

A SPECTROSCOPIC AND CHEMICAL STUDY OF THE COLORATION OF FELDSPARS BY
IRRADIATION AND IMPURITIES, INCLUDING WATER

Thesis by

Anne Marie Hofmeister

In Partial Fulfillment of the Requirements
for the Degree of
Doctor of Philosophy

California Institute of Technology
Pasadena, California

1984

(Submitted September 20, 1983)

ACKNOWLEDGEMENTS

I learned a lot from interacting with my thesis advisor, George Rossman. He originally suggested the project and contributed many valuable ideas along the way. Most importantly, his enthusiasm for scientific research proved to be quite contagious.

The work on amazonite was expedited by E. E. Foord (USGS, Denver). He provided most of the samples and it was his chemical study that prompted this investigation. Discussions with Gene on the geology and chemistry of amazonite pegmatites were extremely helpful. Many others also donated or loaned samples: S. Booth (Zinc Corp. Ltd., Broken Hill, Australia), C.R. Bridges (Bridges Exploration, Ltd., Nairobi Kenya), Gordon Brown (Stanford U.), Rose Cubba, Barclay Kamb, and Sally Rigden (Caltech), Rock H. Currier (Jewel Tunnel Imports, Arcadia, California), Carl Francis (Harvard U.), Subrata Ghose and A. Irving (U. of Washington), E. B. Gray (Z-Gems, Inc., Fallbrook, California), George Harlow and Martin Prinz (American Museum of Natural History), W. F. Larson (Pala International, Fallbrook, California), Roland Reed (El Cajon, California), Robert Reynolds (San Bernardino County Museum, California), Robert Rodgers (Quartzite, Arizona), and J.S. White (Smithsonian Institution, Washington, D.C.). Bob Rodgers gave me a tour of his sunstone claim, and Bob Reynolds showed me the New York Mountains amazonite pegmatite.

Part of the laboratory work was done elsewhere. The EPR and Raman spectroscopies were done using Sunney Chan's facilities in the Caltech Chemistry Division. Craig Martin and Dave Blair taught me how to operate the apparatus and helped me whenever problems arose. The hydrogen manometry was done in Jim O'Neil's laboratory at the USGS Menlo Park facility. Bob Criss taught me how to operate the D/H line and ran the mass spectrometry

analyses for me. IHPV experiments were done in Gordon Brown's laboratory at Stanford under the direction of Mike Hocella. Dave Larsen at JPL arranged for me to use their large irradiator. At Caltech, synthesis and heating experiments were performed in Ed Stolper's laboratory. Julie Paque, Gerry Fine, and Astrid Howard's help with the experiments was invaluable. Magnetic measurements were done in Joe Kirschvink's laboratory.

Special thanks are due to those people who made measurements that I could not do myself: Peter R. Busek (Arizona State University) and Judy Konnert (USGS) did the TEM study of Lake County labradorites, and Bob Criss (USGS, Menlo Park) ran oxygen analyses on similar samples.

Discussions with Professors E. M. Stolper and L. T. Silver greatly helped me progress. I also learned much from talking with Sunney I. Chan (Caltech), Gordon Brown (Stanford), J. R. O'Neil and R. E. Criss (USGS, Menlo Park). My fellow graduate students at Caltech greatly contributed to my growth as a scientist. In particular, many, many thanks go to Stephanie Mattson, Roger Aines, Sally Rigden, Julie Paque, Craig Martin, Cleve Solomon, Henry Shaw, Rose Cubba, Gerry Fine, Terry Smith, and Tom Kuech. Rose and Julie kindly helped type when time was at a premium.

I also wish to thank the technical staff of Caltech for their help. Especially involved were Art Chodos, Martin Ruzek, Randy Heuser, and Vic Nenow. Anne Swatfigure and Betty Johnson worked wonders in turning my scribbling into a nicely typed manuscript.

Much appreciation is due to Professors J'nan Sellery, John Townsend, Robert Wolfe, and Graydon Bell at Harvey Mudd College, and to Lorella Jones and Mike Wortis at University of Illinois for contributing so much to my education in physics and for their concern for my development as a scientist and a person.

This thesis is dedicated to my parents, Delores and Max Hofmeister, and to my sixth grade teacher, James T. Jones, who initially stirred my interest in science.

Financial support for this research was provided by National Science Foundation grants EAR-7919987, EAR-8212540, and EAR-7904801.

ABSTRACT

Spectroscopic techniques allow quantitative measurements of atomic level processes. Of particular interest in mineralogy is application of such methods to determine speciation, site occupancies, ordering, and other physical properties. This thesis presents the results of a spectroscopic (visible, infrared, electron paramagnetic resonance, and resonance Raman), chemical, and experimental investigation on colored and uncolored feldspars. The principal goals were to understand the origin of color and its relationships to other properties of feldspar, and to infer the geologic conditions of color formation. The coloration systems studied include trace amounts of transition metal ions, radiation centers, and inclusions.

Ferrous and ferric iron concentrations in feldspars with low total iron content (<0.32 wt % Fe) were determined from optical and electron paramagnetic resonance (EPR) spectra to better than $\pm 15\%$ of the amount present. Optical spectra indicate that Fe^{2+} occupies two distorted M-sites in plagioclases of intermediate structural state. The linear dependence of the Fe^{2+}/Fe total ratio on An content demonstrates that Fe^{2+} substitutes for Ca. EPR powder spectra show that the number of sites for Fe^{3+} depend on structural state rather than on plagioclase chemistry. The observed linear correspondence of EPR double-integrated intensities with optical peak areas shows that all Fe^{3+} is tetrahedrally coordinated in both plagioclase and disordered potassium feldspar. Microcline perthites show, in addition to tetrahedral Fe^{3+} , an EPR signal due to axially coordinated ferric iron, which is associated with formation of hematite inclusions.

Protons occur as OH^- in plagioclase and sanidine, but as H_2O in microcline. The difference in speciation may be related to temperature of crystallization. Determination of molar absorptivities for IR bands

using H₂O contents from hydrogen manometric measurements, enabled assessment of H₂O contents at the ppm level.

Natural smoky color or smoky color induced by ionizing radiation develops only in potassium feldspars (KAlSi₃O₈) free of water bound in the feldspar structure. Neither fluid inclusion water nor ≡SiOH have an effect. The optical absorption spectra of the smoky color consists of polarized bands at 11600, 16200, 19100, and 27200 cm⁻¹, whose integrated intensities are linearly correlated with the integrated intensity of a broad, asymmetric first derivative at $g_{\text{eff}} = 2.027$ in electron paramagnetic resonance (EPR) spectra. This hole center forms only in KAlSi₃O₈ without structurally bound H₂O, and in microcline is resolved into an asymmetric six-line pattern at $g_{\text{eff}} = 2.024$ and a single derivative at $g_{\text{eff}} = 2.009$ which are Si-O⁻-K and a hole shared between two nonbonding oxygens (NBO) on Si. In analogy to coloring in quartz and glass, the 11600 cm⁻¹ band is caused by a hole trapped between two NBO's on silicon, the 16200 and 27200 cm⁻¹ bands are due to the Si-O⁻-K center, and the 19100 cm⁻¹ band results from a hole trapped on an oxygen attached to two aluminums. Smoky centers do not develop in feldspars with structural water because irradiation mobilizes protons which, while diffusing, destroy centers in their path, and finally then settle in sites similar to their original site. Smoky color also develops in sodic plagioclases, but high Al content inhibits its formation in labradorite.

Amazonite color is intrinsic and controlled by an absorption minimum between three overlapping bands in the ultraviolet and a broad band in β at 630, or one UV band and a broad band in β at 720 nm, or both superimposed. Comparison of EPR to optical integrated intensities shows that all three colors are connected with a first derivative at $g_{\text{eff}} = 1.56$ and two satellites of about 1/7 intensity at g_{eff} of 1.83 and 1.39. Analysis of the EPR

pattern shows that this center is Pb^{3+} 31% of the time, with the hole located on coordinating oxygens for the remaining 69%. This center is only produced in samples which have in addition to Pb, H_2O structurally bound in the lattice. The dependence of color intensity on the smaller molar concentration of structural water or lead implies that lead and structural water in a 1:1 ratio produce color centers in amazonite. The first order reaction kinetics of amazonite color formation by irradiation and the observation that water is not consumed in the process suggests that Pb^{2+} is oxidized to Pb^{3+} by the product OH of the irradiation-induced dissociation of water while H concurrently destroys a hole center on an oxygen, and is followed by the regeneration of the water molecule. The kinetics also show that the radiation necessary for the coloration is provided by internal decay of ^{40}K . The two end-member color types (630 or 720 nm) occur for microcline or orthoclase local structure, respectively. Al/Si disorder increases first locally, and then overall as larger amounts Pb or H_2O are incorporated, so that crystals with intermediate Pb contents have both color types. A spectrally similar blue radiation color also occurs for Pb-bearing sodic plagioclases.

Gemmy labradorite phenocrysts from one Steens Mountain basalt flow in Rabbit Basin, Oregon, sometimes possess a pink schiller, or more rarely a transparent red or green coloration. Direct microprobe analysis of the schiller flakes show that these are metallic copper. XRF analysis of the different colored zones revealed that only the copper content varies with color: colorless samples, or sections of crystals, have 0-35 ppm Cu; greens average 80 ppm Cu; reds average 135 ppm Cu; while schiller bearing labradorites have 50 to 240 ppm Cu. Spectral similarity of the red color to copper-ruby color of glass shows that the red arises from the intrinsic absorption of

colloidal Cu^0 particles that are too small to scatter light (ca. 4 to 22 nm). Spectra from the green regions strongly resemble that of amazonite. Because the temperature of exsolution is subsolidus and proportional to Cu content, diffusion proceeds more rapidly for crystals with higher Cu content and results in formation of larger particles. The Cu^0 reduction at low temperature (800°C) involves formation of hole center (O^-) that is captured by Pb^{2+} to form the green amazonite color (Pb^{3+}). At high temperatures (~ 900 to 1100°C) the reduction of Cu is controlled by whatever reactions occur in the basalt to keep $f\text{O}_2$ along the QFM buffer. Migration of Cu^0 may cause the variation of Cu concentrations in a single sample; but the variation of Cu content among different crystals suggests that the composition of the megacrysts was not constant and changed in response to an increasing copper content in the melt as crystallization of the labradorite proceeded.

The coloration process in feldspar strongly resembles that in glasses for both radiation colors (smoky) and exsolution phenomena (Cu^0 colloids, Cu^0 schiller) and also that of radiation colors in other crystalline solids (smoky quartz, Pb^{3+} or Tl^{2+} in KCl). Although quartz and glass are structurally and chemically similar to feldspar, KCl is not, suggesting that for the most part it is the behavior of the chemical impurity on an atomic level which controls the coloring mechanism.

TABLE OF CONTENTS

	Page
1 INTRODUCTION	1
1.1 Object of the Research	1
1.2 Previous Work	4
a. Color in feldspar: general statement	4
i. Colorless feldspar	5
ii. Feldspar colored yellow by iron impurities	5
iii. Feldspar colored smoky by irradiation	22
iv. Amazonite: feldspar colored blue-green by irradiation	24
v. Blue plagioclase	36
vi. EPR of irradiation centers in feldspar	38
vii. Inclusion colors: general statement	39
Red schiller and red clouded feldspars	39
Black clouded feldspars	42
viii. Sunstones from Lake County, Oregon	43
b. Similar colors in other materials	46
i. Visible and EPR spectroscopy of Cu^{2+}	47
ii. Noble metal colloids in glass	51
iii. Irradiation colors in glass	65
iv. Smoky quartz	71
v. Pb absorptions and EPR of Pb in crystalline solids	75
vi. Blue barite and celestite	88
vii. Effect of proton species on radiation response	90
c. Water in feldspar	99
d. Geology and genesis of amazonite pegmatites	102
e. Geology and geochemistry of Steens Mountain basalts	103
2 METHODS	108
2.1 Spectroscopy	108
a. Visible and near infrared spectroscopy	108
b. Infrared spectroscopy	109
c. Electron paramagnetic resonance (EPR) spectroscopy	110
d. Resonance Raman spectroscopy	110
e. Thermoluminescence	111
2.2 Chemical Analysis	111
a. Electron-microprobe	111
b. X-ray Fluorescence	111
c. Hydrogen manometry	122
d. Thermoanalysis	122
2.3 Synthesis and Heating Experiments	123
a. High pressure synthesis	123
b. Fugacity controlled, atmospheric pressure experiments	123
c. Dehydration and diffusion experiments	124
2.4 Irradiation Experiments	124
a. Artificial irradiation	124
b. Measurement of natural radioactivity	125

3	CONCENTRATION, CHARGE STATE, AND SITE OCCUPANCY OF IRON IN FELDSPAR	126
3.1	Sample Description and Chemistry	126
3.2	Optical Spectroscopy of Fe ²⁺ in Plagioclase	126
3.3	Optical Spectroscopy of Fe ³⁺ in Feldspar	137
a.	Orthoclase and sanidine	137
b.	Andesine and labradorite	137
3.4	EPR spectroscopy of Fe ³⁺	149
3.5	Variation of Fe ²⁺ and Fe ³⁺ Concentrations in Feldspar	163
3.6	Conclusions and Comparison of the Two Spectroscopic Methods	165
4	SPECIATION AND CONCENTRATION OF WATER AND OH IN VARIOUS FELDSPARS	168
4.1	General Statement	168
4.2	Total H ₂ O Concentrations Determined by Hydrogen Manometry	168
4.3	Speciation of "Water" in Feldspar	170
a.	Sanidine: mostly OH	171
b.	Orthoclase: nearly dry	175
c.	Labradorite, andesine, and blue oligoclase: mostly OH	178
d.	Colorless to white microcline: structurally bound H ₂ O	183
e.	Blue-green microcline: mostly fluid inclusion water with some structurally bound water	188
5	SMOKY FELDSPAR: IRRADIATIVE COLORING OF STRUCTURALLY ANHYDROUS FELDSPAR	198
5.1	Sample Description, Chemistry, and Response to Irradiation	198
5.2	Water Speciation Accompanying Smoky Color Formation and Inhibition	201
5.3	Visible and Near-Infrared Absorption by Color Centers in Feldspar	202
5.4	Calculation of Time Necessary for Natural Sanidine Coloration	210
5.5	EPR Spectroscopy of Radiation Centers Near $g_{\text{eff}} = 2$ in Feldspar	215
a.	Description of centers connected with smoky color	215
b.	Correlation of EPR and optical spectra	221
c.	Radiation centers not directly correlated with color	225
5.6	Comparison of Radiation Coloring of Plagioclase to Potassium Feldspar	226
5.7	Proposal of Models for Smoky Feldspar from Comparison with Smoky Quartz and Glass	229
a.	Optical and EPR spectroscopy	229
b.	Effect of proton species on radiation response in feldspar glass, and quartz	232
6	AMAZONITE: IRRADIATIVE COLORING OF STRUCTURALLY HYDROUS, Pb BEARING FELDSPAR	235
6.1	Geologic Occurrence	235
6.2	Chemistry of Samples Studied	237
6.3	Visible Spectroscopy of Amazonite	241
a.	Variation of color in natural samples	241
b.	The effect of radiation on color	253
c.	Spectroscopy of selected samples at liquid nitrogen	261

	temperatures	
	d. Relationship of amazonite color to lead and iron contents	268
6.4	Evidence for Self-Coloration by ^{40}K Decay	273
6.5	Thermoluminescence	278
6.6	EPR Spectroscopy of Centers Associated with Amazonite Color	281
	a. Correlation of EPR with optical results	281
	b. Analysis of EPR signal: Pb^{3+}	287
6.7	Resonance Raman Spectroscopy of Amazonite	289
6.8	The Relationship of Color to Structural Water and Pb Concentrations	294
	a. General statement on response of color to heating and irradiation	294
	b. Dependence of color in a single sample on structural water concentration	294
	c. Evidence for $\text{Pb}:\text{H}_2\text{O} = 1:1$ in color center formation	299
	d. Calculation of Pb^{3+} extinction coefficients and comparison of amazonite color center to Pb^{3+} and Tl^{2+} in KCl	304
6.9	Interrelationships of Al/Si Order/Disorder with Incorporation of Pb and Structural Water in Amazonite	305
6.10	Evidence for Amazonite Coloration of Sodic Plagioclase	312
6.11	Attempts to Synthesis Amazonite	316
6.12	A Model for the Mechanism of Amazonite Coloration	320
7	COLORATION OF LAKE COUNTY LABRADORITE BY EXSOLUTION OF METALLIC COPPER	323
	7.1 Geologic Occurrence	323
	7.2 Description of Colors and Schiller	324
	7.3 Chemistry of the Schiller and the Colored Zones	325
	7.4 Oxygen Isotope Variations Among the Colored Zones	332
	7.5 EPR Spectroscopy	333
	7.6 Magnetic Measurements on the Colored Zones	334
	7.7 Visible Spectroscopy of Lake County Labradorite	336
	a. Characteristics of the colored zones	336
	b. Comparison of red and green colors to transition metal colors	341
	c. Comparison of the green color to amazonite	345
	d. Comparison of the red color to copper-ruby color in glass	348
	7.8 TEM Observations on Red and Green Colored Labradorite	350
	7.9 Dependence of Color and Schiller on Temperature and Oxygen Fugacity	350
	7.10 A Model for the Coloring Mechanism and Exsolution Process in Lake County Labradorite	354
	7.11 Implications of Coloration on Geological Conditions of Formation	358
8	SUMMARY AND CONCLUSIONS	363
	REFERENCES	371
	APPENDIX I Derivation of EPR Parameters for Pb^{3+} in Amazonite	390
	APPENDIX II Blue and Red-Brown Radiation Colors in Barite and Celestite	393
	APPENDIX III Recommendations for Future Studies	405

Figures	page
1.1 Unpolarized absorption spectrum of Itrongay orthoclase from Faye, [1969]	6
1.2 Energy level diagram for a d^5 ion in a tetrahedral site after Manning [1970]	9
1.3 Polarized visible spectra of Itrongay orthoclase from Veremeichik et al [1975]	10
1.4 Single crystal EPR spectra of Fe^{3+} in potassium feldspar	15
1.5 Polarized visible spectra of Lake County labradorite after Bell and Mao [1972]	16
1.6 The linear relation of absorptivity at 1250 nm with iron content after Bell and Mao [1973]	17
1.7 Mossbauer resonance absorption spectra of Fe^{2+} in plagioclase of Apollo 11 after Hafner [1975]	20
1.8 Angular variation of EPR Fe^{3+} spectra in bytownite from Crystal Bay, Minnesota after Scala et al [1978]	23
1.9 Reflectance spectra of blue-green feldspar after Rudenko and Vokhmentsev [1969]	32
1.10 Reflected intensity vs Pb content of amazonites after Zhirov and Stishov [1965]	33
1.11 Amazonite reflectance spectra from Plyusnin [1969]	34
1.12 Relationships of amazonite color to lead and volatile content after Plyusnin [1969]	35
1.13 UV absorption spectra of amazonite after Tarashchan et al [1973]	37
1.14 Cu^{2+} optical absorption spectra in glass after Wong and Angell [1976]	48
1.15 Cu^{2+} optical absorption spectrum in Egyptian blue after Clark and Burns [1967]	49
1.16 Cu^{2+} optical absorption spectrum in $CuAl_2O_4$ after Reed [1974]	50
1.17 EPR spectrum of Cu^{2+} in MgO after Orton et al [1970]	52
1.18 EPR spectrum of Cu^{2+} in $Cu(CH_3COCHCOCH_3)_2$ after Goodman and Raynor [1970]	53
1.19 Visible spectra of gold ruby glass after Williams et al [1981]	57
1.20 Cartoon of the cooling history of copper-ruby glass	63
1.21 Radiation defects in silicate glasses after Griscom [1973]	66
1.22 EPR spectra of H_I and H_{II} centers after Kordas and Oel [1982] and Scheurs [1967]	69
1.23 EPR spectra of $Al-O^-$ hole centers in Smoky quartz after Mackey [1963]	72
1.24 Smoky quartz optical spectrum after Nassau and Prescott [1977]	74
1.25 EPR spectra of Pb^{3+} in KCl after Schoemaker and Kolopus [1970]	78
1.26 Breit-Rabi diagram for Pb^{3+} in ThO_2 after Rohrig and Schneider [1969]	79
1.27 Energy level diagrams for Pb and Tl	82
1.28 Visible spectra of Pb^{3+} in KCl after Schoemaker and Kolopus [1970]	84
1.29 Optical absorption spectra of Tl^0 and Tl^{2+} in KCl after Delbecq et al [1966]	85
1.30 Molecular orbital configurations for Pb^{3+} or Tl^+ after Delbecq et al [1966]	87
1.31 Optical spectra of blue celestite after Bernstein [1979]	89
1.32 Infrared spectra of protons in feldspar after Wilkens and Sabine [1973]	101

1.33	Variation of elements and oxides in Steens Mt. basalts after Gunn and Watkins [1970]	107
2.1	Calibration curves for determination of transition metal oxide concentration from XRF spectra	115
2.2	Comparison of XRF and microprobe analyses for Fe in feldspar	121
3.1	Near-IR absorption spectra of Halloran Springs andesine	129
3.2	Absorption spectra of Serra de Mage anorthite	130
3.3	Near-IR absorption spectra of Lake County labradorite	131
3.4	Gaussian deconvolution of near-IR Lake County labradorite spectra	133
3.5	Gaussian deconvolution of near-IR Halloran Springs andesine spectra	134
3.6	Absorption spectra of Eifel, Germany sanidine	138
3.7	Absorption spectra of Itrongay, Madagascar orthoclase	139
3.8	Gaussian deconvolution of Eifel sanidine spectra	141
3.9	Absorptivity vs FeO content for orthoclase and sanidine	143-144
3.10	Integrated intensity vs FeO content for orthoclase and sanidine	145-146
3.11	Visible spectra of Halloran Springs andesine	147
3.12	Visible spectra of Lake County labradorite	148
3.13	Gaussian deconvolution of visible spectra of Halloran Springs andesine	150
3.14	EPR spectra of potassium feldspars	152
3.15	EPR spectra of microcline-perthites	154-155
3.16	EPR spectra of plagioclase	157
3.17	Numerical integration of EPR Fe ³⁺ spectra	158
3.18	Correlation of EPR integrated intensities calculated by computation and by eq. 2-1	160
3.19	Comparison of integrated intensities for optical and EPR spectra of Fe ³⁺	161
3.20	Dependence of EPR integrated intensity on total iron content	162
3.21	Dependence of Fe ²⁺ /Fe, Fe ³⁺ /Fe and Fe ²⁺ /Fe ³⁺ on An content	164
4.1	Infrared absorptions of OH ⁻ in Eifel sanidine	172
4.2	Near-IR absorption spectra of OH ⁻ in Eifel sanidine	173
4.3	IR spectra of OH ⁻ in Eifel sanidine at liquid nitrogen temperature	176
4.4	IR spectra of Itrongay orthoclase	177
4.5	IR spectra of Lake County labradorite	179
4.6	IR spectra of Lake County labradorite cooled with liquid nitrogen	180
4.7	IR spectra of South Carolina oligoclase at room and liquid nitrogen temperatures	182
4.8	IR and near-IR spectra of H ₂ O in Elizabeth R mine microcline	184
4.9	Correlation of peak intensity between fundamental and overtone modes of water	186
4.10	Dependence of peak intensity in white microcline on total water content	189
4.11	Polarized IR spectra of water in amazonite #19'	190
4.12	Polarized IR spectra of amazonite #5 from Lake George, Colorado	192
4.13	Polarized IR spectra of gemmy green orthoclase #3 from Australia	193
4.14	Polarized IR spectra of OH and H ₂ O in amazonite #6 from Keivy pegmatite, USSR	195
4.15	IR spectra of (NH ₄) ⁺ in Buddingtonite and Amelia, Virginia microcline	196

5.1	Visible absorption spectra of natural and irradiated smoky sanidine	203
5.2	Gaussian deconvolution of sanidine given 0.176 MRads	204-205
5.3	Gaussian deconvolution of irradiated Itrongay orthoclase	206-207
5.4	Visible absorption spectra of irradiated and sun bleached Itrongay orthoclase	208
5.5	Integrated intensity as a function of radiation dose	211-212
5.6	Band area at 7300 cm^{-1} as a function of iron content	213
5.7	EPR spectra of the $g = 2$ region for feldspars other than amazonite	216-220
5.8	Dependence of EPR integrated intensity on dose	223
5.9	Optical integrated intensities of smoky color as a function of EPR integrated intensity of the H center	224
5.10	Absorption spectra of andesine turned smoky by irradiation	227
5.11	Comparison of labradorite spectra before and after irradiation	228
6.1	Polarized absorption spectra of naturally blue, type B amazonite #5	243
6.2	Polarized absorption spectra of naturally green, type G amazonite #3	244
6.3	Polarized absorption spectra of natural, medium green, amazonite #19'	245
6.4	Polarized absorption spectra of natural, medium green, amazonite #32	246
6.5	Polarized absorption spectra of natural, blue-green, type T amazonite #21	247
6.6	Comparison of integrated intensities between the alpha and beta polarizations of amazonites	252
6.7	Comparison of integrated intensities of the UV peaks to that of the sum of the 630 and 720 nm peaks	254
6.8	Visible spectra of the beta polarization of amazonite #19', taken at progressively higher radiation doses	256
6.9	Visible spectra from the beta polarization of amazonite #23 for natural and irradiated samples	258
6.10	Intensity of amazonite color in the 630 to 720 nm region as a function of cumulative radiation dose	260
6.11	Logarithmic plot of $1 - \alpha/\alpha_{\text{max}}$ as a function of cumulative radiation dose	262
6.12	Comparison of visible absorption spectra of a blue amazonite at room and liquid nitrogen temperatures	263
6.13	Comparison of visible absorption spectra in beta of a green amazonite at room and liquid nitrogen temperatures	264
6.14	Comparison of beta polarization for visible absorption spectra of amazonite #21 at room and liquid nitrogen temperatures	263
6.15	Comparison of room and liquid nitrogen temperature absorption spectra in the beta polarization of amazonite #6	264
6.16	Comparison of integrated intensity for chilled and room temperature measurement of amazonites	265
6.17	Dependence of the position of the amazonite peak in the visible region on lead content of natural amazonites	270
6.18	Dependence of the position of the absorption in the visible region on lead content of irradiated amazonites	271
6.19	Dependence of the full width at half height of the visible peak on lead content of natural amazonites	272
6.20	Energy level diagrams for the four types of amazonite spectra	274

6.21	Integrated intensity of the visible absorption in the beta polarization of amazonite as a function of lead content for naturally occurring color	275
6.22	Expanded view of Figure 6.21 in the low lead region	276
6.23	Glow curves for amazonite and other potassium feldspars	279
6.24	First derivative EPR powder spectra of amazonite #12	282
6.25	First derivative EPR powder spectra of 3 amazonite-microclines	283
6.26	Dependence of EPR integrated intensity on integrated intensity of absorption bands in amazonite	286
6.27	Raman spectra of 3 microclines and synthetic $PbAl_2Si_2O_8$	291
6.28	Raman spectra of 3 orthoclases and synthetic $PbAl_2Si_2O_8$	293
6.29	Variation of color with water species in amazonite-orthoclase	298
6.30	Variation of color with structural water by dehydration of amazonite #12	300
6.31	Dependence of color on structural water concentration for dehydrated orthoclase #3"	301
6.32	Dependence of amazonite color on structural water content	302
6.33	Infrared powder absorption spectra of amazonites	306
6.34	Relation between two IR wavelengths in potassium feldspar	308
6.35	Order parameter d/m as a function of water concentration	309
6.36	Order parameter d/m as a function of lead content of amazonites	310
6.37	Absorption spectra of blue sodic plagioclases	313
6.38	Polarized visible spectra of gemmy oligoclase from S. Carolina	315
6.39	Visible spectra of natural, irradiated, and sun-bleached oligoclase	317
6.40	Summary of model for amazonite coloration by irradiation	315
7.1	Dependence of microprobe total and feldspar's An content on copper concentration	328
7.2	Polarized absorption spectra of the red area of Lake County labradorite #200	337
7.3	Polarized absorption spectra of the green area of Lake County labradorite #300	338
7.4	Absorption spectra of α from the four zones of Lake County labradorite #400	339
7.5	Absorption spectra of β from the four zones of labradorite #400	340
7.6	Comparison of alpha spectra at 24°C and -190°C for the red and green colors of Lake County labradorite	342
7.7	Comparison of green labradorite with amazonites	346
7.8	Copper ruby glass and red labradorite visible spectra	349
7.9	Partial phase diagram for Cu^0 and plagioclase	352
7.10	Unpolarized absorption spectra of red labradorite before and after heating	353
7.11	Relationship of Fe, Mn, and Cu trends in the Steens Mountain basalts to Lake County labradorite chemistry	359
7.12	Relationship of MgO , TiO_2 , and Sr trends in Steens Mountain basalts to Lake County labradorite chemistry	360
II.1	Visible absorption spectra of naturally blue barite from Sterling, Colorado	395
II.2	Absorption spectra of the red-brown irradiation color in barite	396
II.3	Dependence of absorption band intensity in barite on dose	397
II.4	EPR powder spectrum of blue barite from Sterling, Colorado	399
II.5	Infrared absorption spectra of the water region of barite from Sterling, Colorado, and blue celestite from Wayne Co., Utah	401-402
II.6	Relationships of blue color in sulfates to IR bands	403

TABLES	Page
1.1 Band positions of tetrahedral Fe ³⁺ in feldspar	8
1.2 Mossbauer parameters of iron in feldspar at liquid nitrogen temperature	11
1.3 EPR parameters of Fe ³⁺ in feldspar	12-13
1.4 Emission excitation energies in cm ⁻¹ of feldspar at room temperature after Telfer and Walker [1978]	19
1.5 Amazonites from Mozambique Pegmatites after Nunes [1974]	27
1.6 Amazonite structural state and Pb content	29
1.7 Analyses of labradorite from Lake Co., Oregon and Crater Elegante, Sonora, Mexico	45
1.8 Conditions for copper-ruby formation after Dietzel [1945]	60
1.9 Noble metal oxygen fugacity transitions in borax glass after Dietzel [1945]	60
1.10 EPR data on Pb ³⁺ in crystalline solids	76-77
1.11 Electronic transitions of Pb and Tl at 77°K	83
2.1 Chemistry of standards made from common colorless Lake County labradorite and oxide powders	113
3.1 Sample description and chemistry of feldspars	127
3.2 Microprobe analysis of selected feldspars	128
3.3 Optical fit parameters of Fe ²⁺ in plagioclase for 1.00 cm thick crystals	135
3.4 Optical spectroscopy parameters of Fe ³⁺ in feldspar	142
3.5 Iron concentrations in feldspar determined by spectroscopy	151
4.1 Total water concentrations on feldspar	169
4.2 Absorption coefficients in Eifel sanidine in cm ⁻¹	174
4.3 Absorptivities of structural water in microcline	185
4.4 Fluid inclusion molar absorptivity in amazonite for alpha or beta on (010)	185
5.1 Sample description, chemistry, and EPR intensities of smoky feldspar	199-200
5.2 Peak parameters used in gaussian fitting of smoky color in feldspar	209
5.3 Integrated intensities of smoky and related bands	209
5.4 EPR parameters for the g = 2 region of amazonite #21, Keivy Pegmatite, USSR	222
5.5 Comparison of color center characteristics of glass, smoky quartz and smoky feldspar	230
6.1 Description and chemistry of blue microcline	238
6.2 Description and chemistry of blue-green microcline	239
6.3 Description and chemistry of green orthoclase, bluish plagioclase and synthetics	240
6.4 X-ray powder data for lead feldspars	242
6.5 Optical parameters of natural amazonites	250
6.6 Optical parameters of the visible peak of natural and irradiated amazonites, 1 cm thickness	255
6.7 Irradiation response of 625 to 720 nm band at selected amazonites	259
6.8 Dependence of amazonite color properties on temperature	267
6.9 Thermoluminescence data for 5.87°C/minute scans	280
6.10 EPR parameters for amazonite signal	285
6.11 Correlation of amazonite resonances with Pb-spar Raman bands	292
6.12 Dehydration and decoloration of amazonite	296

6.13	Infrared water absorptivities, derived water contents, and infrared lattice parameters of amazonites	297
6.14	High pressure synthesis attempts	319
7.1	Microprobe analysis of shiller in Lake County labradorite	327
7.2	Microprobe analysis of labradorite and red glasses	330
7.3	X-ray fluorescence data on labradorite in ppm	331
7.4	Oxygen isotopic measurements of labradorite	332
7.5	EPR intensities for colored labradorites	333
7.6	Magnetic measurements of feldspars	335
7.7	Comparison of known molar absorptivities to those calculated for labradorite	344
7.8	A model for coloration of Lake County labradorite	387
II.1	Sample description and chemistry of barite	394
II.2	Response of blue barite to heating and irradiation	404

1.1 Object of the Research

This thesis presents considerable new data on the origin and mechanism of coloration in feldspar, which involves not only incorporation of trace amounts of metals and water species, but also radiation, exsolution and ordering processes. Colors in crystalline solids and glasses have been the focus of considerable scientific interest partially due to their visual appeal, but moreover because understanding of these phenomena allows insight into atomic-level processes. Naturally occurring colored minerals and gems have an economic value depending on the scarcity and on the beauty of the material and its color. Hence, intense efforts have been made to develop rare colors from common ones, and also to distinguish natural from treated minerals.

The dependence of radiation colors on the presence of chemical impurities was probably first recognized by Goldstein [1902]. Siedentopf [1905] realized that natural coloration of halite was caused by radioactivity and also noted that atoms and colloids (inclusions) give two distinct types of color. The early observations were based on qualitative visual assessment; development of absorption spectral techniques [Roentgen, 1927] marked the transition to modern quantitative studies. Smekal [1928] first recognized the strong influence of crystalline structure on coloration, and Bethe's [1929] development of crystal field theory provided the basis for interpreting spectra directly in terms of electronic transitions of metal ions. Despite these and the more recent developments, even today the specific cause of coloration in many minerals is unknown

[Nassau, 1978].

For feldspar, partial answers exist for many distinct colorations. The yellow color of gemmy crystals is derived from iron substitution [Faust, 1936; Faye, 1969]. Smoky colors are connected with radiation-created aluminum hole centers [Speit and Lehmann, 1976]. The schiller in Lake County labradorite is due to copper-metal inclusions [Andersen, 1917]. Studies of amazonite chemistry by Foord and Martin [1979] strongly suggest that lead is involved in the blue-green color. Yet, major unresolved problems include (1) the coordination of Fe^{+2} , (2) the infrequency of the smoky color, (3) the origin of the copper flakes, and (4) how ordinary uncolored lead can be made to produce color.

The goal of the present investigation was to apply precise spectroscopic techniques (visible, infrared, electron spin resonance, and resonance Raman), chemical analyses of impurities, radiation and heat treatment and forced diffusion to various colored and uncolored feldspars in order to determine the coloration mechanisms and their relationship to other properties of feldspar. It was hoped that a thorough spectroscopic and chemical study, together with supportive experimentation on the feldspars would produce results that could help address the following problems:

- (a) The species, charge state, and site occupancy of the ion(s) responsible for the blue-green color of amazonite and also for the green and red colors of Lake County labradorite.
- (b) The interrelationships of the colors (red, green, and schiller) in Lake County labradorite; and the cause of the zonations both in the feldspars and of the feldspars within the basalts.
- (c) The response of feldspar to radiation.

for the color developed.

- (e) The mechanism and kinetics of coloration in feldspar.
- (f) The physical and geological conditions necessary to produce color (e.g. temperature, fO_2 , irradiative flux).

Considerable progress has been made on all of the above problems. In addition, this work has provided new information on the following:

- (g) Quantitative determination of ferrous and ferric iron concentrations from spectral parameters.
- (h) Quantitative determination of the concentrations of various water species at the ppm level.
- (i) The discovery of a relationship between the speciation of water in feldspar and the mineral's response to irradiation.
- (j) The effect of lead's incorporation on the structural state of the potassium feldspar.
- (k) The stability of Pb^{+3} in the feldspar M-site.
- (l) The process of exsolving copper metal ions from the plagioclase lattice.

Besides providing new spectral and chemical data on feldspar, this thesis attempts to utilize these data towards understanding the physical properties of this mineral. The following discussion therefore concerns a variety of mineralogical problems associated with feldspar, beginning with quantitative determination of Fe^{+2} , Fe^{+3} , and water in the feldspar, continuing with the response of feldspar to irradiation (smoky colors and amazonite) and to exsolving copper metal (Lake County labradorite), and concluding with the mineralogical and chemical implications of the coloring mechanisms as well as the inferred geological conditions of formation. In order to place these data in the proper context, the rest of this chapter will review (1) previous

investigations of the spectral properties, chemistry, and geology of colored feldspars, (2) the spectral properties of similarly colored materials; and (3) preceding work that bears on the related problems of irradiative coloring of solids, the effect of hydrogen species on this process, spectroscopy of lead and copper, and colloidal coloration by metals.

1.2 Previous Work

1.2.a Color in feldspar: general statement

Pure feldspar, free of exsolution and chemical impurities, is colorless. However, minor chemical substituents, inclusions, interference effects from exsolution lamellae, and radiation damage can produce color in the mineral. This section describes previous work on the colored varieties of feldspar, their absorption spectra, and coloration mechanisms. Topics covered include chemical, radiation, and exsolution colors. In particular, chemical impurities produce the yellow color of sanidine, orthoclase and calcic plagioclase. Radiation produces gray or smoky color, or the blue to green color of amazonite and the blue-green color of sodic plagioclase, if the requisite chemical impurities are present. Inclusions create a wide variety of colors: most commonly, pink, brick-red, and grays; but orange, tan and green may also occur. Lastly, aventurine and schiller effects result from inclusions.

This section will not cover exsolution phenomena which can produce a wide range of colors, schiller and chatoyancy. Nor will it concern labradorescence and moonstone effects, which are produced by interference. The interested reader may refer to Ribbe [1975] or Smith [1974, Ch.8].

1.2.a.i. Colorless feldspar

When free of minor substituents and exsolution, feldspar does not absorb light in the visible portion of the spectrum and is, therefore, colorless. The onset of absorption in the ultraviolet region at ~ 320 nm, caused by oxygen to cation charge transfer, is common to many minerals and is most likely due to trace amounts of Fe^{3+} in feldspar [e.g. Faye, 1969]. Absorption in the infrared has been observed in the $3600\text{--}3300\text{ cm}^{-1}$ (3000 nm) region as a result of minor amounts of water in the feldspar [Wilkins and Sabine, 1973; Solomon and Rossman, in prep.]. At longer wavelengths absorption from vibrational motions of the aluminosilicate framework occurs [e.g. Smith, 1974, Sec. 11.2].

1.2.a.ii. Feldspar colored yellow by iron substitution

Iron substitution produces yellow color in sanidine, orthoclase and calcic plagioclase. In the potassium feldspars substitution is accompanied by a reduction of the aluminum content indicating that the iron enters the tetrahedral sites as Fe^{3+} [e.g. Niggli, 1914; Faust, 1936]. Synthesis of amber-yellow KFeSi_3O_8 confirms this substitution [Faust, 1936]. The most outstanding natural examples of iron substitution are sanidine from the Leucite Hills, Wyoming, which contains up to 18% of the KFeSi_3O_8 molecule [Carmichael, 1967], and homogeneous lemon-yellow megacrysts from Itrongay, Madagascar which have up to 12% KFeSi_3O_8 [Coombes, 1954]. Faust [1936] noted that the yellow color of the orthoclase was derived from a general absorption of light at the blue end of the spectrum and ascribed this to large amounts of Fe^{3+} . Faye [1969] correctly attributed the yellow color to strong absorption bands at 417 and 442 nm shown in the unpolarized absorption spectrum of Figure 1.1. Manning's [1970]

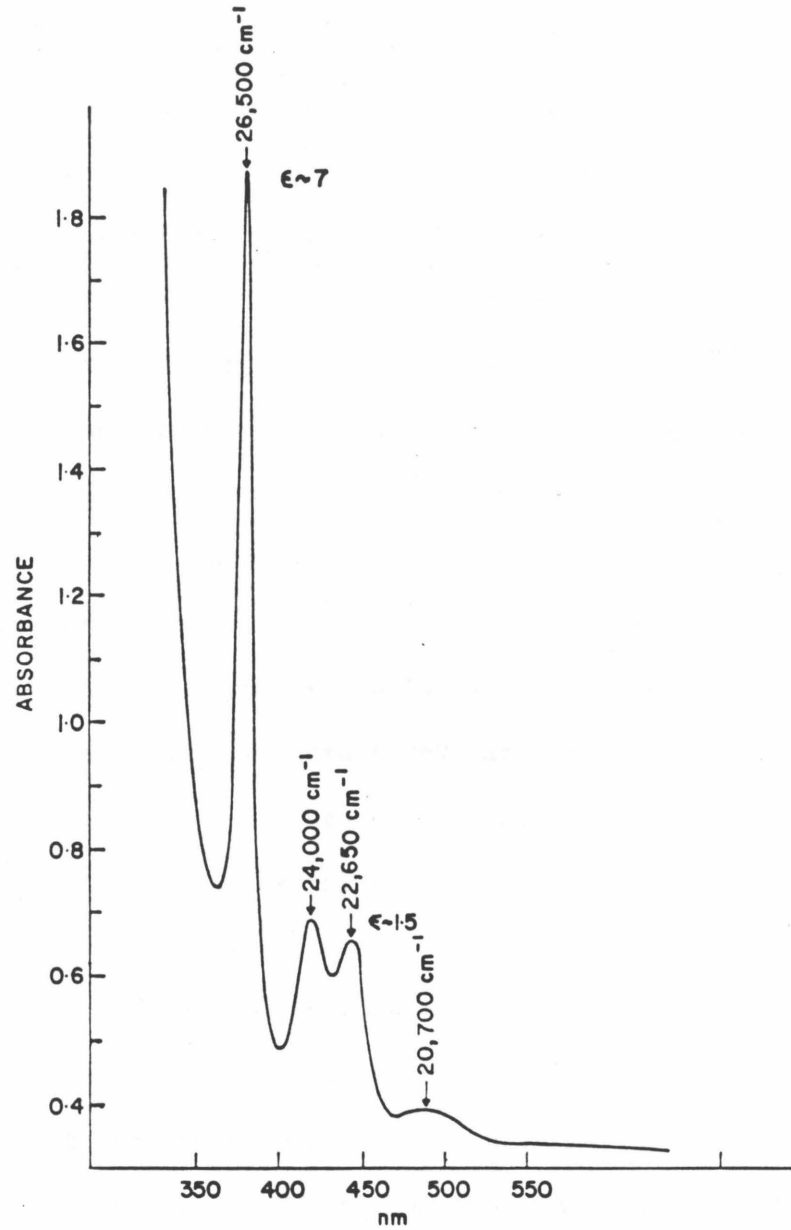


Figure 1.1 Unpolarized absorption spectrum of Itrongay orthoclase, 3.7 mm thick. From Faye [1969].

assignments of the Itrongay orthoclase's bands to d^5 transitions are given in Table 1.1 and depicted on the energy level diagram (Fig. 1.2). Manning [1970] interpreted the increase in extinction coefficient ϵ with increasing energy as proof that the d-d bands borrow intensity from the $O^{2-}-Fe^{+3}$ charge transfer band in the ultraviolet. Veremeichik, et al, [1975] published the alpha and gamma polarizations. Figure 1.3 shows that there is little difference between the spectra and hence no anisotropy apparent to the eye. Except for the weak band at 21000 cm^{-1} , all the absorption bands in the spectrum arise from iron in the tetrahedral site. Veremechik et al [1975] attribute this weak band to Fe^{+3} in hematite inclusions.

Brown and Pritchard [1969] investigated the state of iron in Itrongay orthoclase through Mössbauer spectroscopy. A weak absorption indicates that ferrous iron is present, but at a concentration too low for quantitative analysis. Brown and Pritchard [1969] attribute the strong absorption to Fe^{+3} in distorted tetrahedral sites even though the spectral parameters (Table 1.2) are similar to octahedral Fe^{+3} in other silicates. They attribute this discrepancy to a large amount of covalency for ferric iron in orthoclase and conclude that "Mössbauer spectra alone do not provide a wholly reliable guide to the coordination number of ferric iron in a mineral."

Trivalent iron in K-spar has also been investigated by using electron paramagnetic resonance (EPR) techniques. A summary of the EPR data is given in Table 1.3. Hochli's [1966] data on microcline is consistent with Fe^{+3} replacing Al^{+3} , such that the iron is located in a single site. The broad line width indicates some structural variation of the site [Low, 1968]. Subsequent study of microcline by Marfunin et al [1967] confirmed Hochli's results and also revealed that Itrongay orthoclase has Fe^{+3} in two tetrahedral sites. Marfunin et al [1967] claimed that the site is $T_1(0)$,

Table 1.1 Band positions of tetrahedral Fe⁺³ in feldspar

Itrongay Orthoclase				Lake County Labradorite	
ν (cm ⁻¹)	ϵ †	ν (cm ⁻¹)	Assignment	ν (cm ⁻¹)	ϵ/ϵ_0
Faye, 1969		Veremeichik et al, 1975	Manning, 1970	Bell and Mao, 1972	
26500	7	26300	⁶ A ₁ (S) → ⁴ E(D)	26000	10
24000	1.5	24260	→ ⁴ T ₂ (D)	24000	2
22650	1.5	22720	→ ⁴ A, ⁴ E(G)	22000	1
20700	0.2	20400	→ ⁴ T ₂ (G)	ND	
19000*	weak	17860 16000	→ ⁴ T ₁ (G)	ND	

† ϵ is approximate, units are liter-mole/cm

*approximate peak position from Manning, 1970

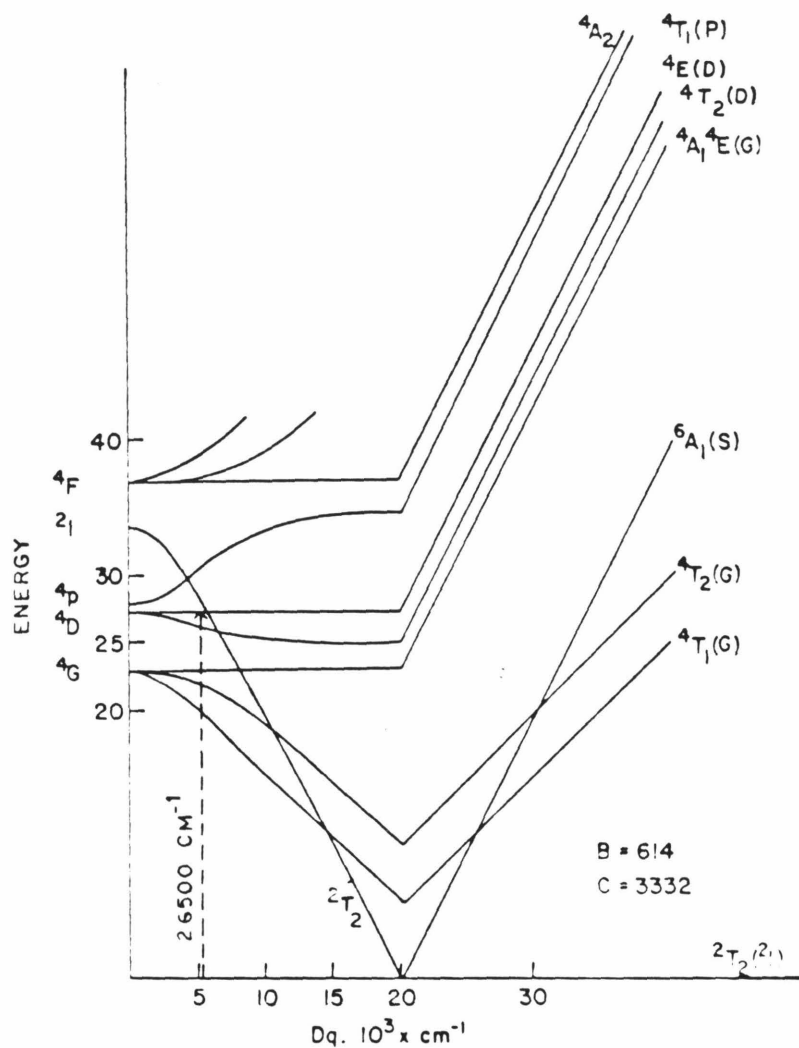


Figure 1.2 Energy level diagram for a d^5 ion in a tetrahedral site. From Manning [1970]. The dotted line indicates the most intense (and highest energy) transition of Fe^{+3} in Itrongay orthoclase.

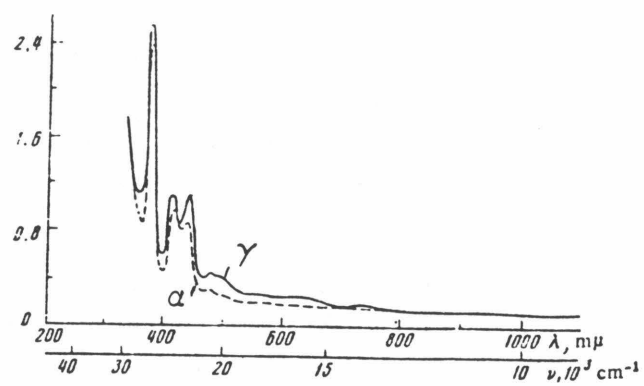


Figure 1.3 The alpha (dashed line) and gamma (solid line) polarizations of Itrongay orthoclase, thickness unknown. From Veremeichik et al. [1975].

Table 1.2 Mössbauer parameters of iron in feldspar at liquid nitrogen temperature

Mineral	Species	Intensity (relative)	Isomer shift (mm/sec)	Quadrupole splitting (mm/sec)	Linewidth at half height (mm/sec)	Reference
Itrongay Orthoclase	Fe ⁺² M-site	1	1.5	2.8	NM	Brown and Pitchard, 1968
"	Fe ⁺³ tet.	9	0.72	0.68	0.65	"
Stillwater Bytownite	Fe ⁺² M-site	-	1.26	2.78	0.39	Schurman and Hafner, 1972
Lunar Anorthite	Fe ⁺² M-site	1	1.40	2.74	0.33	Hafner et al, 1971
"	Fe ⁺³ defects	5	1.10	2.12	0.65	"

Table 1.3 ESR parameters of Fe⁺³ in feldspar

Mineral	Reference	Method	g	g_{eff} of $\pm 3/2$	line width (gauss)	# sites	type
Microcline	Hochli, 1966	Single Xtl 9.9 GHz	2.00			1	tetrahedral
Microcline Khibiv Massif	Marfunin et al 1966	Single Xtl 35 + 9.5 GHz	2.00		20-80	1	tetrahedral
Orthoclase Itrongay	"	"	2.00,2.00,2.05		100-350	2	tetrahedral
Max.Micro. Ukraine	Gaite & Michoulier 1970	Single Xtl 35 Ghz	1.995,2.002,2.002			1	tetrahedral
Microperthite Norway	"	"	2.003,2.003,2.002			1	tetrahedral
Oligoclase An ₂₀ North Karelia	"	"	2.003			1	T ₁ (0)
Oligoclase An ₁₅ Odeganm, Norway	"	"	~ 2 & anisotropic			3	tetrahedral
Labradorite An ₆₈ Lake Co.,Oregon	"	"	"			"	"
Bytownite An ₇₃ Pigeon Pt., OR	"	"	"			"	"
Anorthite An ₁₀₀	"	"	"			"	"
Oligoclase North Karelia	Marfunin et al 1966	Single Xtl 35 + 9.5 GHz	2.001,2.001,2.005			1	tetrahedral

12

Table 1.3 ESR of feldspar, continued

Specimen	Reference	Method	g	g_{eff} of $\pm 3/2$	line width (gauss)	# sites	type
Oligoclase An ₂₂ Hawk Mica Mine, NC	Scala et al 1978	Powder 9.24 GHz		4.3	sharp	1	tet. or oct.
Oligoclase An ₂₉ Mitchell Co., N.C.	"	"		"	"	"	"
Andesine An ₃₂ Kragero, Norway	"	"		"	"	"	"
Labradorite An ₅₀ Labrador, Canada	Scala et al 1978	Single Xtl 9.24 GHz		4.3 4.3-3.9 5.0-5.3	broad " "	1 1 many	tet. or oct. " indistinct
Labradorite An ₆₇ Lake Co., Oregon	"	"		"	"	"	"
Bytownite An ₇₆ Crystal Bay, Minn.	"	"		"	"	"	"
Bytownite Stillwater, Minn	Weeks, 1972	Powder 35 + 9 GHz		4.27		2	oct. or defect
Anorthite Lunar	"	"		"		"	"
Anorthite Lunar	Niebuhr et al 1973	Single Xtl 35.6 + 9.5 GHz		5.02 5.32		1 1	tetrahedral tetrahedral

but their data do not warrant this. Gaite and Michoulier [1970] found that the g-factors of microclines have a slight anisotropy, and also noted that the line width of the ESR spectra increases as the amount of Al/Si order decreases as shown in Figure 1.4. In summary, the ESR of Fe^{3+} in potassium feldspar is potentially useful in understanding the structural state.

Pale yellow colors of bytownite and labradorite can similarly be attributed to Fe^{3+} . About 1/2 weight percent Fe is required to cause color in a millimeter thick crystal. Unlike potassium-feldspar, plagioclases should accommodate Fe^{2+} in the calcium sites, as well as incorporating Fe^{3+} in the tetrahedral sites. Bell and Mao's [1972] optical spectra (Figure 1.5) indicates that both tetrahedral Fe^{3+} and Fe^{2+} in the M-site exist in yellow labradorite from Lake Co., Oregon, because (1) the position and relative intensity of the three high energy peaks are nearly the same as the Fe^{3+} tetrahedral peaks in potassium feldspar (Table 1.1) and because (2) the low energy transition are polarized and positioned similar to Fe^{2+} octahedrally coordinated in other silicates [Bell and Mao, 1973], which is comparable to the 7-coordinated calcium site. The strongly polarized band at 32000 cm^{-1} is probably O^{2-} to Fe^{3+} charge transfer. For lunar plagioclases, Bell and Mao [1973] have demonstrated a linear correlation of the 1250 nm band's absorption coefficient with the concentration of total iron in the sample (Figure 1.6) which substantiates the assignment of ferrous iron to this band.

Emission excitation spectra confirm that Fe^{3+} is present in terrestrial plagioclase, and to a slight extent in the reduced lunar anorthites [Geake et al, 1971, Telfer and Walker, 1975]. Ligand field analysis of the results show that Fe^{3+} occupies distorted tetrahedral sites [Telfer and Walker, 1975

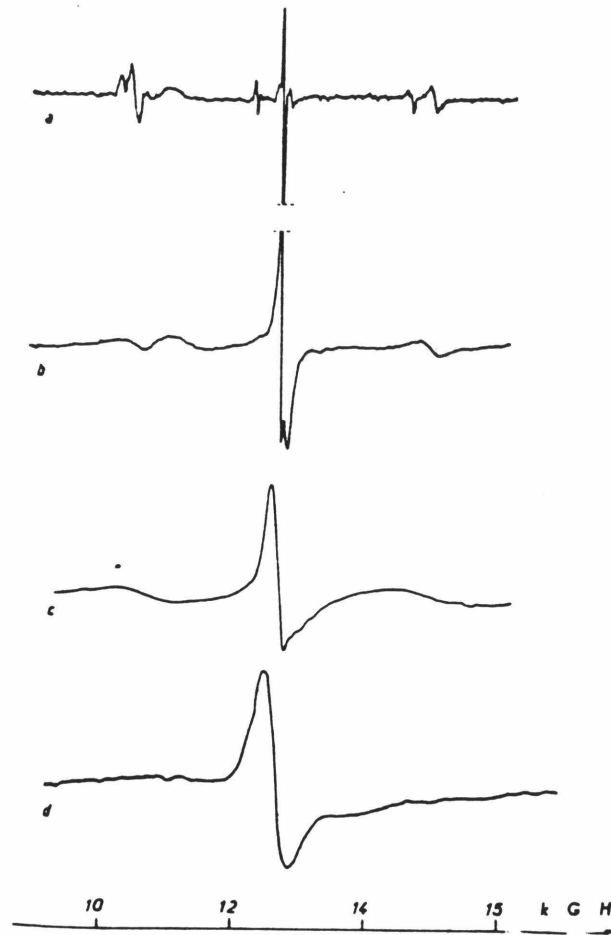


Figure 1.4 Single crystal EPR spectra of Fe^{+3} in potassium feldspar taken at 35 Ghz for one orientation. (a) Twinned Microcline, (b) Adularia from Saint Gothard, Sweden, (c) Orthoclase from Itrongay, Madagascar, (d) Sanidine from Allemagne, France. From Gaité and Michoulier [1970].

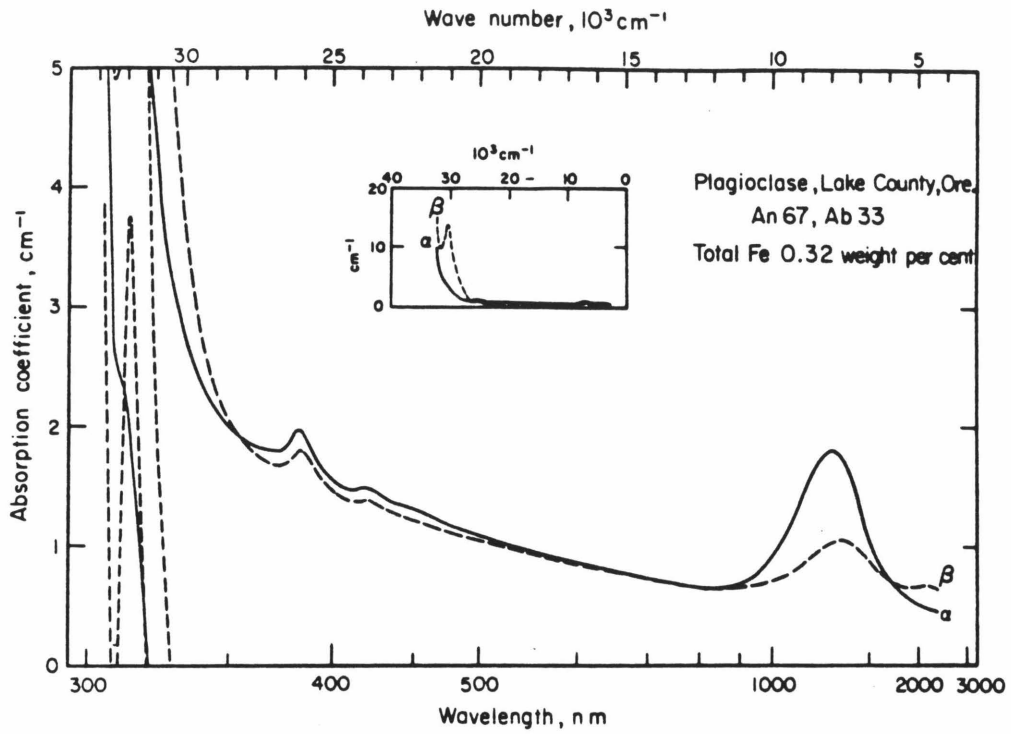


Figure 1.5 The α and β polarizations of Lake County Labradorite showing Fe^{+3} , Fe^{+2} , and $\text{Fe}^{+3}\text{O}^{-2}$ charge transfer (32000 cm^{-1}) bands. The insert is the same spectra in a reduced scale. From Bell and Mao [1972].

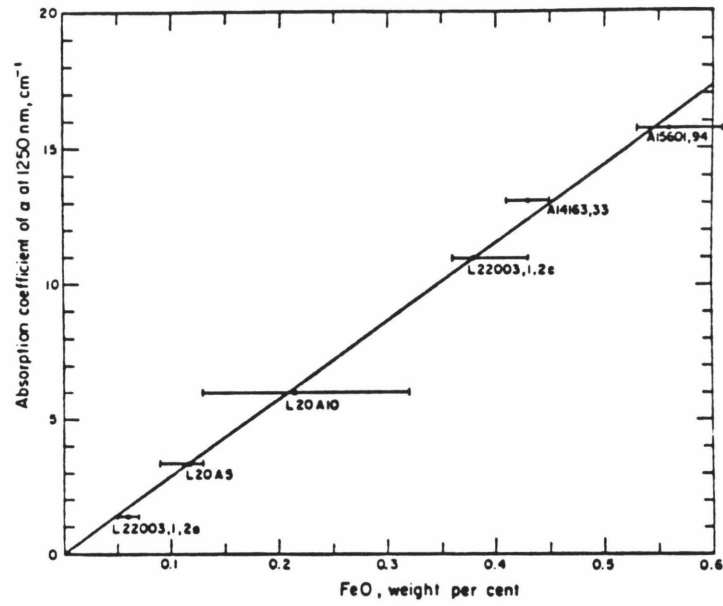


Figure 1.6 The linear relation of the absorption coefficient (cm^{-1}) of crystal-field band at 1250 nm in lunar plagioclase versus weight percentage of FeO determined by electron microprobe. From Bell and Mao [1973].

and 1978]. Both plagioclase and K-spar given similar spectra as indicated by the data in Table 1.4, and the emission excitation spectra are remarkably similar to the absorption spectra in both relative peak intensities [Telfer and Walker, 1975] and positions (see Table 1.1).

Mössbauer spectra of both lunar [Hafner et al, 1971] and terrestrial plagioclases [Schurman and Hafner, 1972] indicate the presence of Fe^{+2} in Ca-sites. For lunar anorthite an additional doublet appears at a slightly lower velocity (marked "T" in Figure 1.7', "C" is the site also seen in Stillwater bytownite). Appleman et al [1971] and Hafner [1972] attribute this doublet to Fe^{+2} in defect sites or substituting for Al^{+3} in tetrahedrallike sites. It is more likely that this "T" site is Fe^{+2} replacing calcium, because the Mössbauer parameters are not dissimilar to those of the "C" site (see Table 1.2) and of octahedral Fe^{+2} in other silicates [cf. Hafner et al, 1971, Table 4], and because anorthite has two pairs of calcium sites which differ structurally resulting in distinct bonding to the B, C, and D oxygens for the two pairs [Smith, 1974, I, p. 110].

Ferric iron has not been identified as a resolved doublet in Mössbauer spectra [Hafner, 1975]. The relatively high intensity of the zero velocity peak has been interpreted as the superposition of a narrow doublet due to Fe^{+3} in tetrahedral sites [Hafner et al, 1971; Schurman and Hafner, 1972]. Considering that the isomer shift for tetrahedral ferric iron in K-spar is large [Brown and Pitchard, 1968] and that the plagioclase T-sites are similar to the K-spar sites (as shown by optical and emission spectra), it is unlikely that a narrow Fe^{+3} doublet is responsible for the asymmetric intensity. At present, the cause is unknown.

EPR studies of trivalent iron in plagioclase, unlike those of

Table 1.4 Emission excitation energies in cm^{-1} of feldspar at room temperature. After Telfer and Walker, 1978

Band Assignment	Bytownite Split Rock Point, Minnesota	Oligoclase Bjordammen, Norway	Albite	Adularia
${}^6A_1(S) \rightarrow {}^4E(D)$	25910	26180	26220	26320
$\rightarrow {}^4T_2(D)$	23600	23540 22690	23580	23760
$\rightarrow {}^4E, {}^4A_1(S)$	22280	22230 20260	22190 20380	22380
$\rightarrow {}^4T_2(G)$	19600	19700 17460	19660 17430	19890 17530
$\rightarrow {}^4T_1(G)$	17160 16010	16250 15230	16250 15070	15860

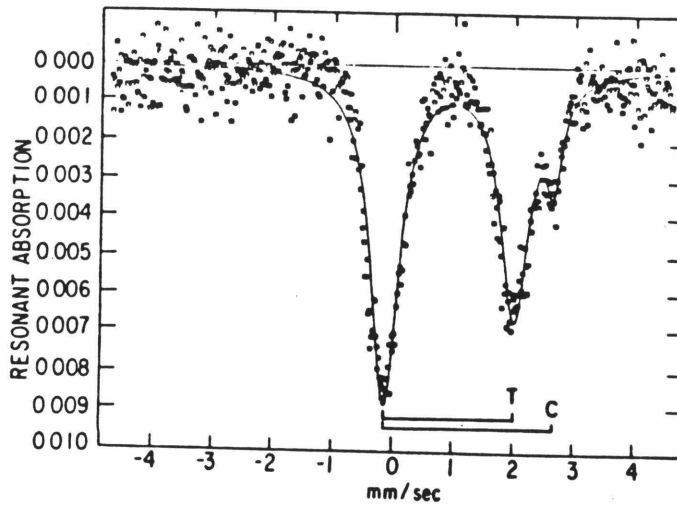


Figure 1.7 Mössbauer resonance absorption spectrum of Fe^{2+} in plagioclase of Apollo 11 basalt #11004 at 77°K . Total iron concentration is 0.3 wt %. "C" is the doublet assigned to Fe^{+2} in Calcium sites. "T" is the doublet due to Fe^{2+} at tetrahedral (?) sites. From Hafner [1975].

microcline, have some conflicts. Table 1.3 summarizes the available literature. Most of the authors assigned Fe^{+3} to tetrahedral sites, but a few [Weeks, 1973; Scala et al, 1978] considered M-sites or defect sites as a possibility. This interpretation stems from earlier erroneous Mössbauer assignments (discussed above). In addition, a discrepancy exists in the number of sites reported for Fe^{+3} for similar feldspars. Measurements on oligoclase (An_{20}) from North Karelia, USSR [Marfunin et al, 1967; Gaité and Michoulier, 1970] showed Fe^{+3} present in a single anisotropic tetrahedral site. Michoulier and Gaité [1972] determined that this site was $T_1(0)$ by fitting the ESR data to a Hamiltonian with fourth order terms. Scala et al's [1978] powder spectra of five different oligoclases and andesines similarly showed one site for Fe^{+3} , whereas Gaité and Michoulier [1970] report 3 sites for some oligoclases. This difference is probably due to structural state: The North Karelia sample has one Fe^{+3} site and is known to be a low-symmetry polymorph, which is analogous to the microcline results. The structural state of the multiple-sited oligoclases was not stated, but it is reasonable to assume that these are disordered in analogy with the K-spar results.

Slightly different problems exist in the number of sites for EPR studies of calcic plagioclases. In an early single crystal study, Gaité and Michoulier [1970] assigned trivalent iron in labradorite, bytownite, and anorthite to three different tetrahedral sites. Because one of the samples (Lake County labradorite) is known to have a high structural state, and thus several different Al sites, a large number of sites for Fe^{+3} seems reasonable. Using powder methods, Weeks [1973] reported two sites for lunar anorthite, both with apparent g-factors of 4.3 for the Kramer's $\pm 3/2$ transition, while Niebuhr et al [1973] reported two sites with apparent g of 5.04 and 5.32

also for lunar anorthite. Because these apparent g -factors of 4.3 will reduce to $g(\text{real})$ of 2, the total number of sites could be 2, 3, or 4. Detailed single crystal work of Scala et al [1978] resolved this discrepancy, by proving that labradorite and bytownite have two different sites with apparent g near 4.3, and another "site" with g effective ranging from 5.0 to 5.3 that actually is the sum of innumerable indistinguishable sites. (Figure 1.8 shows the ESR signals.) It is clear that Fe^{+3} in calcic plagioclases replaces Al^{+3} in the various sites, but connecting the different ESR signals with definite sites in the crystals has not yet been achieved.

1.2.a.iii Feldspar colored smoky by irradiation

Brauns [1909] disclosed that orthoclase, sanidine, and feldspars having a glassy appearance were colored brown (smoky) by radium irradiation (cited by Prizbram, 1956, p. 253). Speit and Lehmann (1976) investigated the smoky color in large transparent crystals of sanidine from the Vokelsfeld area in the Eifel region. In appearance, the crystals are remarkably similar to smoky quartz, except that the sanidine's color is bleached by sunlight [Speit and Lehmann, 1976]. Like smoky quartz, smoky sanidine can be regenerated by ionizing radiation or by electrolytic coloration. Migration of the color towards the cathode in an applied electric field suggests that the sanidine center is a hole [Speit and Lehmann, 1976]. Smoky sanidine has moderately anisotropic visible spectra with bands present at 11500, 13500, 18000, and 27500 cm^{-1} , such that their relative intensities differ for natural and irradiated samples [Speit and Lehmann, 1976]. This is quite different in behavior from smoky quartz (e.g. Sec. 1.2.b.iv). A hydrous species is indicated by broad bands in the infrared, but these are not

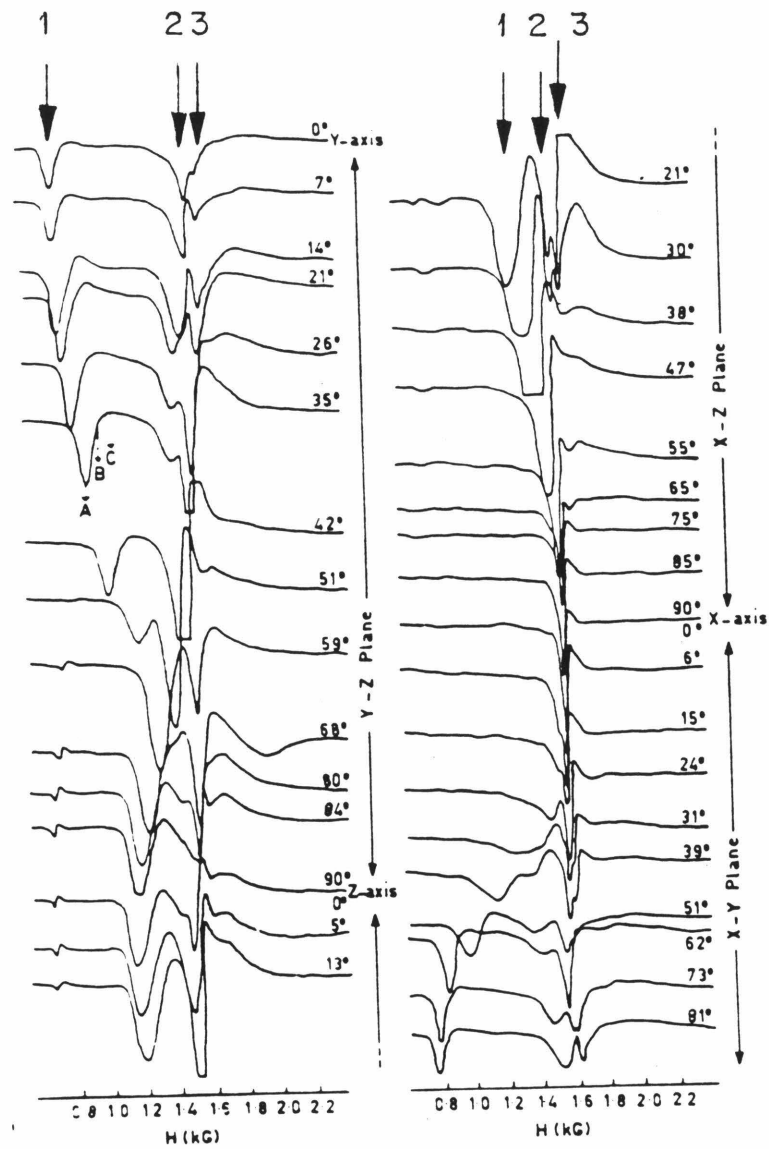


Figure 1.8 Angular variation of Fe^{3+} spectra in bytownite from Crystal Bay, Minnesota with respect to site # 1's magnetic axes. Sites #1, 2, and 3 are indicated by arrows for the 0° and 21° spectra. From Scala et al [1978].

involved in the coloration [Speit and Lehmann, 1976]. The presence of two thermoluminescence bands at 14800 and 21100 cm^{-1} , and existence of both a first and second order reaction for the bleaching kinetics suggest the involvement of multiple sites [Speit and Lehmann, 1976]. The ESR spectrum of smoky sanidine consists of a non-specific single derivative located at g -apparent of 2: no aluminum-hole centers were seen [Speit and Lehmann, 1976]. Because no direct correlation of the ESR spectra with the optical data has been made, any models of the center are at best tentative (cf. Sec. 1.2.b.iii).

1.2.b.iv Amazonite: feldspar colored blue-green by irradiation

According to Hintze [1897], the name amazonstone was originally applied to nephrite and green feldspar found near the Amazon river. Emmerling [1773, as quoted in Hintze, p.1354] restricted the definition to include only feldspar. Breithaupt [1847, p.505] shortened the name to amazonite and confirmed the potassic composition. Since then the name has evolved to imply exclusively triclinic potassium feldspars. However, Rudenko and Vokhmentsev [1969] showed that blue-green oligoclase has amazonite properties. Frondel et al [1966] described a green, lead- and barium-bearing anorthoclase from Franklin, New Jersey. Similarly, Cech et al [1971] described the chemistry and structure of green orthoclase from Broken Hill, New South Wales, and proposed that the name amazonite should include not only blue to green microcline, but also green orthoclase and "other feldspars whose color is similar". General usage, however, has not changed. Accordingly, we will first discuss research on blue potassium feldspars (amazonite).

The earliest investigators of amazonite surmised that the color resulted

from the presence of iron [Koenig, 1876, cited by Odiorne, 1978; Eliseev, 1949; Basset, 1956]; yet as so aptly stated by Basset [1956] "if the green color were due to iron (+2 in the potassium site), then it is difficult to understand why green varieties of all feldspars don't occur." In particular, Basset [1956] noted that amazonites are frequently perthitic, with color concentrated in the microcline lamellae.

Relationships between amazonite coloration and physical properties have been elucidated by a few critical experiments. Eliseev [1949] and Przi Bram (1956, p.253) disclosed that color which was bleached by heat could be restored by X-rays; which implies that amazonite is a radiation-induced color. Oftedal's [1957] data on the decolorization of amazonite through heating suggest that the color loss is a diffusion or decomposition process. Noting that the color is stable below 270°, Oftedal concluded that this is the maximum temperature of formation; and hence that color forms in an "already crystallized and cooled feldspar," and may be attributed to "colour centra." This discovery of amazonites' involvement with radiation is of utmost importance in understanding the physics of the color because it shows that the color is not limited to species such as transition metals (Cr, Cu, V, Fe) and may be a rather complicated process involving defects or impurity ions (see Sec. 1.2.b.iii). The behavior of amazonite centers is apparently not simple because the shade (to the eye) of the restored color sometimes does not match the original, natural color [Shmakin, 1968].

The chemistry of amazonite has been the object of a vast number of studies. Basset [1956] analyzed for Cr, V, and Cu which are known to produce intrinsic green colors. None is present because feldspar lacks the proper octahedral sites. Taylor et al [1960] used emission spectroscopy to determine concentrations of seventeen elements (Li, Na, K, Rb, Cs,

Pb, Tl, Ca, Sr, Ba, Mn, Cu, Co, Ni, V, Sn, and F) in feldspar from a Norwegian pegmatite and concluded there was no chemical difference between the colored and uncolored crystals. Plyusnin [1969] similarly studied Russian amazonites and concluded that Rb, Cu, and Mn were not connected with the color. In contrast with these studies, several investigators have noted the presence of elevated amounts of Pb, Rb, Cs, and Tl in amazonites. A summary of early studies (mostly Russian) reporting increased Pb-contents is given by Cech et al [1971]. More recently, Catanzano and Gast [1960] noted very high amounts of lead in American amazonites. Zhurov and Stishov [1965] measured Pb, Rb, and Tl contents of feldspars and found that color is better correlated with Pb than with Rb or Tl, although several samples did not fit the correlation with lead. Shmakin [1968] detected high Pb, Rb, Cs, and Tl contents in Russian amazonites. Plyusnin [1969] reported increased lead contents in green Russian amazonites. Cech et al [1971] measured 1.2 % PbO in a green orthoclase from Broken Hill, Australia. Nunes [1979] found elevated amounts of Pb, Rb, and Cs in colored feldspars from Mozambique and noted that green amazonites have more lead than blue ones (Table 1.5). Foord and Martin (1979) analyzed Colorado amazonite and found that color-zoned crystals show "an excellent correlation between Pb content and amount of color" (to the eye). They noted enrichment of Rb and Cs, but stated that these "reach a maximum in the growing crystal before the lead" does, and are not correlated with the color. Foord, Martin, Conklin, and Simmons (in prep.) have studied the chemistry, structural state, and occurrence of approximately 100 different amazonites throughout the world. Their investigation embraces a wide range of color, and shows that amazonites with less than 1000 ppm Pb are blue, while the color shifts to green with increasing lead content.

Table 1.5 Amazonites from Mozambique Pegmatites, after Nunes [1979]

Locality	Color	PbO %	Rb ₂ O %	Cs ₂ O %
Santos, Monapo	blue	0.12	0.96	0.06
	blue	0.05	0.66	0.15
	green	0.67	1.69	0.39
	green	0.46	1.52	0.18
	green	0.48	1.51	0.20
Tulua, Nacala	light blue	0.03	0.47	0.03
Pitea, Muiane	light blue	0.03	0.54	0.03
	blue-green	0.14	1.04	0.14
Rio Maria, Morrua	light blue	0.05	0.61	0.06
	green	0.12	0.70	0.06
Vila Machado	green	0.21	1.32	0.10

No other element correlates with color. Foord et al [in prep.] also note that the apparent intensity usually increases as lead concentration increases.

From these papers it appears that the lead contents of amazonite generally range from 0.00X % to 0.0X %, but that some specimens have 0.1 to 0.3 wt % (e.g. Amelia, Virginia, and Franklin, New Jersey, and some Pikes Peak, Colorado localities [Foord and Martin, 1979]; Keivy, USSR [Zhirov and Stishov, 1965]), while a few rare samples have about 1 wt % PbO (Keivy, USSR [Foord and Martin, 1979] and the Broken Hill orthoclase [Cech et al, 1971]).

There is some indication from the X-ray determinations that the structural state of the amazonite is influenced by the lead content. The data of Table 1.6 suggest that crystals with high lead content (>2000 ppm Pb) tend to be disordered, while amazonites with low lead contents are maximum microcline. Synthetic end-member $\text{PbAl}_2\text{Si}_2\text{O}_8$ has been shown to have the feldspar structure [Sorrell, 1962; Scheel, 1971] and form in both the monoclinic (Al/Si disordered) and triclinic (Al/Si ordered) polymorphs [Bruno and Facchinelli, 1972]. Thus, the substitution of lead will not necessarily "force" monoclinic symmetry on the potassium feldspar, but it may be that addition of aluminum through the replacement of K + Si by Pb + Al contributes to the disorder of the system.

There are many indications that color may be correlated with lead. However, some lead-containing feldspars are not colored. One significant exception is an Amelia, Virginia, sample [Foord and Martin, 1979] in which the lead content is 1000 ppm in both green and white portions of the same crystal. Some samples are either much more or much less intense than would be expected from the lead content alone [Foord et al, in prep.]. Colorless feldspars commonly contain 10 to 60 ppm Pb [Smith, 1974, I, p. 101].

Table 1.6 Amazonite structural state and lead content

Location	$\Delta(131,1\bar{3}1)$	PbO, ppm	Reference
Maikyl Pegmatites Kazakhstan	0.91-1.00	90-400	Bugaets, 1967 cited by Cech et al, 1971 Zhironov and Stishov, 1965
Pikes Peak, Colorado	~ 1	<2000	Foord and Martin, 1979
Tordal, Norway	0.96	180	Tibballs and Olsen, 1977
Avdar Massif, Mongolia	0.87	1950	Pivec et al, 1981
Royningsdal, Norway	0.6-0.8	3000	Tibballs and Olsen, 1977
Maikyl Massif, Kazakhstan	0.2-0.78	?	Bugaets, 1967 cited by Cech et al, 1971
Broken Hill, Australia	~ 0	12000	Cech et al, 1971

To account for this type of discrepancy, Zhiron and Stishov [1965] proposed that feldspar has "active" lead which is incorporated by the substitution



wherein the defect actually produces color; and "inactive" colorless lead incorporated by



Plyusnin (1969) discovered a correlation between the color and the amount of water in 10 amazonites, and concluded that a second type of active lead could be incorporated by



The usual oxidation state Pb^{2+} cannot produce color, because its electronic transitions occur in the ultraviolet region (Sec. 1.2.b.v). However, the involvement of radiation in amazonites suggests that an unusual oxidation state or a defect coupled with lead might be involved in amazonite coloration. Using electron spin resonance techniques, Marfunin and Bershov [1970] concluded that Pb^{+1} centers are present in amazonites, but not in other feldspars. This conclusion is suspect because (1) an adequate presentation of the raw data and data analysis was not made, (2) the g values given (1.39, 1.565, and 1.837) are strikingly similar to apparent g's measured for Pb^{+3} in various crystalline solids (Section 1.2.b.v), and (3) Speit and Lehmann [1982] did not find this signal in Australian amazonite. Speit and Lehmann [1982] did observe a Pb-O^- center with $g \sim 2$ and $A \sim 280$ MHz and satellite intensity of 1/7 the central peak's in agreement with Marfunin and Bershov [1970]. Neither set of authors correlated this center with color.

A few researchers have studied the spectroscopy of amazonite. Rudenko and Vokhmentsev [1969] presented the reflection spectra shown in Figure 1.9, and concluded that the color was due to the (absorption) peak at 620

to 670 nm. Zhirov and Stishov [1965] probably used similar data to produce the dependency of amazonite color shown in Figure 1.10. Whether the relative intensity was taken at the reflection maxima ~ 540 nm, or the minima at ~ 640 nm was not stated. Nonetheless, it is interesting to note that the color of the later grown amazonite is more intense for a given lead content than that of an earlier crystallized feldspar.

Sidorovskaya et al's [1982] study of amazonite's thermoluminescence showed that two bands occur at 280 and 490 nm in the neighborhood of 200°C. Because optical absorptions are at higher energies than TL bands, neither TL peak could correspond to the 640 nm absorption. Marfunin [1979] assigned the 290 nm TL band to Pb^{2+} . Sidorovskaya et al [1982] interpreted the TL spectra as arising from an electron trapped in the defect position of eq. 1.1.

Plyusnin [1969] used reflection spectroscopy to study the effect of dehydration on a suite of differently colored amazonites. This suite may have originated from one locality. The reflectance spectra of the natural samples are shown in Figure 1.11. It is important to note that the data Plyusnin used are from the reflection maximum, rather than the absorption maximum which is the better representation of the electronic transition. Plyusnin [1969] calculated the water content of the samples from the measured weight loss upon heating to 900°C by assuming all loss was due to water. Both the reflection intensity and the wavelength were found to correlate with the water content (Figures 1.12 a and b), while the dependence of the intensity on lead content (Figure 1.12 c) has two linear trends for two groups of samples with one sample at variance. (The motion of the reflection maxima is simply due to the shrinking of the absorption peak seen in Figure 1.11, and is not due to any change in the properties of the color center.) Plyusnin's [1969] results definitely indicate that some type of

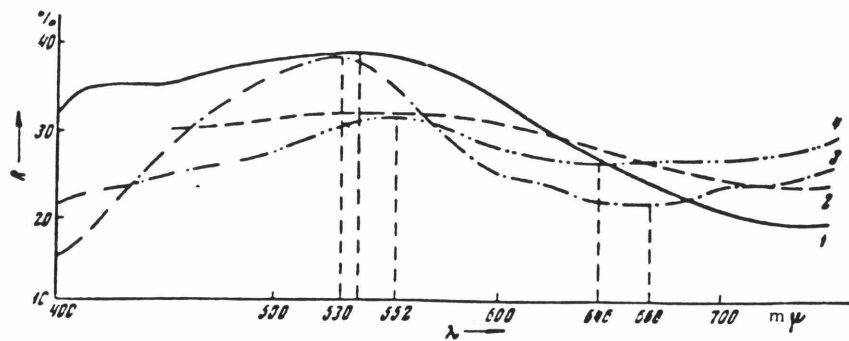


Figure 1.9 Reflectance spectra of blue-green feldspar. From Rudenko and Vohkmentsev [1969],

- _____ (1) Oligoclase An25 (antiperthite)
- (2) Oligoclase An29
- .-.- (3) Microcline, greenish-blue
- .-.-.- (4) Microcline, bluish-green

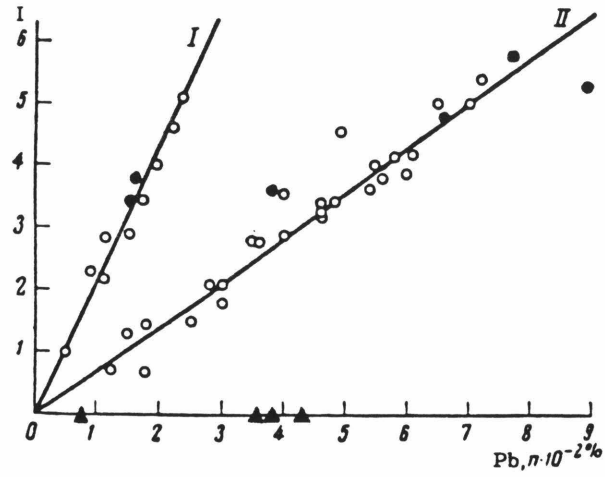


Figure 1.10 Relationship of reflected intensity to lead content of amazonites. From Zhirov and Stishov [1965]. Open circles are blue amazonites, closed circles are green amazonites, triangles are colorless microcline. Curve I represents secondary amazonite growths, while Curve II is primary.

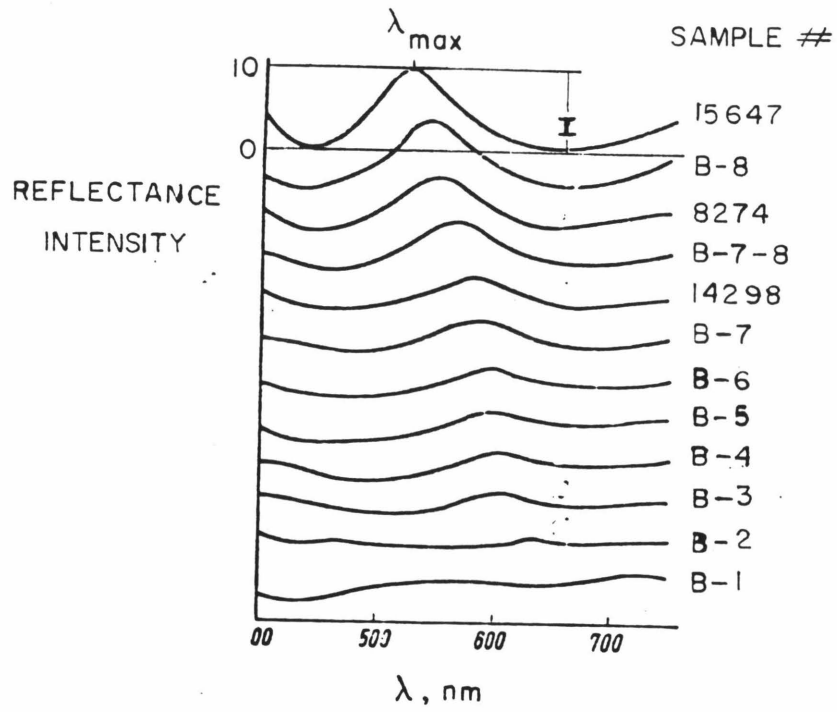


Figure 1.11 Amazonite reflectance spectra. From Plyusnin [1969]. The intensity is relative to sample #15647 which is sealed to 10. The intensity measured (I) is the height of the reflection maxima located at λ_{max} .

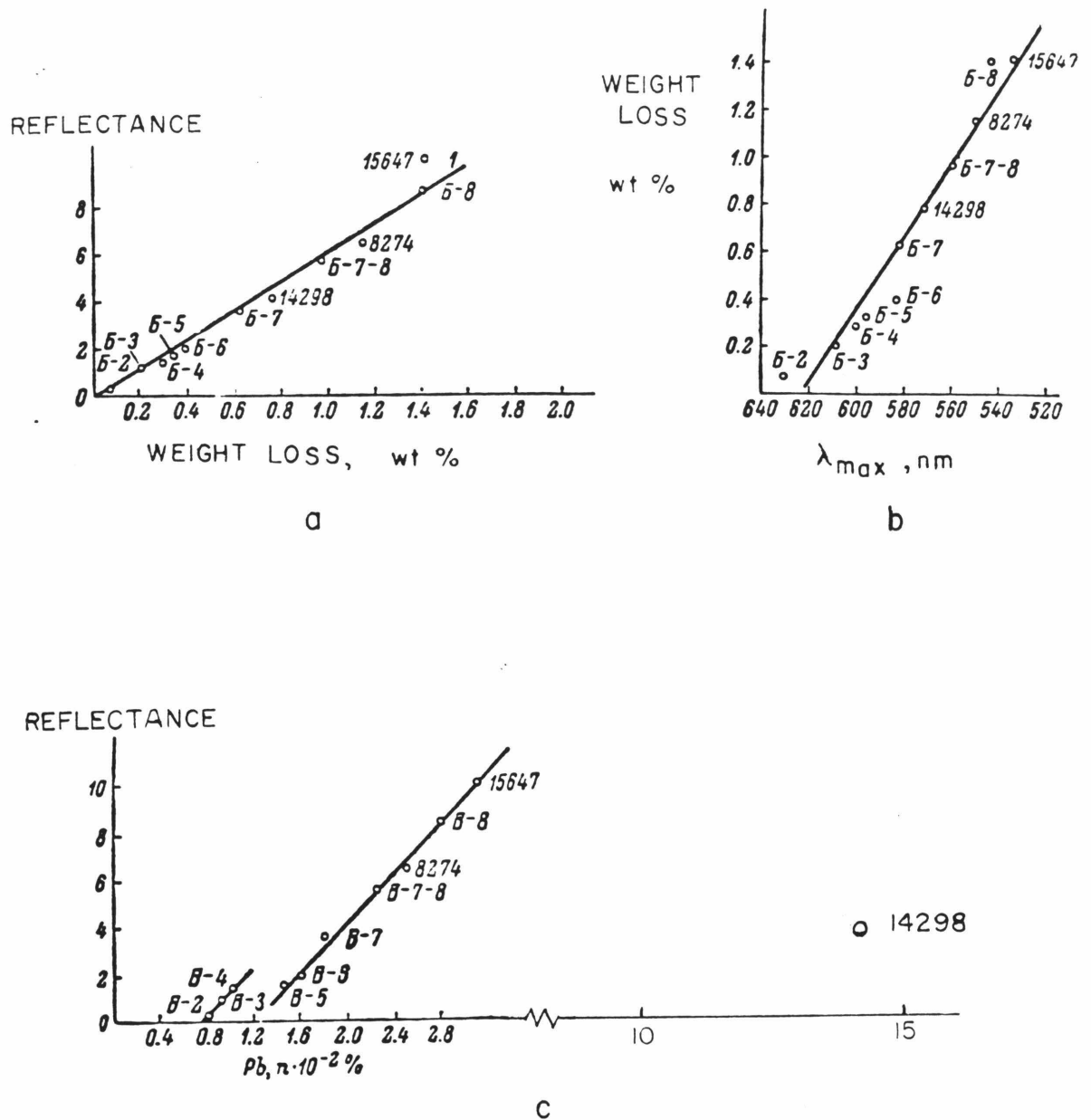


Figure 1.12 Relationships of Amazonite color with lead and volatile content. From Plyusnin [1969].

(a) Relative intensity vs. weight lost upon heating to 900°C. The weight loss was assumed to be water in the form of OH⁻.

(b) Weight lost upon heating vs. wavelength of maximum reflectance.

(c) Relative intensity vs. Pb content of amazonites. Note change of scale for sample #14298.

volatile species (which he surmised was OH^-) is involved; it is also apparent that the volatile concentration is related to the lead concentration, so that whether lead is connected with the color becomes problematic.

Plimer [1967] reported that no water was indicated in Broken Hill orthoclase by infrared spectroscopy. However, his sample was thin, judging from the overall absorbance, which makes his conclusion questionable.

Tarashchan et al [1973] investigated the ultraviolet absorption of amazonite. The UV band at 255 nm (Figure 1.13) is more intense than the color producing bands at 390 and 625 nm [Tarashchan et al, 1973]. The UV spectrum also has a shoulder at 270 nm which the authors did not discuss. The position of the UV band is similar to that of the $^1\text{S}_0$ to $^3\text{P}_1$ transition of Pb^{+2} in alkali-halides (Sec. 1.2.b.v) which led Tarashchan et al [1973] to assign the amazonite transition to Pb^{+2} . That the intensity of this absorption increases upon heating, and then decreased upon subsequent irradiation implies that lead is involved in the coloring: Tarashchan et al [1973] hypothesized that



It is equally likely that



From the diverse chemical and spectral evidence, it appears that lead does participate in amazonite coloration. The mechanism is unknown. The possible role of water remains to be investigated, and the few amazonites that stray from the generally applicable trends have not yet been explained.

1.2.a.v Blue Plagioclase

A pale blue cleavelandite variety of albite (Ab_{94-99}) occurs in the gem pegmatites of Pala [Jahns and Wright, 1951], Mesa Grande, California

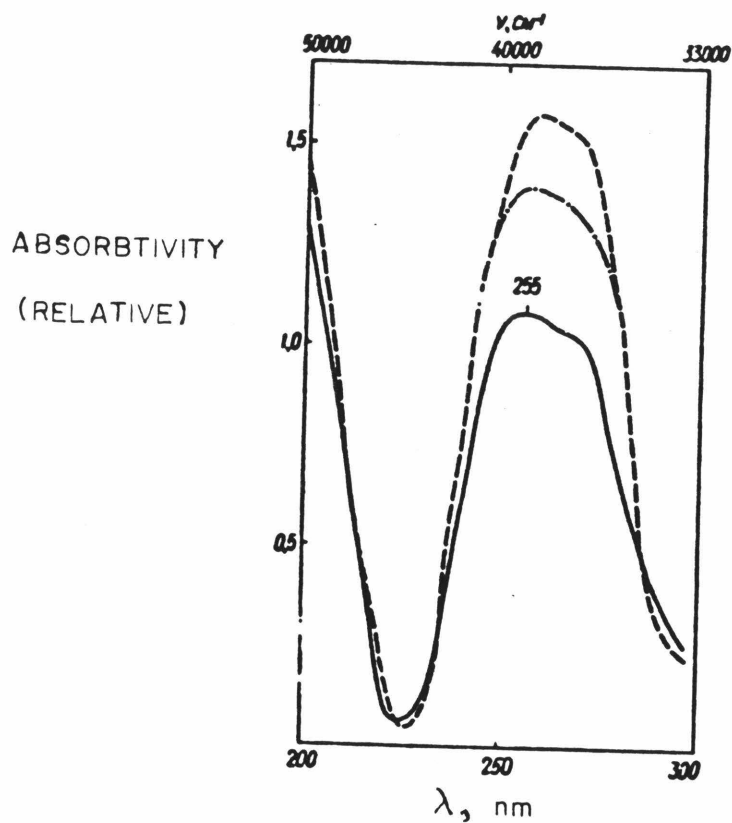


Figure 1.13 Ultraviolet absorption spectra of a blue Russian amazonite. From Tarashchan et al [1973]. The 255 nm band was assigned to 1S_0 to 3P_1 transition of Pb^{+2} . Solid line is the natural specimen; the dashed line is after heating to 5003C; while the dot-dashed line is for irradiation of the sample after heating to 500°C.

[Foord, 1977], and elsewhere. Its color has not been studied. Taylor et al [1960] described a pegmatite in which blue cleavelandite (with a higher lead content than other uncolored cleavelandite in the pegmatite) was associated with amazonite. The blue color of the cleavelandite may be related to the amazonite color, but the appropriate spectral tests have not been performed.

Rudenko and Vokhmentsev [1969] measured the reflection spectra of two blue-green oligoclases (untwinned An_{25} and An_{29} with antiperthite growths of pale blue-green microcline), and compared them to that of amazonite. The only difference is a shift of the reflection minima (which is related to the absorption maxima) 30 to 60 nm towards the red relative to amazonite minima (Figure 1.9). Rudenko and Vokhmentsev heated (300 to 600°C) and X-ray irradiated their samples and noted that the microcline regained its color, but the oligoclase did not. It is not known whether these oligoclases have high lead contents, but the similarity of their reflection spectra to that of amazonite suggests that the blue color arises from the same mechanism. Plagioclase is more weakly and uncommonly colored because it accepts lead into the lattice less readily than $KAlSi_3O_8$ [Smith, 1974, II, p.103].

1.2.a.vi ESR of irradiation centers in feldspar

Besides the Pb^{+1} (?) center and the $Pb-O^-$ center observed in amazonite (See Sec. 1.2.a.iv), many other different radiation signals are revealed in the ESR spectra of feldspar. None of these has yet been quantitatively correlated with color. The various centers reported in the literature have been attributed to Ti^{+3} , $Al-O^- -Al$, $Si-O^- -Si$, $Na-O^-$, $Ag-O^-$ [Marfunin and Bershov, 1970]; Ti^{+3} , $Al-O^- -Al$, $Al-O^-$, $Si-O^- \cdots X$ [Speit and Lehmann, 1982]; NH_3^+ , N^{-2} , $Al-O^-$, and E_1 (which is an electron trapped at an

oxygen vacancy) [Matyash et al, 1982]. All of the centers are anisotropic, and all have g factors near 2. The signals are distinguishable by their fine structure. For details the reader should consult the above references.

1.2.a.vii Inclusion colors: general statement

Feldspar can take on almost any color when it contains colored inclusions. Strictly speaking, these are not feldspar colors, but rather colors of a second, associated phase. White, non-transparent feldspar results from scattering of light from inclusions of alteration products such as clays, or from fluid inclusions [Folk, 1955]. Red color in potassium feldspar is so common that it is frequently a useful diagnostic property for field identification. Grey to black colors are also very common. These two types are mainly related to inclusions of iron oxides and will be discussed in detail for comparison to the thesis results on Lake County labradorite.

Red schiller and red clouded feldspars

Except for the unique Lake County, Oregon, sunstones, to be covered in the next section, red colors in feldspar are comprehensively reviewed by Smith [1974, II, p.614-623]. For completeness, a précis of the original authors' and Smith's work is included.

Red color in feldspar results mainly from inclusions of hematite flakes. If the flakes are oriented, light is preferentially scattered producing iridescence. This play of light and color is known as schiller, or aventurescence, and when present to extreme extent, gives rise to the variety sunstone [Smith, 1974, II, p.614]. Those feldspars having smaller, more dispersed unoriented flakes lack schiller but possess a pink to

brick-red cloudy color.

Andersen (1915) reviewed previous work on aventurine feldspars, and presented a thorough study of the optical properties and effect of heating on red shillers in albites, oligoclases, labradorites and perthites from the U.S. and Norway. From the hexagonal morphology, absorption colors, lack of distinct inherent pleochroism, and presence of iron, he concluded that the lamellae were hematite. Iron hydroxides were ruled out because temperatures greater than 1235°C are needed for feldspars to resorb the flakes. Microcline lamellae attained up to 0.2 mm, while those in plagioclase often measured 3 mm in diameter. From the interference colors, Andersen [1915] determined that the thicknesses ranged from 100 to 400 nm. The lamellae were most numerous on cleavage faces. The lamellae are always oriented on (112), ($\bar{1}\bar{1}2$), (150) and ($\bar{1}50$) planes; the forms (001), (010), (110) and ($\bar{1}\bar{1}0$) are rare. From the lack of lamellae on growth faces, Andersen disallowed simultaneous crystallization as the formation mechanism.

Later studies have confirmed Andersen's results. Kraeft and Saalfeld (1967) showed using electron diffraction that most of the lamellae have Fe₂O₃ structures, and are primarily iron; whereas a few yielded patterns consistent with a hexagonal primitive cell with $a = 5.92 \pm 0.03 \text{ \AA}$ which is unlike that of any known iron oxide. These few lamellae contain in addition to iron, K, Mg, Ca, Al, Si, Cu, Ti, V, Cr, Mn, Co, and Ni [Kraeft and Saalfeld, 1967]. Copley and Gay [1978] examined the aventurine flakes of Norwegian feldspars by preferentially etching the feldspar with HF. Their microanalyses suggest that the flakes are hematite. Copley and Gay [1979] showed that the majority of the inclusions have structures that are ordered or partially ordered forms of α -Fe₂O₃ and chemistries that

approach Fe_2O_3 with minor replacement of cations. They attribute the $a = 5.92 \text{ \AA}$ pattern to a slightly different cation arrangement than $\alpha\text{-Fe}_2\text{O}_3$. Minor amounts of two other unidentified phases sporadically occur within the feldspar [Copley and Gay, 1979]. In studying the orientation of the hematite lamellae, Copley and Gay [1979] found a surprisingly wide scatter of possible orientations, with some clustering around the planes (112) and $(\bar{1}\bar{1}2)$. Like Andersen, Copley and Gay were unable to find a correlation between the platelets' orientation and crystallographic directions within the host feldspar.

Neumann and Christie [1962] showed that averturine cores are usually much more structurally ordered than the surrounding white mantles. Divljan [1960] and Neumann and Christie [1962] showed that there is no correlation between the amount of iron in the crystal and the schiller present. Based on this, the geological location of the Norwegian pegmatites in Mg-metasomatised amphibolitic rocks, and the fact that many non-aventurine feldspars have higher Fe-contents than their averturine counterparts, Divljan [1960] argued that iron is externally derived, rather than internally derived from exsolution.

Red clouded feldspars contain ferric oxides, mostly as hematite, [e.g. Smith, 1974, II, p.618]. The composition for the red feldspars includes anorthite [Isshiki, 1958], potassium feldspar [Ernst, 1960; Riederer, 1965], perthite [Rosenqvist, 1965], and albite [Boone, 1969]. Boone [1969] has made a major contribution to understanding formation of red-clouded feldspar. He observed a gradation of a gray porphyry in the Canadian Gaspé Peninsula from potassic oligoclase-andesine and weakly altered biotite into a red porphyry consisting of hematiferous albite with muscovite inclusions and chloritized biotite. Boone [1969] showed that

formation of the red feldspars results from reaction of ternary feldspars with a vapor phase bearing Fe which was released during decomposition and oxidation of biotite. Consideration of the phase diagram for hematite + feldspar + muscovite + quartz + vapor suggests that this is a low temperature process, occurring between ~ 200 and ~ 500°C [Boone, 1969]. Similar iron metasomatism probably produced red-clouded K-spars, but whether aventurine results from the same mechanism is not clear [Smith 1974, II, p. 623]. Also, the red color of the volcanic transparent anorthite crystals appears to result from exsolution of 0.1 mm platelets on the 001 plane [Isshiki, 1958]. The description and pictures of these lamellae are very similar to that of the schiller in the Lake County labradorite, which suggests that the anorthites belong to a different class of problems. More than one mechanism may be involved in the formation of the red colors [Smith, 1974, II, p. 623].

Black-Clouded feldspars

Smith [1974, II, p.624-629] has extensively reviewed the literature on black inclusions in feldspar.

Intermediate plagioclases are particularly susceptible to this phenomenon, and give the darkest colors [Poldervaart and Gilkey, 1954]. The identity of the minute dark inclusions is not clear, although iron bearing minerals are partially involved as suggested by the mineralogy of the large dark inclusions: iron ore, as well as pyroxene, biotite, spinel, rutile, hornblende, or garnet [Poldervaart and Gilkey, 1954] and also hematite-ilmenite solid solutions [Anderson, 1966]. For the tiny inclusions no spectroscopic or magnetic data are available, but oxides of Fe in mixed valence states, possibly with Ti, would produce a dark color, even in tiny amounts. Andersen's [1915] heating experiments

show that dark inclusions may be produced from red hematite flakes. Like the red-clouded feldspars, black-cloudiness is independent of iron content [Smith, 1974, II, p. 629].

MacGregor [1931] suggested that the dark-cloudiness was caused by exsolution of iron from the lattice as the plagioclase was heated during contact metamorphism. Poldervaart and Gilkey [1954] concluded that an exsolution process was likely for the case of weak clouding, but that intense clouding required introduction of iron into the feldspar. Diffusion of iron through channels produced by the unmixing of the plagioclase explains the restriction of intensely dark clouding to intermediate plagioclases [Poldervaart and Gilkey, 1954]. From these and later studies Smith [1974, II, p.629-630] concluded that water plays a major role in the formation of the dark inclusions; and that chemical migration and/or other minerals are involved. This mechanism is similar to that producing red-cloudiness. Smith [1974, II, p. 630] attributed the difference between the two types to the oxidation state of the inclusions.

1.2.a.viii Sunstones from Lake County, Oregon

Labradorite phenocrysts in a Miocene porphyritic basalt flow near the Rabbit Hills in Lake County, Oregon, are noted for their transparent gemmy quality [Stewart et al, 1966; Peterson, 1972], and have been studied because of their unusual structural state, which is intermediate between high and low, but more similar to high [Stewart et al, 1966; Wenk et al, 1980; Tagai et al, 1980]. The phenocrysts range from 1 to 8 mm in the longest dimension, have coarse albite (and occasionally Carlsbad) twins, and are uniformly An₆₇ except for a rim of An₅₆ to An₆₇ comprising 3 to 8 volume per cent of the crystal [Stewart et al, 1966]. Specimens are

exceptionally clear and commonly are uniformly colorless or straw-yellow [Stewart et al, 1966]. This color is due to iron +3 (see Section 1.2.a.ii) which is a minor component (see Table 1.7 which includes analyses of a similar labradorite from Crater Elegante, Sonora, Mexico).

Besides the common yellow stones, sunstones, and more rarely red and green transparent colors, exist. Early descriptions of these gemstones refer to a Modoc County, California locality [Andersen, 1917; Aitkens, 1937], but it is now clear that the actual occurrence is the Rabbit Hills site [Stewart et al, 1966; Peterson, 1972]. Andersen [1917] noted that these sunstones were much different from the usual varieties (see Sec 1.2.a.vii), consisting of a transparent An_{67} matrix and a schiller due to round, thin, extremely reflective platelets on (001) and (010). The platelets are opaque to translucent green in transmitted light, copper-red in reflected light; range from 10 to 30 μm in diameter, and have thicknesses less than 1 μm [Andersen, 1917]. From these observations and from the presence of trace amounts of copper in the crystals, Andersen concluded that the schiller is metallic copper. (Copper has been detected in plagioclases at levels up to 70 ppm, and either oxidation state should fit in the M-site, but contamination is highly possible [Smith, 1974, II, p. 113-114].) Peterson [1972] reported that the inclusions were a mixture of iron oxide and aluminosilicate according to microprobe analysis, but it is not clear that the platelets would survive the polishing treatment to yield results. The inclusions are definitely not hematite as in other sunstones [Andersen, 1917; Peterson, 1972]. The best identification at present is Andersen's inference of metallic copper from the optics.

A variety of colors have been reported for the labradorite. Some specimens have a red color due to very small, abundant schiller particles [Aitkens, 1937]. Others show fine red, green, or salmon tints [Aitkens,

Table 1.7 Analyses of labradorite from Lake County, Oregon and Crater Elegante, Sonora, Mexico

Locality	Lake County	Lake County	Crater Elegante	Crater Elegante
Reference	Stewart et al 1966	Emmons, 1953 p. 18	Gutmann & Martin 1976	Gutmann & Martin 1976
SiO ₂	51.42	51.08	53.0	53.8
TiO ₂	0.04	0.05	0.09	0.10
Al ₂ O ₃	30.76	31.05	29.2	29.2
Fe ₂ O ₃	0.24	0.43	0.32	0.40
FeO	0.17	0.12	0.19	0.13
MnO	-	0.01	<0.01	<0.01
MgO	0.05	0.22	0.09	0.05
CaO	13.42	13.85	12.4	11.6
SrO	-	0.14	0.105	0.105
Na ₂ O	3.52	3.38	3.86	4.33
K ₂ O	0.23	0.12	0.24	0.28
H ₂ O	0.04	0.06	-	-
Ba	-	0.01	-	-
Li	-	0.0006	-	-
Rb	-	ND	-	-
total	98.89	100.52	99.50	100.00
Mole % An	67.2	68.9	63.9	59.5
Mole % Ab	31.5	30.3	34.7	38.9
Mole % Or	1.3	0.7	1.4	1.6

1937]. The colors vary in both tone and intensity, and change to the eye as the sample is rotated in natural lighting [Carlson and Kircher, 1976]. The range of colors is derived from various combinations of the weakly pleochroic yellow with two strongly pleochroic colors. One appears red-orange in total, but is orange or light reddish-purple in polarized light; the other appears blue-green overall, but is blue-green, orange, or colorless in polarized light [Carlson and Kircher, 1976]. Peterson [1972] reported that no chemical differences in microprobe analyses were found among the colorless, red, green, and yellow with schiller zones, but that trace amounts of iron, copper, manganese and titanium were found. An interesting question is whether the red and green colors are associated with the allegedly copper platelets (cf. Section 1.2.b.ii) or with iron or with the other transition metals present. (Cu^{2+} is discussed in Section 1.2.b.i.) Charge transfer is a distinct possibility. Another is colloidal copper (see Sec. 1.2.b.ii).

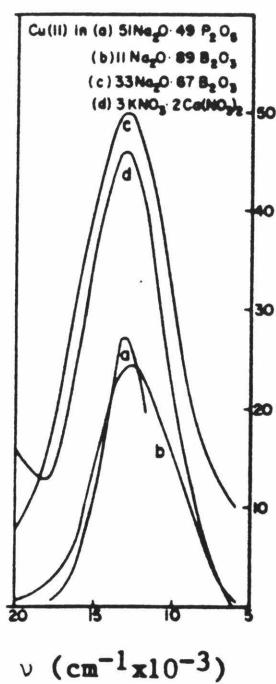
1.2.b Similar colors in other materials

This section offers a cornucopia of coloring phenomena that could be related to coloration of feldspar. In anticipation of the labradorite results, the spectroscopy of Cu^{2+} is discussed, and the reduction of Cu^{1+} to Cu metal and its subsequent exsolution in glass is covered in detail. The general subject of irradiation effects in glass is included. Details are given for smoky quartz, because of its similarity to smoky feldspar. Blue barite and celestite are briefly mentioned because their spectra resemble that of amazonite. In anticipation of the amazonite results, the visible, ultraviolet, and EPR spectroscopy of lead are extensively described, and the effect of hydrogen ions on irradiation colors is covered in detail.

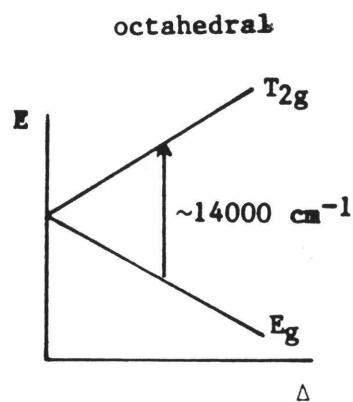
1.2.b.i Visible and ESR spectroscopy of Cu^{+2}

As a major element constituent, divalent copper is known to cause the blue-to-green colors of minerals such as diopside $\text{CaSiO}_2(\text{OH})_2$ [Newham and Santoro, 1967], azurite $\text{Cu}_3(\text{CO}_3)_2(\text{OH})_2$, malachite $\text{Cu}_2\text{CO}_3(\text{OH})_2$ and turquoise $\text{CuAl}_6(\text{PO}_4)_4(\text{OH})_8 \cdot 5\text{H}_2\text{O}$. In minor amounts Cu^{+2} also colors glasses [e.g. Weyl, 1951, p. 154-167], calcite CaCO_3 , and smithsonite ZnCO_3 blue or green. The colors are easily explainable by crystal field theory. Copper +2 has a d^9 configuration, so in an octahedral field, it will have one transition, E_g to T_{2g} , that will give a broad, unpolarized absorption. However copper +2 is susceptible to Jahn-Teller distortions, so that distorted octahedral sites are energetically favorable [e.g. Griffith, 1961, p. 300]. This leads to splitting of the energy levels and extra absorption features. For comparison, Figure 1.14 shows the optical absorption spectra and band assignments for Cu^{+2} impurities octahedrally coordinated in various glasses [Wong and Angell, 1976, p.287]; Figure 1.15 shows Cu^{+2} octahedrally and tetrahedrally coordinated in spinel CuAl_2O_4 [Reed, 1973]; and Figure 1.16 shows Cu^{+2} in square-planar coordination in Egyptian blue ($\text{BaCuSi}_4\text{O}_{10}$) [Clark and Burns, 1967]. The blue to green colors are due to the transmission maxima. It is significant that the band positions for octahedral and square planar coordinations are nearly the same and that the chemistry does not exert a strong influence on the spectra. Apparently, copper distorts its environment to achieve energetically favorable sites. If Cu^{+2} were located in the feldspar-site, its absorption spectra should consist of a broad band centered on 630-850 nm, that may or may not be polarized.

EPR spectroscopy of Cu^{+2} is well known (see for example [Goodman and Raynor, 1970] p. 313-324; Abragam and Bleaney, 1970, p. 455-466] and

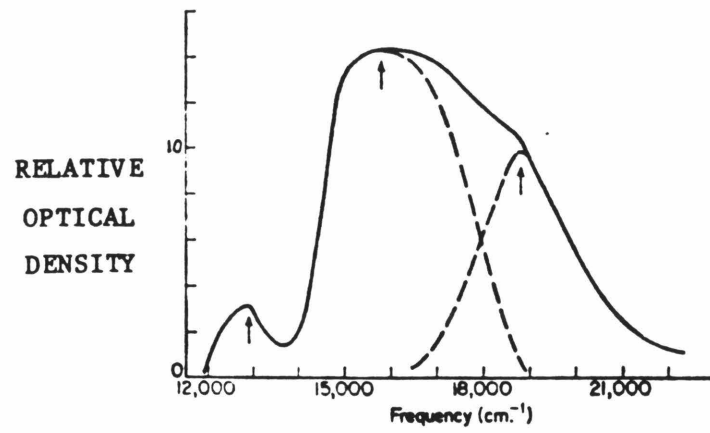


a

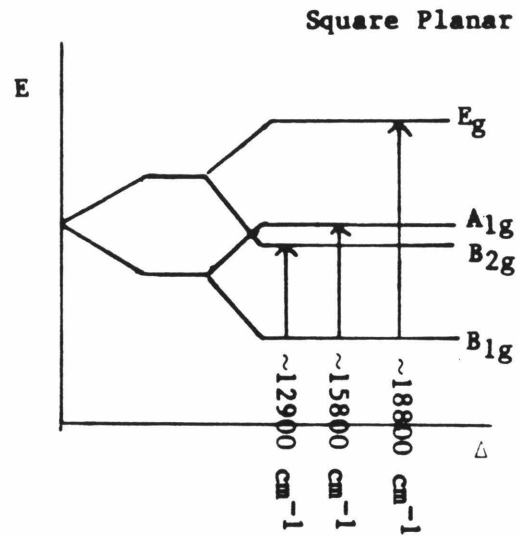


b

Figure 1.14 Optical absorption spectra and energy level diagram for Cu^{2+} octahedrally coordinated in glass. The spectra are from Wong and Angell [1976, p. 287].

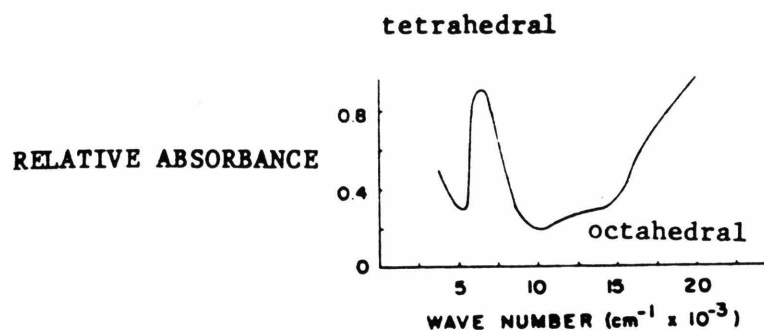


a

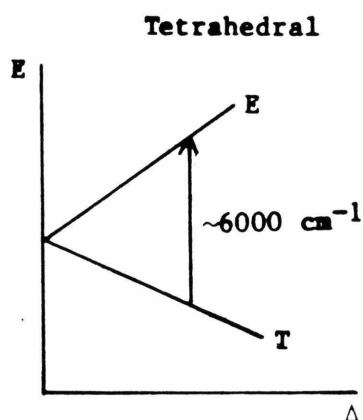


b

Figure 1.15 Optical absorption spectrum and energy level diagram of Cu^{2+} in square planar coordination in Egyptian blue $\text{BaCuSi}_4\text{O}_{10}$. From Clark and Burns [1967].



a



b

Figure 1.16 Optical absorption spectrum of Cu^{2+} in tetrahedral (6000 cm^{-1} band) and octahedral (12000 cm^{-1} band) coordination in CuAl_2O_4 . From Reed, [1973]. Although Cu occupies octahedral sites 67%, the intensity of the **octahedral** band is much less than that of the tetrahedral band because of the selection rules [e.g. Burns, 1970]. The energy level diagram is for tetrahedral Cu^{2+} .

references in both. The single unpaired electron of Cu^{+2} would undergo one transition in a magnetic field, except that interactions of the electron with the copper nuclei having nuclear spin I of $1/2$, split the one transition into $2I + 1$. Copper's EPR spectra are further complicated because two isotopes exist with only slightly different EPR characteristics, and because Cu^{+2} is subject to Jahn-Teller distortions. For highly symmetric octahedral sites, the latter effects serve to broaden the spectra giving the four first derivatives seen in Figure 1.17 [e.g. Abragam and Bleaney, 1970, p. 465-466]. For very distorted sites, both effects are apparent in the EPR spectra (Fig. 1.18), but the four first derivatives still stand out. For feldspar with Cu^{+2} in the irregularly coordinated M-site, EPR spectra similar to Fig. 1.18 are expected.

1.2.b.ii Noble metal colloids in glass

As will be shown in Chapter 7, the colors in Lake County labradorite are related to the exsolution of copper metal. This section will discuss a similar process in a different, but well-studied medium.

Depending on the size of the metal colloid, several kinds of color can be produced in glass. The largest colloids, ranging from $\sim 0.5 \mu\text{m}$ ($5 \times 10^5 \text{ nm}$) to $\sim 1000 \text{ nm}$ yield aventurine effects in reflected light [e.g. Weyl, 1951, p. 421]. Moderately large colloids of about 1000 nm to a few hundred nanometer produce an opaque, colored glass (copper hematine) [Weyl, 1951, p. 421]. Colloids ranging from several hundreds of nanometers to $\sim 70 \text{ nm}$ scatter light, giving a cloudy-brown or livery color in reflected light, but a blue color in transmission [Williams et al, 1981]. Small colloids ranging from about 70 nm to a few nanometers do not scatter light, but produce color through the intrinsic absorption of the metal

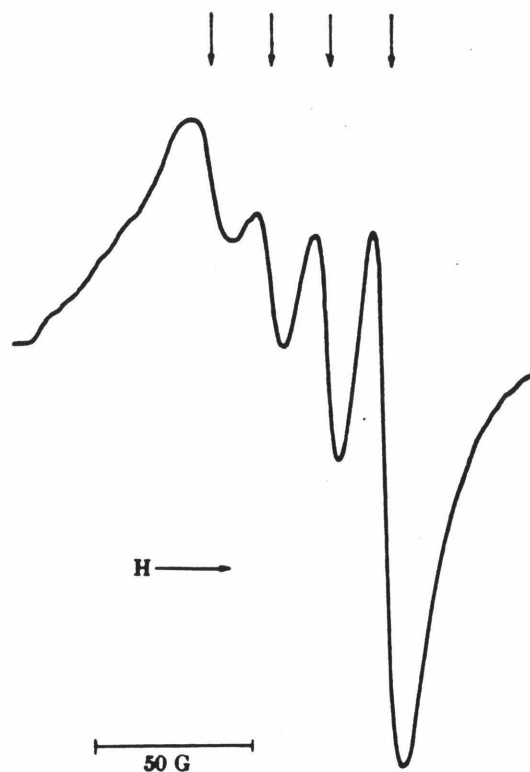


Figure 1.17 EPR first derivative spectra of Cu^{2+} for nearly octahedral coordination of Cu^{2+} in MgO at 77K. From Orton et al [1961]. Jahn-Teller distortions tend to broaden the transitions so that the differences in hyperfine structure of the two $I = 3/2$ nuclei Cu^{63} and Cu^{65} disappear. For Cu^{2+} in MgO , the g -factor is 2.19 and the A -factor is $190,000 \text{ cm}^{-1}$. The arrows indicate the four transitions due to nuclear spin of $3/2$.

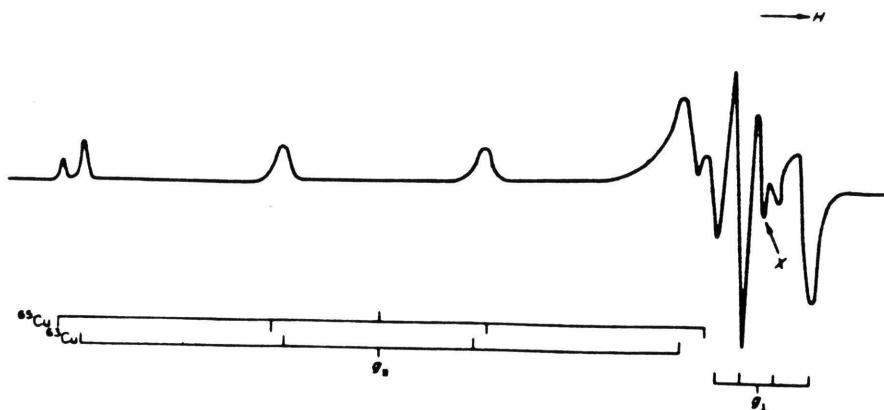


Figure 1.18 EPR of distorted octahedral coordination of Cu^{2+} in $\text{Cu}(\text{CH}_3\text{COCHCOCH}_3)_2$ in CHCl_3 at 77K. From Goodman and Raynor [1970]. The hyperfine structure for the two isotopes is visible here. g_{\parallel} is 2.285; g_{\perp} is 2.042; A_{\parallel} is $175 \times 10^4 \text{Cu}^{-1}$; A_{\perp} is $28.2 \times 10^4 \text{cm}^{-1}$. The line marked x is a forbidden transition.

(copper-ruby) [e.g. Weyl, 1951, p. 420-423]. Very small particles will not produce color, but the upper limit for the size of these colorless colloids is not precisely known. For each of these types, the physical origin of the color, along with the conditions needed to produce the color, will be discussed in detail. The behavior of copper metal in glass will be stressed, but the effects of silver and gold in glass will be included where pertinent. Lastly, the mechanisms of colloid formation will be examined in order to explain why different size colloids (colors) develop under various conditions.

Aventurine effects in glass are equivalent to those in feldspar, except that the metallic flakes are not oriented. Goldstone is the commercial name for aventurine glass with metallic copper inclusions (and was used by Aitkens [1937] to describe Lake County sunstone). Although this glass has been manufactured since ancient times, the nature of color formation was not understood until Wohler [1843] noted that the habits of the shiller (triangles, hexagons, and cubes) were identical to copper crystals precipitated from salts and concluded that aventurine in glasses was also due to precipitation of metallic copper [referenced in Weyl, 1951, p. 420-423]. Auger [1907] separately analyzed the flakes by dissolving the glass matrix, thereby proving that the aventurine is due to Cu^0 [referenced in Weyl, 1951, p. 423]. The composition of the base glass is not fixed, although alkali-silicate glasses are commonly used. To produce aventurine effects a few % of copper oxide is needed [e.g. Tress, 1962b], and also some type of reducing agent [Fremy and Clemandot, 1846; as referenced in Weyl, 1951, p. 422]. Cooling under moderate to strong reducing conditions is necessary to produce aventurization because it permits exsolution of metallic copper at high temperatures and thus low

viscosities so that large flakes form [Dietzel, 1945]. Slow cooling aids this process [Weyl, 1951, p. 422-423; Tress, 1962b].

Copper hematinone glass is opaque and bright red due to precipitation of metallic copper [Weyl, 1951, p. 421-423; Tress, 1962b]. It is distinguished from aventurine by having smaller, but more abundant Cu^0 clusters which are numerous enough to produce opacity and too small to produce a metallic reflection [Ebell, 1874, as cited in Weyl, 1951, p. 423-424]. Hematinone is made from low viscosity glass such as lead glass with >5% copper oxide, iron oxide, and sometimes tin oxide [Weyl, 1951, p. 422; Tress, 1962b]. The glass must be cooled quickly under reducing conditions, and then either held at 800°C for several hours [Tress, 1962b], or reheated [Weyl, 1951, p. 423-424]. The essential difference between hematinone and aventurine glasses is the heat treatment: the more rapid cooling of the hematinone provides many small nuclei and the later heat treatment allows growth of the colloids to remove any copper left in the glass [Weyl, 1951, p. 424].

The transparent copper-ruby, silver-yellow, and gold-ruby colors are a classical representation of glasses colored by colloids, and have been the object of many scientific investigations. Reviews on the history of the ruby-colors and on the scientific research are given by Dietzel [1945], Stookey [1949a], Weyl [1951, p. 331-435], and Williams et al [1981]. The scientific basis for understanding the ruby color was established by Faraday [1857]. His experiments on metal films and solutions proved that the intense red colors of hydrosols are due to the presence of finely subdivided metallic gold particles; that the gold's colloidal color is unaffected by the surrounding medium suggests that the red color is intrinsic. Faraday [1857] deduced that the color of ruby glass is due to

metallic gold in separated and diffuse particles. Through ultramicroscope observations, Ebell [1874; referenced by Weyl, 1959, p. 403] concluded that the colors of copper-ruby and silver-yellow glasses were also due to metallic particles, and that the differences in the properties of copper-ruby, hematine, and aventurine were caused by variation in crystal size. Zsigmondy [1909] confirmed the existence of colloidal gold in gold-ruby glasses and demonstrated that the colloids have a wide range of sizes. Using an ultramicroscope, Zsigmondy observed colloids as small as 40 nm, and postulated that the gold even existed in metallic clusters of atomic dimensions. (This is the origin of the metallic solution hypothesis.) Mie's [1908] theoretical treatment along with Steubing's [1908] extension and experiments on the optical properties of colloidal metals showed that the color results from absorption, not light scattering. Further theoretical study by Gans [1912] showed that gold ruby color results from spherical particles. (For an English summary of these early analyses and for later theoretical developments see Stookey et al [1978]; Perenboom et al [1981] and references cited in both.) Both theory and observations agree that the upper limit for a good ruby color is about 70-100 nm. The lower limit may be about 2 nm, because this is the smallest size for which colloidal gold particles still give X-ray patterns identifiable as metallic gold [Scherrer and Staub, 1931]. Gold particles at this range produce an intense absorption band at ~ 530 nm [e.g. Weyl, 1951, p. 375] while silver colloids absorb at ~ 415 nm [e.g. Stookey et al, 1978], and copper at ~ 550 nm [e.g. Weyl, 1951, p. 431]. (See Figure 1.19.) The extinction coefficient of these colors is probably large because concentrations of only 10 ppm Ag^0 are sufficient to produce readily observable color [Stookey et al, 1978].

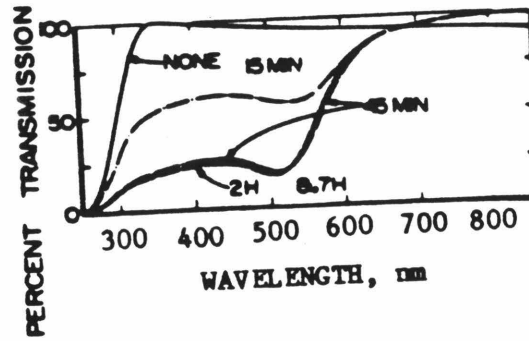


Figure 1.19 Visible spectra at gold ruby glass taken after various stages in annealing (none, 15 min, 45 min, 2 hour, 8.7 hours) for a glass with 0.04 % Au and 0.20% SnO₂. From Williams et al [1981].

Sometimes at the onset of color formation, silver bearing glasses are red [Forst and Kreidl, 1942] while gold glasses are purple [Weyl, 1959, p. 378]. These less common colors have been attributed to irregularly shaped particles by Weyl [1951, p 378]. Later work on silver bearing glasses by Stookey and Araujo [1968] and Stookey et al [1978] has proved that varying the elongation of the silver particles does indeed yield a wide range of colors through the combination of one absorption band at 360 nm and another in the visible whose position depends on the eccentricity. (For spherical particles, the bands merge at 415 nm.) Stookey et al [1978] developed the elongated particles through nucleation of Ag° on grains of sodium and silver halides. This development explains Forst and Kreidl's [1942] observation that introduction of silver as a halide allows production of the silver-red color, while addition of Ag_2O to the glass does not.

In summary, the transparent colors of ruby- and related glasses are due to the absorption of light by small noble metal clusters too small to scatter light. (This phenomenon is not limited to glasses: implantation of Au° in rutile (TiO_2) also yields absorption spectra of small metal aggregates [Guermazi et al, 1980].) If the noble metal colloids do obtain sizes large enough to scatter light (~ 70 to 300 nm), then the ruby-glass is spoiled and a livery color appears. The absorption colors are modified by the scattering colors so that the glass appears blue in transmission [Weyl, 1951, p. 370]. Light reflected from the colloids is brown [Williams et al, 1981]. (Colors purely due to scattering will occur if the metal is not noble, but alkalic. Although I will not discuss the details of this coloration it is of interest that colloidal coloring by alkali metals has been observed in minerals such as alkali halides [see

e.g. Hobbs et al, 1974; Schulman and Compton, 1962, Ch. IX] and fluorite [e.g. Bill and Calas, 1978].)

The chemistry and heat-treatment for small colloid formation in ruby glass has been the focus of many studies. Ebell [1874; cited in Weyl, 1951, p. 424] observed that ruby-color developed in glasses with copper oxide and tin on Fe_3O_4 under reducing conditions. Williams [1914; cited in Weyl, 1951, p. 426] showed copper-ruby formation is strongly dependent on the heat treatment (melting temperature, rate of cooling, and annealing or striking temperature), and that factors such as base glass composition and copper oxide content are of minor importance, except that addition of lead oxide increases the brilliance of the ruby color. Copper contents are however limited to 0.2 wt %, although in high lead content glasses up to 2% Cu_2O can be added and the glass will still give a good ruby [Weyl, 1951, p. 428 & 432]. Dietzel [1945] showed that additions of polyvalents such as SnO , FeO , As_2O_3 , Sb_2O_3 , Ce_2O_3 or PbO were essential to good ruby-color formation and that oxygen fugacity in the melt dictated the results (see Table 1.8 and 1.9). Without the polyvalents, a livery color (spoiled ruby) will develop [Stookey, 1949a]. Ruby color develops upon slow cooling, but is usually induced in a colorless quenched glass through annealing [Dietzel, 1945]. This process is reversible, so the glass can be cycled from colorless to red and back [Tress, 1962]. Copper, silver, and gold bearing glasses behave nearly the same except that with increasing nobility, increasing f_{O_2} and decreasing metal contents are needed to produce intense, transparent colors [Dietzel, 1945; Stookey, 1949a].

To account for these observations, two types of theories for the mechanism of coloration have been proposed. The metallic solution proponents, originally Zsigmondy [1909; cited in Stookey, 1949a], held

Table 1.8 Conditions for Copper-ruby formation [Dietzel, 1945]

% H ₂ in N ₂ -H ₂ mixture	Color of borax-glass with 0.1 % CuO	Color of borax-glass with 0.1 % CuO and 0.5 % SnO ₂	EMF (volts)
0	blue	blue	0.09
1.0	light blue	light blue	0.45
1.3	colorless	red patches	0.48
2.9	light grey	colorless if quenched; clear, bright red if slowly cooled	0.56
5.8	light grey with exsolved Cu ⁰ flakes	"	0.63
33.	"	"	0.87

Table 1.9 Noble metal oxygen fugacity transitions
in borax-glass [Dietzel, 1945]

Transition	fO ₂
Cu ⁺² → Cu ⁺¹	10 ⁻³ to 10 ⁻¹⁰
Cu ⁺¹ → Cu ⁰	2x10 ⁻¹²
Ag ⁺¹ → Ag ⁰	~ 10 ⁻²
Au ⁺¹ → Au ⁰	~ 10 ⁴

that the metal dissolves in the melt as atoms; cooling develops nuclei; and reheating causes coagulation and growth of the colloids to coloring size. The ionic solution proponents, (originally Rose [1848] and Silverman [1932], as cited by Stookey [1949a]) held that the metals dissolved as ions and that low temperature heat treatment reduces the metal which then exsolves and aggregates. Experimental evidence indicates ionic solution:

- (1) Color develops once pO_2 in the glass melt falls below a specific value, which increases with increasing nobility [Dietzel, 1945].
- (2) Because of the extreme nobility of gold, oxidizing agents are required for gold-ruby formation [Silverman, 1952] otherwise gold precipitates [Dietzel, 1945; Stookey, 1949a]. Copper-ruby, on the other hand, requires mildly reducing conditions [Dietzel, 1945; Stookey, 1949a].
- (3) Irradiation of gold-bearing glass also containing a photo-reducing agent such as cerium produces gold-ruby color [Stookey, 1949b].

There is uniform agreement that copper and silver are ionically coordinated in glass, yet a few researchers still contend that gold at least partially solvates as metal in the glass. Weyl [1953] reasoned that the addition of Pb to the gold glass allowed solvation of Au^0 in the network because Pb^{+2} is electronically asymmetric [e.g. Wells, 1962, p. 245] such that its Pb^{+4} side would bond to the glass network and its Pb^0 side would be compatible with Au^0 (similar reasoning holds for tin.) This cannot be correct because Williams et al [1981] were able to hold gold in solution (or precipitate it) in a polyvalent-free glass by controlled thermal treatment. Tress [1962a and b] argued that gold exists as both Au^0 and Au^{+1} in glass in a fixed ratio depending on fO_2 , T, and the chemistry of the glass. This is correct, but the question then is, to what degree is gold incorporated as Au^0 ? Because the ruby-glasses have at most 10 ppm gold,

it is not the gold which controls its oxidation state, but rather the other constituents in the glass, or external conditions. Gold must be initially ionically incorporated because (1) Stookey [1949a and b] and Dietzel [1945] showed that reduction induces precipitation and color so that there cannot be a significant amount of Au° in solution in a glass without the color forming and (2) gold-ruby colors form in the same manner as copper-ruby or silver-yellow colors which require initial ionic solution.

Several different reactions have been proposed for the reductions leading to the ruby colors: (1) Simple dissolution of the oxide [Auger, 1907; as cited by Dietzel, 1945]; (2) Self-reduction: $\text{Cu}_2\text{O} = \text{Cu}^\circ + \text{CuO}$ [Granger, 1923; as cited by Dietzel, 1945]; and (3) Reduction mediated by a polyvalent: $\text{Cu}_2\text{O} + 2\text{FeO} = 2\text{Cu} + \text{Fe}_2\text{O}_3$ [Beyersdorfer and Beyersdorfer, 1943; as cited by Dietzel, 1945]. For photosensitive glass, reaction (2) does lead to copper-ruby color [Stookey, 1949b]. Reaction (1) does occur in copper bearing glasses, but lends toward production of large colloids. Copper-ruby is produced by reaction (3) or similar reactions with polyvalents such as As, Sn, Sb, Se, Te, Pb, Sb or the like. The development of copper-ruby colors can be explained by the change in chemical equilibria curves with temperature (see Fig. 1.20). In all cases, the glass melt is initially at a certain oxygen fugacity. Most components in the glass do not undergo oxidation/reduction reactions and will not affect the fugacity. However, copper and the polyvalents (Sn for example) do have temperature and fugacity dependent oxidation states, and these do have an effect on the state of the glass. If the glass is slowly cooled in a controlled atmosphere, then the path will lie along a constant $f\text{O}_2$ line, and this will lead to an increase in the oxidant/reductant ratio. Thus, for glasses with copper (and without tin), if the glass begins colorless

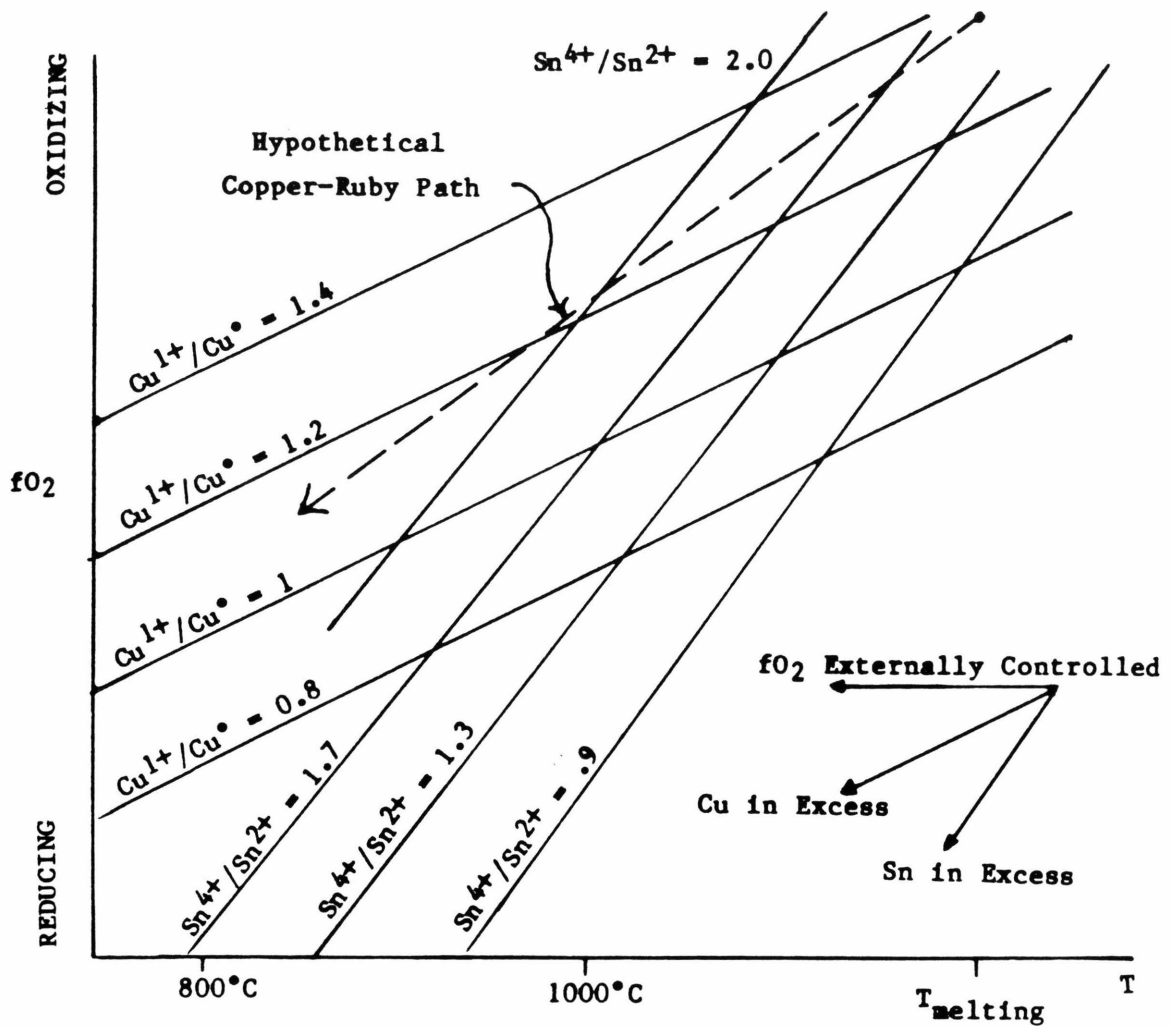


Figure 1.20 Cartoon of the cooling history of copper-ruby glass. The curves of constant $\text{Cu}^{1+}/\text{Cu}^{\circ}$ ratio and constant $\text{Sn}^{4+}/\text{Sn}^{2+}$ ratio are sketched here. Their exact position is not known, but the steeper slope of the Sn curves is a certainty [e.g. Tress, 1962a]. Vectors are shown for the thermal path the glass would follow for the three cases: f_{O_2} is constant, CuO is the only multi-charged substituent, or SnO is the only multi-charged substituent. For the case of copper ruby glass cooled slowly, the path will be in between the Cu-in-excess and Sn-in-excess lines as indicated by the dashed line. In this way, the copper will be reduced at low temperatures so that exsolution and aggregation is limited to small flakes.

(high $\text{Cu}^{+1}/\text{Cu}^{\circ}$), it will remain colorless, but if it begins with a low $\text{Cu}^{+1}/\text{Cu}^{\circ}$, it will exsolve metal at high temperatures. In the later case, the concurrent low viscosity permits aggregation of large to moderately large flakes (adventurine or hematine) depending on cooling rate [cf. Dietzel, 1945]. If the amount of CuO is high, or if the fugacity is not externally controlled, then the thermal path will follow the line of constant $\text{Cu}^{+1}/\text{Cu}^{\circ}$ ratio [cf. Tress, 1962a]. In this case, copper may exsolve over a range of temperature, producing both large and small flakes (livery-ruby color). For copper-free glasses, with a large amount of tin (SnO_2), the thermal path can be buffered along the line of constant $\text{Sn}^{+4}/\text{Sn}^{+2}$ [cf. Tress, 1962]. For glasses with both CuO and SnO_2 , the thermal path depends on the ratio of Cu to tin and on the extent of external fugacity control. For glasses with higher amounts of tin than copper, the thermal path falls between the copper and tin in excess paths (see Fig. 1.20) so that as the glass cools $\text{Cu}^{+1}/\text{Cu}^{\circ}$ decreases as $\text{Sn}^{+4}/\text{Sn}^{+2}$ increase. Thus, with the proper initial oxygen fugacity, reduction and exsolution will occur at a low temperature, resulting in smaller colloids and copper-ruby color [Dietzel, 1945].

In summary, color-production is dictated by the oxygen fugacity within the glass. This can be effected by external agents, but it is the presence of internal buffers (such as $\text{Pb}^{+4}/\text{Pb}^{+2}$ ratio) that allow copper-ruby formation. The size of the colloid depends on the temperature at which reduction of Cu^{+1} to Cu° is initiated. This can be attributed to the glasses strong viscosity dependence on temperature; apparently high viscosity inhibits growth of colloids. Aggregation probably occurs by diffusion. Small angle X-ray scattering experiments by Williams et al [1981] show that Ostwald ripening does not occur: once colloids are formed, the larger ones do not grow at the expense of smaller ones during later heat treatment.

1.2.b.iii Irradiation Centers in Glass

Ionizing radiation (X-rays or γ -rays) frees electrons in solids primarily through Compton scattering. The free electrons then migrate through the lattice freeing less tightly bound electrons and creating electron deficient regions (holes) [e.g. Lell et al, 1966]. Pre-existing defects such as vacancies, interstitial atoms, multivalent impurities, or non-bridging oxygens trap some of the electrons and holes [e.g. Bishay, 1970]. Figure 1.21 schematically depicts several of these traps in a stylized two-dimensional glass structure. (The defects are described in the figure caption). Traps which absorb visible light are known as color centers. Because this property makes them amenable to spectroscopic study, color centers have been the focus of a great deal of research. Properties of the color centers have been deduced from the effect of irradiation, heat treatment and oxygen fugacity on the optical spectrum [see e.g. Wong and Angell, 1976, p. 356]. Similarly, the charge state of the center has been determined by adding multivalents such as Ce^{+3} , which reacts with holes to form Ce^{+4} [Stroud, 1962] or conversely by adding electron scavengers such as Fe^{+3} [Mackey et al, 1966a] or Pb^{+2} , Ag^{+1} , or Cd^{+2} [Treinin, 1968, pp. 543 and 562]. However, absolute identification of the center can only be achieved through correlation of optical intensity with ESR spectral intensity. Identification is difficult because: (1) The visible and ultraviolet spectrum of most irradiated glasses is composed of several broad overlapping peaks ranging from 250 nm to 1250 nm [Bishay, 1970] which arise from many different centers and (2) Factors such as structure, composition, trace impurities, fO_2 and temperatures of radiation and annealing do influence the optical absorptions [e.g. Bishay, 1970; Wong and Angell, 1976, p. 357]. Accordingly,

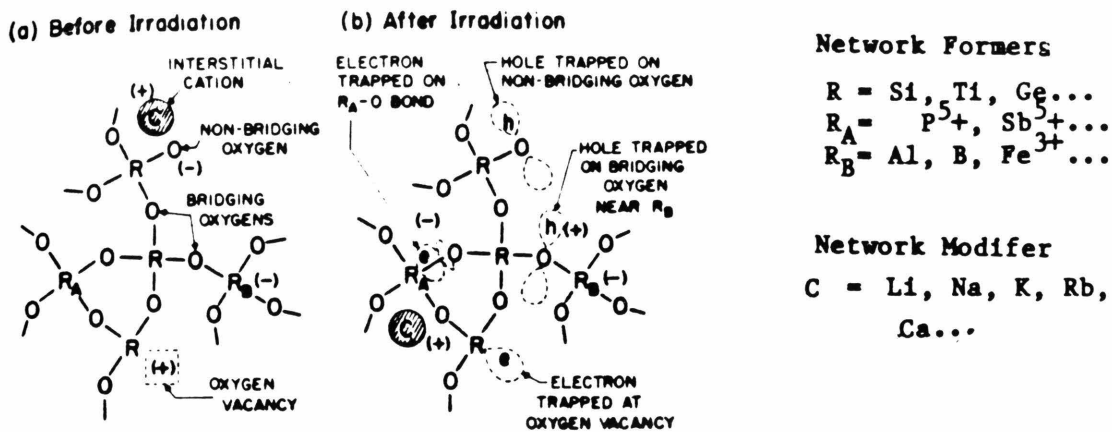


Figure 1.21 Radiation defects in silicate glasses. From Griscom [1973].

Schematic diagram of a silica glass showing the relationship of pre-existing defects (a) with radiation-induced paramagnetic centers (b). As shown, the trapped species are locally charge compensated. However, individual trapped holes and electrons would be much more distant than depicted here. The common traps illustrated are: (1) E1 center. An oxygen vacancy occurring next to a silicon produces a region of positive charge which can trap electrons. (2) X-hole traps. If a +3 charge network former like Al is tetrahedrally coordinated, and isolated from a charge compensating cation, then the complex has a net negative charge and will attract holes. Usually the hole is located on a coordinating cation. Charge compensated defects will also form hole centers if the cation is "ejected" by radiation. (3) Non-bridging oxygens. Addition of alkalis to SiO₂ glass creates singly bonded oxygens and a region of negative charge which can trap holes. (4) Interstitial cations. These have been shown to trap electrons in borate glasses and may do the same in silicate [Griscom, 1973]. (5) X-electron traps. Tetrahedral coordination of Ge or P in silicate glass results in centers with an affinity for electrons. Stability of the trap increases when an interstitial cation is located nearby.

the nature of color centers is broadly understood, but considerable controversy remains over the details of interpretation [see Wong and Angell, 1976, p. 355]. Much of the difficulty in understanding how radiation damage affects glasses stems from the fact that the irradiative states are highly dependent on the temperature and time scale of observation [Wong and Angell, 1976, p. 359]. Hence, care must be taken in comparing results.

This section will discuss irradiative colorations relevant to feldspar coloration: (1) color centers in alkali- and alumino-silicate glasses; (2) Pb-associated color centers; and (3) the apparent predominance of hole over electron centers. A later section will cover the influence of hydrogen and water on irradiative coloring of glasses and minerals. For further details of the irradiation process the reader should consult reviews by Lell et al, 1966; Treinin, 1968; Bishay, 1970; Griscom, 1973; Wong and Angell, 1976, Sec. 6.5; and Friebele and Griscom, 1979].

In alkali-silicate and alumino-silicate glasses, as in most irradiated glasses, visible absorptions are generally associated with oxygen-related hole centers while ultraviolet absorptions are often connected with electron centers [Bishay, 1970; Griscom, 1973]. Weeks and Nelson [1960] and Nelson and Weeks [1960] have shown that high energy bands at 200 to 250 nm arise from electron centers similar to E_1 and E_2 of (smoky) quartz. Stroud [1962] determined that the absorptions at 440 and 620 nm in silicate glasses with low alkali content were hole centers by addition of Ce^{+3} to the glass. Comparison of the behavior of these optical bands with radiation treatment and variation of alkali content of the glass, and to the response of the overlapping EPR signals near $g=2$ (H_2 and H_3) suggests that the 420 nm band is associated with H_2 and the 620 nm band is related to H_3 [Stroud, 1962;

Scheurs, 1967]. Scheurs [1967] proposed that H_2 is a hole trapped at two non-bonding oxygens, while H_3 is a hole trapped at three non-bonding oxygens. Kordas and Oel [1982] separated the two ESR signals (which they refer to as H_I and H_{II}) by computer modelling of the signals at different temperatures (Figure 1.22). Kordas and Oel [1982] correlated H_I (H_2) with the optical bands at 310 and 510 nm in silicate glasses with high alkali content and concluded from computer modelling that the center is a hole on a non-bonding oxygen near a silicon ion. This partially confirms the suggestions of Stroud [1962] and Scheurs [1967], because the 440 nm band shifts to 510 nm with increasing alkali content [Yokota, 1954]. The 620 nm band has not been quantitatively correlated with any EPR features. Conversely, neither have the EPR centers such as the hole H_3 (H_{II}) [Kordas and Oel, 1982] or the aluminum-oxygen hole [see Lell et al, 1966] been firmly linked with optical absorptions. But, it is likely that H_3 (which Kordas and Oel [1982] concluded was a hole trapped at two non-bonding oxygens near a silicon) is connected with the 620 nm band [Cohen and Makar, 1982].

In addition to the above intrinsic centers, alkali-silicate and alumino-silicate glasses are colored by impurities such as Ti, Ga, Sm, Yb, Eu, Mn, U, [Smith and Cohen, 1964] and Ce [Stroud, 1962]. Additives not only color the glass in the unirradiated state, but also can react with radiation to form supplementary absorption bands [Lell et al, 1966] or can serve to inhibit previous color centers [e.g. Treinin, 1966]. The consequences depend on the type of impurity and factors such as f_{O_2} and temperature. For example, addition of a few % of Ti to alkali silicate glass under reducing conditions suppresses the 440 and 620 nm hole bands while adding another band at 540 nm [Smith and Cohen, 1964]. In general,

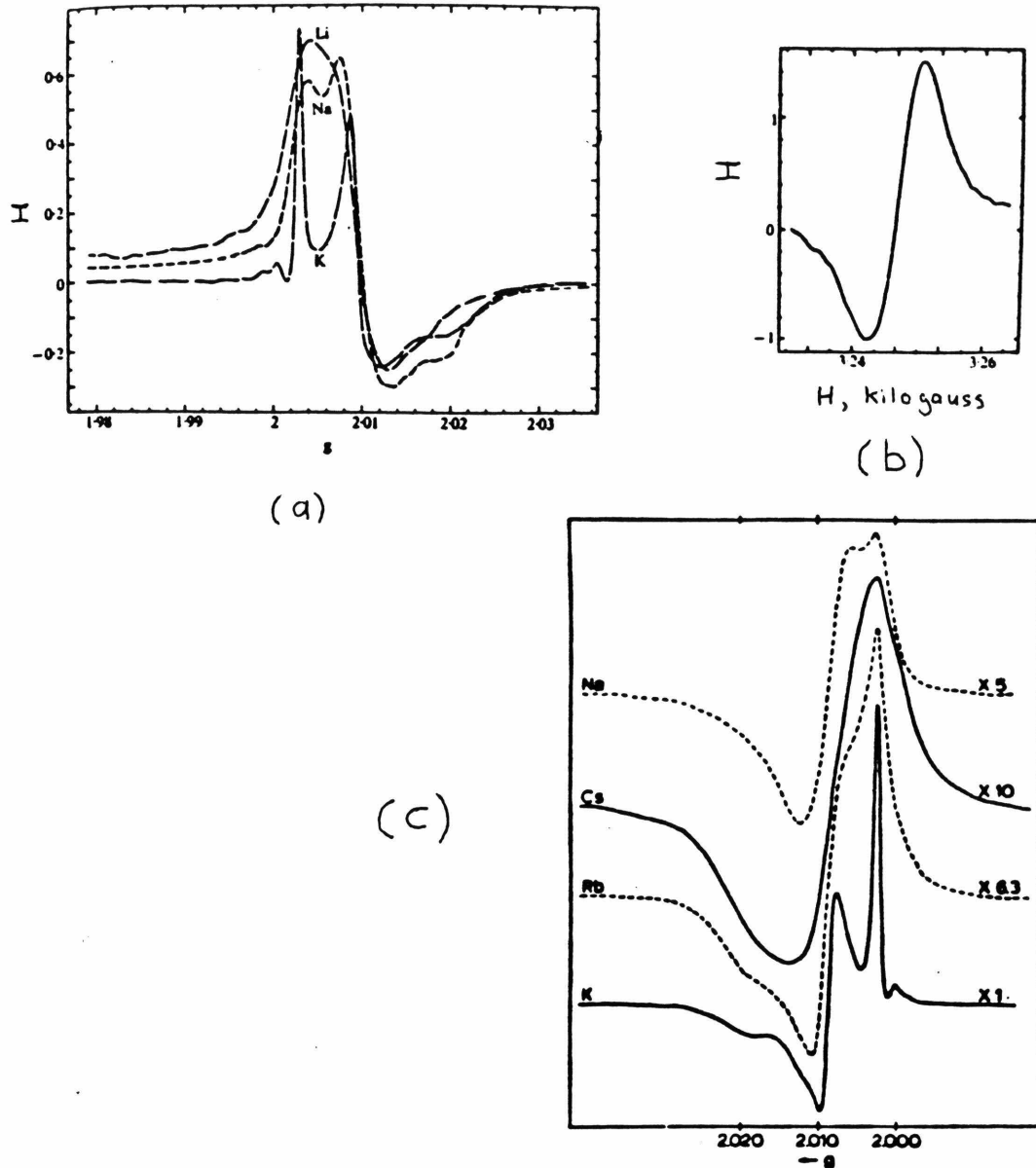


Figure 1.22 EPR spectra of the H_I and H_{II} centers in glass.

(a) Dependence of the shape and position of H_I center ($SiO^- - X$) on the type of alkali [Kordas and Oel, 1982]. (b) Shape of the H_{II} center for sodium silicate glass: for potassium silicate glass the position is the same, but the width is about 60% of that shown [Kordas and Oel, 1982]. (c) Shape of the combination of the two centers for glasses $X_2O \cdot 9 SiO_2$ [Scheurs, 1967].

multivalency is required for the cation to influence irradiative coloring and the result is determined by the efficiency with which the impurities, hole, and electron centers compete for the electrons and holes migrating during irradiation [e.g. Lell et al, 1966].

Incorporation of lead as an impurity ion in glass has been shown to suppress color center formation [Barkatt et al, 1981], but by itself has not been demonstrated to cause irradiative coloring. Minor additions of lead to glass do result in blue fluorescence after uv or cathode stimulation [Weyl, 1951, p. 489], but this is probably related to ultraviolet (~ 200 nm) Pb^{+2} transitions.

Glasses with lead as a major component exhibit several types of color centers. For example, lead silicate glasses have two broad absorption bands at 525 and 570 nm arising from an unknown center [Barker et al, 1965]. Lead borate glasses have a band at 825 nm, the intensity of which first increases with lead content and then decreases for PbO greater than about 35% [Bishay and Maklad, 1966]. This and the response of the color to oxidation and reduction suggest that the center is an electron trapped near lead [Bishay and Maklad, 1966]. However, an independent EPR study of lead silicate and lead borate glasses by Kim and Bray [1968] has shown that neither type possesses a paramagnetic center with features indicative of lead nuclei; instead, both glass-types develop ubiquitous O^- hole centers through irradiation which are probably interstitial. Thus, no color centers present in Pb-bearing glasses have been directly connected with lead, and the absorption spectra produced by irradiation remain unexplained.

For irradiated complex oxide glasses, the most commonly observed EPR signals come from oxygen-associated hole traps [Griscom, 1973]. In pure

silica glass, electron signals of E_1 and E_2 centers are easily distinguished [e.g. Weeks and Nelson, 1960a,b] but their intensity decreases as alkali content increases [Griscom, 1973]. No such correlation exists for hole centers, so that an apparent discrepancy exists between the number of hole and electron centers in high-alkali glasses [Griscom, 1973]. In particular, computer simulations of broad band signals in borate glasses suggest that the "hidden" electrons are trapped on alkali ions or shared among alkali clusters [Griscom, 1973]. It is not known whether these broad band ESR signals correlate with any optical bands, including the 520 to 830 nm bands which occur in high alkali borate [Arafa and Bishay, 1969]. Friebele and Griscom [1979] have suggested that electrons may be commonly trapped in pairs, in which case no EPR signal would be produced.

1.2.b.iv Smoky Quartz

A large number of investigations have been applied towards elucidating the nature of smoky quartz aluminum centers. Weil [1975] cited 125 references in his comprehensive review on aluminum centers in α -quartz. This section will briefly recapitulate Weil's [1975] summary and will review pertinent work since 1975.

Smoky color develops upon irradiation (with neutrons, γ or X-rays) of α -quartz with aluminum impurities. In unirradiated crystals, aluminum substitutes for silicon, with charge compensation occurring through local interstitial incorporation of H^+ , Li^+ or Na^+ [Weil, 1975]. EPR experiments and analyses thereof have firmly established that irradiation produces an unpaired electron which is trapped at one of the two oxygens closest to an aluminum ion [Griffiths et al, 1954; O'Brien, 1955]. (See Figure 1.23.) At approximately liquid nitrogen temperatures, this "hole" is shared

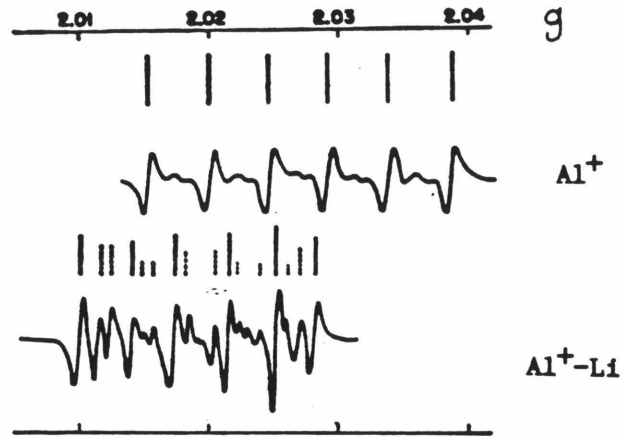


Figure 1.23 Smoky quartz's EPR derivative spectra and line positions for two kinds of aluminum oxygen hole centers in quartz. From Mackey [1963]. The spectrum labeled Al^+ is of an uncompensated center. The spectrum labeled Al^+-Li is of a center with a nearby lithium compensator. Both are for the magnetic axis parallel to \underline{c} at 77K.

between the two closest oxygens [Taylor and Farnell, 1964]; while at room temperature the hole migrates among all four coordinating oxygens [Schnadt and Schneider, 1970]. Irradiation creates the center by independently displacing an electron and the compensating cation to other trapping sites in the crystal such as Ge or Ti [e.g. Weil, 1975]. The complications that arise when the compensation is a hydrogen ion rather than an alkali ion will be discussed in Section 1.2.b.vii.

Early optical studies [see Weil, 1975 and references therein] attributed the smoky color to two anisotropic bands (A_1 at ~ 620 nm and A_2 at ~ 460 nm). Nassau and Prescott [1975 and 1977] have shown that the smoky color is actually produced by the A_3 band at 428 nm (shown in Figure 1.24) which correlates with the aluminum-hole center seen in the ESR, and that the A_1 and A_2 bands by themselves produce a blue color and are not correlated with the ESR center. Schirmer's [1976] calculations suggest that the A_3 band results from hopping of the electron between the oxygens. Cohen and Makar [1982] have suggested that A_2 is analogous to H_2 and A_1 is analogous to H_3 , where H_2 and H_3 are hole centers in alkali-silicate glasses as discussed in Section 1.2.b.iii.

Also present in smoky quartz are the E_1 and E_2 bands [Nassau and Prescott, 1975]. These bands are located at 210 and 230 nm respectively [Lell et al, 1966] and have been shown to arise from electron centers: E_1 is an electron trapped at an oxygen vacancy [Weeks, 1956; Weeks and Nelson, 1960 a,b], and E_2 is an electron trapped at SiO lattice vacancy with a proton nearby [Weeks, 1963]. The vacancy in the lattice could equally well be SiO₂ [Lell et al, 1966].

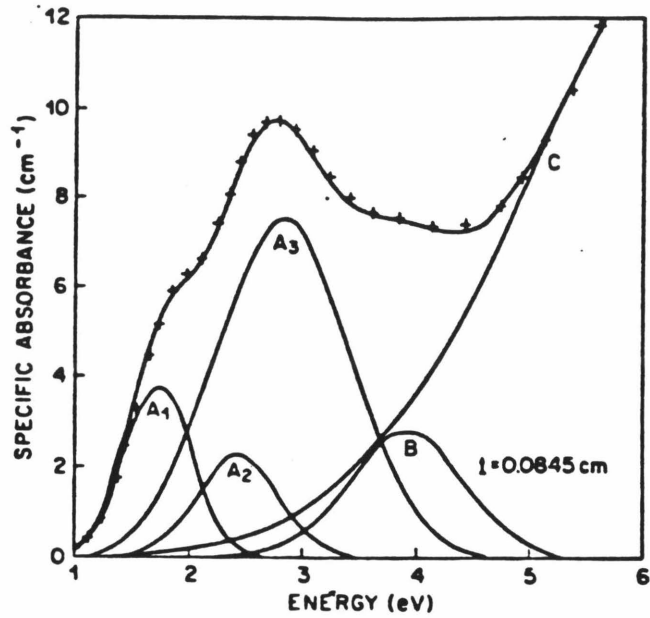


Figure 1.24 Smoky Quartz Optical Spectrum. This gaussian decomposition is of the π spectrum of a smoky quartz crystal after saturation with X-rays. From Nassau and Prescott [1977]. Only band A_3 at 2.9 eV is connected with the EPR signal and the smoky color. Then bands at A_1 and A_2 by themselves yield a blue color. A_1 is at 1.85 eV. A_2 is at 2.55 eV.

1.2.b.v Pb absorption spectra and EPR of Pb in crystalline solids

Unlike glasses, crystalline materials commonly yield features attributable to lead upon irradiation. The lead ion can only produce EPR spectra if its oxidation state is +1 or +3. Because the magnetic properties of lead nuclei are distinct from those of any other elements (21% of lead exists as Pb^{207} with nuclear spin of $1/2$, while the rest have $I = 0$; see Goodman and Raynor, 1970, Table I), an EPR lead signal is unique. This easily identifiable signal must consist of one large peak with two smaller peaks each having $1/7$ the intensity of the large one [Goodman and Raynor, 1970, p. 219; Born, 1970]. Such spectra have been observed in 14 different crystalline solids (including natural calcite) which possess lead impurities and have been irradiated (see Table 1.10). A typical signal and its Breit-Rabi diagram are shown in Figure 1.25 and Figure 1.26. The EPR-lead signal is characterized by (1) a g -value near $g_{\text{free}} = 2.0023$ for the $I=0$ isotopes, (2) an apparent g -value < 2 for the $I = 1/2$ Pb^{207} isotope, (3) a large isotropic hyperfine splitting constant (A) for Pb^{207} , (4) substantial reduction of A from the free ion value, (5) small ($\sim 0.1\%$) anisotropy in A , and (6) presence of superhyperfine structure for ligands other than oxygen (see Table 1.10). Characteristics 1, 3, 5, and 6 require an electron in an $^2S_{1/2}$ state [Goodman and Raynor, 1970, p. 167; Born et al, 1976; Nishi et al, 1977], so that Pb^{+3} ($5d^{10}6s^1$) must be the resonance state rather than Pb^{+1} ($5d^{10}6s^26p^1$).

Table 1.10 shows that the g values of the $I = 0$ centers deviate both positively and negatively from the spectroscopic splitting factor of the free electron (2.0023). In general, a positive deviation indicates a hole center [Goodman and Raynor, 1970, p. 197], but admixture of ligands with

Table 1.10 Compilation of EPR data on Pb³⁺ impurities in crystalline solids

Host	Reference	Radiation	g(I=0)	A ²⁰⁷ cm ⁻¹	ΔA cm ⁻¹	g(I=1/2) (approx.) gauss	Super- hyperfine intensity	Prob. on Pb %	Coord. # of Pb	Coord. ligand	Max. Temp Pb ³⁺ was observed K
free ion	Schawlow et al 1949	-	-	2.60	-	-	-	100	-	-	-
calcite CaCO ₃	Popescu & Grecu 1975	γ, X	2.0056	1.262	0.001	-	ND	49	6	CO ₂ ²⁻	280
CaWO ₄	Born et al 1970,71,74	X	1.99	1.276	0.0013	7600	strong	40	4	WO ₄ ²⁻	215
KCl	Schoemaker & Kolopus 1970	γ, X	2.034	1.100	~ 10 ⁻⁸	8000	weak	41	6	Cl ⁻	220
PbF ₂	Nishi et al 1977	γ, n°	2.007	1.57	~ 0	7100	strong	60	8	F ⁻	200
ZnO	Born et al 1971b	not stated	2.013	0.808	~ 0	-	ND	31	4	O ²⁻	-
ZnSe	Holton & Watts 1969	γ	2.0729	0.6249	~ 0	-	ND	23	4	Se ²⁻	200
ZnTe	Suto & Aoki 1968	γ	2.133	0.523	0.02	-	ND	20	4	Te ²⁻	200
CaO	Born et al 1971b	γ, X	1.999	1.07	ND	-	ND	41	6	O ²⁻	200
CaSe	Yamashita & Asano 1976	not stated	2.173	0.6832	ND	>5000	present	24	4	Se ²⁻	200

Table 1.10 EPR of Pb^{3+} , continued

Host	Reference	Radiation	$g(I=0)$	A^{207} cm^{-1}	ΔA cm^{-1}	$g(I=1/2)$ (approx.) gauss	Super- hyperfine intensity	Prob. on Pb %	Coord. # of Pb	Coord. ligand	Max.Temp Pb^{3+} was observed K
ThO_2	Rohrig & Scheider 1969	γ	1.968	1.229	0.007	6500	ND	48	8	O^{2-}	300
$\text{Y}_3\text{Ga}_5\text{O}_{12}$	Andlauer et al 1973	X	2.002	1.264	BLD	7500	ND	49	8	O^{2-}	300
$\text{Lu}_3\text{Ga}_5\text{O}_{12}$	"	X	2.001	1.272	"	-	ND	50	"	"	"
$\text{Y}_3\text{Al}_5\text{O}_{12}$	"	X	2.002	1.339	"	"	"	52	"	"	"
$\text{Lu}_3\text{Al}_5\text{O}_{12}$	"	X	2.000	1.383	"	"	"	53	"	"	"

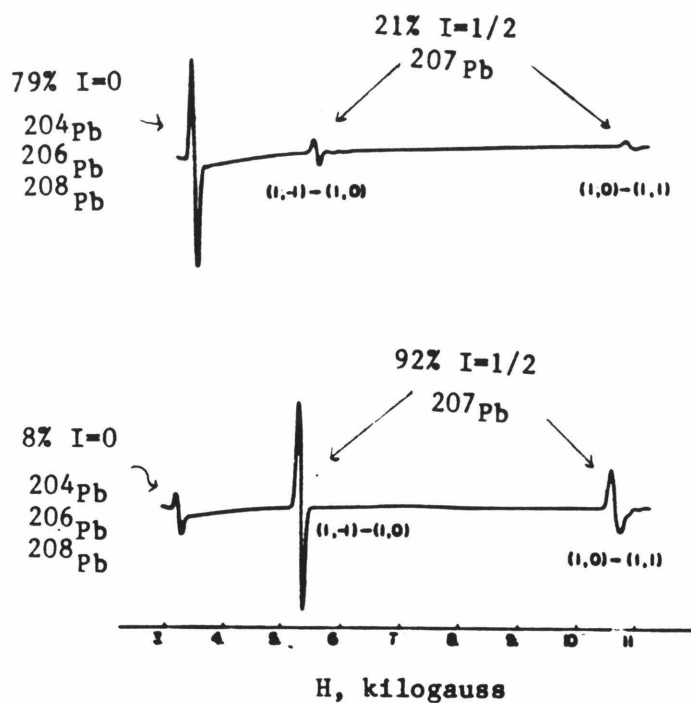


Figure 1.25 ESR spectra of Pb^{3+} in KCl. From Schoemaker and Kolopus [1970]. Both spectra were obtained at LN_2 temperatures after irradiation. The upper spectrum is from a crystal with normal lead. The lower spectrum is from a crystal enriched in Pb^{207} . The high field transition of the $I=1/2$ nucleus is weaker than the low field transition because in the strong field limit the former is forbidden [Schoemaker and Kolopus, 1970].

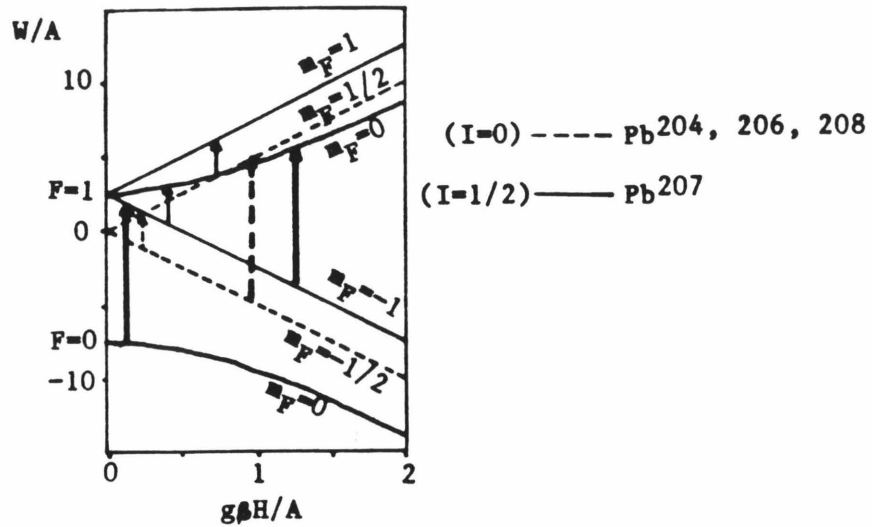


Figure 1.26 Breit-Rabi diagram for Pb^{+3} energy levels and transitions in ThO_2 . From Rohrig and Schneider [1969]. The solid lines are for the $I=1/2$ isotope, while the dashed lines are for the $I=0$ isotopes. The short thin arrows indicate 9.2 GHz transitions while the long thick arrows indicate 35 GHz transitions. Note that the $I=0$ transition is physically in between the $I=1/2$ transitions for 35 GHz excitation.

s-state ions will also lead to a positive g-shift [Watanabe, 1966]. The frequent occurrence of Pb^{+3} ions with g values less than 2.0023 suggests that the transition observed is the s-electron, rather than the s-hole, but does not mandate it. In either case, the probability P that the s electron or hole is located on Pb^{+3} is given by

$$P = \frac{A}{A_{free}} \cdot \frac{g_{free}}{g} \quad (1.6)$$

[Watanabe, 1966; Iida and Watanabe, 1968]. P less than 100% indicates sharing of the electron with the ligands. For the compounds listed in Table 1.10, the hyperfine splitting constant A is considerably reduced from the free ion value leading to probabilities from 20 to 60%. For the more ionic solids having oxygen ligands, P ranges from 31-53%. Note that delocalization is favored for tetrahedral coordination (P = 31 to 40%) over octahedral sites or duodecahedral sites (P = 41 to 53%) in agreement with Watanabe's [1966] theory of $S_{1/2}$ ions. The delocalization shows that the lead complex is alternating between $Pb^{+4} - Pb^{+3}$ or $Pb^{+3} - Pb^{+2}$. That the lead ions enter the crystal as Pb^{+2} suggests that the complex alternates between Pb^{+3} and Pb^{+2} . The frequent accompaniment of the lead center by electron centers [Born et al, 1970; Schoemaker and Kolopus, 1970; Popescu and Grecu, 1975; Nishi et al, 1970] corroborates that the lead center is a hole center.

The relative stability of the Pb^{+3} hole center is indicated by its behaviour with temperature. The centers are created by irradiation at liquid nitrogen temperatures; however, several centers persist even at room temperatures (see Table 1.10). Ostensibly, the electron delocalization (implied by the A-factor) contributes to the stability of the hole centers. That Pb^{+3} ($5d^{10}6s^1$) is isoelectronic with the stable Au^0 atom may also aid in its formation [Andlauer et al, 1973].

The ordinary oxidation state, Pb^{+2} , does not produce color, but the excitation of one of its 6s electrons to a 6p level (as shown in Figure 1.27) does produce absorptions in the ultraviolet. The wavelengths for these transitions and for those of isoelectronic Tl^{+1} are listed in Table 1.11. Oscillator strengths which are available for Tl^{+1} are also listed. For thallium and lead in the same environment (KCl) the transitions occur at nearly the same energy for the higher energy peaks while the energy of the lowest transition is only slightly smaller for lead than thallium. In contrast, substitution of lead into different matrices does affect the energy of the transitions.

Color may be associated with the Pb^{+3} hole center in some of the lattices. The apparent intensity of the yellow color in synthetic garnets is correlated with the Pb^{+3} centers [Andlauer et al, 1973]. However, the crystals do have 0.007 Fe per formula unit which could give a yellow color. Born et al [1972] observed that scheelite is colored brown by X-rays but did not discern whether this is due to the Pb^{+3} or V_k -electron centers. Mita [1965] observed luminescence at 621 and 478 nm which may be connected with Pb^{+3} . Synthetic KCl has unpolarized absorption bands at 216, 303, and 465 nm (Figure 1.28) which have the same thermal formation and decay properties as the Pb^{+3} EPR signal but not the electron trap's signal [Schoemaker and Kolopus, 1970]. Similarly, irradiation of KCl doped with Tl^{+1} has also been observed to develop color [Delbecq et al, 1966]. Initially, the spectra of Figure 1.29a are observed, along with a 367 nm absorption due to Cl_2^- centers. Delbecq et al [1966] attributed this to Tl^0 , and made the band assignments listed in Table 1.11. Heating the crystal creates new absorption bands. Delbecq et al [1966] attributed the changes to diffusion of Cl_2 which recombines with both Tl^0 and Tl^{+1}

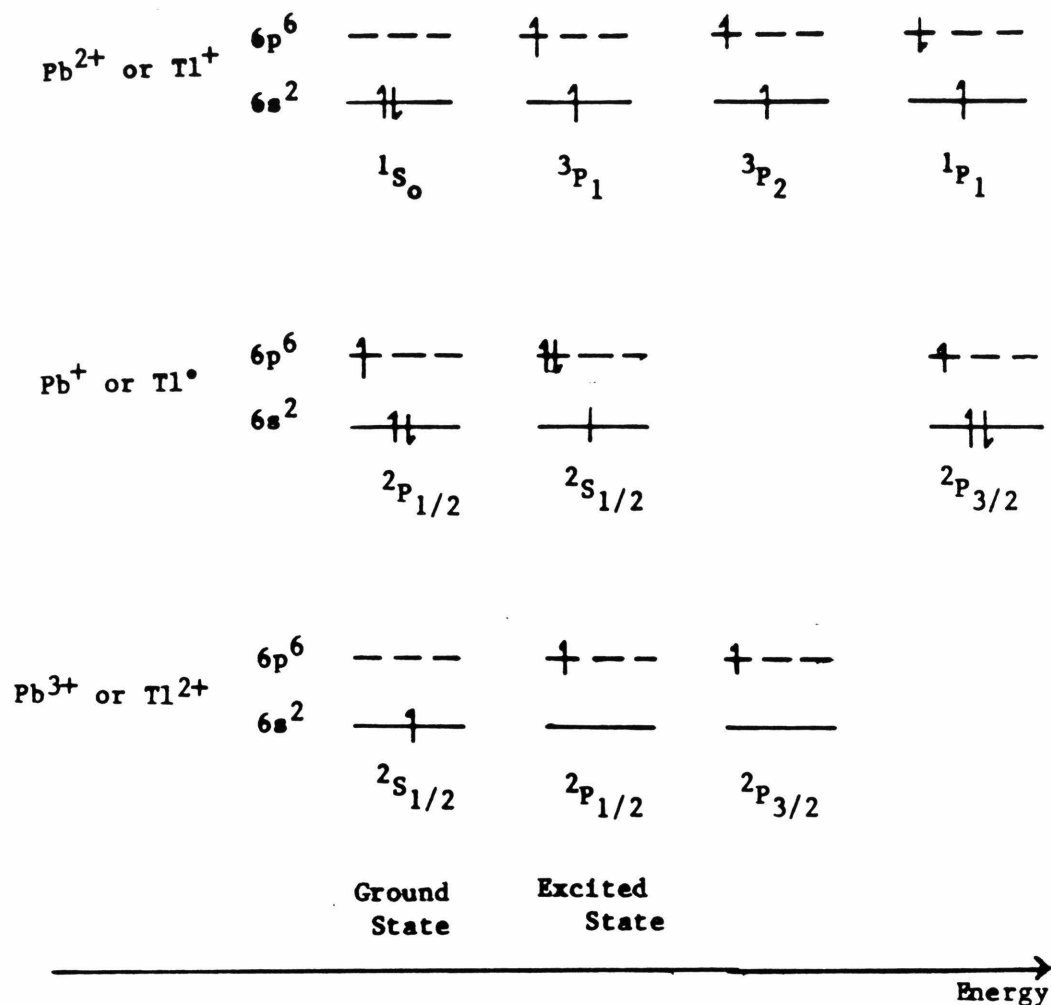


Figure 1.27 Energy level diagrams for S to P electronic transitions of Pb on Tl for different charge states. The ground states are shown on the right, and all excited states are on the left. The relative energies of the states are schematically indicated. Each state is labeled with spectroscopic notation, $2S+1L_J$. Note that some states appear the same but differ in energy because the J value for a single configuration can vary from $|L+S|$, $|L+S-1|$ to $|L-S|$.

Table 1.11 Electronic transitions of lead and thallium at 77 K

Transitions	KI:Pb ⁺²	NaCl:Pb ⁺²	KCl:Pb ⁺²	Na-Si-O glass:Pb ⁺²	KCl:Tl ⁺¹	
	λ nm	λ nm	λ nm	λ nm	λ nm	f#
A $^1S_0 \rightarrow ^3P_1$	350	272	271.5	230	247	0.08
B $^1S_0 \rightarrow ^3P_2$	300	209	211		209	0.007
C $^1S_0 \rightarrow ^1P_1$	273	202	202.5		196	0.48
		198	199			
		195	195.5			
D' charge transfer	253	186.5	191.5		ND	
D excitation	230	~150	~150		ND	
Reference	Hashimoto & Ohiwa 1980	Onaka et al 1965	Onaka et al 1965	Parke & Webb 1973	Delbecq et al 1966	

Transitions	KCl:Pb ⁺³		KCl:Tl ⁺²	
	λ nm		λ nm	f#
? $^2S_{1/2} \rightarrow ^2P_{1/2}$	465		364	0.13
?	303		294	0.22
?	hidden by Pb ⁺² band		262	0.14
?	216		220	0.23
Reference	Schoemaker & Kolopus 1970		Delbecq et al 1966	

Transitions	KCl:Tl ⁰	
	λ nm	f#
$^2P_{1/2} \rightarrow ^2P_{3/2}$	1500	10^{-4}
$^2P_{1/2} \rightarrow ^2P_{3/2}$	1260	10^{-4}
?	640	0.03
$^2P_{1/2} \rightarrow ^2S_{1/2}$	380	0.48
Reference	Delbecq et al 1966	

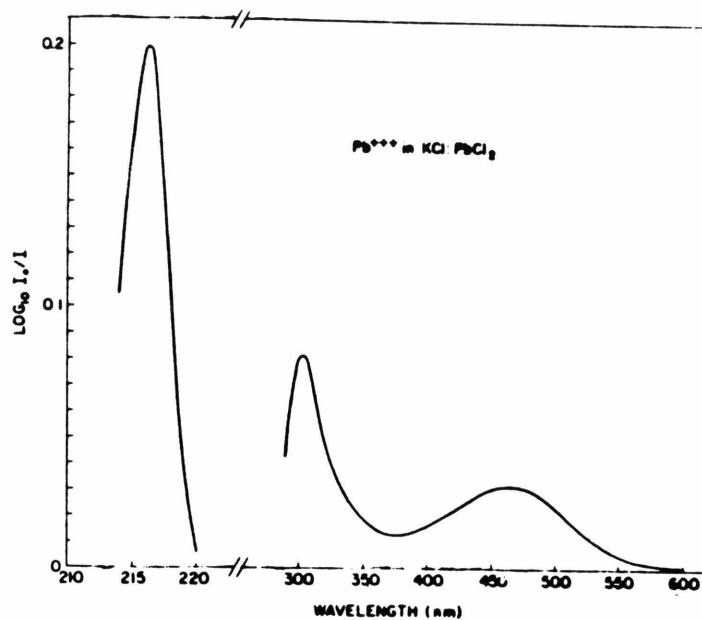
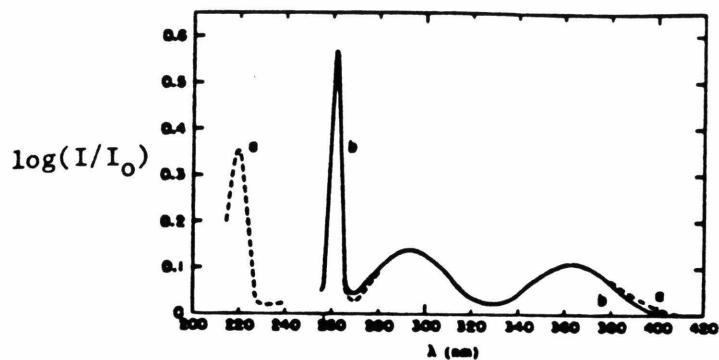
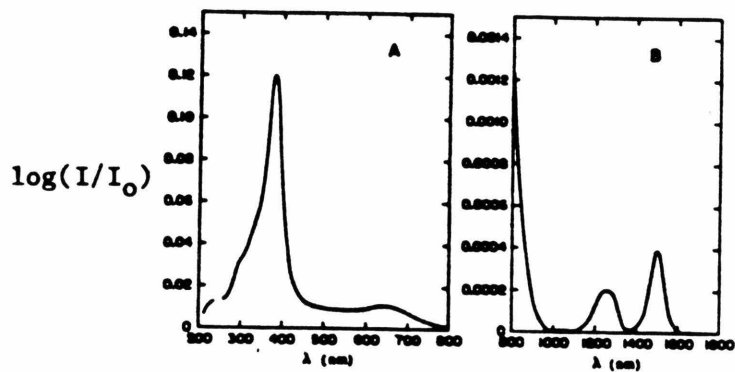


Figure 1.28 Unpolarized spectrum of Pb^{3+} at 77K in a 1 mm thick KCl crystal with about 1% $PbCl_2$ impurities. From Schoemaker and Kolopus [1970]. Bands due to Pb^{2+} occurring between 220 and 290 nm were omitted for clarity. These overrode any Pb^{3+} signal that may have existed at these wavelengths.



a



b

Figure 1.29 Optical absorption spectra of Tl° and Tl^{2+} in KCl at 77K. From Delbecq et al [1966]. (a) Unpolarized spectrum of Tl^{2+} for a 12 mm thick KCl crystal originally having 1.3 mole % Tl^{+} , which was irradiated and warmed to remove Tl° [Delbecq et al, 1966]. Curves marked a and b were determined by two methods. (b) Unpolarized spectra of Tl° for a 12 mm thick crystal doped with Tl^{+} and then irradiated at liquid nitrogen temperatures. A and B are have different intensity scales.

to produce both Tl^{+1} and Tl^{+2} . Delbecq et al [1966] isolated the spectra for Tl^{+2} (shown in Figure 1.29b) by subtracting the peaks of the Tl° still left after heating. Peak positions are listed in Table 1.11. Dreybrodt and Silber [1967] confirmed the assignment of Delbecq et al [1966] of the optical bands to Tl^{+2} by EPR spectroscopy.

Electronic assignments for the transitions of the different charge states can be made with varying degrees of confidence. Absorption spectra of Pb^{+2} and Tl^{+1} in alkali halides have been extensively studied and successfully correlated with the transitions listed in Table 1.11 and depicted in Figure 1.27 [e.g. Hashimoto and Ohiwa, 1980]. The similarity of the Tl° electronic transitions to those of Tl^{+1} coupled with the oscillator strengths of Tl^{+1} bands makes Delbecq et al's [1966] assignments seem plausible, except that the weak band at 640 nm was not accounted for. In contrast, electronic transitions for Pb^{+3} or Tl^{+1} cannot be reliably assigned, because these states could involve admixtures of molecular orbitals. Figure 1.30 shows the transitions involving bonding and non-bonding ligands proposed by Dreybrodt and Silber [1967]. Such transitions would occur with the oscillator strengths ($f = 0.1$ to 0.3) observed [Dreybrodt and Silber, 1967]. Another possibility would be transitions from d-like orbitals, as depicted in Figure 1.30 if the 6s orbital has some p character. Other complications are the $^2S_{1/2}$ to $^2P_{1/2}$ or $^2P_{3/2}$ transitions and the likelihood of Jahn-Teller distortions for the Pb^{+3} excited states. For these reasons, the color producing absorption bands of Pb^{+3} and Tl^{+2} have not been positively correlated with electronic transitions.

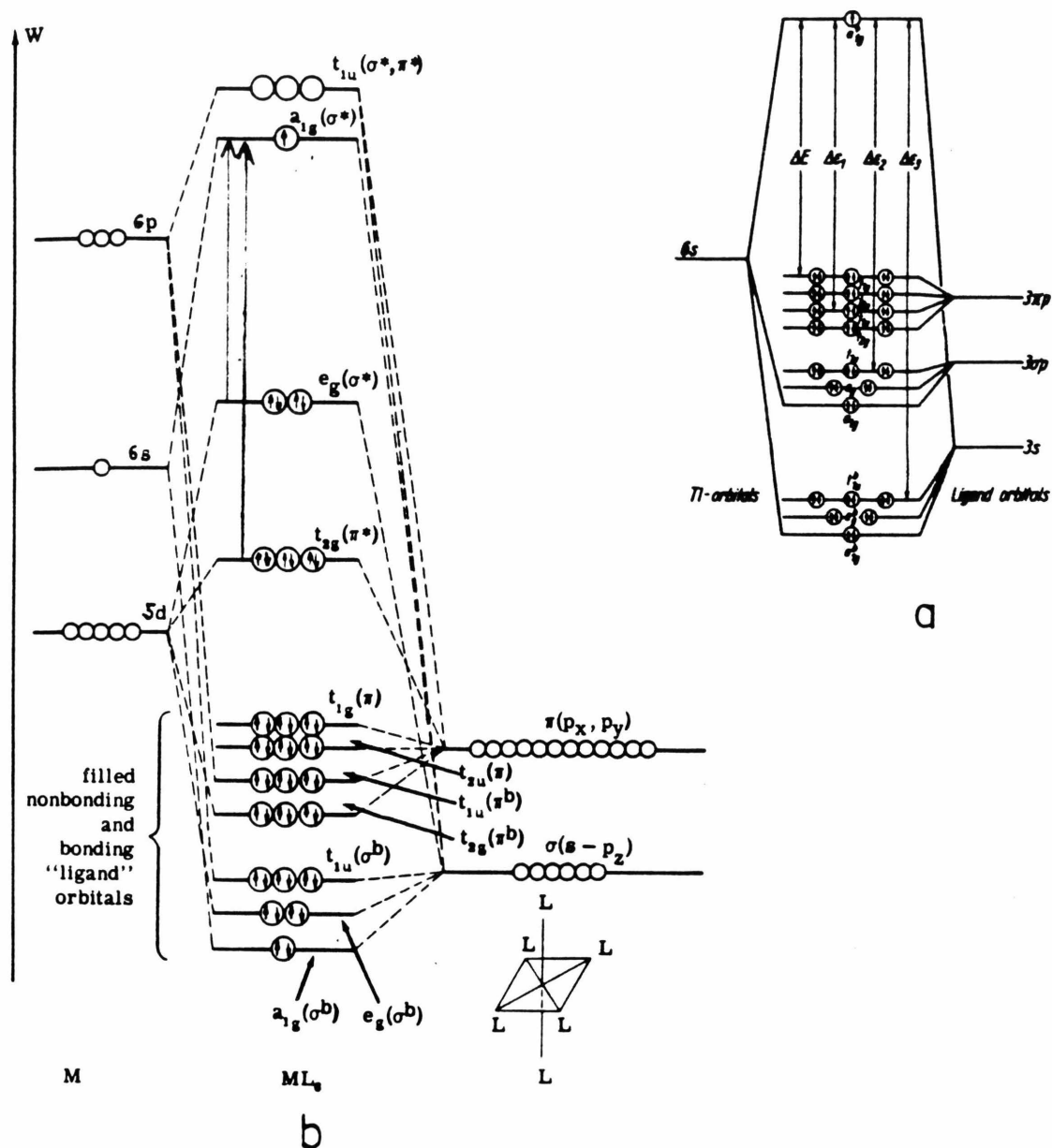


Figure 1.30 Molecular orbital configurations for Pb^{3+} or Tl^{+} .

(a) From Dreybrodt and Silber [1967]. The four spectroscopic bands observed by Delbecq et al [1966] were assigned to various transitions from the ligand-like orbitals to the nonbonding a_{1g}^* as shown by the long arrows. (b) Given by Ballhausen and Gray [1964, p. 103] Two other possible transitions are indicated by the long arrows.

1.2.b.vi Blue Barite and Celestite

The common pale blue color of celestite (SrSO_4) or barite (BaSO_4) is a radiation color because the color can be removed by heat and returned by radiation and because the mineral is thermoluminescent [Przibram, 1956, p. 241]. Blue celestite's unpolarized absorption spectrum as shown in Figure 1.31 consists of two broad overlapping peaks at 620 ± 5 nm and 575 ± 5 nm, superimposed on a UV band peaking below 400 nm [Bernstein, 1979]. The unpolarized spectrum of blue barite is similar except that the peaks are at 640 and 595 nm; this shift to lower energy is consistent with barite's larger unit cell [Bernstein, 1979], and implies that the same mechanism applies to both minerals. The blue color in sulfates results from a transmission window between the ultraviolet tail and the broad bands near 600 nm. This is remarkably similar to amazonite color (see Sec. 1.2.b.iv) not only in spectroscopic appearance but also because both colors are induced by radiation.

The mechanism for coloration is not understood, but the experimental data are suggestive. Schulman et al [1952] have shown that pure synthetic SrSO_4 is uncolored by radiation but that synthetic SrSO_4 with 0.1 to 1.0 mole % Na_2SO_4 or K_2SO_4 added are colored by X-rays approximately in proportion to the alkali content. The reflectance spectra of the synthetics have broad minima at around 580 to 600 nm [Schulman et al, 1952] which is similar to that expected for the natural samples. Also, Bernstein [1979] found an exponential relationship of bleaching time with potassium content for celestites, but found no correlation with any other impurities [Fe, Mg, Ba, Ca, or Na]. If the color is produced by some type of electron trap, then incorporation of a monovalent cation in a divalent salt should result in coloration because charge compensation mechanisms such as

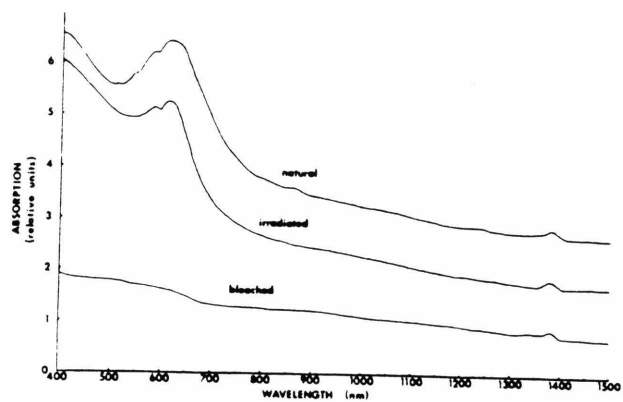


Figure 1.31 Unpolarized Optical Spectra of Blue Celestite from Bernstein [1979]. The major absorptions are at 620 ± 5 nm, 575 ± 5 nm, and < 400 nm. The spectrum of blue barite is similar, except that the peaks are displaced by +20 nm.

(1) K^+ (substitutional) + K^+ (interstitial) replacing one Sr^{+2} or
 (2) $2K^+$ replacing $2Sr^{+2} + SO_4$ would provide favorable sites for
 electron traps [Schulman et al, 1952]. Bernstein's [1979] data suggests
 a correlation of the time needed to bleach the color with potassium
 content. However, Wells et al [1983] examined zoned celestite with
 colorless, gold-orange, and blue regions and found that the gold-orange
 regions have higher iron concentrations, while the blue areas have six
 times the lead content than the others. ESR measurements (summarized by
 Bernstein [1979] reveal multiple paramagnetic centers which have been
 attributed to O^- , SO_2^- , SO_3^- and SO_4^- . Such species are likely to result
 from irradiation of sulfate; however, none of the detected ESR signals
 have been directly correlated with the intensity of the color. Thus the
 blue color of barite and celestite is connected with the effect of radiation
 on sulfates with impurities, but whether that species is lead or potassium
 or some other trace element is unknown.

1.2.b.vii Effect of proton species on radiation response

The literature contains ample data indicating that water and hydrogen
 influence radiation coloring not only in nominally anhydrous materials
 such as glass, quartz, alkali halides, but also in hydrous phases such
 as the mineral brazilianite and in alkali-ice glasses. The main effect
 in glasses is to suppress coloration, but in certain instances enhancement
 occurs. For glasses, the specific response to gamma or X-ray irradiation
 depends on the impurity content, but OH concentration higher than impurity
 concentration inhibits color center formation [e.g. Acocella et al, 1982].
 Arnold and Compton [1959] showed that small amounts of OH in pure silica
 glass inhibited formation of the C electron center (which absorbs at 215

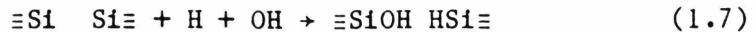
nm) but enhanced the 257 nm band for liquid nitrogen temperature X-ray irradiation. For room temperature gamma-irradiation of H₂O-rich pure silica, Weeks and Lell [1966] showed that the intensity of the 220 nm band due to E centers varied linearly with OH infrared absorption intensity (except for very low OH concentrations) in a manner suggesting that OH was disabling the electron center by mending the dangling bonds left by the oxygen vacancy (see Fig. 1.21 for a picture of the E center). Weeks and Lell [1966] also observed a decrease in the 550 nm (hole center) absorption band, and no enhancement of the 257 nm band. Faile and Roy [1970] revealed that color suppression also occurs for H₂ impregnated samples irradiated at room temperatures, and that this is accompanied by strong increase in OH infrared bands. Color centers did form at liquid nitrogen temperatures implying that diffusion of hydrogen is a part of the suppression process [Faile and Roy, 1970]. Both Faile and Roy [1970] and Shelby [1979] assigned the 2200 cm⁻¹ peak in glass to the species SiH. This peak is more likely to be an Si-OH combination stretching-bending mode [e.g. Bartholomew et al, 1980]. Shelby [1979] showed that irradiation of H₂ impregnated silica produces Si-OH species in proportion to (radiation dose * original H₂ concentration)^{1/2}. The square root relationship with dose is observed in formation of other types of defects but is not adequately explained [Shelby, 1978].

The effect of protons on the irradiative response of "less than pure" silica glass is slightly more complicated depending on the amount and type of impurity present. Van Wieringen and Kats [1957] noted that water bearing alkali and alkali-earth silicate glasses were colored less by irradiation than when dry. Canina and Priqueler [1962] observed that silica glass with equally low concentrations of OH and Al was colored by

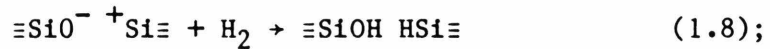
irradiation while silica with only OH at $10^{20}/\text{cm}^3$ was uncolored. Faile [1969] showed that hydrogen impregnation in complex glasses suppressed color formation except when high concentrations of Pb^{+2} or Ti^{+4} were present. Friebele et al [1978] observed that for a given glass composition, increased OH content produced a less colored glass. Lead-silicate was not an exception to this rule, but the inherently intense absorptions of lead silicate glass causes it to be more highly colored than other glasses of similar OH content [Friebele et al, 1978]. The response of alkali silicate glass with high water contents is virtually identical to that of silica. Acocella et al [1982] showed that absorption bands at 440 and 620 nm along with the overlapping EPR signals H_2 and H_3 decreased drastically with increasing H_2O content and that OH is formed from H_2O during irradiation. Similarly, in borosilicate glass formation of the boron-oxygen hole center is repressed by H_2 gas impregnations of greater than 0.2 mole %. In diametric opposition, Mackey et al [1970] observed that the intensity of the 450 nm band in borosilicates increased linearly with hydroxyl absorption for low OH concentration. Possibly, a threshold of water content is necessary before the repressive effects are seen.

From these observations on glasses the following mechanisms are suggested. The observations mandate that the irradiation process disassociates H_2 or H_2O within the glass to form the species SiOH [Faile and Roy, 1970; DiSalvo et al, 1922; Hartwig, 1977; Shelby, 1979; Acocella et al, 1982]. It is likely that the disassociation proceeds by formation of atomic hydrogen because H° has been observed in irradiated glass [e.g. Van Wieringen and Kats, 1959]; and also because the primary products of water radiolysis are H and OH [Draganic and Draganic, 1971, p. 23]. However, formation of the species H^+ and OH^- cannot be ruled

out. Electron color center formation could be suppressed by occupation of oxygen vacancies through the reaction



which would prevent E centers from forming [e.g. Lell et al, 1966]; but evidence for SiH is lacking. Pre-existing E centers ($\equiv\text{Si}^{\ominus}-\text{Si}\equiv$) would be similarly destroyed with the electron finding another trap or recombining with a hole [e.g. Lell et al, 1966]; another possibility is formation of SiOH and interstitial H°. Faile and Roy [1970] proposed that bonds broken during irradiation could be mended by pairs of atomic hydrogen



but again, the evidence for SiH is poor. Similar reactions could occur with water, because two SiOH groups would result. A related mechanism could also occur involving non-bridging oxygens present before irradiation [DiSalvo et al, 1972] which would serve to prevent hole center formation, and would result in SiOH bonds which have been observed in infrared spectra.

For crystalline quartz, there are two color centers which require the presence of protons to form. One is a center in which Ti^{3+} occupies a Si site and a proton charge compensator is bound interstitially nearby [Rinneberg and Weil, 1972]. The response of this center to proton content has not been studied. The other is the E₂ center which absorbs at 230 nm and consists of an electron trapped at a hydrogen compensated SiO vacancy [Weeks, 1963] or SiO₂ vacancy [Lell et al, 1966]. For crystals having an appreciable concentration of E₂ centers, the E₁ center (an electron trapped at an oxygen vacancy) does not readily form unless the E₂ center is bleached by heating at 250 to 300°C whereupon subsequent irradiation develops E₁ centers but not E₂ [Nelson and Weeks, 1960]. Because the precursor oxygen vacancies are likely to exist in quartz, this result

suggests that the hydrogen ions present mend E_1 centers in quartz in the same manner as they mend E centers in glass, namely by filling in the vacancy. The similar behavior of protons in quartz and glass is corroborated by the observation of interstitial atomic hydrogen in EPR spectra of irradiated quartz [Weeks and Abraham, 1964; Perlson and Weil, 1974] and in glass [von Wieringen and Kats, 1957].

In contrast to the E_2 band, the formation of Al-hole centers in quartz is adversely affected by the presence of protons [e.g. Weil, 1975]. Smoky color can be induced in quartz by electrolysis in N_2 but not in H_2 [Hafele, 1960]. Bambauer's [1961] comparison of the optical absorption coefficient of 460 nm with Li and H contents in quartz implies that Al centers compensated by H do not produce the smoky color, but that the lithium compensated centers do. Mackey [1963] confirmed Bambauer's suggestion by EPR studies at liquid nitrogen and room temperature. Mackey [1963] showed that Al-hole centers form only at LN_2 temperature in a hydrogen compensated crystal, and that warming to room temperature destroys the centers, whereas uncompensated Al-hole centers are stable even at room temperature. Apparently, room temperature diffusion is sufficient to return the hydrogen displaced by radiation to the Al-site where it can eliminate the hole.

Kats [1962] used infrared spectroscopy to study the mechanism of hydrogen displacement in synthetic and natural quartz by irradiation. He showed that there are about 40 different sites for hydrogen in the crystal including H alone, H near various alkalies, and H near aluminum. X-ray irradiation decreases the intensity of alkali-associated hydrogen bands while increasing that of aluminum-associated bands and forming new alkali-hydrogen bands [Kats, 1962, p. 259]. He suggested [ibid, p. 194]

that irradiation removes both alkali and hydrogen whereupon the hydrogen diffuses back to the alkali site, forming a new IR absorption band. Kats [1962, p. 164] noted that smoky color develops only in quartz that has a low overall water content with OH mainly distributed among Al-associated centers. Quartz with high water content and many different IR bands turns yellow (citrine) with irradiation. Heating of the colorless or yellow quartz at 1000°C will remove the alkali associated hydrogen bands, leaving the Al-H bands at 3311, 3371, and 3435 nm, and allowing smoky color to develop upon irradiation [Kats, 1962, p. 193-195, 257]. The smoky color would not be due to the Al-H centers [e.g. Weil, 1975] but to other uncompensated Al-O hole centers.

Kats' [1962] observations on the connection of smoky color and OH bands has been verified and expanded by Krefft's [1975] electrolysis experiments on quartz. When electrolysis was performed under vacuum, a well-defined color front moved across the crystal: at the color front, OH bands and OH-alkali bands were transformed to the OH-Al bands of 3310, 3321, and 3435 cm^{-1} [Krefft, 1975]. She showed that removal of hydrogen in the crystal proceeds by this same conversion of unstable to stable bands. The effect is somewhat reversible in that electrolysis of quartz in moist air, H_2 , or H_2O will force incorporation of protons as OH (3472 cm^{-1} band) which will prevent smoky coloration and allow yellow to develop [Krefft, 1975].

Hydrogen may also play a role in the formation of the other radiation colors in quartz: citrine and amethyst. Citrine is known to have high lithium [Bukarnov and Markova, 1969] and high water contents [Kats, 1962]. Gamma irradiation of Li-rich quartz decreases the intensity of the OH bands associated with Li and makes a new OH band associated with Li at

3408 cm^{-1} and also intensifies the OH-Al band at 3371 cm^{-1} [Kats, 1962, p. 194]. Heating the crystal slightly removes the yellow color and restores the original intensity of the bands [Kats, 1962, p. 194]. When smoky-citrine zonation occurs, the Li-OH defects are mostly contained in the citrine zones [Bukarnov and Markova, 1969]. EPR study of citrine by Maschmeyer et al [1980] has shown that citrine has two aluminum-oxygen hole centers both of which are quite different from the aluminum-oxygen hole center present in smoky quartz. Despite the known involvement of H, Li, and Al in the centers, the EPR data is not sufficient to elucidate the structure of the citrine centers at present [Maschmeyer et al, 1980].

In contrast, amethyst color is not correlated with OH content [Kats, 1962, p. 275-279]. Ongoing study of zoned amethyst-citrine by R. Aines [Ph.D thesis, in prep.] suggests that the presence of molecular water inhibits amethyst formation while aiding citrine formation.

In the alkali-halides, hydrogen can occupy halogen or interstitial sites and can also be incorporated as hydroxyl. Although these species do not directly cause visible color, they are associated with absorption bands in the ultraviolet and their interaction with irradiation can indirectly produce color. According to Schulman and Compton [1962, p. 163-168], and Watts [1977, p. 291], substitutional H^- forms the U center which absorbs light around 190-290 nm. UV, gamma, or X-ray irradiation moves the hydrogen atom to an interstitial site, so that one electron is remaining to create an F-center and thus, color. Ultraviolet and X-ray irradiation of OH-bearing alkali halides can similarly create an F-center and interstitial atomic hydrogen [Schulman and Compton, 1962, p. 168 and 185].

The irradiative response of hydrogen ions in stoichiometrically hydrous minerals has received scant attention. The available literature concerns

two minerals. Hill and Lehmann [1978] have shown through EPR that X-ray irradiation of brazilianite produces atomic hydrogen. Irradiation also changes the green color to yellow, which Hill and Lehmann [1978] attribute to reduction of Fe^{+3} to Fe^{+2} by the atomic hydrogen. Faile [1969, p. 89] showed that hydrogen impregnated beryl $\text{Be}_3\text{Al}_2\text{Si}_6\text{O}_{18}$ is not colored by a Gigard dose of X-rays whereas a similar untreated sample turns dark from such a dose.

Study of γ -radiation's effect on high spin iron complexes ($\text{FeSO}_4 \cdot 7\text{H}_2\text{O}$, $(\text{NH}_4)_2\text{Fe}(\text{SO}_4)_2 \cdot 6\text{H}_2\text{O}$, $\text{NH}_4\text{Fe}(\text{SO}_4)_2 \cdot \sim 1.5\text{H}_2\text{O}$, and $\text{Fe}^{2+}_x \cdot 2\text{H}_2\text{O}$) by Gutlich et al [1968] has shown that the two compounds of higher water content were oxidized to ferric sulfates by the γ -radiation, while the lower water content sulfates were unchanged. Gutlich et al [1968] proposed that radiation disassociated water molecules into the radicals H and OH, and that the radical OH oxidized the iron, itself becoming OH^- .

The effect of radiation on aqueous alkali hydroxide glasses i.e. "alkaline ices" has been studied in depth [see reviews by Kevan, 1969 and Wong and Angell, 1976, Ch. 6]. Trapped electrons, which produce a broad absorption at 580 nm, were first observed in irradiated, frozen (77 K) solutions of water with alkali hydroxide by Schulte-Frohlinde and Eiben [1962]. Their EPR results implied that the trapped electrons are solvated by molecular water. Subsequent studies have shown that 77 K irradiation not only traps electrons, but also creates atomic hydrogen and O^- hole centers in all alkaline ices of greater than about 5 to 15 molar alkali-hydroxide [Kevan, 1969, p. 68-69]. The radical OH, which is observed in pure irradiated ice [e.g. Kevan, 1969, p. 60-63], is not observed in alkali ices because any OH formed reacts with OH^- to form O^- and H° [e.g. Wong and Angell, 1976, p. 377]. The hole center O^- absorbs ultraviolet

light at about 240 nm [Kevan, 1969, p. 70]. The electrons are trapped at a variety of sites as indicated by the broad absorption band [e.g. Wong and Angell, 1976, p. 372]. If transition metal cations or alkali metal oxyanions such as NaHSO_4 are added to an alkali ice then the H° and O^- traps are still formed, but the electrons created by irradiation react with the cations or oxyanions instead of forming "solvated" electron traps [e.g. Kevan, 1969, p. 80-82]. Thus, the response of alkali ices to irradiation, like that of glasses, can be modified by impurities present; yet the ubiquitous centers H° are O^- dominate.

These diverse examples divulge that irradiation of hydrogen bearing glasses and minerals creates atomic hydrogen which diffuses through the lattice and is trapped at existing defects. Very often the defect in which hydrogen is eventually trapped is related to the defect from which the H° was removed. There is evidence that alkali atoms are also displaced by irradiation, and that the difference of behavior between alkali and hydrogen atoms is that hydrogen can diffuse at room temperature. Atomic hydrogen by itself forms radiation centers that absorb ultraviolet light. Atomic hydrogen can eliminate both hole and electron centers by several processes: displacing electrons, mending broken bonds, attaching itself to non-bonding oxygens, and by replacing positive charges with H^+ . In summary, the species water and hydroxyl react with radiation to form mobile reactive species which modify the glasses' or minerals' response to irradiation in a manner depending on the total chemistry of the phase.

1.2.c Water in feldspar

The presence of water, especially at high pressures, has been known to effect such various processes in feldspar as the rate of oxygen exchange [e.g. Yund and Anderson, 1978], exsolution and ordering in K-spar [e.g. Parsons, 1978]; and ease of plastic deformation [e.g. Tullis and Yund, 1980]. (There is some indication that water is involved in amazonite coloration [Plyusnin, 1969] (see Sec. 1.2.a.iv).) Water does not appear to affect coherent exsolution, but rather aids in the coarsening of the lamellae [Parsons, 1978]. Yund and Tullis [1980] demonstrated that even a trace of water influences the rate of Al/Si disordering in albite and microcline, such that increasing the amount of water increases the rate. They argued that water is probably the principal factor controlling the structural state of the feldspar in many rocks.

Two mechanisms have been proposed to explain the role of water in these processes. Donnay et al [1959] suggested that water aids structural transformations and ion exchange by hydrolyzing the tetrahedral oxygen bonds. O'Neil and Taylor [1967] envisioned that rapid exchange occurred by fine scale dissolution and reprecipitation at the reaction front passing through the crystal. These mechanisms have very different implications for the speciation of water within the feldspar. That of Donnay et al [1959] implies water should be present as the species SiOH, while O'Neil and Taylor's [1967] mechanism would favor molecular water. Fluid water in vacuoles is a common feature observed in feldspars, but the state of water at the structural level is not understood. Wilkins and Sabine [1973] and Solomon [in prep.] have addressed this issue through infrared spectroscopy.

All specimens of andesine, adularia, orthoclase, labradorite, and anorthoclase which Wilkins and Sabine [1973] examined gave spectra with

broad diffuse bands between 3000 and 3750 cm^{-1} as shown in Figure 1.32. The only feldspar having a sharp line spectrum was albite from Amelia, Virginia. Through deuteration, Wilkins and Sabine proved that the sharp bands between 3400 and 3600 cm^{-1} were due to OH. Wilkins and Sabine [1973] concluded that the broad peaks were due to water, but they did not assign the spectra to a particular species.

As part of his Ph.D. thesis, G. C. Solomon has studied the speciation of water in feldspars from igneous environments. A synopsis of his results on K-spar is given here. Solomon has determined that water in pegmatitic potassium feldspar exists in two modes. The first type is molecular water which is crystallographically oriented with its two-fold rotation axis nearly parallel to the y direction and its molecular plane parallel to (001) as indicated by the polarization of two anisotropic stretching bands at 3620 and 3550 cm^{-1} and a stretch-bend combination mode at 5130 cm^{-1} . Solomon and Rossman [1979] assigned this type to molecular water in the M-site. They assigned the second type to molecular water absorbed in microvacuoles because its absorptions were much less pleochroic. (These are the bands at 3440 and 3280 cm^{-1} and a combination mode at about 5200 cm^{-1} .) The M-site water is removed from the feldspar at temperatures near 700°C, while the microvacuole water leaves at about 200°C [Solomon and Rossman, 1979].

In plagioclase phenocrysts from Lake County, Oregon, and Crater Elegante, Sonora, Mexico, protons occur in low (~ 0.1 wt%) concentrations and are speciated as OH^- rather than H_2O [Solomon and Rossman, 1982]. Solomon and Rossman interpreted the difference in speciation as relating to the higher proportion of H_2O in more hydrous melts.

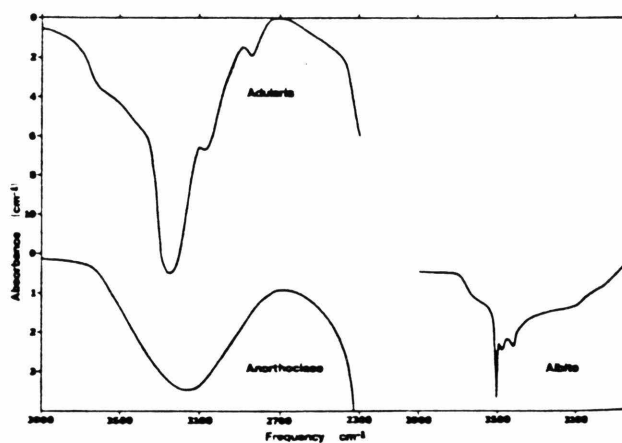


Figure 1.32 Unpolarized infrared spectra from single crystals of adularia (Van Nalps, Switzerland), anorthoclase (Mt. Franklin, Australia) and albite (Amelia, Virginia) from [Wilkins and Sabine, 1973]. The authors' electrolytic measurements showed that the adularia has 0.08 wt % H₂O. This gives an extinction coefficient of 120 liters/mole·cm at 3250 cm⁻¹ for the adularia.

1.2.d Geology and genesis of amazonite pegmatites

Some amazonite occurs in granites, but for the most part this mineral is found in pegmatites. This rock type is characterized by a very coarse-grained texture and is generally believed to crystallize from a water-rich magma or supercritical fluid. Pegmatites typically, but not entirely, are associated with granitoid intrusives. They can be classified in three types: homogeneous, layered, or concentrically zoned [cf. Jahns, 1959]. In particular, amazonite pegmatites can be homogeneous [e.g. Plimer, 1976] or zoned [e.g. Foord and Martin, 1979].

Several origins are possible for pegmatites. Those associated with granitoids can be synchronously emplaced [Orville, 1960], leading towards compositions identical to the parent, or can segregate from the parent-melt resulting in a fractionated composition [Cameron et al, 1949, p. 5-7 and 105]. Those not associated with intrusives are derived by partial melting, and possibly fractionation, of country rocks during metamorphism [e.g. Plimer, 1971]. Amazonite pegmatites in Colorado were apparently fractionated from the magma which formed the 1 byr old Pikes Peak Batholith [Foord and Martin, 1979]. Amazonite pegmatites at Broken Hill, Australia, were derived from partial melting of pelitic rocks which was associated with the dewatering of nearby lead and zinc rich sulfide ore bodies late in the history of the 1.5 to 0.9 byr old metamorphism [Plimer, 1976]. Many Russian researchers have argued that amazonite pegmatites are formed by a metasomatic process, but Barasov et al [1971] showed that Russian amazonites formed during the late stages of magmatic crystallization.

Conditions of amazonite pegmatite formation vary from 1 to 3 kilobars [Hutchinson, 1976] and about 500°C (formation of microcline) for the

Colorado amazonites to as high as 5 to 10 kilobars and 750 to 800°C for the Broken Hill metamorphism [Binns, 1964]. This suggests that the physical parameters may not be important. Apparently, the basic requirements for amazonite pegmatite formation are fluidized felsic magmas rich in Pb and other elements such as Rb, Cs, and Tl [cf. Foord and Martin, 1979; Plimer, 1976].

Another requirement for amazonite pegmatites may be great age. E. E. Foord [pers. comm.] has noted that many of the one hundred amazonite pegmatites he has studied are Precambrian with the exception of : the New York Mountains, California, which is associated with the Cretaceous Teutonia Quartz Monzonite [Hewett, 1956]; possibly Amelia, Virginia, which could have been either emplaced or metamorphosed at 280 my; Cretaceous pegmatites in granite near Jefferson and Nye counties, Nevada; Mineral Hill, Pennsylvania; Hawthorne, Nevada; and the Conway Granite, New Hampshire. The age may be associated with the time needed to develop the radioactivated coloration, or perhaps the proper magma chemistry needed to develop amazonite fluids only occurred in abundance in Precambrian times.

1.2.e Geology and geochemistry of the Steens Mountain Basalts

The Lake County labradorites (sunstones of Rabbit Hills) described in Section 1.2.a.viii occur as phenocrysts in highly porphyritic basalt flows which are petrographically equivalent to the Steens Mountain Basalt (60 miles to the east) and also to the Abert Rim Basalts (10 to 15 miles southwest) [Stewart et al, 1966]. The sunstone bearing flow itself varies from ~ 3 meters thick and covers about 7 square miles [Peterson, 1972]. The flow rests upon a red cindery baked zone which in turn covers non-porphyritic basalts [Peterson, 1972]. The sunstone bearing basalt is

holocrystalline, exhibiting intergranular and diktytaxitic textures, and ophitic clinopyroxene [Stewart et al, 1966]. The labradorite phenocrysts (An_{67} with 0 to 8% rims of about An_{50}) comprise 10 to 55 % of the rock [Stewart et al, 1966]. The groundmass consists of >50% An_{60} microlites; 21% augite; 16% olivine which is partially altered to iddingsite; 8% magnetite; 2% calcite; and 2% voids [Stewart et al, 1966].

From the X-ray study of the phenocrysts, Stewart et al [1966] concluded that the labradorite "formed by primary crystallization in a magma chamber at temperatures greater than $1100^{\circ}C$ and under relatively uniform conditions.... Rapid, but small, fluctuations of temperature and pressure during eruption and extrusion caused oscillatory zoning and resorptions observed in the rims.... Crystallization of the outer, less calcic rim occurred during eruption. The intermediate structural state of both core and rim indicates rapid cooling and low vapor pressure of volatiles, as expected for (very thin) flows.... The higher structural state of the outermost shell and of the groundmass feldspar reflects a compositional effect on the (fast) rate of attaining a given structural state during cooling." Wenk et al [1980] did a structural refinement on Lake County and Surtsey, Iceland, An_{67} labradorites using both X-ray and neutron diffraction which showed that the Lake County phenocrysts were not cooled as rapidly as the Surtsey crystals.

The topmost 1000 meters of the Steens Mountain sequence in southwestern Oregon consists of thin flows of holocrystalline olivine-basalt with a diktytaxitic texture, the most notable characteristic being a high content (up to 60%) of glassy-appearing labradorite laths which are nearly uniform in size [Fuller, 1931]. Chemically, the basalts are distinguished by their high alumina and high titania contents ($SiO_2 = 47-51\%$, $Al_2O_3 = 16-18\%$,

Fe_2O_3 and $\text{FeO} = 11\%$, $\text{CaO} = 8-10\%$, $\text{TiO}_2 = 3\%$, $\text{MgO} = 3\%$, $\text{K}_2\text{O} = 1\%$) [Fuller, 1931, p. 121]. The high alumina is explained by the high feldspar content. Ti is probably present as titanomagnetite [Gunn and Watkins, 1970]. These flows are an extrusive equivalent to anorthosite, which makes their high fluidity "all the more remarkable" [Fuller, 1931].

The Steens Mountain Basalts have been dated at 15.5 ± 0.3 m.y. [Baksi et al, 1967]. Paleomagnetic studies of the flows by Watkins [1969] have shown that the entire lava sequence was extruded in a short period (2000-50000 yrs) when the geomagnetic field was changing polarity [discussed by Gunn and Watkins, 1970].

Chemical analysis of 63 out of 70 successive flows by Gunn and Watkins [1970] have generally confirmed Fuller's observations, and in addition have revealed that chemical differences exist among the different flows: lavas that are enriched in Al are also enriched in Ca and Sr, and are depleted in Ti, Fe^{2+} , Fe^{3+} , K, Mn, Mg, P, Rb, Ba, Ni, and Cu. Silica content is nearly constant [Gunn and Watkins, 1970]. The copper content of the flows ranges from 0 to 400 ppm, averaging about 200 ppm.

Vertical profiles of the chemistry show that the lavas occur as eight distinct groups of 3 to 12 lavas each [Gunn and Watkins, 1970]. From the chemical variations (Figure 1.33) Gunn and Watkins concluded that all the lavas originated from a parent magma which was intermediate between a high alumina tholeiite and an olivine tholeiite, and that the chemical trends are due to fractional crystallization of plagioclase (and sometimes olivine) coupled with extrusion of both fractionated liquid and labradorite cumulates. Gunn and Watkins [1970] interpreted the cyclic nature of chemical variations as evidence for successive recharging of the magma chamber.

Helmke and Haskin's [1973] study of the concentration of rare earth

elements as well as Co, Sc, and Hf in these same basalt samples disclosed that clinopyroxene fractionation also occurred, that the parent magma was specifically equal to the average composition of Gunn and Watkin's group "E" lavas, and that this magma could have been produced by partial melting of olivine-pyroxene rock. In particular, Helmke and Haskin [1973] showed that the europium signature strongly suggests that plagioclase accumulation occurred for some of the lava groups.

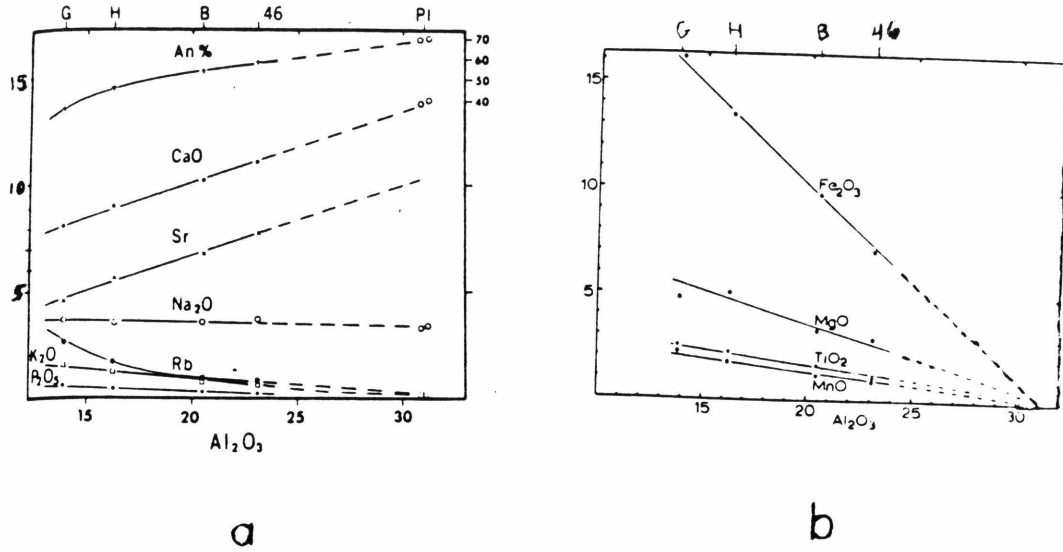


Figure 1.33 Variation of elements and oxides in the Steens Mt. Basalts as a function of Al_2O_3 . From Gunn and Watkins [1970]. (a) Felsic components. (b) Ferromagnesian group oxides. For both (a) and (b) G,H, and B are the averages for groups of lavas. 46 is a single lava. Pl is a bytownitic plagioclase unrelated to the basalts. Rb is in ppm/10; Sr is in ppm/100; all others are in wt %.

2.1 Spectroscopy

2.1.a Visible and near infrared spectroscopy

Optically oriented slabs of plagioclase were obtained by first orienting a chip from a crystal using a polarizing microscope with a universal stage while orienting the crystal on another universal stage. Usually a Bxa optical figure was used. This oriented slab was next cut with a diamond saw, roughly ground with diamond wheels, and checked for the proper optical orientation. When this was properly established the crystal was polished on parallel sides with alumina powder or diamond paste down to 0.3 micron grit. For the third optical direction, the slab was cut and polished at right angles to one optic axis, if possible. For potassium feldspar, the (010) and (001) cleavages were used for orientation because these are exactly oriented optically for the high temperature phases, and oriented within a few degrees for microcline. Sample thicknesses, as measured by a micrometer, ranged from 0.1 mm to a few centimeters.

Occasionally cleavage faces or unoriented unpolished faces were used when the material was unsuitable for orientation, or available in limited quantities, or too precious to grind.

Polarized spectra were obtained with Glan Thompson prism calcite polarizers in a Cary 17I spectrometer in approximately the 280 to 2800 nm range. The Cary is not equipped with polarizing microscopes which makes it necessary to use sample areas of about 100 square micrometers or larger.

Low temperature spectra were taken in two locally constructed liquid

nitrogen dewars. For both, the sample was held in a vacuum in position on an aluminum or brass block which was partially sitting in liquid nitrogen. The sample temperature was measured using a thermocouple attached to the metal block near the sample.

The raw spectral data from the Cary, along with the appropriate baseline spectra were digitized on a Tektronix 4956 with the aid of a Tektronix 4052 computer. Spectra were then baseline subtracted and the corrected spectra were stored in data files and also drawn by the Tektronix 4662 plotter through use of computer programs written by G.R. Rossman and modified by S.M. Mattson. Using programs written by S.M. Mattson, visible peaks were fit to gaussians; IR peaks were fit to Lorentzians, and UV tails were fit to the following equation:

$$\text{absorbance} = C_1 \exp(C_2/\lambda) \quad (2.1)$$

[Urbach, 1953; Davydov, 1968].

2.1.b Infrared spectroscopy

For single crystal studies, samples were optically oriented in the same manner as for visible spectroscopy. Usually the same sections were used for both methods, except that water-rich microclines required very thin slabs for infrared work.

Spectra were obtained with gold wire grid polarizers on a silver bromide substrate in a Perkin Elmer 180 (PE-180) spectrometer in the 4000 to 2000 cm^{-1} range. Wire screens of known absorbance were measured at 4000 cm^{-1} under the same conditions as the sample for calibration. Low temperature spectra were taken using a specially constructed liquid nitrogen dewar with KBr windows.

The raw spectral data were digitized and rescaled using the computing

equipment and programs described in Section 2.1.a, except that a baseline correction was not necessary.

Powder spectra were obtained on the same instrument (PE-180) in the 4000-380 cm^{-1} range. The samples were prepared by grinding 0.7 mg feldspar with 200 mg KBr with a mortar and pestle, and then forming a flat disk (1 cm diameter) with a press. The disk was heated at $\sim 80^\circ\text{C}$ several hours under vacuum to drive the absorbed water off. Spectra data were digitized.

2.1.c. Electron paramagnetic resonance (EPR) spectroscopy

EPR spectra were taken at liquid nitrogen temperature on a Varian E-line X-band spectrometer at about 9.2 Ghz. All samples examined were coarsely ground powders of 30 to a few hundred milligrams in weight. Itrongay orthoclase was used as a reference for intensity calibration.

The raw data was digitized and plotted with Tektronix equipment. A simple line integral algorithm was used to double integrate baseline subtracted spectra. The baselines were approximated from either heat-bleached amazonites or iron free feldspar, depending on whether amazonite color or Fe^{3+} was being studied at that time. The area was also estimated from

$$\text{Area} = \frac{(\text{signal height}) \cdot (\text{signal width})^2}{(\text{gain}) \cdot (\text{sample weight}) \cdot (\text{modulation amplitude}) \cdot (\text{power})^{1/2}} \quad (2.2)$$

2.1.d Resonance Raman spectroscopy

Raman spectra were obtained using a commercial Spectra-physics argon laser with a tunable dye option and a double monochromator, which was interfaced to a SCAMP computer. Large (centimeter sized) slabs of crystal were placed in the sample holder so the laser beam was reflected from a polished oriented surface or a cleavage face. Raman spectra were digitized using the Tektronix computing equipment. Baseline subtraction was not necessary.

2.1.c Thermoluminescence

Thermoluminescence curves were recorded with a JPL-NASA thermoluminescence photometric system which consists of an Ilex Optical Company #4 Acme synchron photomultiplier tube (PMT) attached to an amplifier circuit and a light-proof sample chamber with a sample holder that is heated between two electrodes at a constant rate (5.48°C/sec). Several hundred milligrams of sample can be heated. A thermocouple is used to convert the heating voltage to a temperature. Glow curves are produced by recording PMT output versus heating voltage on an x-y recorder. This gives the total light intensity given off by the sample as a function of temperature.

2.2 Chemical Analysis

2.2.a Electron microprobe

Quantitative chemical analyses for major and minor oxide components were made using an automated MAC-5-SA3 electron microprobe crystal spectrometer and an ORTEC Si(Li) solid state detector interfaced with an NS 880 multichannel analyzer and a PDP-8/L computer. Operating conditions were 15 kV accelerating voltage and 0.05 A sample current. Data was collected and analyzed by using standard programs for feldspar [e.g. Chodos et al, 1973] or two modified versions which would analyze either for PbO or for CuO and Ag₂O instead of TiO₂.

2.2.b X-ray fluorescence

This section describes the method developed by the author for quanti-

tative chemical analysis of minor and trace elements in feldspar by using a commercial Kevex Micro-X 7000 wavelength-dispersive analytic X-ray fluorescence spectrometer equipped with Quantex-Ray® software.

Samples were run as polished sections, crystals in the rough, or powders loaded into a plastic cylinder (1" diameter) with a thin mylar film for the bottom to minimize attenuation of the X-rays. Enough powder was used to cover the bottom of the container unless sample quantity was limited. Background spectra were collected on the thin mylar film. Standards were prepared from powders of (1) feldspars with known amounts of iron, lead, strontium as determined by microprobe analysis or by previous investigators; and (2) various small amounts (< 4 wt. %) transition metal oxides finely ground and dispersed in a powder of Lake County labradorite. CuO , Cr_2O_3 , and Fe_2O_3 were the oxides added for one set of standards; MnO_2 and TiO_2 were added to labradorite for a second set. The oxide contents of these standards are given in Table 2.1.

Data were collected using Kevex's Quantex-Ray programs. Different targets were used to optimize analysis for the various elements. (A germanium target was used for transition metals; a silver target was used for lead and strontium.) For each target, a standard set of peak parameters (position and width) was used for all elements of interest. Background data were collected for 400 seconds. Data on samples and standards were collected until 5000 counts were accumulated for silicon or 800 seconds elapsed, whichever took less time. Kevex's programs were used to determine the number of counts acquired for each element. The background counts were removed from this raw data by subtracting a time-proportioned background; for example,

$$I(\text{Si}) = \text{corrected integrated counts}(\text{Si}) = \text{total sample counts}(\text{Si}) - (\text{sample acquisition time}/400 \text{ sec}) \cdot \text{background counts}(\text{Si}).$$

Table 2.1 Chemistry of standards made from common colorless Lake County labradorite and oxide powders

Sample/ Oxide	Lab-Fe-Cr-Cu #2	Lab-Fe-Cr-Cu #1	Lab-Fe-Cr-Cu #5	Lab-Ti-Mn #3	Lab-Ti-Mn #4	Lab-Ti-Mn #6	Labradorite (probe data)
SiO ₂	47.03	48.3	49.50	46.00	47.8	50.4	51.7
TiO ₂	-	-	-	5.85	4.02	1.27	0.09
Cr ₂ O ₃	1.90	1.95	0.87	-	-	-	-
MnO	-	-	-	4.20	2.87	0.91	-
FeO _{total}	4.25	1.85	2.19	0.36	0.38	0.40	0.41
CuO	2.83	2.91	1.31	-	-	-	-

To determine the chemistry from the corrected integrated counts, it was necessary to compare the corrected integrated count for the element of interest to an internal standard. To determine the amount of transition metals, silicon was chosen for the internal standard because this element was known to be constant for the different kinds of feldspar (i.e. labradorite, or potassium feldspar) and had been accurately determined by microprobe analyses. Calibration curves of Fig. 2.1 were derived by plotting the known oxide content of the standards against

$$\frac{I(\text{element})}{I(\text{Si})} \cdot \frac{\text{wt \% SiO}_2}{51.7}$$

In this way, the weight percent of the oxide could be read directly from the curve. In practice, it was easier to use a linear equation fit to the curves to calculate the oxide concentrations in the various samples. The transition metal concentrations determined in this manner are accurate to $\pm 10\%$, except that copper oxide concentration is only accurate to $\pm 15\%$.

A similar method was used for the determination of iron in microclines, except that feldspars with known amounts of iron (i.e. Itrongay orthoclase and Eifel sanidine) were used as standards. Accuracies are again limited to $\pm 10\%$. To check the accuracy of the iron determinations of both plagioclase and potassium feldspars, the XRF analysis of FeO (total) was plotted against microprobe determination of iron content. The one-to-one correlation shown in Fig. 2.2 suggests that the XRF method is reliable within the stated error ($\pm 10\%$), and the the XRF method has a 'blank' of 0.002 wt% FeO.

Similarly, lead and strontium contents were determined by using several amazonites with known PbO concentrations as lead standards and Crater Elegante labradorite (analyzed by Gutmann and Martin [1976]) as the strontium standard. Because analysis of these elements required use

Figure 2.1

Calibration curves for determination of transition metal oxide concentration from X-ray fluorescence spectra. The horizontal axis is the oxide content in weight percent of the standards described in Table 2.1. The vertical axis is the integrated counts of the oxide divided by the integrated counts of silicon, and normalized to 51.7 wt % SiO₂ (which is the silica content of AN₆₇ labradorite). Both oxide and silica counts were background subtracted.

- (a) FeO_{total}. For this curve, Fe₂O₃ is recalculated as FeO. The two lines on the graph are for K α ₁ and K α ₂ peaks.
- (b) CuO
- (c) Cr₂O₃
- (d) MnO
- (e) TiO₂

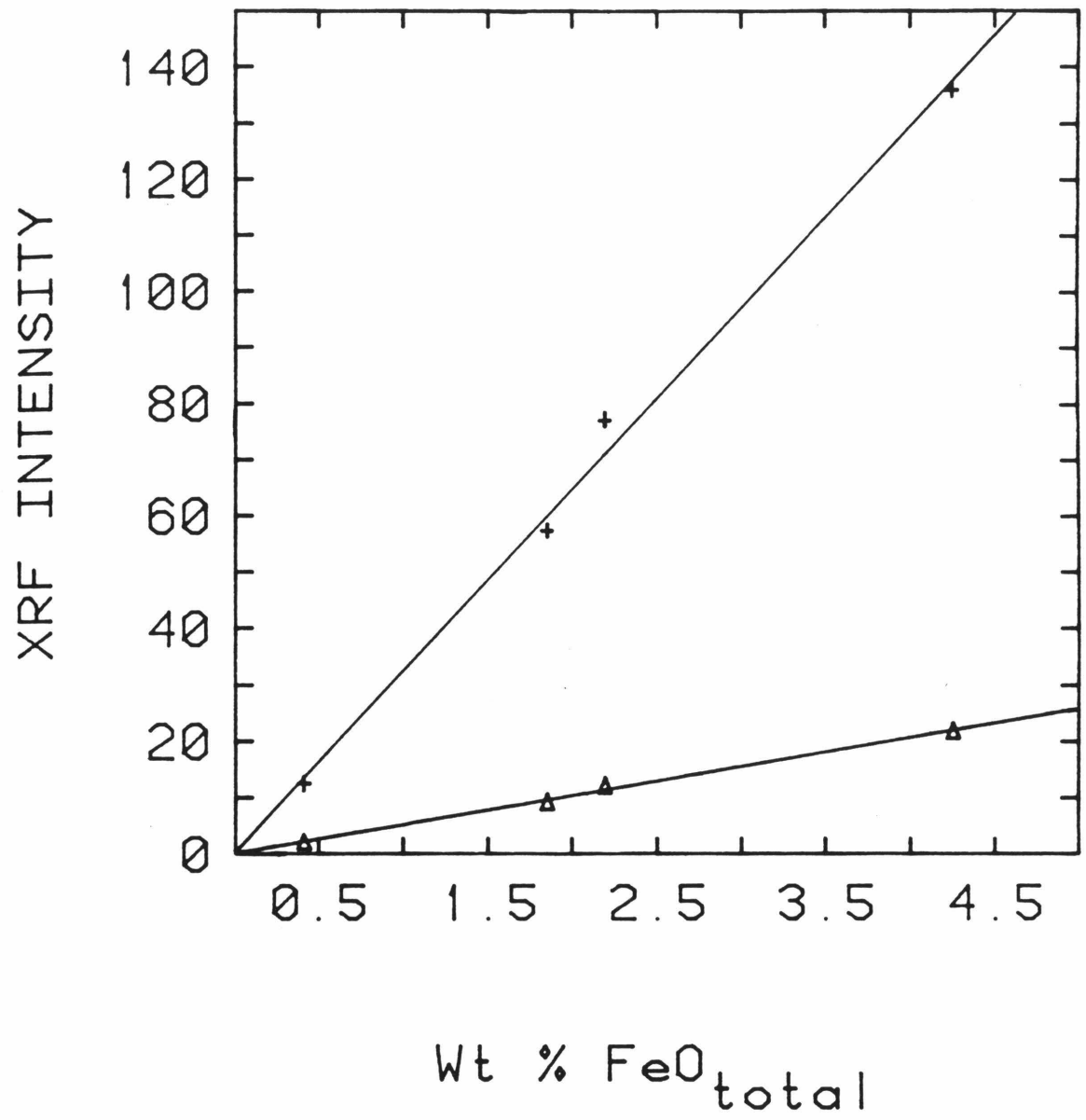


Figure 2.1a

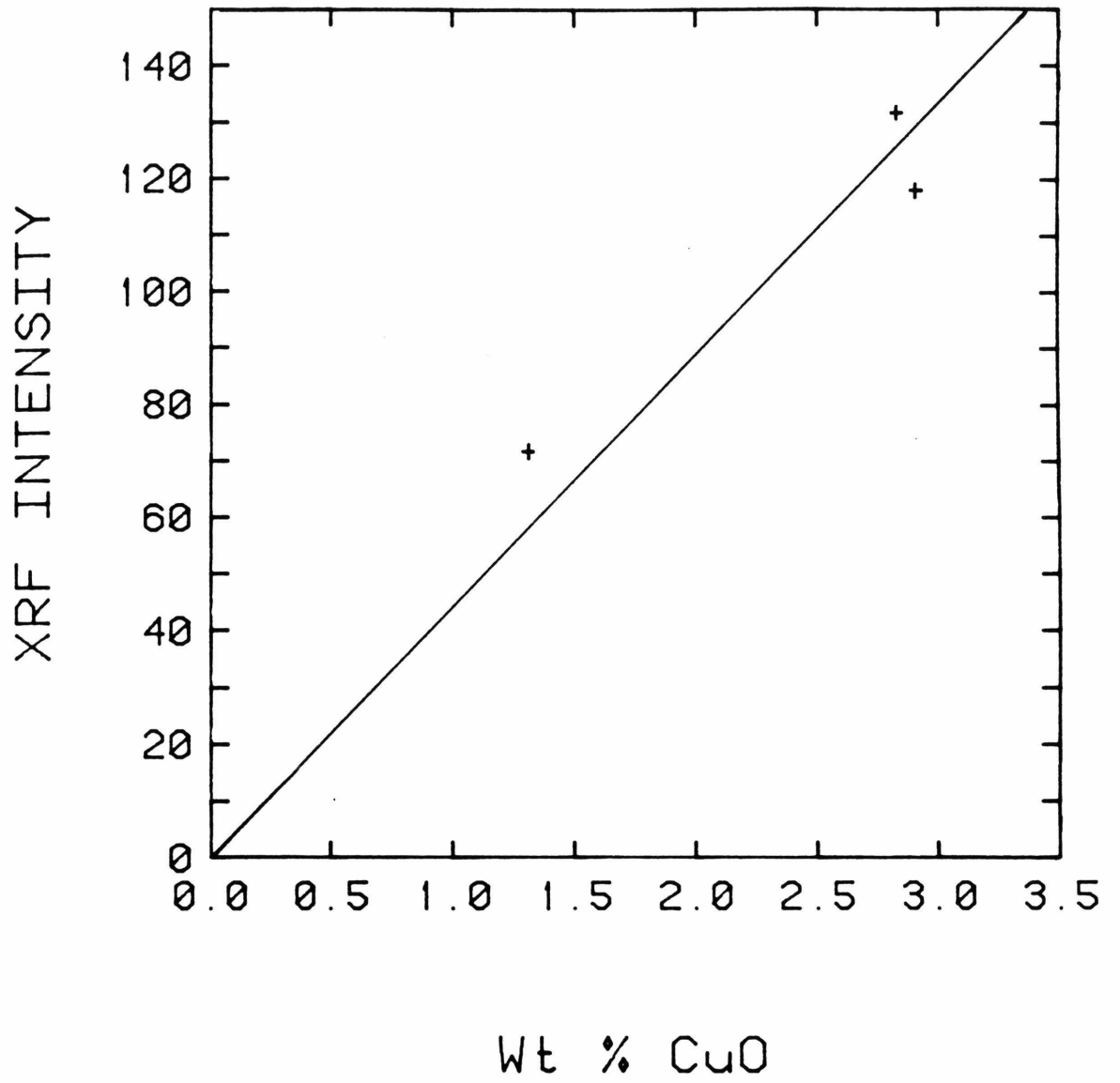


Figure 2.1b

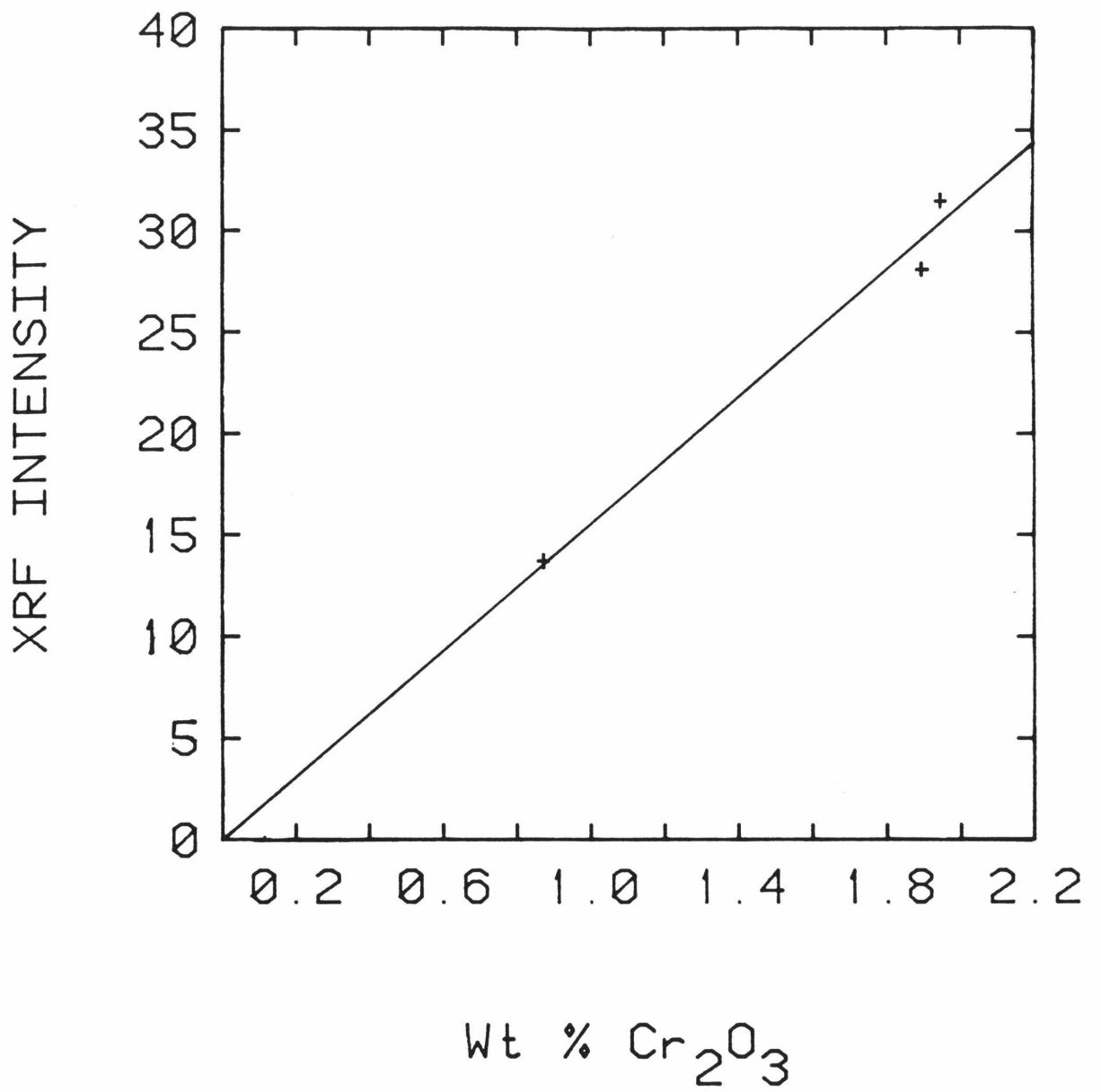


Figure 2.1c

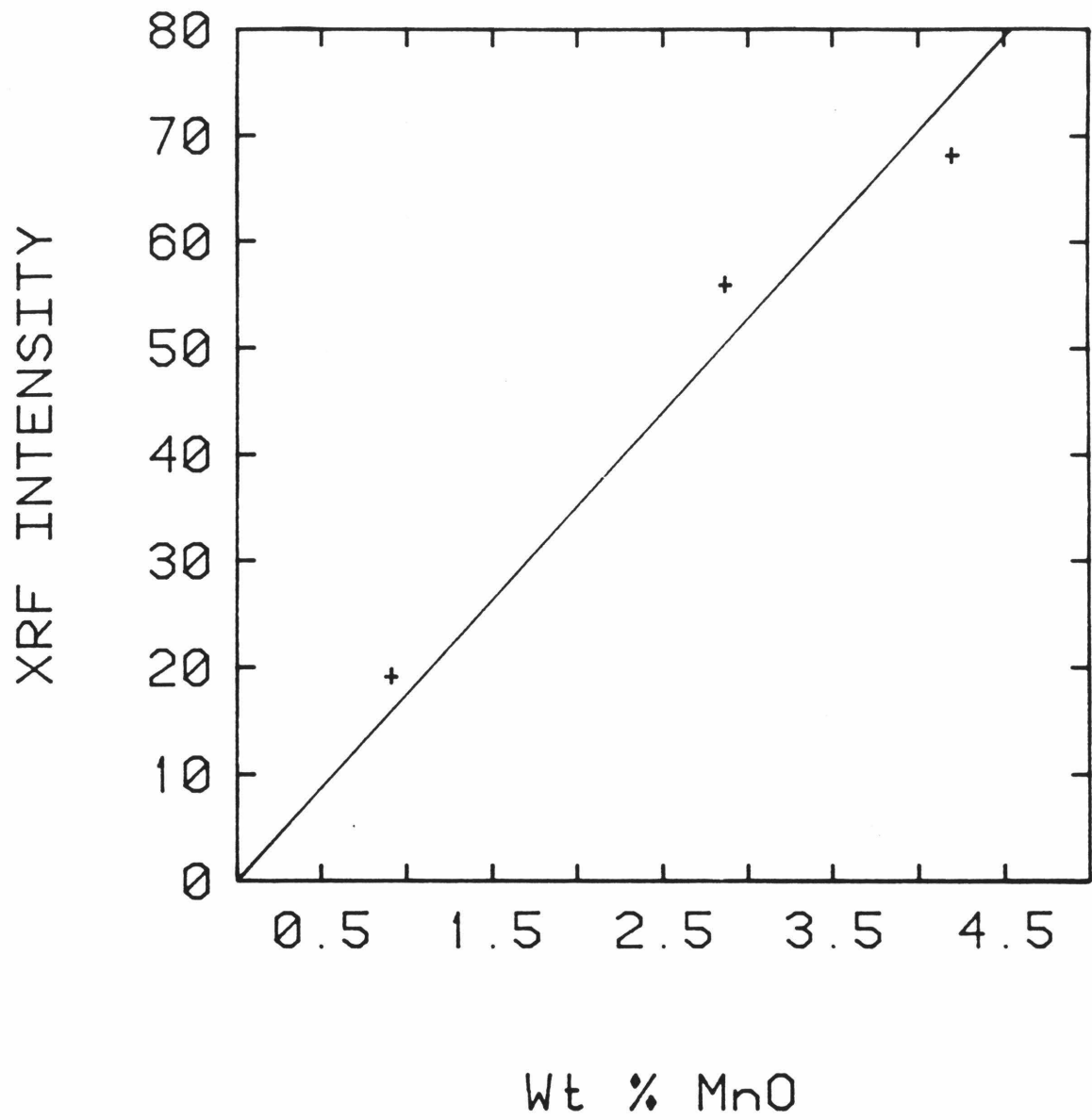


Figure 2.1d

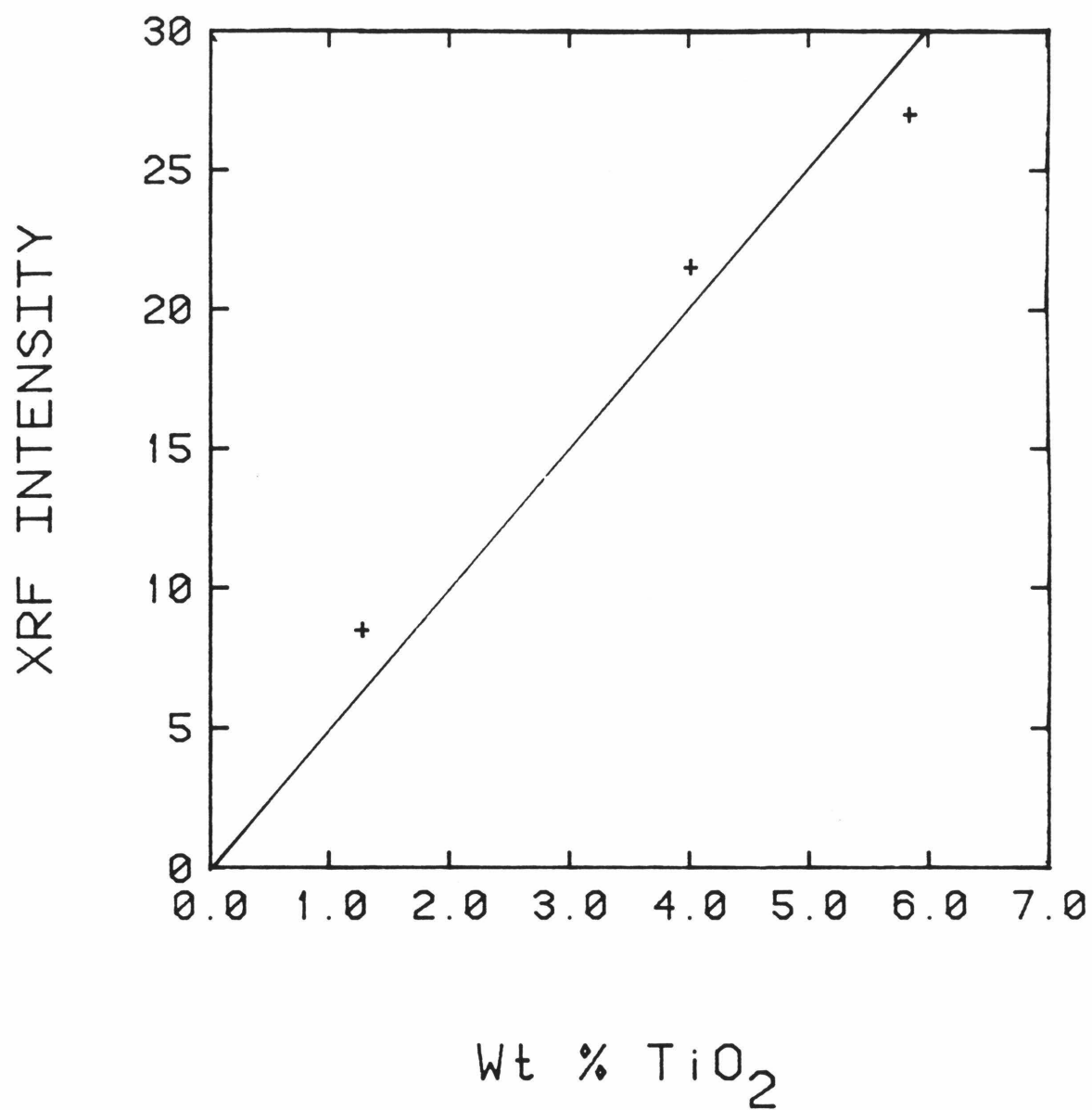


Figure 2.1e

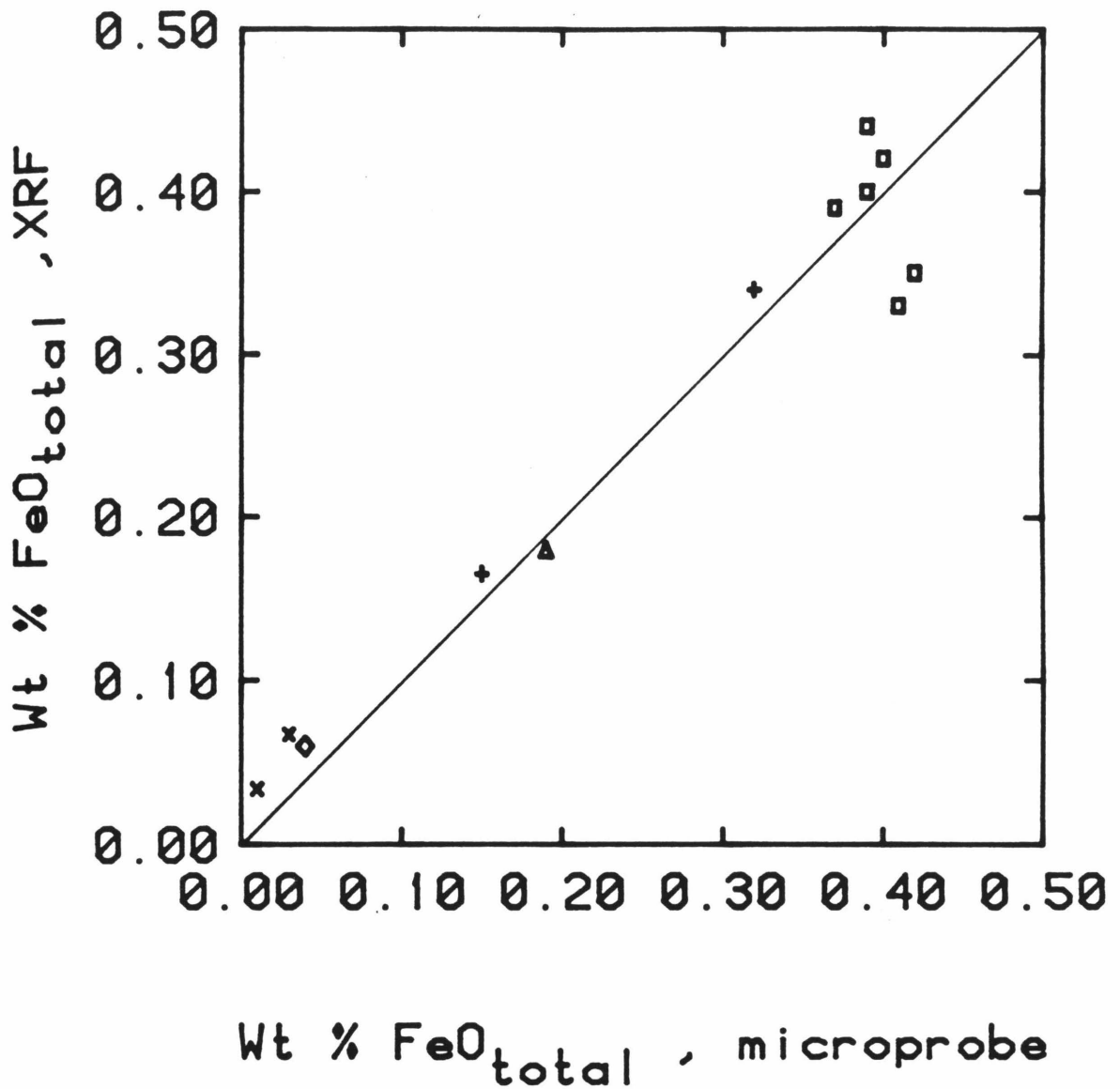


Figure 2.2 Comparison of X-ray fluorescence and microprobe analyses for iron in feldspar. Iron content is calculated as weight percent of FeO* which is Fe₂O₃ and FeO combined. The XRF analysis is plotted on the vertical axis. For the microprobe, analyses of less than 0.1 wt % are below the limits of detection and hence unreliable. Microcline analyses are indicated by an "x"; sanidine or orthoclase by a plus sign; oligoclase by a diamond, andesine by a triangle, and labradorite by a square.

of a silver target, the silicon peak was too weak to be used as the internal standard, so that iron's $K\alpha_1$ peak was used instead. This produced less accurate analyses; strontium and lead concentrations were determined using XRF are ± 15 to 20%.

2.2.c Hydrogen manometry

Hydrogen extractions were made in the stable isotope laboratory of the U.S.G.S. at Menlo Park. About 0.5 grams of feldspar fragments were loosely crimped in a molybdenum foil packet, placed in a platinum crucible inside a Pyrex-quartz reaction vessel, and heated at $\sim 150^\circ\text{C}$ under vacuum overnight. Next, a radio-frequency generator was used to heat the mineral to $\sim 1400^\circ\text{C}$, which allows for complete release of water and H_2 gas into the vacuum line. The water evolved was frozen into a LN_2 cold-trap, and H_2 was converted to water using a hot ($\sim 550^\circ\text{C}$) Cu-CuO furnace and then frozen. The water was then passed several times through a hot ($\sim 700^\circ\text{C}$) uranium furnace to completely convert it to H_2 gas, which could be manometrically measured. The volume of gas and the sample weight were then used to compute the weight % of total water removed from the feldspar.

For those samples with sufficiently large gas volumes, mass spectrometer analyses were made with a double collecting mass spectrometer. The data was corrected to standard mean ocean water (SMOW) using a computer program and analyses of standard waters.

2.2.d Thermoanalysis

Heat flux differential scanning calorimetry (DSC) and thermogravimetric (TG) analyses of feldspar were carried out simultaneously in a Mettler TA2000C system. Feldspar powder was weighed and placed in 70 ml platinum

cups. Alumina powder was used as a reference. The sample was heated under nitrogen from room temperature to 1000°C at a rate of 5 to 10°C per minute. A baseline was made by reheating the dehydrated sample.

2.3 Synthesis and Heating Experiments

2.3.a High pressure synthesis

High pressure experiments were conducted both at Caltech and at Stanford. At Caltech synthesis was attempted in a 1/2"-piston-cylinder apparatus similar to that of Boyd and England [1960]. Sample assembly and run procedures used were similar to those described by Chipman and Hayes in Johannes et al [1971], except that tungsten-rhenium thermocouples were used and a crushable alumina spacer was used instead of pyrophyllite. Samples of crushed feldspar or oxide powders were loaded into a platinum capsule (1 mm o.d.), and ~ 5 microliters of purified water were added. The capsule was pinched and spot welded. Runs were made between 3 and 10 kb and 600-900°C, and were from 8-24 hours long.

At Stanford, experiments were conducted in an internally-heated pressure vessel (IHPV). Platinum capsules (3 mm diameter) were loaded with 5 or 6 small (<1 mm) chips of Elizabeth R-Mine white microcline (Micro-1") and water, and then were crimped and welded. Runs were performed at ~ 2 kbar and 700° for 48 hours.

2.3.b Fugacity controlled, atmospheric pressure experiments

Experiments at atmospheric pressure were performed in a Deltech PT-31-VT low-inertia laboratory furnace which was regulated by a Eurotherm temperature controller. Oxygen fugacities were controlled either H₂-CO₂

gas mixtures or CO-CO₂ gas mixtures. A solid electrolyte sensor, calibrated at the Fe/FeO buffer was used to measure fO₂. Samples were suspended on platinum wire loops, of about 3 mm diameter. Runs were conducted between 850 and 1500°C for 3 to 24 hours.

2.3.c Dehydration and diffusion experiments

Dehydration of samples was done in air in a Lindberg solar basic furnace at temperatures between 200 and 1000°C. The samples were heated in a fused silica boat.

Diffusion of cations into feldspar was accomplished by heating the sample in a molten PbCl₂ (and other chlorides) at ~ 800°C overnight. The melt was contained in a ceramic crucible and heated in a Temco furnace regulated by a Honeywell temperature controller.

2.4 Irradiation Experiments

2.4.a Artificial irradiation

Samples of feldspar were artificially irradiated both at Caltech and at JPL. The source used at Caltech is cesium-137 which produces 0.66 MeV gamma rays and is currently giving doses of 1.41 MRads/day. Jet Propulsion Laboratory has cobalt-60 source which produces 1.33 and 1.173 MeV gamma rays and is somewhat stronger, currently giving doses of 6.25 MRads/day. The irradiation dose was recorded when the samples were removed from the irradiators. Most samples were irradiated at room temperature, but a few were irradiated while inside a styrofoam dewar filled with liquid nitrogen.

2.4.b Measurement of natural radioactivity

The natural radioactivity of amazonites was measured with a 8 inch well Harshaw NaI scintillator matched window assembly with three photomultiplier tubes. The detector assembly is designed to view large (~ 4" diameter) crystals. The detector assembly is isolated from external sources by lead brick housing, and its output is processed by a Canberra Industries Multichannel analyzer #8100. Counts were accumulated as a function of energy for a recorded time, usually one day. Background was obtained by counting when the sample chamber was empty. The instrument was calibrated by measuring the radiation from a Cs-137 source.

CONCENTRATION, CHARGE STATE, AND SITE OCCUPANCY OF IRON IN FELDSPAR

3.1 Sample Description and Chemistry

Table 3.1 gives details for the various feldspars examined in this section. Table 3.2 lists microprobe analyses for the specific samples, except for the amazonites and white microclines which are listed in Tables 6.1 to 6.3, and the Lake County labradorite which is similar to analyses in Tables 1.7 and 7.2, and perthite #4876 which was not analysed. Only samples with gemmy, twinfree areas were suitable for optical spectroscopy study, while all could be studied by EPR methods. Anorthite from the Serra de Mage meteorite was chosen as the Fe^{2+} standard for optical spectroscopy because fugacity conditions in a meteorite imply that little if any trivalent iron exists therein. Iron-rich orthoclase from Itrongay was used as the Fe^{3+} standard for both optical and EPR studies because Fe^{2+} can only be present in very low amounts as indicated by Mössbauer spectroscopy [Brown and Pritchard, 1969].

3.2 Optical Spectroscopy of Fe^{2+} in Plagioclase

Near-infrared absorption spectra of plagioclase (Figs. 3.1 to 3.3) show up to four broad bands due to Fe^{2+} . The features in the alpha and beta polarizations of labradorite (Figure 3.3) are similar in shape and position to those published by Bell and Mao (1972), and to each other, while the gamma spectrum is quite different from either set. From the complete spectral data on the labradorite four bands are visually discernable: one at 8000 cm^{-1} in α and partially in β , one at 7200 cm^{-1} in γ , one at 5300 cm^{-1} in γ , and one at 4600 cm^{-1} in α and β .

Table 3.1. Sample Description and Chemistry of Feldspars

Feldspar	Locality	Sample Number	Description	MICROPROBE ANALYSES				XRF Fe Total wt %	Optical Data Available	EPR * Integrated Intensity	EPR* DI †
				OR mole %	AB mole %	AN mole %	Fe total wt %				
Sanidine	Eifel, Germany	GRR 2/11/81	Gemmy, smoky	85.8a	14.2	0.0	0.12	0.13	Table 4	107	185
Orthoclase	Irongay, Madagascar	P-490	Gemmy, yellow	89.5 ^b	10.5	0.0	0.30	Standard ≅0.30	Table 4	NM	NM
"	"	GRR 7/7	"	91.4 ^b	8.6	0.0	0.25	0.26	NM	256	451
Orthoclase- Amazonite	Broken Hill, Australia	NDHC-68	Transparent green	92.0 ^{c,d}	7.8	0.2	BLD [‡]	0.009	BLD	2.6	5
Microcline	Elizabeth R Mine, CA	Micro-1	White perthite	93.5 ^d	6.5	0.0	<0.02	0.003	BLD	2.9	4
"	Perth, Ontario	8048	Red perthite	95.3 0.5	4.7 99.3	0 0.2	0.09 0.17	0.204	NM	MS†	NM
"	Riverside Co., Calif.	4786	Pink perthite	-	-	-	-	0.052	NM	MS†	NM
"	New York Mts., CA	19'	Green perthite	90.7 ^d	9.3	0.0	0.01	0.015	NM	MS†	NM
Oligoclase	S.Carolina	81228 Harvard	Gemmy, pale blue	1.6 ^e	81.3	17.2	0.03	0.05	BLD	13.5	126
Andesine	Halloran Springs, CA	AND-100	Gemmy, some Fe _x O inclusions	3.6 ^e	65.7	30.8	0.15	0.11- 0.17	Tables 3 & 4	43.2	333
Labradorite	Lake County, Oregon	GRR 3/1/76	Gemmy, yellow coarse twins	0.7 ^f	33.8	66.0	0.31	0.31	Tables 3 & 4	69.0	523
Labradorite	Crater Elegante, Mex.	CE-100	Gemmy, yellow fine twins	1.3 ^g	30.1	68.6	0.29	0.30	NM	70.0	468
Anorthite	Serra de Mage Meteorite	AMNH 3782-6	Turbid, yellowish Fe inclusions	0.2 ^e	6.0	93.8	0.07	NM [‡]	Table 3	NM	NM

* For 100 mg of sample and EPR run conditions of 1.0 mW, 1 Gauss modulation amplitude, x 1 gain. ‡ Below Level of Detection
 † Not Measured. ‡ Multiple species for iron prevented quantitative analysis. ¶ Double Integral, numerically calculated.
 † See Table 2 for complete microprobe analysis; and Spencer (1937) for similar material. ‡ See Coombs (1954) for analysis
 of similar material. † See Cech et al. (1971) for analysis of similar material. ‡ See Foord, Martin, Conklin, and
 Simmons (in prep.) for analysis of similar material. † See Table 2 for complete microprobe analysis. ‡ See Stewart et
 al. (1976) for analysis of similar material. † See Gutman and Martin (1976) for analysis of similar material.

Table 3.2 Microprobe Analysis of Selected Feldspars

	Sanidine Eifel	Perthite 8048	Perthite 8048	Orthoclase P490	Orthoclase 7/31/76	Oligoclase S.Carolina	Andesine Halloran	Labradorite Mexico	Anorthite 3782-6
SiO ₂	63.14	64.34	69.23	64.56	64.85	62.28	59.59	51.27	44.29
TiO ₂	BLD*	BLD	BLD	BLD	BLD	BLD	0.06	0.04	BLD
Al ₂ O ₃	18.48	17.92	19.30	17.98	17.06	22.94	25.86	28.85	36.22
FeO _{total}	0.15	0.09	0.17	0.38	0.32	0.04	0.19	0.37	0.09
MgO	BLD	BLD	BLD	BLD	BLD	BLD	BLD	0.07	BLD
BaO	0.79	0.17	0.13	0.12	0.16	BLD	BLD	BLD	BLD
CaO	BLD	BLD	0.05	0.01	BLD	3.94	6.97	16.15	19.46
Na ₂ O	1.59	0.53	12.13	1.22	0.94	10.33	8.21	3.91	0.68
K ₂ O	14.60	16.05	0.10	15.01	15.19	0.30	0.67	0.27	0.32
Total	98.77	99.10	101.10	99.34	98.53	99.83	101.4	100.96	100.8
Or	85.8	95.3	0.5	89.0	91.4	1.6	3.6	1.35	0.2
Ab	14.2	4.7	99.3	11.0	8.6	81.3	65.7	30.06	6.0
An	0.0	0.0	0.2	0.0	0.0	17.2	30.8	68.58	93.8

*Below Level of Detection.

#Not Measured.

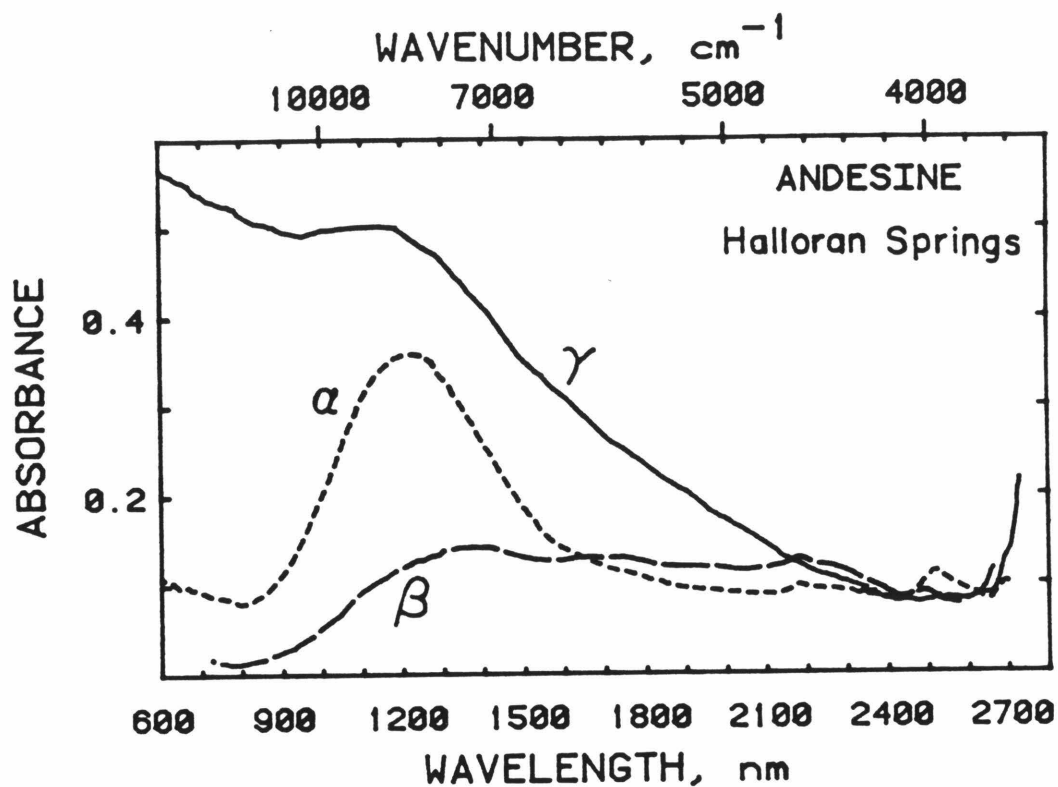


Figure 3.1. Near infrared optical absorption spectra of andesine from Halloran Springs, California, showing the broad band M-site Fe^{2+} features at about 1200 nm and possibly at 1800 to 2400 nm. Total iron content is 0.15 wt% Fe, part of which is ferrous. The rise in absorbance of the gamma spectrum towards short wavelength is due to scattering from fractures and inclusions. The small, sharper features at 2200, 2500, and 2750 nm are due to OH^- .

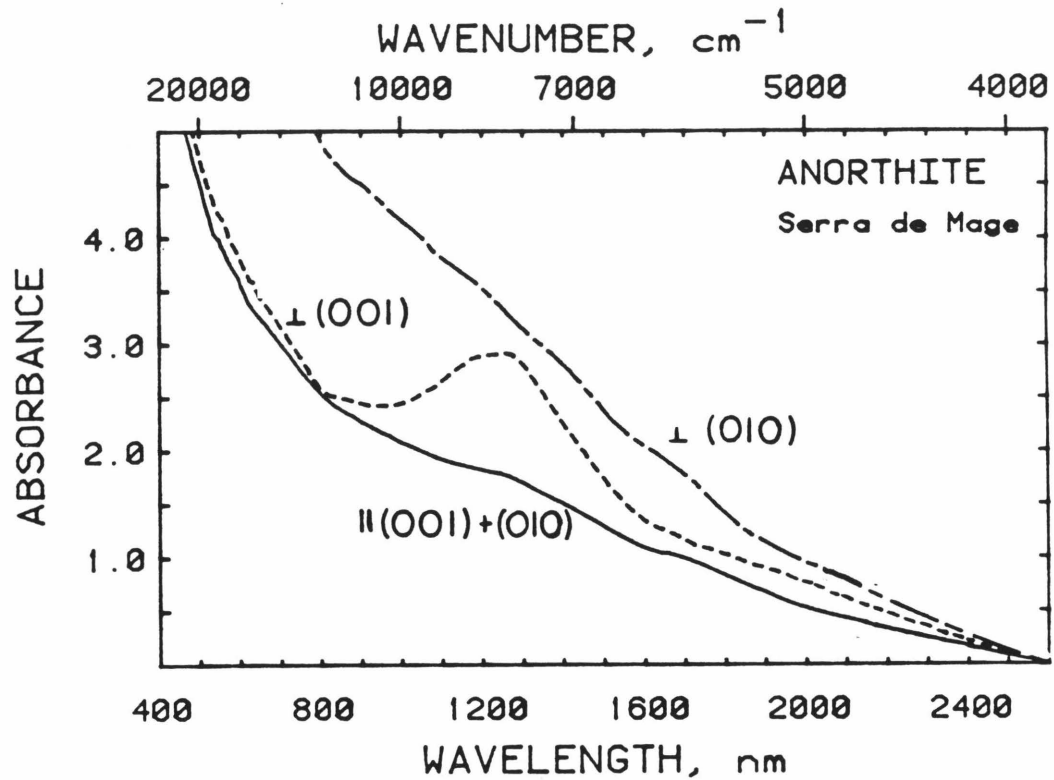


Figure 3.2 Absorption spectra of anorthite from the Serra de Mage meteorite showing broad-band M-site Fe^{2+} features at 1250 nm. Total iron content is 0.07 wt% Fe^{2+} . Spectra normalized to 1.0cm thickness. The weak features near 2300 nm may be part of the baseline. The strong rise of absorbance at shorter wavelengths is due to scattering from twin planes. Because of fine scale twinning, spectra were taken on cleavage faces.

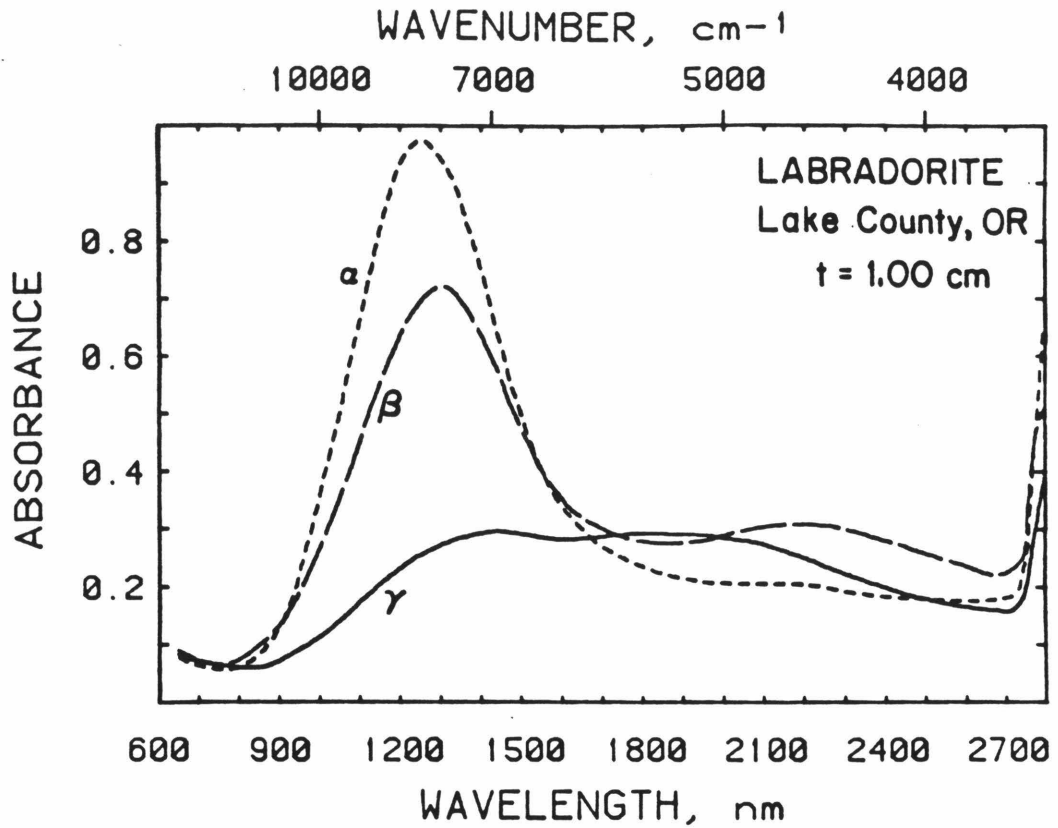


Figure 3.3 Near-infrared absorption spectra of labradorite from Lake County, Oregon. Bands at 1250, 1400, 1850, and 2200 nm are due to ferrous iron. The rise towards the infrared is due to OH⁻.

As discussed by Bell and Mao (1972), Fe^{2+} is located in the M-site in the feldspar structure. Fe^{2+} in a site of low symmetry usually produces two absorption bands in the near-infrared portion of the spectrum (Goldman and Rossman 1977). The presence of four absorption bands in the labradorite spectra indicates two structurally different Fe^{2+} sites. Any one polarization could be fit with a limited range of four Gaussian peaks, but all three polarizations (α , β , or γ) could not be fitted with the same four Gaussian peaks (Figures 3.4 and 3.5 and Table 3.3). This implies that either (1) the component peaks are not Gaussians, or (2) there are more than four components and thus more than two Fe^{2+} sites. In view of the intermediate structural state of the labradorite, (Stewart et al, 1976), a continuum of microenvironments for each of the two principal sites is likely to exist giving rise to asymmetric peaks. These two principle sites may correspond to the "C" and "T" doublets seen in Mössbauer spectroscopy of lunar plagioclases [Hafner et al, 1971].

The Fe^{2+} features in the andesine and anorthite spectra (Figures 3.1 and 3.2) bear an overall resemblance to those of the labradorite. The variation of relative peak intensities and apparent band positions among the three samples can be attributed to the difference in orientation of the optic axes with respect to the crystallographic axes for the three plagioclases. For the andesine, two bands can be seen at 8000 ($\alpha\gamma$) and 7200 cm^{-1} (β). There are indications of additional absorption bands at lower wavenumbers in the Gaussian decomposition of the andesine, which were obscured by OH overtones in the wavelength plot (Fig. 3.1). That the coordination environment of Fe^{2+} in the andesine is probably similar to that in labradorite is corroborated by the similar Gaussian fits (Table 3.3). The lower quality of the anorthite spectra due to scattering and small sample size prevents

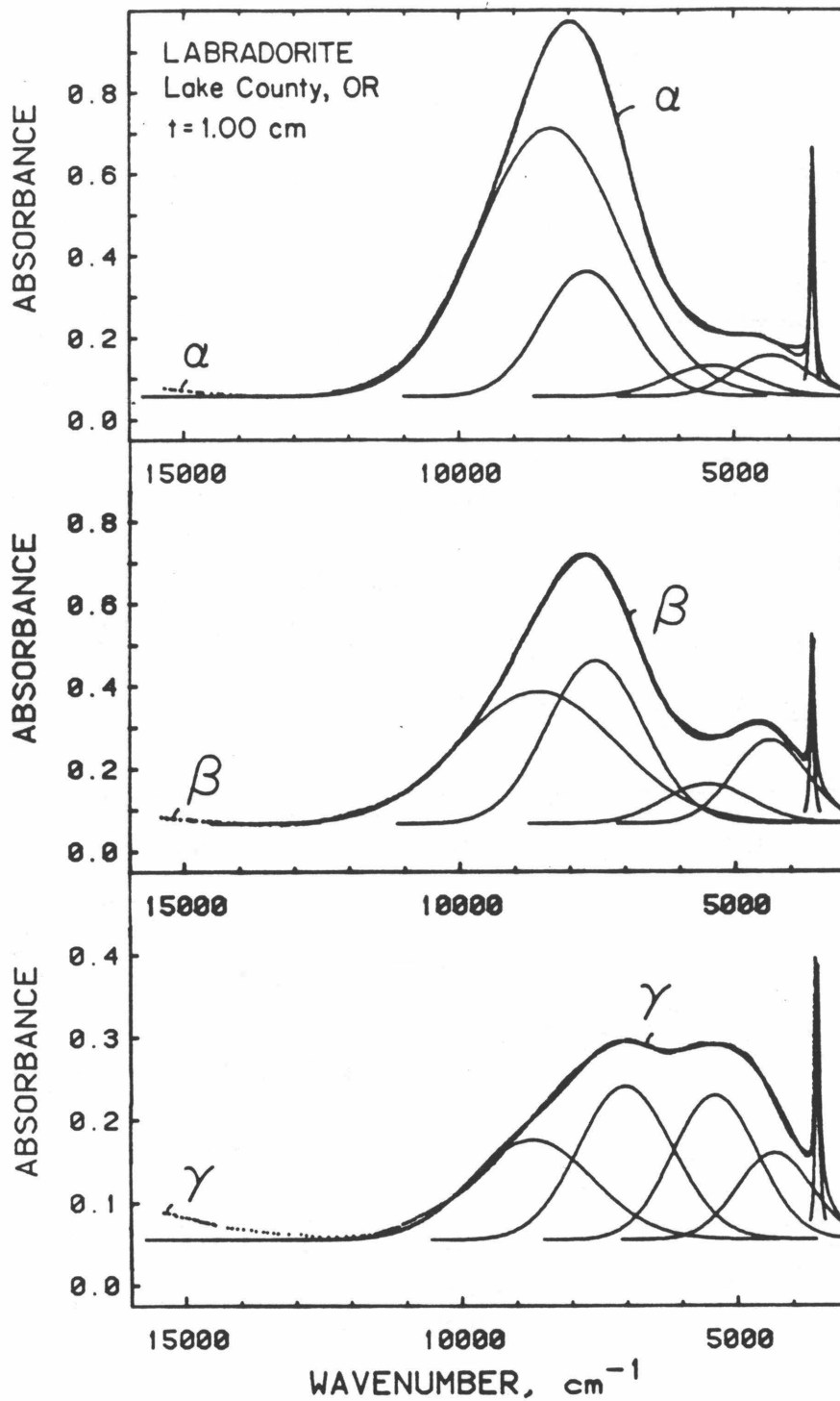


Figure 3.4 Gaussian deconvolution of Lake County labradorite near infrared spectra. The sharp peak at 3570 cm^{-1} is due to OH; all other features are due to Fe^{2+} . The actual spectra are plotted as dotted lines. Gaussian components and the calculated spectra are solid lines. More than four components are required to fit the three polarizations.

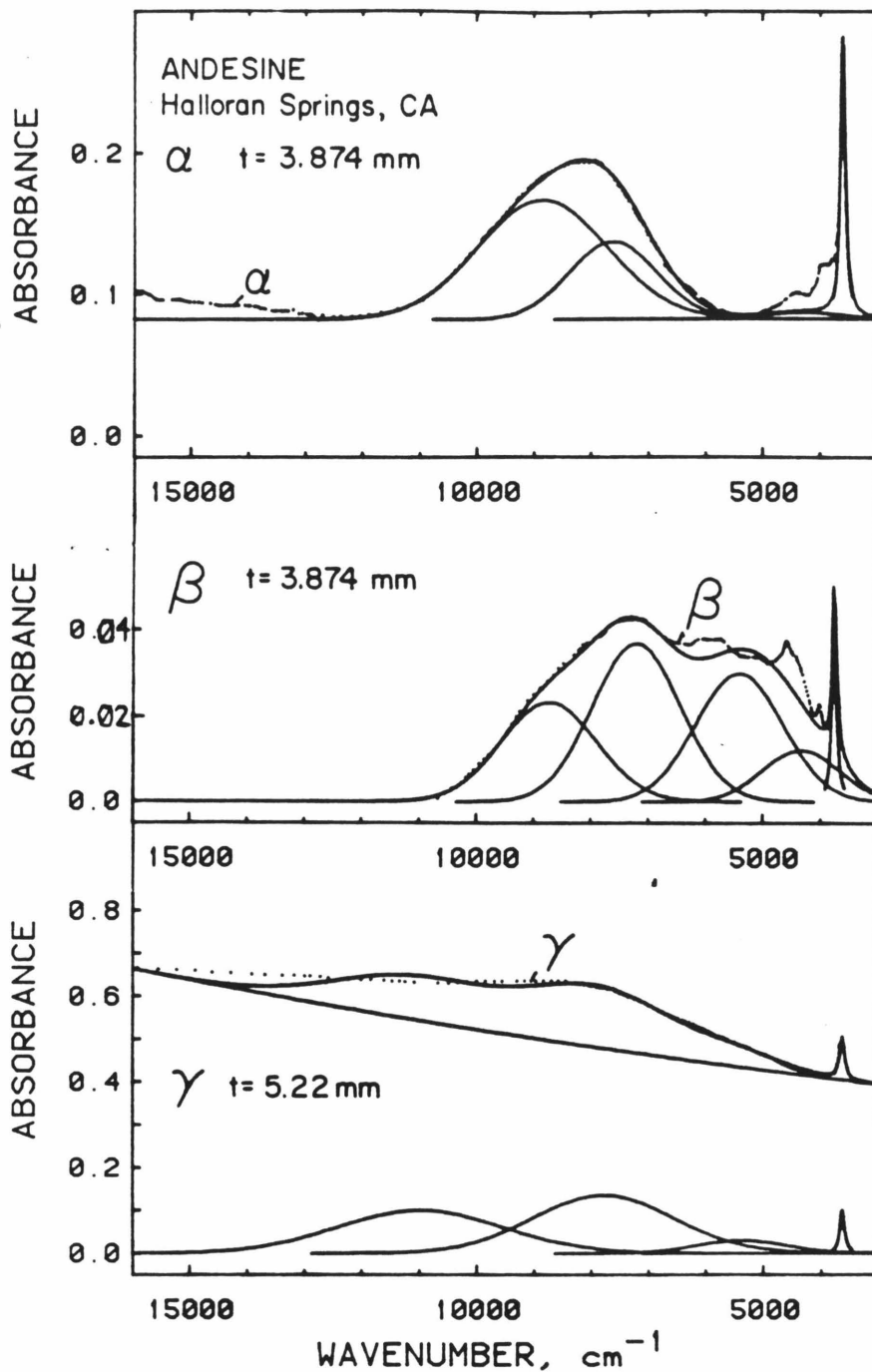


Figure 3.5 Gaussian deconvolution of Halloran Springs andesine. The actual spectra are plotted as dotted lines. Gaussian components and the calculated spectra are solid lines. OH^- bands are superimposed on the ferrous bands near 5000 cm^{-1} . γ is poorly resolved due to scattering.

Table 3.3 Optical Fit Parameters for Fe²⁺ in Plagioclase for 1.00 cm-thick Crystals

Mineral	Polarization	Energy cm ⁻¹	1/2 Width¶ cm ⁻¹	Abs cm ⁻¹	I.I.* cm ⁻²	Energy cm ⁻¹	1/2 Width cm ⁻¹	Abs cm ⁻¹	I.I.* cm ⁻²
Andesine	α	8850	2650	0.219	619	7620	1800	0.142	272
Halloran Springs	β	8730	1950	0.299	622	7200	1800	0.478	915
	γ	~8000	~1500	~0.8	~300	-	-	-	-
Labradorite	α	8340	3050	0.655	2127	7680	1900	0.305	617
Lake County	β	8550	3380	0.320	1152	7500	2060	0.395	867
	γ	8730	2600	0.121	335	7030	2010	0.186	398
Anorthite†	⊥ (001)	9500	2500	0.58	1554	7800	2000	1.31	2798
Serra de Mage	∥ (001+010)	8000	~2000	~0.10	~200	-	-	-	-
	⊥ (010)	-	-	-	-	-	-	-	-
Andesine cont.	α	-	-	-	-	4340	1580	0.013	22
	β	5410	1780	0.387	734	4340	1580	0.155	261
	γ	-	-	-	-	-	-	-	-
Labradorite cont.	α	5410	1850	0.075	148	4340	1580	0.100	168
	β	5480	1850	0.095	187	4340	1580	0.202	340
	γ	5410	1780	0.175	332	4340	1580	0.105	177

*Integrated Intensity.

¶ Full width at half height.

†Intensity was not measurable due to poor resolution below 5000 cm⁻¹.

determination of the number of absorption bands. Resolution in the high energy region is sufficiently good to see that only one band exists. This suggests that the site occupancy of Fe^{2+} in the meteoritic plagioclase differs from the terrestrial plagioclases. However, the orientation of the optical axes may be such that the two bands near 1250 nm were merged into one, so that the variation of site occupancy is intriguing, but unproven.

The impossibility of resolving the plagioclase spectra into a definite number of Gaussian peaks (Figures 3.4 and 3.5 and Table 3.3) and the variation of orientation of optical axes among the samples limits the number of meaningful quantities derivable from the spectral parameters to two: namely, the integrated intensities of each of the high and low energy absorption bands averaged for the three polarizations. Unfortunately, the area of the low energy peak ($\sim 5000 \text{ cm}^{-1}$) is unreliable for the andesine and anorthite because of its low contrast with the baseline. Taking this into consideration, the ferrous iron content of the terrestrial plagioclases can be computed in two ways. The first assumes that the lower energy bands are proportional to the higher so that the iron content is represented by the integrated intensity near 1250 nm, that is,

$$[\text{Fe}^{2+}] = \frac{[\text{Fe}^{2+}] \text{ anorthite} \cdot \text{Integrated Intensity} (\sim 8000 \text{ cm}^{-1} \text{ peak})}{\text{Integrated Intensity} (\sim 8000 \text{ cm}^{-1} \text{ of anorthite})} \quad . \quad (3.1)$$

The second way assumes that the spectra were good enough to resolve all the Fe^{2+} bands so that the anorthite's iron content is described by the area of its one band, while the terrestrial plagioclases require all band areas to correctly assess divalent iron concentrations:

$$[\text{Fe}^{2+}] = \frac{[\text{Fe}^{2+}] \text{ anorthite} \cdot \text{Total Integrated Intensity} (8000+5000 \text{ cm}^{-1} \text{ peaks})}{\text{Total Integrated Intensity} (\sim 8000 \text{ cm}^{-1} \text{ of anorthite})} \quad . \quad (3.4)$$

Equation (3.1) gives 0.085 wt% Fe^{2+} for the labradorite, while equation (3.2) gives up to 0.103 wt% Fe^{2+} . Both numbers are comparable to ferrous iron contents derived by wet chemical analysis: 0.13 (Stewart et al, 1966) and 0.09 wt% Fe (Emmons 1953, p. 18). For the andesine eq. (3.1) gives 0.023 wt% Fe^{2+} and equation (3.2) gives 0.026 wt% Fe^{2+} . The uncertainty in iron content from eq. (3.1) is $\pm 11\%$ while that from eq. (3.2) is $\pm 15\%$, which mostly arises from the uncertainty in the chemical analysis of the anorthite, but partially from the uncertainty in measuring the optical band area ($\pm 2\%$ for the 5000 cm^{-1} band). Gemmy samples like the labradorite give accurate and reproducible results. However, the variable internal quality due to fractures, twinning, or inclusions in some samples limits both the usable thickness and area for optical spectroscopy and results in a steep baseline due to scattering, and thus reduces the accuracy of the data. Equation (3.1) is probably better because the anorthite may have some intensity near 5000 cm^{-1} which was not apparent in the small sample measured. Equation (3.2) gives comparable results because most of the intensity for the Fe^{2+} optical transitions lies in the $\sim 8000 \text{ cm}^{-1}$ band.

3.3 Optical Spectroscopy of Fe^{3+} in Feldspar

3.3.a Orthoclase and sanidine

Optical spectra of sanidine and orthoclase show evidence only of Fe^{3+} in tetrahedral sites. The concentration of Fe^{2+} , if present at all in the M-site, was estimated at less than 0.002 wt% by comparison with the anorthite spectrum. This is small compared to both the total iron content of the sample and the error in its chemical analysis. The spectra of the sanidine (Figure 3.6) and the orthoclase (Figure 3.7) differ only slightly if the absolute intensity of the Fe^{3+} bands is not considered. Because of the

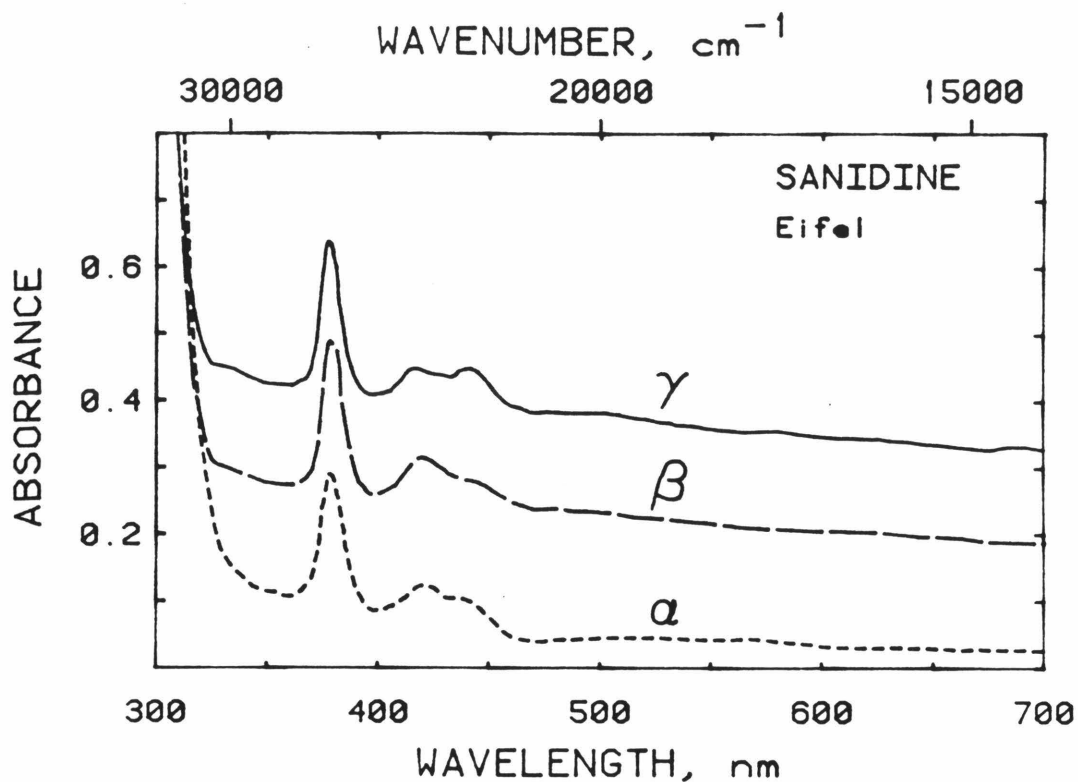


Figure 3.6. Optical absorption spectra of sanidine from Eifel, Germany, showing tetrahedral Fe^{3+} features between 350 and 400 nm. Total iron content is 0.123 wt% Fe. Spectra normalized to 1.0 cm thickness. The absorption rise towards the ultraviolet is due to oxygen to iron charge transfer. The sample was heated at 400°C for 0.5 hours to remove its natural smoky color which otherwise would be superimposed on the iron spectrum.

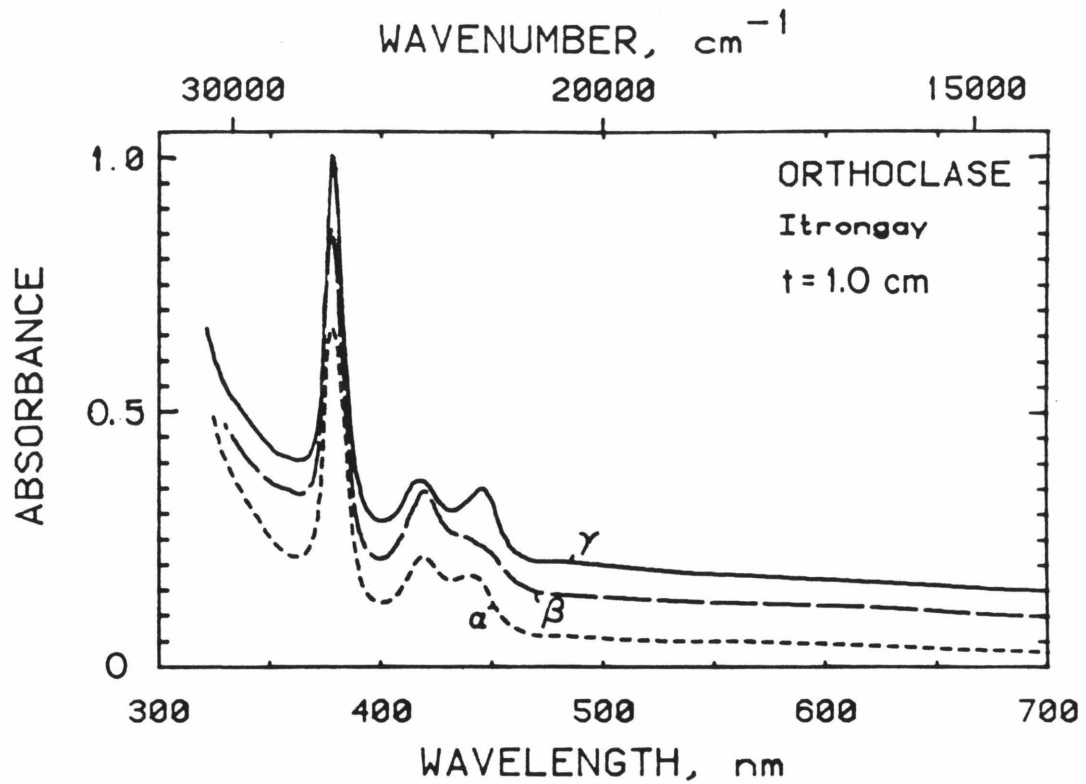


Figure 3.7 Optical absorption spectra of clear, lemon-yellow orthoclase from Itrongay, Madagascar. Iron content is 0.30 wt% Fe^{3+} . The yellow color is due to the absorptions at 418 and 445 nm. All absorptions are due to Fe^{3+} . There may be absorptions near 500 nm, but these are comparable in intensity to the noise.

weak pleochroism, these polarized spectra resemble the unpolarized spectrum of Faye [1969], and are similar to the alpha and gamma spectra recorded by Veremeichik et al [1975]. (See Section 1.2.a.ii.)

The Gaussian fits to the orthoclase (not shown) and sanidine spectra (Fig. 3.8) are nearly identical, as shown by the listing of peak parameters (Table 3.4). The Gaussian fits show that slight differences exist between the orthoclase and sanidine in the intensity ratios (α/β ; β/γ ; α/γ) for each of the transitions. Despite the differences, nearly linear correlations exist between iron content and absorptivity and between iron content and integrated intensity for each polarization (Figure 3.9 and 3.10).

The deviation from linearity in Figures 3.9 and 3.10 may be real because it is larger than both the uncertainties in measurement and the small amount of ferrous iron that is possibly present (<0.003 wt%). The deviation could be interpreted as arising from (1) the intensity stealing mechanism of Manning [1970] wherein the d-d transitions nearer to the O^{2-} to Fe^{3+} charge transfer band borrow more energy from it, and/or (2) real differences in extinction coefficients presumably due to structural variations. Intensity stealing would produce a nonlinear extinction coefficient because the absorption bands have finite width, so that the taller, wider at the base peak would receive an extra "boost" in intensity.

3.3.b Andesine and Labradorite

The spectra of andesine (Figure 3.11) and labradorite (Figure 3.12) resemble the spectra of Fe^{3+} in potassium feldspar except that the peaks are broader and shifted to slightly lower energies. The oligoclase spectrum (Chapter 6) exhibits a shoulder near 26200 cm^{-1} which is undoubtedly due to Fe^{3+} , but is too weak for quantitative analysis. The α and γ polarizations

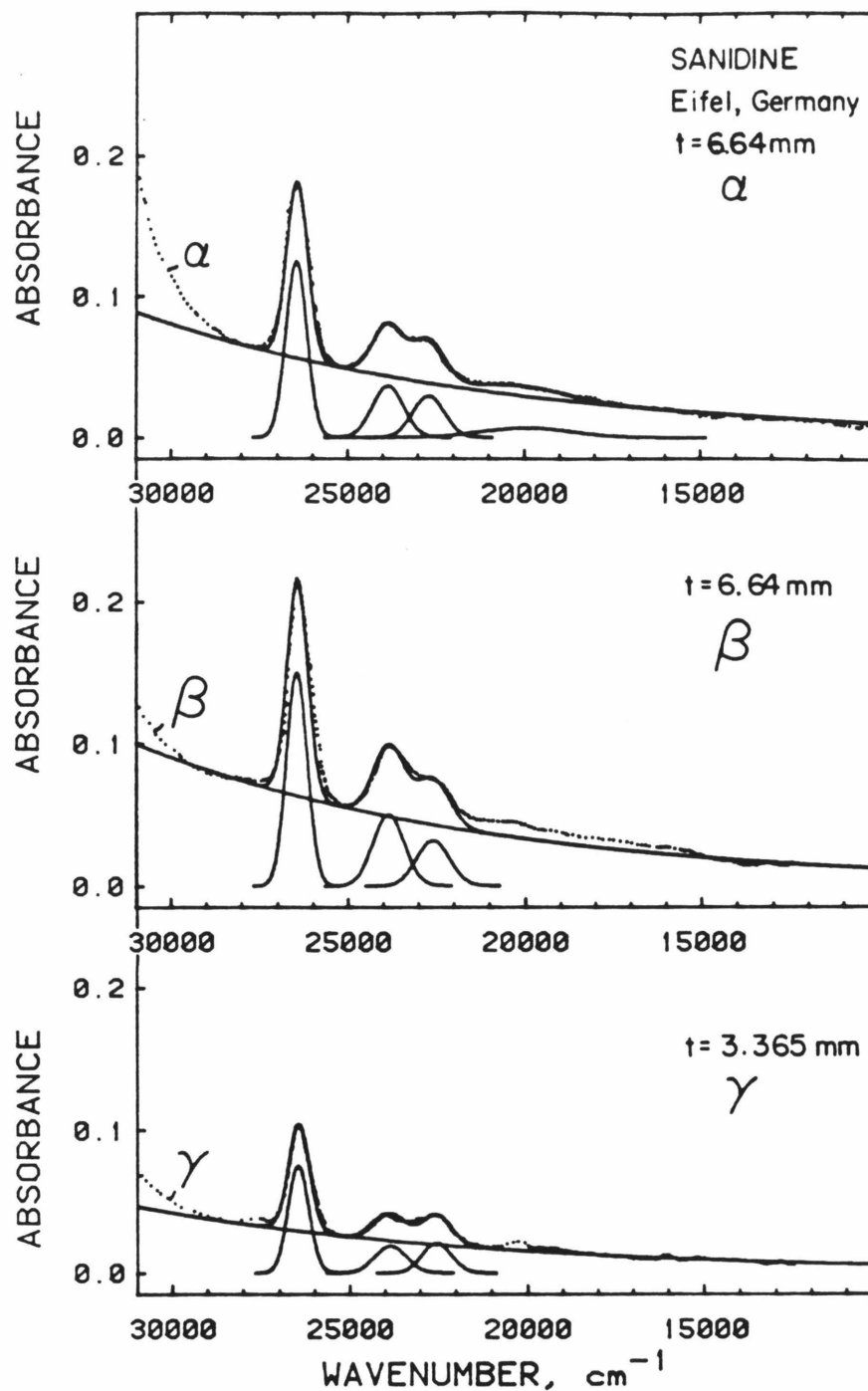


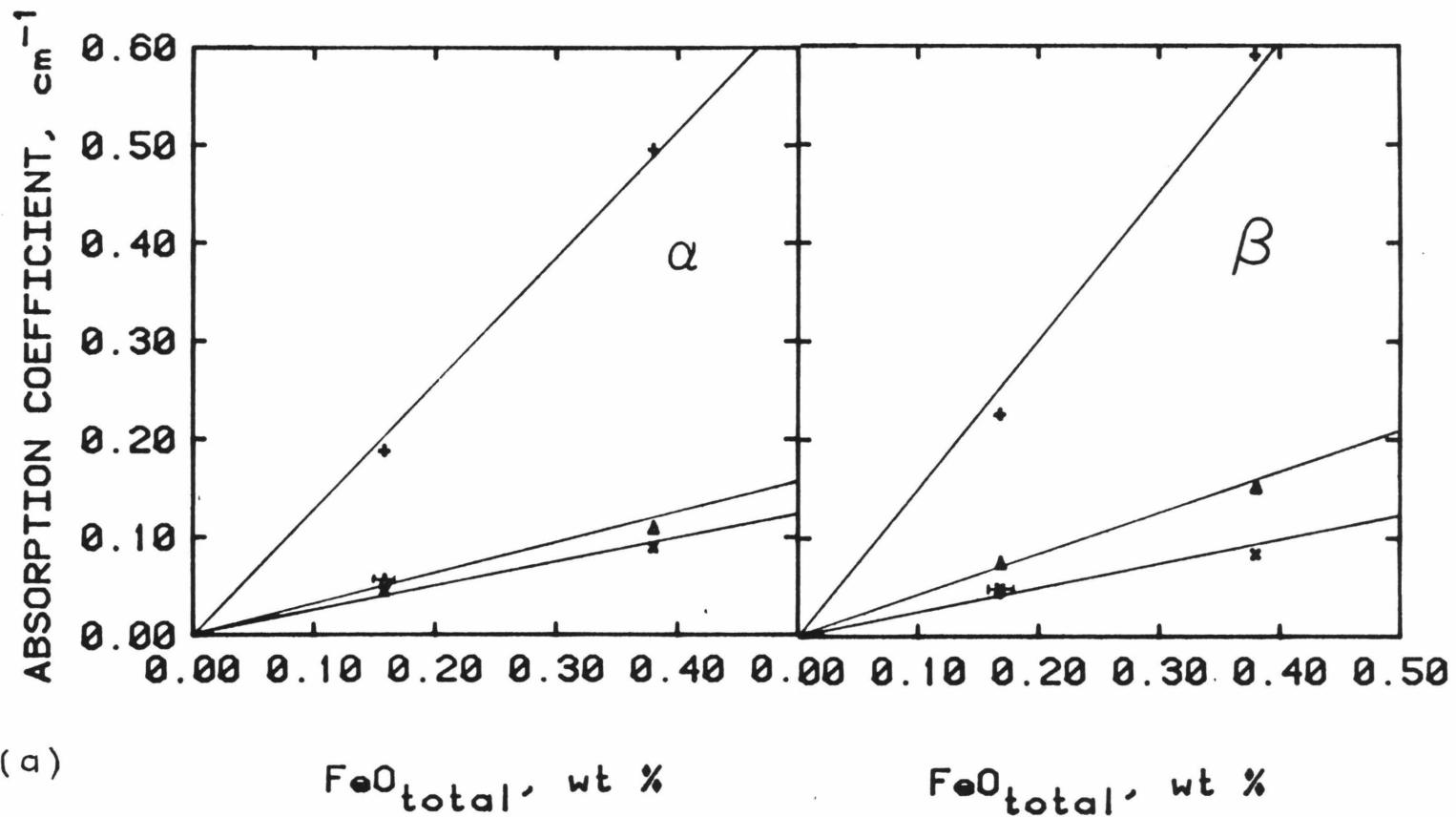
Figure 3.8 Gaussian deconvolution of the polarized absorption spectra containing the visible region of clear sanidine. Iron content is 0.123 wt% Fe^{3+} . All absorption bands are due to tetrahedral Fe^{3+} . The baselines were approximated by Equation 2.1. The baseline, component peaks, and calculated spectra are solid lines. The spectral data are plotted as dots.

Table 3.4 Optical Spectroscopy Parameters of Fe³⁺ in Feldspars

Sample	Polarization	${}^6A_1(S) + {}^4E(D)\dagger$				${}^6A_1(S) + {}^4T_2(D)\dagger$				${}^6A_1(S) + {}^4A, {}^4E(G)\dagger$			
		Energy cm ⁻¹	1/2-Width cm ⁻¹	Abs cm ⁻¹	I.I.* cm ⁻²	Energy cm ⁻¹	1/2-Width cm ⁻¹	Abs cm ⁻¹	I.I.* cm ⁻²	Energy cm ⁻¹	1/2-Width cm ⁻¹	Abs cm ⁻¹	I.I.* cm ⁻²
Orthoclase	α	26450	690	0.495	364	23850	1040	0.109	121	22650	1050	0.089	100
Itrongay	β	"	"	0.591	434	"	"	0.153	169	22600	1070	0.084	95
	γ	"	"	0.640	470	"	"	0.106	117	22500	970	0.116	119
Sanidine	α	"	700	0.188	140	"	1040	0.055	60.9	22700	1050	0.044	49.7
Eifel	β	"	690	0.226	166	"	"	0.075	83.4	22600	1090	0.048	55.9
	γ	"	"	0.223	164	"	"	0.056	62.5	22550	970	0.062	64.5
Oligoclase S.Carolina	α	~26200	?	~0.03	-	-	-	-	-	-	-	-	-
Andesine	α	26200	800	0.150	128	23650	950	0.070	70.5	22390	1300	0.057	84.7
Halloran	β	"	"	0.181	154	23750	"	0.062	62.7	"	1400	0.036	50.0
Springs	γ	"	"	0.182	155	"	"	0.042	42.6	"	"	0.057	82.8
Labradorite	α	26130	900	0.270	259	23700	990	0.066	69.6	22350	1250	0.060	79.9
Lake CO	β	26030	"	0.220	211	23650	900	0.065	62.3	22390	1300	0.045	62.3
	γ	25980	"	0.292	280	23580	"	0.039	41.1	22310	1250	0.074	98.5
		${}^6A_1(S) + {}^4T_2(G)\dagger$				${}^6A_1(S) + {}^4T_1(G)\dagger$							
		Energy cm ⁻¹	1/2-Width cm ⁻¹	Abs cm ⁻¹	I.I.* cm ⁻²	Energy cm ⁻¹	1/2-Width cm ⁻¹	Abs cm ⁻¹	I.I.* cm ⁻²				
Andesine	α	20000	1600	0.018	50.0	16000	1600	0.018	30.8				
cont.	β	"	1700	0.047	84.1	16200	1700	0.018	32.8				
	γ	"	1800	0.036	69.3	-	-	-	-				
Labradorite	α	-	-	-	-	-	-	-	-				
cont.	β	20000	1600	0.019	32.4	16800	1600	0.012	20.4				
	γ	19950	1600	0.021	35.8	16800	1600	0.012	20.4				

*Integrated Intensity was calculated for 1.00 cm thick crystal.

†Assignments for tetrahedral Fe³⁺ in feldspar made by Manning (1970).



(a) α and β . (b) γ and average.

Figure 3.9 Absorptivity as a function of iron content for orthoclase (0.38 wt % FeO) and sanidine (0.15 wt % FeO) for the three polarizations and their average. + denotes 26400 cm^{-1} band, Δ is the 23850 cm^{-1} band, and x represents the 22650 cm^{-1} band. The orthoclase symbol is about the size of the error bars, but the uncertainty in the sanidine's iron content is larger as shown.

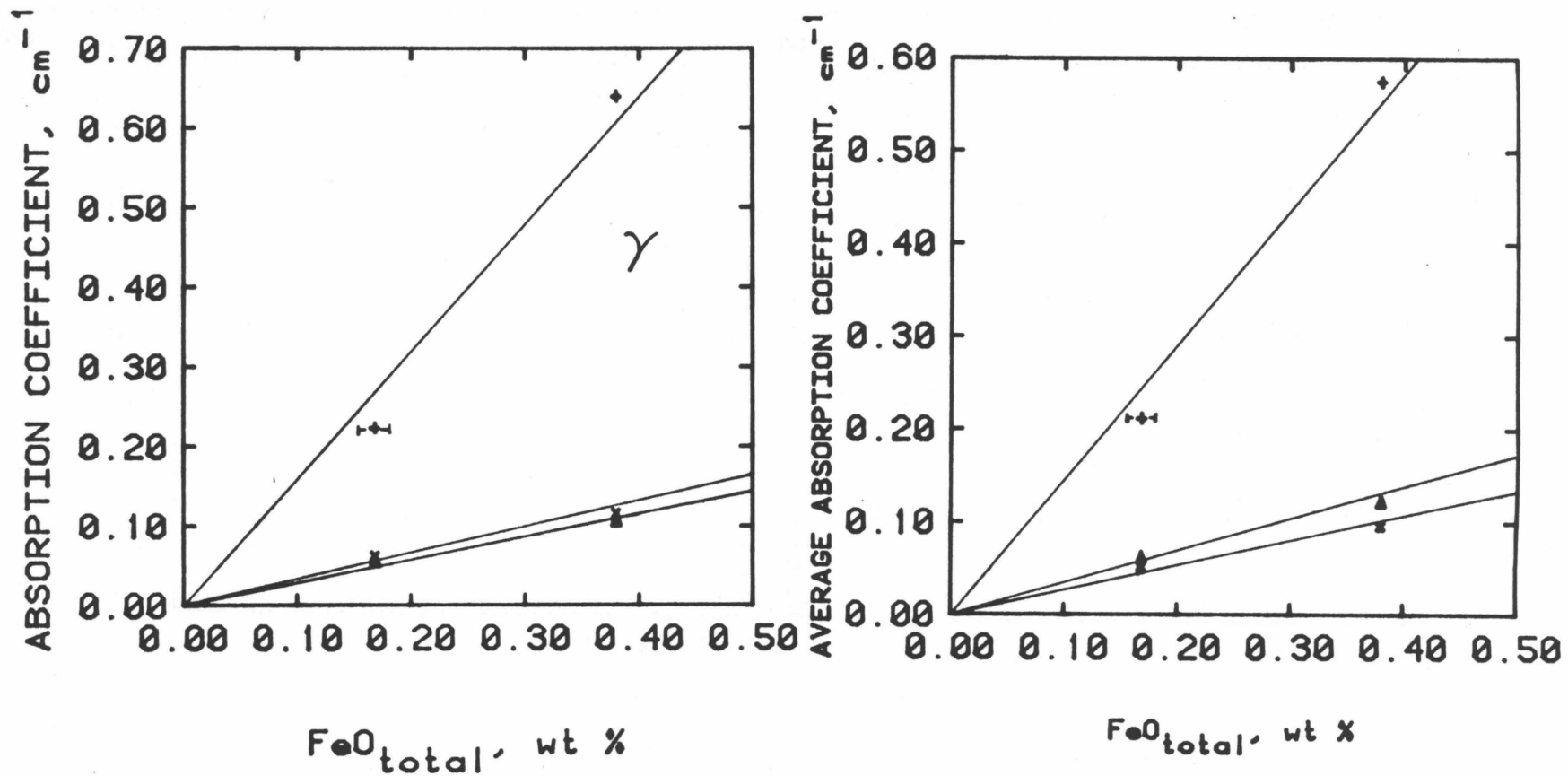


Figure 3.9 b

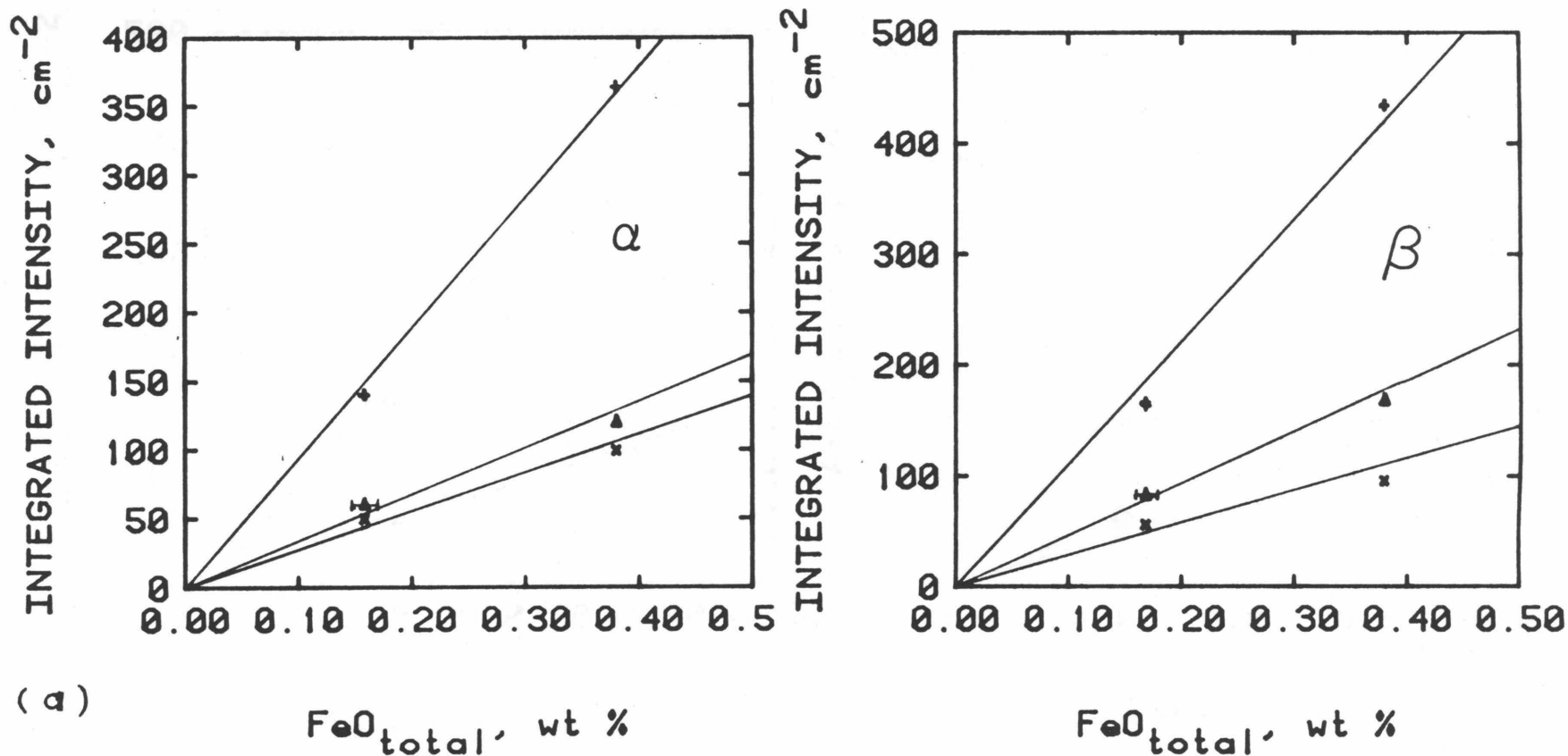


Figure 3.10 Integrated intensity (I.I.) as a function of iron content for orthoclase (0.30 wt% Fe^{3+}) and sanidine (0.12 wt% Fe^{3+}) for the three polarizations and their average. + denotes 26400 cm^{-1} band, Δ is the 23850 cm^{-1} band, and x represents the 22650 cm^{-1} band. The orthoclase symbol is about the size of the error bars, but the error in the sanidine's iron content is larger as shown. (a) α and β . (b) γ and average.

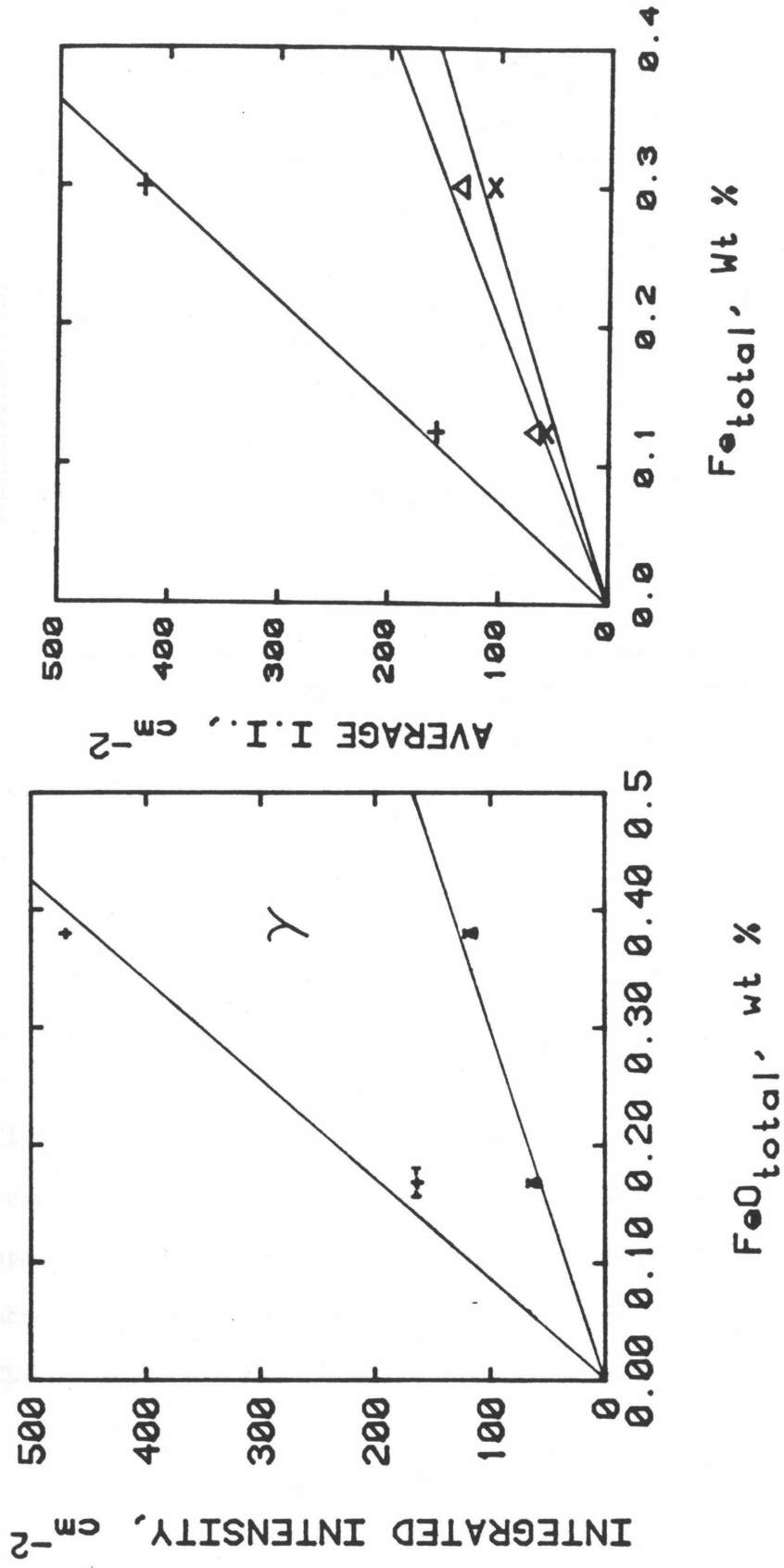


Figure 3.10 b

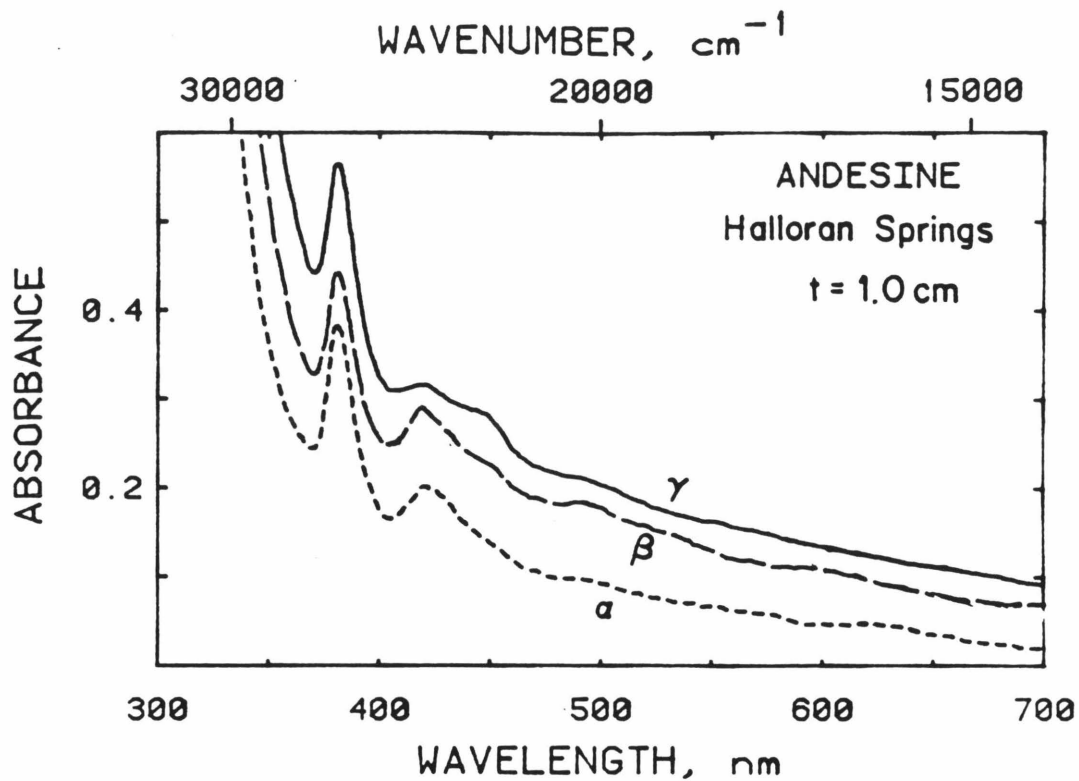


Figure 3.11 Polarized absorption spectra in the visible region of andesine from near Halloran Springs, California. This is a continuation of the spectra of Figure 3.1. Spectra are normalized to 1.0 cm thickness. Absorption features in this region arise from tetrahedral Fe^{3+} transitions. The spectra were displaced vertically from each other for clarity.

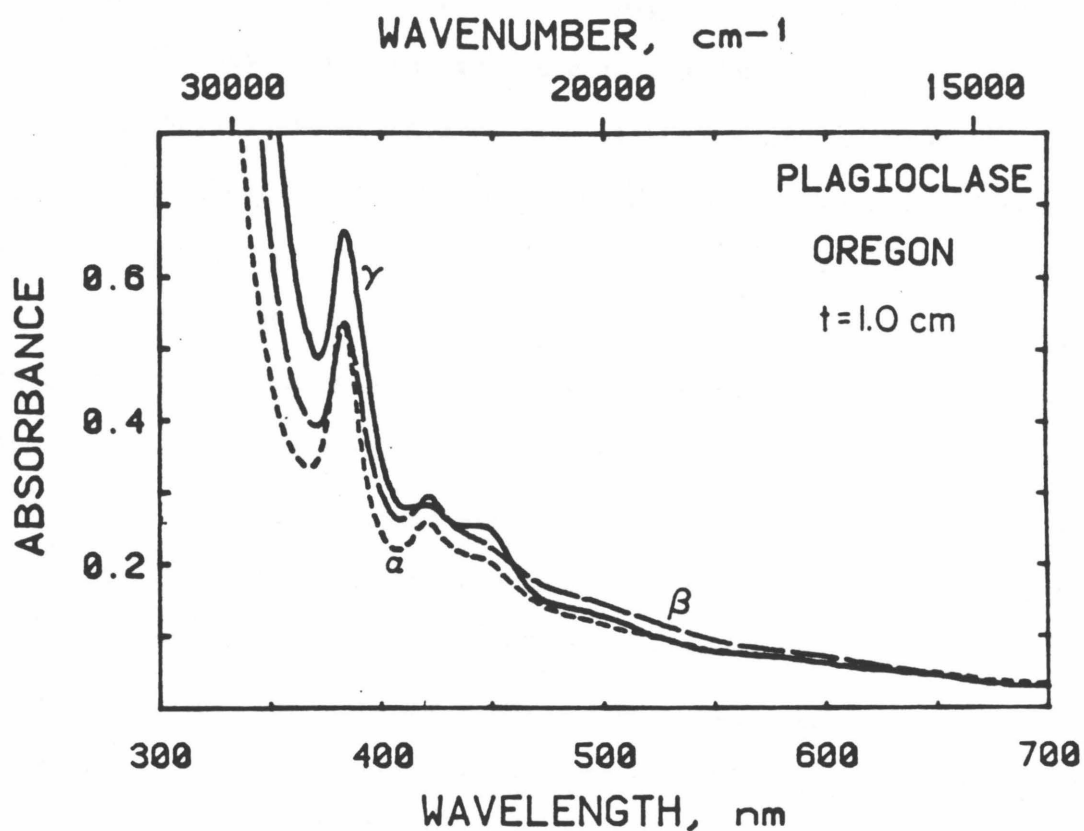


Figure 3.12 Polarized absorption spectra in the visible region of labradorite from Lake County, Oregon. This is a continuation of the spectra of Figure 3.3. Absorption features in this region arise from tetrahedral Fe^{3+} transitions. The rise towards the ultraviolet is due to O^{2-} to Fe^{3+} charge transfer.

of the labradorite resemble Bell and Mao's [1972] spectra.

The Gaussian fit parameters for the high energy transition (Fig. 3.13- and Table 3.4) show that although the polarization of the 26200 cm^{-1} transition of the andesine is similar to that of the potassium feldspars, the labradorite's differs strongly. This requires comparison of spectral parameters averaged for the three polarizations to determine Fe^{3+} concentrations. The different widths of the plagioclase and potassium feldspar absorptions demand that comparison must be made using integrated intensities, not absorptivities. The most accurate iron contents were obtained by using the $\sim 26200\text{ cm}^{-1}$ transition, and are listed in Table 3.5. The uncertainties stated primarily represent the uncertainty in the linear fit between the potassium feldspars' iron content and the average integrated intensity of their absorptions. The data in Table 3.5 show that within the stated errors the sum of optical determinations of Fe^{2+} and Fe^{3+} for the two plagioclases equals total iron content as determined by microprobe analysis. This substantiates the validity of the assumption that similar average integrated extinction coefficients apply to all feldspars studied.

3.4 EPR Spectroscopy of Fe^{3+}

EPR spectra of powdered potassium feldspars mainly consist of features due to high spin Fe^{3+} (Section 1.2.a.ii). Some have features near effective g factor (g_{eff}) of 2.0 due to radiation centers [Matyash et al. 1982; Speit and Lehmann, 1982; Chapter 5]. Figure 3.14 shows a strong first derivative at $g_{\text{eff}} = 4.3$ and a weaker satellite near $g_{\text{eff}} = 9.7$, both of which characterize high spin Fe^{3+} in a low symmetry environment [Golding et al, 1978]. Our results are similar to powder spectra of low-Ca plagioclase [Scala et al, 1978]. Large linewidths (100 to 190 gauss) for Fe^{3+} in

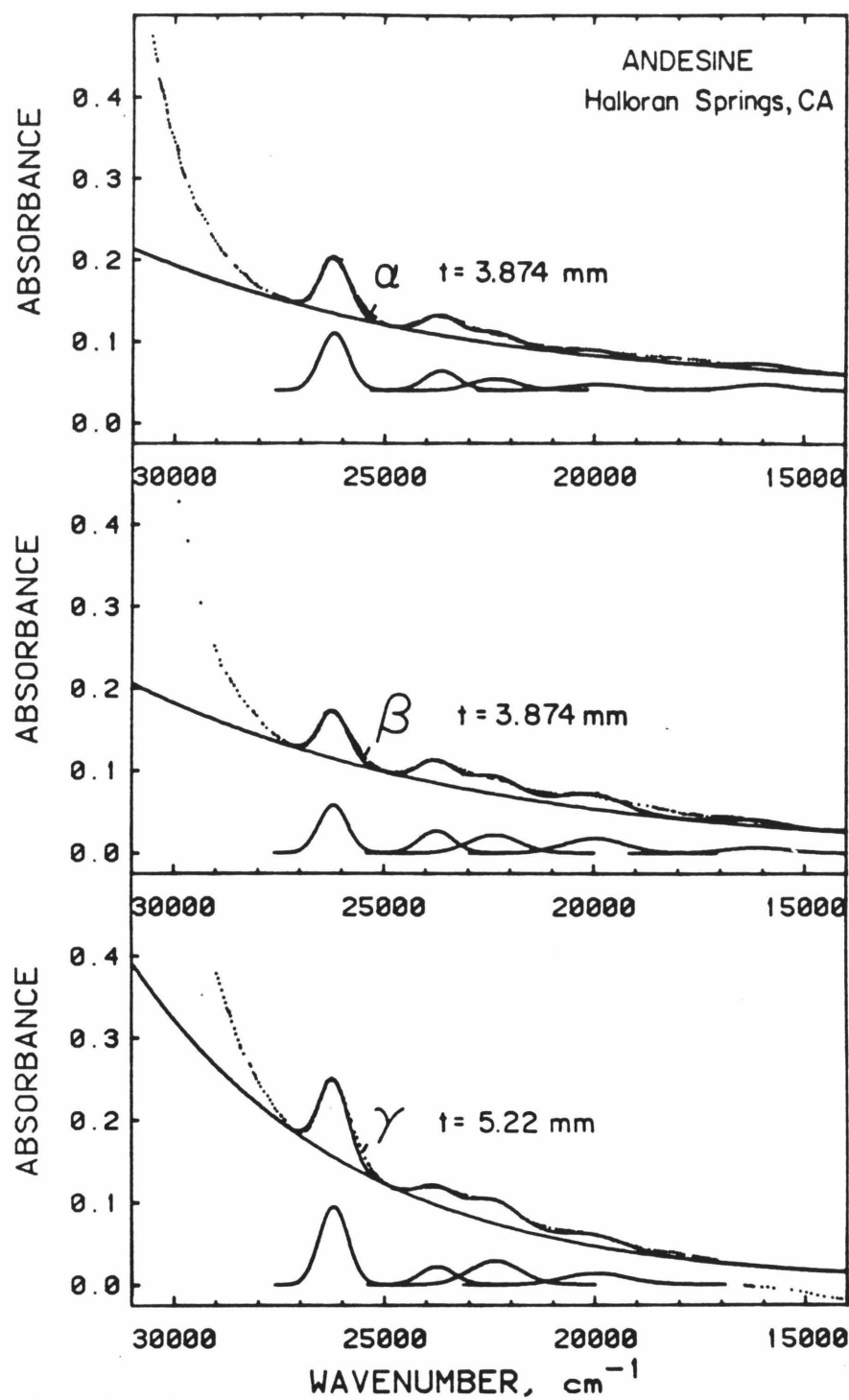


Figure 3.13 Gaussian deconvolution of the Halloran Springs andesine's visible spectra. Baselines were approximated from Equation 2.1. Simulation of the UV charge transfer band was not attempted. The baseline, component peaks, and the calculated spectra are solid lines; the spectral data points are the dots.

Table 3.5 Iron Concentrations in Feldspar Determined by Spectroscopy

Feldspar	X-Ray ^a	Optical Spectroscopy		EPR Spectroscopy	
	Total Fe wt% Fe ±0.008	Fe ²⁺ wt% Fe	Fe ³⁺ wt% Fe	Fe ³⁺ wt% Fe Method 1 ^d	Fe ³⁺ wt% Fe Method 2 ^d
Oligoclase, S. Carolina	0.039	<0.0015 ^b	0.03 ± 0.01	0.035 ± 0.005	Standard ±0.039
Andesine, Halloran Spg.	0.15	0.025 ± 0.003	0.11 ± 0.008	0.13 ± 0.01	0.125 ± 0.015
Labradorite, Lake County	0.31	0.09 ± 0.01	0.18 ± 0.008	Standard ±0.18 ± 0.01	0.199 ± 0.05
Labradorite, Crater Elegante	0.30	NM ^c	NM	0.183 ± 0.01	0.203 ± 0.03
Orthoclase, Irongay	0.26-0.30	<0.002	Standard ^e ± 0.30	Standard ^e ± 0.26	
Sanidine, Eifel	0.123	<0.002	Standard ^e ± 0.123	Standard ^e ± 0.123	
Amazonite, Broken Hill	0.009	<0.005 ^b	<0.04	0.0028	
Microcline, Elizabeth R	0.003	NM	NM	0.0031	

^a Iron contents greater than 0.01 wt% were measured using the electron microprobe, those below were measured using XRF.

^b Limits of detection depend on sample thickness.

^c Not Measurable because of twinning and/or turbidity.

^d Method 1 involves using the optically determined Fe³⁺ content for the labradorite. Method 2 involves assuming the oligoclase has all ferric iron.

^e A linear fit of these two samples in Fig. 3.10b or 3.20 was used to compute iron contents for the other K-spars.

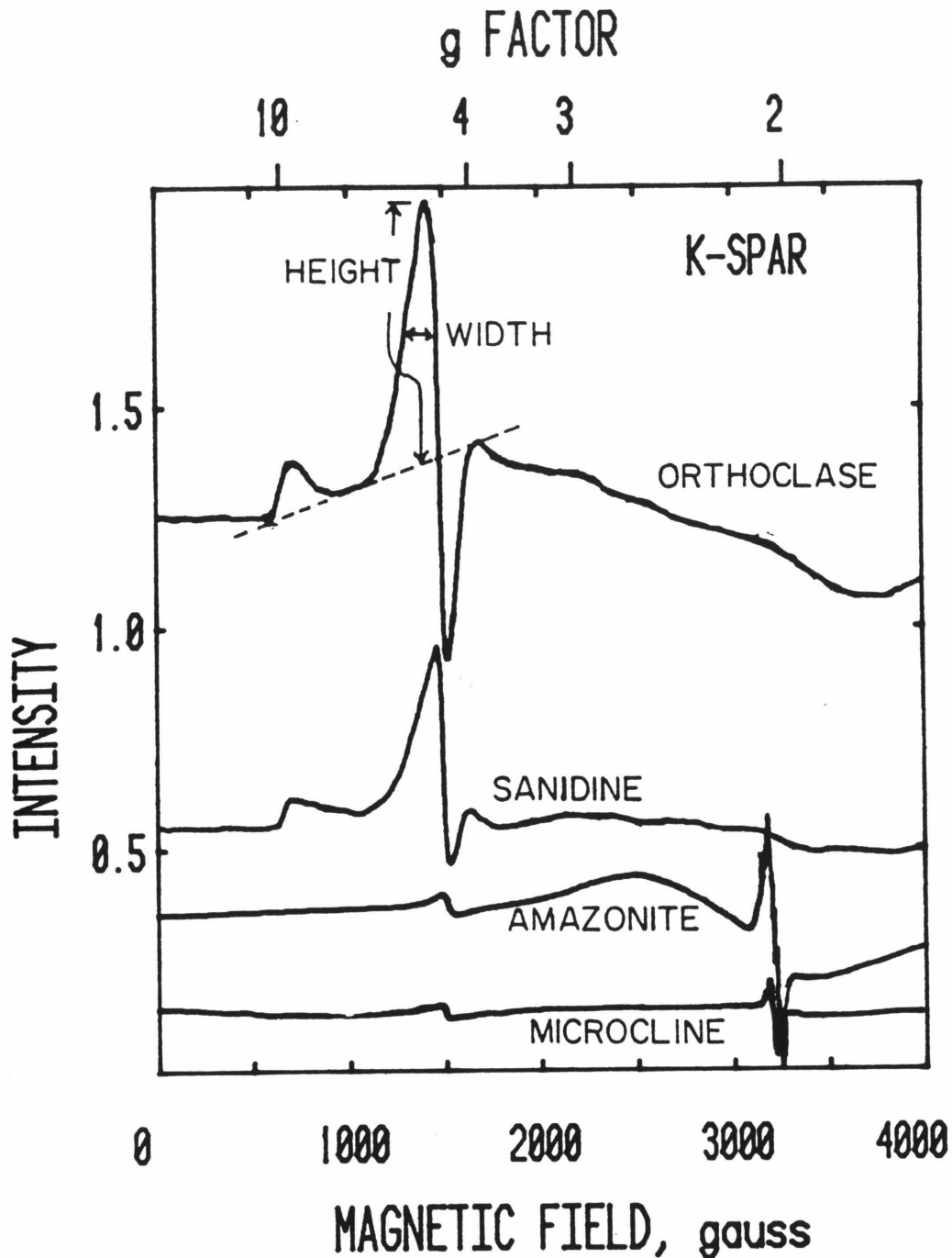


Figure 3.14 EPR first derivative powder spectra of potassium feldspars. The signals were scaled for 100 mg sample weight, 1.0 mWatt power, x 100 gain, and 1 Gauss modulation amplitude. g_{eff} Factors are approximate. The large features near $g_{\text{eff}} = 9.7$ and 4.3 are due to Fe^{3+} . Sharp signals near $g_{\text{eff}} = 2$ and the broad band near 2.18 in the amazonite are radiation centers. The baseline, width and height shown were used to calculate integrated intensity.

disordered potassium feldspar were observed previously [Marfunin et al, 1966; Gaite and Michoulier, 1970]. Because of this large linewidth, these powder spectra do not reveal multiple sites for Fe^{3+} which were detected in single crystal EPR studies of disordered potassium feldspars [Marfunin et al, 1966].

EPR spectra of most microclines (Fig. 3.15) were complicated by an additional first derivative at $g_{\text{eff}} = 3.2$, and smaller satellites at $g_{\text{eff}} = 30, 15, 12.3, 7.1, \text{ and } 5.9$. Except for the feature at $g_{\text{eff}} = 30$, these additional bands are correlated with the intensity (to the eye) of the pink color. The pink color (see Section 1.2.a.vii) results from small, dispersed hematite flakes, which suggests that these EPR features are associated with the hematite or its precursors. A strong isotropic first derivative signal at $g_{\text{eff}} = 3.3$ along with weaker satellites at $g_{\text{eff}} = 7.3, 6, 2$ (and possibly 5) should occur for Fe^{3+} in a tetragonal or axial environment [Golding et al, 1977]. These theoretical values are close to the observed values of the first derivative at $g_{\text{eff}} = 3.2$ and of the two satellites at 5.9 and 7.1 in the pink feldspars, indicating that this iron species is distinct from tetrahedrally coordinated Fe^{3+} . I propose that the axially coordinated Fe^{3+} represents an intermediate stage in deposition of hematite within the feldspar, or possibly results from hematite flakes on a unit cell scale. Because of the multiple siting of Fe^{3+} and lack of suitable standards, determination of Fe^{3+} contents from EPR spectra of the pink perthites was not attempted.

The broad band at $g_{\text{eff}} = 1.8$ in feldspar has been assigned to clusters of magnetically interacting iron (Speit and Lehmann, 1982). The increase in intensity of this signal with the strength of the red color (i.e., hematite concentration) supports this hypothesis. Because the broad band at $g_{\text{eff}} =$

Figure 3.15 EPR first derivative spectra of pink microcline perthites, scaled so that the height of the $g_{\text{eff}} = 4.3$ peaks are equal, and arranged in order of decreasing intensity of red color from top to bottom. g -Factors are approximate because the frequency ranges from 9.17 to 9.188 GHz. Features near $g_{\text{eff}} = 4.3$ and $g_{\text{eff}} = 9.7$ are due to Fe^{3+} in the feldspar lattice. Features near $g_{\text{eff}} = 3.2, 5.0, 7.1, 12.3,$ and 15 appear to be correlated with the red color, and can be attributed to axially coordinated iron. Small features in the red perthite between g_{eff} of 2 and 3 are also likely due to axially coordinated Fe^{3+} . Broad bands at $g_{\text{eff}} = 2.3$ and 1.8 are due to clusters of magnetically interacting iron. These features are obscured by radiation centers at $g_{\text{eff}} = 2$ in the New York Mountains' amazonite.

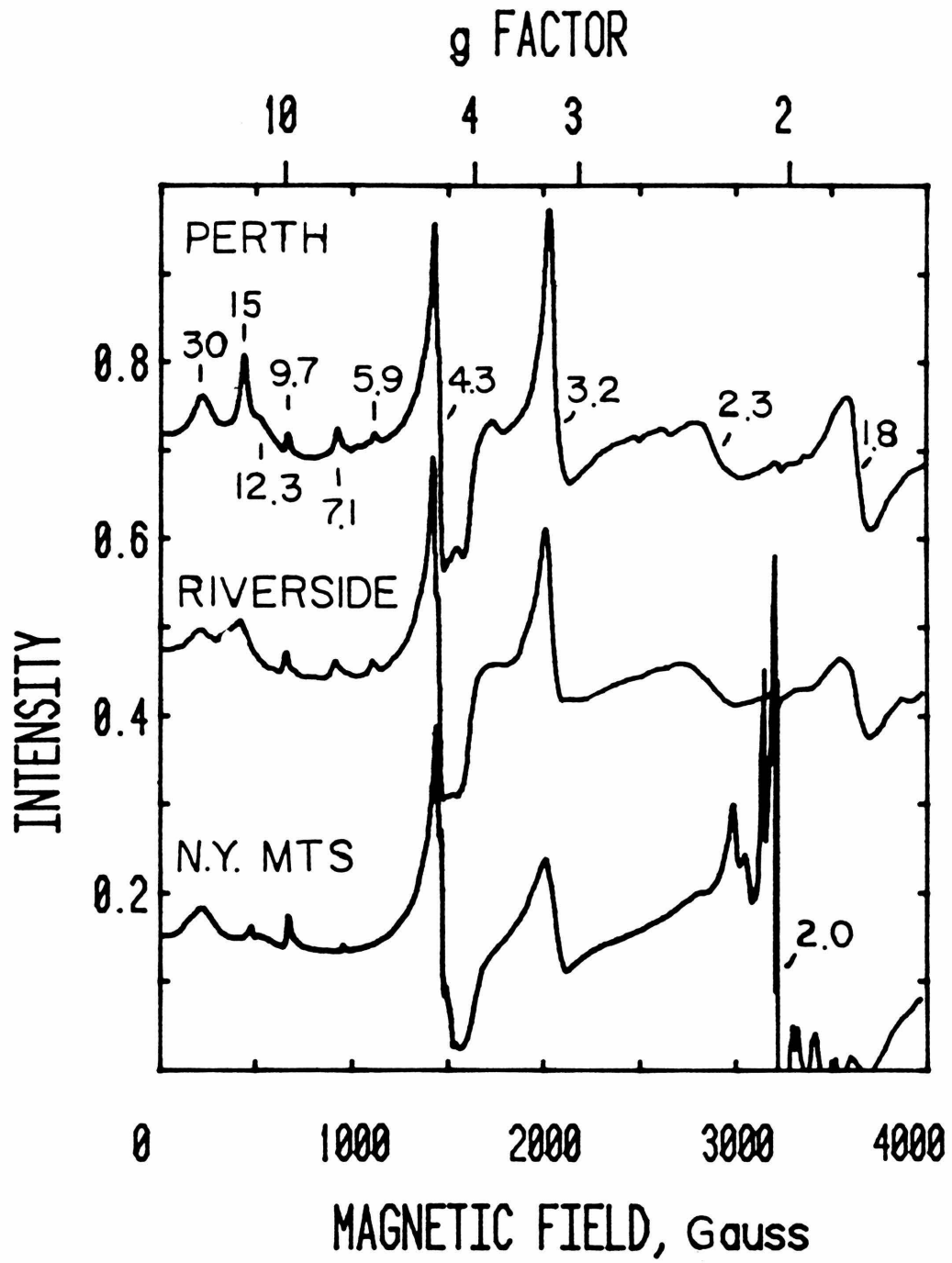


Figure 3.15

2.3 is also more intense in the hematite-rich samples, a similar origin is suggested. The very broad band at $g_{\text{eff}} = 2.18$ in the EPR spectrum of the low iron amazonite (Fig. 3.14) cannot be due to magnetically interacting iron; it may be due to a type of electron radiation damage center modelled by Griscom [1973].

EPR powder spectra of plagioclases (Fig. 3.16) are similar to those of the disordered potassium feldspars (Fig. 3.14), except for peak shape. These results are in agreement with single crystal studies of plagioclase [Scala et al, 1978] except that the two signals observed at $g_{\text{eff}} = 4.3$ in the single crystal spectra are not distinguishable in my spectra, and the signal at $g_{\text{eff}} = 5$ which Scala et al [1978] observed in high-Ca plagioclase spectra is discernible only in the powder spectra of the oligoclase. Probably the stronger $g_{\text{eff}} = 4.3$ signal in the powder spectra of the labradorite masks the weaker signal at $g_{\text{eff}} = 5$. Thus, the EPR spectra of low-Ca plagioclase are not detectably different from that of high-Ca plagioclase as implied previously [Gaité and Michoulier, 1970; Scala et al, 1978]. The similarity of the andesine and oligoclase spectra to those of the two structurally intermediate labradorites [Stewart et al, 1966; Gutmann and Martin, 1976] suggests that the distribution of Fe^{3+} among tetrahedral sites is influenced more strongly by changes in the feldspar lattice due to both Al/Si ordering resulting from thermal history, than by differences in anorthite content.

Integrated intensities for the EPR spectra were calculated from both equation (2.2) and by using a simple line integral to double integrate digitized baseline-subtracted spectra. Figure 3.18 shows that the numerically calculated absorption spectra for the feldspars strongly depends on both peak shape and baseline. The numerically calculated double integrals for these and the other feldspars are given in Table 3.1. Because the correla-

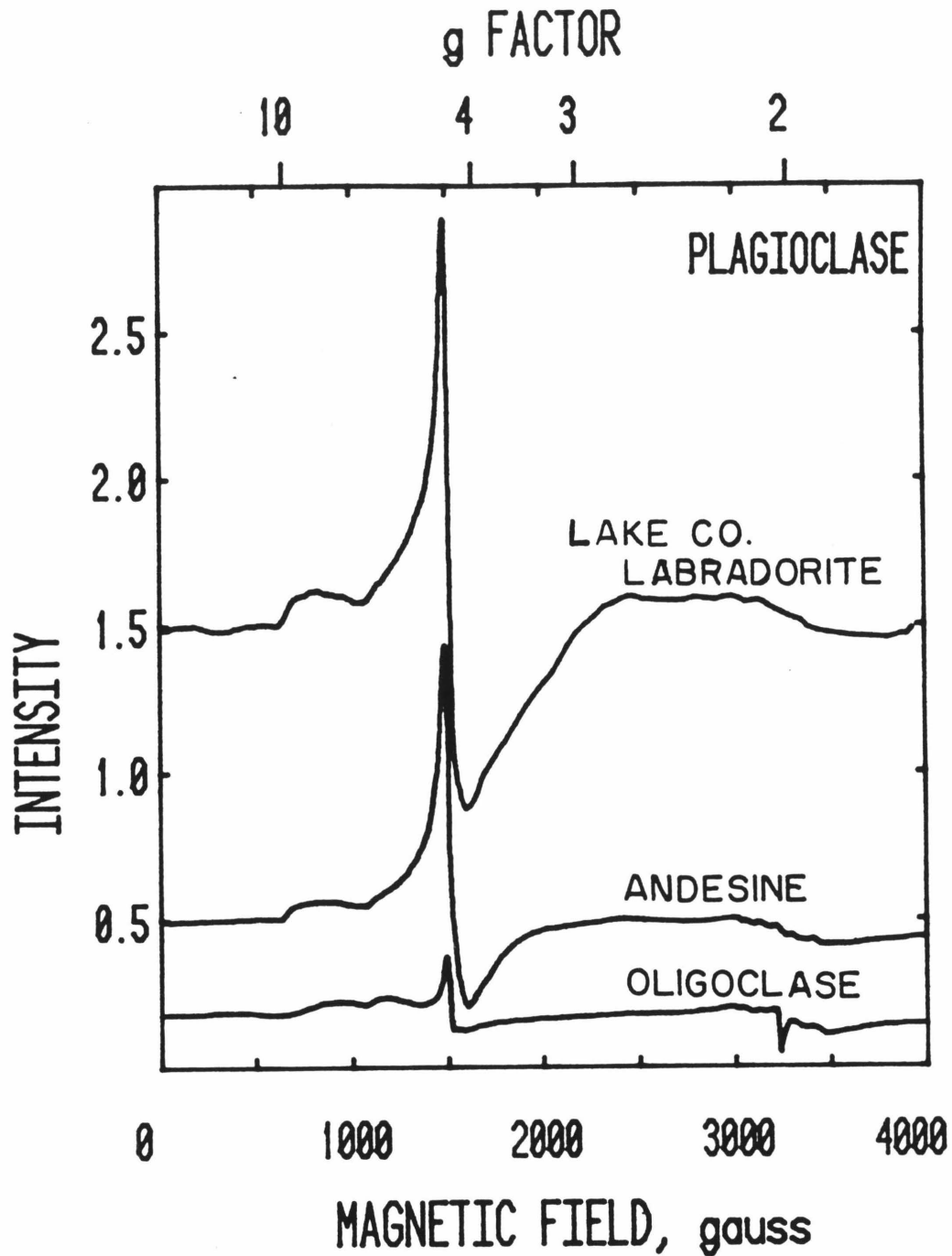


Figure 3.16 EPR first derivative powder spectra of plagioclase feldspars, scaled to 100 mg sample, 1.0 mW power, 1 Gauss modulation amplitude, and $\times 100$ gain. g -Factors are exact. The Lake County labradorite spectrum which is shown is also similar to the Crater Elegante labradorite spectrum. The features near $g_{\text{eff}} = 9.7$ and $g_{\text{eff}} = 4.3$ are due to Fe^{3+} , while the features near $g_{\text{eff}} = 2$ are radiation centers.

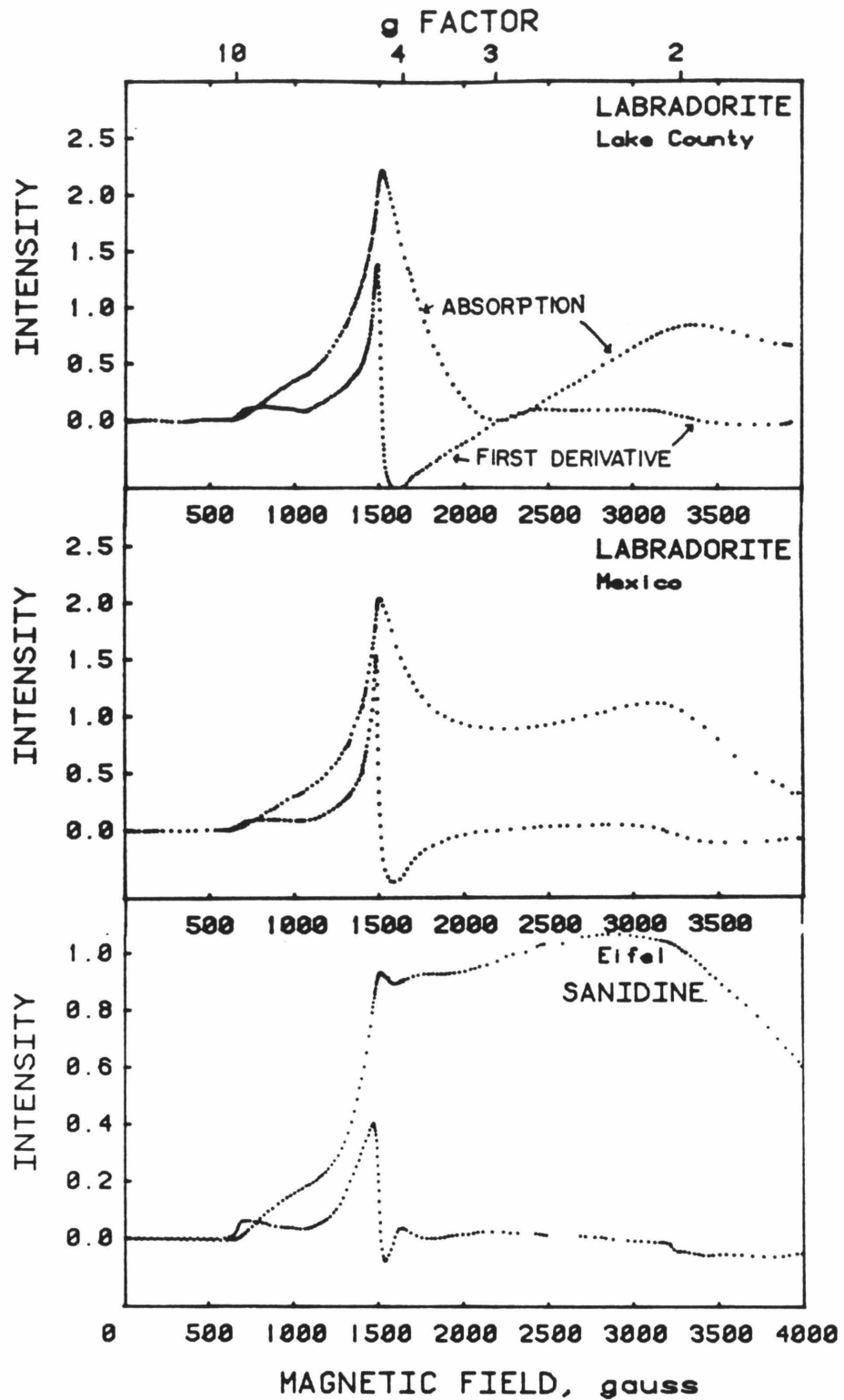


Figure 3.17 Numerical calculation of absorption curve of both labradorites and the sanidine. The data (first derivative) is scaled for 100 mg, 1 mW, 1 Gauss modulation, and x100 gain, while the calculated absorption curve is for x10 gain. g-Factors are approximate.

tion between the numerically-calculated and formula-calculated integrated intensities is linear (Figure 3.18), and because the numerical method is less accurate due to the baseline approximations required, the data from equation (2.2) are presented hereafter in this thesis.

Comparison of the EPR integrated intensity (Table 3.1) with the average of the integrated intensities of the Fe^{3+} transitions in the optical spectra near 26200 cm^{-1} (Figure 3.19) shows separate linear correlations for the potassium feldspars and the plagioclases. The existence of the linear correlation proves that the EPR signals near $g_{\text{eff}} = 4.3$ arise from tetrahedral Fe^{3+} . The separate correlations for potassium feldspar and plagioclase are due to the drastic differences in EPR peak shape (which is caused by the different numbers of sites for ferric iron for the two types of feldspar).

The integrated intensity of the potassium feldspars' EPR spectra is linearly dependent on iron content (Fig. 3.20) which supports the assumption that virtually all iron in potassium feldspars is trivalent. This correlation was used to compute Fe^{3+} concentrations for the two potassium feldspars with low amounts of iron. Table 3.5 shows that the EPR determination of iron content is comparable to the XRF analysis. Differences for the amazonite may be due to sample inhomogeneity, insofar as different crystals from the same locality were used for the two measurements.

The integrated intensities of the plagioclase EPR spectra monotonically increase with total iron content (Figure 3.20). Because the dependence of EPR integrated intensity on ferric iron concentration differs for potassium feldspar and plagioclase, the Fe^{3+} concentration in plagioclase was calculated by two methods: (1) Based on the absence of Fe^{2+} in its optical spectrum, assume that the oligoclase has only ferric iron and use its EPR integrated

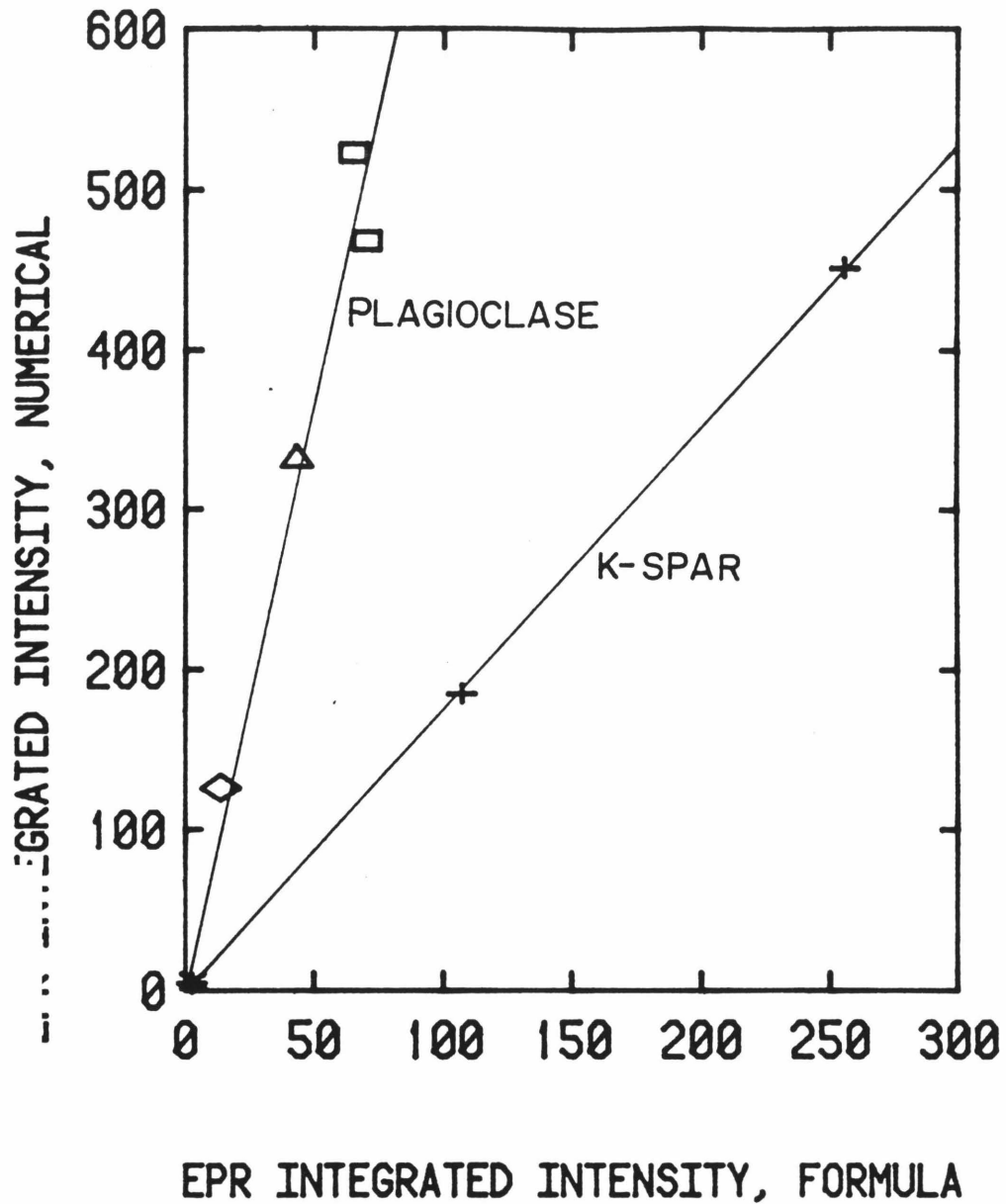


Figure 3.18 Correlation of EPR integrated intensities calculated by computer algorithm and by equation 2.1. Squares are labradorite, diamonds are andesine, Δ is oligoclase, + are orthoclase or sandine, and x is microcline. Integrated intensities were scaled for 100 mg sample weight, 1 mW power, 1 Gauss modulation amplitude, and x100 gain.

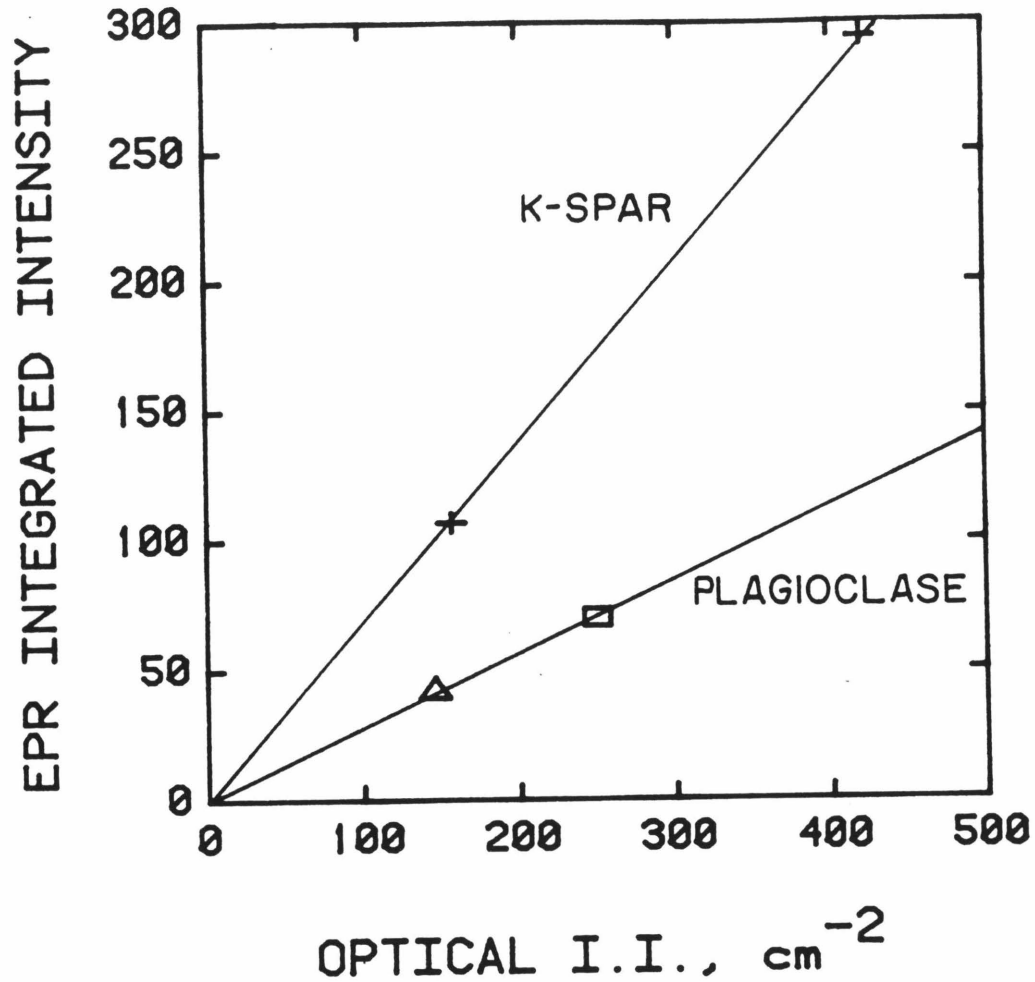


Figure 3.19 Comparison of integrated intensities of optical and EPR bands due to Fe^{3+} in feldspars. The integrated intensity was calculated from eq. 2.1 and is scaled for a sample weight of 100 mg, 1 mW power, 1 G modulation amplitude, and $\times 100$ gain. + denotes sanidine or orthoclase, Δ is andesine and square represents labradorite. Because optical and EPR spectra were obtained on different samples of Itrongay orthoclase with different iron contents, the EPR I.I. of the orthoclase was multiplied by the ratio of the iron contents of the two samples to produce a proper comparison. The separation of the potassium feldspar and plagioclase trend is due to their different dependences of EPR integrated intensities on iron concentration.

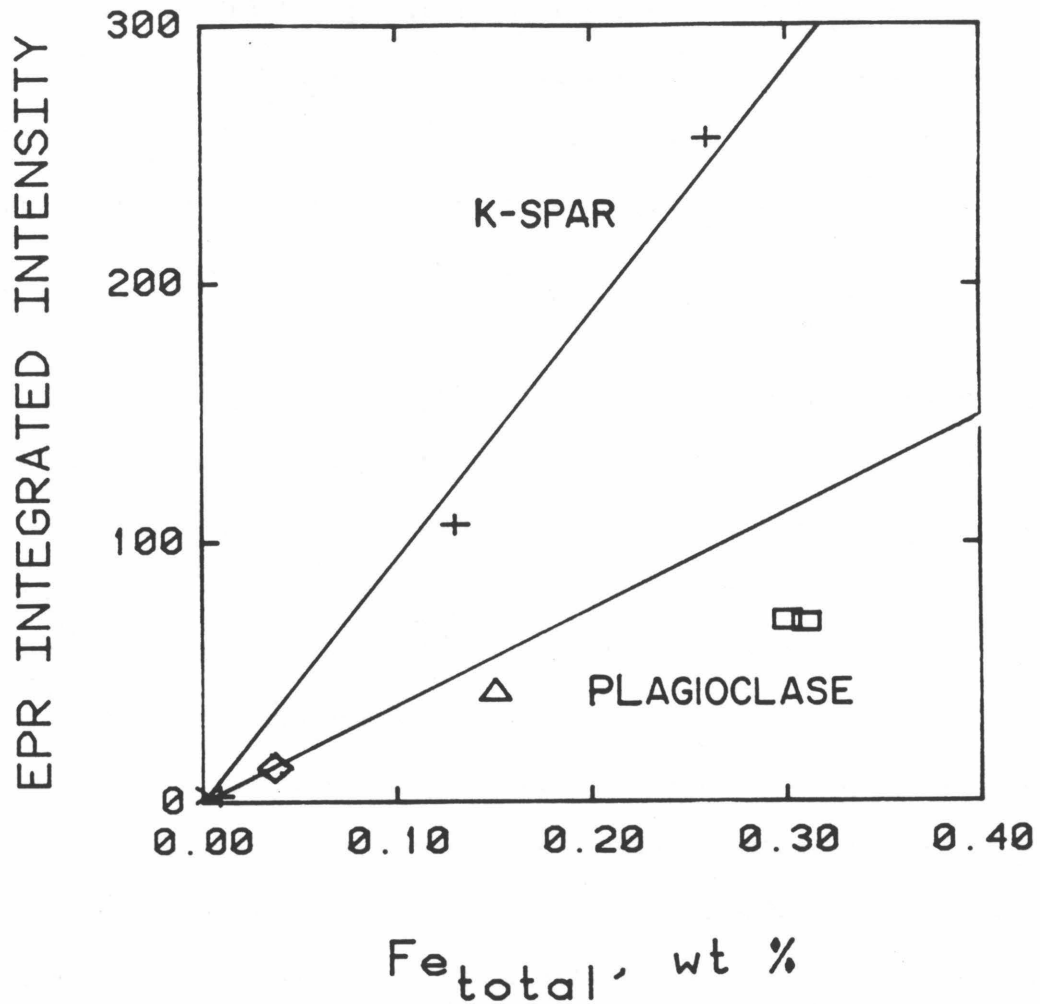


Figure 3.20 Dependence of EPR integrated intensity of feldspars on total iron content as wt% Fe. The integrated intensity was calculated from eq. 2.2 and is scaled for a sample weight of 100 mg, 1 mW power, 1 G modulation amplitude, and x100 gain. x denotes microcline, + orthoclase or sanidine, diamond for oligoclase, Δ for andesine, and squares for labradorite. The trends for potassium feldspars and plagioclases are separate due to different peak shapes. The potassium feldspar trend is linear because the iron is essentially all ferric. The plagioclase trend shows nonlinearity due to incorporation of ferrous iron. The straight line denotes where plagioclases with exclusively ferric iron should plot.

intensity and iron content to calculate Fe^{3+} for the other plagioclases, or (2) Use the EPR integrated intensity and the Fe^{3+} concentration determined optically for the labradorite to calculate amounts of ferric iron for the others. Results from both methods are the same within experimental errors (Table 3.5), and are equivalent to the optical determination of Fe^{3+} .

3.5 Variation of Fe^{2+} and Fe^{3+} Concentrations in Plagioclase

Figure 3.21 shows that the $\text{Fe}^{2+}/\text{Fe}_{\text{total}}$ ratio increases with increasing anorthite content for the four plagioclases examined. The strong influence of the topology of the aluminosilicate framework on the M-atom's environment [Smith, 1974, p. 113] suggests that the increase of $\text{Fe}^{2+}/\text{Fe}_{\text{total}}$ with anorthite content is related to the number of favorable sites for Fe^{2+} as more calcium and aluminum are incorporated. Although the $\text{Fe}^{3+}/\text{Fe}_{\text{total}}$ ratio decreases with anorthite content, Fe^{3+} concentration actually increases with anorthite content simply because the aluminum content doubles in going from An 0 to An 100. The regularity of the iron dependence on the anorthite content may be attributed to the similarity of the plagioclases: all are in an intermediate [Gay, 1955] to a high structural state [Stewart et al, 1960; Gutmann and Martin, 1976]; except for the oligoclase, all are basaltic phenocrysts, so they probably crystallized in an Fe-rich liquid near the QFM buffer. The oligoclase is probably from a pegmatite, which means that the liquid would be less Fe-rich and more reducing. If the melt were controlling the Fe^{2+}/Fe ratio in the feldspar, then a higher Fe^{2+}/Fe ratio for the oligoclase would occur than for the basaltic phenocrysts. The opposite is true, suggesting that the availability of proper (Ca-like) sites controls the Fe^{2+}/Fe ratio in the feldspar.

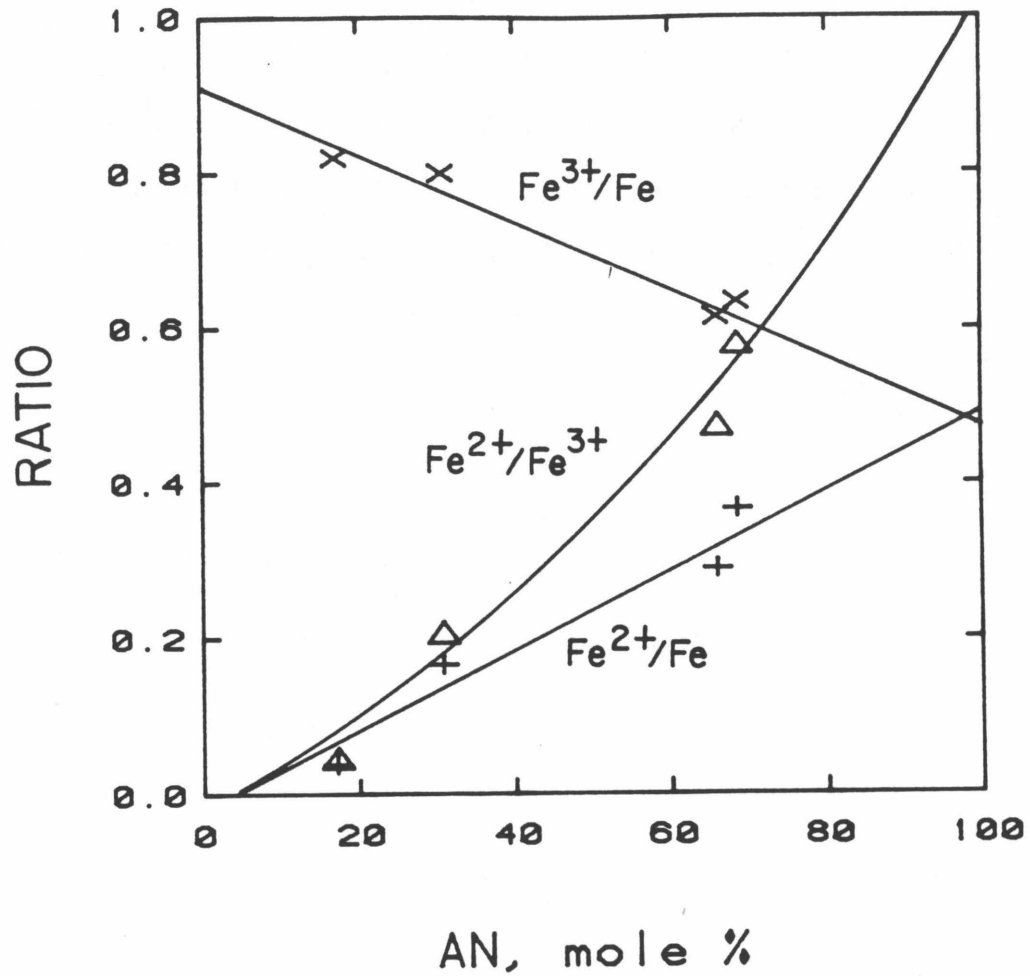


Figure 3.21 Dependence of Fe^{2+}/Fe and Fe^{3+}/Fe and Fe^{2+}/Fe^{3+} ratios on plagioclase feldspar composition, which is represented as mole % anorthite. Plus signs are Fe^{2+}/Fe . X's are Fe^{3+}/Fe . Triangles are Fe^{3+}/Fe^{2+} . The lines are the best fit to the data for Fe^{2+}/Fe and Fe^{3+}/Fe . The line for Fe^{2+}/Fe^{3+} was computed from the ratio of the other lines.

3.6 Conclusions and Comparisons of the Two Spectroscopic Methods

I have shown that optical spectroscopy can be used to directly determine both Fe^{2+} and Fe^{3+} concentrations, and that EPR spectroscopy can determine Fe^{3+} concentrations for feldspars to better than $\pm 15\%$ of the amount present. The two methods are complementary. The optical technique is limited to feldspars that have a transparent region which is thick enough to produce an analyzable spectrum. Specifically, for Fe^{2+} determinations, 0.002 wt% Fe^{2+} is about the limit of detection for a crystal thickness of 1.0 cm; for Fe^{3+} determinations, 0.04 wt% Fe^{3+} is about the limit of detection for a crystal thickness of 1.0 cm. The method can tolerate some scattering by inclusions, but the quality of the spectra and, hence, the accuracy of the concentrations is detrimentally affected.

In contrast, requirements for EPR determinations are much less stringent. Fine scale twinning and turbidity should cause no problems. About 25 mg of sample is needed to detect concentrations of about 0.1 wt% Fe^{3+} . Concentrations of 0.001 wt% Fe^{3+} probably could be detected with 200 mg of feldspar, but at these low amounts resolution of the EPR spectra becomes increasingly difficult. Another limitation of the EPR technique is saturation: the method should become unfeasible with large amounts of iron (~ 0.5 to 1.0 wt% Fe^{3+}). For such feldspars, if practical, optical spectroscopy would be preferable.

Both techniques are limited by the availability of suitable standards and the accuracy of their chemical determinations. For example, Itrongay orthoclase worked well as the Fe^{3+} optical standard for all feldspars, and as the Fe^{3+} EPR standard for disordered potassium feldspars, but separate standards are needed for EPR determinations of Fe^{3+} in plagioclase and in maximum microcline. Synthesis of standards with known iron concentrations and oxidation states may improve the accuracy of the results.

The accuracy of the iron concentrations determined by spectroscopy is $\pm 10\%$ for EPR method and ± 11 to 15% for optical study. The uncertainty mainly arises from the inaccuracy of the data. Errors from analysis of the spectra are comparatively minor, except when drastic baseline corrections are needed to compensate for poor quality spectra. One unknown contribution is the variation of integrated extinction coefficients among the various feldspars studied. Because peak area linearly depends on iron concentration for potassium feldspar and because the sum of the optically determined Fe^{2+} and Fe^{3+} concentrations of plagioclases equals the total iron content, I conclude that the variation of optical integrated extinction coefficients is a minor perturbation. The tetrahedral site does not change much in size (mean T-O distances vary from 0.1642 to 0.1643 to 0.168 Å from Or to Ab to An [Smith, 1979, p.88 and 111]), which may serve to equalize optical integrated extinction coefficients. Differences between the tetrahedral sites are manifest in the peak shape of both the optical and the EPR spectra, the EPR being more sensitive to site distortions. Although the M-site changes drastically across the plagioclase series, integrated extinction coefficients remained essentially constant. This observation and the virtual absence of ferrous iron in potassium feldspar suggests that Fe^{2+} is incorporated into specific, Ca-like sites which do not experience major structural variations across the plagioclase compositions examined.

In summary, optical spectra of Fe^{2+} in structurally intermediate to high plagioclases show that iron replaces calcium in two distorted sites. Variation of optic axes orientation and possibly of site occupancy among the two sites of the different plagioclases precludes use of peak absorptivities for determination of Fe^{2+} content and requires use of average band areas. By comparing band areas, Fe^{2+} contents were determined for two plagioclases

with mixed valences. Comparison of optical spectra of iron in plagioclase and potassium feldspars shows that Fe^{3+} is tetrahedrally coordinated, and that the plagioclase Fe^{3+} sites are similar to those of potassium feldspar. By comparison of optical peak areas, Fe^{3+} contents were determined for the plagioclases. That the sum of the optically determined Fe^{2+} and Fe^{3+} concentrations equals that of total iron supports the feasibility of this method. In a similar manner, EPR integrated intensities were used to determine Fe^{3+} contents. Because different numbers of iron sites were present in plagioclase and potassium feldspar (the number of sites being related to the structural state of the feldspar), several comparisons utilizing various standards were made to calculate Fe^{3+} contents. Agreement of the two methods with each other and with optical data indicated that the EPR determination of iron content is equally feasible.

SPECIATION AND CONCENTRATION OF WATER AND OH IN VARIOUS FELDSPARS

4.1 General Statement

This chapter strictly concerns how much "water" is present and how it is speciated in the different feldspars studied (smoky sanidine, yellow orthoclase, labradorite, blue plagioclases, colorless microcline, and amazonite). The following chapters will relate the data presented here to radiation coloring and radiation resistance of feldspar. Descriptions and chemistries of the gemmy feldspars (sanidine, orthoclase, and plagioclase) are given in Tables 3.1 and 3.2, while data on the amazonites can be found in Tables 6.1 to 6.3. Fluid inclusions were observed visually only in Broken Hill #3" amazonite at 3 μm sizes. If present in the other feldspars, fluid inclusions are less than 1 μm in the maximum dimension. In microclines, turbidity associated with fluid was observed, but individual inclusions could not be resolved with the microscope.

4.2 Total H₂O Concentrations Determined by Hydrogen Manometry

Eight different specimens were selected for total water content measurements. The results presented in Table 4.1 show that the water concentration ranges from about 0.05 to 0.20 wt % for microclines and is roughly 0.017 wt % for sanidine. These measurements are precise (roughly $\pm 1\%$), but the amount of water evolved may involve a blank of 1 $\mu\text{mole H}_2\text{O}$ [R.E. Criss, pers. comm., 1982]. For the microclines, the blank merely increases the uncertainty to about $\pm 5\%$. For the sanidine, the inclusion of a blank means that the water content could range from 0.013 to 0.018 wt%.

Three samples were measured several times to gauge the repeatability of the results and the homogeneity of the samples. For two of the samples

Table 4.1 Total Water Concentrations in Feldspar

Sample	Locality	Number	Weight, grams	H ₂ O, μmoles	H ₂ O wt%	H ₂ O, mole/liter	δD _{smow}
Sanidine	Eifel	13755	0.4170	4.0*	0.017*	0.0243*	ND ⁺
Microcline	Elizabeth R Mine CA	13757	0.5118	39.0	0.14	0.200	-46
		7	0.3861	21.5	0.10	0.143	-68
Microcline	White Queen Mine, CA	25a	0.4367	36.0	0.15	0.214	-60
		25b	0.4460	31.5	0.13	0.185	ND
Amazonite	Broken Hill	13756 (=3")	0.2689	17.5	0.12	0.171	-133
Amazonite	Lake George CO	5a	0.4246	18.5	0.07	0.100	-82
		5b	0.5019	15.5	0.06	0.089	-95
"	"	12a	0.4088	24	0.09	0.129	-78
		12b	0.4023	33	0.15	0.214	-83
"	"	12c	0.4740	44.5	0.17	0.243	-92
		9	0.4111	19.5	0.09	0.129	-78
Amazonite	Keivy USSR	21	0.4655	28	0.11	0.157	-83
Uncertainty			<u>+0.002</u>	<u>+ 0.2*</u>	<u>+0.002*</u>	<u>+0.002*</u>	+1

*The hydrogen content could be affected by the blank of about 1 μmole, so that for the sanidine, the H₂O concentration could range from 0.018 to 0.026 mole/liter and for the microclines, the error could be + 5% of the measured value.

+ Not determined

(#25 and #5) the two measurements are the same considering the experimental error. The water content of the third sample (#12) varies by a factor of two. Because one of the measurements (#12b) was done on a single chunk of feldspar, and because most amazonites are inhomogeneously turbid to the eye, it is likely that the fluid inclusion water (turbidity) varies for this sample and the others. Repeatability occurs in the measurements due to the large sample weight used (1/2 gram).

Deuterium ratios were also measured and are reported as δD_{smow} in Table 4.1. The Broken Hill orthoclase is metamorphic and has a low δD value. The other feldspars are all pegmatitic and have values within the range of normal magmatic waters. It is interesting that the δD values of the white microclines (all of Cretaceous age) range from -46 to -68, while δD values of the amazonites (except #3), all of which are Precambrian in age, range from -78 to -95. The lowered value for the older samples may result from hydrothermal alteration, or may represent differences in the composition of magmatic waters with time, or may indicate differences due to individual pegmatites.

4.3 Speciation of "Water" in Feldspar

To distinguish between fluid inclusion water, isolated H₂O molecules, and hydroxyl, comparisons were made between infrared spectra taken in the fundamental OH stretch region at room and liquid nitrogen temperatures; and also between the infrared fundamentals and near-infrared combination modes. Freezing allows distinction of fluid inclusions from the other species because it shifts the wavenumber of the fundamental stretch of liquid water from 3400 to 3200 cm⁻¹, while increasing the intensity. Speciation as H₂O is revealed by the presence of 2 fundamental stretches

in the infrared region and by a stretch-bend combination mode at about 5260 cm^{-1} (1900 nm), whereas SiOH (and probably AlOH) groups exhibit a stretch-bend mode at 4545 cm^{-1} (2200 nm) [Scholze, 1966; Bartholomew et al, 1980].

Because the near IR bands are much weaker than the fundamentals in the IR, different pieces of the same sample were utilized for the two measurements except for the glassy samples (sanidine, orthoclase, and the various plagioclases). For these cases, a sample larger than 1 cm was not available, so absorbance in the near IR was run at ten times expansion.

4.3.a Sanidine: mostly OH

The chemistry of smoky sanidine from basalt flows in the Eifel district of Germany is discussed in Section 3.1. Chapters 3 and 5 discuss the visible and EPR spectroscopy of this sample.

Infrared spectroscopy of sanidine reveals broad absorption bands that are grouped in two pairs according to their polarizations (Figure 4.1). No change was seen in the spectra after irradiation and mild heating (400°C for 1/2 hr). Dehydration of the crystal at 900°C for 3 days showed a reduction in all four bands of 65 to 80% of the original intensity. However, the bands at 2460 and 2560 cm^{-1} cannot be due to "water", and are probably lattice overtones, because they are present in "dry" orthoclase (Fig. 4.4) at about the same intensity.

Near-infrared absorption spectra of Eifel sanidine show evidence of weak bands at 1400, 2200, and 2500 nm (7090 , 4545 , and 4000 cm^{-1} ; Figure 4.2). Band intensities for these and the IR fundamentals are listed in Table 4.2. The 1900 nm mode is no more intense than the spectral noise (0.001 cm^{-1}). Because the extinction coefficient of the 1900 nm band

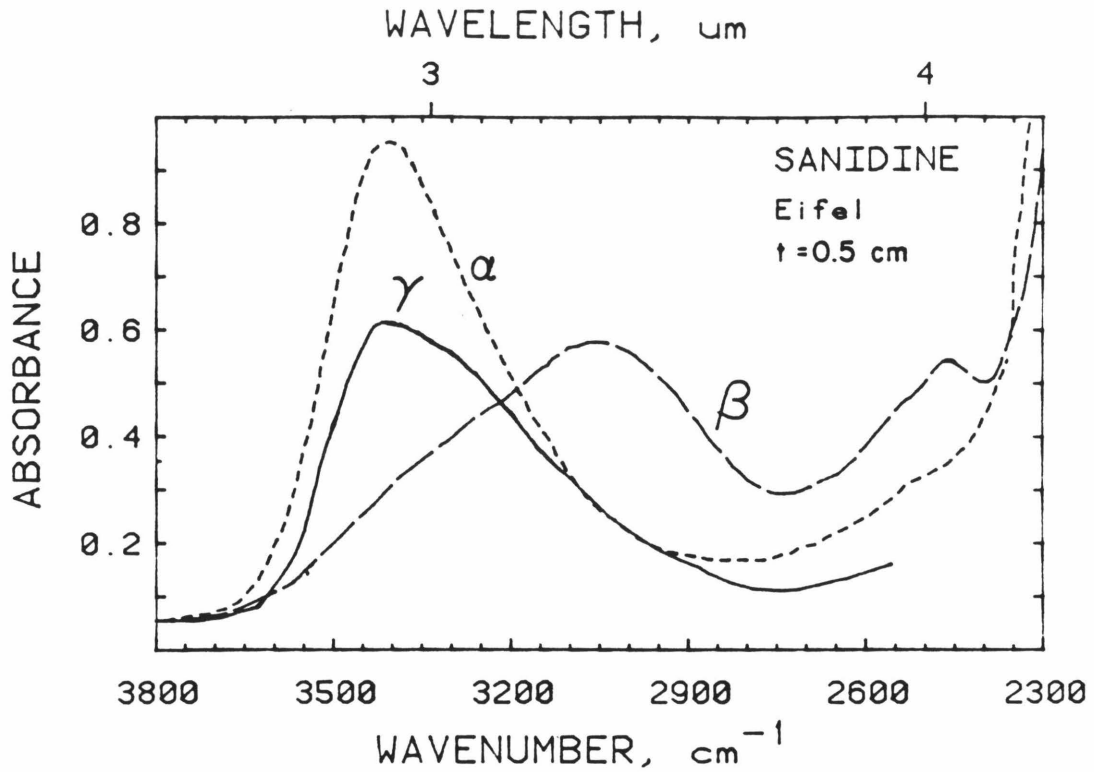


Figure 4.1 Polarized infrared absorption spectra of "water" in smoky sanidine from the Eifel district, Germany. Two bands are present at 3430 and 3050 cm^{-1} . The differences in energy and polarization indicate two very different sites. The bands near 2600 cm^{-1} are due to lattice modes.

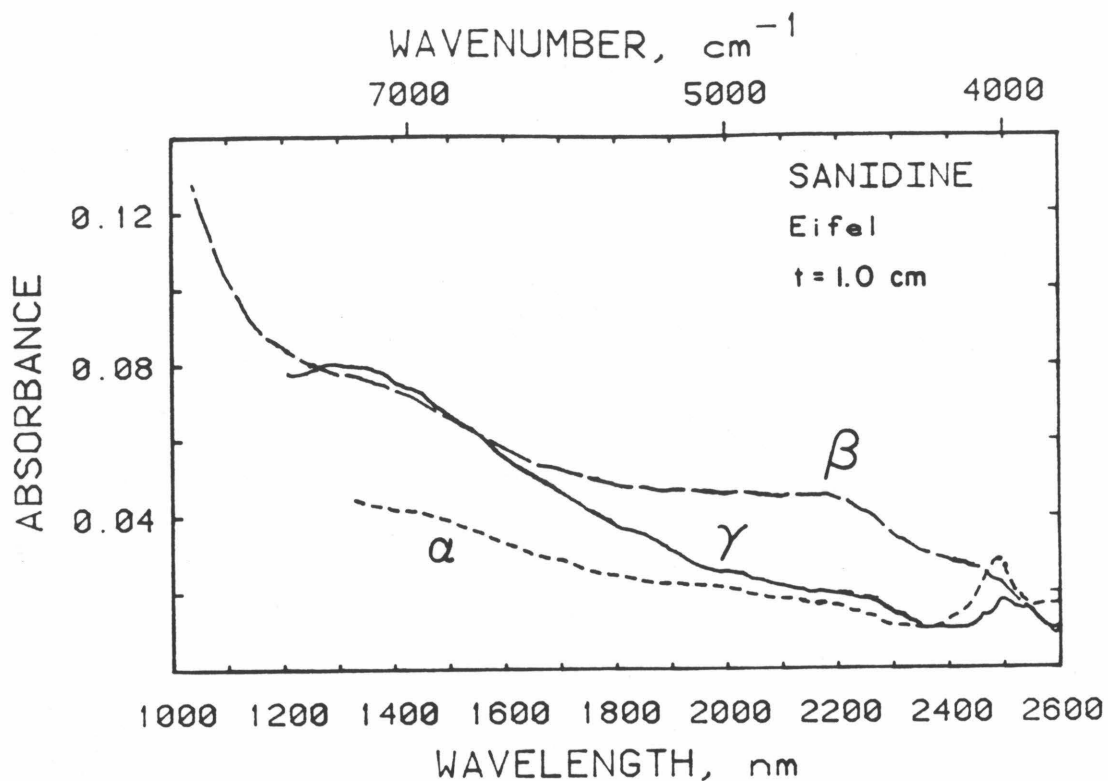


Figure 4.2 Polarized near infrared absorption spectra of smoky sanidine from Eifel. (Same crystal as in Figure 4.1). Absorption bands due to water or OH are seen at 1400 and 2500 nm. A band due only to OH is visible at 2200 nm. If the H_2O band at 1900 nm is present, it is below the noise level, which shows that most of the protons present are due to SiOH or AlOH .

Table 4.2 Absorption Coefficients in Eifel Sanidine in cm^{-1}

Species	OH+H ₂ O	H ₂ O	OH	OH+H ₂ O	OH+H ₂ O	OH+H ₂ O
λ , cm^{-1}	7090	5240	4545	4000	3450	3030
$I(\alpha)$, cm^{-1}	0.001	0	0.003	0.012	1.71	0.26
$I(\beta)$, cm^{-1}	0.006	0	0.004	0.005	0.43	0.73
$I(\gamma)$, cm^{-1}	0.012	0	0.015	0.008	1.05	0.33
Average, cm^{-1}	0.006	0	0.0073	0.0083	1.06	0.44
ΔI , cm^{-1}	$\pm .001$	$\pm .001$	$\pm .001$	$\pm .001$	$\pm .01$	$\pm .01$
$\epsilon_{\text{ave}}\#$, 1/mole·cm	0.28	-	0.31	0.39	50	20
	± 0.05		± 0.008	± 0.07	± 8	± 4
$\epsilon_{\text{glass}}^*$, 1/mole·cm	0.12	1.00	0.55	ND	33	-
$\epsilon_{\text{glass}}^*$, 1/mole·cm	0.21	1.76	0.98	0.95	67	-

* Bartholomew et al (1980) K-Na-Zn-Al-Si-O glass

+ Stolper (1982) basalt, rhyolite, albite glass

The E calculated could be higher by a factor of 1.3 if the water determination were affected by a blank

in glass is roughly twice that of the 2200 nm X-OH stretch-bend mode [Bartholomew et al, 1980] and the extinction coefficients are roughly the same in quartz [Aines and Rossman, 1983, in press], molecular water in the sanidine comprises less than 15% of the total water. Therefore, the two peaks at 3030 and 3450 cm^{-1} in the fundamental region represent two kinds of hydroxyl groups.

IR spectra of the sanidine taken at liquid nitrogen temperatures show an increase of up to 20% in band intensity, a shift of the 3030 and 3450 cm^{-1} bands to 3000 and 3360 cm^{-1} , and the appearance of a distinct band at 3200 cm^{-1} (Figure 4.2). The appearance of the 3200 cm^{-1} band suggests that some of the water in the sanidine is present as fluid inclusions (which must be smaller than about 1 μm from microscope examination). The growth of the 3200 cm^{-1} band probably caused the shift of the 3450 cm^{-1} band but could not have resulted in the shift of the 3030 band to 3000 cm^{-1} . This change represents a lengthening of the primary band. Also, the growth of the 3200 cm^{-1} band probably contributed to the apparent increase in the other bands. Thus, most ($\sim 90\%$) of the water present in sanidine is bound as two kinds of hydroxyl represented by the 3030 and 3450 cm^{-1} bands.

Extinction coefficients calculated by using the total concentration of water in sanidine are presented in Table 4.2, along with extinction coefficients of glass. The uncertainties reported for the extinction coefficient are due to the uncertainty in the water content. These are larger than the error induced because a small amount of the total water ($\sim 7\%$) is due to fluid inclusions. The extinction coefficients are comparable to those of glass for all bands.

4.3.b Orthoclase: nearly dry

Figure 4.4 shows very weak absorptions in yellow Itrongay orthoclase

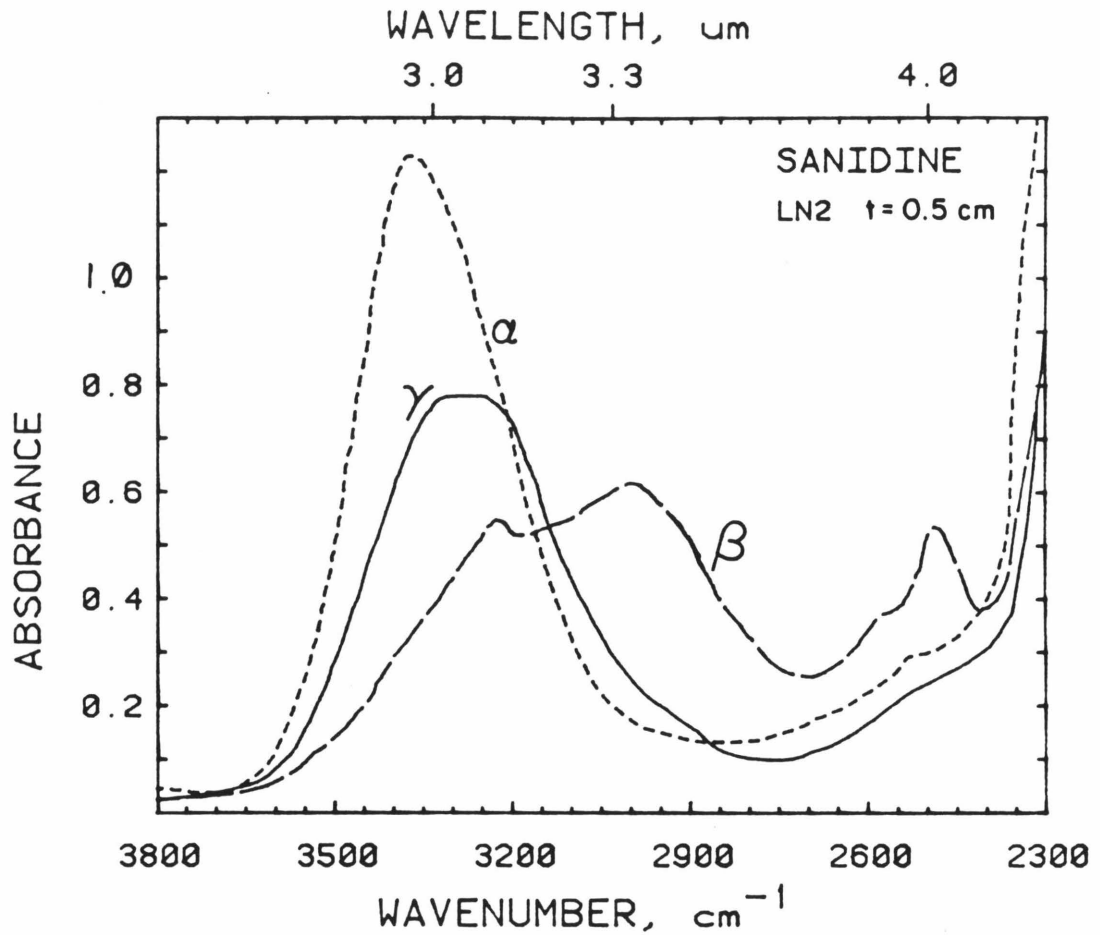


Figure 4.3 Polarized infrared absorption spectra of smoky sanidine near liquid nitrogen temperatures. The 2 bands shown in Figure 4.1 have shifted upon cooling to 3380 and 3000 cm^{-1} , while slightly increasing in intensity. A new sharp band appears at 3200 cm^{-1} , which indicates that some fluid inclusion water is present.

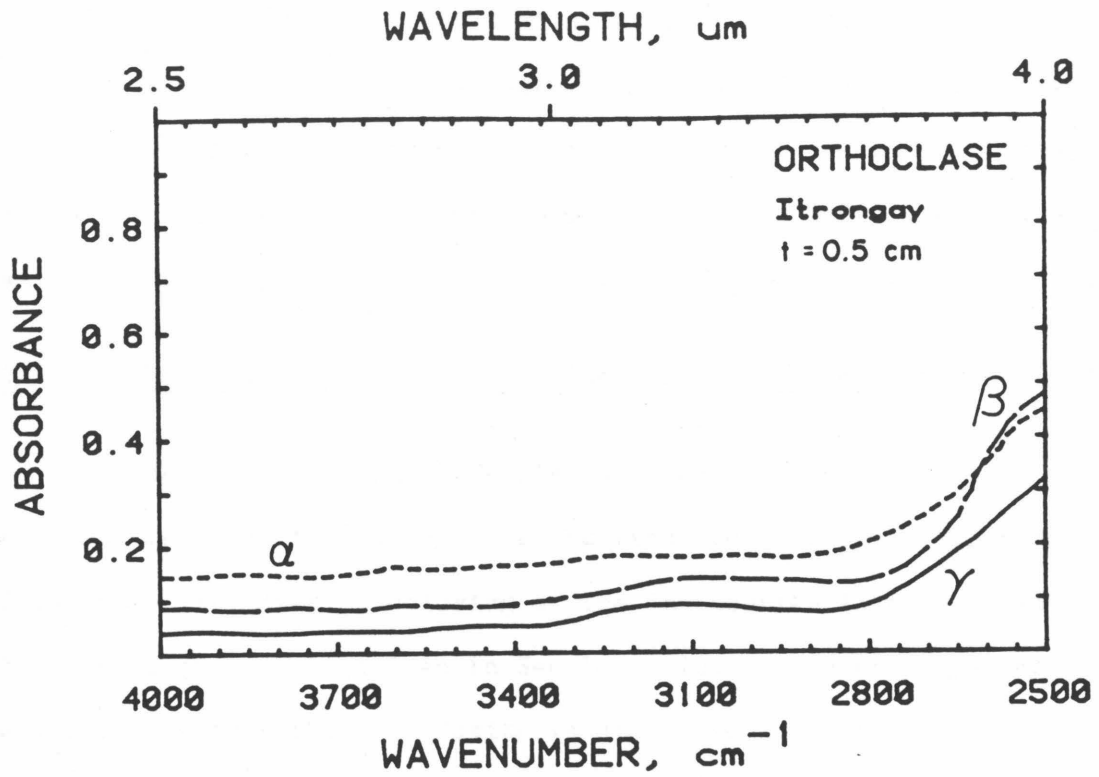


Figure 4.4 Polarized infrared absorption spectra of gemmy yellow orthoclase from Itrongay, Madagascar. Weak bands are present near 3100 and 3450 cm^{-1} . Spectra were offset for clarity. The bands near 2600 cm^{-1} are equal in intensity to those of the much more hydrous sanidine (Fig. 4.1), which shows that these are lattice mode overtones.

near 3030 and 3450 cm^{-1} . The similarity of their positions to that of the sanidine suggests that the water in the orthoclase is most likely OH. Application of the extinction coefficients in Table 4.2 to Itrongay orthoclase intensities suggests that this feldspar has 0.002 ± 0.0004 wt % H_2O as OH.

4.3.c Labradorite, andesine, and blue oligoclase: mostly OH

The chemistry of the three plagioclases studied by infrared spectroscopy is given in Chapter 3, along with spectroscopy of iron in these feldspars. Irradiation coloring of the labradorite is covered in Chapter 5 and that of the oligoclase in Section 6.10. Study of copper metal exsolution within the labradorite is discussed in Chapter 7.

The IR spectra of water in labradorite consists of a shoulder at 3600 cm^{-1} and broad bands near 3100 and 3400 cm^{-1} (Figure 4.5). The 3600 cm^{-1} band is nearly isotropic and is probably the result of alteration (clay). Similar bands have been previously assigned to OH^- [Wilkins and Sabine, 1973]. Spectra taken at liquid nitrogen temperatures show a sharpening of the two broad peaks, an increase in intensity of less than 10%, and a slight shift in position to 3150 and 3360 cm^{-1} (Figure 4.6). Strong absorptions of ferrous iron in the near IR thwarted observation of stretch-bend modes in this particular sample, but in others from the same locality, the OH^- mode at 2200 nm was observed, but not the 1900 nm mode of H_2O . Thus, it is likely that water in the labradorite is speciated the same as in the sanidine because of the similar band positions and behavior with temperature. The differences in polarization bands result from the different crystallographic orientations of the optic axes in the two feldspars. Thus, water in labradorite mostly consists of Si-OH and Al-OH with a small amount of

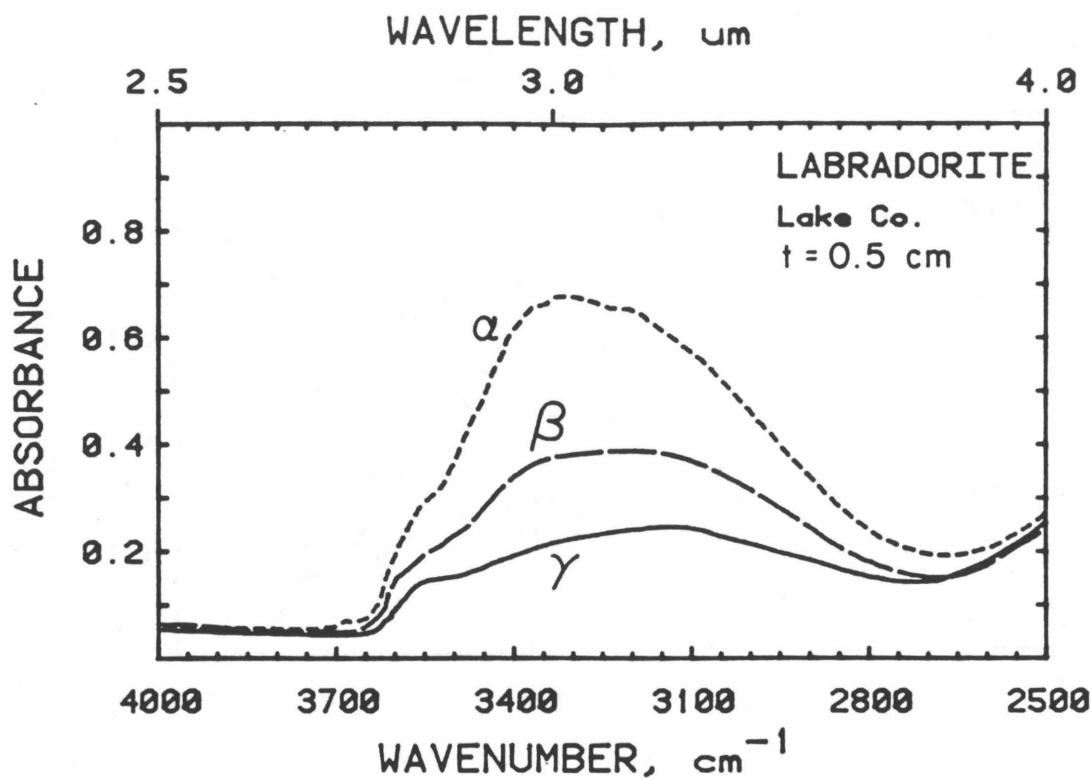


Figure 4.5 Polarized infrared absorption spectra of yellow, gemmy labradorite from Lake County, Oregon. Two broad bands are present near 3400 and 3100 cm^{-1} . The shoulder at 3600 cm^{-1} is nearly isotropic and indicates the presence of OH^- , possibly in alteration products.

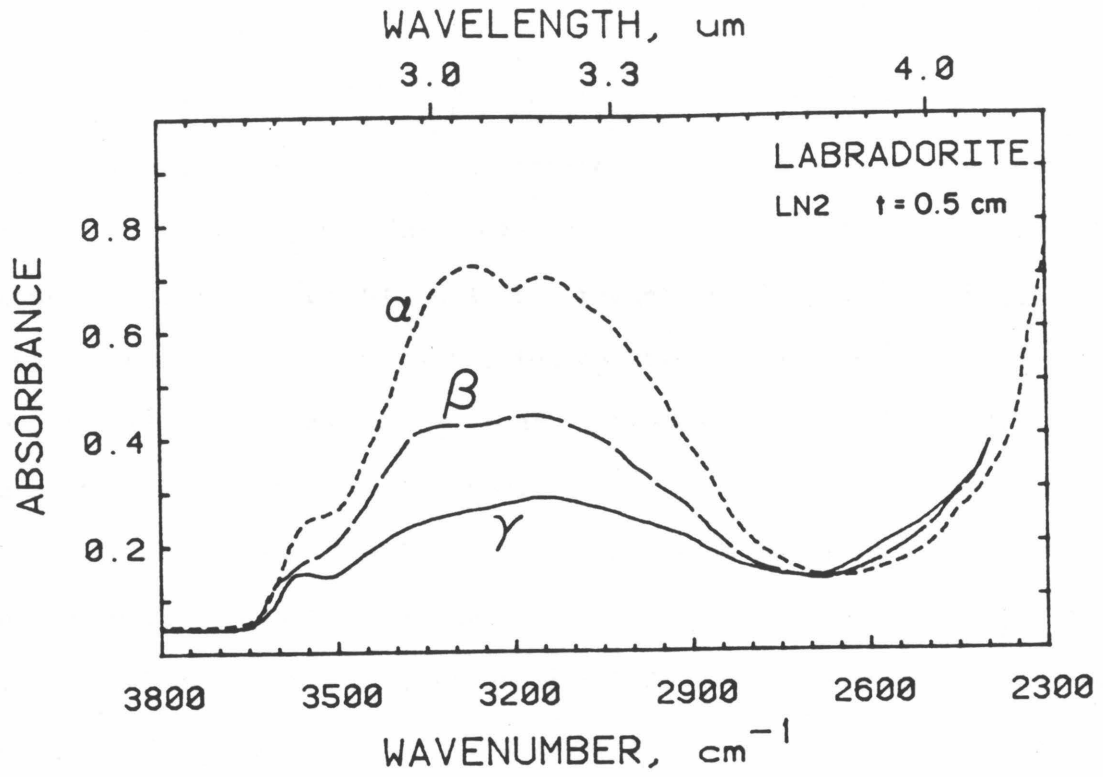


Figure 4.6 Polarized infrared absorption spectra at liquid nitrogen temperature of the same crystal of Lake County labradorite as in Figure 4.5. Cooling reveals bands at 3660, 3330, 3150, and 3050 cm^{-1} . No bands are present near 2500 cm^{-1} . Intensities are at most 10% greater for the cooled labradorite, so that very little water is present as fluid inclusions.

fluid inclusion water.

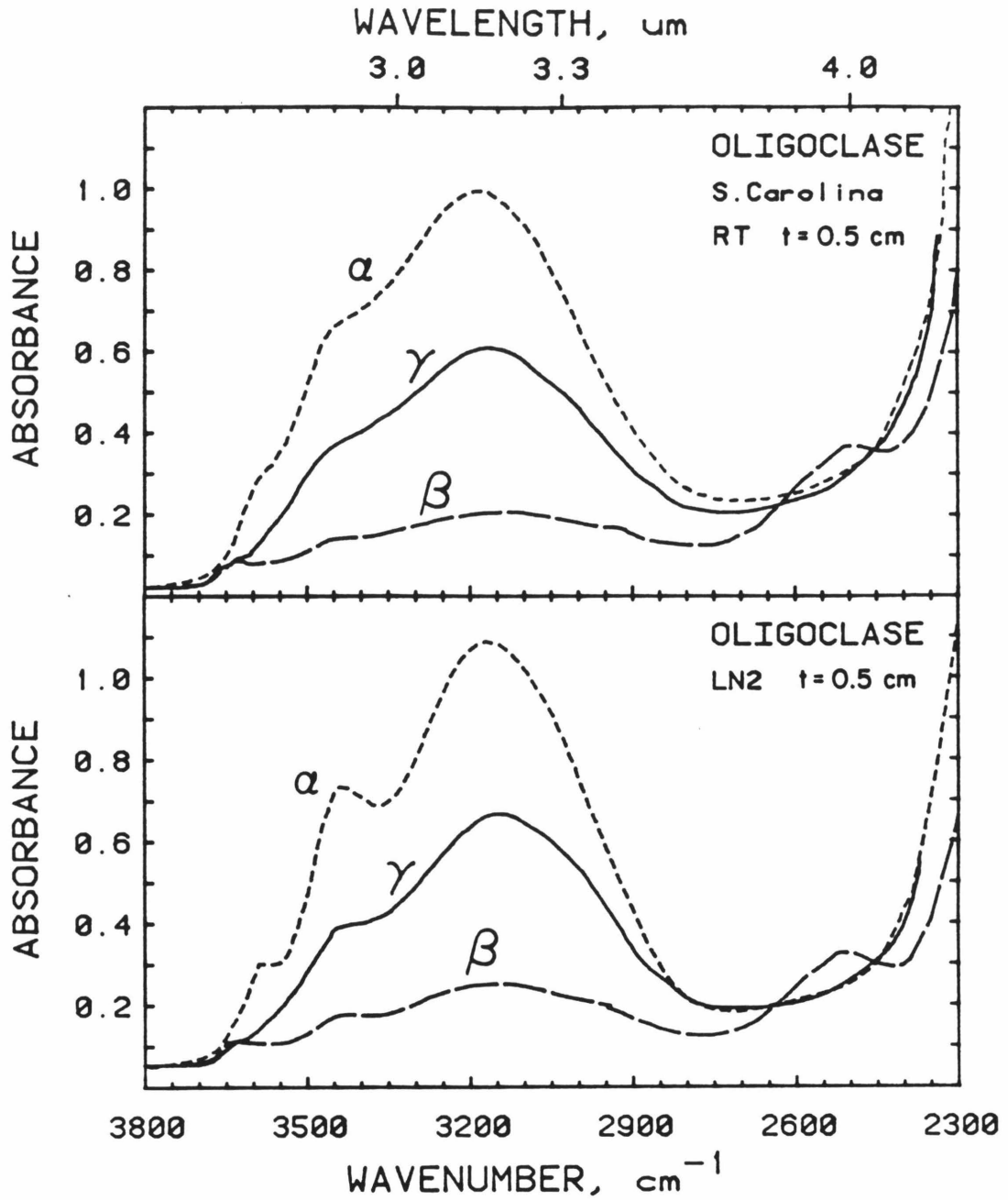
Andesine from Halloran Springs, California, possesses infrared spectra very similar to that of the labradorite. Figure 3.1 shows the near infrared spectra of this sample. The presence of the 2200 nm band indicates OH⁻ groups. A band due to H₂O could be present, but is obscured by Fe²⁺ absorptions. Because the extinction coefficient of the OH band is roughly 1/2 of that of the H₂O band, I conclude that most of the andesine's water is present as SiOH and AlOH.

Blue oligoclase from South Carolina yields infrared spectra similar to the sanidine and labradorite (Figure 4.7). Like labradorite, the oligoclase spectra has a weak shoulder 3700-3600 cm⁻¹ which is probably due to alteration products, and broad asymmetric absorptions in the water region. Features shared with sanidine are two strong peaks in beta at 2500 and 2600 cm⁻¹ (which are due to lattice vibration overtones), and two distinct peak positions within the broad bands at 3170 and 3450 cm⁻¹.

Freezing of the oligoclase with liquid nitrogen shows only a 10% increase of intensity at 3200 cm⁻¹ and a very slight sharpening of the bands. This behavior is similar to that of both the sanidine and labradorite, and shows that less than 10% of the total water is present as fluid inclusions.

Measurement of the oligoclase in the near infrared region showed that the 2200 nm band due to OH is weakly present. The 1900 nm band due to H₂O was not detected in a 1 cm sample. The lack of the 1900 nm band, and the similarity of the oligoclase spectra to that of the sanidine, suggests that nearly all the protons in sanidine occur as hydroxyl.

Because total water contents were not measured, extinction coefficients cannot be determined for OH in plagioclase. The molar absorptions of OH



4.7 Polarized infrared spectra of gemmy, pale blue oligoclase from South Carolina. Absorptions at 3700, 3450, and 3180 are probably due to different types of OH^- in the feldspar. The small change upon cooling shows that only a small proportion of the protons can be present as fluid inclusions. Lattice overtones occur near 2500 cm^{-1} .

in sanidine can be used to estimate the OH concentration as H₂O in plagioclase:

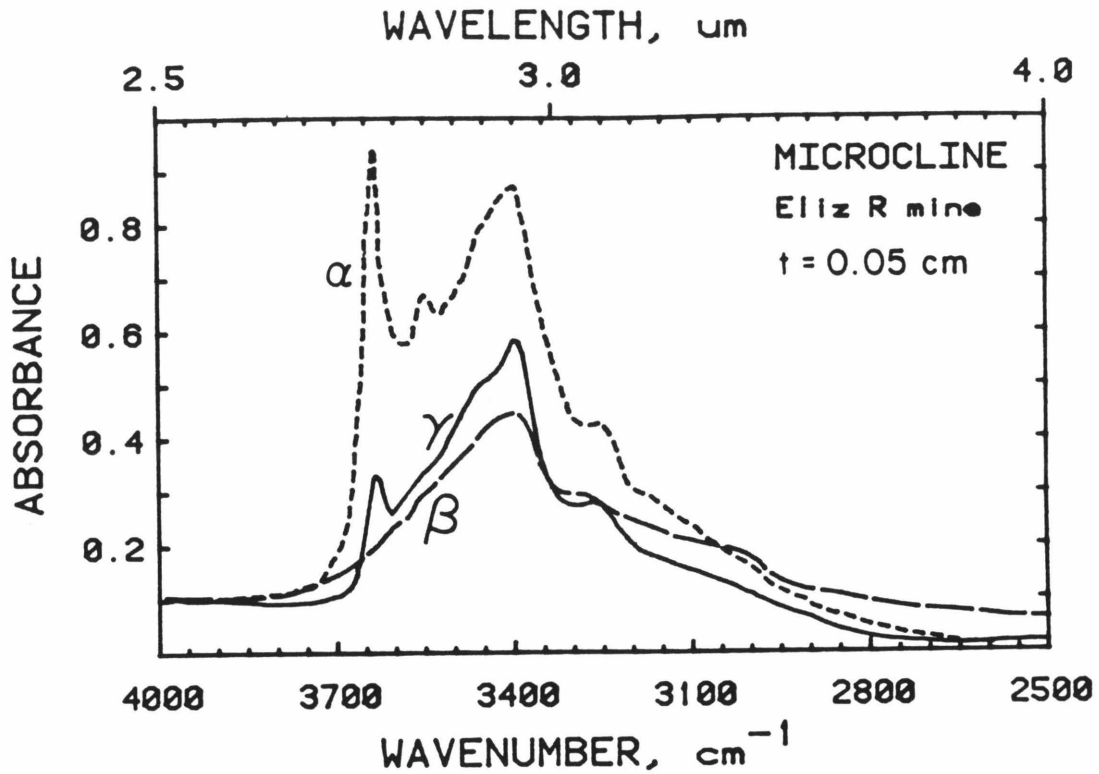
oligoclase	0.020 wt% H ₂ O
andesine	0.052 wt% H ₂ O
labradorite	0.013 wt% H ₂ O

The uncertainty is \pm 20% due to the uncertainty in the molar absorptivity of sanidine.

4.3.d Colorless to white microcline: structurally bound H₂O

The gemmiest regions of three microclines from the Elizabeth R mine and one from the White Queen mine (Pala District, California) were examined spectroscopically. For all cases, two pairs of polarized bands were seen: One pair (3630 and 3550 cm⁻¹) is strongly polarized in alpha and weakly in beta. The other pair (3400 and 3250 cm⁻¹) is less strongly polarized. The best resolved spectra are presented in Figure 4.8, and are similar to spectra observed by G.C. Solomon [in prep.].

Near-infrared spectra were taken on thicker sections of the same crystal. For all cases, strongly polarized bands of H₂O were seen at 1900 and 1950 nm, but OH bands were not detected at 2200 nm in agreement with Solomon and Rossman [1979]. The intensities of the two combination stretch-bend bands and of the two largest of the four IR fundamentals are listed in Table 4.3. Plotting each of the two near-IR bands against each of the two IR bands (Figure 4.9) shows that weak correlations exist between all possible pairs. The poor correspondence is probably due to sample inhomogeneities between the different pieces used. Yet, a general increase of the 1900 nm absorptions with the fundamentals is apparent. This trend along with the absence of the 2200 nm X-OH band indicates that



a

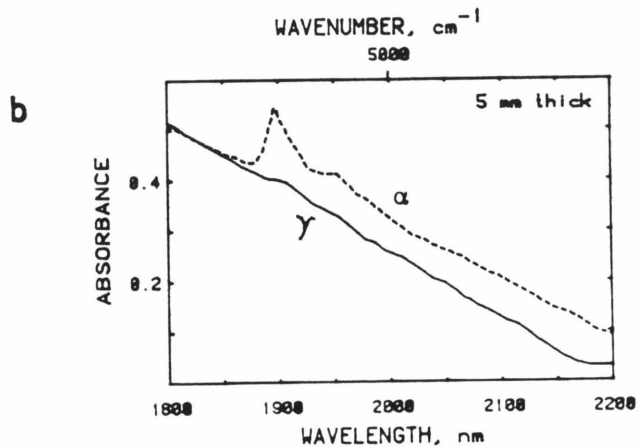


Figure 4.8 Polarized infrared absorption spectra of a gemmy area of white microcline #7, Elizabeth R mine, CA. (a) IR region. Absorption bands are present at 3630, 3550, 3460, 3400, 3250, and 3050 cm^{-1} . (b) Near-infrared region. Bands are seen at 5250 cm^{-1} (1900 nm) and 5100 cm^{-1} (1950 nm). The weak bands at 3450 and 3050 cm^{-1} are probably due to XOH species similar to sanidine. The 2 combination modes and the remaining 4 bands in the IR are due to two different types of water molecules.

Table 4.3 Absorptivities of Structural Water in Microcline

Sample	Number	Polarization	I(5790) cm ⁻¹	I(5130) cm ⁻¹	I(3630) cm ⁻¹	I(3400) cm ⁻¹
White Queen Mine CA	25	α	0.62	0.322	25 ± 1	23 ± 1
Elizabeth R Mine CA	1	α	0.447	0.239	18.2	18.8
	13579	α	0.391	0.218	18.1	17.8
	7	α	0.270	0.120	17.2	15.6
		β	ND	ND	1.3	7.14
		γ	~ 0	~ 0	4.6	9.90
		ave				
ε(#7, α), l/mole·cm			1.9	0.84	120	110
ε(#7, ave), l/mole·cm			ND	ND	54	76

Table 4.4 Fluid inclusion molar absorptivity in amazonite for α or β on (010)

Sample	Number	H ₂ O, mole/l	I(3430), cm ⁻¹	ε †, l/mole·cm
Lake George, Colorado	5	0.095 ± 0.005	2.45	26 ± 2
"	9	0.129 ± 0.013	2.77	21 ± 2
"	12	0.20 ± 0.05	4.26*	21 ± 2

* Average of four pieces

† Average molar absorptivity is 23 ± 2 l/mole·cm

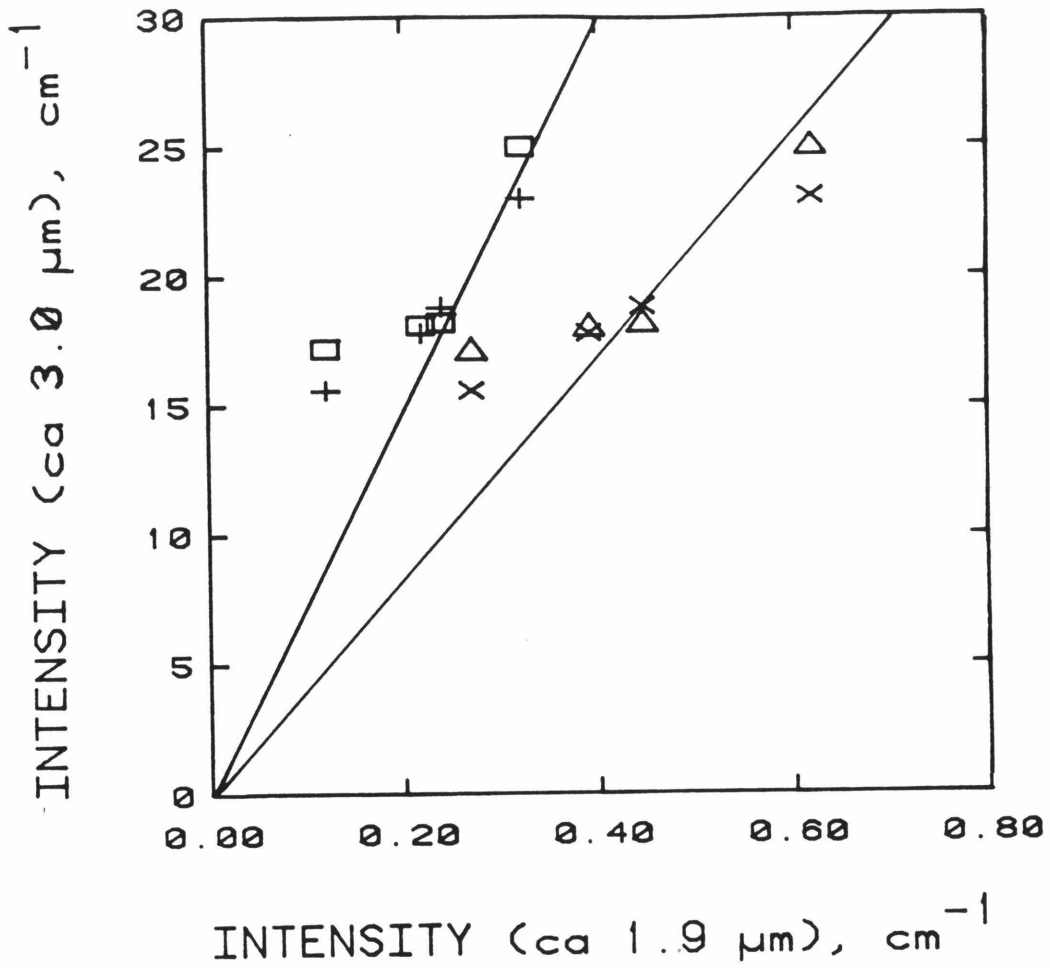


Figure 4.9 Correlation of peak intensity in the OH stretching mode (ca. 3 μm) with H₂O combination stretching-bending mode (ca. 1.9 μm) for the alpha polarizations of white microcline from the Pala district. Triangle, 5760 vs. 3630 cm⁻¹. X, 5760 vs 3400 cm⁻¹. Square, 5130 vs 3630 cm⁻¹. + 5130 vs 3400 cm⁻¹. Weak correlations exist for all pairs of bands. Neither pair fits better than the other.

water is present as H₂O in these microclines. Because IR spectra taken on microcline #7 at liquid nitrogen temperatures were not detectably different from the room temperature polarized spectra on the same chip, water indicated by the bands at 3630, 3550, 3400, and 3240 cm⁻¹ in the IR and 5130 and 5260 cm⁻¹ (1950 and 1900 nm) in the near-infrared occurs as isolated molecules in the feldspar structure (structural water), which agrees with Solomon's [in prep.] conclusions based on the separation of the peaks. The most likely site for the water is the M site, due to its size. Charge balance could be obtained by substitution of a divalent cation for a nearby K⁺, or by replacing an Al³⁺ ion with Si⁴⁺, because electrostatic equilibrium extends further than nearest neighbors [e.g. Smith, 1974, Vol. I, pp. 79, 95, 100]. There is no spectral evidence of H₃O⁺. Other likely sites are microfractures and microvacuoles [Solomon, in prep.] or other defects in the feldspar structure.

Besides the two pairs of absorptions in the infrared, weaker bands present at 3450 and 3030 cm⁻¹ in the microcline are polarized in alpha + gamma, and beta respectively (Figure 4.8). This suggests that some water in microcline occurs in the same mode as the sanidine. Because these fundamental vibrations are much weaker than the others in the microcline, temperature effects might not be observed for these bands, and the corresponding overtones would not be observed in samples less than several centimeters thick. Because turbidity in these microclines limits usable thicknesses to under 1 cm, direct correlation of the 3450 and 3030 cm⁻¹ fundamentals with stretch-bend combinations was not possible, so that assignments of these bands in microcline must rely on observations of sanidine.

Application of the sanidine extinction coefficients to the 3400 cm⁻¹

band in alpha in the microcline, implies that the OH concentration is 0.05 wt% as H₂O. Because this is the same size as the error (due to the blank) in the total water content, the amount of OH present can be ignored in computing molar absorptivities for structural water in microcline. Figure 4.10 shows that peak intensity is weakly dependent on total water concentration. However, a linear fit through the origin and two of the three samples is possible for all of the four peaks. The linear fit suggests that the weak dependence is due to inhomogeneity of water in the samples, such that the thin piece of the White Queen mine crystal and the thick piece of sample #1' did not have the same water content as the slab used in hydrogen manometry. The most accurate molar absorptivities were obtained from sample #7, and these are included in Table 4.3. The average of the molar absorptivity for the three polarizations of the fundamentals is similar to that of OH in sanidine and OH and H₂O in glass (Table 4.2).

4.3.e Blue-green microcline: mostly fluid inclusion water with some structural water

Chemistry and spectroscopy (other than IR) of amazonites will be covered in Chapter 6. This section deals strictly with speciation and concentration of water in amazonite. Only the infrared region will be discussed, because the blue microclines are too turbid and the green orthoclases are too small for detection of water bands in the near-IR.

A typical IR spectrum of amazonite shows mostly broad bands (Figure 4.11). The polarizations taken on the more turbid face (001) are much more intense than those from the gemmy face (010); however, the spectra within each pair are nearly the same. These facts suggest that the broad bands arise from the fluid inclusions which cause the turbidity.

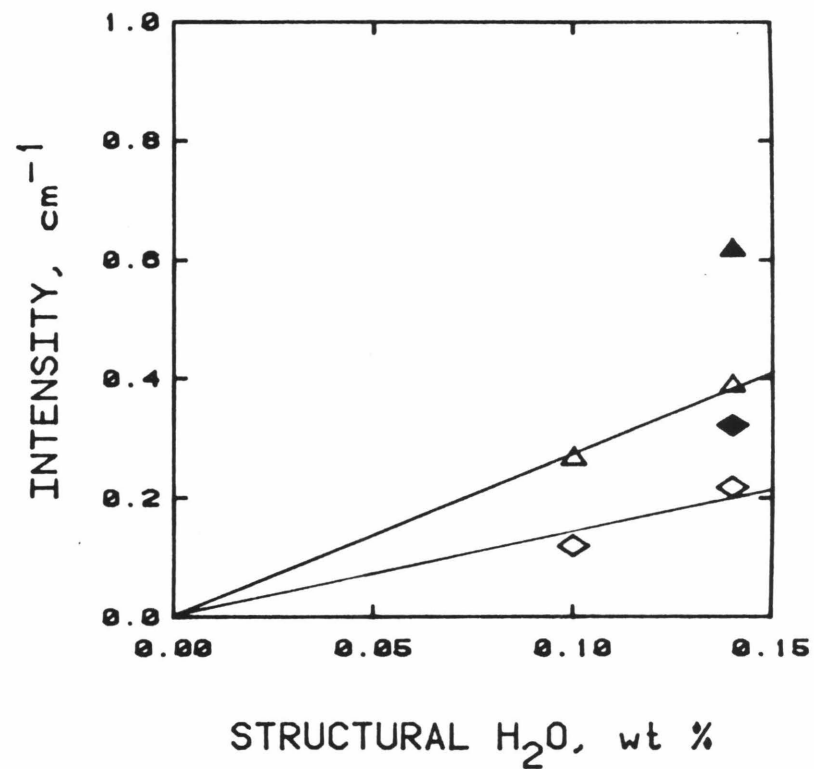
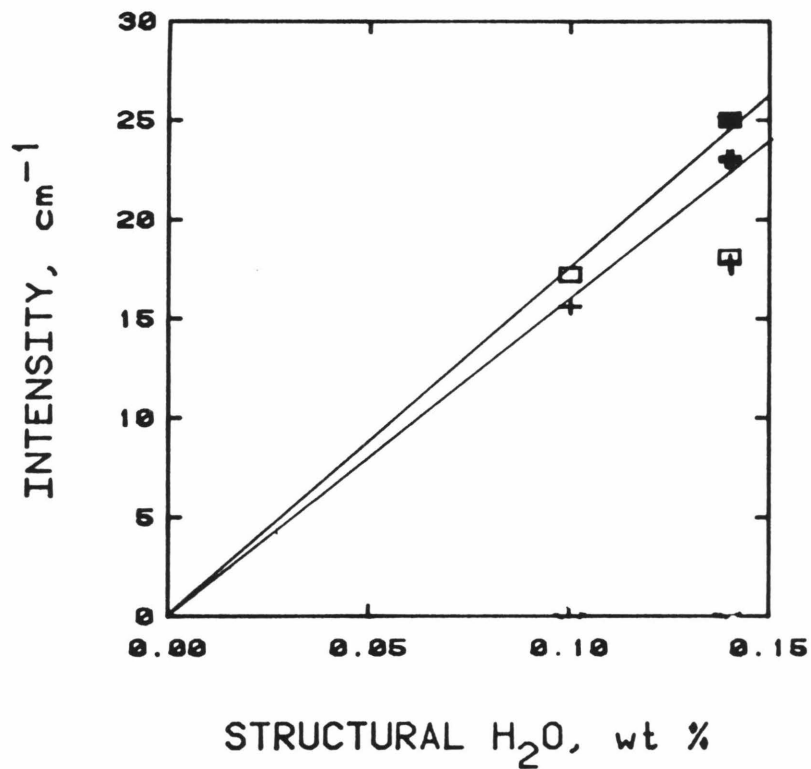


Figure 4.10 Dependence of peak intensity in alpha on total water concentrations of white microclines. Triangle, 5760 cm^{-1} band. Diamond, 5130 cm^{-1} band. Square, 3630 cm^{-1} band. +, 3400 cm^{-1} band. Filled symbols are for the White Queen sample. Peak intensity weakly depends on concentration because of inhomogeneities of water in a single crystal.

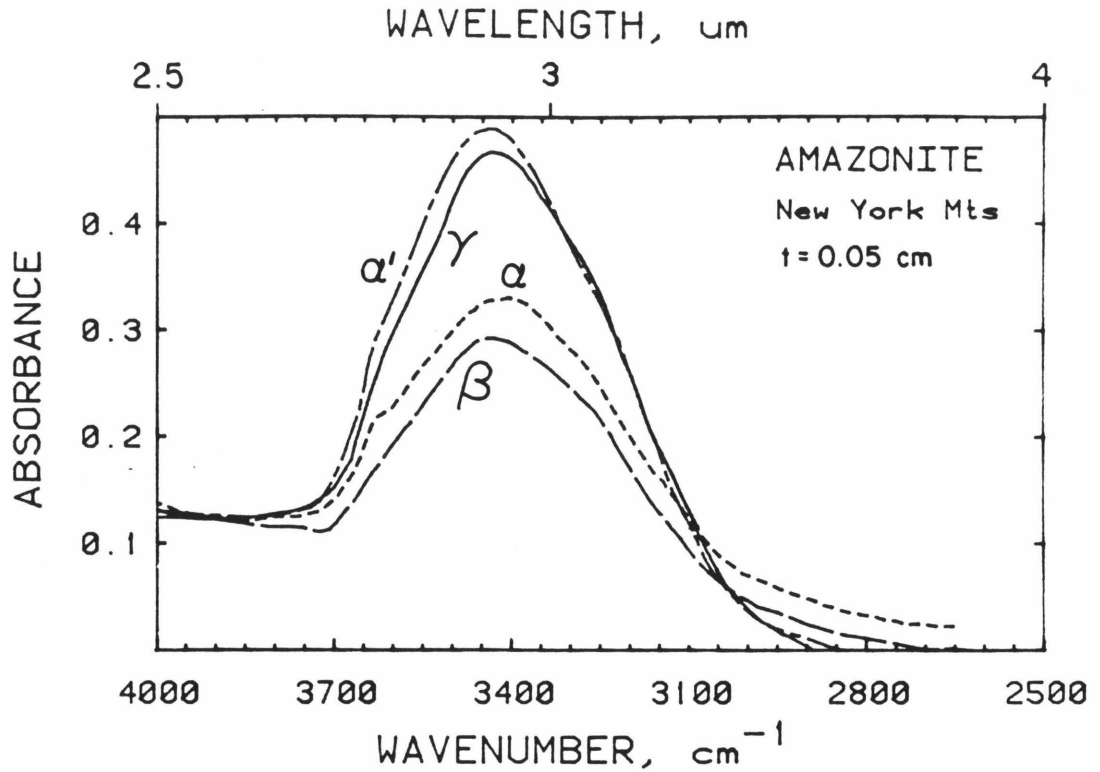


Figure 4.11 Polarized infrared spectra of amazonite #19'. α and β were taken on (010). γ and α' were taken on (001). The pair of spectra from the more turbid face (001) has much more water than the pair from the gemmier face (010). Little difference in band shape exists between the two spectra of each pair.

A variable amount of anisotropy exists in amazonite IR spectra at 3630 and 3240 cm^{-1} . These positions are the same as those of structural water peaks in white microcline (Sec. 4.3.d) and suggest that a small portion of water in amazonite may be incorporated within the feldspar structure.

Comparison of typical amazonite IR spectra taken at room temperature and near liquid nitrogen temperature (Figure 4.12) shows that freezing splits the broad bands into three components, doubles the intensity, and shifts the central absorption to 3200 cm^{-1} , which proves that the broad, isotropic (with respect to one face) bands are due to fluid inclusions.

Slight anisotropy at 3630 and 3440 cm^{-1} are shown in the IR spectra of the Colorado amazonite chilled with liquid nitrogen (adjusting for baseline differences). Slight anisotropy also exist at these positions in the room temperature spectra which shows that these bands are a separate from the fluid inclusion water.

Typical IR spectra of gemmy green orthoclase from Australia are shown in Figure 4.13. Small differences occur between pairs of spectra taken on the same cleavage face, while a large amount exists between spectra taken on different faces. Most of the intensity difference between α of (010) and α of (001) arises from the broad band at 3400 cm^{-1} , which was attributed to fluid inclusion water in microcline. From the band profile and position and the presence of microscopic (ca 1 μm) fluid inclusions in orthoclase, I conclude that the broad band in orthoclase results from the fluid inclusions. Anisotropy between spectra on the same face occurs at all four band positions for structural water in microcline (3630, 3550, 3440, and 3240 cm^{-1}), which shows that two different kinds of structural water are present. (Both types are probably present in microclines, such that a higher ratio of fluid to structural water in the

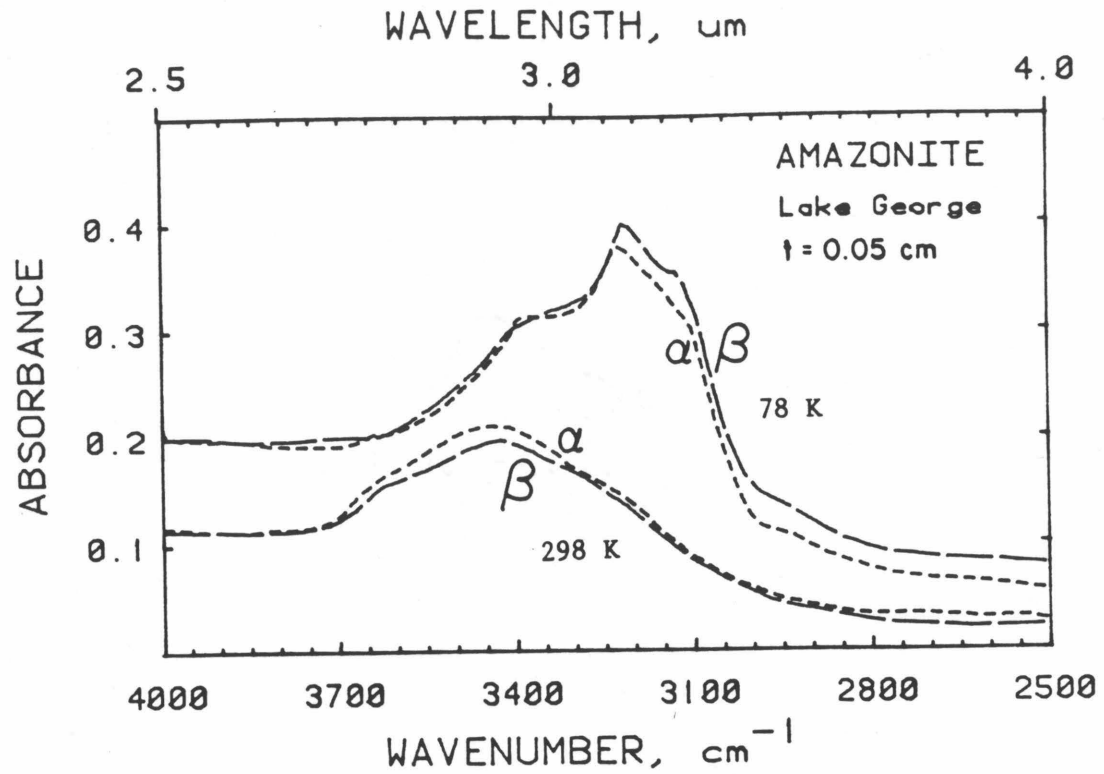


Figure 4.12 Polarized infrared spectra of amazonite #5 from Lake George, Colorado. The lower pair was taken at room temperature, while the upper pair was taken after the sample was cooled with liquid nitrogen. The splitting, shifting, and intensification of the IR bands upon freezing proves that liquid water is present in the feldspar.

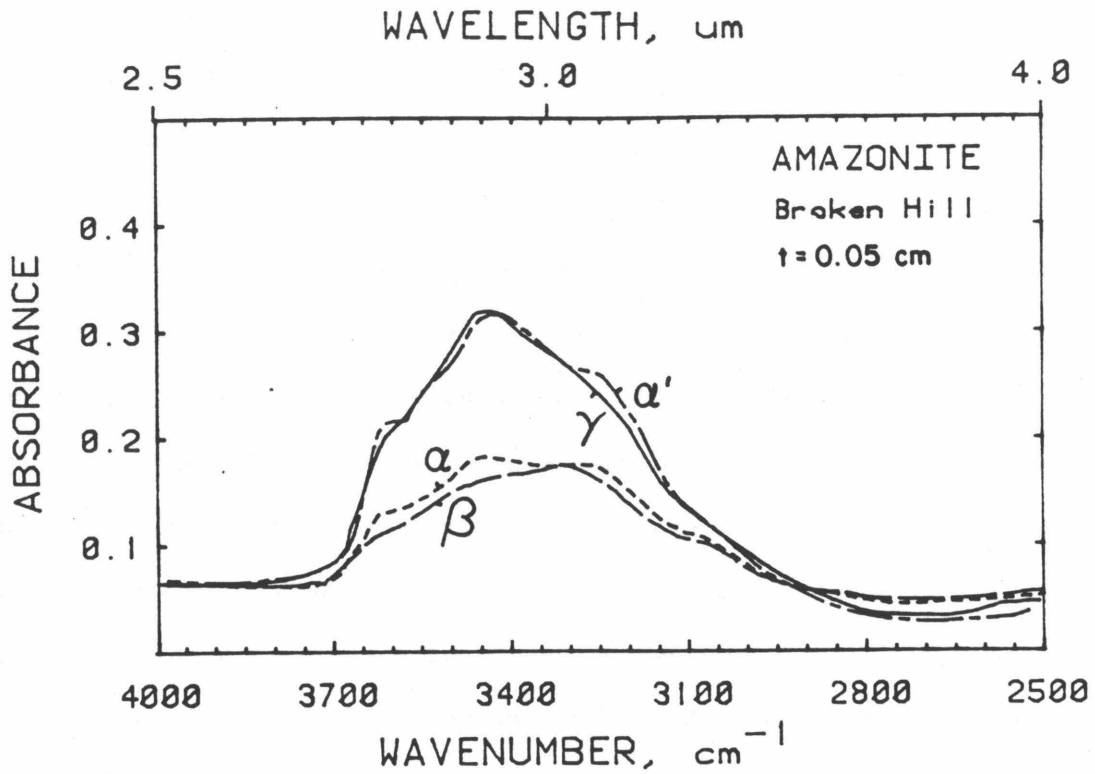


Figure 4.13 Polarized infrared spectra of gemmy green orthoclase #3 from Australia. Spectral data were scaled from 1 mm and 1.6 mm thick samples. The $\gamma\alpha'$ pair is from (001) while $\alpha\beta$ are from (010). Slight anisotropy exists between different peaks of the two pairs, while an overall difference in intensity exists between the two pairs, especially near 3450 cm^{-1} .

microcline leads to masking of all but the 3620 cm^{-1} peak. A band is weakly present at 3050 cm^{-1} , which may indicate XOH groups similar to those of sanidine.

Another type of water which is frequently present in amazonites is manifested by two bands near 3700 and 3640 cm^{-1} (Figure 4.14). The intensity of the higher energy band is much greater if the baseline due to the broad band fluid inclusion water is (visually) subtracted. Because hydroxyl from various types of clay absorbs near these wave numbers, and because these samples are turbid, I conclude that clays are indicated by absorptions near 3700 and 3640 cm^{-1} . Anisotropy present in the amazonite spectra is most likely due to structural water.

The presence of the ammonium ion is indicated in both green and white microcline from Amelia, Virginia. Figure 4.15 shows IR spectra of two Amelia microclines, along with the spectrum of buddingtonite $(\text{NH}_4)\text{AlSi}_3\text{O}_8 \cdot (1/2\text{ H}_2\text{O})$. Bands in the buddingtonite spectra at 3410 , 3300 , 3175 , 3060 , 2840 , 1770 , 1680 , and 1440 cm^{-1} are similar in position to those of $(\text{NH}_4)^+$ at $3040 + \nu_L$, 3145 , 3080 , 2800 , 1680 , and 1400 cm^{-1} (where ν_L is a lattice mode) [Nakamoto, 1978, p. 135]. The "extra" bands at high energy and near 1700 cm^{-1} in the buddingtonite may be due to combinations with a second lattice mode or may be associated with water. The two bands at 3700 and 3650 are probably clay. Features in the microclines at 3440 , 3330 , 3070 , and 2840 cm^{-1} give a similar band profile to the ammonium absorptions in buddingtonite, which strongly suggests that NH_4^+ is present in these microclines. The Amelia samples also show evidence of fluid inclusion water (broad band underlying the sharper absorptions) and for the green sample, structural water (3630 cm^{-1} band in alpha). The cause of the 3550 cm^{-1} band in α in the white microcline is not known.

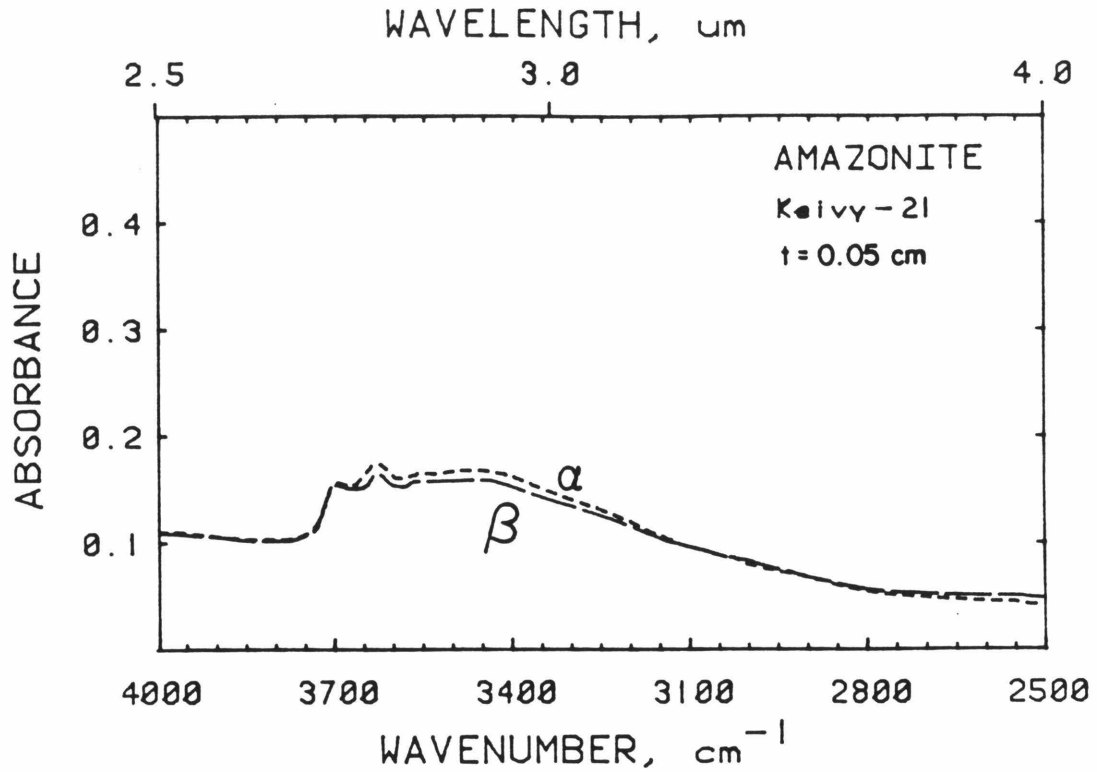


Figure 4.14 Polarized infrared spectra of green amazonite #6 from Kola Peninsula, USSR. Spectra were scaled from a 0.825 mm sample. Broad band fluid inclusion water is indicated, along with alteration products (3700 and 3640 cm^{-1} bands) and a slight amount of structural water (anisotropy at 3620 and 3440 cm^{-1}).

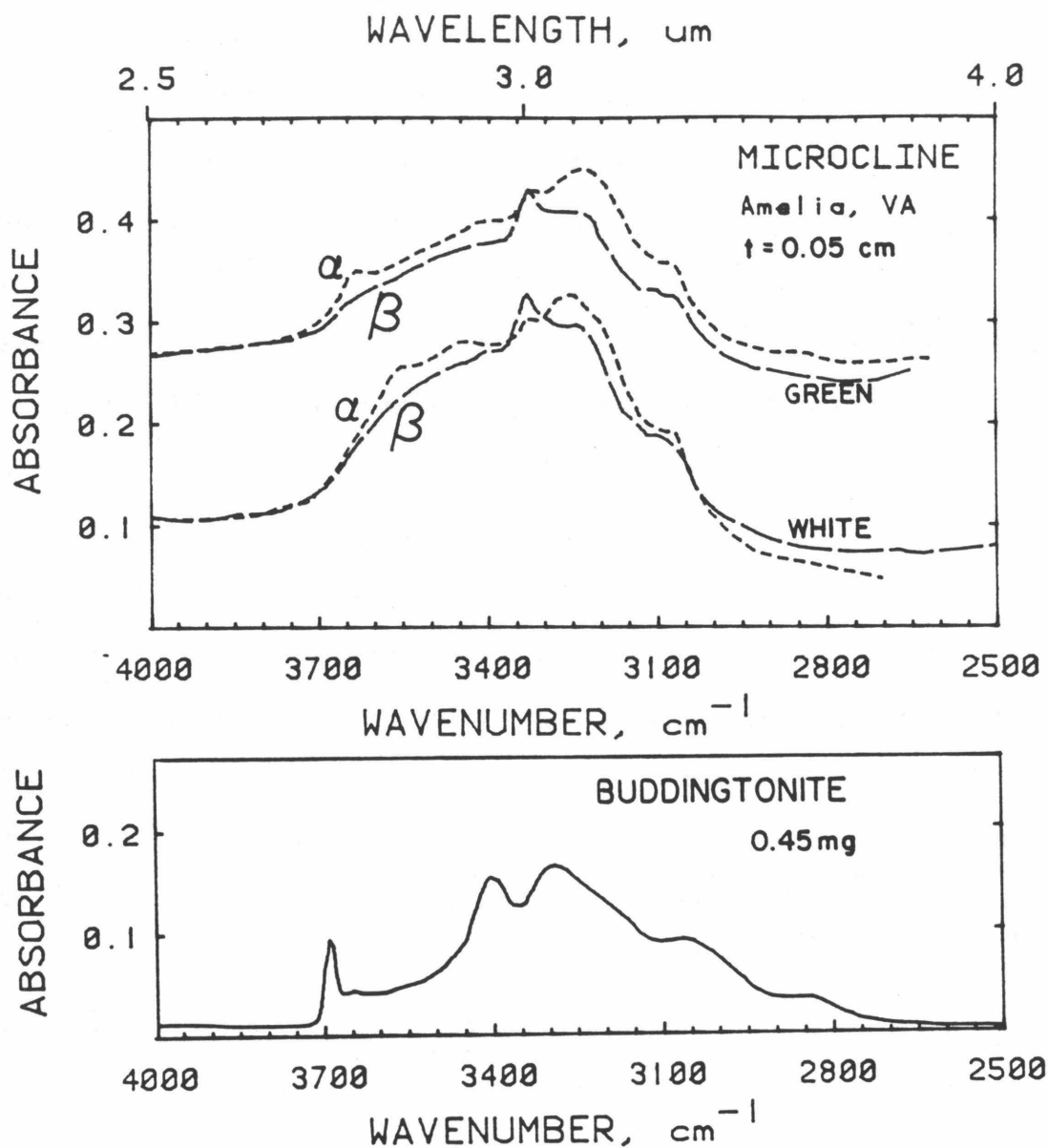


Figure 4.15 Polarized infrared spectra of green and white microcline from Amelia, Virginia, along with an unpolarized buddingtonite spectrum. Microcline spectra are plotted as 0.5 mm thickness; buddingtonite as 0.45 mg in a 200 mg KBR pellet. Peaks near 2840, 3070, 3145, and either 3300 or 3410 cm^{-1} are associated with $(\text{NH}_4)^+$. One of the 3300 or 3410 cm^{-1} peaks is connected with water, as are the remaining peaks in the spectra.

The diverse species indicated in the infrared occur with different frequency in amazonite. All of the 21 amazonite samples studied had fluid inclusion water. In addition, nineteen samples showed a slight amount of anisotropy at 3620 cm^{-1} which I conclude is due to structural water. (See Table 6.13 for a list of these samples, and their water contents.) Seven samples (#'s 21, 6, 20, 26, 32, 3', and 3'') had OH^- due to alteration products (clays). Two samples (#'s 22 and 24) from Amelia, Virginia, contained $(\text{NH}_4)^+$.

Molar absorptivities were determined for the broad band water by using peak intensities and the total water contents of Table 4.1. From Table 4.4, molar absorptivities of fluid inclusions at 3420 cm^{-1} vary slightly among the three samples which have mostly broad band water. The variation is probably due to both inhomogeneities in fluid inclusion concentration, and a slight amount of structural water in the amazonites. The average for the three samples is $23 \pm 2\text{ l/mole}\cdot\text{cm}$, which is considerably lower than molar absorptivities for structural water ($76\text{ l/mole}\cdot\text{cm}$ at 3400 cm^{-1}) and OH ($50\text{ l/mole}\cdot\text{cm}$ at 3456 cm^{-1}).

A molar absorptivity for the 3700 cm^{-1} band due to alteration products can be estimated from Figure 4.13, the total water content (0.15 mole/liter), and the average fluid inclusion molar absorptivity. The intensity at 3420 cm^{-1} is 1.54 cm^{-1} , which implies that 0.067 mole/liter of the water is in fluid inclusions. If the remainder of the water is OH of alteration products, then its molar absorptivity at 3700 cm^{-1} is $12 \pm 2\text{ l/mole}\cdot\text{cm}$. The amount of structural water is roughly 0.002 mole/l, which will not affect the calculation.

CHAPTER 5

SMOKY FELDSPAR: IRRADIATIVE COLORING OF STRUCTURALLY ANHYDROUS FELDSPAR

This chapter presents and correlates the features present in optical (visible to infrared) and EPR spectroscopy for natural, heat-bleached, and irradiated smoky feldspar. The properties of the feldspar centers, including the influence of water on response to radiation, are compared to those of smoky quartz and irradiatively colored alkali- and alumino-silicate glasses. Based on our observations, the above comparison, and models previously proposed for smoky quartz and glasses [Nassau and Prescott, 1975; Scheurs, 1967; Kordas and Oel, 1982; Cohen and Makar, 1982], we propose a model for the smoky colorations in feldspar.

5.1 Sample Description, Chemistry, and Response to Irradiation

Feldspars used in this study are listed in Table 5.1. Complete chemical data on the amazonites are listed in Tables 6.1 to 6.3; data for the remaining feldspars are listed in Tables 3.1 and 3.2.

Gemmy sanidine from the Volkesfeld area of the Eifel region is naturally light brown-grey. Itrongay orthoclase turns deep blue-grey with irradiation. Like sanidine, this color fades in sunlight or with heating. Amazonites (microcline and orthoclase colored blue-green by radiation) frequently have a grey tinge. Heating can permanently remove the blue-green color, whereupon the grey color develops through irradiation. Gamma-irradiation of white microcline does not induce color, unless the feldspar is dehydrated beforehand or irradiated at liquid nitrogen temperature, in which case, the grey color fades upon warming to room temperature. Chemically, the microcline differs only slightly from the other two potassium feldspars in that it has less iron. Iron is not involved in the irradiative coloring because the EPR

Table 5.1 Sample Description, Chemistry, and EPR Intensities

Sample and Number	Locality	Chemistry ^a	Fe ^a wt%	Treatment ^b	Color	H ₂ O wt%	Proton Species	EPR I.I. ^g	
								H	ΣAl-O ⁻
Sanidine 13757	Eifel, Germany	Or ₈₆ Ab ₁₄	0.12	None	Smoky	0.017 ^d	OH	80	Very weak
				400°C+0.176 MR	Smoky	0.018	OH	262	ND
				400°C+0.35 MR	Smoky	0.018	OH	333	ND
				400°C+2.82 MR	Dark Smoky	0.018	OH	595	~0
Orthoclase 13762	Itrongay, Madagascar	Or ₉₀ Ab ₁₀	0.25	None	Yellow ^c	0.001	OH	ND	ND
				2.82 MR	Blue-grey	ND ^e	-	#	#
				7.02 MR	Blue-black	ND	-	ND	ND
Perthite 13757(1")	Elizabeth R Mine, Calif.	Or ₉₄ Ab ₇	0.003	None	White	0.14 ^d	H ₂ O*	0	0
				28.4 MR	White	ND	-	0	0
				900°C	White	<0.006	H ₂ O*	ND	ND
				900°C+2.4 MR	Grey	ND	-	1658	300
Orthoclase ^f 13756 + 28	Broken Hill, Australia	Or ₉₂ Ab ₈	0.009	None	Green	0.004	H ₂ O*	1	-
						0.064	H ₂ O ^f		
				400°C+6 MR	Grey	0.0034	H ₂ O*	1	-
				0.05	H ₂ O ^f				
Amazonite 13758(19')	New York Mts., California	Or ₉₁ Ab ₉	0.015	None	Green	0.001	H ₂ O*	1	~350
				400°C+28MR	Grey	0.18	H ₂ O ^f		
						-	-	1	-
Amazonite 21	Keivy Pegma- tite, USSR	Or ₉₆ Ab ₄	0.03	None	Blue-green	0.001	H ₂ O*	1	-
						0.051 ^d	H ₂ O ^f		
				400°C+ ~10 MR	Grey	ND	-	1	-
				900°C+1.3 MR	Grey	ND	-	2240	86
Amazonite 5,9,12	Lake George, Colorado	Or ₉₅ Ab ₄	0.04	None	Blue	0.001	H ₂ O*	1	-
						0.090 ^d	H ₂ O ^f		
				400°C+ ~10 Mr	Grey	0.0005	H ₂ O*	1	-
						0.037	H ₂ O ^f	1	-

Table 5.1 Sample Description, Chemistry, and EPR Intensities (Continued)

Sample and Number	Locality	Chemistry ^a	Fe ^a wt%	Treatment ^b	Color	H ₂ O wt%	Proton Species	EPR I.I. ^g	
								H	ΣAl-O ⁻
Oligoclase Harvard 81228	S. Carolina	Or ₂ Ab ₈₁ An ₁₇	0.04	None 1.17 MR	Blue Grey-green	0.020 0.020	OH OH	ND	ND
								340	~600
Andesine 13759	Halloran Spgs., California	Or ₃ Ab ₆₆ An ₃₀	0.15	None 5.46 MR	Colorless Smoky	0.052 ND	OH ND	0	~500
								ND	ND
Labradorite 13761	Lake County, Oregon	Or ₁ Ab ₃₃ An ₆₆	0.31	None 11.28 MR	Yellow ^c Med.Yellow	0.013 ND	OH -	0	~320
								0	320

^aChemistry and iron contents from Hofmeister and Rossman (1983, in press). For K-feldspars and oligoclase all iron is ferric. For the labradorite, Fe³⁺ = 0.18 wt% and Fe²⁺ = 0.12 wt%. For andesine Fe³⁺ = 0.11 wt% and Fe²⁺ = 0.03 wt%. Or = KAlSi₃O₈. Ab = NaAlSi₃O₈. An = CaAl₂Si₂O₈.

^bRadiation doses are total doses. All heating done for 1/2 hour.

^cNatural yellow colors are due to high iron contents.

^dIndicates water determined by hydrogen manometry. Others were determined from the molar absorptivities of these samples. For sanidine, ε averaged for the three polarizations is 50 ± 8 liter/mole·cm. For white microcline, ε in α at 3620 cm⁻¹ is 120 liter/mole·cm. For amazonite, ε in α on (010) at 3400 cm⁻¹ is 23 ± 2 liter/mole·cm.

^eNot Determined.

^fFluid inclusion water.

^{*}Structurally incorporated water.

^gUnits are relative. H is the hole center at g_{eff} = 2.027, ΣAl-O⁻ is the sum of the aluminum related hole centers. Broad band is the wide electron center near g_{eff} = 2.0.

[#]Signals were overlapping.

[†]Signal obscured by baseline.

[‡]H_I and H_{II} signals occur instead of H.

[§]Optical study was on 13756; EPR work done on AMH#28

spectra of iron in the sanidine are unaffected by heating or X-ray irradiation [Speit and Lehmann, 1976], and because the response of amazonites is independent of iron content.

5.2 Speciation of H₂O Accompanying Smoky Color Formation and Inhibition

Feldspars which become smoky from irradiation possess low total water concentrations (Table 5.1 and Section 4.2) and broad absorptions near 3400 cm⁻¹ which indicate ≡XOH (Section 4.3.a). Molecular water in Eifel sanidine comprises less than 15% of the total "water," the remainder being ≡XOH⁻. For the sanidine, no changes were seen among spectra taken before and after irradiation and mild heating (400°C for half an hour), confirming Speit and Lehmann's [1976] observations.

Microcline uncolored by radiation possesses a series of four sharp polarized bands in the IR and two near 1900 nm (Section 4.3.c) indicating molecular water in a structural site, and also has much higher water concentrations (Table 5.1; Section 4.2). The feldspar M-site is the most likely candidate, considering its size, bonding, and capability of distorting to incorporate impurities. Infrared spectra taken of this structural water show no changes before and after irradiation, yet this species is always present in potassium feldspars uncolored by radiation.

Amazonites contain mostly fluid inclusion water as indicated by the formation of ice bands in the infrared spectra at low temperatures (Section 4.3.e). A small, variable amount of structural water is also present. If amazonite is decolorized by thermal treatment, it then can be turned grey by gamma ray irradiation, only if this structural water is also driven off in the heat treatment. Residual fluid inclusion water, if present, does not influence the results of the irradiation.

5.3 Visible and Near-Infrared Absorption by Color Centers in Feldspar

The spectra of naturally smoky and irradiated sanidine (Figures 5.1 and 5.2) resemble that of Speit and Lehmann [1976], but differ slightly in peak positions. This difference may be due to curve fitting or to baseline corrections. Irradiated Itrongay orthoclase has similar spectra (Figure 5.3). The variation in relative band intensities between natural and irradiated samples are partially related to dose: long exposures increased the band near 15000 cm^{-1} in gamma and the UV tail (cm^{-1}) of the deeply colored orthoclase. Spectral measurements of this same sample after sun-bleaching of the color (Figure 5.4) show that the middle energy peak has two broad components at roughly 16200 and 19100 cm^{-1} which vary in relative intensity among the three polarizations: the 19100 cm^{-1} peak dominates the γ spectra, the 16200 peak is much stronger than the 19100 cm^{-1} band in β , while in α , the intensities are approximately equal. Thus, the apparent shift in position for the $\sim 17000\text{ cm}^{-1}$ band between the natural and induced colors is due to varying intensities of the two components (19100 and 16200 cm^{-1}) with radiation dose, but the cause of the shift of the lower energy peak from 11390 (natural) to 11600 cm^{-1} is unknown.

Quantitative measures for the absorptions present in smoky feldspar were derived from a computer fit to 5 gaussian peaks and an approximation of the UV tail by equation 2.2. The peak parameters used are listed in Table 5.2 and the integrated intensities of the bands in orthoclase and sanidine are listed in Table 5.3 as a function of dose.

The intensity of the band near 11600 cm^{-1} can be precisely determined by method, but the overlap of the bands near 16200 and 19100 cm^{-1} lends an indeterminate amount of error. The presence of the ultraviolet tail

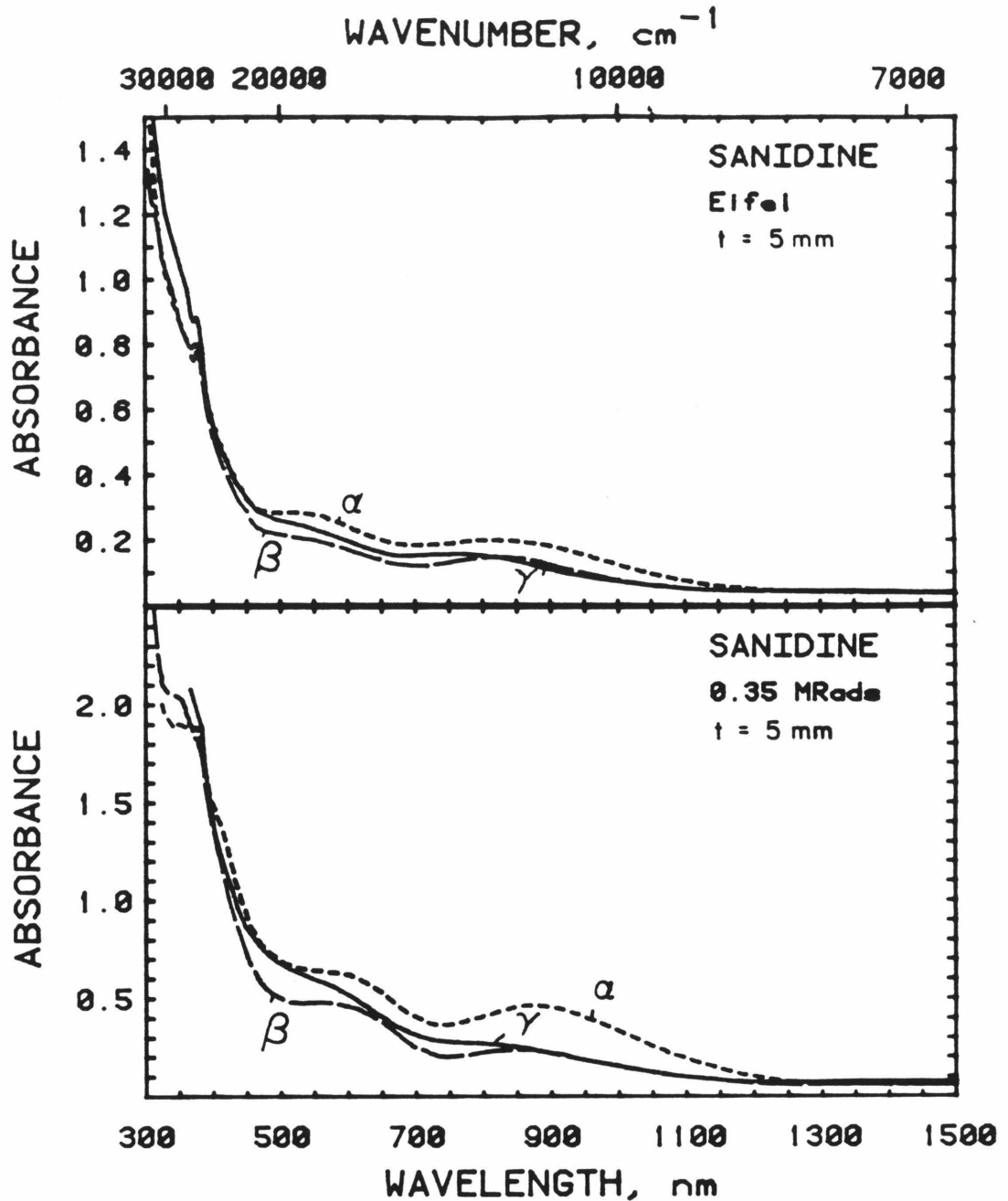


Figure 5.1 Visible absorption spectra of natural (top) and irradiated (bottom) smoky sanidine from the Eifel district, Germany. The small sharp bands at 380 nm are due to Fe^{3+} . All other bands are radiation induced. The peak positions and relative intensities of the bands differ slightly between the natural sample and the sample that was heat-bleached and then given a 0.35 MRad dose of gamma-rays.

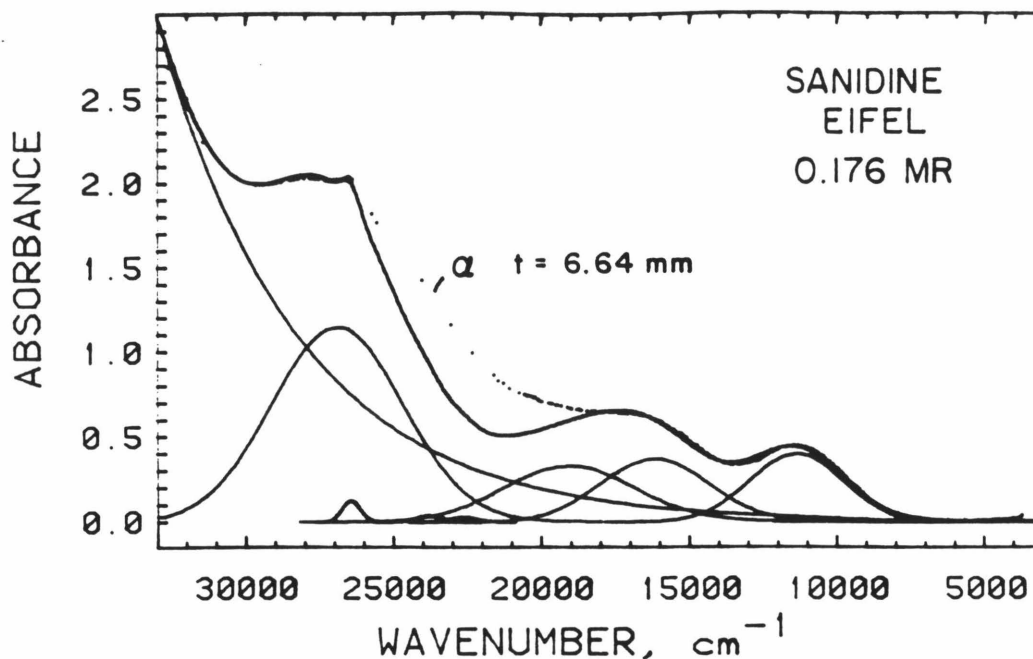
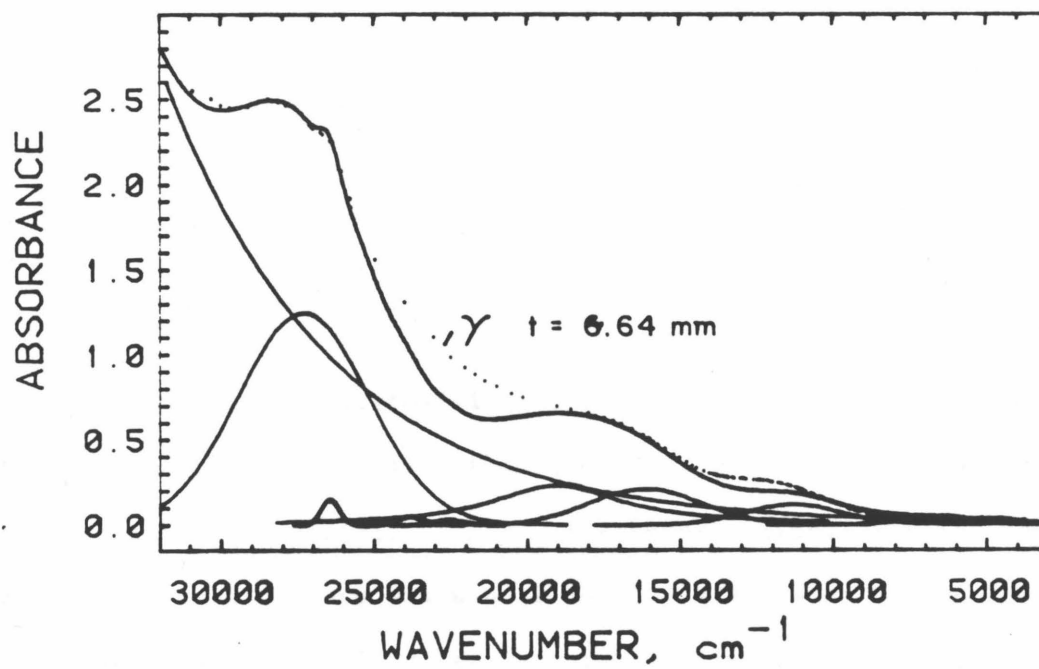
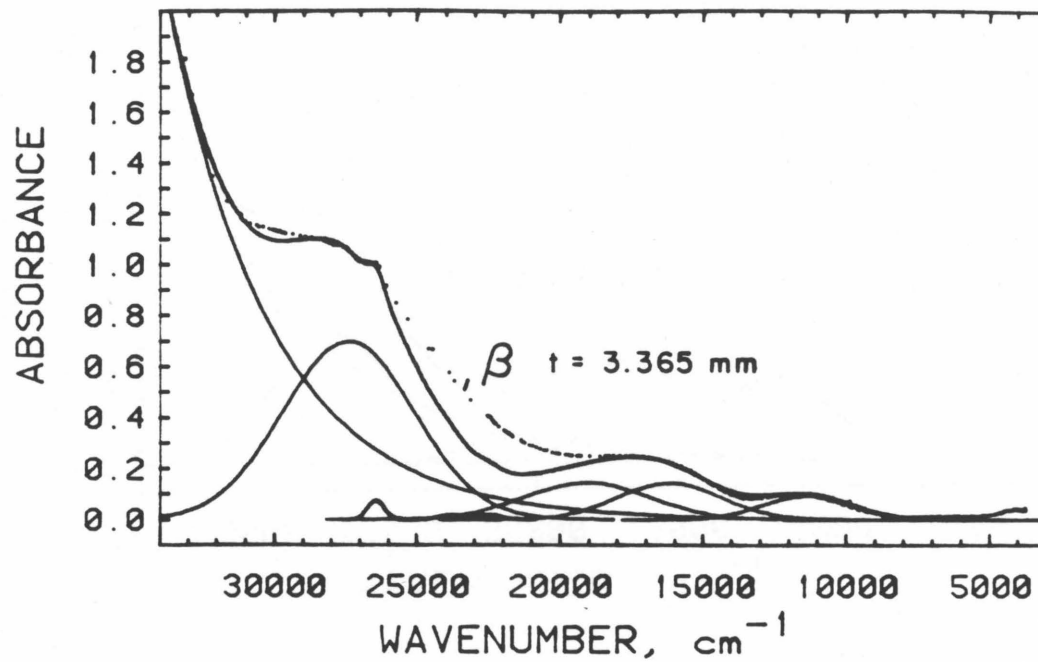


Figure 5.2 Gaussian decomposition of the polarized visible and near-infrared spectra of Eifel sanidine, irradiated 0.176 MRads. Thicknesses and polarizations are indicated on the spectra. Ferric iron transitions (small, sharp peaks near 380 nm) are partially masked by the large tail from the ultraviolet. All other features are irradiation bands. Spectral data are represented by the dots. Gaussian components, UV tail, and the calculated spectra are solid lines. The UV tail was computed using Equation 2.1. The same component peaks were used to calculate all smoky absorptions, except that the energy for the 27200 cm^{-1} was allowed to vary slightly.



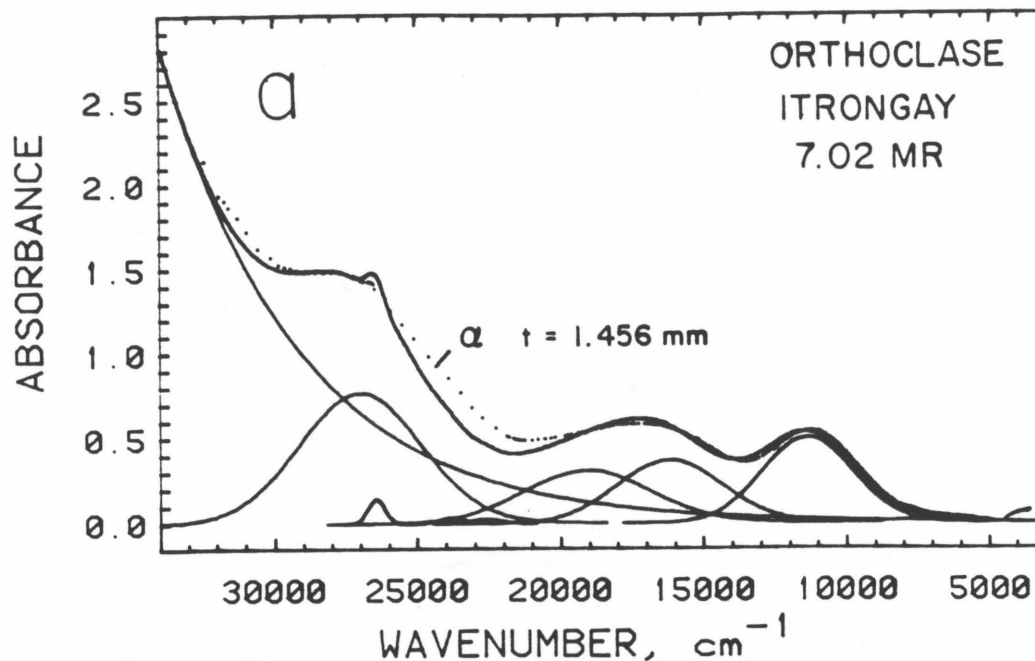
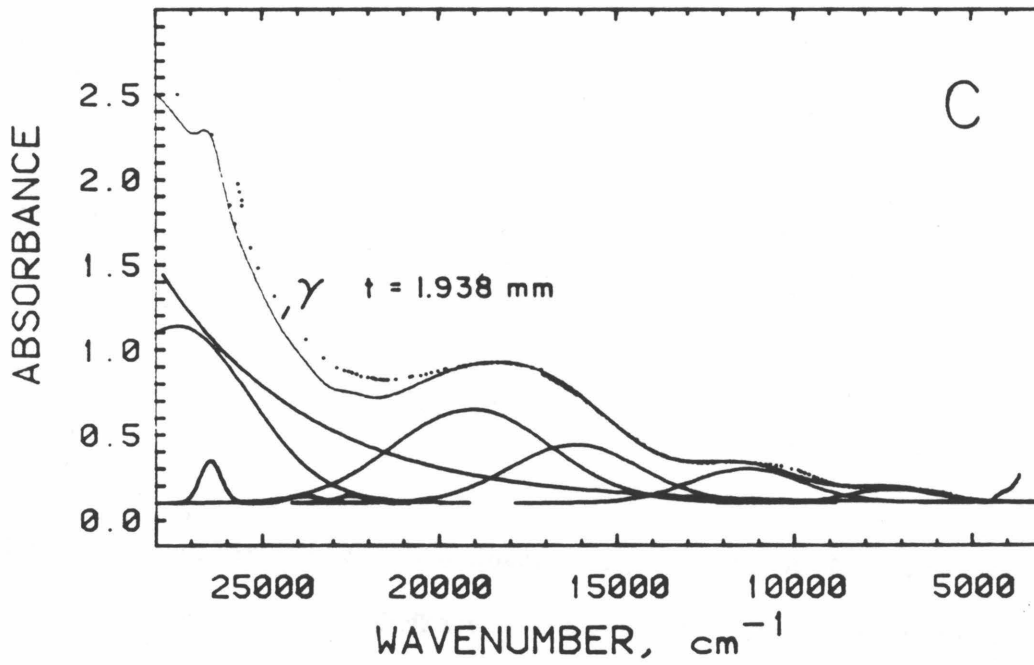
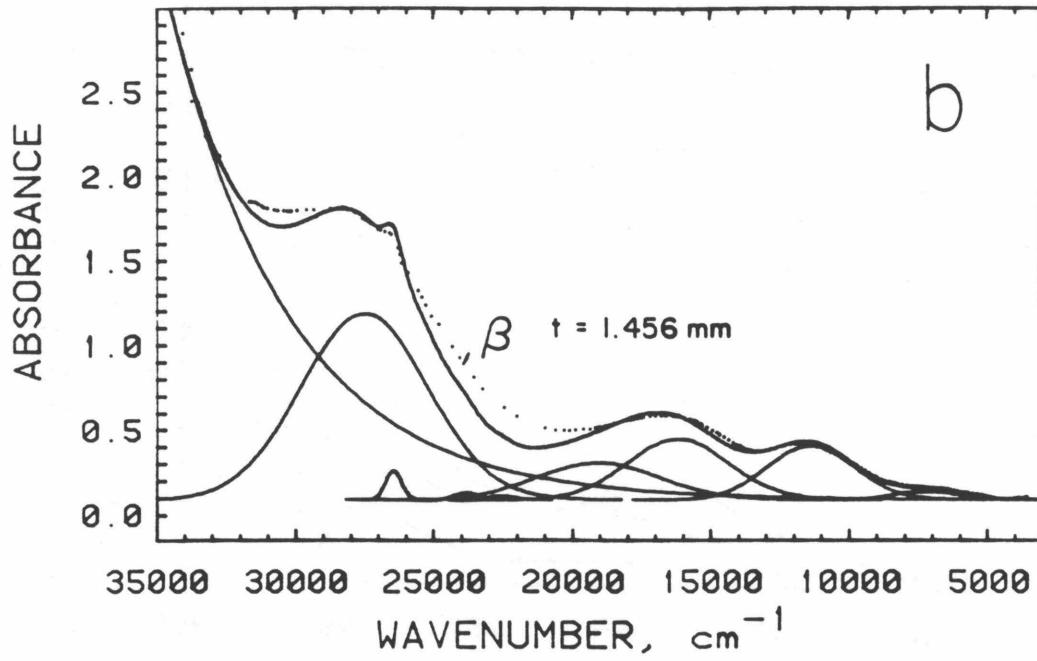


Figure 5.3 Gaussian decomposition of the polarized visible and near-infrared spectra of Itrongay orthoclase, irradiated 7.02 MRads. (a) α polarization. (b) β polarization. (c) γ polarization. Ferric iron d-d transitions (small, sharp peaks near 380 nm) are masked by the large tail from the ultraviolet. All other features are irradiation bands. Spectral data are represented by the dots. Gaussian components, UV tail, and the calculated spectra are solid lines. The UV tail was computed using Equation 2.1. The same component peaks were used to calculate all smoky absorptions, except that the energy for the 27200 cm^{-1} was allowed to vary slightly.



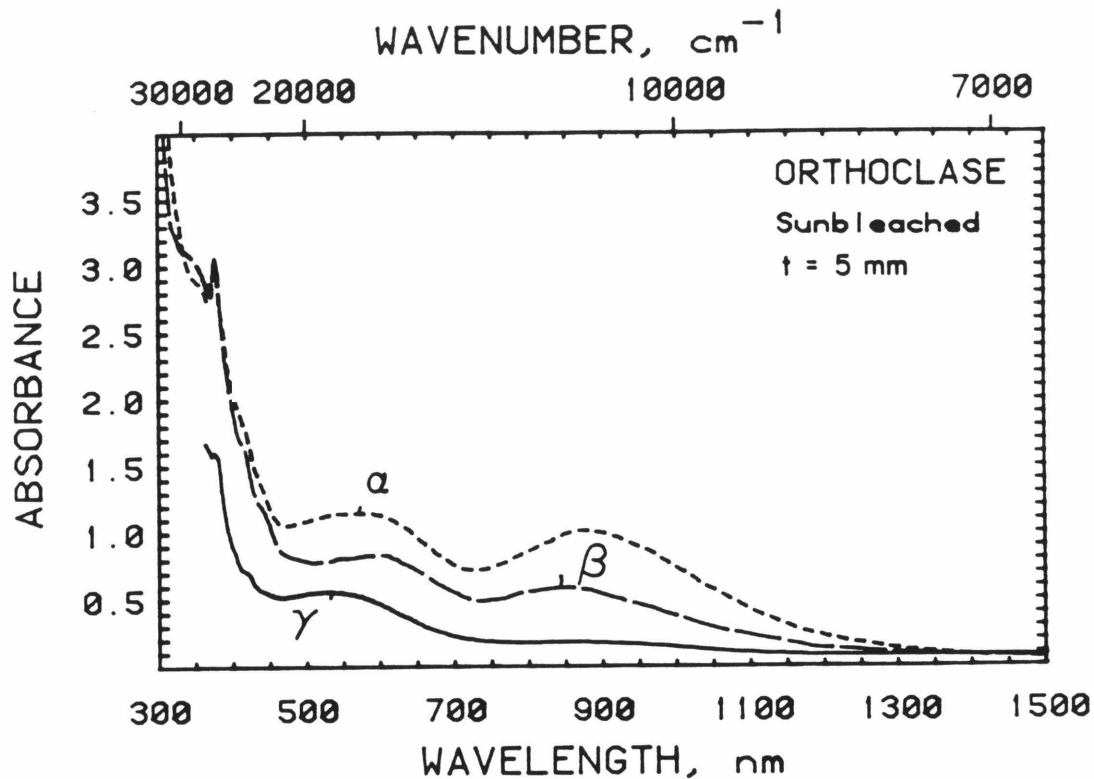


Figure 5.4 Polarized visible absorption spectra of Itrongay orthoclase which was irradiated 7.02 MRads and then bleached by exposure to sunlight. Much lower intensity of the 27200 cm^{-1} (340 nm) band allows resolution of the Fe^{3+} band at 380 nm. The polarization of the bands in the orthoclase differs slightly from the sanidine (Fig. 5.1).

Table 5.2 Peak Parameters Used in Gaussian Fitting of Smoky Color in Sanidine and Orthoclase

Designation		Position, cm ⁻¹	1/2-width, cm ⁻¹	Polarization
7300	irradiated	7300	2800	$\beta > \gamma > \alpha$
11600	natural	11600	3700	$\alpha > \beta > \gamma$
	irradiated	11390	3700	$\alpha > \beta > \gamma$
16200	either	16200	4300	$\alpha > \beta > \gamma$
19100	natural	19100	5200	$\alpha > \gamma > \beta$
	irradiated	"	"	$\gamma > \alpha > \beta$
27200	natural	27200 ± 300	5000-5200	$\alpha > \beta > \gamma$
	irradiated	"	"	$\beta > \gamma > \alpha$
uv tail	natural			$\gamma > \beta > \alpha$
	irradiated			$\beta > \gamma > \alpha$

Table 5.3 Integrated Intensities of Smoky and Related Bands

Designation			11600	16200	19100	27200	7300
Mineral	Dose, Mrads	Polarization	I.I., cm ⁻²				
Sanidine	Natural	α	1202	897	1507	2900	
		β	770	750	784	3190	
		γ	697	709	980	3298	
	Heated 0.176	$\alpha\beta\gamma$	0	0	0	0	
		α	2370	2250	2750	9590	
		β	1112	1970	2390	11960	
	0.350	γ	712	1448	2830	9980	
		α	2770	2830	2751	9760	
		β	1770	2245	2715	13990	
	2.82	γ	1009	1862	3002	10023	
		α	5565	6277	6700	26346	0
		β	3161	4627	4606	19750	354
Orthoclase	Natural	γ	2225	2955	6700	24560	0
		$\alpha\beta\gamma$	0	0	0	0	
		α	10820	9120	8370	25600	205
	2.82	β	6764	8180	6465	33170	1023
		γ	2360	4580	11070	31190	600
		α	13530	11640	11789	28160	410
7.02	β	8660	11321	8370	43440	1010	
	γ	4070	8030	15712	27340	1230	

which increases radiation dose further reduces the accuracy of measuring these peaks, and greatly complicates determination of the 27200 cm^{-1} peak intensity. Despite these limitations, band intensity correlates with radiation dose (Fig. 5.5). The three lower energy bands grow at comparable rates whereas the growth of the 27200 cm^{-1} band is roughly triple any of the others. A similar initial steep increase of color and later shallower linear rise has been observed in irradiated glasses, and have been explained by two processes: (1) the initial coloring of defects present before irradiation and (2) the later production and coloration of defects [Levy, 1960].

For the orthoclase with 0.3 wt% Fe^{3+} , the appearance of a band at 7300 cm^{-1} with increased dosage may be connected with formation of Fe^{2+} or possibly some type of iron-associated center, because a linear correlation of peak area with Fe content was observed (Figure 5.6). However, a reduction of intensity of the Fe^{3+} bands was not observed either in the EPR or optical absorption spectra, so that assignment of this band is tenuous.

5.4 Calculation of Time Necessary for Natural Sanidine Coloration

Comparison of the integrated intensities of the natural sanidine to that of a crystal irradiated 0.176 MRads (Table 5.3) suggests that the cumulative dose received by the natural sanidine was about 0.1 MRads. For water, 1 Rad is equivalent to the release of 6.24×10^{13} eV/gram H_2O [Draganic and Draganic, 1971, p. 210]. For feldspar, the energy release is about the same:

$$1 \text{ Rad} = 2.43 \times 10^{13} \text{ eV/gram KAlSi}_3\text{O}_8. \quad (5.1)$$

Radioactive decay follows the equation

$$N = N_0 \exp(t(\ln 1/2)/\tau) \quad (5.2)$$

where τ is the half-life, t is time, N is the number of particles, and N_0 is the initial number of particles. Differentiating gives

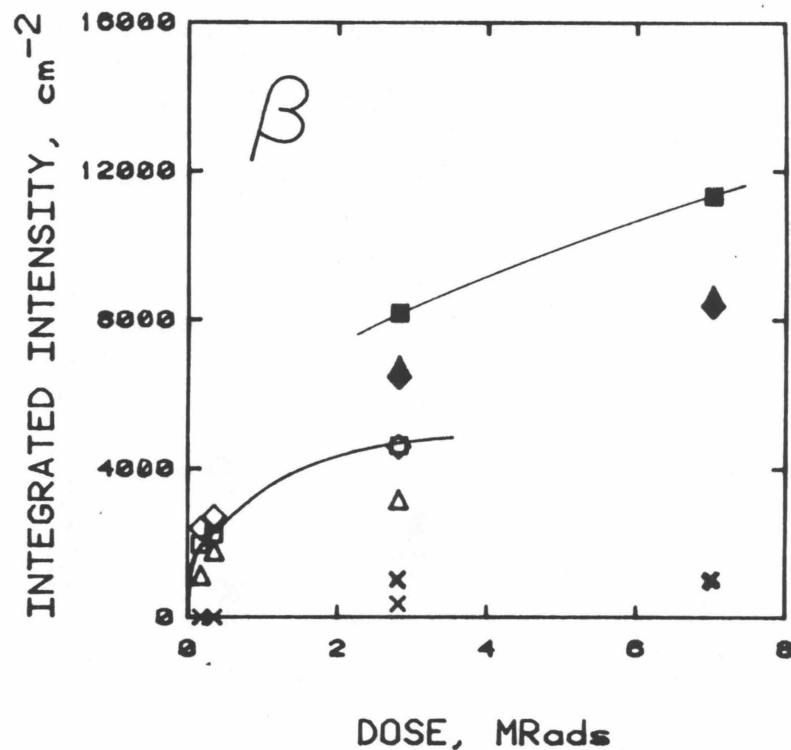
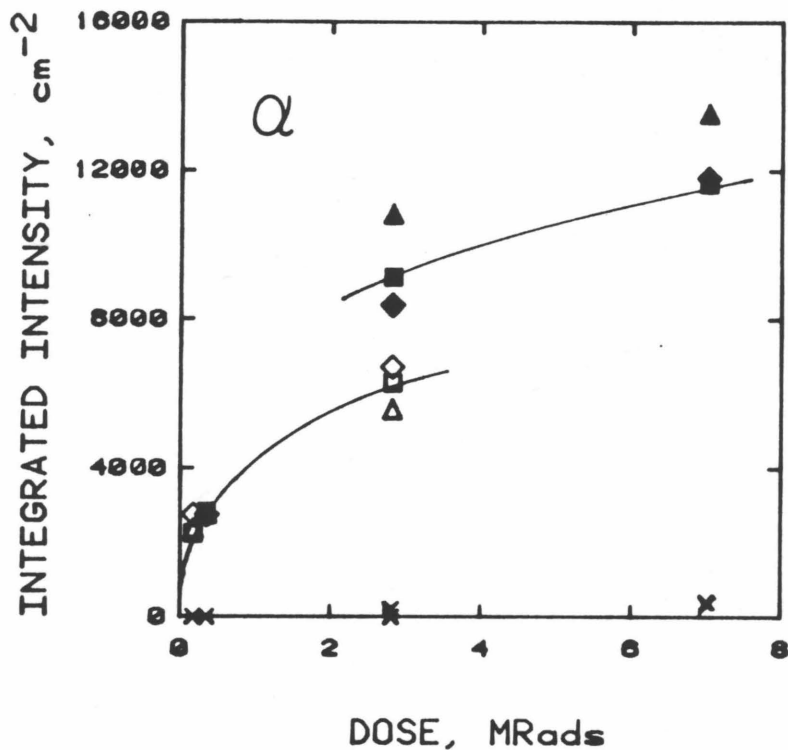
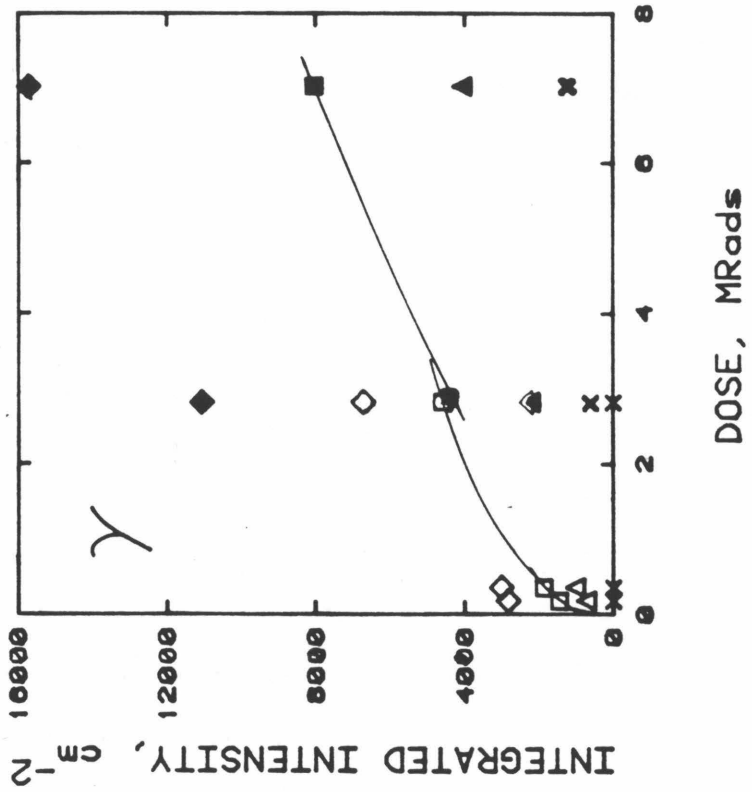
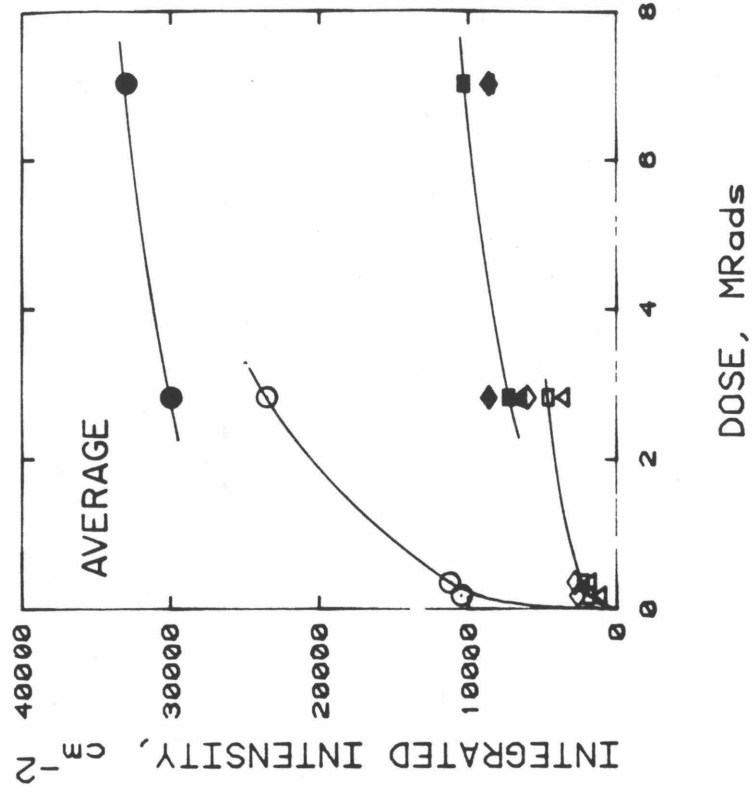


Figure 5.5 Integrated intensity (I.I.) of absorption peaks present in smoky feldspar as a function of radiation dose. I.I. were taken from computer generated fits of gaussians for each of the three polarizations and their average. Circle, 27500-26900 cm^{-1} peak. Triangle, 19100 cm^{-1} peak. Diamond, 16200 cm^{-1} peak. Square, 11390-11600 cm^{-1} peak. X, 7300 cm^{-1} band. Open symbols denote sanidine. Filled symbols denote orthoclase. The knee in the curves indicates that growth of the color centers may proceed by two different reaction kinetics.



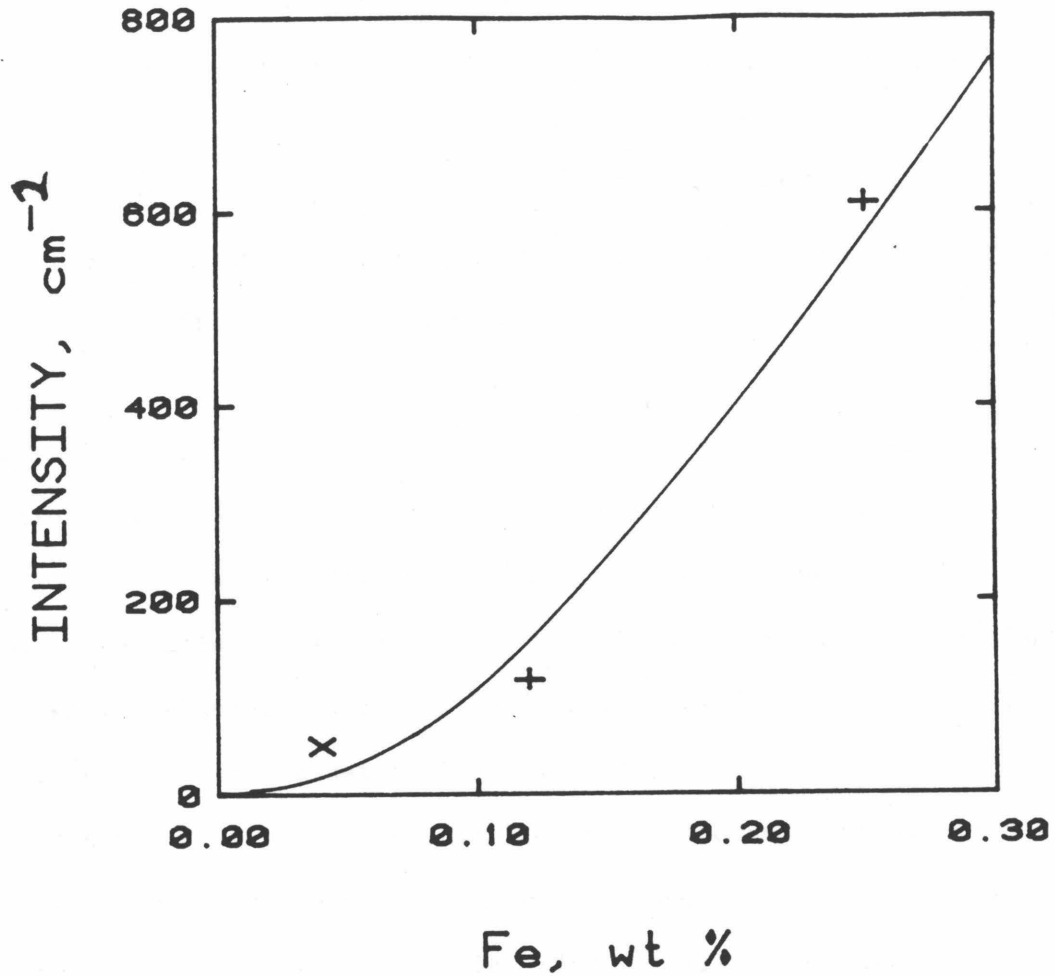


Figure 5.6 Dependence of the band area of the peaks at 7300 to 9100 cm^{-1} on iron content. Crosses are potassium feldspar. X is oligoclase. The trend indicates that iron may be associated with this peak. Tentatively, the $\sim 7300 \text{ cm}^{-1}$ band is assigned to ferrous iron in the tetrahedral site created from Fe^{3+} by radiation.

$$dN/dt = -N(\ln 1/2)/\tau . \quad (5.3)$$

^{40}K comprises 1.18×10^{-2} % of the potassium isotopes, has a half-life of 1.28×10^9 years, and produces 1.4 MeV gamma rays 10% of its decays and 1.3 MeV betas 90% of its decays [Weast, 1973, p. B-225]. Because of the long half-life, the number of ^{40}K atoms have been nearly constant over the Tertiary. Thus, a simplified equation suffices:

$$\Delta t = \tau \Delta N / N(\ln 1/2). \quad (5.4)$$

ΔN is the number of decays, which can be related to the dose through equation 5.1. Thus, the number of decays can be approximated by

$$\Delta N = \text{Dose (in rads)} \cdot (6.24 \times 10^{13} \text{ eV/gram}) / 1.3 \text{ MeV}. \quad (5-5)$$

Combining equations 5.4 and 5.5 and using appropriate conversion factors (279 g/mole feldspar and 6.02×10^{23} atoms/mole) gives an estimate for the time required to color natural sanidine of 0.06 Myrs.

Volcanic activity in the Eifel district occurred throughout the Tertiary, dominantly in the Miocene (12-26 myr), but some eruptions took place in Pleistocene time (<2 myr) [Luettig, 1980, p. 111]. The geologic age of the sanidine would thus provide much more radiation flux than indicated by the sample's present color. Considering that the color bleaches at about 156°C or upon exposure to sunlight [Speit and Lehmann, 1976], a much longer time than the calculated 10^5 years could be necessary to keep the increase in color in pace with the removal, so that it is highly likely that internal decay of ^{40}K within the feldspar provides the radiation energy for the natural color. The gamma particles from the ^{40}K should penetrate the sample far enough to give the even color observed because gamma particles from the cesium source with similarly low energy evenly color large (several centimeter diameter) crystals during short exposures. Betas will only penetrate about 1 mm, but even coloration should occur from their emission because the K atoms are dispersed.

5.5 EPR Spectroscopy of Radiation Centers near $g_{\text{eff}} = 2$ in Feldspar

5.5.a Description of centers correlated with smoky color

In both natural and irradiated smoky feldspars, a broad (~ 100 G) slightly asymmetric first derivative is present at $g_{\text{eff}} = 2.027$ (Figure 5.7a). This center (designated by H in analogy to the nomenclature in the glass literature) is also present in irradiated orthoclase. In white microcline the H center can be induced by γ radiation only if structurally bound water is removed beforehand by heating. The breadth of the signal in microcline indicates the presence of disorder. This disorder is substantiated by the superposition of an Al-O^- -Al signal (see below) because aluminum ions are isolated from each other in maximum microcline, and also by the band widths of the lattice modes in the IR spectrum.

The H center is also induced by irradiation of microcline-amazonites (Figures 5.7 b, c, and d) which have been thermally disordered as indicated by broadening of linewidths in the infrared absorption pattern and by the presence of an Al-O^- -Al EPR pattern. A combination of two centers which vary in relative intensity is found in amazonite #21 and the same sample #21 that was first heated (but not disordered) and then colored grey by irradiation. One center consists simply of a single first derivative at $g_{\text{eff}} = 2.009$ with a 20-Gauss width. The second complex center consists of six lines (five of which are nearly equally spaced at intervals of 55 to 68 Gauss) centered at $g_{\text{eff}} = 2.024$. The intensity of the low complex center in most samples is so low that the outermost satellites disappear into the noise (Figures 5.7 b and d). This led previous workers to attribute the complex center to a three-line pattern derived from Pb-O^- -X [Marfunin and Bershov, 1970, Speit and Lehmann, 1982]. In the well-resolved signal, the double-integrated intensity (Equation 2.2) of either inner satellite is more

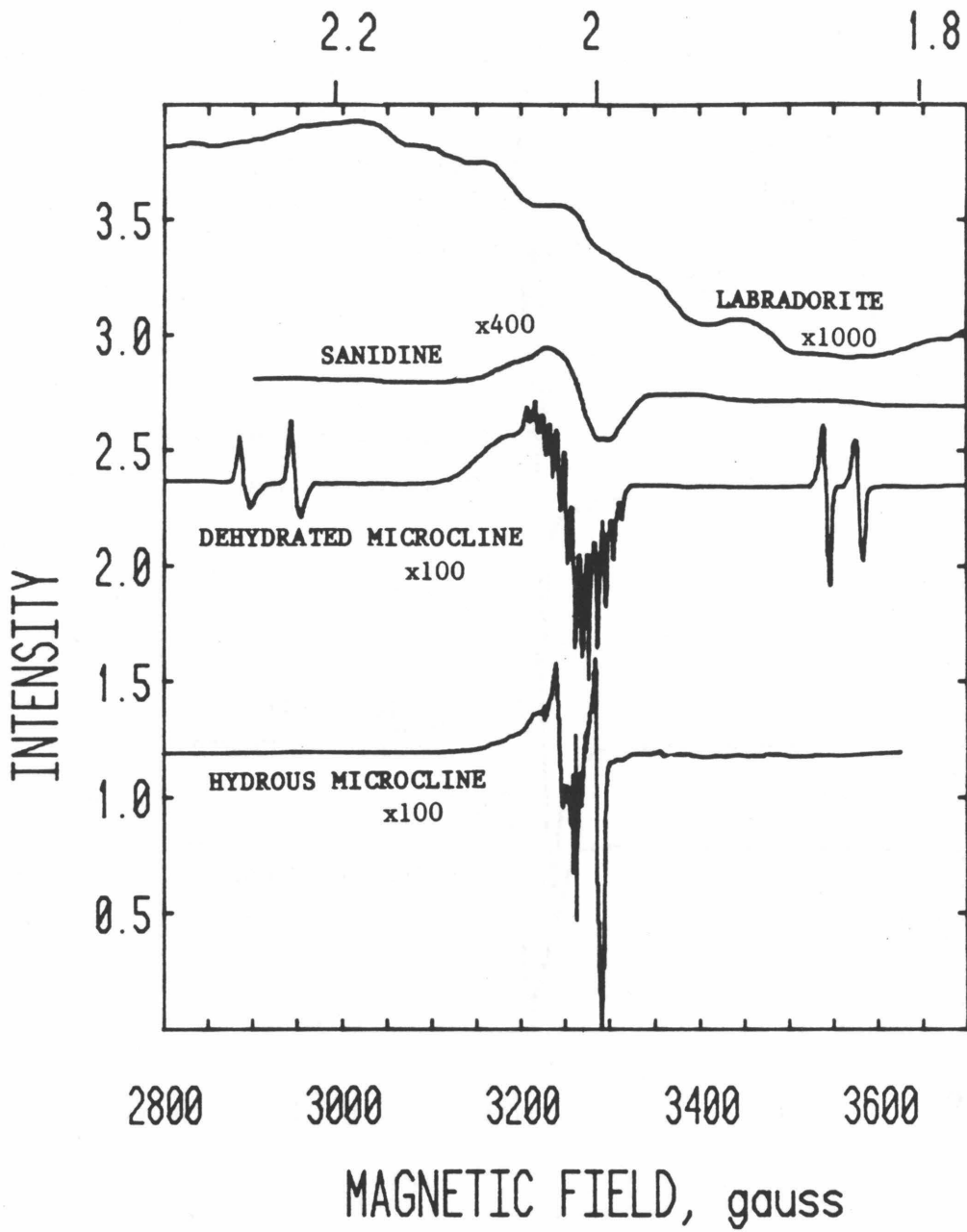
Figure 5.7 EPR spectra of radiation centers near $g_{\text{eff}} = 2$. Intensities are scaled for run conditions of 1.0 mWatt, 1 Gauss modulation amplitude, and 100 mg of sample weight. Gains are designated. (a) H and Al-centers. Frequencies were 9.225 GHz for the labradorite, 9.264 GHz for the sanidine, 9.200 GHz for the dry microcline, to 9.178 for the wet microcline. Both smoky sanidine and grey (dry) microcline possess a slightly anisotropic first derivative near $g = 2$. For the labradorite, the sextet hyperfine structure is due to Al-O^- center. For the wet microcline, a variety of first derivatives is seen, all relatively narrow (<40 G wide) and all concentrated around $g = 2$.

(b) H_I and H_{II} . The signals near $g = 2$ are not connected with the blue-green color because they return after heat-bleaching. The peak at 1.83 is connected with amazonite color (Section 6.6). Frequencies were 9.20 GHz for disordered microcline, and 9.194 for the others. For the natural Keivy sample, seven lines are distinguishable. Predominance of one of these lines in the heated and irradiated Keivy sample shows that there are two centers: a simple one-line center and a complex 6-line center. Further heating disordered the sample, whereupon the EPR lines are broadened and one asymmetric signal develops. The natural orthoclase shows the same two centers in different proportions and slightly broader linewidths than the microcline. For lowered intensity of the complex center, the weakest satellites are not resolved.

(c) H_I , H_{II} , and Al-O^- in green amazonites. Dehydrated samples turned grey and developed the signals near $g = 2$ after irradiation. Frequencies ranged from 9.188 to 9.2, so that g -factors are approximate. The dashes indicate the positions of the Al-O^- centers. "A" indicates the amazonite center. An additional line occurs in the Broken Hill spectra at 3260 Gauss.

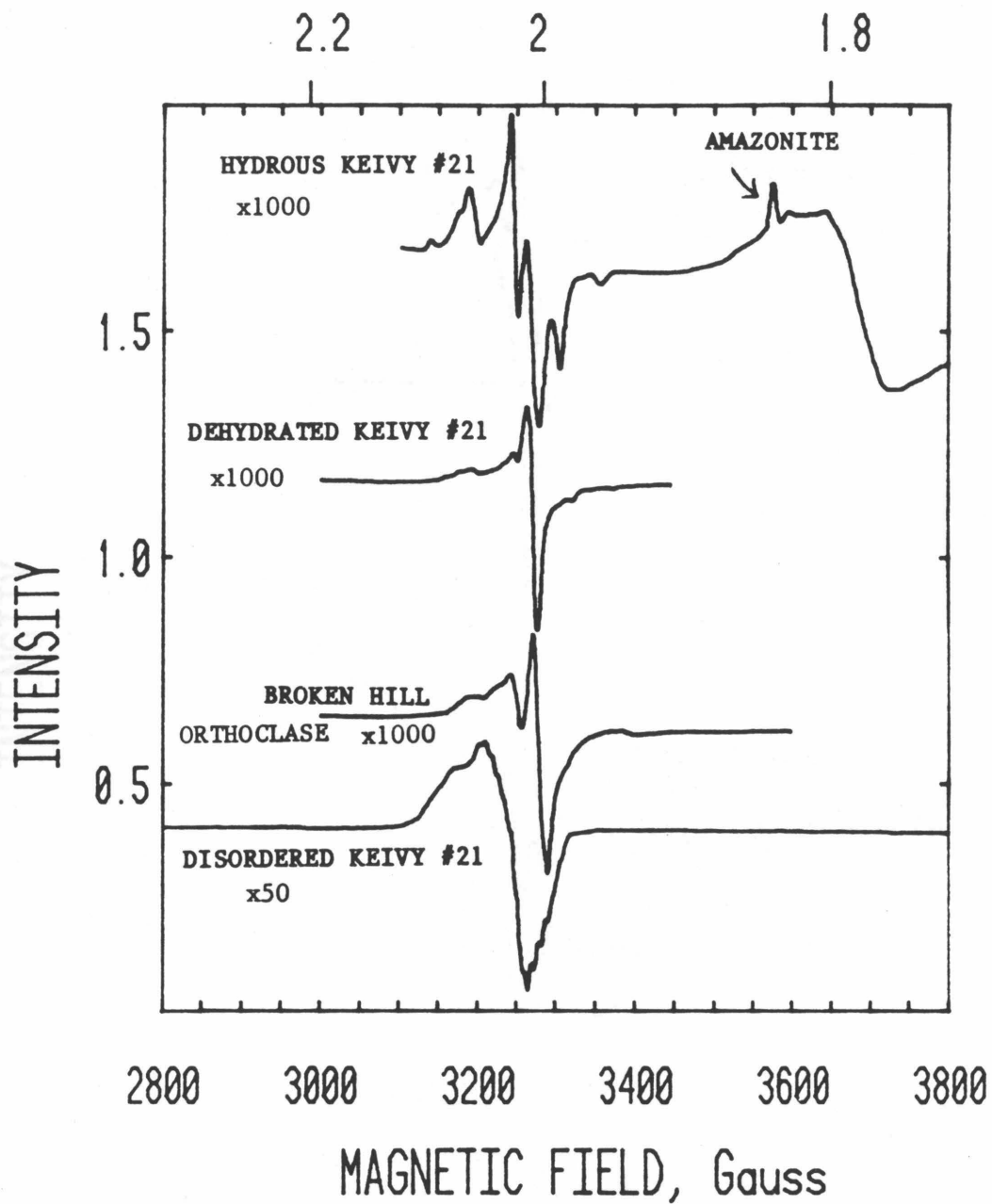
(d) H_I , H_{II} , and Al-O^- in blue amazonites. Frequencies were all 9.914 GHz. The oligoclase spectra is shifted because it was taken on a contracted scale.

g FACTOR



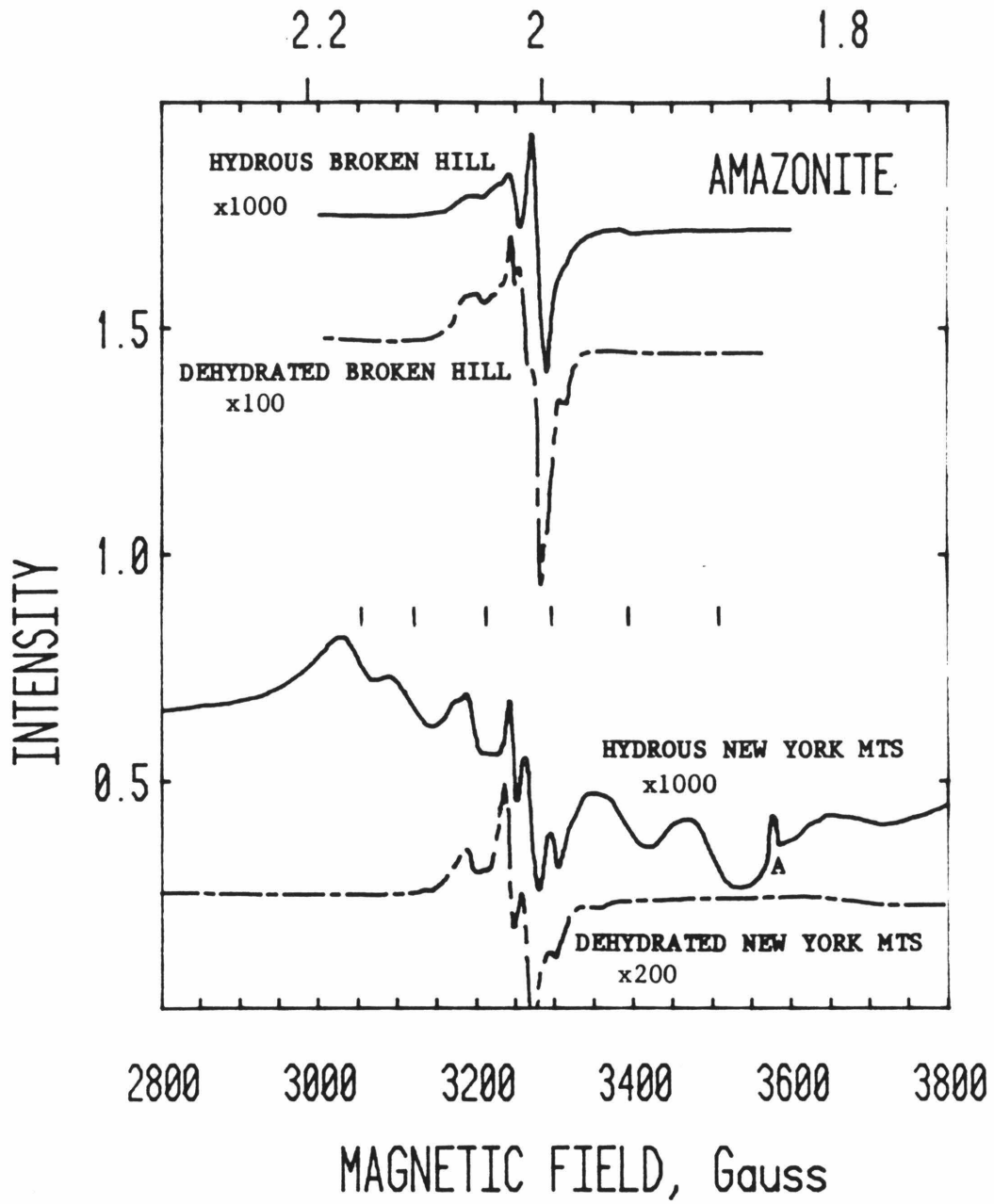
a

g FACTOR



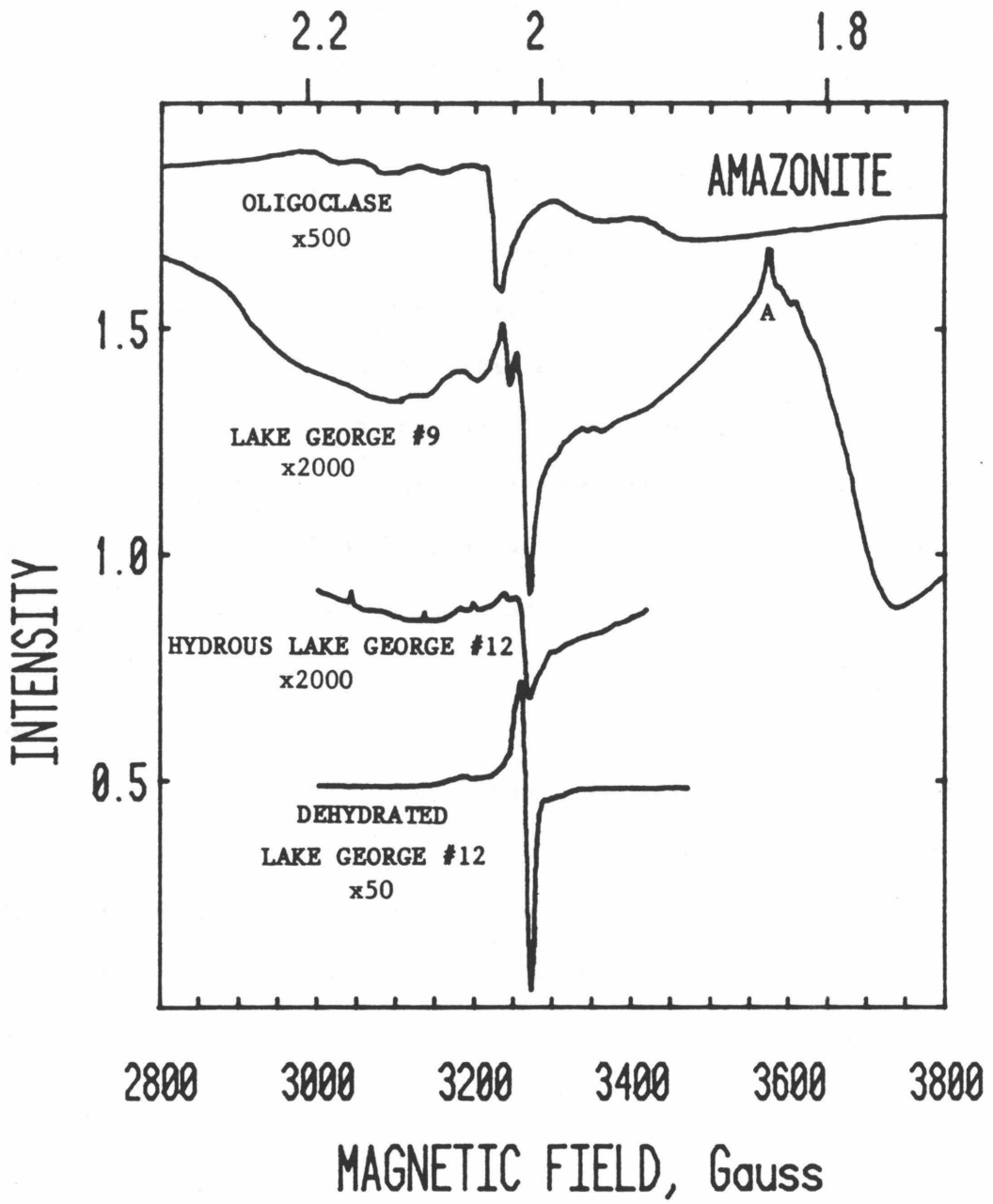
b

g FACTOR



C

g FACTOR



d

than 0.4 times that of the central peak (Table 5.4), which rules out involvement of lead ions in the center because the predicted ratio of satellite to central peak intensity for Pb is 0.143 (e.g., Goodman and Raynor, 1970, Table 1 and page 219).

If the linewidths of the two centers were doubled, they would combine to yield the asymmetric H center pattern of the disordered Keivy sample. This interpretation is supported by the width of the Fe^{3+} pattern in sanidine which is double that of microcline, and is further corroborated by the association of smoky color with the two EPR patterns in microcline but with the one (combined) pattern in sanidine. Intermediate behavior occurs in the EPR pattern of Broken Hill orthoclase which gives an envelope similar to the H center in sanidine (Figures 5.7 b and d).

The increase in intensity of the H centers in sanidine with radiation dose (Fig. 5.8) follows a similar initial steep rise and then shallow increase as did the absorption bands. The H center in the dehydrated microcline is much more intense than that of the sanidine for the same dose. This could be either due to different EPR extinction coefficients for the two polymorphs (as is the case for Fe^{3+} EPR bands) or to different response of the feldspar to radiation or both. The rate of growth of radiation centers and the maximum color obtained definitely would be sample specific, and dependent on factors such as thermal history.

5.5.b Correlation of EPR and optical spectra

To determine which optical absorptions in the smoky sanidine are related to the H center, band intensities were plotted as a function of the intensity of the H center (calculated by Equation 2.2). All bands correlate with the H center, within the uncertainty of peak parameter determinations (Fig. 5.9). The correlation with the 19100 cm^{-1} band is the weakest, because

Table 5.4 EPR Parameters for the $g = 2$ region of Amazonite #21,
Keivy Pegmatite, USSR

Center	Magnetic field Gauss	g	Relative Height	Relative Integrated Intensity	Total Width Gauss
H _I (complex)	3135	-	0.043	0.052	
	3175	-	0.157	0.294	
	3190	-	0.270	0.729	
	3247	2.023	1.000	1.000	240
	3305	-	0.304	0.376	
	3369	-	0.059	0.165	
H _{II} (simple)	3270	2.009	-	-	45

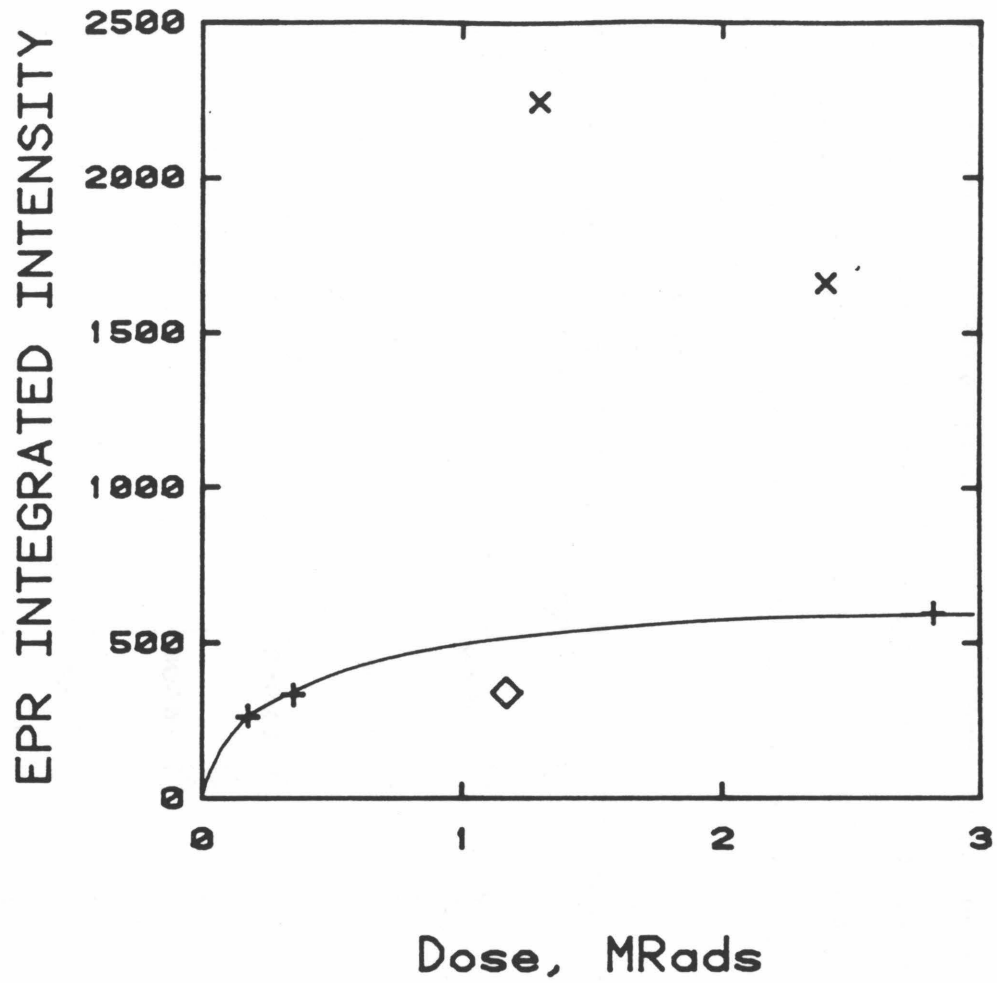
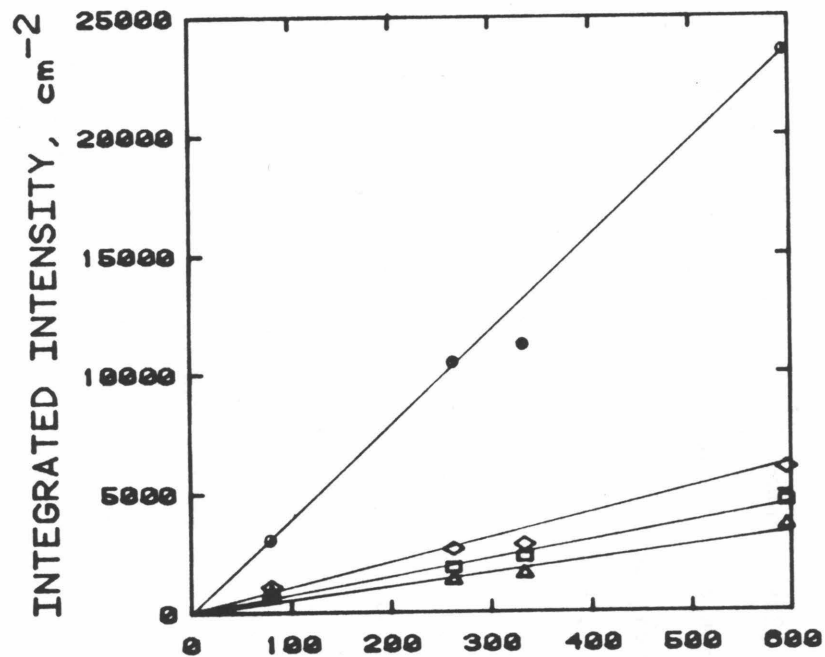
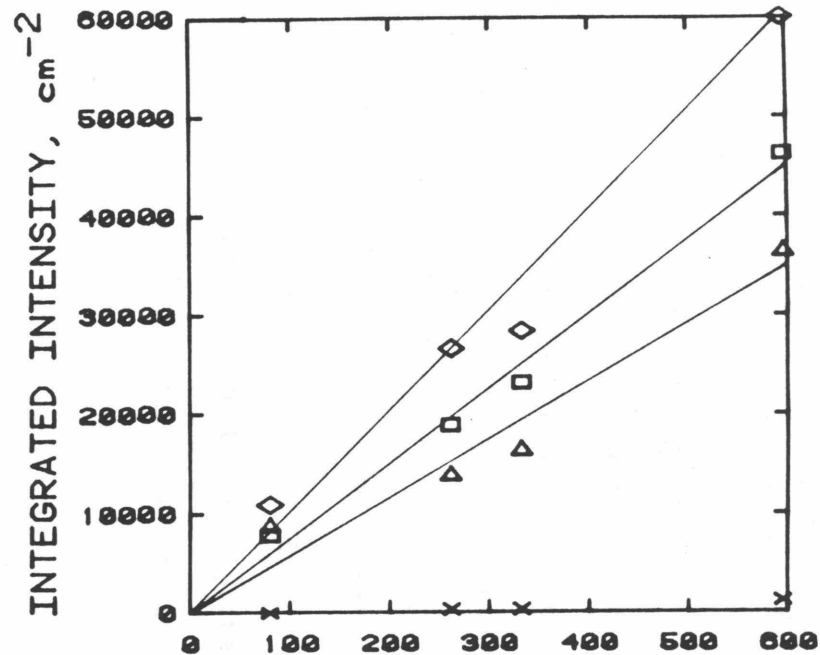


Figure 5.8 Dependence of EPR integrated intensity on dose. Intensities were scaled for 100 mg, 1 mW, 1 G modulation amplitude, and x100 gain. Crosses, sanidine. X, dehydrated and disordered microcline. Diamond, oligoclase. The curve for the sanidine resembles the behavior of the absorption bands with dose. Different samples develop centers at varying rates.



EPR II



EPR II

Figure 5.9 Optical integrated intensity of the absorption bands in smoky sanidine vs EPR integrated intensity of hole center H in sanidine. Symbols are the same as those in Fig. 5.5. Optical I.I. were averaged for the three polarizations, except for the 27200 cm^{-1} peak, which was averaged for α and β alone because this peak is poorly resolved in gamma. Linear correlations exist for all bands.

measurements of this band's parameters are the least reliable.

5.5.c Analysis of radiation centers not directly correlated with color

The EPR spectrum of natural amazonite 13758 (Fig. 5.7 c), andesine, and labradorite (Figs. 3.16 and 5.7 a) and also γ -irradiated orthoclase and oligoclase (Fig. 5.7 d) includes a pattern with six broad (50 Gauss) equal intensity first derivatives. A similar pattern in microcline with narrow line width was attributed to Al-O^- [Matyash et al., 1982]. Both patterns are probably caused by the same center; disorder present in our samples would produce a broader signal. [cf. Gaite and Michoulier, 1970].

Superimposed on the pattern of the H center in both disordered microclines (Figs. 5.7 a and b) is a set of 13 narrow (8.8 G) hyperfine lines of varying intensity which is similar to the Al-O^- -Al center pattern observed in potassium feldspars and albite by [Ioffe and Yanchevskaya, 1968; Marfunin and Bershov, 1970; Speit and Lehmann, 1982]. The two lines observed in excess of the eleven expected may be due to two additional sharp centers similar to those seen in hydrous microcline. Also present in the EPR spectrum of the dehydrated microcline are two pairs of $I = 1/2$ signals ($g_{\text{eff}} = 2.025$, $a = 0.056 \text{ cm}^{-1}$ and $g_{\text{eff}} = 2.031$, $a = 0.065 \text{ cm}^{-1}$) that occur in an intensity ratio of 0.78. The intensity ratio and isotropic hyperfine coupling, a , do not agree with those for any of the $I = 1/2$ isotope pairs [DuVarney and Garrison, 1975; Goodman and Raynor, 1970, Table LVI]. The signals could be due to the radicals H° or PO_3^{2-} in two very different sites, because these traps have a -values of about 0.05 cm^{-1} [Marfunin, 1979, Ch.7], but dehydration at 900°C should have removed such substituents. At present, we have no model for these centers.

Irradiated microcline with structurally bound water yields an EPR

spectrum very different from dry microcline or potassium feldspars with mostly OH (Fig. 5.7 a). Neither the H center, nor the Al-O^- , Al-O^- -Al, or any other aluminum-related center is present. EPR spectra similar to the large first derivative at $g_{\text{eff}} = 1.994$ have been attributed to Ti^{3+} [Marfunin and Bershov, 1970; Speit and Lehmann, 1982]. This signal is similar to an electron trap in sodium-silica or potassium-silica glasses [Stroud et al., 1966], but we do not have enough information either to confirm this assignment or to determine the causes of the other signals.

A single sharp line at g_{eff} of 2.015 with 10 Gauss width is seen in irradiated Broken Hill Orthoclase (Fig. 5.7 c). This center is some type of e^- trap and may be related to the E centers of quartz and glass [e.g. Lell et al, 1966].

5.6 Comparison of Radiation Coloring of Plagioclase to Potassium Feldspar

For the three plagioclases examined, smoky color could only be induced in the sodic feldspars. The $\sim 16000 \text{ cm}^{-1}$ band dominates the visible spectra of the naturally blue oligoclase (Section 6.10), but irradiation did develop the UV tail and bands near 12500 and 9100 cm^{-1} , along with the H and Al-O^- centers (Fig. 5.7 d). The 9100 cm^{-1} band may be due to ferrous iron, but cannot be positively assigned. The andesine spectra are very similar to those of the smoky sanidine, having bands at 12000 , 16600 and 29000 cm^{-1} , plus a strong UV tail (Figure 5.10). EPR spectra were not taken of the irradiated andesine, but natural andesine shows the Al-O^- center (Fig. 3.16).

In non-smoky labradorite, a definite increase in the UV tail occurs upon irradiation (Fig. 5.11). Difference spectra also indicate the presence of a weak 27200 cm^{-1} band with an intensity of 0.1 cm^{-1} , but no other radiation-associated absorption bands were resolvable, and neither was the H center observed in EPR spectra. The different behavior of the labradorite

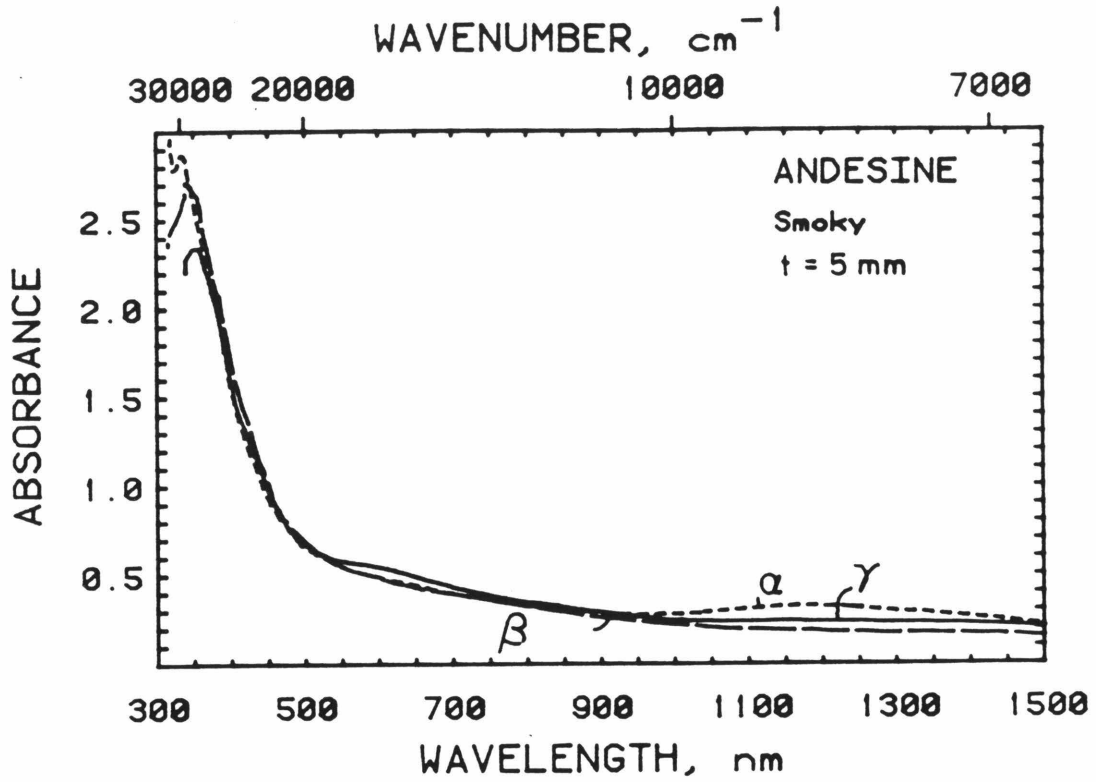


Figure 5.10 Polarization absorption spectra of smoky color in andesine from Halloran Springs, California. Dose, 5.46 MRads. The broad band at 1200 nm is due to ferrous iron in the M-site (Section 3.3.b). Weak bands are present at 650 and about 430 nm. A strong band is seen near 350 nm. The smoky color mostly arises from the intense UV tail.

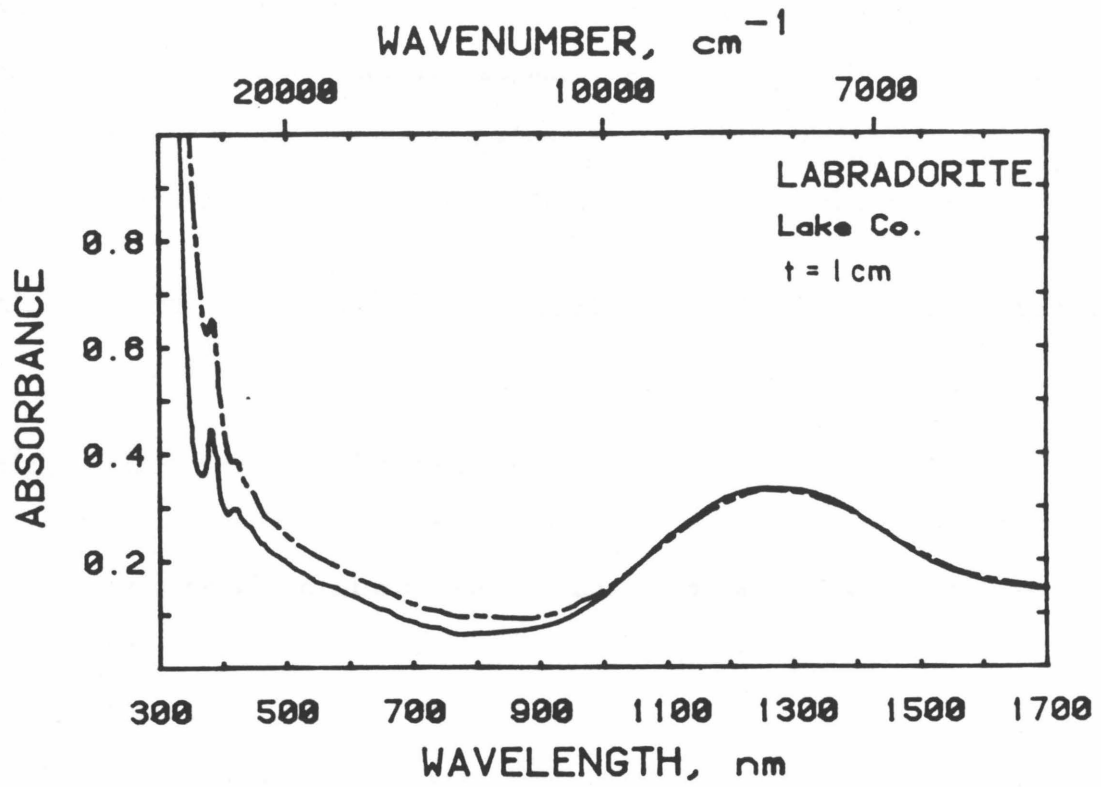


Figure 5.11 Unpolarized optical absorption spectra of natural and irradiated gemmy laboradorite from Lake County, Oregon. Irradiation increases the tail from the ultraviolet, which deepens the yellow color. Sharp bands near 380, 415, and 440 nm are due to Fe^{3+} in tetrahedral sites.

cannot be ascribed to proton speciation, because all have OH (Section 4.3.c). The absence of smoky color in labradorite is likely due to increased incorporation of Al because for glasses, the 16100 and 22000 cm^{-1} bands do not form when Al content exceeds alkali content [Karapetyan et al, 1964].

5.7 Proposal of Models for Smoky Feldspar from Comparisons with Smoky Quartz and Glass

5.7.a Optical and EPR spectroscopy

Table 5.5 summarizes the optical, EPR, and color suppression properties of hydrous species in glass, quartz, and feldspar. The general behavior of glasses was covered in Section 1.2.b.iii. The most pertinent points are restated here.

In alkali-silicate glasses, two overlapping EPR signals occur near $g_{\text{eff}} = 2$. Kordas and Oel [1982] separated the two ESR signals through computer modelling of the signals at different temperatures, correlated H_I with the optical bands at 32700 and 19600 cm^{-1} in alkali silicate glasses, and concluded that the center is a hole on a non-bonding oxygen near a silicon ion with an alkali nearby. The H_{II} center modelled as a hole trapped between two nonbonding oxygens near a silicon [Kordas and Oel, 1982] is probably connected with an absorption at 16100 cm^{-1} because both respond similarly to radiation treatment and variation of alkali content of the glass [Stroud, 1962; Scheurs, 1967].

In α -quartz smoky color develops upon irradiation if aluminum ions are present. Irradiation creates a hole center on an aluminum ion [Griffiths et al, 1954; O'Brien, 1955] by not only displacing an electron to other trapping sites in the crystal but also displacing the compensating cation [e.g. Weil, 1975]. The aluminum-hole center has been correlated with the A_3

band at 23360 cm^{-1} which produces one type of smoky color; another blue-smoky color results from absorption bands A_1 at 14900 cm^{-1} and A_2 at 20530 cm^{-1} [Nassau and Prescott, 1975 and 1977]. Cohen and Makar [1982] have suggested that A_2 is analogous to H_2 (H_I) and A_1 is analogous to H_3 (H_{II}).

For smoky feldspar, four bands are observed at consistently higher wavelengths than in glass or smoky quartz (Table 5.5). We have found that all absorptions in feldspar are connected with the intensity of the H center. The shape of the H center's EPR signal is similar to that reported for the overlapping H_I and H_{II} EPR spectra in glass by Scheurs [1967] and Kordas and Oel [1982]. The width of the H center is broader in proportion to the increase in width for the $Al-O^-$ center from glass to feldspar (Table 5.5), so that the difference can be attributed to structure. Moreover, the shapes and locations of the simple and complex centers in microcline (which together comprise the H center) resemble those of H_{II} and H_I in glass, respectively, especially for the case of the potassium ion (which gives five sharp lines [Kordas and Oel, 1982]). We conclude that the H center in feldspar is equivalent to the sum of the H_I and H_{II} centers in glass and that the simple and complex centers in microcline are the same as H_I ($Si-O^- -K$) and H_{II} (hole shared between two NBO's attached to a Si, with compensators nearby), respectively. In analogy with Kordas and Oel's [1982] results, we suggest that the bands in feldspar near 32700 and 16200 cm^{-1} result from H_{II} (with K^+ or possible Na^+) nearby, and that the 11600 cm^{-1} band is related to H_I .

The $Al-O^-$ or $Al-O^- -Al$ centers were not measurable in sanidine irradiated with 2.82 Mrads, but the $Al-O^-$ center was observed for an orthoclase, strongly colored by an absorption band near 19100 cm^{-1} , which was irradiated with 2.4 or 7 Mrads. For smoky quartz, the 23360 cm^{-1} band is assigned to the $Al-O^- -Al$ center [Nassau and Prescott, 1975; 1977] while

the two lower energy bands are assigned to hole centers similar to H_I or H_{II} [Cohen and Makar, 1982]. This suggests by analogy that the third highest energy in smoky feldspar should be connected with a hole near aluminum. The presence of the $Al-O^-$ center in non-smoky labradorite suggests that this may not be connected with the 19100 cm^{-1} band, but the different chemistry of this feldspar may alter the energy of the absorption. Speit and Lehmann [1982] have suggested that the $Al-O^- -Al$ center was connected with smoky color, specifically the 11600 cm^{-1} band. We propose that the $Al-O^- -Al$ center is connected with the 19100 cm^{-1} band in analogy to smoky quartz and not the closely related $Al-O^-$ center because this trap was observed in feldspars without smoky color. The hole centers H_I , H_{II} , and $Al-O^- -Al$ probably develop at similar rates because formation of the Al center requires displacement of a cation to an interstitial position which would lead to formation of an H_I or H_{II} trap.

The 27200 cm^{-1} band is probably due to a second transition of H_I , as is the case for glass [Kordas and Oel, 1982]. Alternatively, because similar peaks in quartz and glass have been attributed to electron centers [Mackey et al, 1966b; Cohen and Makar, 1982], the 27200 cm^{-1} band may be an electron center (or centers) complementary to the hole centers.

The UV tail is partially ascribed to some type of electron trap, but some of its intensity is derived from O^{2-} to Fe charge transfer [e.g. Faye, 1969].

5.7.b Effect of proton species on radiation response in feldspar, glass, and quartz.

Section 1.2.b.vii discusses how H_2O , OH , and H_2 inhibit radiation coloring of Al and Si related hole centers and various electron traps

in glasses and quartz at room temperature. The results are summarized in Table 5.5. The observations on glass mandate that the irradiation process disassociated H_2 or H_2O within the glass to form the species $SiOH$ [Faile and Roy, 1970; DiSalvo et al, 1977; Hartwig, 1977; Shelby, 1979; Acocella et al, 1982]. For quartz and glass, formation of atomic hydrogen H° by irradiation has also been observed [Van Wieringen and Kats, 1959; Weeks and Abraham, 1964; Perlson and Weil, 1974]. Formation of color centers in these samples at liquid nitrogen temperatures implies that diffusion of hydrogen is a part of the suppression process [Faile and Roy, 1970].

In potassium feldspar, radiation coloring is suppressed if water is structurally present as H_2O . Water in the form of fluid inclusions or OH does not influence coloration. Three bands at 11600, 16200, 19100, and 27200 cm^{-1} and correlated hole centers on silicon or aluminum do not develop unless the structural water is removed by heating. Neither does irradiated wet microcline develop the yellow color which results from intensification of the UV tail. This behavior is similar to that of both glass and smoky quartz except that OH in feldspar was not demonstrated to inhibit irradiation coloring. OH may inhibit coloring because orthoclase which had one tenth the water of sanidine was colored twice as dark by the same dose of gamma rays. Radiation probably moves protons bound as OH in the feldspar, but this would have a very small effect on coloration because OH concentrations are low. Unlike quartz and glass, atomic hydrogen was not observed in the EPR spectra, nor was a change apparent in the IR spectra of the water or OH after irradiation. However, the formation of color centers in hydrous feldspar irradiated at liquid nitrogen temperatures suggests that a similar mechanism occurs in the feldspar; namely, that irradiation frees atomic hydrogen which diffuses to sites similar to those from which they were removed,

destroying centers in their path. I suggest that in feldspar irradiation disassociates water into the radicals H and OH. The hydroxyl radical could mend broken bonds or electron centers by



such that the electron recombines with a freed hole or another trap. H would diffuse and attach itself to a hole trapped on an NBO, forming another SiOH or AlOH bond, and releasing a hole. Similar mechanisms involving SiOH have been proposed for glass and quartz by Faile and Roy [1970] and DiSalvo et al [1972] as discussed in Section 1.2.b.vii.

CHAPTER 6

AMAZONITE: IRRADIATIVE COLORING OF STRUCTURALLY
HYDROUS, Pb-BEARING FELDSPAR

Most of this chapter will focus on the blue to green variety of potassium feldspar known as amazonite. The final section will describe the characteristics of blue plagioclase, comparing them to those of "amazonite".

6.1 Geologic Occurrence

This section summarizes observations made on two amazonite-bearing pegmatites. One is located in a saddle in granitic rocks east of Lone Pine Station, California, at $117^{\circ}58.8'$, $36^{\circ}37.8'$. The granitic rocks are labeled Mesozoic on the Death Valley Sheet (compiled by C.W. Jennings [1958]). The other pegmatite is in the New York Mountains, California, 3/4 mile south of Giant Ledge Mine ($115^{\circ}7.5'$, $35^{\circ}14.5'$). The pegmatite intrudes carbonate rocks, but is probably associated with the Cretaceous Teutonia Quartz Monzonite [Haskell, 1959].

The Lone Pine amazonite pegmatite consists of stringers and pods a few centimeters to upwards of 40 cm long, which are distinctly zoned. An aplitic border separates the coarser grained quartz, feldspar, and biotite from the host granitic rocks. The coarse grained quartz is smoky. The amazonite is often, but not always, next to smoky quartz. The blue feldspars are usually the coarsest grains, but finer grained amazonite occurs bordering the aplite. All colors are the same value (7.5 blue-green on the Munsell chart) but vary in intensity from nearly white to bright. The color boundary is sharp near the aplite edge of the pegmatite pockets, but within the pocket, the zonation of color is irregular. Single crystals may have a mottled appearance in blue and white coloration.

The New York Mountains pegmatite is tabular in shape (1.2 m by 5 m) and vertically layered. The present level of exposure is frozen in with

quartz, but a small pocket was found near the surface [Robert Reynolds, pers. comm.] The specimens excavated from this pocket are on display at the San Bernardino County Museum near Riverside, California. From north to south, the layers across the dike are aplite (30 cm), coarse-grained amazonite (15 cm), fine-grained, white potassium feldspar with mica and quartz (45 cm), and aplite (45 cm). Quartz from this pegmatite is a milky grey and does not darken after 10 MRads of γ -irradiation. The blue-green color is mostly contained in the coarsest grained zone, but three or four stringers of amazonite occur in the fine-grained zone parallel to the other layers. These stringers have crystals slightly larger than the white potassium feldspar, are about 1 cm wide, and are sporadically located within the fine grained zone.

The color of the amazonite in the New York Mountains pegmatite is remarkably consistent in value (medium blue-green, 2.5 BG on the Munsell chart) and ranges only slightly in intensity. Boundaries between the blue-green and white potassium feldspar are sharp ($\ll 1$ mm). Occasionally a zone of light blue feldspar of about 5 mm thickness is seen between the white and deeper blue-green. In this case, the boundary between the white and the blue is sharp, but the color grades over about 1 mm between the pale blue to deep blue-green. This type of zonation may occur within a single crystal.

Formation of amazonite requires a pegmatitic environment enriched in lead and other elements (see Section 1.2.d). The process forming the color must be relatively constant over the duration of crystallization because the value of the color within both the Lone Pine Station and New York Mountains amazonite pegmatites is nearly constant. Yet some variability exists because a range of intensities of the blue amazonite color can be seen at Lone Pine Station, and because the colors differ for the two pegmatities. The

restriction of color to the coarsest potassium feldspars suggests that the proper trace element chemistry resulting in formation of amazonite develops in the latest stages of crystallization.

6.2 Chemistry of Amazonites Studied

Tables 6.1 to 6.3 give descriptions and chemical analyses for all amazonites studied. Most of the samples were provided by E. E. Foord (USGS, Denver) and comprise part of the amazonites he has studied. As discussed in Section 1.2.a.iv, Dr. Foord's chemical analyses indicate that lead is involved in the coloration, such that higher lead contents give more intense colors and a truer green color. As indicated in Tables 6.1 to 6.3, Foord's suite of amazonites embraces the known range of color and lead contents, and includes the exceptions to his chemical trends (#14, 15, 18, 22, 9, 20, 26).

Samples provided by others were analyzed using the microprobe which quantitatively analyzed PbO contents as low as 0.05 wt%. I also analyzed samples from Dr. Foord's suite which either had high lead contents or were samples I had used in several spectroscopic measurements as representatives of the various amazonite colors (#12, 9, 6, 22). Lead content for the plagioclase were determined by XRF because they were too low to detect with the microprobe. Lead and iron contents for low lead potassium feldspars (Table 6.1 and 6.2) are emission spectroscopic analysis from Foord, Martin, Conklin, and Simmons [in prep.].

The samples studied are both typical and atypical of amazonite colors and chemistries. It was hoped that spectroscopically characterizing a wide range of samples would help to reveal the origin of the color.

The synthetic feldspar $\text{PbAl}_2\text{Si}_2\text{O}_8$ was made by grinding and mixing the appropriate proportions of oxides together, and then heating the

Table 6.1 Description and Chemistry of Blue Microcline

Sample #	1" 13757	7	8 (78-3)	14	15	16	23	4 DMNH-10934*	5	12
Locality	Elizabeth R Mine, CA	Elizabeth R Mine, CA	Wigwam Creek, CO	Hawthorne, Nevada	New York Mts, CA	Lansverk Norway	India	Wigwam Creek, CO	Lake George, CO	Lake George, CO
Description	Perthite, Gemmy impart	Perthite Turbid	Perthite Turbid, mottled	Perthite Turbid	Turbid Perthite	Perthite Turbid	Coarse Perthite, Zoned	Perthite Zoned	Perthite w/whitecap	Perthite Turbid
Color Munsell#	White NR9.25	White NR9.0	Pale blue 7.5BG9/2	Brn blue 2.5B8/4	Dingy grey 5Y9/2	Blue 7.5BG7/8	Blue 7.5BG7/6	Blue 7.5BG7/7	Dk Blue 7.5BG6/8	Blue 7/5BG7/8
Provided by	G. Brown Stanford	E.E.Foord USGS	E.E.Foord USGS	E.E.Foord USGS	E.E.Foord USGS	E.E.Foord USGS	S. Ghose U of Wash	E.E.Foord USGS	E.E.Foord USGS	E.E.Foord USGS
Microprobe										
SiO ₂	65.73						62.53			65.62
TiO ₂	0.09						ND			trace
Al ₂ O ₃	18.46						18.00			18.32
FeO _{total}	BLD						BLD			trace
MgO	BLD						BLD			BLD
BaO	BLD						BLD			0.04
CaO	BLD						0.01			
Na ₂ O	0.69						0.58			0.48
K ₂ O	15.02						14.85			16.35
PbO	ND						0.05			ND
Total	100.5						96.01			100.8
Or	95.7						94.3			95.7
Ab	4.3						5.6			4.3
An	0						0.1			0
XRF: Fe	0.004						ND			0.041
PbO	-						ND			-
Emission Spectroscopy†										
Fe	-	<0.001	0.01	0.015	0.030	0.015	-	0.030	0.030	0.02
Pb	-	0.005	0.015*	0.020	0.030	0.030	-	0.045*	0.050	0.070
Methods‡	IR, TL EPR	VIS, IR TL, RR	VIS, IR TL	VIS, IR TL	VIS, IR	VIS, IR TL	VIS, IR TL	VIS, IR TL, RR	VIS, IR TL	VIS, IR, TL RR, EPR, Scnt

All analyses are in weight%, except that Or, Ab, An are in mole %.

*Emission spectroscopic analysis is from [Foord and Martin, 1979]

†All emission spectroscopy data, except for samples with* are from [Foord, Martin, Conklin, and Simmons, in prep]

‡IR = infrared. VIS = visible. TL = thermoluminescence. EPR = electron paramagnetic resonance. RR = resonance Raman.

Scnt = scintillator measurement of natural radiocativity.

Table 6.2 Description and Chemistry of Blue-green and Green Microcline

Sample #	18	22	24	9 78-16*	19' 13758	21	20	6	32	26
Locality	Joseph Bukuru Paddock, Nigeria	Amelia, VA	Amelia, VA	Crystal Peak, CO	New York Mts, CA	Keivy Peg. Kola Pen. USSR	Monapo Mozambique	Keivy Peg., Kola Penn. USSR	Pearl, Routt Co., CO	Genessee Mnt, CO
Description	Very turbid microperthite	Perthite	Perthite Turbid	Perthite Turbid	Turbid Perthite	Has coarse wht albite blebs	Turbid perthite	Has coarse wht albite blebs	Coarse Perthite	Turbid w/grey inclusions
Color Munsell#	Grey/grn 10G7/4	Green 10G7/8	White N9.5	Grn blue 5BG6/8	Blue grn 2.5BG7/6	Dr.B-grn 2.5BG5/6	medgrn 7.5BG8/6	malachite grn 7.5G6/8	Green 5G9/2	grey/gr 5G9/2
Provided by	E.E.Foord USGS	E.E.Foord USGS	E.E.Foord USGS	E.E.Foord USGS	R.Reynolds San Berdo Co. Museum	S.Rigden R.Cubba Caltech	E.E.Foord USGS	E.E.Foord USGS	E.E.Foord USGS	E.E.Foord USGS
Microprobe										
SiO ₂		64.00	63.12	63.02	64.03	62.83		63.52	64.37	62.09
TiO ₂		ND	ND	ND	ND	ND		ND	ND	ND
Al ₂ O ₃		17.85	17.73	17.82	17.90	18.15		18.20	18.53	18.47
FeO _{total}		BLD	BLD	0.05	0.01	0.03		BLD	BLD	B
MgO		BLD	BLD	BLD	BLD	BLD		BLD	BLD	BLD
BaO		BLD	BLD	0.03	BLD	Trace		0.05	0.44	0.42
CaO		BLD	BLD	0.02	BLD	BLD		BLD	Trace	BLD
Na ₂ O		0.56	0.43	0.70	0.97	0.47		0.50	0.65	0.62
K ₂ O		15.50	13.30	15.65	14.62	15.29		15.46	15.53	15.07
PbO		0.085	0.12	0.20	0.19	0.20		0.83	0.81	1.10
Total		98.0	94.70	97.5	98.0	96.7		98.6	100.3	97.8
Or		94.8	95.2	93.7	90.7	95.5		95.3	94.2	93.8
Ab		5.2	4.8	6.3	9.3	4.5		4.6	6.2	5.7
An		0	0	0	0	0		0.1	0.1	0.01
XRF: Fe		ND	ND		0.013	0.026				0.041
PbO		ND	ND							
Emission Spectroscopy†										
Fe	0.15	0.07	0.03				0.015	0.03	0.07	0.015
Pb	0.07	0.10*	0.10*	0.12*			0.30	1.0*	0.7	0.7
Methods‡	VIS, IR, TL	VIS, IR TL	VIS, IR TL	VIS, IR TL, EPR	VIS, IR RR, EPR	VIS, IR, TL RR, EPR, Scnt	VIS, IR TL	VIS, IR TL, RR		VIS, IR

All analyses are in weight%, except that Or, Ab, An are in mole %.

*Emission spectroscopic analysis is from [Foord and Martin, 1979]

†All emission spectroscopy data, except for samples with* are from [Foord, Martin, Conklin, and Simmons, in prep]

‡IR = infrared. VIS = visible. TL = thermoluminescence. EPR = electron paramagnetic resonance. RR = resonance Raman.

Scnt = scintillator measurement of natural radiocativity.

Table 6.3 Description and Chemistry of Green Orthoclase, Bluish Plagioclase and Synthetics

Sample #	3	3'	3" 13756	28	29 H-81228	30	31	PbAl ₂ Si ₂ O ₈
Locality	Broken Hill Australia	Broken Hill Australia	Broken Hill Australia	Broken Hill Australia	South Carolina	Africa	Mozambique	Synthetic
Description	Grey inclusions	Transparent	Transparent w/fluid inclusions	Transparent	Gemmy Oligoclase	Gemmy Albite	Gemmy Albite	Cloudy, some glass
Color Munsell#	Grey-grn 2.5G7/2	Med green 2.5G7/6	Green 2.5G6/8	Grey-grn 2.5G7/2	Pale blue 7.5BG9/2	Pale blue 7.5BG9/2	Pale blue 7.5BG9/2	Creamy 2.5GY9/2
Provided by	E.E.Foord USGS		S.Ghose & A. Irving U of Wash	S.Booth Zinc Corp.	C.Francis Harvard U		W.Larson Pala Intl.	A.Hofmeister Caltech
<u>Microprobe</u>								
SiO ₂	63.00	62.59	61.70		62.0	67.22		
TiO ₂	ND	ND	ND		ND	BLD		
Al ₂ O ₃	18.56	18.52	17.63		22.76	20.69		
FeO _{total}	trace	BLD	BLD		0.04	BLD		
MgO	BLD	BLD	BLD		BLD	BLD		
BaO	0.04	0.07	0.16		BLD	0.11		
CaO	trace	BLD	0.05		3.82	1.40		
Na ₂ O	0.59	0.91	0.79		10.51	11.03		
K ₂ O	14.94	14.71	14.45		0.31	0.20		
PbO	1.79	1.60	1.80		trace	ND		
Total	98.95	98.54	96.50		99.65	100.68		
Or	94.2	91.3	92.1		1.6	1.1		
Ab	5.7	8.7	7.6		82.0	92.4		
An	0.1	0	0.3		16.4	6.5		
XRF: Fe	-	-	0.009		0.05	0.026		0.028
PbO	-	-	-		0.035	0.018		-
SrO	-	-	-		0.04	BLD		-
<u>Emission Spectroscopy†</u>								
Fe	0.05							
Pb	2.0							
Methods‡	VIS, IR TL	VIS, IR TL, EPR	VIS, IR TL, RR, EPR	EPR	VIS, IR EPR	VIS	VIS	RR, IR X-ray

All analyses are in weight%, except that Or, Ab, An are in mole %.

*Emission spectroscopic analysis is from [Foord and Martin, 1979]

†All emission spectroscopy data, except for samples with* are from [Foord, Martin, Conklin, and Simmons, in prep]

‡IR = infrared. VIS = visible. TL = thermoluminescence. EPR = electron paramagnetic resonance. RR = resonance Raman.

Scnt = scintillator measurement of natural radioactivity.

mixture in a covered platinum crucible at 900°C for two days. The result was a mixture of glass and small crystals (<0.5 mm) which were optically anisotropic. X-ray powder data for the synthetic is similar to that of lead feldspars synthesized previously [Sorrel, 1962; Scheel, 1971] and also resembles that of sanidine (Table 6.4) which shows that the synthetic used in this work is also a feldspar.

6.3 Visible Spectroscopy of Amazonite

6.3.a Variation of color in natural samples

Amazonite color is intrinsic because it originates in the gemmy areas of the crystal. The turbid regions scatter light, giving the specimen an overall color and an opaque or translucent appearance. Except for the orthoclase from Broken Hill and an intermediate microcline from Genessee Mountain, Colorado, all amazonites examined were perthitic, with colored microcline lamellae and white albite lamellae. The color of a single sample is almost always constant in hue, but variable in intensity, giving a mottled appearance.

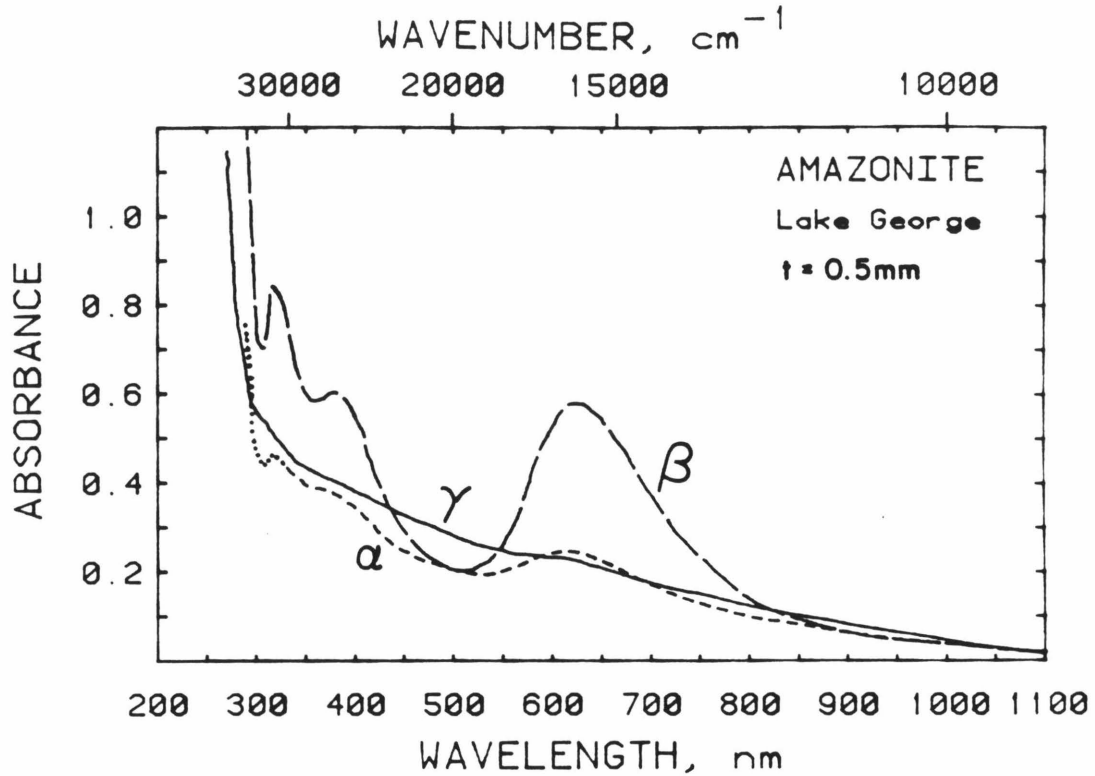
Most amazonites are greenish-blue (7.5 BG on the Munsell chart), but the color to the eye encompasses all values between this and green with a slight amount of yellow (2.5 G), (see Tables 6.1 to 6.3). The intensity varies strongly, and some samples have, in addition to the blue-to-green color, a greyish cast. It is notable that the two extremes of color are connected with two polymorphs of potassium feldspar: samples with the bluest colors are microcline while all yellowish green samples are orthoclase.

The remainder of this section discusses the optical spectroscopy of 21 amazonites, presenting results on the "typical" blue color, as well as the more exotic green colors. Figures 6.1 to 6.5 show representative

Table 6.4 X-ray Powder Data for Lead Feldspars

PbAl ₂ Si ₂ O ₈ (this work)		PbAl ₂ Si ₂ O ₈ (Scheel, 1970)		PbAl ₂ Si ₂ O ₈ * (Sorrel, 1962)		Sanidine (Scheel, 1970)	
d,nm	I/I ₀	d,nm	I/I ₀	d,nm	I/I ₀	d,nm	I/I ₀
.651	51	.658 } .653 }	100	.662	79	.665	6
.604	22			.598	40		
.581	35	.581	32				
		.460	20			.423	52
.396	33	.395	15	.397	14	.395	10
		.381	35	.383	40	.387	6
				.380	35	.378	52
.360	37	.361	20	.363	26	.362	11
				.352	35	.355	12
.346	72	.345	72	.348	95	.346	31
		.326 } .324 }	50	.331	100	.333	100
.328	100			.326	56	.328	60
.324	54			.302	40	.323	52
.300	38	.300	25	.293	19	.300	31
.292	31	.292	8	.278	38	.277	14
.276	48	.277	35			.261	17
.257	91	.257	60	.257	74	.258	35

* This has some potassium impurities



+

Figure 6.1 Polarized absorption spectra of naturally blue type B amazonite #5 from Lake George, Colorado. The three broad bands at 630, 385, and 330 nm are connected with amazonite color. The finely spaced dots indicate where the alpha spectrum was estimated from a spectrum of the same chip after irradiation. The slow rise towards the ultraviolet is due to scattering from turbid regions, and from the perthite lamellae. The steep rise is probably due to both oxygen-metal charge transfer bands, and to Pb^{2+} absorptions near 255 nm.

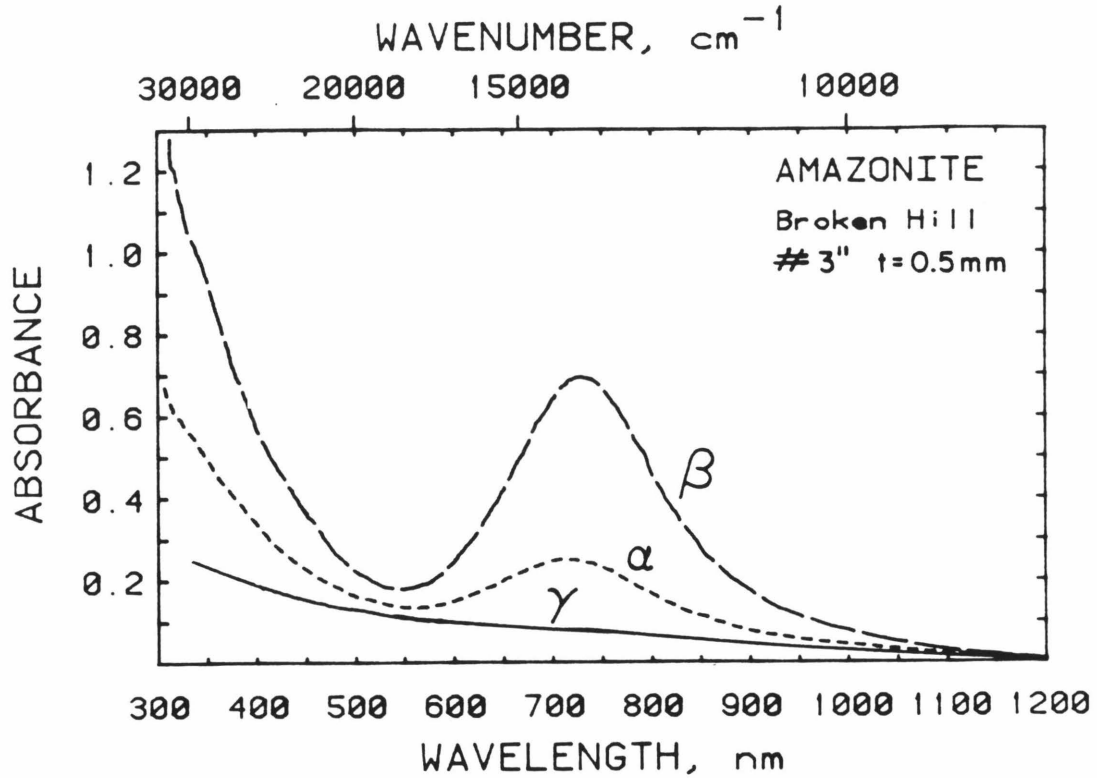


Figure 6.2 Polarized absorption spectra of naturally green, type G amazonite #3" from Broken Hill, Australia. The broad band at 720 nm is connected with the color. This sample is close to gem quality so that very little scattering contributes to the spectra. A band may be weakly present near 360 nm. The UV tail is markedly polarized in the same scheme as the amazonite peak at 720 nm.

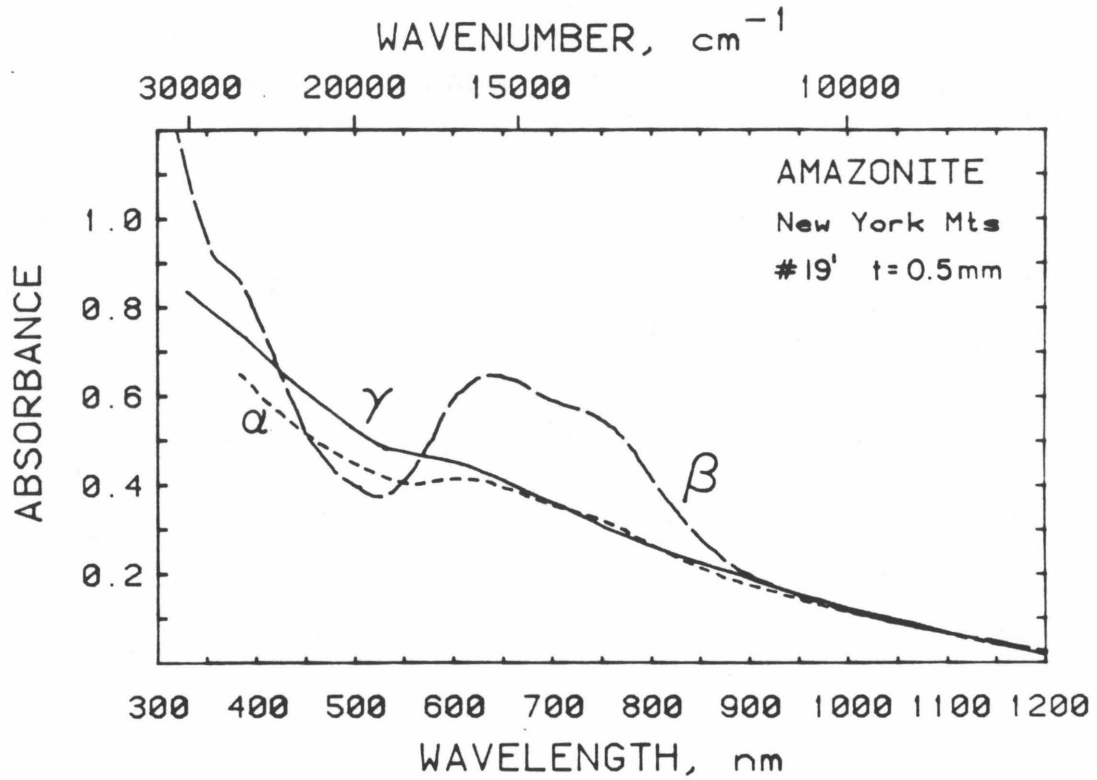


Figure 6.3 Polarized absorption spectra of natural, medium green, amazonite #19' from New York Mountains, California. This type D sample shows that both the 720 and 630 nm peaks are present. Strong scattering in this turbid sample prevented resolution of the higher energy peaks.

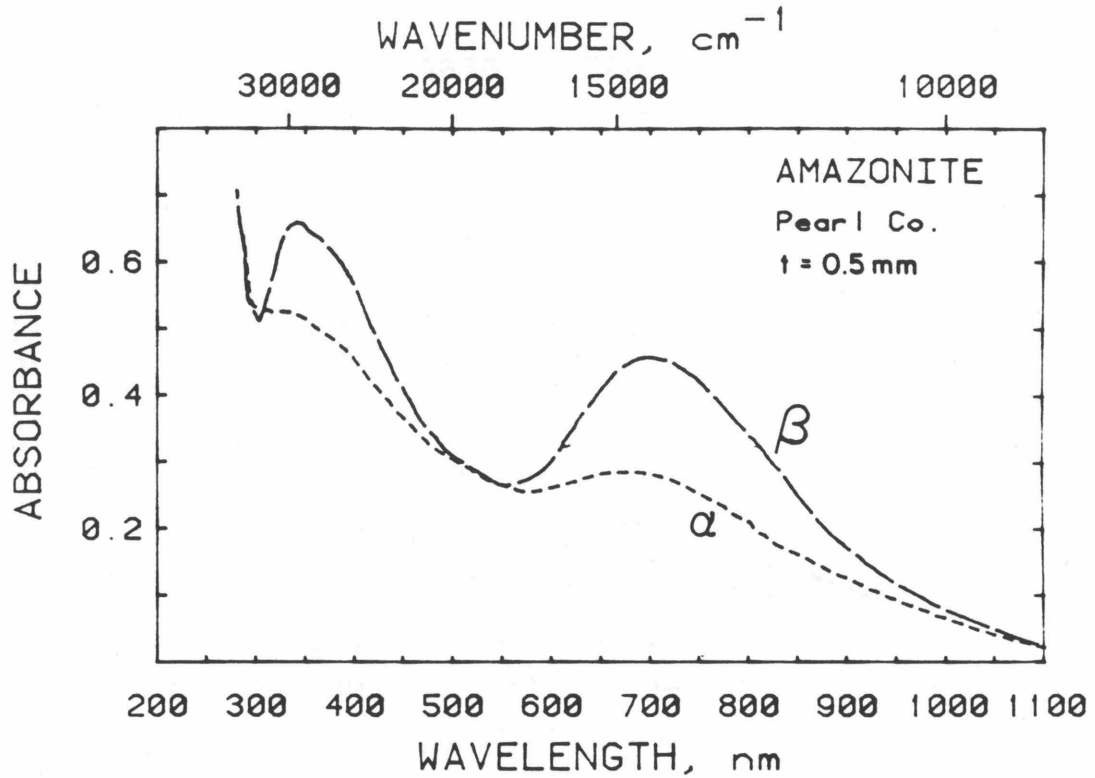


Figure 6.4 Polarized absorption spectra of natural, medium green amazonite #32 from Routt County, Colorado. The relative intensity of the 630 and 720 nm bands is such that superposition gives one apparent very broad band. This sample has much less scattering than the other two type "D" amazonites so that its high energy bands appear very intense.

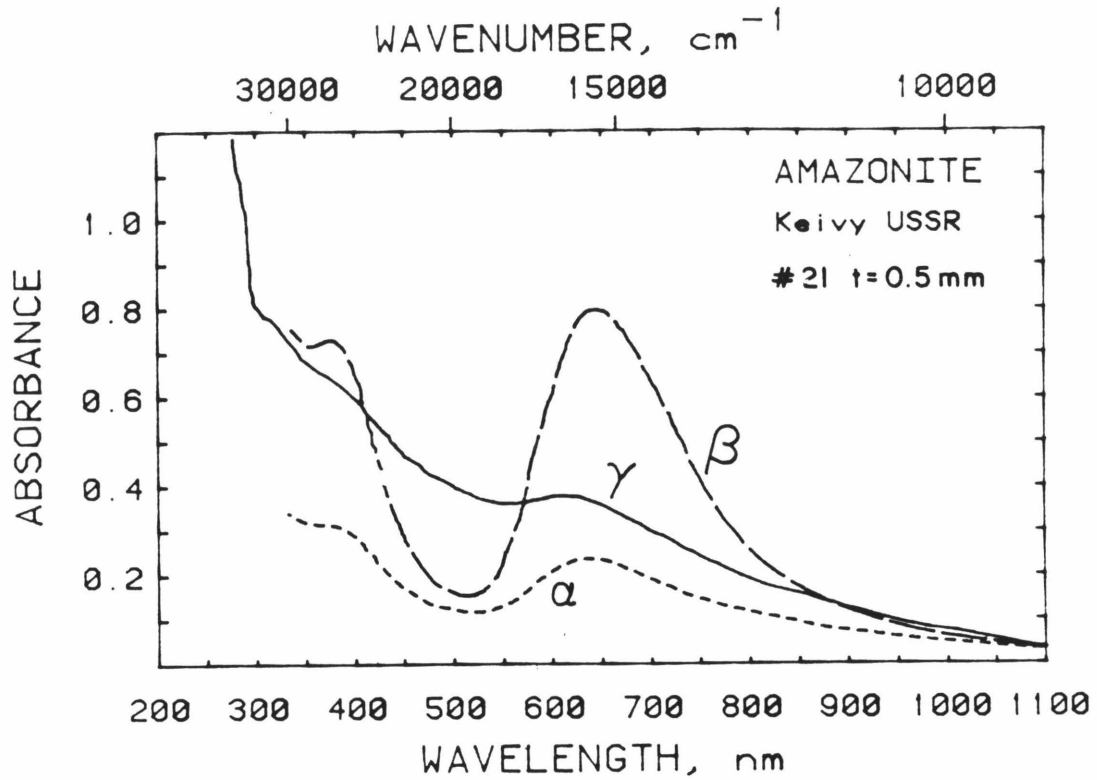


Figure 6.5 Polarized absorption spectra of natural blue-green type T amazonite #21 from Keivy pegmatites, USSR. The most intense absorption for the type T color is shifted to 643 nm and is broader than the singlet of the blue amazonites. Broad bands are also present at 385 nm (shown here) and revealed at 330 nm by irradiation.

samples of the various types of spectra seen. The optical spectra of amazonites have the following features in common. Amazonite peaks are strongly polarized in the beta direction (perpendicular to the (001) face), weakly present in alpha, with little to no intensity in the gamma direction (nearly perpendicular to the (010) face). The component of the peaks in the gamma direction is due to scattering because it is lowest for the least turbid microclines and zero for the gemmy orthoclases; therefore, the gamma component will be ignored in analysis of the spectra. No features were seen in the near infrared beyond about 1000 nm. All amazonites have one or two overlapping broad bands of 3000 to 4500 cm^{-1} width which are slightly asymmetric and centered at 625 to 720 nm. All amazonites have a strong tail from the ultraviolet that is most intense in β and least intense in γ and thus similar to the visible absorption bands. Samples with a band at 625-650 nm have two additional absorptions at 385 and 330 nm. The combination of these absorption features leaves a transmission minimum in the blue to green region which gives amazonite its range of colors. The features seen in the absorption spectra are probably equivalent to the broad bands noted previously in reflection spectra of amazonite by Rudenko and Vokhmentsev [1969].

Examination of absorption spectra of amazonites from 14 different localities around the world has revealed that there are only a few distinct color types. Figure 6.1 shows the optical spectra of a perthite that is an end-member blue (type B), defined as possessing three broad polarized absorptions at 625, 385, and 330 nm along with a UV tail. The transmission minima occurring near 500 nm produces a somewhat greenish blue color. Figure 6.2 shows the optical spectra of an orthoclase which is an end-member green (type G) having one band at 720 nm plus a UV tail. The transmission minima at 540 nm results in a true green color. A weak absorption band or bands are

present near 320-350 nm in this and other type G samples (#26). The 720 nm peak appears broader than the 630 nm peak, but conversion of wavelength to energy units shows that the 720 nm peak is slightly narrower.

With one exception, the variation in amazonite color is produced by superposition of these two end-member types. Figures 6.3 and 6.4 show optical spectra of three microclines having doublets (type D). For the low intensity sample, the two peaks are clearly resolvable, but for the higher intensity samples the sum of the two bands gives one very broad ($\sim 4500 \text{ cm}^{-1}$) apparent peak. Spectroscopy at liquid nitrogen temperature (Section 6.3.c) resolves the two bands for these samples, or irradiation can change the relative intensity of the two peaks, to reveal a doublet structure (Section 6.3.b). In the type D amazonites, the variation in relative intensity of the 720 and 630 nm peaks produces a gradual shift in the transmission window, and thus results in the continuous variation of hue between the two end-member types.

Figure 6.5 shows the one exception. The turquoise color (type T) is produced by a shift in the largest peak to 643 nm. This peak is broader than the 630 nm peak but is not as broad as the doublet, nor can it be resolved into a doublet either by irradiation or at low temperatures. Yet, the spectra are very similar to that of the blue amazonites, having both the 385 and 330 nm bands. This type T sample could possibly be a doublet with mostly the B band, such that the G band is too weak for resolution by the above methods.

Table 6.5 presents complete analyses of these representative samples plus a few others. The position, width, and intensity were measured directly from spectral data after estimating the baseline by hand. Integrated intensity was estimated by multiplying the full width at half height $W_{1/2}$

Table 6.5 Optical Parameters of Natural Amazonites (1cm Thickness)

Type	Sample	Visible Peak				UV-Vis Peak				UV Peak			
		ν cm ⁻¹	$W_{1/2}$ cm ⁻¹	I cm ⁻¹	II cm ⁻²	ν cm ⁻¹	$W_{1/2}$ cm ⁻²	I cm ⁻¹	II cm ⁻²	ν cm ⁻¹	$W_{1/2}$ cm ⁻¹	I cm ⁻¹	II cm ⁻²
Bl singlet	8 β	16000	>2500	1.13	>2825	26200	3000	0.6	1800			ND†	
	α	"		~ 0		"		~ 0				ND	
"	5 β	16050	3350	8.4	28140	25780	3500	5.5	19250	30770	2700	6.1	16470
	α	16000	"	1.7	5700	"	"	1.1	3850			ND	
"	12 β	16000	3350	10.1	33840	26000	3500	6.6	23100			ND	
	α	"	"	2.2	7370	"	"	1.3	4550			ND	
"	9 β	16000	3450	8.72	30080	25800	3150	5.9	18585	30860	2850	5.9	16815
	α	"	"	1.15	3970	"	"	1.15	3625			ND	
Blue grn Singlet	21 β	15530	3760	13.16	49480	25700	4000	8.16	32600	30824		ND*	
	α	"	"	2.7	10260	"	"	1.32	5300			ND*	
Doublet	23 β	15700	3760	3.50	13160	26000	3350	2	6700	3000	?	2	6000
	α	15880	3400	0.71	2430	"	"	0.4	1340			ND	
"	22 β	14840	4380	4.40	19270	25700	3900	3.52	13730	31100	3000	3.96	11900
	α	"	"	1.10	4820	"	"	0.50	2000	"	"	0.50	1500
"	19 β	14840	4500	6.84	30800	26000	3350	4.21	14100			ND	
	α	"	"	1.68	7600	"	"	weak				ND	
"	6 β	14840	4230	12.1	51180	26000	3700	9	33300			ND	
	α	"	"	2.2	9300	"	"	1.6	5900			ND	
"	32 β	14180	4090	5.26	21510	25600	3800	4.21	16000	29000	3050	4.56	13900
	α	"	3800	1.75	6660	"	"	1.75	6650	"	"	1.75	5350
Grn singlet	26 β	13710	3100	4.20	13020	28500?		v wk†		31300?		v wk	
	α	"	"	0.95	2950			ND				ND	
"	3" β	13700	3000	11.10	33300			?		29400?		v wk	
	α	"	"	2.94	8820			?		"		"	

* This band is weakly present in gamma, and strongly present in an irradiated sample in beta and moderately in alpha
† Very weak
‡ Not determined

by the intensity. Peak fitting by computer was attempted, but the baseline (which is a combination of a UV tail and scattering) could not be adequately modelled by either a scattering curve (absorbance = C/λ^5) or by absorbance = $C_1 \exp(C_2/\lambda)$ [Urbach, 1953; Davydov, 1968], so that computer fitting did not give accurate areas for the peaks. Use of direct measurements does not allow resolution of the two peaks for the doublet types, so that average intensity and total areas are listed in Table 6.5. Also, the parameters of the two higher energy peaks are less accurately measured because the baseline is less well defined in the low wavelength region due to scattering.

The data in Table 6.5 show that the energy and the width of the 625 nm band are consistent among type B samples, 16050 cm^{-1} and 3400 cm^{-1} , $\pm 50 \text{ cm}^{-1}$ respectively. The 385 nm band is less well resolved, giving a wider spread in energy and width ($25850 \pm 150 \text{ cm}^{-1}$ and $3350 \pm 150 \text{ cm}^{-1}$, respectively). Its properties were the same for both type B and type D, but the width of this peak may be slightly larger for the type T amazonite. The 330 nm peak was measurable only in a few of the less turbid samples, but its energy and width (30900 and $2900 \pm 200 \text{ cm}^{-1}$) were less well constrained. The two type G samples show very weak absorptions in the UV which may be due to a minor contribution from the two peaks of the blue type, but could equally well be the equivalent of the middle energy peak for the type G, with the highest energy absorption occurring further out in the ultraviolet.

Figure 6.6 shows that the integrated intensity in the alpha polarization is linearly correlated with that in the beta polarization for each of the 625 to 720 nm peaks and the 385 nm peak. (There were insufficient data on the 330 peak to establish this correlation.) Slight deviations are probably due to scattering. The largest deviations occur for the doublet types, whose integrated intensity was less accurately determined.

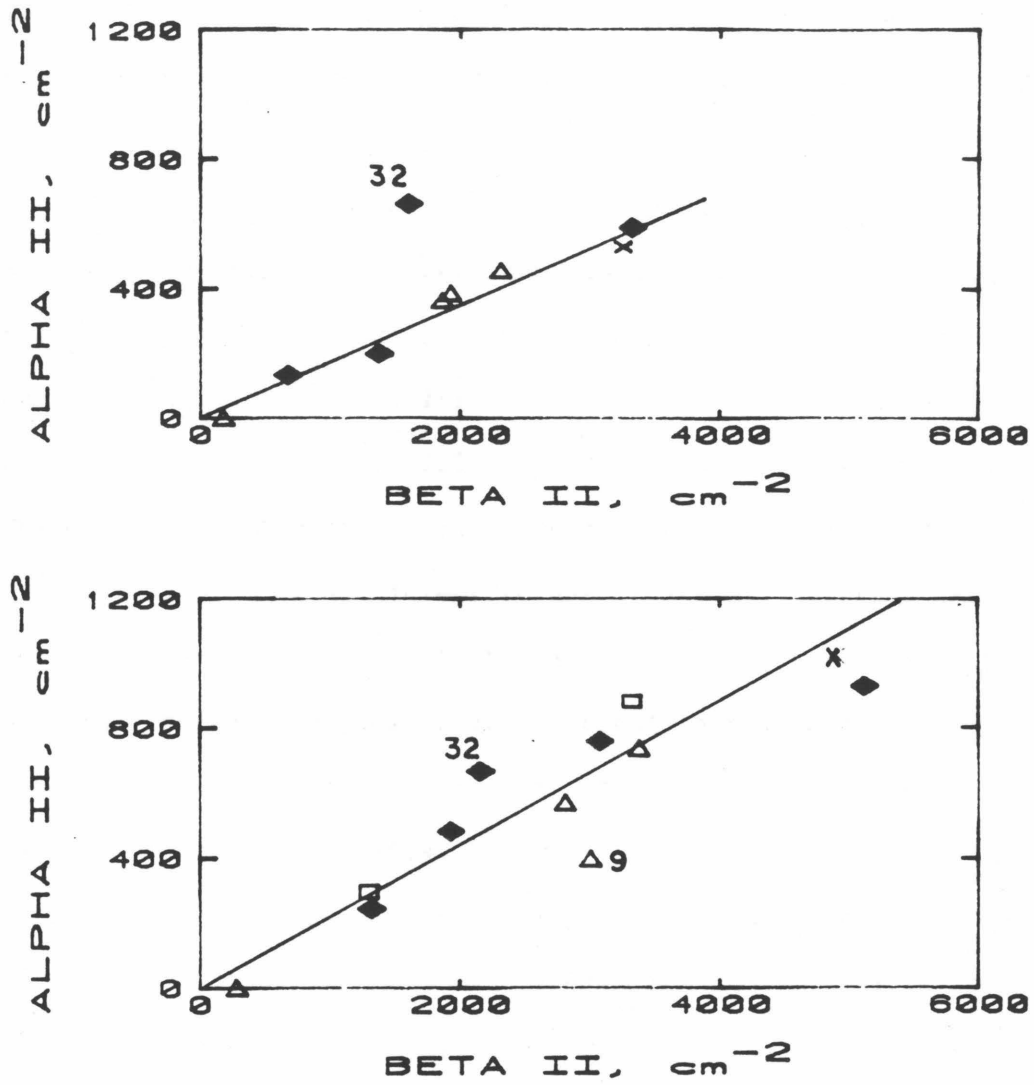


Figure 6.6 Comparison of integrated intensities (II) between the alpha and beta polarizations of amazonites. Triangle = type B. Diamond = type D. Square = type G. X = type T. The upper graph is of the 385 nm peak, while the lower is for the sum of 630 and 720 nm peaks. A few "exceptions" to the trends are labeled with their sample numbers.

The correlation shows that one polarization is needed for computation of amazonite color parameters, so that further discussions and comparisons will rely on the beta polarization exclusively.

Figure 6.7 shows that the integrated intensities for both the 385 and 330 nm peaks are linearly dependent on that of band(s) at 625-720 nm for the type B samples and almost all of the doublets. The one exception is a doublet having subequal intensity for the 625 and 720 nm peaks, which substantiates that the 625, but not the 720 nm band is connected with the UV absorptions. The correlations of Figure 6.7 show that using the parameters of the peak(s) at 625 to 720 nm is sufficient to quantitatively describe amazonite color. For comparison of samples of the blue type or of the green type, intensity suffices, because the peak width is consistent within each type. However, comparison of the doublet types or intercomparison of the four types requires use of integrated intensity.

Table 6.6 summarizes the optical properties of the 630-720 nm absorption of all amazonites examined, and categorizes the samples in terms of the different spectral types (B, G, D, T).

6.3.b Effect of radiation on amazonite color

As indicated by the data in Table 6.6, amazonite color can increase, decrease, or remain the same. This means that the chromophore is not in equilibrium, so that color should not be compared to the chemistry unless the sample is irradiated close to saturation. Of the 16 samples tested, 7 increased and 9 decreased. The changes did not follow any one color type, except that the one type T sample decreased. Changes were both major and minor in both directions. One obvious effect was to change the relative intensity of the two peaks in the doublet. Figure 6.8 shows that the peak at 720 nm grew faster than the one at 625 nm during irradiation of amazonite

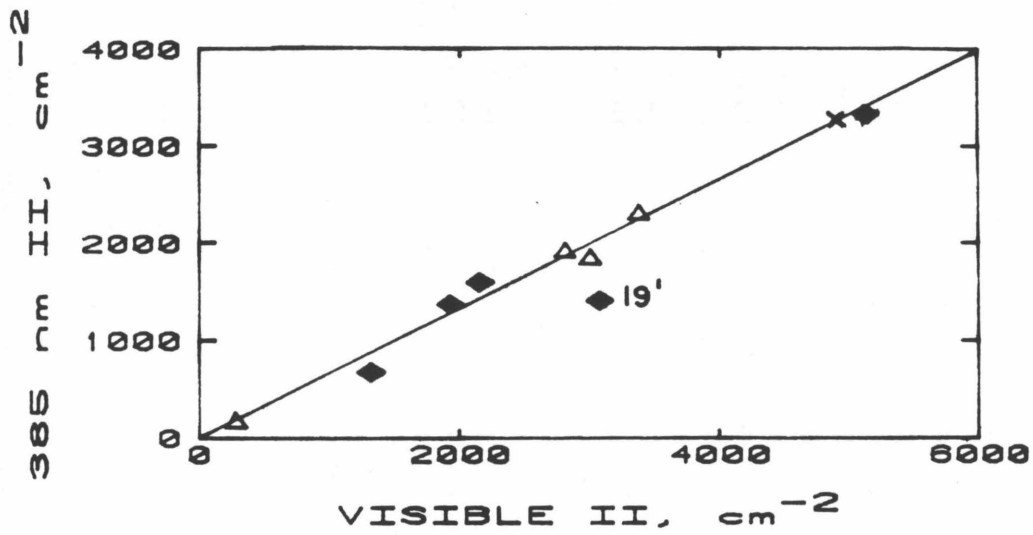
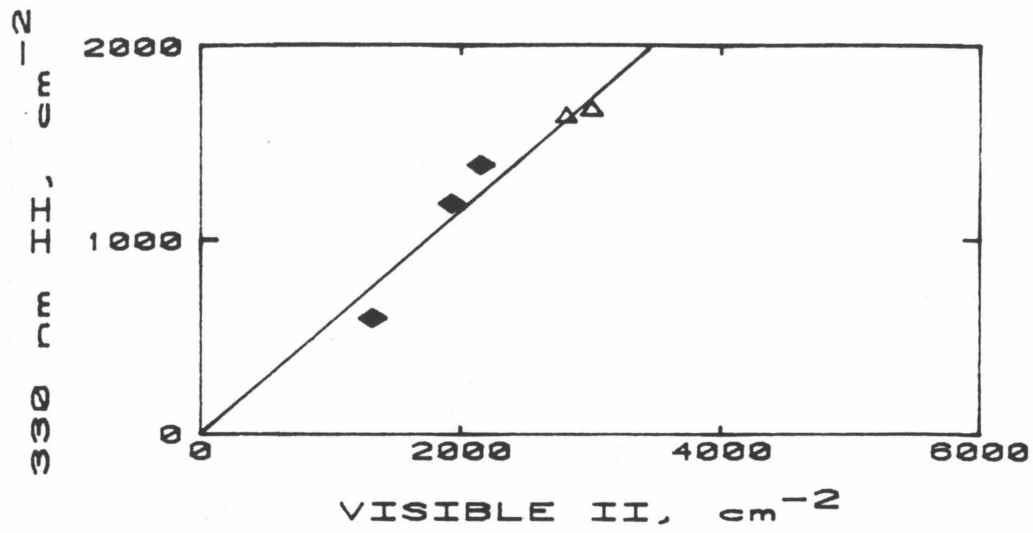


Figure 6.7 Comparison of integrated intensities of the UV peaks to that of the sum of the 630 and 720 nm peaks. 330 nm, top. 385 nm, bottom. Only one sample deviates from trend (#19') but its 385 nm peak area is poorly determined due to scattering.

Table 6.6 Optical Parameters of the Visible Peak of Natural and Irradiated Amazonites of 1 cm thickness

Sample#	Type	Natural Color				Irradiation Response				
		$1/\lambda$ cm ⁻¹	$W_{1/2}$ cm ⁻¹	I cm ⁻¹	II cm ⁻¹	Dose MRads	$1/\lambda$ cm ⁻¹	$W_{1/2}$ cm ⁻¹	I cm ⁻¹	II cm ⁻²
8	B	16000	>2500	1.13	> 2825	ND	-	-	-	-
14	B	16103	3165	10.74	33980	10	15970	3175	9.34	29650
15	B	15880	>2500	0.7	1750	ND	-	-	-	-
16	B	16100	3170	3.83	12141	ND	-	-	-	-
23	D	15700	3760	3.50	13160	66	14810	~4600	3.24	~14912
4	B	15900	3280	5.95	19516	35	15900	3300	4.68	15440
5	B	16050	3350	8.40	28140	11	16000	3260	8.7	28362
12	B	16000	3350	10.1	33840	28	16000	3330	11.2	37300
18	B	15900	>3200	1.4	4480	ND	-	-	-	-
22	D	14840	4380	4.40	19270	18.3	14810	~4700	2.93	~13800
9	B	16000	3450	8.72	30080	77	16000	3470	4.78	16600
19	D	14530	~4700	5.09	~23920	51	14000	4550	4.65	21160
19'	D	14840	4500	6.84	30800	76	14840	5000	9.36	46800
21	T	15530	3760	13.16	49480	91	15625	3900	11.2	43680
20	D	14640	4650	7.35	34180	37	13950	4550	6.69	38440
6	D	14840	4230	12.1	51180	17.8*	14900	4410	10.9	48069
26	G	13710	3100	4.2	13020	69.1	13710	3300	4.45	14690
32	D	14180	4090	5.26	21510	ND	-	-	-	-
3	G	13900	~4000	2.06	~8240	17.8	13780	3120	5.44	16970
3'	G	13920	~3600	6.3	22680	51.0	13610	3370	6.25	21060
3''	G	13700	3000	11.1	33300	94	13700	3000	13.4	40200

* Data taken 2 months after irradiation when the peak was symmetric. Spectra taken immediately after irradiation was slightly assymmetric with more 720 component.

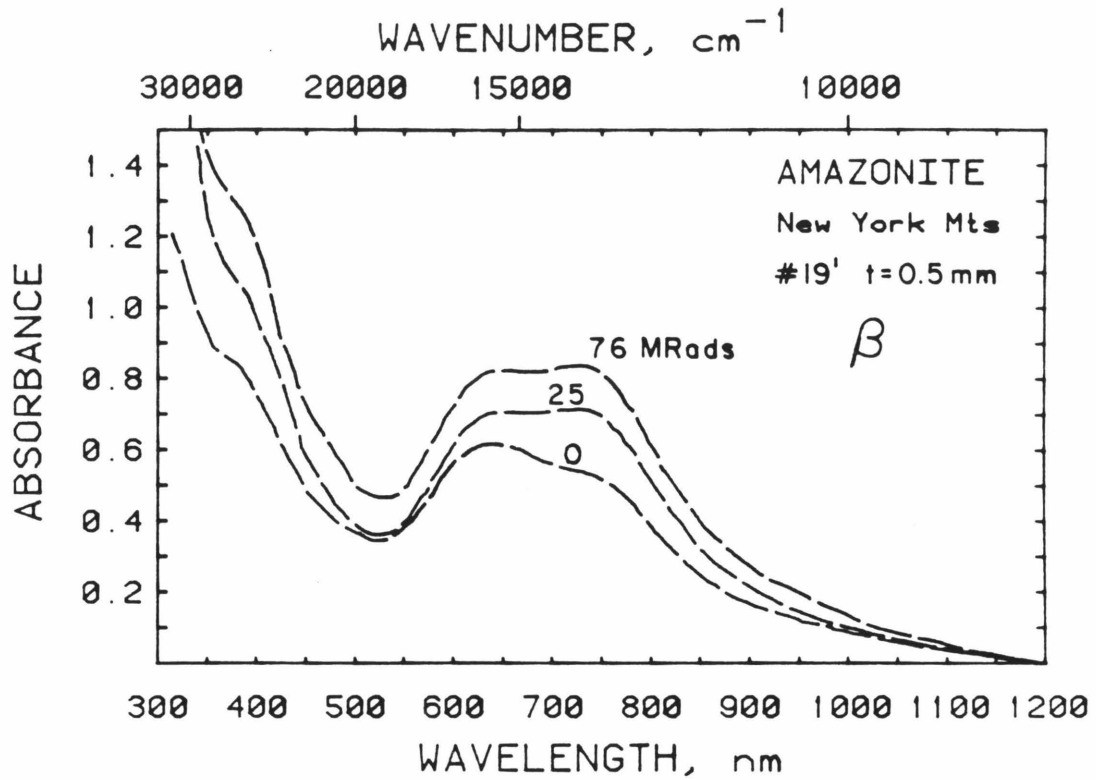


Figure 6.8 Visible spectra of the beta polarization of amazonite #19', taken at progressively higher radiation doses. Doses labeled are cumulative. Irradiation increases all bands associated with amazonite color, including the UV tail. In this sample, the 720 nm band grows more than the 630 nm band.

#19'. The different growth rates of the two peaks lead to changes in the shape and width of this and other doublet configurations. One sample, #23, which appeared to be an asymmetric type B before irradiation, became an obvious doublet after irradiation (Figure 6.9).

In order to understand the kinetics of amazonite coloration, the color of samples from each of the color types was monitored as the sample was irradiated. Table 6.7 records the change in intensity of the visible peak as a function of dose. Coloration is rapid at first, then slower. As shown in Figure 6.10, saturation of the color occurs at about 100 MRads for the two samples which were bleached before the series of irradiations (#3" and 12), and at slightly lower doses (perhaps 70 MRads) for the samples which were only irradiated (#19' and 3"). Notably, samples which were heated do not reach as intense a color as similar samples which were not heated. This point and the reason some amazonite colorations decrease upon irradiation will be discussed in Sections 6.8 and 6.12.

By fitting the data in Table 6.7 to different rate laws, I determined that the increase in coloration follows first order kinetics: let X be the number of color sites present at a given time, and C the maximum number available, then,

$$\frac{dx}{dt} = -k(C-X). \quad (6.1)$$

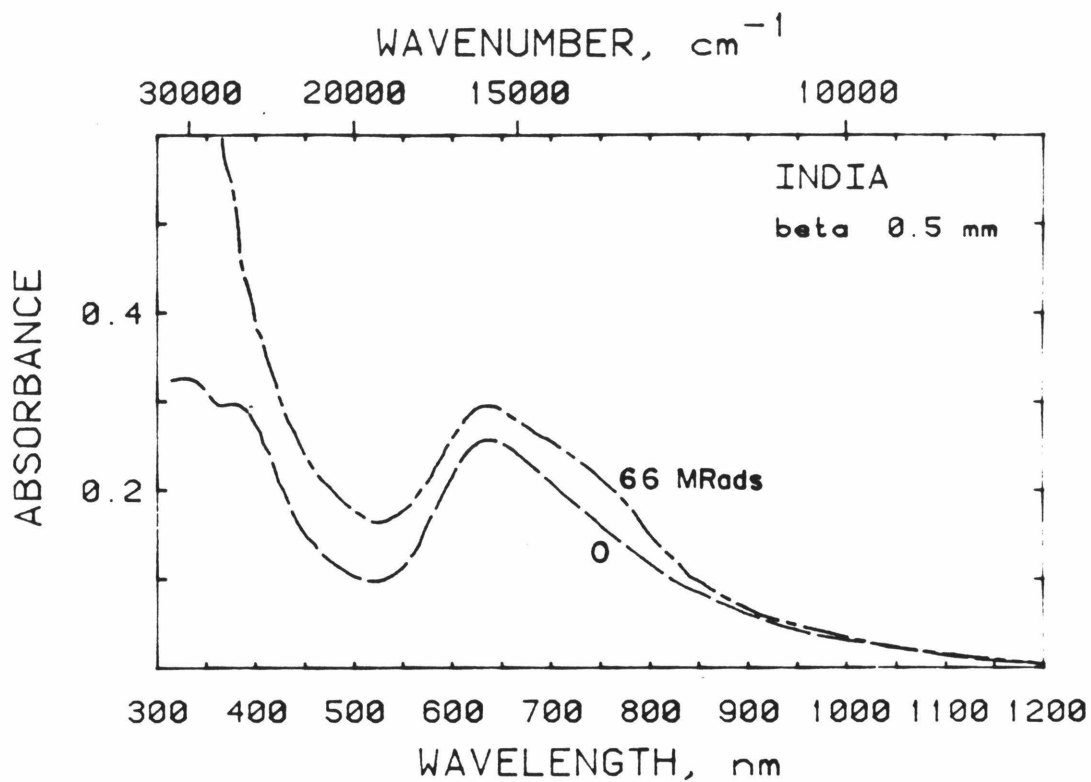
Integration from 0 to t gives

$$\ln \frac{C-X}{C-X_0} = kt. \quad (6.2)$$

Another way to write this is

$$\ln (1-X/C) = k_1t + k_2. \quad (6.3)$$

To apply this equation to the data, I used the radiation dose as the time variable, the intensity of color to represent the number of color sites,



+

Figure 6.9 Visible spectra from the beta polarization of amazonite #23 for natural and irradiated samples. Before irradiation, the weak 720 nm peak added a low energy "tail" to the 630 nm band. Irradiation preferentially increased the 720 nm band, revealing a doublet structure. A strong increase in the UV band with radiation obscures the 2 higher energy transitions.

Table 6.7 Irradiation Response of 625 to 720 nm Band of
Selected Amazonites

Sample#	$W_{1/2}$ cm^{-1}	$C,$ cm^{-1}	Dose, MRads	$I,$ cm^{-1}	$1-I/C$	$k_1,$ MRads^{-1}
12 heated B	3300	9.70	0	4.1	0.58	-0.0277
			6	4.8	0.51	
			20	6.5	0.33	
			45	8.1	0.165	
			70	8.9	0.082	
			121	9.5	0.021	
3" G	3000	14.00	0	9.5	0.321	-0.0230
			11	10.1	0.279	
			29	11.2	0.200	
			40	12.4	0.114	
			67	13.1	0.064	
			94	13.4	0.040	
145	13.85	0.011				
3" heated (300°) G	3000	6.5	0	3.2	0.508	-0.0230
			18	4.1	0.369	
			29	4.8	0.262	
			56	5.4	0.169	
			83	6.0	0.077	
19' D	4500	9.37	0	6.7	0.284	-0.0852
			15	8.4	0.103	
			25	9.0	0.0039	
			76	9.36	0.001	
4 B	3300	-	0	5.95		
			10	5.75		
			35	4.68		
21 T	3800	-	0	13.16		
			25	11.7		
			91	11.2		

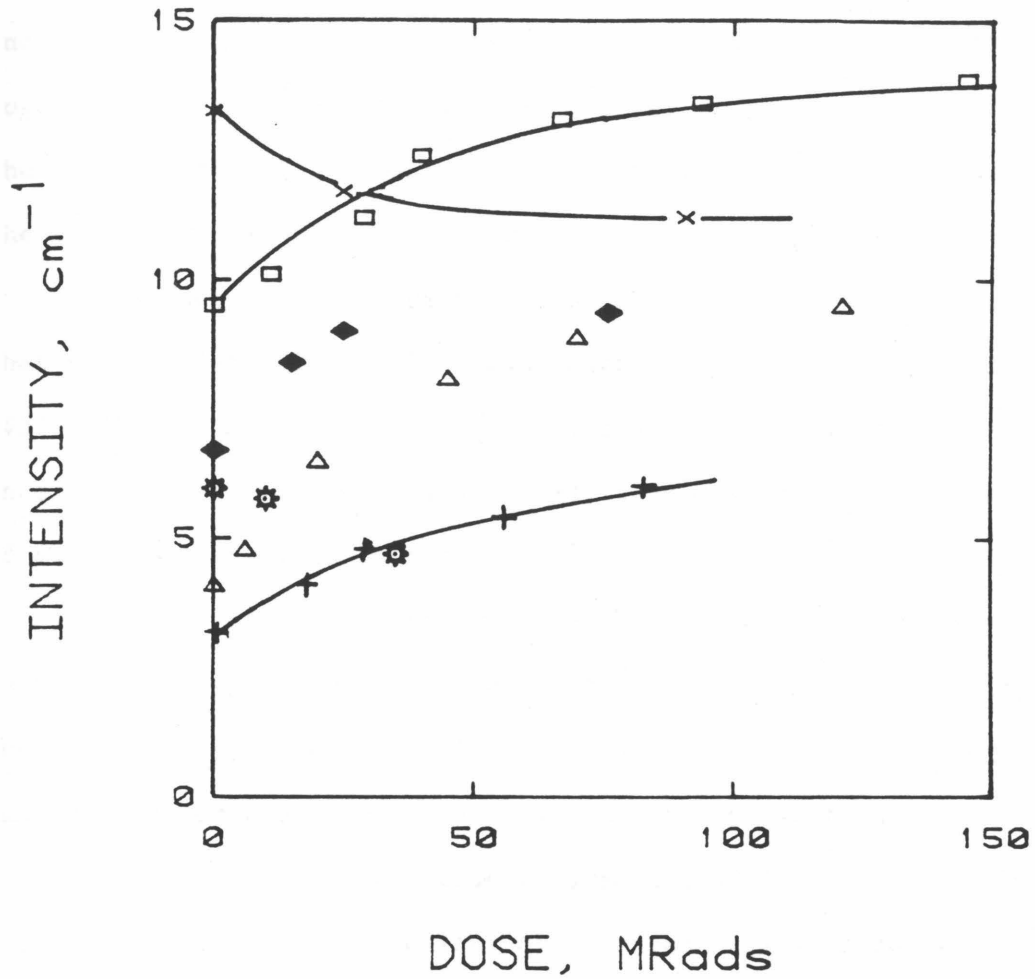


Figure 6.10 Intensity of amazonite color in the 630 to 720 nm region as a function of cumulative radiation dose. Triangle = B #12. Diamond = D #19'. Square = G #3". + = G #3", heated to 400°C for 1/2 hour before irradiation. Star = B #4. X = T #21. Saturation of color is approached near 100 MRads for almost all samples.

and estimated C from the saturated color. Figure 6.11 shows that the natural logarithm of $(1 - I/C)$ is a linear function of the dose for three samples. The fourth sample (#3", heated) was not plotted because of clutter. It has the same slope as the #3" unheated sample.

The slopes (rate constant, k_1) of the three types of colors differ, such that the doublet (#19') colors much more rapidly than the two singlets (#3" and 12). The differences are likely to be sample-specific and not inherent to the different color types, considering the varied responses of all samples to irradiation.

The first order kinetics implies that amazonite coloration is limited to a specific number of sites in the feldspar. This suggests that a certain chemical entity, or structural or chemical configuration is needed for amazonite coloration. It also shows that the production of electrons or holes is sufficiently large that it does not delay the transformation of precursor site to the amazonite color center. First order kinetics do not require a one step reaction, but do show that there is one rate limiting step in the production of color.

The kinetics will be further discussed in section 6.12 which concerns the mechanism of coloration.

6.3.c Spectroscopy of selected samples at liquid nitrogen temperature

Spectra of all four types of amazonite color were taken in a liquid nitrogen dewar. Figures 6.12 - 6.14 show that upon cooling the feldspar to liquid nitrogen temperature, the absorption shifts to slightly higher energy, while sharpening and intensifying. For the broad doublet, cooling resolves the two absorption bands (Figure 6.15). Table 6.8 lists peak parameters at room and $1N_2$ temperatures. Although peak intensity nearly doubles, the area under the absorption is nearly constant or increases slightly.

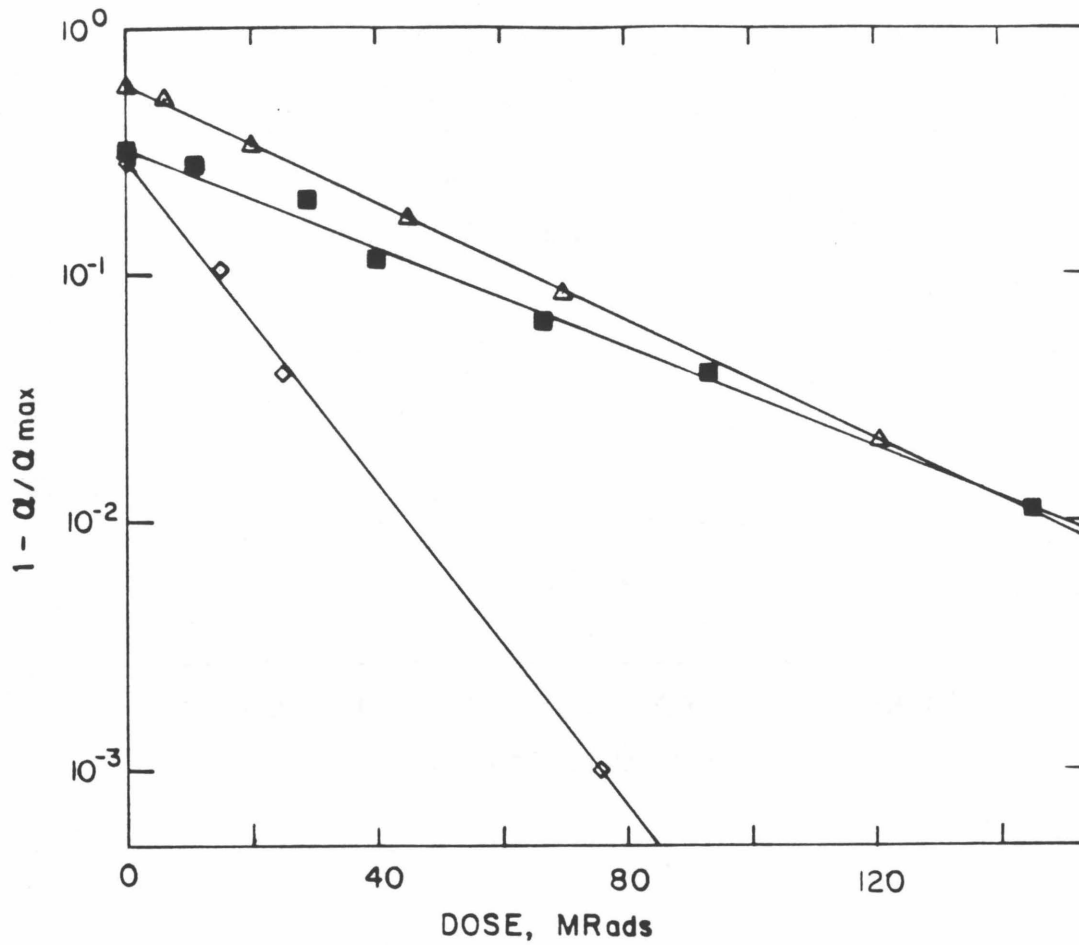


Figure 6.11 Logarithmic plot of $1 - \alpha/\alpha_{\max}$ as a function of cumulative radiation dose. Triangle = B #12. Diamond = D #19'. Square = G #3''. The constants differ for each sample (see Table 6.7). The linear correspondence implies first order kinetics. The different types of samples have different slopes and thus different rate constants.

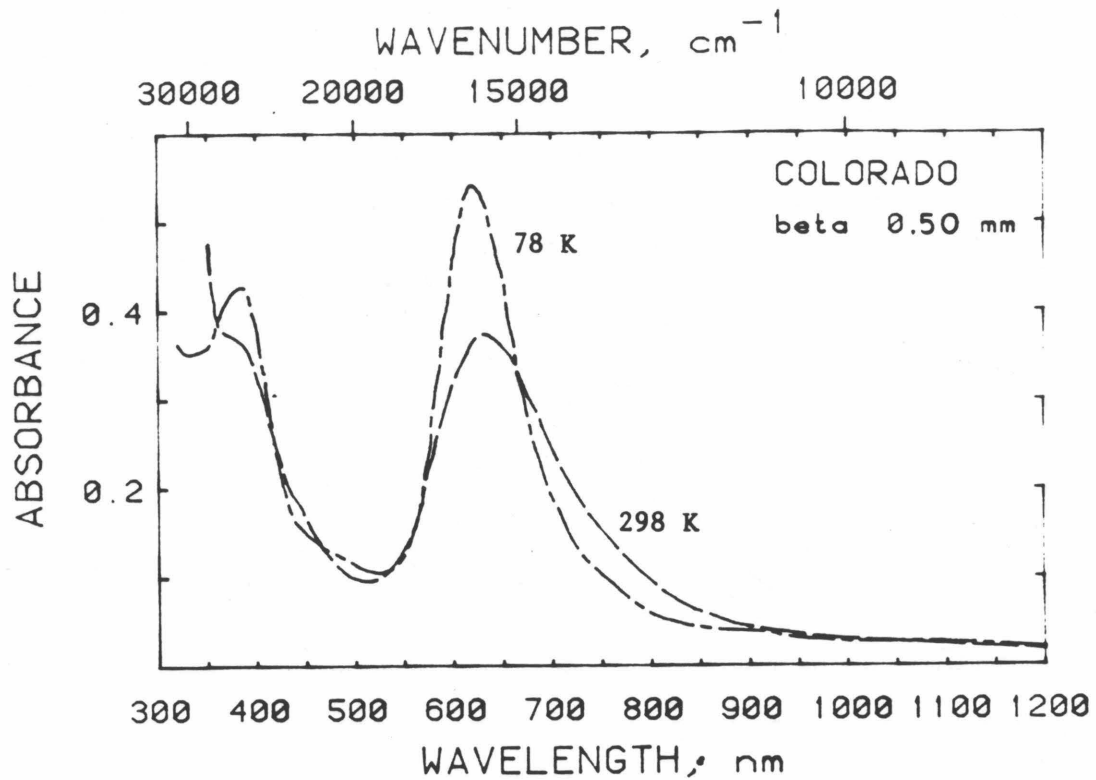


Figure 6.12 Comparison of visible absorption spectra of a blue amazonite (type B, #4) at room and liquid nitrogen temperatures and chilled in a liquid nitrogen dewar. Both absorptions sharpen and increase in intensity strongly such that the peak area is nearly constant. The peak position shifts to slightly lower wavelengths.

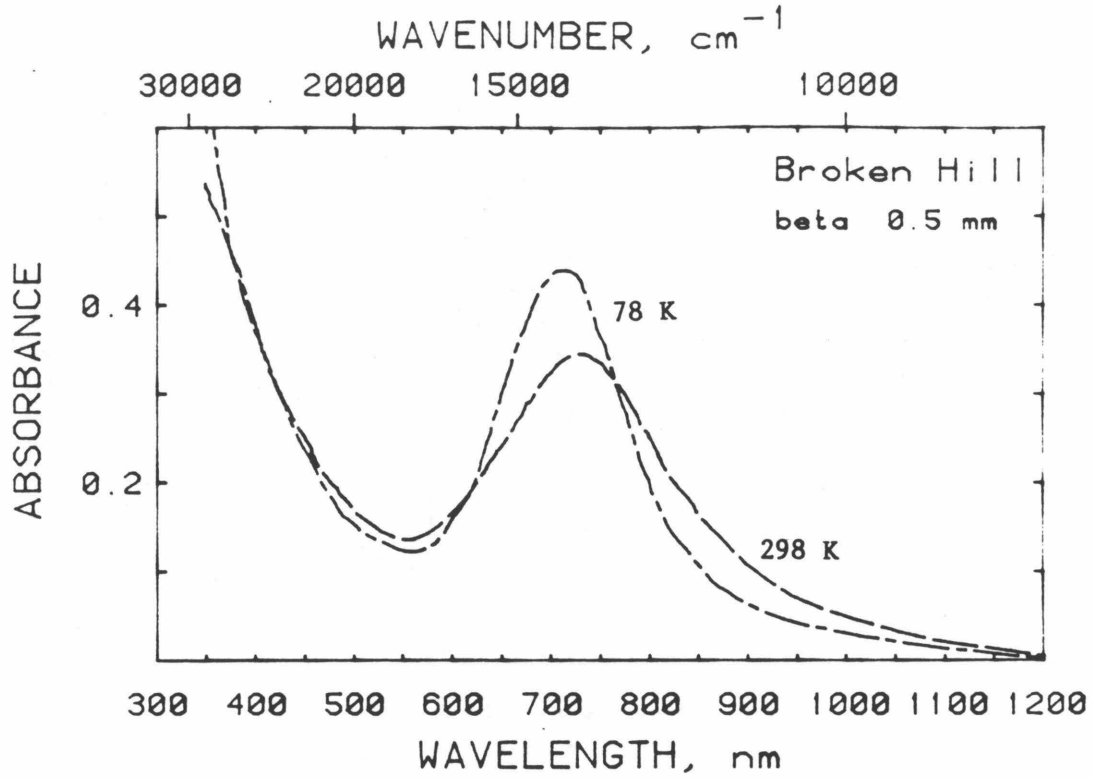


Figure 6.13 Comparison of visible absorption spectra in beta of a green amazonite (type G, #3) at room and liquid nitrogen temperatures. The green band sharpens and increases in intensity, similarly to the blue (Figure 6.11), and also shifts to higher energy.

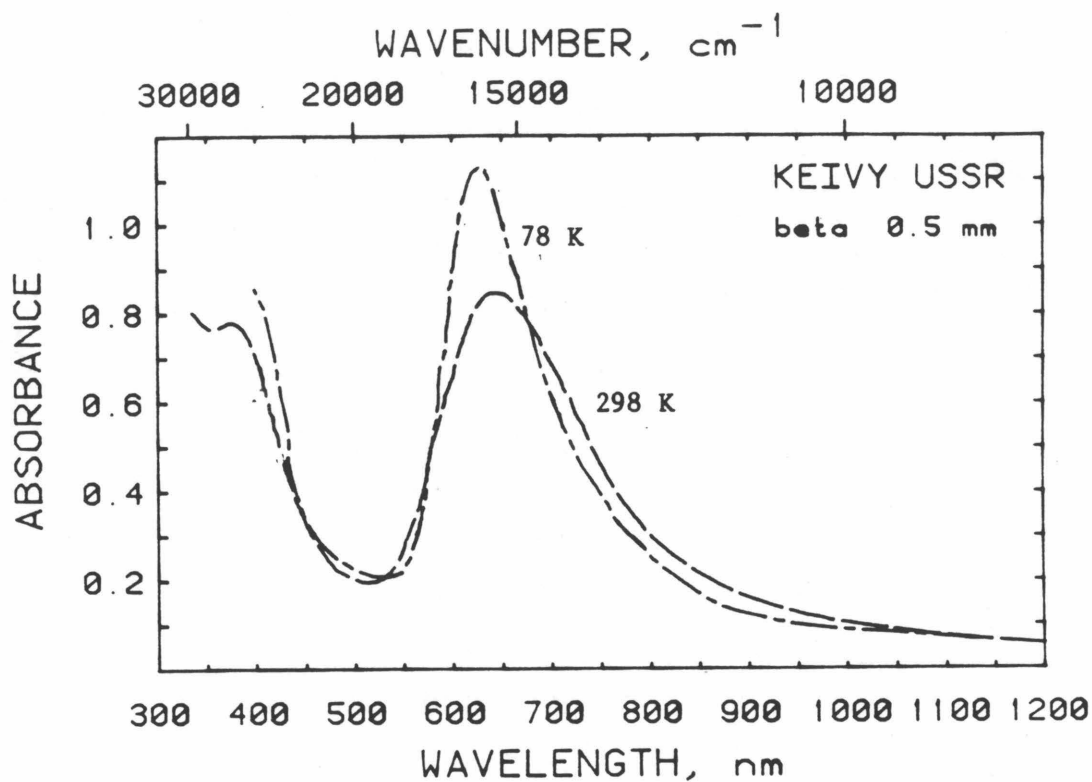


Figure 6.14 Comparison of beta polarization for visible absorption spectra of amazonite #21 (type T) at room and liquid nitrogen temperatures. Upon chilling, the peak position shifts to slightly higher energy, the peak sharpens and increases strongly in intensity, again keeping constant area (in energy dimension).

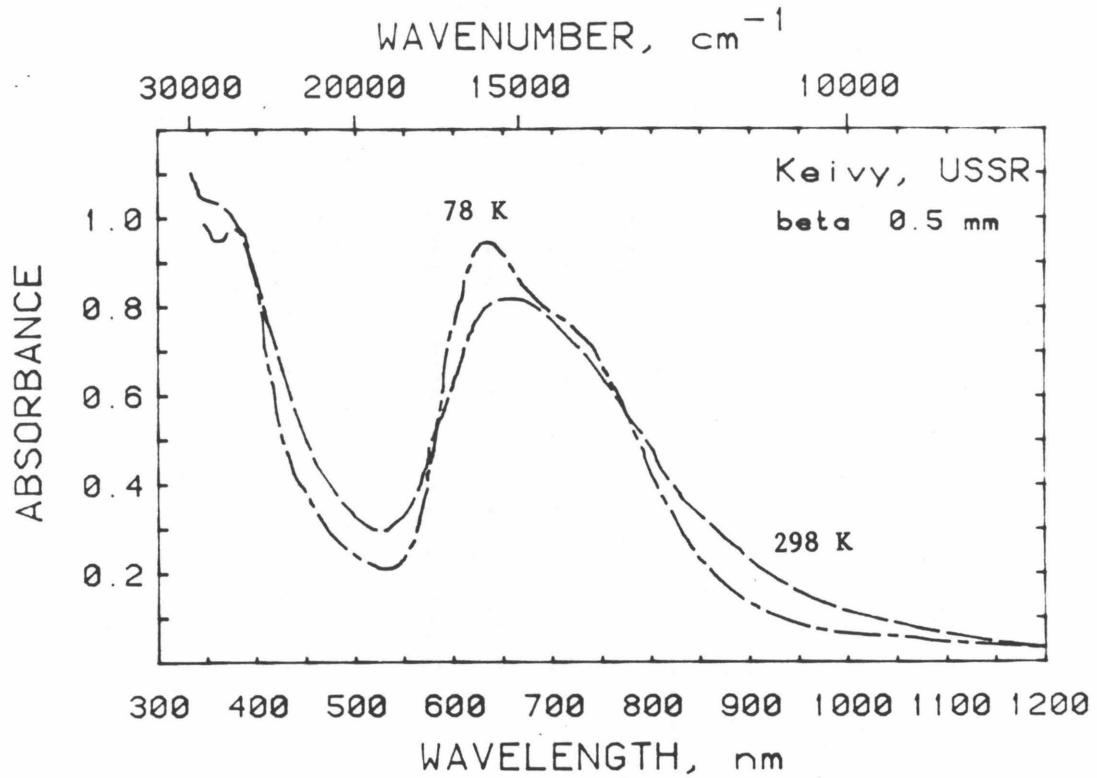


Figure 6.15 Comparison of room and liquid nitrogen temperature visible absorption spectra in the beta polarization of amazonite #6 (doublet type). The two bands in the visible spectra are poorly resolved at high temperatures, but cooling clearly reveals the doublet structure. Sharpening also occurs for the 385 nm band and the UV tail.

Table 6.8 Dependence of Amazonite Color Properties on Temperature

Sample# and type	Dose, MRads	Color at Room Temperature				Color at Liquid N ₂ Temperature			
		$1/\lambda$ cm ⁻¹	$W_{1/2}$ cm ⁻¹	I cm ⁻¹	II cm ⁻²	$1/\lambda$ cm ⁻¹	$W_{1/2}$ cm ⁻¹	I cm ⁻¹	II cm ⁻²
4 B	10	15900	3320	5.75	19090	16210	2310	9.24	21340
3 G	17.8	13780	3120	5.44	16970	14060	2950	7.125	21020
6 D	0	~14900	4410	11.6	51156	15150*	4450	3.63	60653
21 T	0	15530	3760	13.16	49480	15850	2600	19.04	49500

* Components at 15900 and ~13900 cm⁻¹; 15900 component is larger

The area increase for the doublet (#6) is likely to be overestimated due to the change in peak shape, so that on the average, no change in peak area with temperature is seen for these four samples (Figure 6.16).

Conservation of peak area with cooling suggests that the electronic transition producing the color does not involve intervalence charge transfer, because IVCT usually produces a strong increase in area. An allowed electronic transition, or d-d exchange is more likely the cause of amazonite color because either of these mechanisms could produce bands with constant area during cooling.

6.3.d Relationship of amazonite color to lead content

As discussed in section 1.2.b.IV, Foord et al [in prep.] have shown that the hand-specimen color of amazonite becomes greener, and usually, but not always, more intense with increasing lead content. Quantitative spectroscopic measurements are in agreement with Foord, Martin, Cocklin, and Simmons's [in prep.] observations, but show that there are many exceptions.

Figure 6.17 shows that the energy of the peak in the visible region decreases as lead content increases. Because the color depends on the transmission minima, this makes samples with higher lead samples greener. Figure 6.17 also shows that type B (blue) amazonites have peak energies near 16000 cm^{-1} and low ($< 0.2\text{ wt}\%$) lead contents; type G amazonites have energies near 13800 cm^{-1} and high ($>1\%$) lead contents; and the doublets fall in between in both peak energy and lead content. Because irradiation tends to increase the type G peak more than the type B (Section 6.3.b), irradiated doublets have lower energies (Figure 6.18) and give a poorer correlation.

The peak width at half height shows two distinct trends with lead content (Figure 6.19). At low lead contents, $W_{1/2}$ increases sharply with PbO content. A maximum is reached near $0.2\text{ wt}\%$, and thereafter $W_{1/2}$

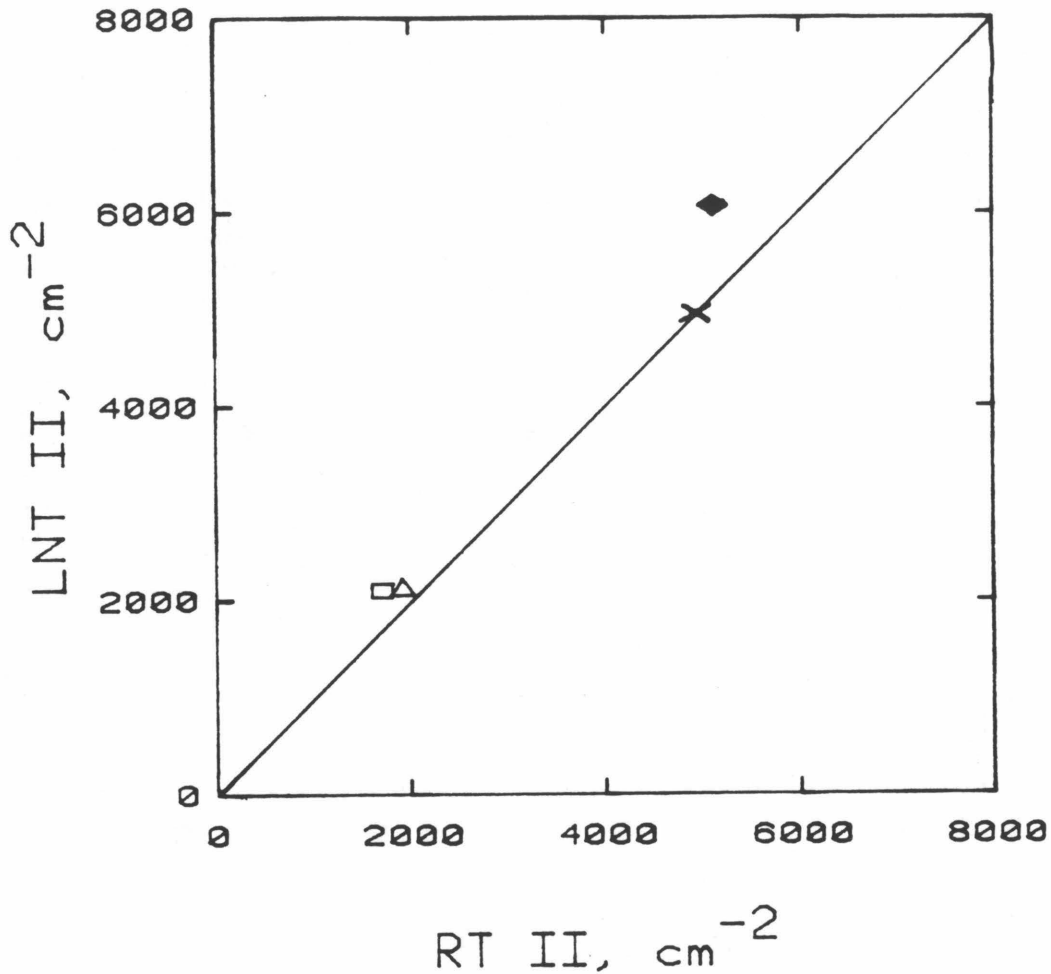


Figure 6.16 Comparison of integrated intensity (II) for chilled and room temperature measurement of amazonites. Triangle = B #4. Diamond = D #6. Square = G #3. X = T #21. Except for the doublet, the correspondence of peak areas is nearly one-to-one. An increase in peak area of as much as 15% may occur, as indicated by sample #6. This sample's area is slightly overestimated at low temperature because of the structure in the doublet region, so that the actual increase in area is somewhat less than 15%.

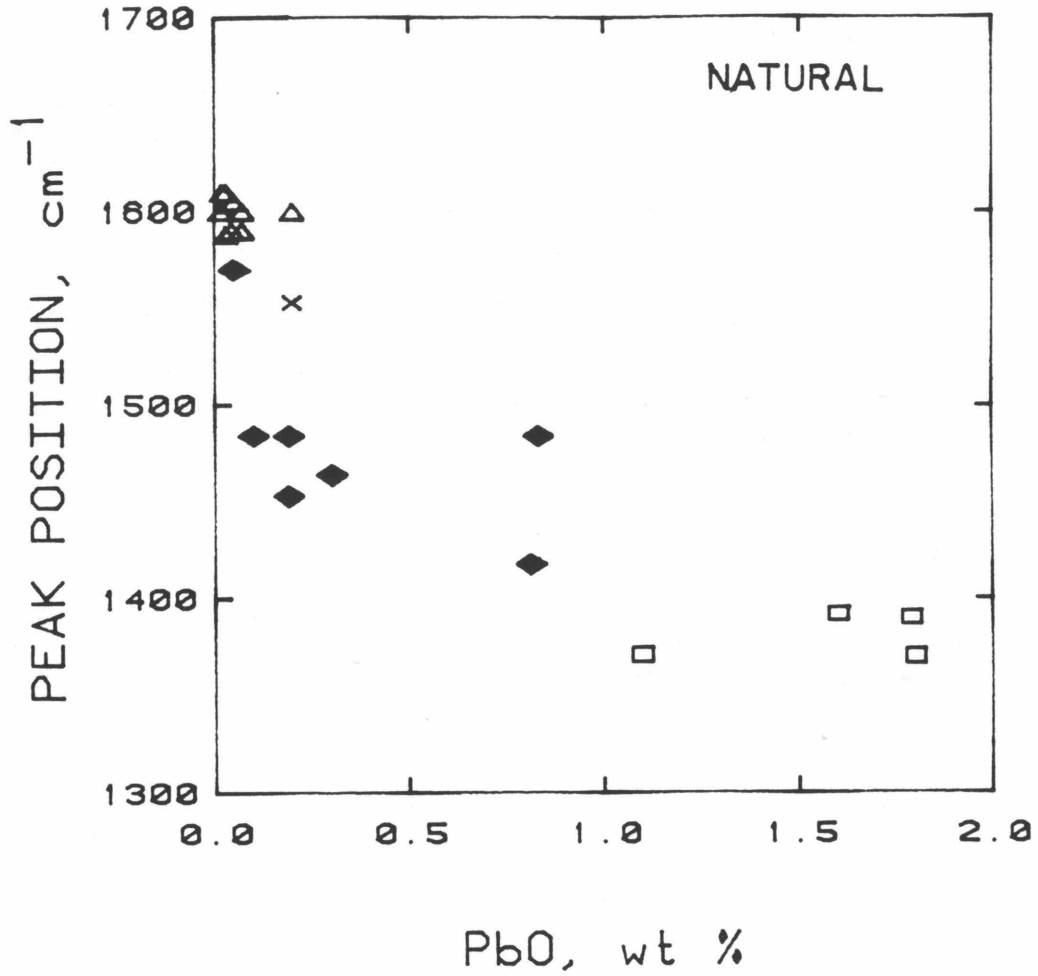


Figure 6.17 Dependence of the position of the amazonite peak in the visible region (in wavenumbers) on lead content of natural amazonites. Triangle = type B. Diamond = type D. Square = type G. X = type T. A decrease in peak energy as lead content increases is seen, along with grouping of the different amazonite color types over certain ranges of lead content. Error bars are roughly the size of the samples.

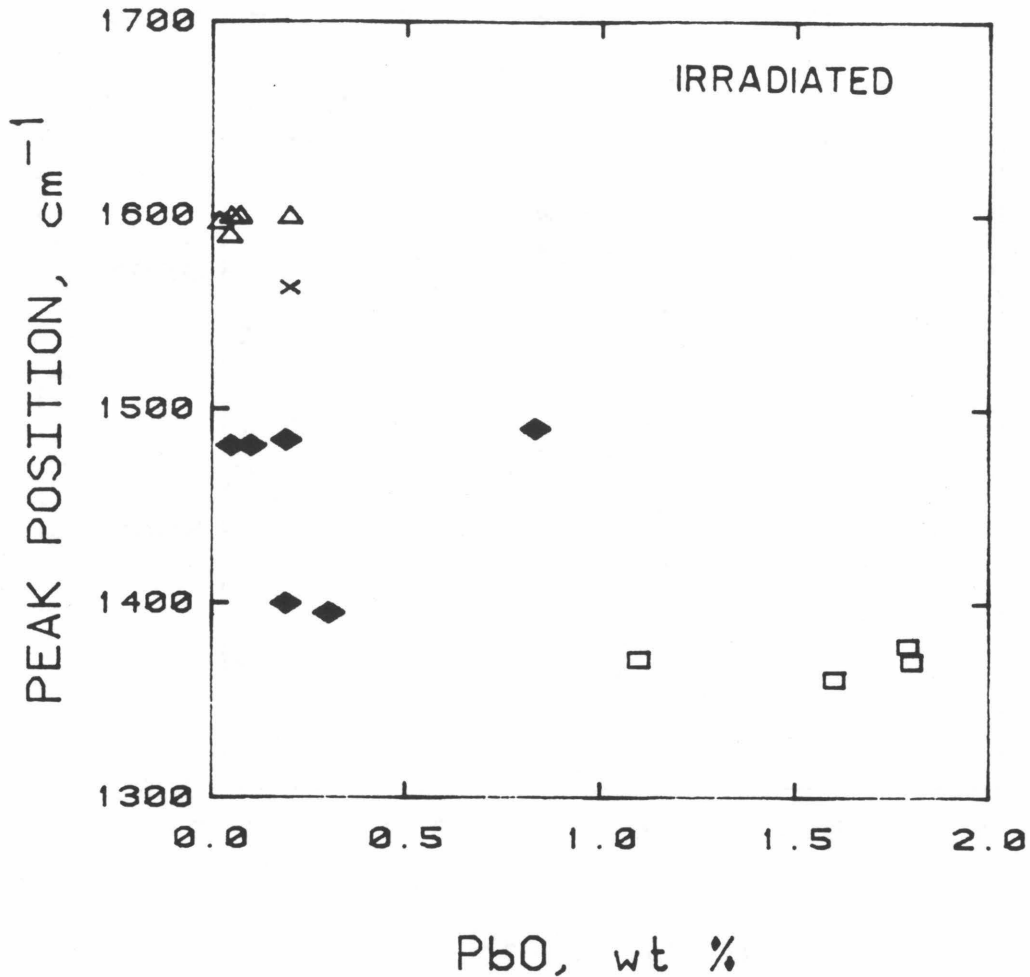


Figure 6.18 Dependence of the position of the absorption in the visible region on lead content of irradiated amazonites. Triangle = type B. Diamond = type D. Square = type G. X = type T. A wider range of peak energies at low lead content occurs because irradiation preferentially develops the 720 nm peak. This diagram shows that there are two distinct energies (at 16000 and 13800 cm^{-1}), with the exception of the type T sample and with intermediates forming by addition of the two peaks. The blue samples occupy a much more restricted range in lead contents than the other types.

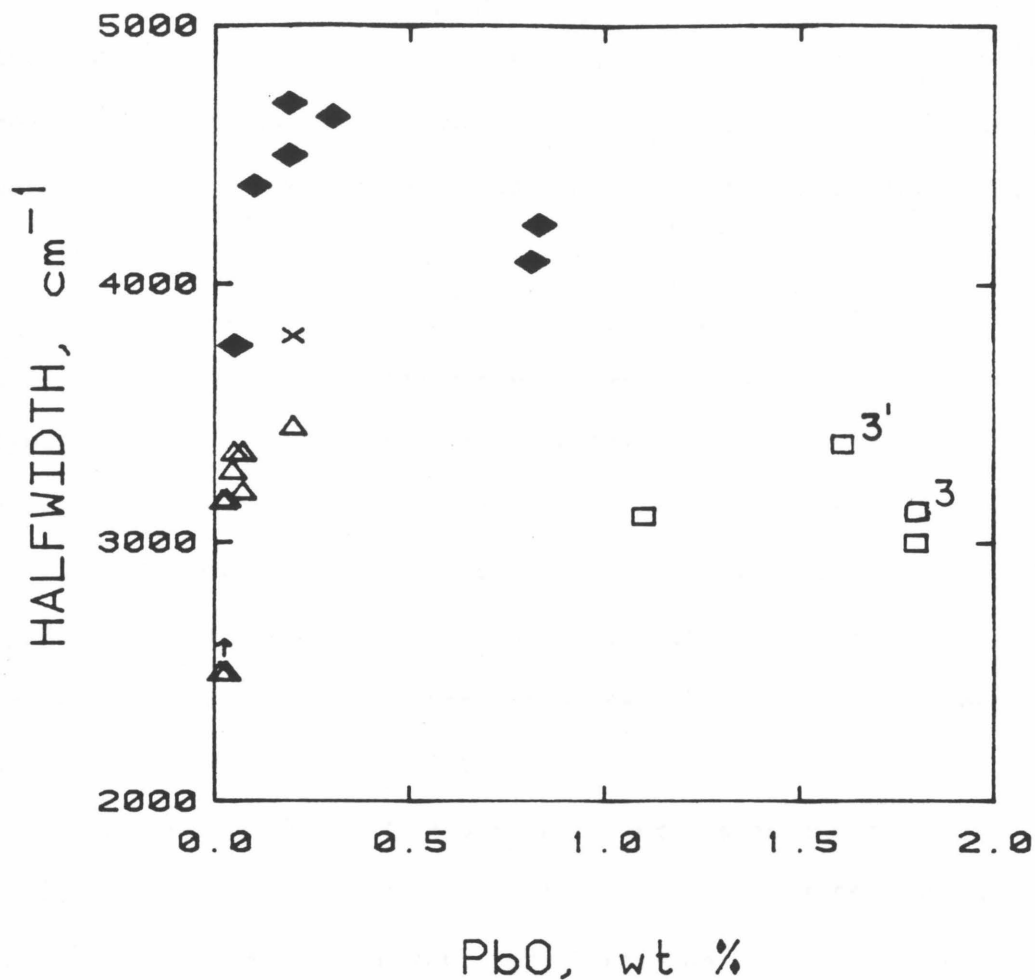


Figure 6.19 Dependence of the width of the visible peak at half height on lead content of natural amazonites. (For samples 3 and 3', the irradiated half-width was used because the low intensity of the peak in the natural samples made measurement of the halfwidth inaccurate.) A strong increase with Pb initially occurs, and then the half-width gradually decreases with Pb for the high lead samples. This indicates that the proportion of the green to blue peak in amazonites increases with lead content and is likely to be controlled by lead content. Around PbO of 0.2 wt%, the ratio is roughly 1.

decreases with increasing PbO. Because the B and G samples group around the low widths, this trend can be interpreted as an increase of the G component, over the B component until no component remains. This quantitatively shows that samples become greener with increasing lead content.

Figure 6.20 illustrates the absorptions present in each of the color types and the range of lead content observed for each. The two end-member types (B, G) are restricted to the extremes of lead contents observed in amazonites. However, the doublet types and the one type T sample show overlap with each other and the type B. Lead is apparently a major factor in determining amazonite color type. The other factor is probably structure because the type G samples are orthoclase while the type B samples are microcline. This will be elaborated on in Section 6.9.

Figures 6.21 and 6.22 shows that there is some correlation of integrated intensity with lead content for each of the different types of color. For example, three of the four type G samples fall on such a trend and six of the eight doublets occupy another trend (Fig. 6.21). Seven of the ten type B samples increase in intensity with increasing lead content (Figure 6.22). Graphs of irradiated color versus lead content are very similar. The lack of a common trend, and the many exceptions to the trends, for the various color types suggests that another factor in addition to lead is necessary for the coloration. Dehydration experiments suggest that this is water (see section 6.8).

6.4 Evidence for Self-Coloration of Amazonite by ^{40}K Decay

The natural radioactivities of three amazonites were measured with a scintillator and counter. All three samples produced a peak at 1.4 Mev.

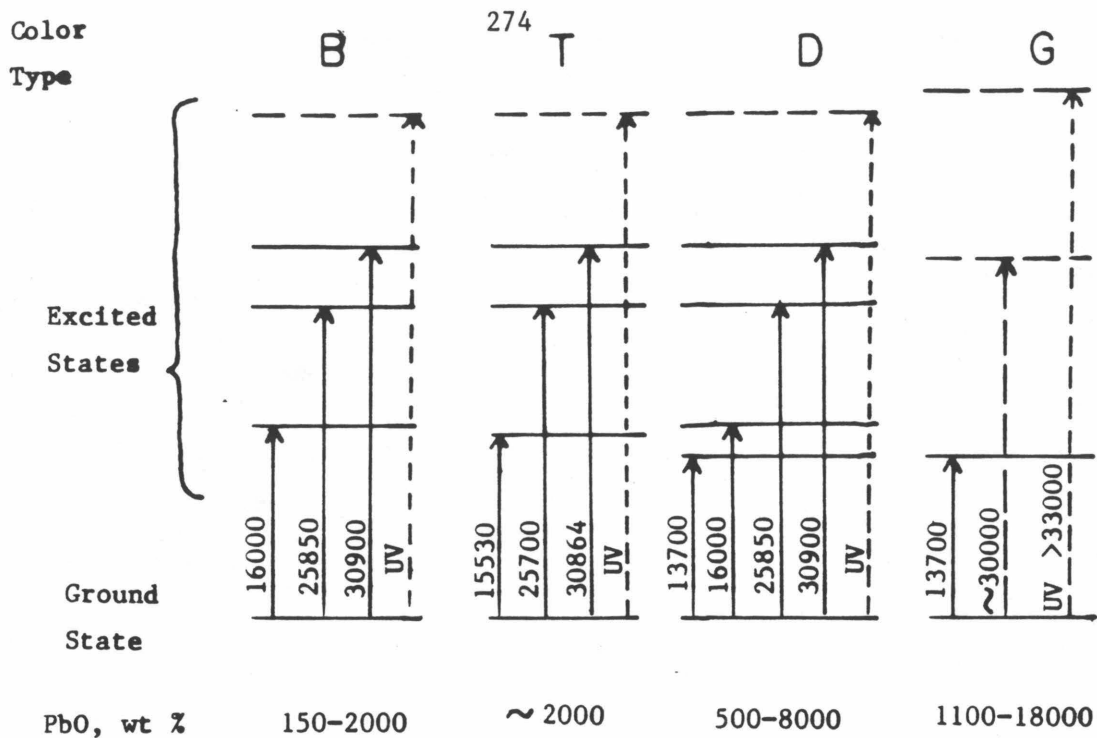


Figure 6.20 Energy level diagrams for the four types of amazonite spectra. Arrows indicated transitions, solid where accurately measured, dashed where approximate, and dotted where inferred. Transitions are tabled by the energy in cm^{-1} . A transition to the UV is connected with amazonite color, but its energy was not determined.

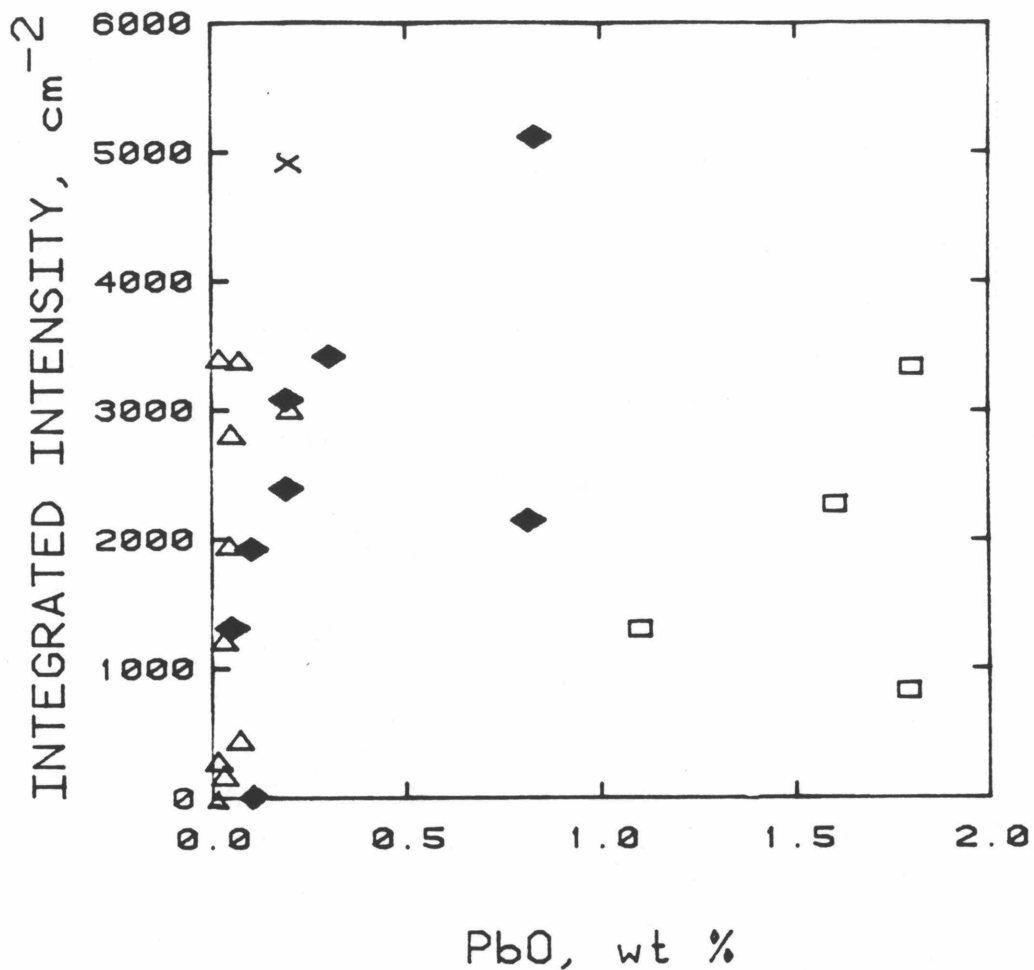


Figure 6.21 Integrated intensity (II) of the visible absorption in the beta polarization of amazonite as a function of lead content for naturally occurring color. Triangle = type B. Diamond = type D. Square = type G. X = type T. For low lead contents, intensity generally increases with lead content, but this correlation is very poor, and beyond 0.5 wt% no clear cut trend is visible.

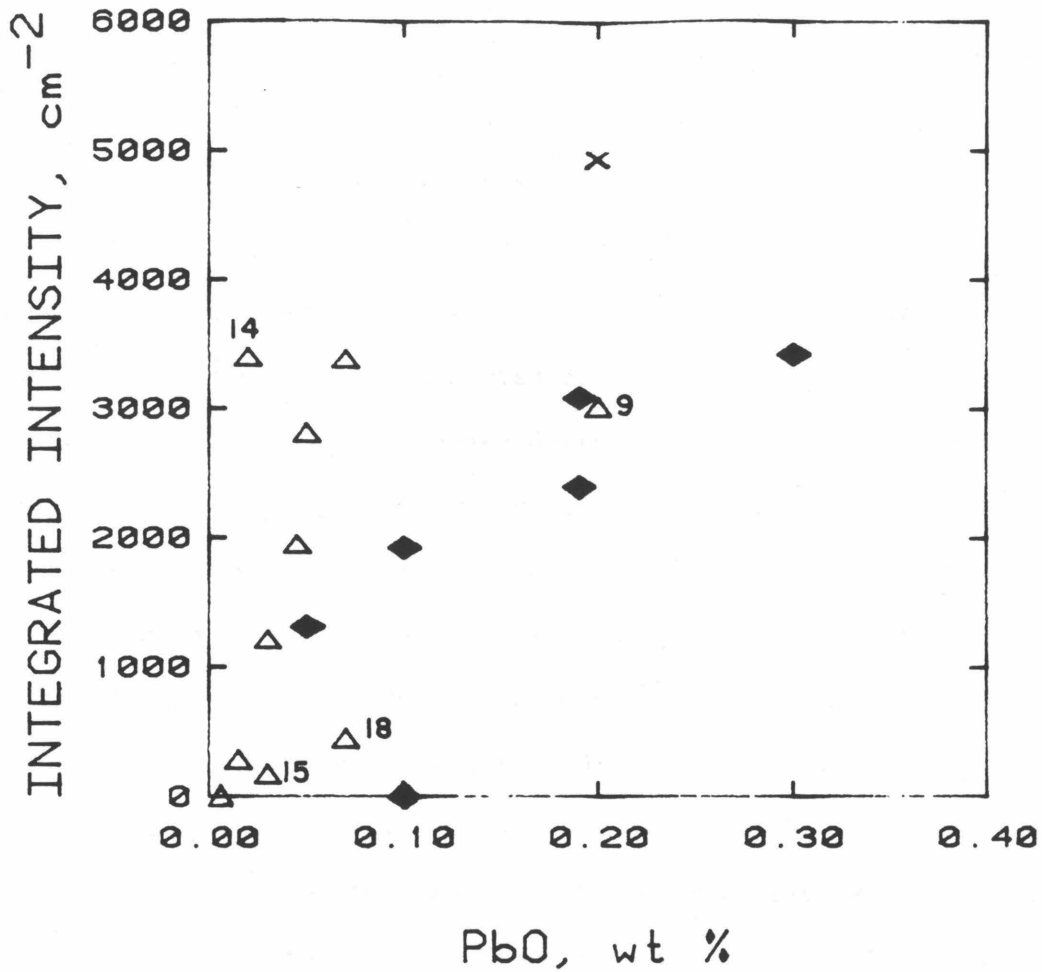


Figure 6.22 Expanded view of Figure 6.21 in the low lead region. Symbols are the same as in Figure 6.21. Some points are labeled by sample number. No correspondence of peak area with lead concentration is apparent for the blue samples, but integrated intensity in the doublets correlates with Pb for 6 out of 8 samples. This trend probably results from an increasing proportion of the 720 nm band with Pb.

Background subtracted values of radioactivity are:

Amazonite #12 (Colorado, blue), 6.5×10^6 counts/yr/gram

#21 (USSR, bluish), 6.5×10^6 counts/yr/gram

Caltech #7561 (Minas Gerais, Brazil, blue), 5.7×10^6 counts/yr/gram

(Background counts were 1.6×10^8 /year; #21 weighed 68 grams, while the others weighed about 28 grams). The similar values for radioactivity and the correspondence of the measured decay energy with that of gammas and betas (see section 5.4) released during potassium-40 decay suggests that decay of ^{40}K within amazonites produces their natural radioactivity.

The time needed to develop the natural color by self-irradiation can be calculated in two ways. The first method is to use the measured radioactivities, while the second is to use the potassium-40 content as in section 5.4. For both methods, we use the total dose from the cesium source which would induce an intensity similar to the natural intensity. From section 6.4, this is roughly 100 Mrads for the Colorado blue samples (#12) or Broken Hill orthoclases, but only 40 Mrads for New York Mts (#19). For both methods we also use the conversion factor $1 \text{ MRad} = 6.24 \times 10^{13} \text{ MeV/gram}$ (eq. 5.1).

Using the measured radioactivity of 6×10^6 cts/yr/gram gives 770 myr for the Colorado and Broken Hill amazonite colorations and 300 myr for the New York Mountains coloration. The second method (see section 5.3.b) gives much smaller values of 34 myr and 14 myr, respectively. The dissimilar answers for the two methods may be because the measured emissions from the sample would consist of only gammas due to penetration distances and would predict a time nine times longer because beta decay occurs 90% of the time. These ages are the maximum needed for coloration because both are based on the present radioactivity of ^{40}K . Because the half life of the isotope is large (1290 Myrs), the ages calculated are not grossly overestimated.

The ages of the samples are about 1 byr for the Colorado and Broken Hill localities [Hutchinson, 1976; Binns, 1964], and 60-120 myr for the Teutonia Quartz Monzonite of the New York Mountains [Hewett, 1956]. Comparison of the calculated times for coloration to these geologic ages suggest that gamma decay of ^{40}K could be entirely responsible for the coloration of both Precambrian and Cretaceous samples, while beta decay provides ten times the flux needed. Thus, amazonite color can be produced by internal decay of ^{40}K . The fact that the color of the samples is not saturated suggests that beta decay does not convert precursor sites to amazonite color centers. Irradiation with a beta source could resolve this question.

6.5 Thermoluminescence

Glow curves were made with both natural and irradiatively colored amazonites as well as amazonites decolorized by heating and several non-amazonites. This method does not discriminate between wavelengths of light emitted; it merely records intensity of light (including blackbody radiation) given off as the sample is heated. For potassium feldspars, five thermoluminescence (TL) peaks were distinguishable at about 160, 200, 255, 300, and 340°C. Examples of the various TL peaks are shown in Figure 6.23. Table 6.9 lists the temperature and relative intensity of the TL peaks for all samples measured. Many amazonites (#14, 9, etc.) did not thermoluminesce.

The data in Table 6.9 show that only the lowest temperature glow peak (at 160°C) is exclusively seen in amazonites. None of the higher temperature peaks can be connected with the blue-green color, because these are present in white, grey, or pink potassium feldspars. Because the 160°C TL peak is weakly present in only one natural amazonite, but

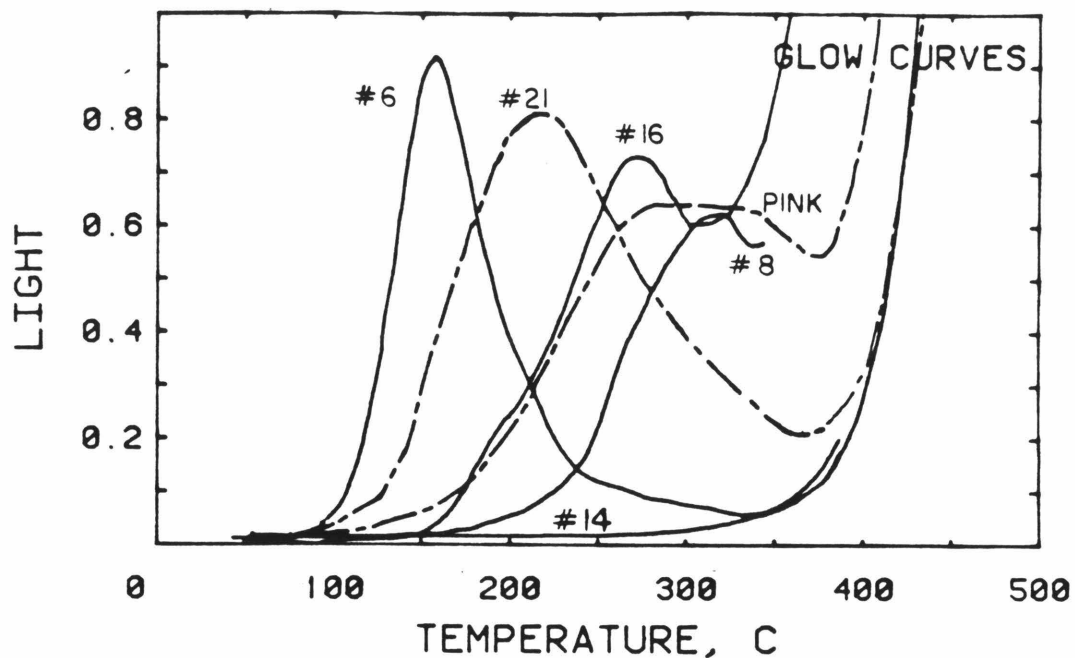


Figure 6.23 Glow curves for amazonite and other potassium feldspars. Light intensities are relative. All curves were taken with a heating rate of $5.9^{\circ}\text{C}/\text{sec}$. Gains are $\times 1$ except that sample #16 is plotted as $\times 10$, and sample #8 is plotted as $\times 5$. Solid lines are amazonite; dashed-dots lines are other colors. #6, Keivy green, after 25 MRads. #21, Keivy, grey, heated and irradiated. #16, Landsverk, blue, natural. Pink, perthite of unknown location. #8, Lake George, pale blue, natural. #14, Nevada, bright blue, natural.

Table 6.9 Thermoluminescence Data for 5.87°C/minute Scans

Category	Sample#	Color-type*	Dose, MRads	Tl ₁ , [¶] °C	Tl ₂ , °C	Tl ₃ °C	Tl ₄ , °C	Tl ₅ , °C
Other	1	white					290M	
	7	white				250W		
	7	white	7			240M		
	22	white				250VW		
	Perthite Little 3 Mine Ramona, CA	pink				270VS		340VS
		grey-brown					285S	
Heat-bleached								
amazonites	12	grey	20				305VS	
	21	grey	?		205VS			
Natural								
amazonites	8	B					315M	
	14	B						
	16	B			195W	270M		
	23	D			200VW			
	4	B				265M		
	5	B				270S		
	12	B				245M		
	22	D				250VW		
	9	B						
	19'	D				270M		
	21	T		160W				
	20	D						
	6	D						
	3	G					250W	
	3"	G						
Irradiated								
Amazonite	4	B	18		205VS		290VS	
	12	B	20	160VS				
	18	B	?	160W				
	6	D	.25	160VS				

* B, 630 nm singlet. T, 642 nm singlet. G, 720 nm singlet. D, doublet.
[¶] S = strong, m = medium, w = weak, v = very

strongly induced in several samples upon irradiation, this peak is probably not directly associated with the color, but may be due to a center complementary to the amazonite center.

As discussed on page 31, Sidorovskaya et al [1982] showed that heating amazonite at a temperature between 50 and 200°C results in emission of light around 490 nm. This band could be connected with the absorption band at 380 nm, because luminescence occurs at lower energies than absorption. If the connection is correct, then the 380 nm band does not result from the same color center which produces the 630 nm band.

6.6 EPR Spectroscopy of Centers Associated with Amazonite Color

6.6.a Correlation of EPR with Optical Results

EPR first derivative powder spectra were taken of at least one of each of the 4 different amazonite color types. Spectra were also run on chips from the sample which were heated to remove the amazonite color, and then irradiated to reveal centers extraneous to the blue-green color. For Broken Hill orthoclases, no signal could be attributed to the green color, but for all microclines investigated, a distinct set of signals was observed in the blue-green but not in the heat-bleached and irradiated samples. (The several centers which were observed near $g = 2$ in both green and decolorized and irradiated samples are discussed in Section 5.5.)

The amazonite center (Figure 6.24) consists of a large first derivative near $g_{\text{eff}} = 1.56$ with two smaller satellite absorption features at $g_{\text{eff}} = 1.83$ and 1.39 . Some specimens have two or three of these sets (Figure 6.25), such that one set dominates in intensity. It is possibly significant that the sole amazonite in the type T category possesses three sets, and that the B sample with two sets has a relatively broad and asymmetric peak in comparison

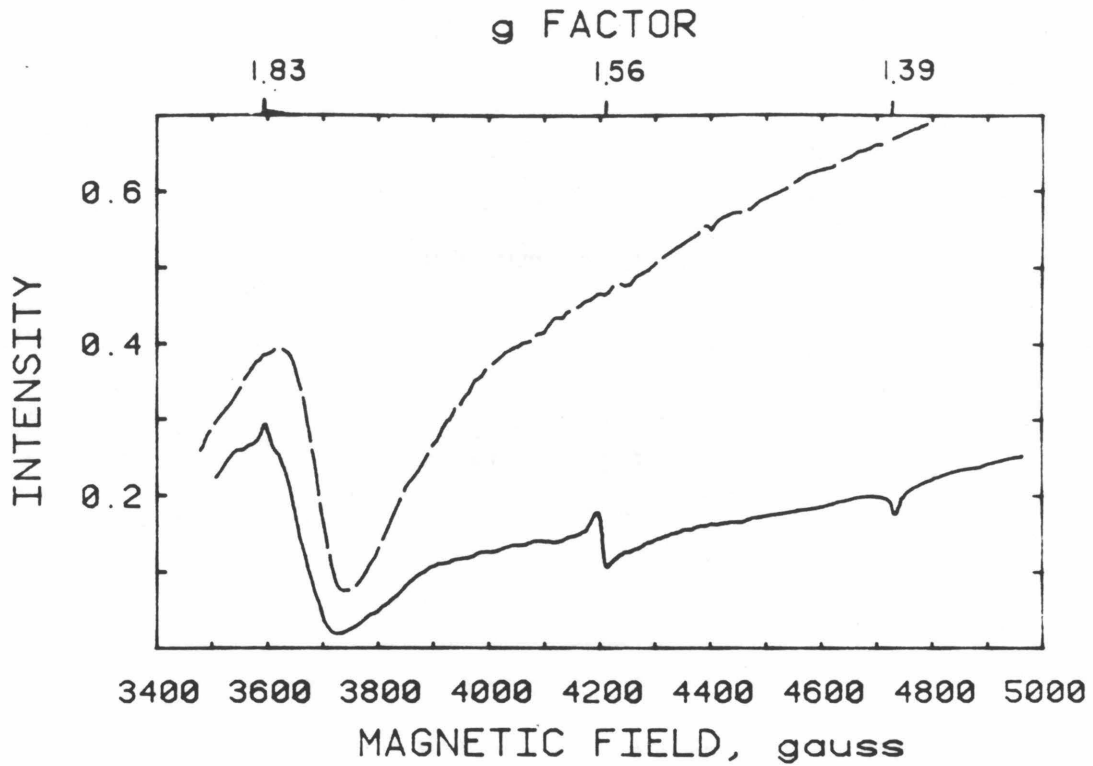


Figure 6.24 First derivative EPR powder spectra of amazonite #12 from Lake George, Colorado. Solid line, natural blue color (type B). Dot-dashed line, the same sample heated at 900° for 1/2 hour and irradiated (grey). Spectra are scaled for 100 mg sample weight and run conditions of 1.0 mW, 1G modulation and x1000 gain. Features near $g_{\text{eff}} = 1.83$, 1.56, and 1.39 must be connected with amazonite color. The large, broad band near $g_{\text{eff}} = 1.8$ is probably due to hematite inclusions.

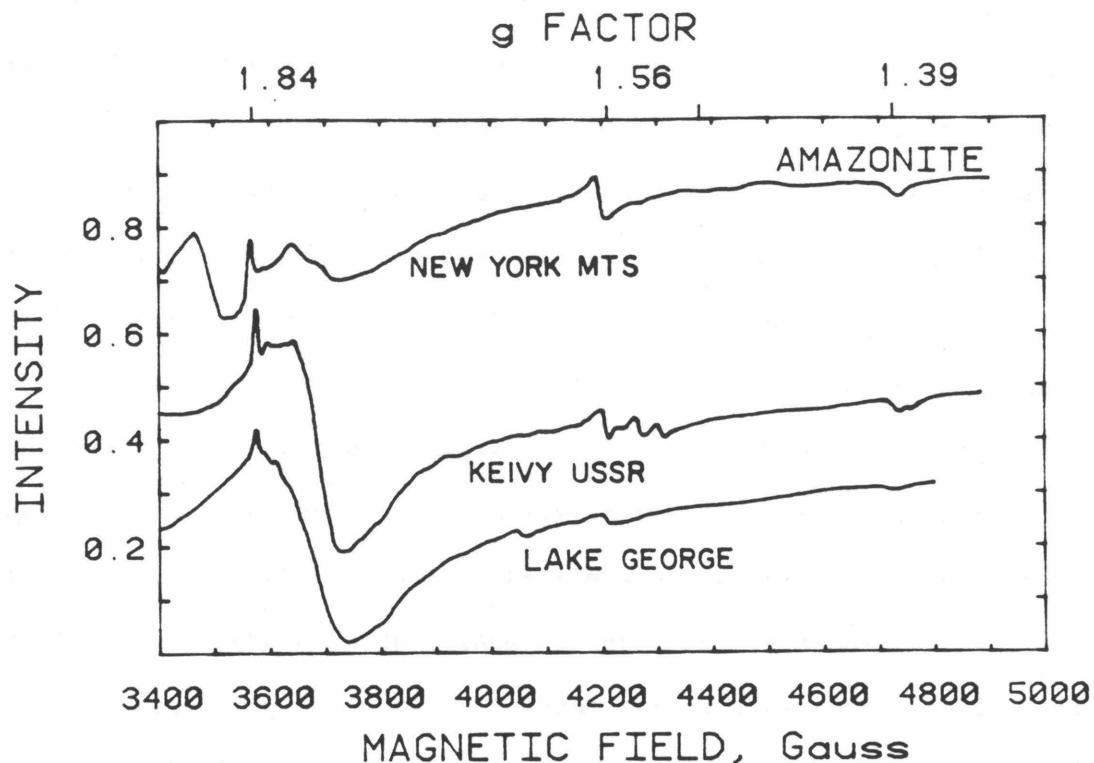


Figure 6.25 First derivative EPR powder spectra of three amazonites. Top, #19', doublet from New York Mountains, 28 MRad dose. Middle, #21, type T, Keivy USSR, natural. Bottom, #9, blue amazonite from Lake George, Colorado, natural. Spectra were scaled for 100 mg sample weight and run conditions of 1.0 mW, 1G modulation and x1000 gain. The broad feature near $g_{\text{eff}} = 1.8$ is due to hematite inclusions. Smaller features near 3430 and 3640 Gauss are due to the Al-O^- hole center (shown in Figure 6.27). The small sharp features at $g_{\text{eff}} = 1.84, 1.56, \text{ and } 1.39$ are connected with amazonite coloration. All samples have the same features as did amazonite #12, but #9 and #21 show additional similar features at slightly different positions, and with much lower intensities.

to other type B's, and deviates from the correlations of the optical parameters discussed in Section 6.3.b and 6.3.d.

Integrated intensities for each feature were calculated by equation 2.2, and are listed in Table 6.10 along with g_{eff} and the frequency for the spectra. EPR I.I. are most accurate for the sharp signal near $g_{\text{eff}} = 1.83$, but very imprecise for the broad signals near $g_{\text{eff}} = 1.39$.

To compare the EPR centers to the color, the sum of the integrated intensity for each region ($g_{\text{eff}} = 1.83$, etc.) was plotted against the sum of the integrated optical intensity in the alpha and beta polarization for the peak in the visible. The sum was necessary because sample #9 deviates from the correspondence of intensity in alpha to that in beta due to scattering. Figure 6.26 shows that a linear correlation with color exists for each of the three EPR regions with only the type D sample deviating from the trends. The deviation may be due to the method of calculating optical peak areas or differences in optical extinction coefficient for the B and G peaks. The real isotopic differences between this Cretaceous sample (#19) and the three Precambrian amazonites would produce a shift in the direction observed but with a much smaller magnitude (discussed below). The deviation cannot be accounted for by using the intensity of only the 625 nm component for the "color" of sample #19'. Therefore, the EPR signals near $g_{\text{eff}} = 1.83$, 1.56, and 1.39 not only directly correlated with the amazonite color, but all variations (types B, D, T, and therefore G) arise from the similar color centers.

It is puzzling why amazonite EPR signals were not observed in green orthoclase. The answer is likely to be the disorder: EPR signals due to Fe^{3+} are roughly twice as broad in orthoclase as in microcline [Marfunin

Table 6.10 EPR Parameters for Amazonite Signal

Sample Number	Optical		EPR						Frequency, GHz
	Color Type	II,* cm ⁻²	g	II¶	g	II	g	II	
12	B	41210	1.829	0.0663	1.564	0.038	1.390	0.20	9.194
9	B	34050	1.837	0.0428	1.560	0.186	1.383	§	9.194
			1.815	<u>0.010</u>	1.62	<u>0.11</u>	1.376		
21	T	59740	1.836	0.076	1.562	0.330	1.387	0.163	9.194
			1.826	0.012	1.540	0.136	1.381	0.062	
19'(28MRads) D		56700	1.835	0.088	1.562	0.620	1.380	0.381	9.165
			(+ 200)	(+ 0.002)	(+ 0.002)	(+ 0.002)	(+ 0.002)	(+ 0.002)	

* Integrated intensity summed together for the beta and alpha polarizations

¶ Integrated intensity calculated for x100 gain, 100 mg sample, 1 mw power, 1 Gauss modulation

§ Two signals were not resolvable

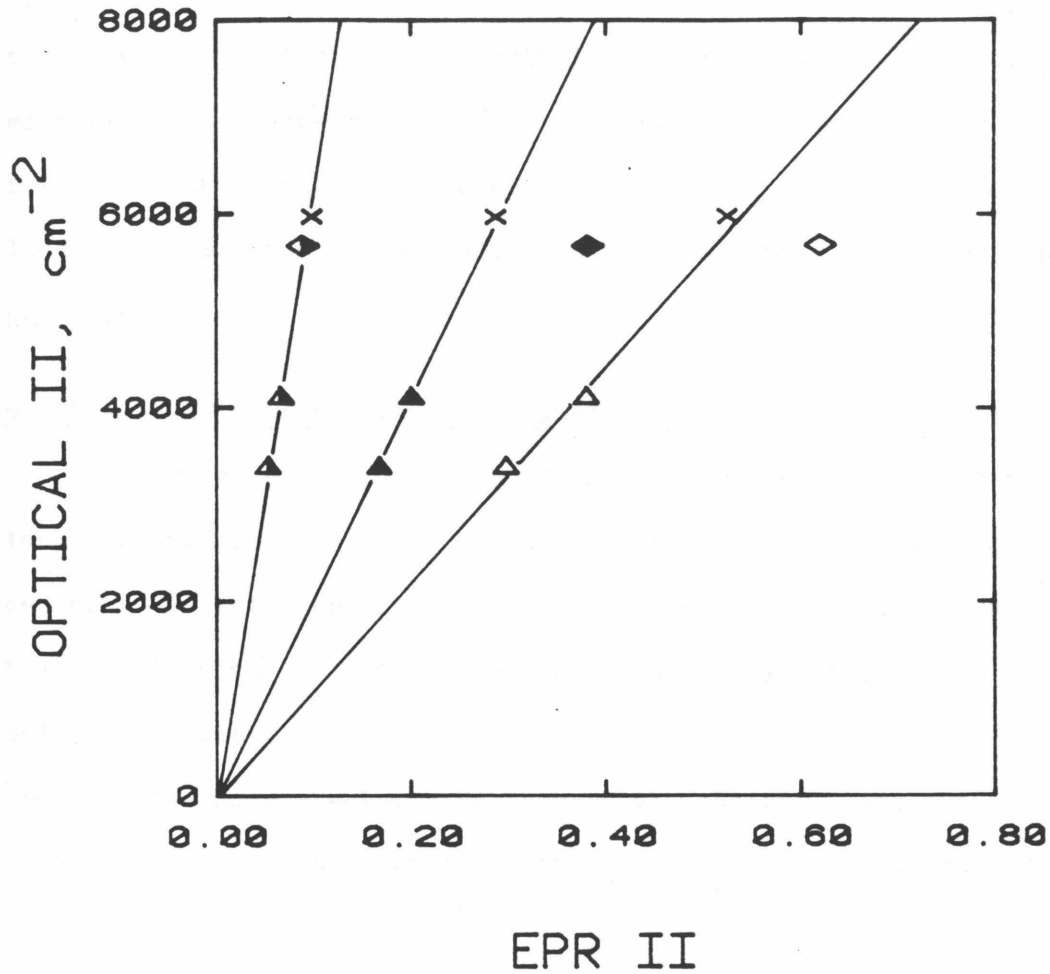


Figure 6.26 Integrated intensity (II) of the EPR signals associated with amazonite color as a function of the sum of the integrated intensity of the peak(s) in alpha and beta near 630 to 720 nm. Triangle, type B. Diamond, type D. X, type T. The lines are labeled with g_{eff} for the three EPR signals. EPR II scaled for 100 mg sample weight, and run conditions of 1 mW, 1G modulation and x1000 gain. The type D sample departs from the correlation for two of the EPR signals. This may be due to its younger age (hence different isotopic ratio) or different extinction ratios for the 620 and 720 nm bands.

et al, 1966; Gaité and Michoulier, 1970; Section 3.4] which suggests that the amazonite signal is probably much broader in orthoclase than in microcline. Broadness in a low intensity signal could easily render it invisible with respect to the noise. Possibly, EPR spectroscopy at liquid helium temperature would reveal an amazonite EPR signal in the green orthoclase.

6.6 Analysis of EPR amazonite signal: Pb^{3+}

The characteristics of the EPR signal can be used to determine the ion, its charge state, and the delocalization of charge in the color center. The large central first derivative with two satellites implies that the isotopes of the element involved mostly possess zero nuclear spin, but a small portion consists of $I = 1/2$. From Figure 6.26, the ratio of the more precise satellite to the central component, R , ranges from 5.5 to 7.1. Theoretically, this ratio is predicted from the isotopic abundances by

$$R = (2I+1) \cdot \% (I = 0) / \% (I) \quad (6.4)$$

[Goodman and Raynor, 1970, p. 219]. The element whose abundances today most closely approach the experimentally determined ratio is lead (21.1% $I = 1/2$, 78.9% $I = 0$, $R = 7.5$). The only other elements which give comparable ratios are Sn (16.7% $I = 1/2$, 83.3% $I = 0$, $R = 0$), W (14.3% $I = 1/2$, 86% $I = 0$, $R = 12$), and Pt (33.7% $I = 1/2$, 65.3% $I = 0$, $R = 39$). No other elements have similar isotopic abundances [Goodman and Raynor, 1970, Table I]. Precambrian lead (which is appropriate for most amazonites) would give a slightly lower ratio. The model of lead isotopic change by Stacey and Kramers [1975] gives $R = 7.1$ for 1 byr old Pb, which is similar to that of recent lead. Not only is the value of R for Pb closest to the experimental ratio, but Pb is strongly concentrated in amazonites while Pt, Sn, and W have

not been noted (See 1.2.b.iv and 6.2). Thus, Pb colors amazonite blue to green.

Lead is almost certainly located in the M-site of the feldspar because of its size and charge. Pb^{2+} with an ionic radius of 1.20 Å could easily substitute for K^+ with an ionic radius of 1.33 Å. Synthetic solid solutions have been made between $PbAl_2Si_2O_8$ and $KAlSi_3O_8$ [Scheel, 1971].

The EPR spectra of Figure 6.25 appear isotropic and show a very large splitting between the $I = 1/2$ satellites which suggests that the hyperfine interaction, a , is very large. These two characteristics implicate an "s" state rather than a "p" state so that the charge state of the lead ion must be Pb^{3+} . This agrees with previous studies of the EPR spectra in lead doped, irradiated crystals (see Section 1.2.b.v).

Because of the large isotropic hyperfine interaction, the intermediate field case is used to describe the spectrum. When the electron is more strongly coupled to the central nucleus than to the external magnetic field, the energy levels of the system (neglecting superhyperfine interactions) are

$$W(F, m) = 1/4 ha - g_n \mu_n B_m \pm \frac{1}{2} ha (1 + 2 mz + z^2)^{1/2} \quad (6.5)$$

where $z = (-g\mu_B + g_n\mu_n)B/ha \quad (6.6)$

[DuVarney and Garrison, 1975; Ramsey, 1956, p. 86; Breit and Rabi, 1931].

B is the magnetic field, a is the isotropic hyperfine coupling constant, h is Planck's constant, μ_B is the Bohr magneton, μ_n is the nuclear magneton of the lead nucleus, and g_n and g are the nuclear and electron spectroscopic splitting factors. F is the quantum number $|I \pm S|$, which in the case of lead is 1 or 0, and m is the component of F along the external magnetic field. The plus sign is used when $F = 1$, and the minus sign for $F = 0$. A sketch of the energy levels is shown in Figure 1.26, along with

possible transitions. For the case of amazonite, the $I = 0$ transition occurs at a magnetic field value in between the two $I = 1/2$ transitions. Thus one transition for the $I = 1/2$ pair is from the state $(F, M) = (0, 0)$ to $(1, -1)$ while the other is from $(1, -1)$ to $(1, 0)$. This differs from previous cases of Pb^{3+} (section 1.2.b.v), so that a detailed derivation of a and g as functions of the resonance conditions (the frequency and magnetic field) was necessary.

Calculations in Appendix I show that $a = 0.852 \text{ cm}^{-1}$ and $g = -2.189$. The positive deviation of $|g|$ from the free electron value of 2.0023 implies a hole center. Using equation 1.6, the probability that the hole is on the lead is 31%, which means that the complex alternates between Pb^{3+} and Pb^{2+} or that the hole is delocalized. These values are similar to those of Pb^{3+} observed in other irradiated compounds (Table 1.10), although the probability is lower than that measured for octahedral sites. This may result from contraction of the M-site around the smaller Pb^{3+} nucleus.

The amount of anisotropy can be estimated from the line widths of the three peaks

$$\delta a = |\Delta B_2 - \Delta B_c| (1 - a/2\nu)^2$$

or

$$\delta a = |\Delta B_1 - \Delta B_c| (1 + a/2\nu)^2 \quad (6-3)$$

For amazonite #12, the satellite line widths are $\Delta B_2 = 27 \pm 2 \text{ G}$ and $\Delta B_1 = 15 \pm 1 \text{ G}$, while the central line is $23 \pm 1 \text{ G}$, so that the anisotropy is less than 2%. This small value is expected for an s state, and is similar to that observed for other Pb^{3+} centers (Table 1.10).

6.7 Resonance Raman Spectroscopy of Amazonite

Resonance Raman spectra were taken on each of the four types of

colors by exciting the crystal with a wavelength (619 nm) inside the amazonite absorption. For comparison, spectra were also taken on bleached specimens (in the same orientation) and on white microcline #7, Itrongay orthoclase (Caltech #8000) and synthetic $\text{PbAl}_2\text{Si}_2\text{O}_8$. Because of a steep baseline from the direct beam, data were collected at wave numbers greater than 150 cm^{-1} . Unfortunately, this precludes examination of the lower energy metal-oxide stretching modes which are likely to be involved with the chromophore. It was hoped that the modes of M-O stretching coupled to O-Si-O bending (500 cm^{-1} region in IR) would confirm the 3+ charge state of the lead in the colored feldspars.

Figure 6.27 shows that some of $\text{PbAl}_2\text{Si}_2\text{O}_8$ Raman modes are shifted to larger wavenumbers in comparison to KAlSi_3O_8 . This is expected because the vibrations above 200 cm^{-1} depend mostly on the lattice. From comparison of the grouping and assignments of modes in the IR by Iiishi et al [1971], the bands labeled R_4 to R_6 are modes involving O-Si-O bending coupled to M-O stretching, bands R_3 and R_2 are Si-O-Si (or Al) deformation, and mode R_1 is a M-O stretching. The change in frequency due to substitution of Pb for K increases the frequency in accordance with simple physics.

$$\nu = C(K/M)^{1/2} \quad (6.8)$$

The change is small because the lattice mostly controls the frequencies of vibration.

If the oxidation state of the lead was increased, then the frequency of the bands should increase. Changes of $\pm 1 e$ observed in oxides produce shifts of 10 to 100 cm^{-1} [Nakamoto, 1978, Table II - 6e]. For the type T (Figure 6.27) and type B amazonites, increases were observed in the R_2 , R_4 , and R_6 bands relative to the bleached samples, which is the same as the ordinary microcline. The increase in R_6 in the microcline is likely

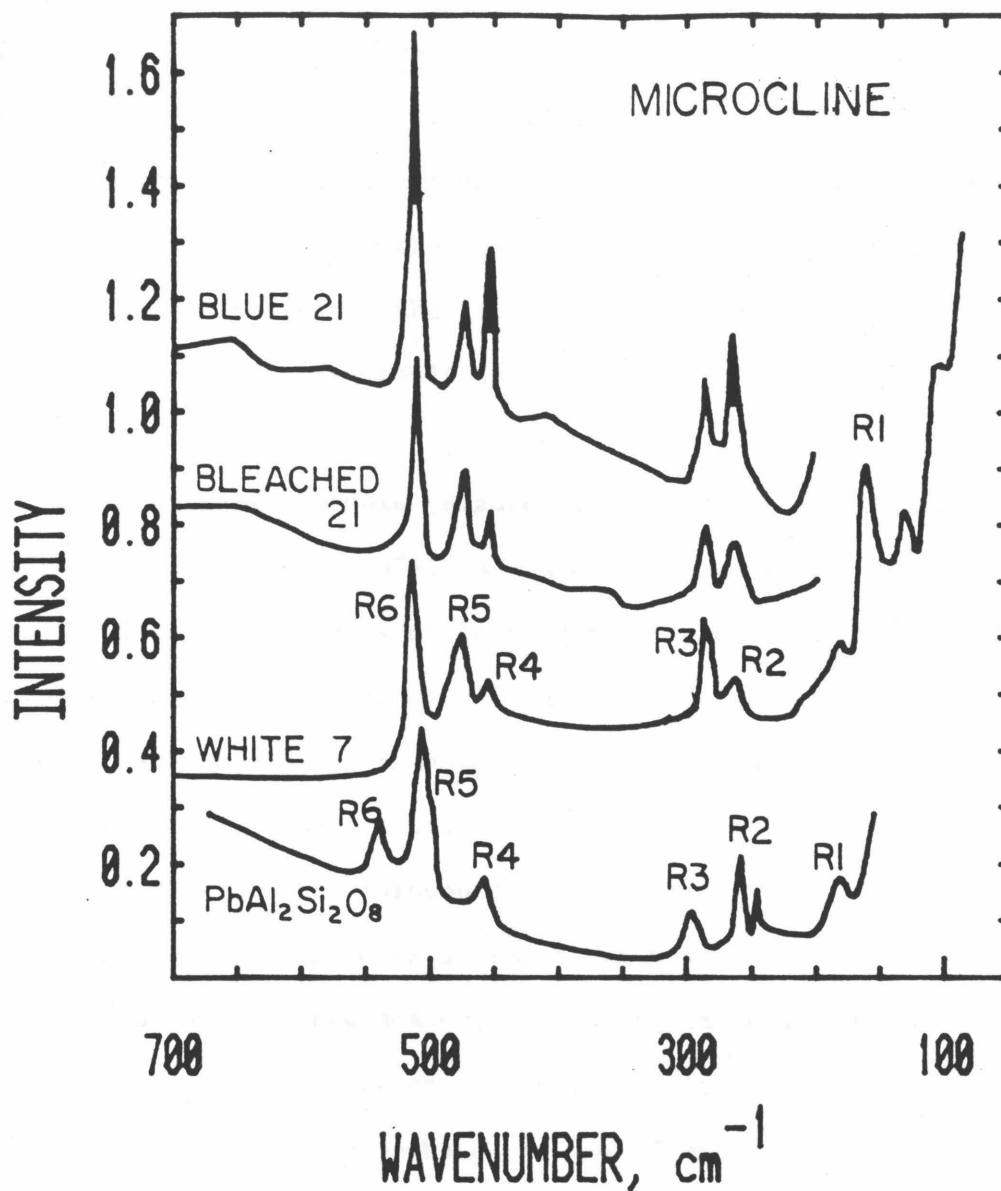


Figure 6.27 Raman spectra of three microclines and synthetic $\text{PbAl}_2\text{Si}_2\text{O}_8$. Run conditions were 619 nm excitation, 80 mW power, 400/800 slits. More than 12 scans were collected for each sample, and these data were added and smoothed. The intensities of the three microcline spectra are scaled so that the absorption at 475 cm^{-1} is of equal height. Shaded areas of the green sample indicate increases due to resonance. Labels R_1 to R_6 indicate possible correlations of modes between the microclines and $\text{PbAl}_2\text{Si}_2\text{O}_8$.

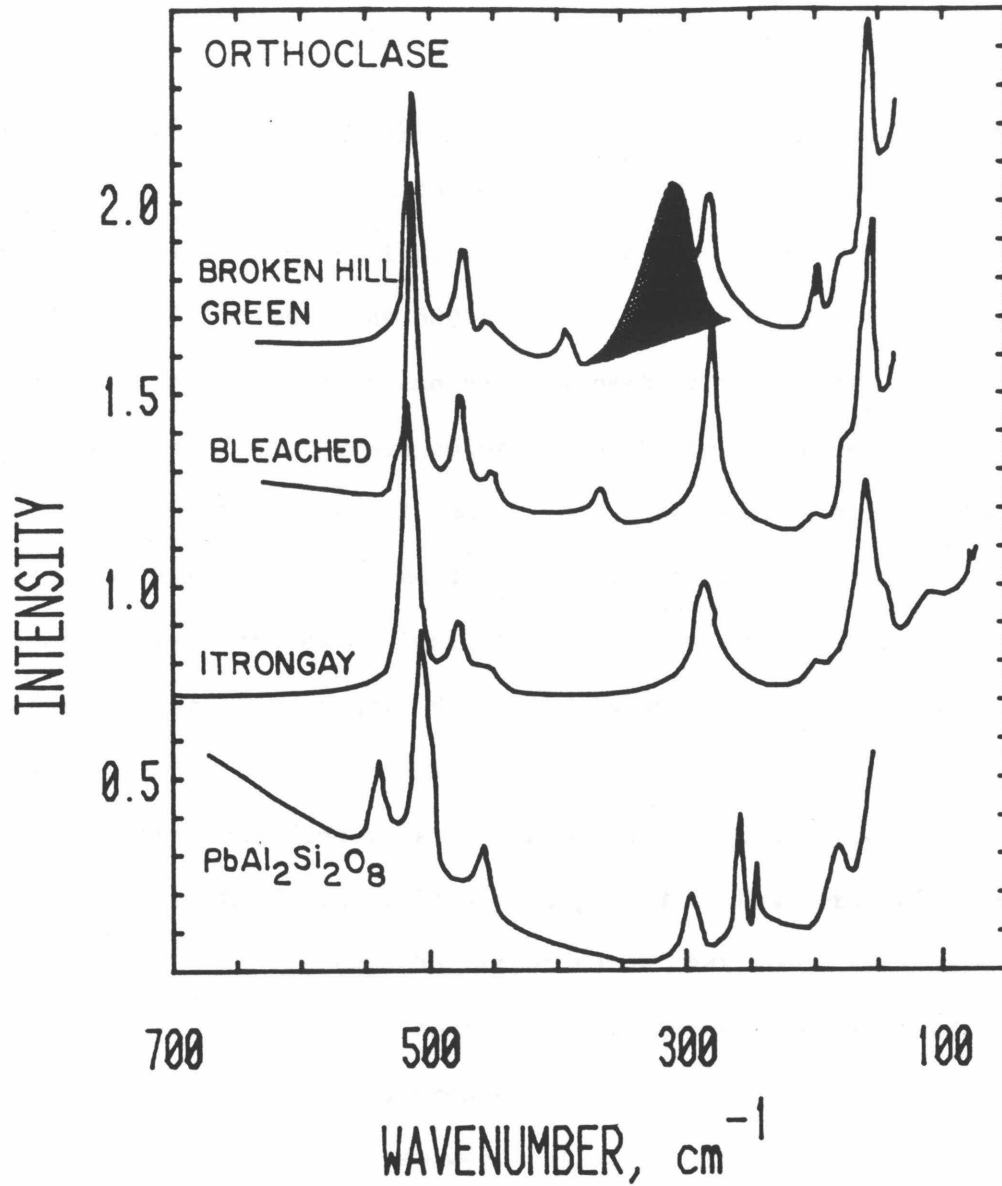
due to an R_5 component from Pb ion because this vibration is both closest to R_6 in $KAlSi_3O_8$ and the most intensive in the lead feldspar. The shifts in frequency in the microclines are small and positive (Table 6.11). The small magnitude is below the lower end of that expected and may be due to the lattice's control on the vibrational frequency. The positive changes suggest Pb^{3+} , but this result is not definitive due to the small shifts involved.

For the type G sample (Figure 6.28), resonance produces two new intense bands at 198 and $\sim 310\text{ cm}^{-1}$. Because frequency shifts are limited to about 100 cm^{-1} , the bands of lead feldspar above 450 cm^{-1} could not be involved in the resonance at 310 cm^{-1} , so that one of the lead feldspar's vibrations below 300 cm^{-1} must be the source. Therefore, the frequency shift observed in the orthoclase is positive, which substantiates that Pb^{3+} (not Pb^{1+}) is the chromophore.

The different response of the B and G amazonites is probably structural. The type D intermediate amazonite shows resonances similar to those of both the type B and type G, which suggests that it has an intermediate microcline structure or perhaps domains of microcline and amazonite.

Table 6.11 Correlation of Amazonite Resonances with Pb-feldspar Raman Bands

RAMAN VIBRATION (cm^{-1})	$PbAl_2Si_2O_8$ Synthetic	Green Orthoclase 3"	Doublet Microcline 19'	Blue Microcline 12 or 21	Wavenumber Shift
R1	183	198	NB	NA	+15
R2	250	310	261 285	260	+10 to +60
R3	295			--	+15
R4	450	--	--	452	0 to +2
R5	506	--	511	511	+5



†

Figure 6.28 Raman spectra of three orthoclases and synthetic PbAl₂Si₂O₈, 619 nm excitation; 80 mW; 400/800 slits, >12 scans, smoothed. Shaded areas of the green sample indicate resonance peaks.

6.8 The Relationship of Color to Structural Water and Pb Concentrations

6.8.a General statement on response of color to heating and irradiation

Previous studies indicated that amazonite color could be removed by heat and regenerated by irradiation (section 1.2.a.iv). This is true only if heating is below about 500°C and of short duration (less than about 1/2 hour). Otherwise, color can be only partially restored. After extensive heating, the blue or green color cannot be redeveloped, but instead, a smoky color occurs (Sections 5.2 and 5.7.b). The heating apparently removes an essential ingredient of amazonite color. Structural changes do not occur at such low temperatures as indicated by very similar infrared lattice patterns before and after heating. Diffusion is suggested insofar as permanent destruction of color proceeds more rapidly as temperature increases. It is doubtful that the lead ions themselves are diffusing because D is about 5×10^{-11} at 500°C [Smith, 1974, V. II, p. 169]. However, volatile species are likely to be lost at the temperatures over which amazonite color is partially destroyed. The next sections discuss how detailed studies of the amount of hydrous species present in amazonite, their dehydration, and the concurrent loss of color showed that structural water is an integral part of amazonite colorations.

6.8.b Dependence of color in single samples on structural water content

Pieces of crystals from each of the two end-member color types (B and G) were heated at various temperatures for 1/2 hour, and then irradiated at a fixed dose. The changes in volatiles present were monitored by infrared spectroscopy. As discussed in section 4.3.e, water in amazonites occurs mostly as fluid inclusions, and partially as structurally bound H₂O, even in the gemmiest of samples (Broken Hill orthoclase). Heating

decreased the concentrations of both of these species at similar rates, as indicated by the band intensities at 3620 and 3440 cm^{-1} (Table 6.12). Irradiation did not affect the shape or intensity of the bands in the infrared, but the intensity of amazonite color developed for the pieces heated at different temperatures roughly corresponds to the absorbances of both fluid inclusions and structural H_2O (Table 6.12).

To differentiate which proton species is involved, infrared measurements of the water regions in all amazonites were made and are presented in Table 6.13. The IR absorptivities were related to concentrations by using ϵ determined for structural H_2O in white microcline (120 $\text{l/mole}\cdot\text{cm}$ in alpha at 3620 cm^{-1} ; Section 4.3.d) and ϵ for fluid inclusions in amazonite (23 $\text{l/mole}\cdot\text{cm}$ in alpha on 010 at 3440 cm^{-1} ; Section 4.3.e). Uncertainties are ± 1 ppm for structural water concentrations greater than about 7 ppm. Concentrations below 5 ppm are affected by a "blank" of that size due to the difficulty of measuring the height of the 3620 cm^{-1} peak on top of the fluid inclusion band. Uncertainties in the fluid inclusion water contents are $\pm 10\%$.

A naturally occurring variation of color, fluid inclusion water, and structural water occurs for the 3 samples from Broken Hill which otherwise are the same chemically (nearly identical PbO contents). Figure 6.29 shows that color depends on structural water and not fluid inclusion water for the three Broken Hill orthoclases plus the high Pb orthoclase from Colorado (#26). (The samples were irradiated to develop the maximum color possible and to equalize variations due to exposure to radiation.) The correlations also suggest that a blank of about 3 ppm exists in structural water content.

For the type B sample (#12) which was dehydrated, the color developed after irradiation is linearly dependent on structural water concentrations

Table 6.12 Dehydration and Decoloration of Amazonite*

Sample	Temp °C	Color cm ⁻¹	Saturation Color, cm ⁻¹	I(α, 3620)¶ cm ⁻¹	Structural H ₂ O, ppm	I(α, 3440)§ cm ⁻¹	Fluid Inclusion H ₂ O, ppm
#12 Lake							
George, CO	-	10.9		0.34	19	4.44	1450
	250	10.4		0.196	11	2.82	930
	300	10.0		0.429	25	5.0	1600
	350	9.23		0.173	10	2.39	790
	400	6.30	9.70	0.130	7.5	1.56	520
	500	3.80		0.087	5.0	1.11	370
	550	4.11		0.100	5.8	1.78	590
	650	5.2		0.130	7.5	0.87	290
	700	1.9		0.082	4.7	0.48	160
	750	1.6		0.089	5.0	0.50	170
	800	0.6		0.06	3.3	0.47	160
#3" Broken Hill, Australia							
	-	10.0	14.0	0.64	37	2.0	670
	100	7.8		0.8	46	1.6	530
	200	7.4		0.75	43	1.5	500
	300	3.1	6.5	0.66	38	1.6	530
	450	1.8		0.60	34	1.5	500
	600	1.0		0.12	7	1.0	330
	800	0.2	0.3	0	0	0.7	230

* All samples were heated 1/2 hour. #12 was irradiated about 40 MRads. #3" was irradiated 30 MRads.

+ Absorptions due to fluid inclusions and clays were subtracted
Only intensity due to fluid inclusions is included

Table 6.13 Infrared Water Absorptivities, Derived Water Contents, and Infrared Lattice Parameters of Amazonites

Sample Number	I(α , 3620)¶ cm ⁻¹	Structural H ₂ O, ppm	I(α , 3440)§ cm ⁻¹	Fluid Inclusion H ₂ O, ppm	λ_{18} μm	λ_{15} μm	d/m
7	12.2	1000	~ 0	~ 0	18.68	15.45	1.40
8	~ 0.2	~ 12	2.47	820	18.69	15.44	3.63
14	0.7	42*	5.00	1670	18.64	15.44	2.72
15	~ 0.03	~ 2*	~ 25	8000	18.62	15.47	1.57
16	0.23	14	7.0	2300	18.63	15.45	3.61
23	0.16	9	1.76	590	18.64	15.44	3.64
4	0.10	7	2.1	700	18.62	15.47	4.54
5	0.31	18	2.69	900	18.61	15.46	1.58
12	0.34	19	4.4	1470	18.64	15.43	2.88
12 heated	0.196	11	2.82	940	-	-	-
18	~ 0	~ 0	~ 56	~ 18000	18.65	15.46	0.49
22	0.28	15	2.35	780	18.63	15.45	2.30
24	~ 0	~ 0	4.05	1350	18.63	15.44	1.30
9	0.15-0.2	8-12	2.76	920	18.69	15.44	2.94
19	0.20	12	9.1	3000	18.64	15.46	3.07
19'	0.25-0.42	13-23	5.8	1930	18.65	15.47	1.69
21	0.13-0.27	7-15	1.60	530	18.62	15.44	3.10
20	~ 0.15	~ 8	~ 1.7	~ 560	18.64	15.46	3.06
6	~ 0.12	~ 7	1.58	530	18.66	15.47	3.92
32	~ 0.20	~ 12	2.53	840	18.69	15.46	1.18
26	0.25	14	4.90	1630	18.67	15.44	0.83
3	0.31	17	2.5	840	18.51	15.56	0.21
3'	0.41	22	2.11	700	-	-	0.15
3''	0.64	35	2.0	670	18.48	15.56	0.57

* Molar Pb < molar H₂O

¶ Absorptions due to fluid inclusions and clay subtracted

§ Absorptions only due to fluid inclusions

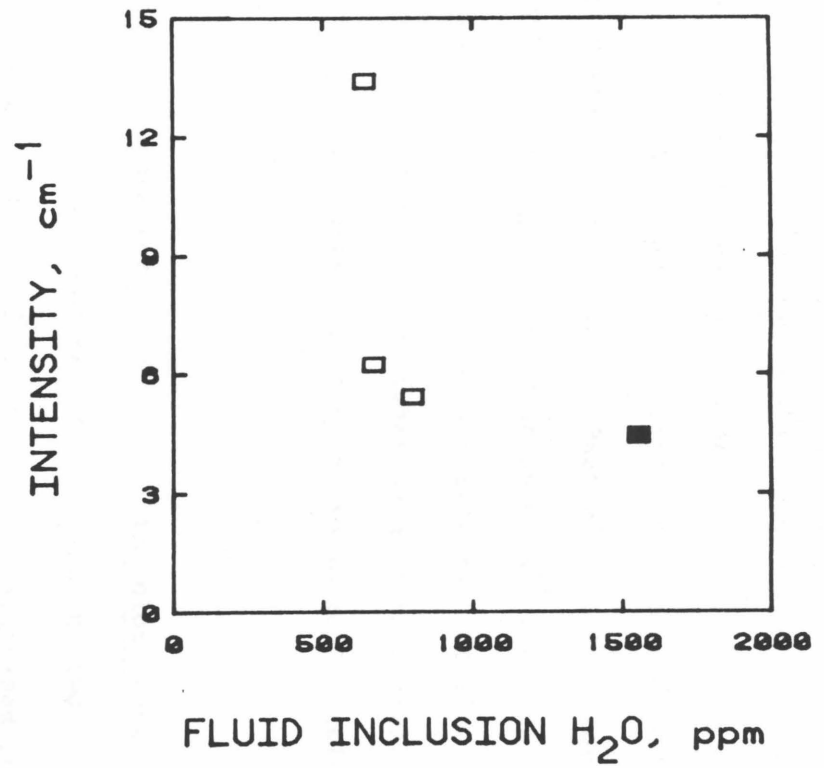
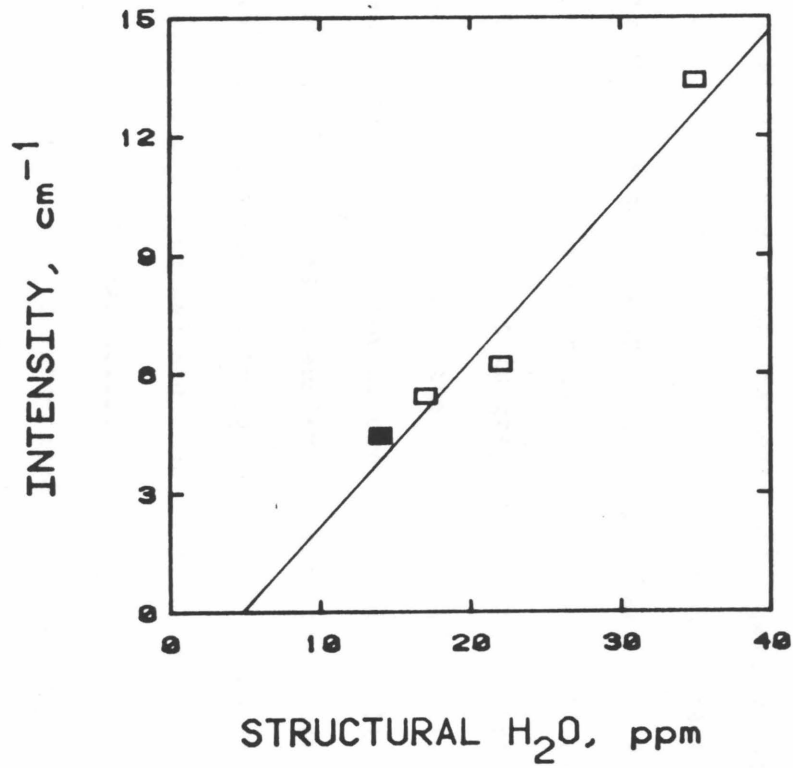


Figure 6.29 Variation of color with water species in amazonite-orthoclase. (a) Water bound structurally. (b) Water occurring as fluid inclusions. Color was enhanced by radiation and measured at 720 nm for these type G amazonites. The filled square is sample #26. Open squares are samples from Broken Hill #3, 3', and 3".

for less than 12 ppm H₂O (Figure 6.30), with saturation in color occurring about 12 ppm. This shows that some but not all of the structural water is involved in amazonite color centers. The type G sample (#3") which was dehydrated shows a non-linear increase of color with structural water concentration (Fig. 6.31). Part of this behavior may be attributed to conversion of H₂O to an OH at 3600 cm⁻¹ upon heating (G.C. Solomon, in prep.) which interferes with measurement of the 3620 cm⁻¹ band. The other part may be that at the higher water concentrations (> 15 ppm), not all of the structural water is involved in amazonite coloration as shown in Figure 6.30.

6.8.c Evidence for Pb: H₂O = 1:1 in color center formation

Of the 23 amazonites studied, all but two have more molar Pb than molar H₂O (Tables 6.1 to 6.3 and 6.13). As discussed in section 6.3.d, the integrated intensity of amazonite color poorly corresponds with Pb content. To test if the color corresponds to water concentrations, a plot of integrated intensity against ppm structural water was made for the 21 samples having more molar Pb than molar H₂O. Sample 14 and 15 with less molar Pb than H₂O were also included on this graph by plotting their effective water concentration which is defined as the amount of molar water equal to their molar lead. Weak trends are seen for natural color, but well defined trends exist between irradiation enhanced intensity and structural water content (Figure 6.32). Irradiation was used to bring the colors to their maximum intensity (or minimum in a few cases) and thus to eliminate differences in coloration due to varying natural exposures.

The dependence of integrated intensity on structural water content for the two endmember types (blue singlet and green singlet) shows that

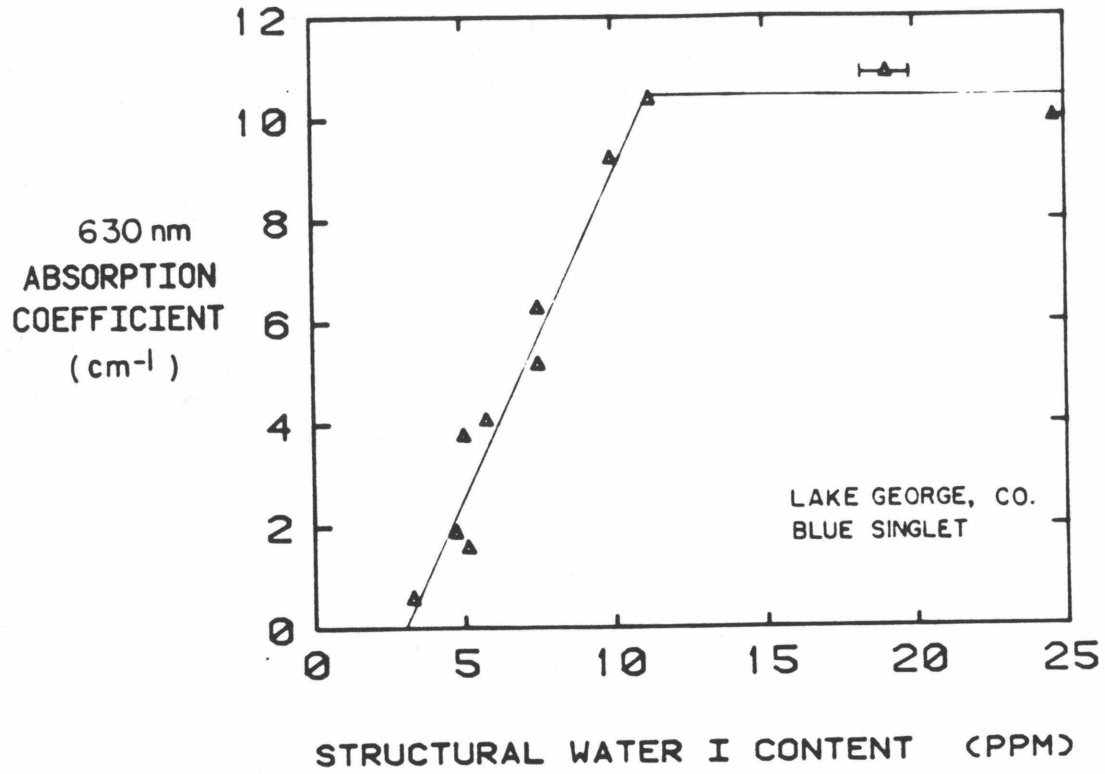


Figure 6.30 Variation of color with structural water by dehydration of amazonite #12, Type B from Lake George, Colorado. Dose, 40 MRads. The correlation is linear below 12 ppm H₂O. Saturation occurs at higher structural water concentrations.

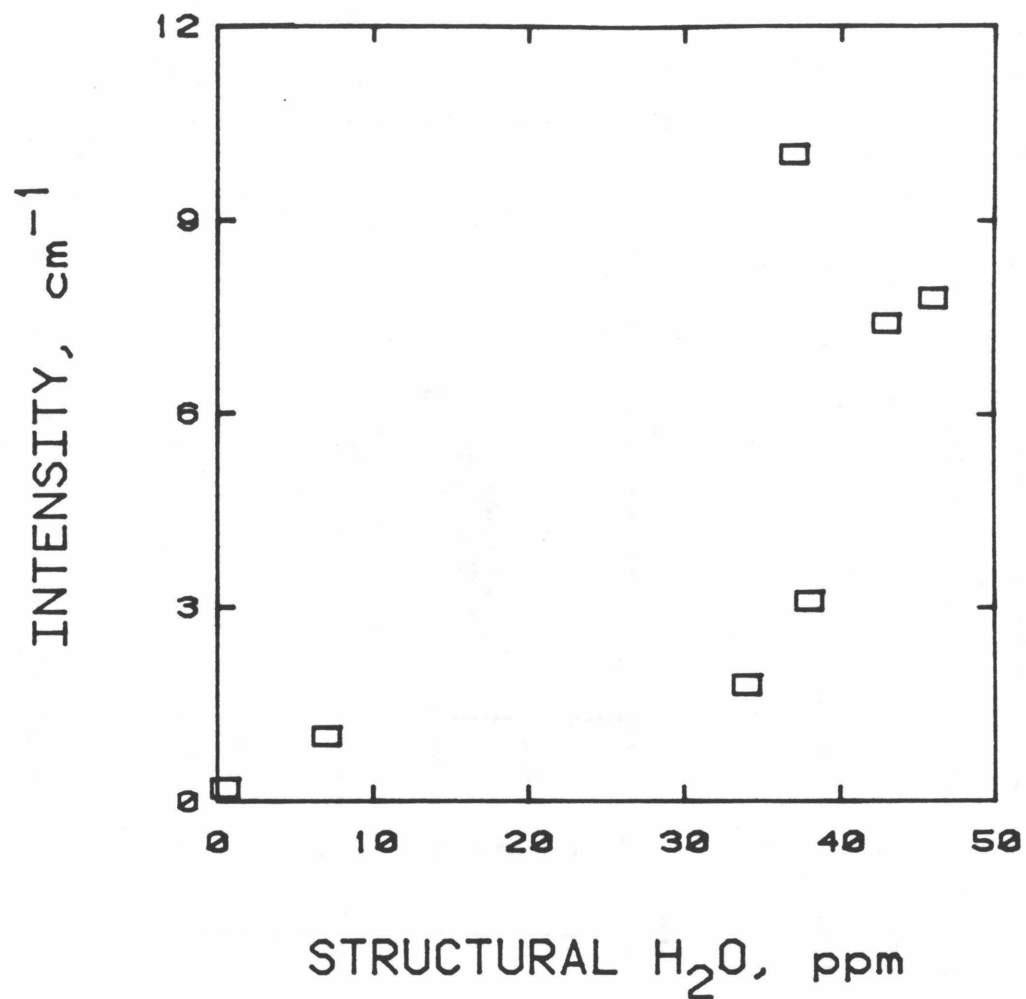


Figure 6.31 Dependence of color on structural water concentration for dehydrated orthoclase #3". Type G, Broken Hill, Australia. Dose 30 MRads. The correlation is nonlinear for the high structural water contents.

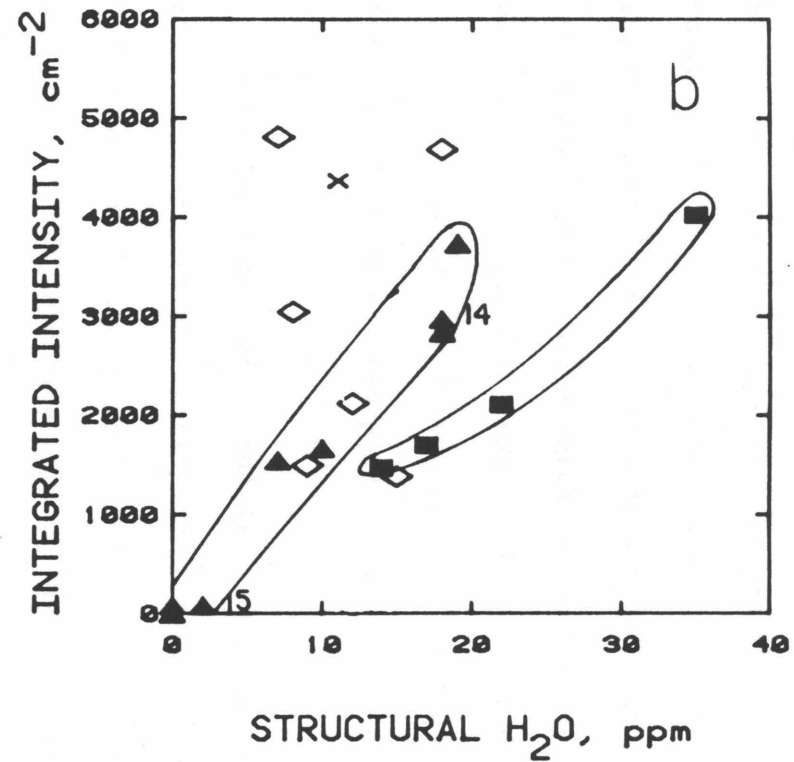
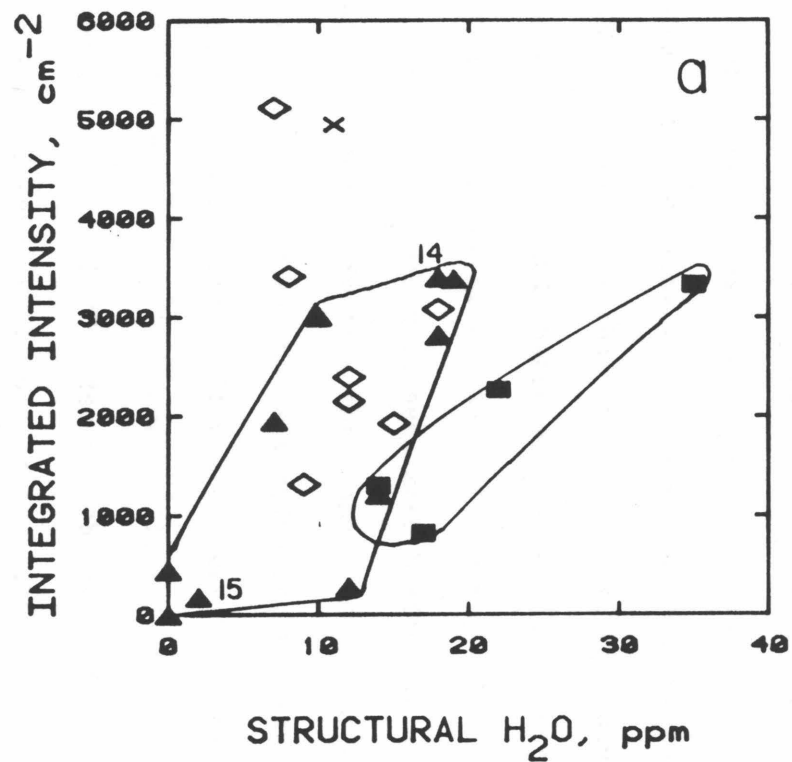


Figure 6.32 Dependence of amazonite color on structural water content. (a) Natural color. (b) Irradiation enhanced color. Filled triangles, type B blue singlets. Open diamonds, type D doublets. Filled squares, type G green singlets. X, type T blue-green singlet. The two numbered samples have molar water in excess of molar lead, and were plotted where their molar water equals their molar lead. Data point envelopes enclose the two end-member color types. Both a triangle and a diamond (not shown) intersect the origin of both graphs. The increases and decreases of color upon irradiation produce more constrained trends for the B and G types.

water is the limiting factor in coloration for samples with more molar Pb than molar H₂O. The fact that the effective water contents of samples #14 and 15, which have more molar H₂O than Pb, plot on the same trend strongly suggests that Pb and H₂O occur in a one to one ratio to develop amazonite color centers. Some doublets do not occur within the trends defined by the type B and type G samples which may be related to the partitioning of the water among the two different types of color sites. The one type T sample also plots outside the B or G trends, but this is almost certainly due to differences among molar absorptivity for the three different types of amazonite singlet.

From the ranges of Pb and H₂O concentrations in amazonite, and the lattice parameters and density of potassium feldspar, the likelihood of the H₂O being near Pb can be estimated. On the average amazonites have 20 ppm structural water, and blue samples have 450 ppm Pb while the green samples have 18000 ppm Pb. These concentrations show that on the average one H₂O molecule occurs per 4500 potassium ions, and blue samples have one Pb ion per 1500 potassium ions while greens have one Pb ion per 40 potassium ions. These numbers show that statistically, H₂O molecules in the blue amazonites have about a 0.06% chance of having the closest M site occupied by a Pb ion, while H₂O in the green amazonites has about a 1% chance. Statistically, Pb and H₂O should occur in separated M-sites in all amazonite types. Thus, either H₂O is affecting the transformation by gamma rays of Pb²⁺ to Pb³⁺ from afar, or Pb and H₂O are being incorporated together in potassium feldspar as it forms. If H₂O affects the irradiative transition regardless of distance to Pb, then eventually all ordinary lead would be transformed to the chromophore Pb³⁺. Because the intensity even of saturated samples does not depend on Pb content (Section 6.3.d), then the effect of H₂O in

the creation of color is limited in space. For Pb^{3+} to form, structural water must occur close to the lead ion. It is likely that much of the structural water is incorporated with Pb during growth, but that part of the structural H_2O occurs separately. If this proportion varies slightly among the amazonites, the trends seen in Figure 6.32 would definitely occur along with a significant amount of deviations.

6.8.d Calculation of extinction coefficients and comparison of amazonite color center to Pb^{3+} and Tl^{2+} in KCl

Extinction coefficients can be calculated from the two trends in Figure 6.32b by using effective molar lead contents which are equal to the molar water concentrations. For type B amazonite, $\epsilon = 4300 \text{ l/mole}\cdot\text{cm}$, and for type G, $\epsilon = 2500 \text{ l/mole}\cdot\text{cm}$. Oscillator strengths can be calculated from

$$f\# = 4.8 \times 10^{-9} \epsilon W_{1/2} \quad (6-9)$$

where $W_{1/2}$ is the full width at half height. This gives $f\#$ equal to 0.066 for type B amazonite color and $f\#$ equal to 0.038 for type G color for the Pb^{3+} absorptions in the visible. The oscillator strength for the 385 nm peak (using Figure 6.7) is 0.044, and that of the 330 nm peak is 0.038. These oscillator strengths are comparable, but slightly lower than those of isoelectronic Tl^{2+} in KCl (0.13 to 0.23: Delbecq et al, 1966). Oscillator strengths of Pb^{3+} have not been previously measured (See section 1.2.6.V).

The number of bands for Pb^{3+} in potassium feldspar is three for type B and one for type G. For Pb^{3+} and Tl^{2+} in KCl, 4 bands were observed, but two were at UV wavelengths not investigated in this study. For the type B amazonite, the fourth band may be the shoulder at 270 nm observed by Tarashchan et al [1973].

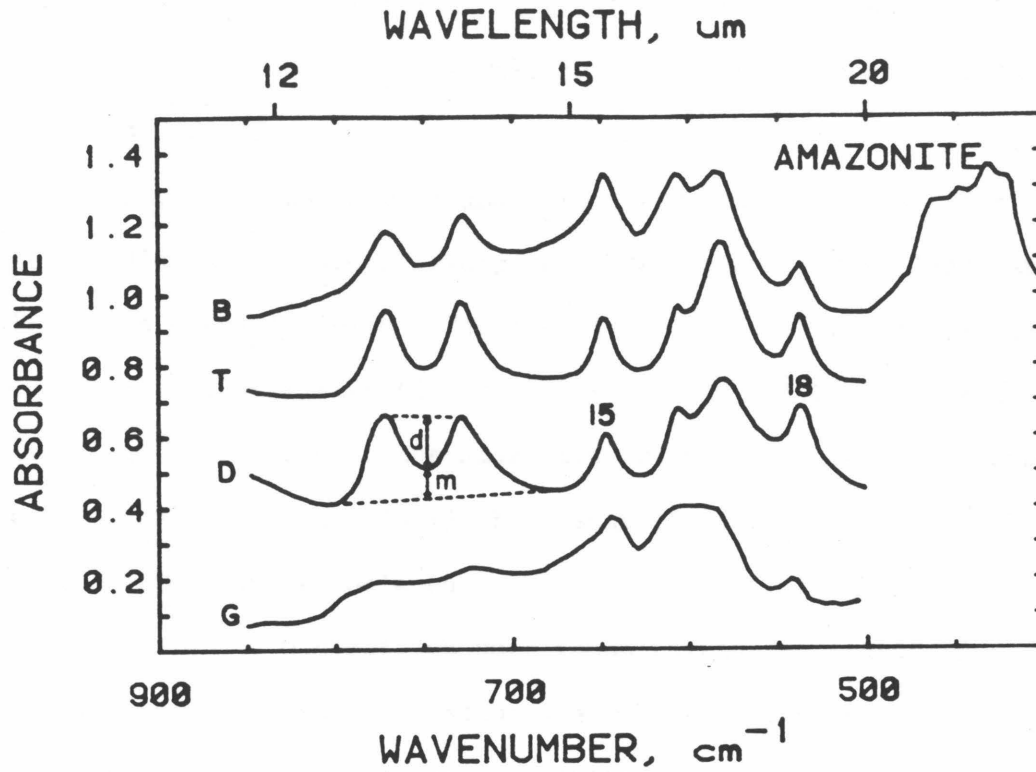


Figure 6.33 Infrared powder absorption spectra of amazonites. B, #4 from Wigwan Creek. T, #21 from Keivy, USSR. D, #19' from New York Mts. G, #3" from Broken Hill, Australia. Spectra were offset for clarity. The positions of the bands numbered 18 and 15 μm were used as a measure of Al/Si order/disorder, as was the ratio d/m , where d and m are the intensities indicated near 13 μm .

overlap to the average height of the two peaks was also measured for the amazonites, but because this measure was found to be proportional to d/m , it was abandoned.

Figure 6.34 shows that amazonites give the same trend for λ_{18} versus λ_{15} as did the potassium feldspars of Hafner and Laves [1957] and Martin [1968; as cited in Smith 1974, Vol. I, p. 520]. Microclines (all perthites) occur as a cluster near (18.65 μm , 15.45 μm). Orthoclases are separate and diagonally offset. The amazonite orthoclases are at the upper end of the trend (near the microclines) which suggests that these are relatively well ordered for orthoclases.

Because the microclines were found to cluster together using the peak position method, peak separation was used as the measure of Al/Si order. The order/disorder is apparently limited in amazonites by the amount of structural water involved in coloration (Figure 6.35a). The order also seems to be limited by the amount of fluid inclusion water (Figure 6.35b). It is possible that fluid inclusion water formed from structural water during cooling and ordering so that the two concentrations are related. It is also possible that a disordered feldspar may hold more water.

Yund and Tullis [1980] previously showed that the rate of disordering increased with higher concentrations of water. Figure 6.35 suggests that the rate of ordering is diminished by high concentrations of water; possibly, comparisons between laboratory disordering experiments and geologic ordering processes cannot be made.

Order in amazonites is further influenced by lead content (Table 1.6). With increased incorporation of Pb into the potassium feldspars, the maximum amount of order that is possible decreases (Figure 6.36), such that at very high Pb content ($\sim 2\%$) only orthoclase occurs. The various color types are

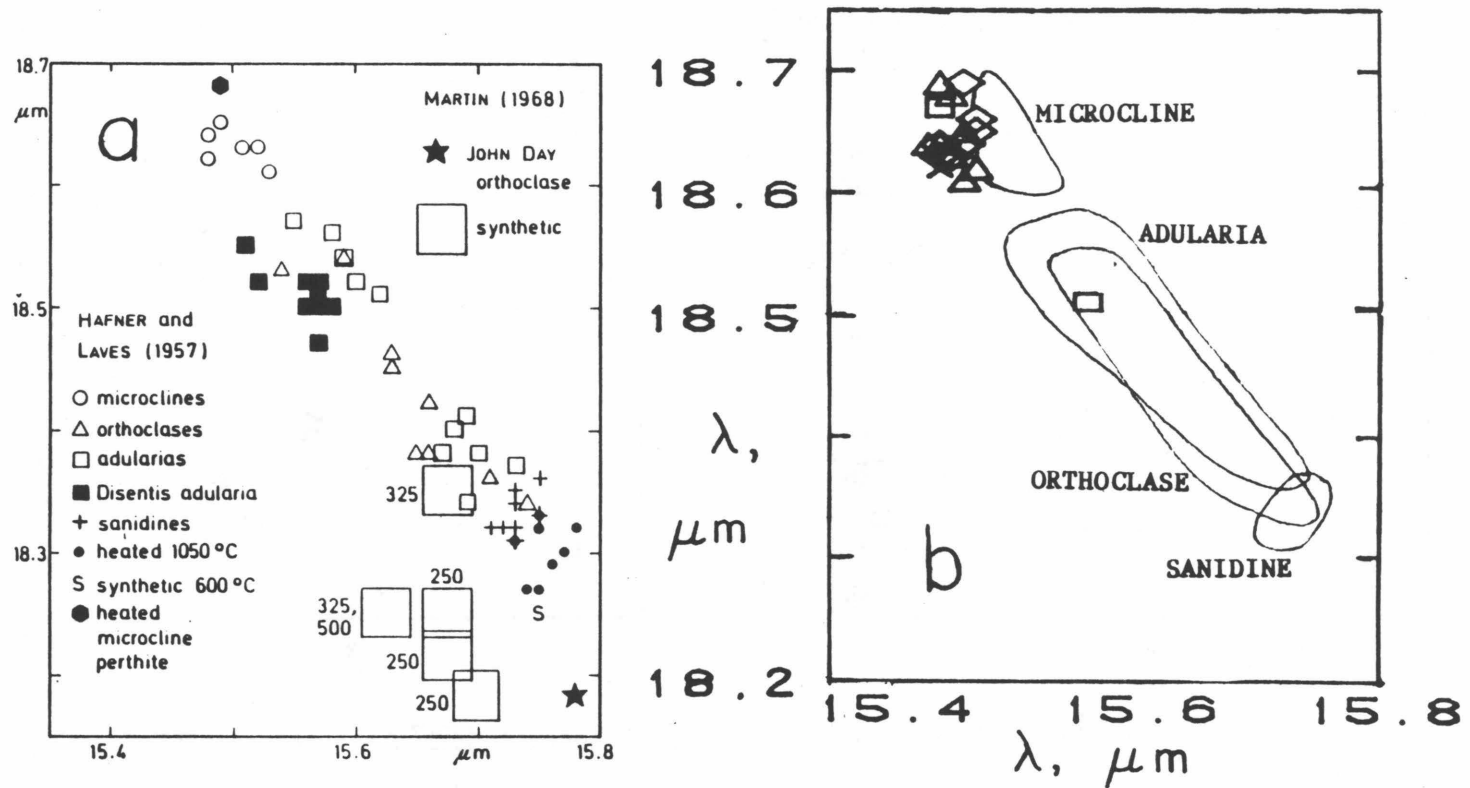


Figure 6.34 Relation between two IR wavelengths in potassium feldspar. (a) Data from Hafner and Laves (1957) and Martin (1968) as depicted by Smith (1974, I, p. 520). (b) Data for amazonites of this thesis. Triangles, blue singlets. Diamonds, doublets. Squares, green singlets. X, blue-green singlet. Dots, white potassium feldspars related to amazonites. The microcline amazonites cluster at the upper end. The orthoclase-amazonites fall nearer to microclines than to the sanidines of (a).

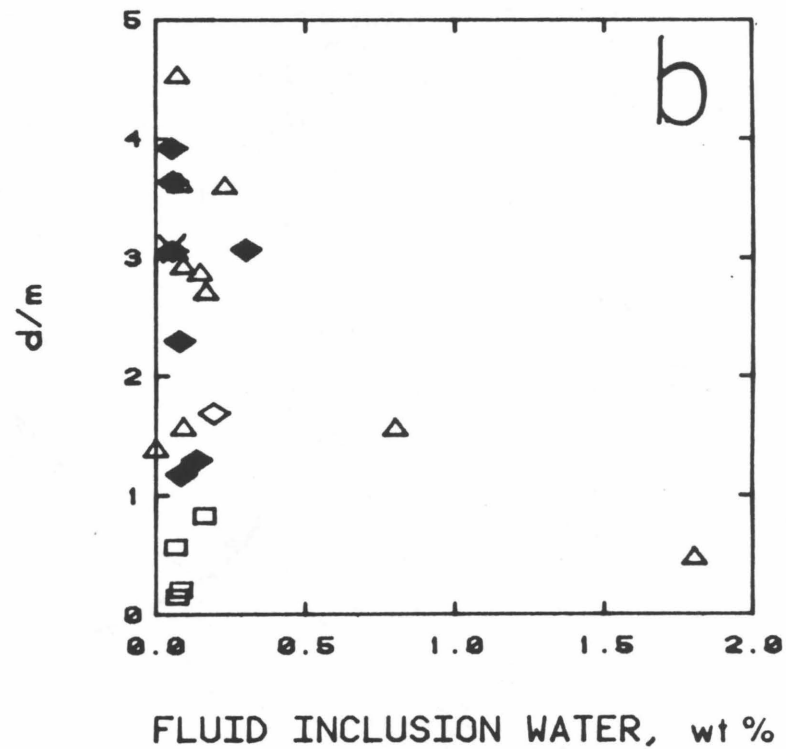
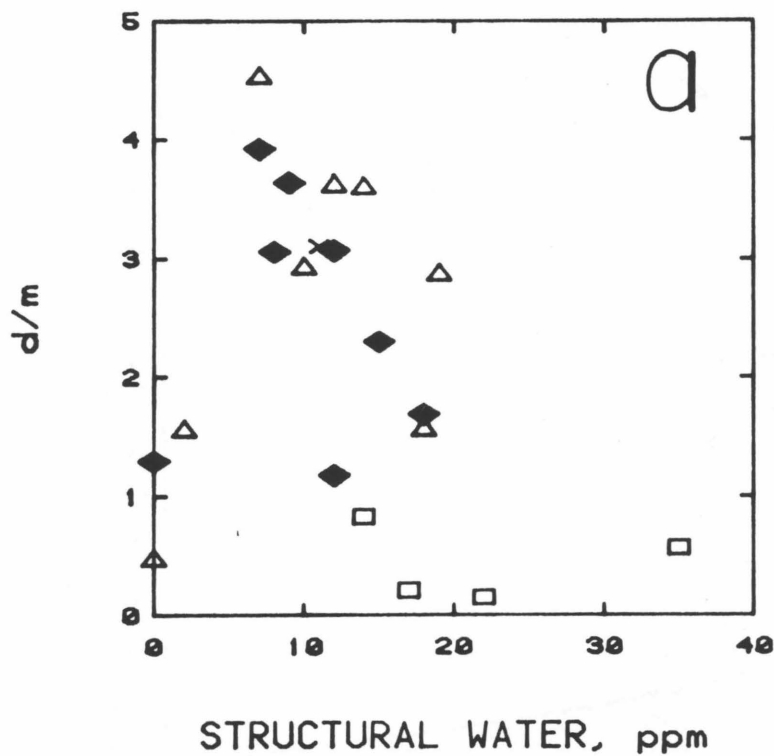


Figure 6.35 (a) Order parameter d/m as a function of structural water concentration. For sample #14 effective water concentration was used because only part of the water is involved in amazonite color. Symbols are the same as in Figure 6.34b. The upper limit to the order parameter depends linearly on the amount of structural water incorporated in the amazonite. (b) Order parameter as a function of fluid inclusion water concentration, same symbols. Order decreases as more water is incorporated in the feldspar.

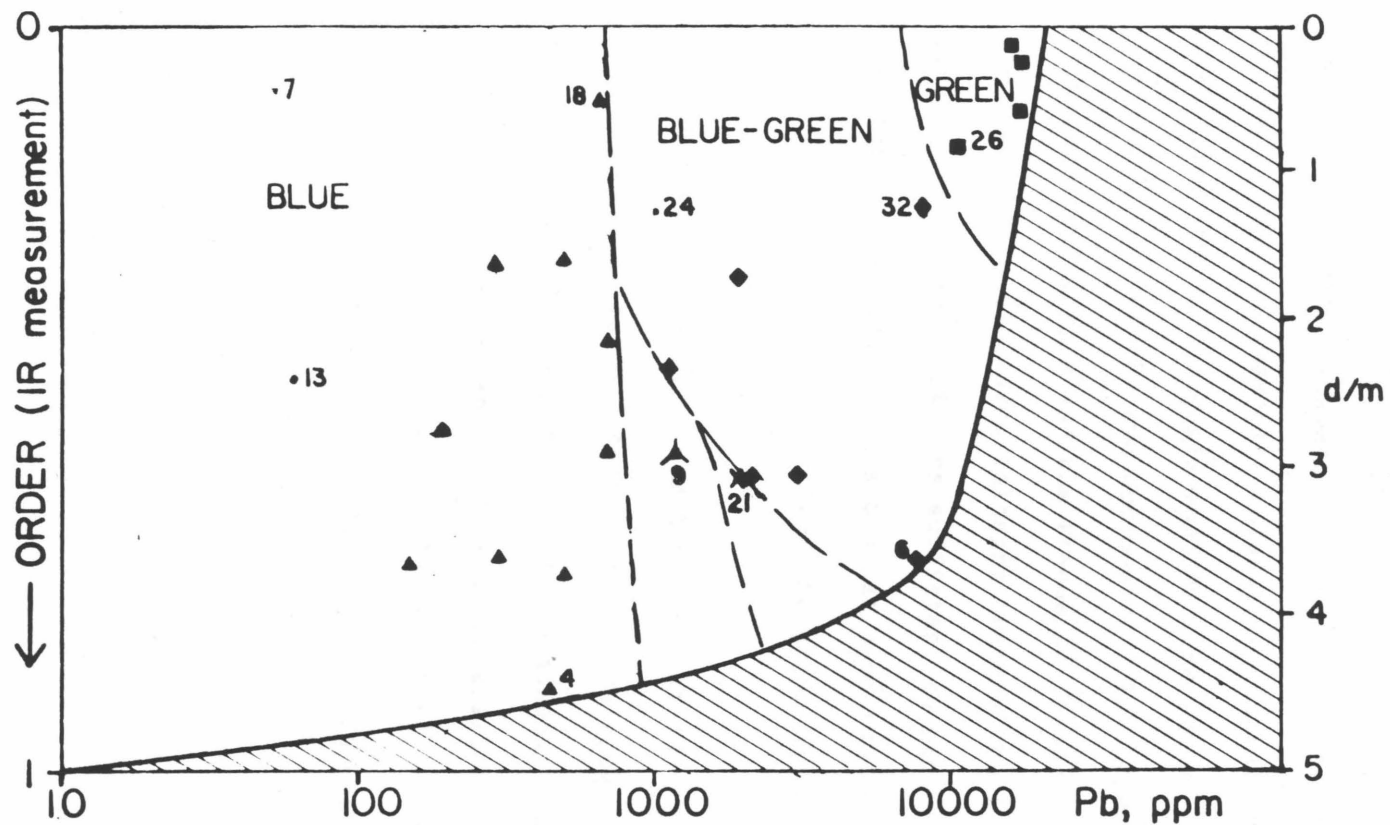


Figure 6.36 Order parameter d/m as a function of lead content of amazonites. Dots, uncolored. Triangles, type B. Diamond, type D. Square, type G. X, type T. Triangle plus lines, type B with additional EPR Pb^{3+} signals. The graph was sectioned according to color type. Dashed lines also show the boundaries of amazonite formation. As more lead is incorporated, the maximum amount of order that is possible decreases.

restricted to specific amounts of Pb content and ordering. Type B (blue singlets) occur at low Pb contents. Type G (green singlets) is limited to high Pb and low order. Doublets (D) have intermediate Pb content and an intermediate order parameter. At intermediate Pb content and high amount of order, unusual amazonite coloration occurs, such as the Keivy #21 sample with three EPR Pb^{3+} signals and the Lake George #9 with two EPR Pb^{3+} signals. The association of the two end-member color types (B and G) with the two structural polymorphs and the trends of Figure 6.36 suggest that incorporation of Pb into potassium feldspar changes the lattice locally, such that large amounts (about 2%) are sufficient to produce an overall orthoclase structure. Amazonite with a doublet spectrum must have both "orthoclase" and "microcline" sites for Pb^{3+} even though on the average the crystals are microcline.

The type T amazonite and blue singlet #9 with multiple EPR amazonite sites are likely to represent intermediate stages in the conversion of microcline to orthoclase by Pb incorporation. The additional EPR sites can only be slightly distorted from the solitary site seen in low Pb type B amazonites, because sites completely distorted to "orthoclase" do not give an EPR signal at liquid nitrogen temperature. The slight distortion of microcline sites is expected to produce a small shift in the energy of the optical bands, as observed for type T sample #21 (400 cm^{-1}). Sample #9 exhibits less distortion in the EPR and a smaller optical shift (200 cm^{-1}), which corroborates the supposition of intermediate structure of amazonite sites.

6.10 Evidence for Amazonite Coloration of Sodic Plagioclase

Pale blue colors occur in cleavelandite and oligoclase (Section 1.2.b.v). Visible spectra taken from cleavage faces of three gemmy blue sodic plagioclases (two albites from Africa and oligoclase from South Carolina, Figure 6.37) show that the blue color arises from a broad band similar to that which produces amazonite color in potassium feldspar. The natural band in sodic plagioclase is centered from 605 to 645 nm, has a full width at half height of about 4000 cm^{-1} , and has an intensity from 1.7 (oligoclase) to 2.4 (albite) approximately in the beta polarization. Unlike potassic amazonite, companion bands at 360 and 380 nm were not observed. Other features present are sharp bands at 383 and 421 nm, indicating ferric iron in tetrahedral sites, and a weak broad band at 1100 to 1200 nm in the albites which may indicate ferrous iron in an M-site (Section 3.2)

The similarity of the blue plagioclase spectra to those of amazonite is suggestive, but for the plagioclase blue to be designated amazonite, proof that Pb^{3+} is the chromophore is needed. This was tested directly by EPR spectroscopy, but no signature attributable to Pb^{3+} was observed in the oligoclase. (Neither albite was tested.) The absence of the Pb^{3+} signal in EPR does not rule out amazonite coloration, because this signal was not observed in any of the orthoclase amazonites, probably due to the disorder present and the accompanying broad signals. The gemmy nature of the oligoclase suggests an intermediate structural state, because peristerite is the typical low temperature polymorph at low anorthite contents [Gay, 1955]. Thus, the structure of these plagioclase samples probably prohibits direct confirmation of Pb^{3+} as the chromophore.

The amazonite mechanism can be tested indirectly by comparing other characteristics of the color. Thus, for the blue color in plagioclase

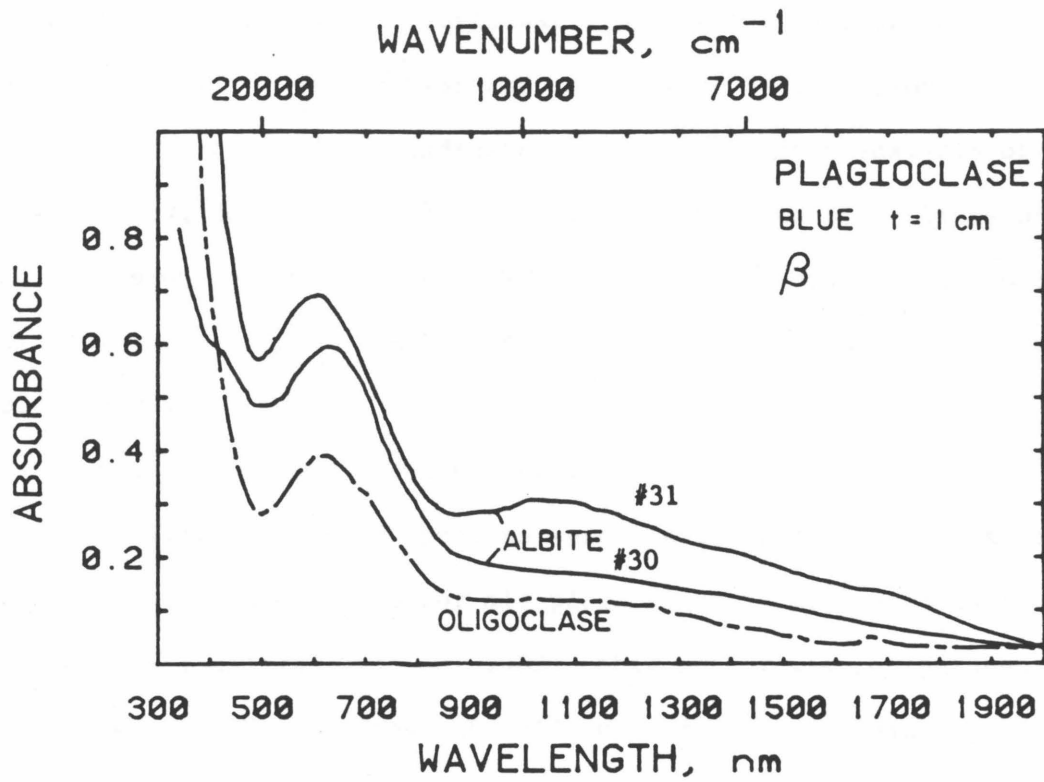


Figure 6.37 Visible spectra of blue sodic plagioclases. The spectra were taken on 010 perpendicular to 001, so the polarization is nearly beta. Spectra were scaled for 1.0 cm.

to be amazonite, the visible spectra must be similar in polarization and band shape, lead and structural water must exist in plagioclase, and the color must be removed by heat and regenerated by radiation.

A trace of lead was indicated in the microprobe analysis of oligoclase (Sample #29, Table 6.3). By comparing intensities of Pb lines of plagioclase to potassium feldspar through XRF, the lead contents were estimated at $\pm 30\%$ of the amount present. Albite #30 has 180 ppm Pb, while oligoclase #29 has 350 ppm Pb.

Structural water was not detected by IR spectroscopy of the oligoclase (Section 4.3.c); instead, protons were speciated at OH^- . Because OH^- speciation has been noted for all plagioclase investigated so far (Section 4.3.c), [Solomon and Rossman, 1982], this matter was not pursued further.

Figure 6.38 shows that the 612 nm band in oligoclase is polarized in beta. This is similar to amazonite color which is also polarized in beta, because in both cases beta is nearly perpendicular to (001). For albite, the band is probably in beta, as suggested by spectra taken on the 010 cleavage face (Figure 6.37). The band width for the plagioclases (4000 cm^{-1}) is wider than that of the singlet bands ($3200\text{ to }3750\text{ cm}^{-1}$) the potassium feldspar, but narrower than that of the doublet (4500 cm^{-1}). The position of the band in plagioclase is similar to the type B or T color of potassium feldspar, but only one band was observed as is the case for type G. Because band structure is certainly related to the structure of the feldspar, the plagioclase spectra should be more like type G of the orthoclases.

That the blue color of plagioclase can be removed by heat was demonstrated by Rudenko and Vokhmentsev [1969]. These experiments were not repeated because of the possibility of total destruction of color as observed for the Russian plagioclases and in some potassium amazonites, and also

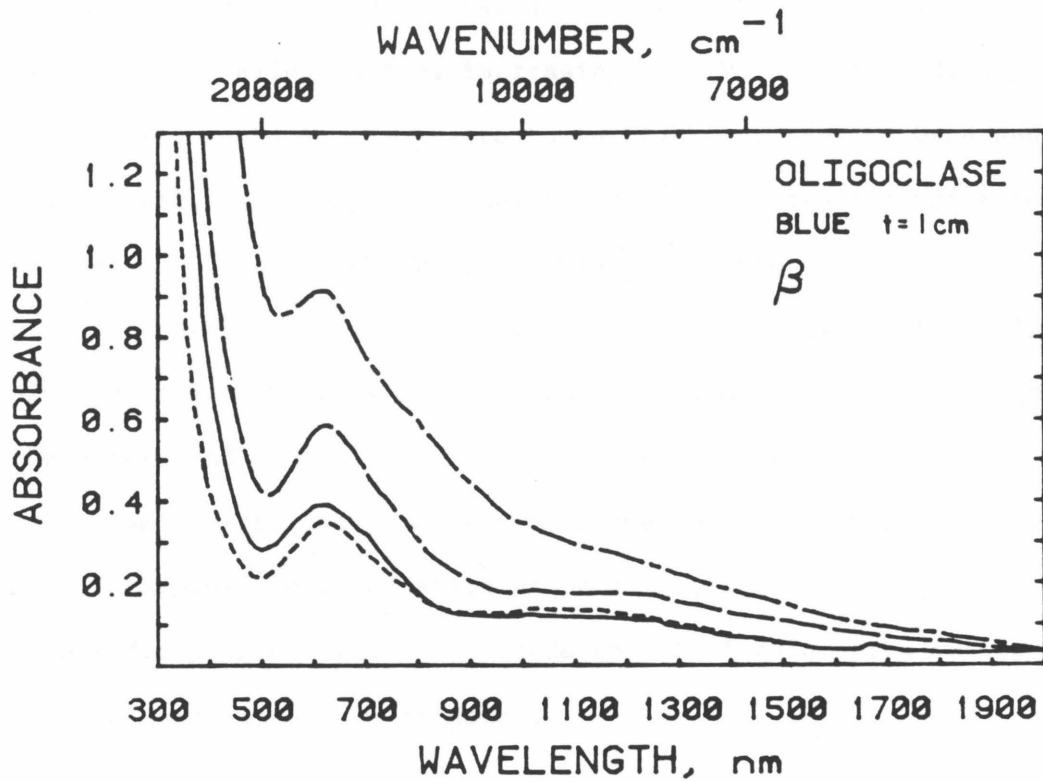


Figure 6.38 Polarized visible spectra of blue gemmy oligoclase from South Carolina. Spectra are scaled for 1.0 cm thickness. The blue color results from the polarized, broad band in beta at 614 nm, which strongly resembles the type T band in potassic-amazonite.

because of the scarcity of the blue plagioclase samples.

Radiation not only increased the intensity of the blue color, but also added a yellow cast by increasing the UV tail, and added a band at 850 nm (Figure 6.39). Exposure to sunlight removed the band and reduced the UV tail, which suggests that these features are analogous to smoky coloration of sanidine (Ch. 5). This is corroborated by observation of the H center (Section 5.4) in the EPR of blue oligoclase, but not in the other plagioclases. The blue color is not affected by sunlight, but bleaching the other bands shows the 614 nm band more clearly.

Based on similarities of band shape, position, width, and polarization, and of response to irradiation and heating, and on the presence of lead in blue sodic plagioclases, I conclude that Pb^{3+} coloration occurs here, as in blue-green potassium feldspars.

6.11 Attempts to Synthesize Amazonite

Three approaches were used in endeavors to synthesize amazonite: ion exchange of feldspar in molten $PbCl_2$; ion exchange in lead-chlorite-water solution, and high pressure cooking of oxides plus water or feldspar plus water. None were successful.

Ion exchange was performed with mm sized chips of both microcline (sample #1") and adularia (St. Gotthard, Switzerland). Irradiation of samples did not produce a blue-green color in any portion of the sample. Microprobe determinations of samples polished at an angle showed that most of the lead was deposited on the surface (probably as some type of oxide) but that a slight amount of lead penetrated into the sample, possibly up to a micrometer in depth. Because samples of similar microcline (0.25 mm thick) were completely dehydrated by the same temperatures and times the

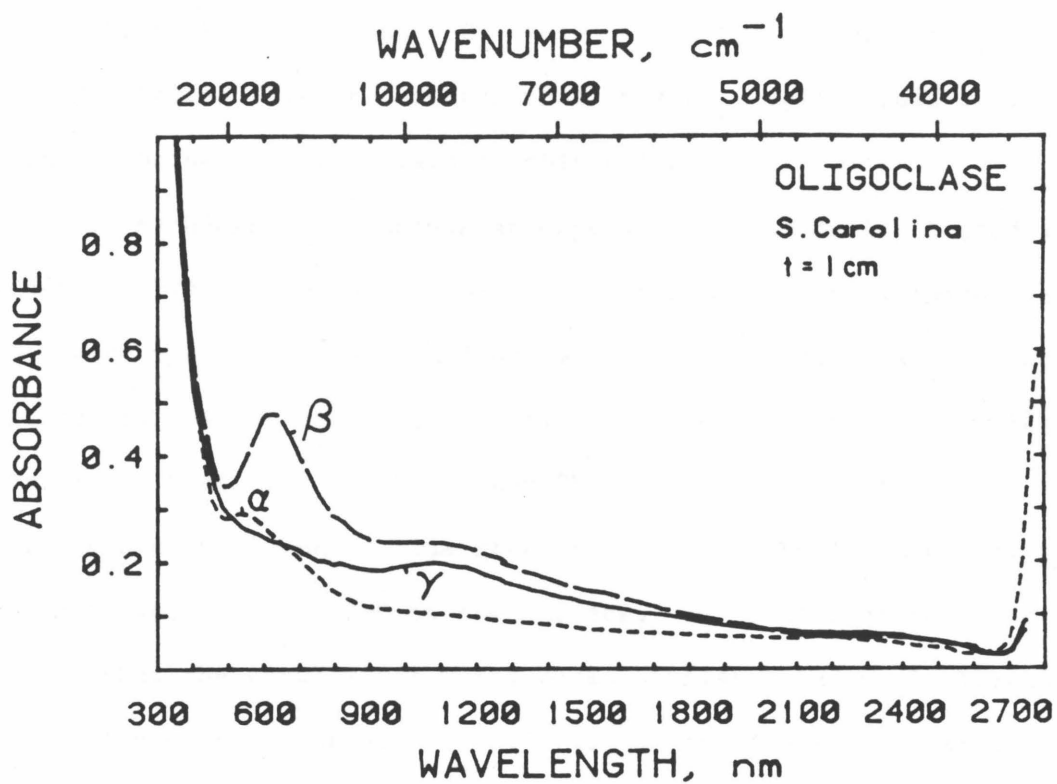


Figure 6.39 Visible spectra of natural, irradiated, and sun-bleached oligoclase. The orientation is nearly beta [on (010) perpendicular to (001)]. Irradiation develops a band at 850 nm and enhances the UV tail. Sunlight removes these effects and reveals that the 614 nm band was also increased by gamma-radiation.

ion exchange experiments were performed at, it is highly likely that the feldspars cooked in molten PbCl_2 were dehydrated deeper than the lead ions penetrated. It is doubtful that amazonite color could be produced even in the wettest feldspars by this method.

Ion exchange in brine was attempted in an internally heated pressure vessel (IHPV) at Stanford with Prof. Gordon Brown's permission. Samples used were again colorless, hydrous microcline 1" from the Elizabeth R Mine, California. After the run, the chips had a opaque yellowish white coating similar to that seen in the molten PbCl_2 exchanges. Irradiation of these samples did not induce a blue-green coloration. Microprobe analysis of the chips showed 0.34 wt% PbO on the surface. IR spectra of polished samples showed that the samples had water peaks similar to natural microcline: the absorption coefficient at 3620 cm^{-1} of the treated sample was 20/cm, while similar untreated samples give 18/cm. The higher absorptivity of the treated sample is within the range seen in feldspars from the Pala pegmatites. It is likely that the lead was entirely deposited as a coating on the surface so that a proper feldspar structure with lead and water substituents was not formed in the brine exchange experiment.

Table 6.14 summarizes the run conditions for synthesis attempts with the Clifton press. In this series of experiments, pressures were initially chosen to duplicate the inferred formation conditions of the Colorado pegmatites. Calibration of the press by G. Fine showed that pressures below 8 kbar were unreliable, such that the sample tube is probably not pressurized below about 8 kbar. Thus, the three earliest runs were likely near atmospheric pressure, which explains the bubbles (outgassing) in the highest temperature run. The fourth and final run was made at 8 kbars and 700°C which is similar to the metamorphic conditions for the Broken Hill amazonite,

Table 6.14 High Pressure Synthesis Attempts

Starting Material	P*,kb	T,°C	Time,hrs	Results	Comments
Oxides KAlSi ₃ O ₈ :0.1 wt % Pb	~3	900	6	Glass w/bubbles	Above liquidus, H ₂ O exsolved
	"	700	1.5		
	"	500	2.5		
Oxides KAlSi ₃ O ₈ : 2wt%Pb	3	650	23	Powder	Subsolidus
Broken Hill Amazonite, #3", dehydrated	3.6	650	24	Powder	Subsolidus
Keivy USSR Amazonite #21, dehydrated	8.0	700	23	Powder	Subsolidus

* Pressure calibration by G. Fine revealed that the early runs nominally at 3 kb were probably not pressurized.

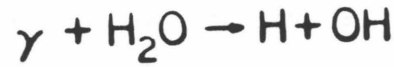
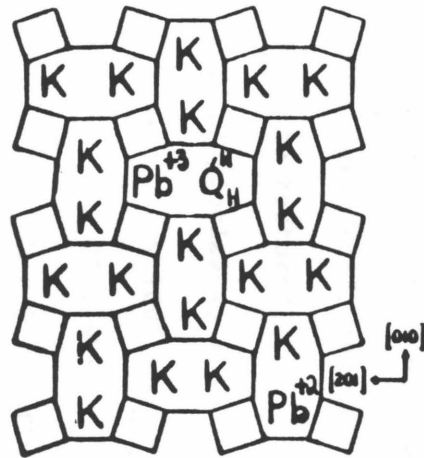
but apparently still below solidus for the Keivy USSR amazonite.

None of the methods described resulted in blue feldspar. It is possible that use of the press at higher temperatures at 8 kbars could produce amazonite. A better approach would be use of hydrothermal bombs, which allow larger quantities of material in a run. Use of gels and longer run times could overcome sluggish feldspar nucleation, and would help to diffuse the essential ingredients (Pb and H₂O) through the batch.

6.12 A Model for the Mechanism of Amazonite Coloration

In developing a model to explain how amazonite color is produced, the following observations must be accounted for: 1) The chromophore is Pb³⁺, such that the hole spends 31% of its time on the lead and the remainder on coordinating oxygens; 2) Irradiation is necessary to produce the color; 3) The maximum coloration developed (i.e. the number of color sites) depends on the concentration of structural water; moreover, a one to one ratio of Pb to H₂O for the color sites is indicated; 4) The structural water bands are unchanged by radiation; 5) Different color types depend on the structure of the feldspar, both locally and overall; 6) H₂O prevents smoky coloration.

I propose that amazonite coloration proceeds as illustrated in Fig. 6.40. The prime prerequisite is incorporation of Pb and H₂O in the pairs of M-sites which closely approach each other. Lead incorporated by itself does not transform into Pb³⁺, and is hence "inactive". Gamma radiation from ⁴⁰K disassociates water molecules, forming the radicals H and OH. The mobile component, H, diffuses. The stationary component oxidizes a nearby oxygen, forming OH⁻ and an O⁻ hole center. This hole is shared with the adjacent Pb ion, forming Pb³⁺ and thus amazonite color.



RADIOLYSIS
OF WATER:

H DIFFUSES



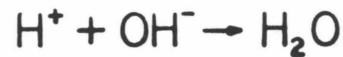
HOLE CENTERS
CREATED



AMAZONITE
COLOR



ISOLATED HOLE
CENTERS RUINED



WATER
RECYCLED

Figure 6.40 Summary of model for amazonite coloration by irradiation.

Right-hand side, schematic of feldspar structure, showing inactive lead Pb^{2+} , and active lead which is incorporated near H_2O in an M-site.

Lefthand side, list of steps in the process of conversion of Pb^{2+} to Pb^{3+} by irradiation activated water.

Meanwhile, the radical H probably encounters an SiO^- -K hole center (smoky center) which was created by radiation and reduces it. Finally, the proton settles in a stable site, most likely one similar to that from which it was removed.

It may be questionable that the water is recycled. However, H_2O is the stable form of hydrogen in microcline, and quartz has been shown to exhibit similar motion of hydrogen ions and final location in stable sites [e.g. Kats, 1962, p.194]. Also, smoky color is faint in amazonites, but is strongly developed once the water is removed. The migration of the H radical through the lattice and its synchronous oxidation can account for suppression of smoky color. Finally, the proposal of OH being stationary and being involved in the oxidation of lead is absolutely necessary: if the oxidizing agent were mobile, then all Pb in the amazonite could be converted to Pb^{3+} , which clearly does not occur.

Occasionally, amazonite color decreases upon irradiation. This behavior can be accounted for in this model as the removal of an H_2O molecule from a color producing site in that electrons independently released by irradiation could recombine with Pb^{3+} ; and without the neighboring water molecule, the site could not be restored.

For blue plagioclases, a slightly different mechanism is proposed:



There is not enough atomic hydrogen to eliminate all smoky (O^-) centers, so that some form upon irradiation along with the amazonite.

CHAPTER 7

COLORATION OF LAKE COUNTY LABRADORITE BY EXSOLUTION OF METALLIC COPPER

7.1 Geologic Occurrence

The sunstone bearing basalt flow is located in Township 33 south, Range 24 east, section 11, 6 miles north of Rabbit Hills in Lake County, Oregon. The sunstone flow covers about two square miles, and has been set aside by the state as a public collecting locality (except for two small claims). Previous work on this and related flows is discussed in Section 1.2e. This section summarizes my observations and those of Robert Rodgers (who is mining one of the claims) on the distribution of the colored phenocrysts within the flow.

The sunstone flow is at least three meters thick, and is underlain by a reddish mudstone about 10 cm thick. The basalt is holocrystalline, highly vesiculated, and consists of approximately 40% labradorite phenocrysts which can attain a maximum dimension of 6 cm. The topography is flat. Outcrops are rare, but the surface is studded with phenocrysts weathered out from the flow. The labradorite is mined by digging pits and sifting weathered basalt.

Almost all of the labradorites possess only a yellow hue due to tetrahedral Fe^{3+} . However, in two small areas of about 1/8 square mile each approximately 90% of the phenocrysts are of this ordinary type, but (as a rough estimate) 9% possess a pink schiller, 1% have a red tint, and 0.1% are green. These colors will be described in detail in Sections 7.2 and 7.4. Within the colored-phenocryst bearing areas, the colored feldspars seem to group together, forming "pods". One pod can contain mostly one type of colored stone, but usually a mixture of ordinary labradorite and the more unusual colored varieties occurs. No differences were noted

between basalt containing colored phenocrysts and basalt containing ordinary phenocrysts. The flow appeared contiguous.

A schiller very similar to that of the Lake County labradorite was observed in phenocrysts from a basalt flow of Crater Elegante, Sonora, Mexico. The geology of this occurrence is described by Gutmann [1976].

7.2 Description of Colors and Schiller

Previous work on colors occurring in Lake County labradorite is discussed in Section 1.2.a.viii. Most crystals are gemmy, and twinned on a centimeter scale. All are yellow due to Fe^{3+} in tetrahedral sites. For a millimeter thick crystal, the hue is like pale straw. This color is covered in Chapter 3, and will not be discussed here. Two other tints exist: red or green. The red is similar to the color of candied apples and varies from pale pink to deep red, independently of crystal thickness. The red is weakly pleochroic. The green color is strongly anisotropic with a polarization scheme of true green/orange/colorless, such that the combination gives muddy tones. The green also varies in intensity independently of crystal thickness. For the most deeply colored crystals, the green color blends into a bluish green.

The schiller can give a distinctly pink cast to the entire crystal when viewed in reflected light. The schiller consists of platelets up to 40 μm in diameter and about 0.2 μm thick oriented on (010) and (001). In reflected light, the platelets are extremely bright, copper-pink in color, and isotropic by themselves, although the optics of the feldspar may cause apparent anisotrophy. The platelets have a conchoidal texture. In transmitted light, the platelets are opaque in the center, but translucent brown on the edges. A few platelets on the surface were white in

reflected light.

The colors and schiller can occur separately or in any combination in a single crystal, although the latter is more common, and green rarely occurs alone. Frequently, the color is confined to one area of the crystal, although it may cross twin planes and cracks. Color occurs both at the edges and in the centers of crystals. Zonations are common, the sequence being colorless, green, red, and then schiller. The red grades into the schiller, but boundaries between the colorless and green or the green and red are sharp. Zonation can be in parallel layers, concentric or irregular. If it is concentric, then the green always encircles the red. Irregular zonations consist of green and red overlapping or schiller interspersed through a green or red bearing lath.

Schiller in labradorite from Crater Elegante similarly consists of small copper-red, highly reflective platelets (10 μm diameter, $<0.2 \mu\text{m}$ thick) oriented on (010) and (001). (Most schillers in feldspar are unoriented as discussed in Section 1.2.a.vii.) The platelets are usually clustered in groups of 3 to about 50. Schiller occurs in about 10% of the phenocrysts I have examined. The schiller was not described by Gutmann [1977]. Chemically and structurally, the labradorites from the two localities are very similar [Stewart et al, 1967; Gutmann and Martin, 1976]. The only detectable differences are the existence of tubular voids and fluid inclusions in the Crater Elegante phenocrysts [Gutmann, 1977 and 1974], and their finer scale twins (0.1 mm).

7.3 Chemistry of the Schiller and the Colored Zones

Microprobe analyses were acquired from the schiller flakes by polishing the crystal at a small angle (about 3°) to the (001) plane containing the platelets. Three platelets on two crystals were partially removed by the

polishing. Analyses of the exposed crescents listed in Table 7.1 show that copper is present in variable amounts. The other elements present occur in the correct proportions for feldspar, having no excess silicon, and both major and minor elements close to those of the pure labradorite (Table 1.7). This shows that the analysis was picking up some feldspar, and that the schiller flake is some type of copper mineral. The copper-oxide content determined is proportional to the microprobe total (Fig. 7.1) demonstrating that copper is in the metallic state, and confirming Andersen's 1917 microscope observations. Recalculation of copper as Cu^0 (rather than CuO) and subtraction of the excess oxygen from the microprobe total gives recalculated totals near 100% (Table 7.1).

Because no silver was detected for the highest copper analysis, its proportion in the flakes can be no more than 10%. No elements other than copper and those present in the labradorite were observed in the energy dispersive spectrum during analysis, suggesting that the schiller could be pure copper metal.

Copper content (as CuO) also depends somewhat on anorthite content of the feldspar (Fig. 7.1). For a low percentage of copper in the analysis (i.e. mostly feldspar occupying the microprobe beam), the correspondence is weak, but a definite drop in anorthite content is apparent for analysis consisting largely of schiller. If the copper exsolved from the lattice, then this correspondence suggests that copper originally occupied a calcium-like site. Ferrous iron, as shown in Chapter 3, similarly substitutes for calcium.

Because of the smaller size and sparsity, analysis of the schiller in Crater Elegante was not attempted. From the similar appearance and orientation of the flakes, it is likely that the schiller in Crater Elegante

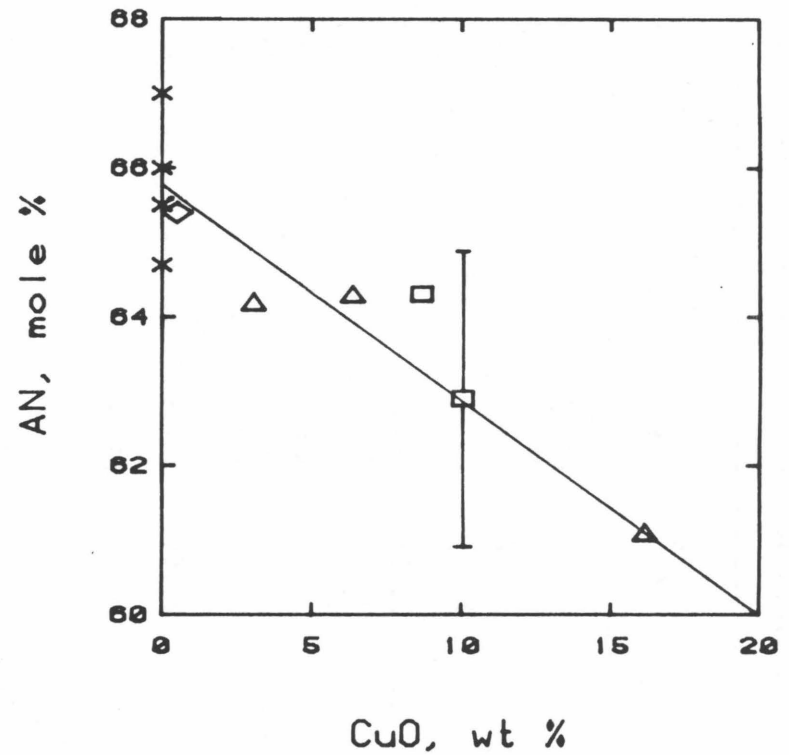
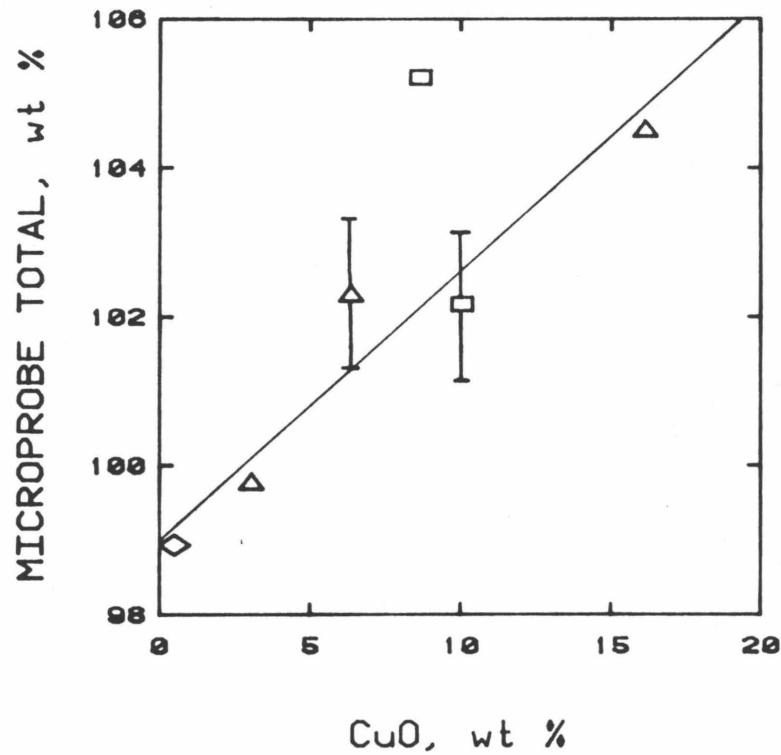


Figure 7.1 Dependence of microprobe total and feldspar's An content on copper concentration. Triangles, shiller #110-B1. Squares, shiller # 110-B2. Diamond, Shiller # 106-B1. X, data from labradorite analysis apart from shiller. Error bars indicate experimental uncertainty.

Table 7.1 Microprobe Analysis of Schiller in Lake County Labradorite

Sample No. Point No.	110-B1 1	110-B1 2	110-B1 3	110-B2 1	110-B2 2	106-B1 1
SiO ₂	45.34	48.23	48.29	46.12	48.48	48.89
TiO ₂	0.02	0.05	0.04	0.04	0.03	0.04
Al ₂ O ₃	27.02	30.13	30.47	28.86	30.13	30.91
FeO _{total}	0.41	0.44	0.46	0.40	0.43	0.44
MgO	0.14	0.15	0.12	0.12	0.12	0.11
CaO	11.39	12.95	13.25	12.48	13.23	13.92
Na ₂ O	3.92	3.89	4.00	3.98	3.98	3.98
K ₂ O	0.12	0.13	0.12	0.12	0.12	0.13
MnO	BLD†	BLD	BLD	BLD	BLD	trace
CuO	16.14	6.34	3.03	10.15	8.67	0.49
AgO	BLD	BLD	BLD	BLD	trace	BLD
Total	104.52	102.31	99.79	102.17	105.22	98.94
Total*	100.49	100.73	99.03	99.66	99.66	98.82
Or	0.8	0.8	0.7	0.7	0.7	0.7
Ab	38.1	34.9	35.1	36.3	35.0	33.9
An	61.1	64.3	64.2	62.9	64.3	65.4

*Total recalculated assuming all copper is in the metallic state

†Below limit of detection

labradorite is also copper metal.

Microprobe and XRF analyses were performed on the differently colored areas of the phenocrysts to determine if any particular chemistry was associated with the color types. Major elements are consistent: orthoclase content is constant and equal to 0.6 to 0.7 mole % while anorthite content varies slightly from 64.7 to 67 mole % (Table 7.2). Copper was below the limit of detection (<0.02 wt%). Iron contents were constant within experimental uncertainty ($\text{FeO} = 0.41 \pm 0.02$ wt%). Titanium was constant and low, except for the red zone. Both the major and trace element chemistries of the colored and uncolored Lake County labradorites are similar to those of phenocrysts from Crater Elegante (Table 7.2). Analyses reported here are also similar to published analyses (Table 1.7).

X-ray fluorescence analyses of the differently colored zones in the phenocrysts show that the impurities Fe, Ti, Cr, Mn, Cu, and Sr are present, but that only the copper content varies with the color by more than a factor of 10 (Table 7.3). Moreover, stones without color zones have very low Cu, and the copper concentration increases from colorless to green to red to schiller, which is the sequence seen in layered and concentrically zoned samples. The variations seen in other elements are only slightly larger than the experimental uncertainty. A larger titanium content for the red zones was not observed. Trace element concentrations observed in two labradorites from Crater Elegante were similar, except for higher SrO and possible TiO_2 contents. Copper was detected in the piece without schiller, but was very low in one sample with schiller. This may be due to the sparsity of the flakes (there were only 5 in the chip which was powdered for analysis).

The copper content measured for a heavily schillered piece (#106)

Table 7.2 Microprobe Analysis of Labradorite and Red Glasses

Location	Lake County, Oregon					Crater Elegante Sonora, Mexico		Cu-ruby	Aventurine
	91§	92§	80	70	106	13760	200	Glass	Glass
Sample No.									
Color	-	Green	Red	Schiller	Schiller	-	Schiller	Red	Schiller
SiO ₂	51.56	51.84	51.62	51.53	50.44	51.27	53.08	60.03	59.18
TiO ₂	0.07	0.06	0.12	0.15	0.05	0.04	0.06	0.04	0.02
Al ₂ O ₃	29.96	30.05	29.43	29.88	30.97	28.85	29.73	0.27	1.48
FeO _{total}	0.04	0.42	0.39	0.41	0.43	0.37	0.39	1.38	2.27
MgO	0.17	0.15	0.15	0.15	0.12	0.07	0.06	0.04	0.16
BaO	trace	0.05	0.05	BLD¶	ND†	BLD	0.03	0.05	BLD
CaO	13.40	13.20	13.26	13.89	14.11	16.15	12.04	8.00	6.62
Na ₂ O	3.73	3.76	3.92	3.69	3.94	3.91	5.54	2.50	0.62
K ₂ O	0.12	0.13	0.13	0.11	0.12	0.27	0.33	5.40	0.45
CuO	NM	NM	NM	NM	BLD	NM	NM	0.13	1.25
PbO	BLD	BLD	BLD	BLD	NM	BLD	BLD	1.01	BLD
Total	99.40	99.70	99.10	99.70	100.18	100.96	101.20	78.8*	72.0*
Or	0.7	0.7	0.7	0.6	0.7	1.35	1.73	-	-
Ab	33.3	33.8	34.6	32.4	33.3	30.06	44.65	-	-
An	66.0	65.5	64.7	67.0	66.0	68.58	53.62	-	-

* Low total of glass is probably due to boron content

† Not determined

¶ Below limit of detection

§ Different sections of the same crystal

Table 7.3 X-Ray Fluorescence Data on Labradorite in ppm

Location Color	Lake County, Oregon†						Modoc Co, CA	Crater Elegante, Sonora	
	Common	Colorless	Green	Red	Schiller	Average	Schiller	Colorless	Schiller
CuO	<20	45	100	170	80-300	<40?	54	120	<20
FeO	4000	4300	3500	3900	3600	4000	~ 4900	3900	4400
SrO	550	530	570	570	580	560	ND	=1020	=1020
TiO ₂	750	560	350	650	550	600	~ 730	*	730
Cr ₂ O ₃	25	45	10	35	10	30	17	<10	29
MnO	55	80	65	40	30	65	~ 0	<10	60
PbO						<100	ND	<50	<50

*BaO present prevented determination of TiO₂

†Average of 3-5 samples for each color; Common refers to crystals without colored zones, colorless indicated zones from colored crystals

‡SrO content is the average of those measured by Gutmann and Martin [1976]

was 300 pm CuO. From microscope observations, this crystal is about 0.001 volume % schiller, assuming a platelet thickness of 0.2 μm . If the schiller is pure copper then the crystal's copper content would be 440 ppm CuO. The calculated value is slightly higher than the measured XRF value because the maximum platelet thickness was used. The closeness of the two values supports the conclusion that the schiller is nearly pure Cu.

The presence of a high amount of copper in colored zones, and especially in the red areas which often grade into schiller suggests that the colors are associated with formation of the copper schiller.

7.4 Oxygen Isotope Variation among the Colored Zones

R.E. Criss (USGS, Menlo Park, CA) analyzed several samples of Lake County labradorite to test whether the various types of stones have different $\delta^{18}\text{O}$ values. His results are:

Table 7.4 Oxygen Isotopic Measurement of Labradorite

Locality	Sample Number	$\beta^{18}\text{O}$ per mil	Color Type
Lake Co	AvRAL	6.1	common (23 analyses)
"	1600	6.1	common stone occurring with colored
"	1200	6.1	schiller
"	1300	6.2	red
"	1000	6.4	colorless part of red #1100
"	1700	6.5	green
Crater Elegante	100 (13760)	6.1	colorless
"	200	6.2	schiller

All of the above values are within the normal range for plagioclase from unaltered basaltic flows (e.g. Taylor, 1968). There may be a slight tendency for the colored and particularly the green stones to have higher $\delta^{18}\text{O}$ values, although the results are equivocal given the analytical uncertainty of ± 0.2 per mil [R.E. Criss, pers. comm., 1983]. Such a $\delta^{18}\text{O}$ difference, provided that it exists, could indicate that the common and colored stones either (1) formed from different magmas, or (2) formed under somewhat different conditions.

7.5 EPR Spectroscopy

Only two types of signals were observed in the differently colored zones of the labradorite: one pattern results from Fe^{3+} in tetrahedral sites (Section 3.4) while the other is attributed to the Al-O hole center (Section 5.5). EPR integrated intensities for the Fe^{3+} signal at $g_{\text{eff}} = 4.3$ were calculated from equation 2.2, for sample weight of 100 mg, 2.0 mw power and 1G modulation:

Table 7.5 EPR Intensities for Colored Labradorite

Locality	Sample Number	Color	EPR I.I.
Lake County	13761	common	69.0
"	1500	green	68.0
"	70	red	70.0
"	1300	schiller	70.8
Crater Elegante	100	colorless	70.2
"	200	schiller	67.0

Because the analytical uncertainty is $\pm 10\%$ (Section 3.4), the EPR I.I. are equivalent for all colors and for both localities and are roughly equal to the 0.18 wt% Fe^{3+} which was determined optically for Lake County #13761 (Section 3.3a). Because the total iron concentrations are also the same within experimental uncertainty, the ferrous iron concentrations should be nearly equal for the differently colored areas (to $\pm 10\%$).

7.6 Magnetic Measurements on the Colored Zones

Feldspar crystals were cleaned with HCl. Their magnetic moments were measured with a cryogenic magnetometer both before and after impulse magnetization (courtesy of J. Kirschvink, Caltech). Because of the smallness of the measured magnetic moment (Table 7.6) contamination could drastically affect the results. The uniformly high values of sample #200 from Crater Elegante are therefore suspect. Otherwise, the magnetic moments are small, unaffected by cooling to liquid nitrogen temperature, and unaffected by prior magnetization. Neither could the colored zones be distinguished by their magnetic moments (μ). Similar magnetic moments were measured for disordered potassium feldspars with entirely ferric iron. The observations indicate that little, if any, magnetic interaction occurs in the colored labradorite, and that the different types all respond the same.

Table 7.6 Magnetic Measurements of Feldspars

Locality	Sample No.	Color	μ (RT) ¶	μ (1N ₂) ¶	μ^* (RT) ¶	μ (bkgrnd) ¶	Fe ³⁺ /Fe _{tot}
Lake Co.	13761	Colorless	620	830	570	40	0.6
"	-	Green	70	130	60	40	"
"	-	Red	140	280	25	40	"
"	-	Schiller	200	430	350	40	"
Crater E	100	Colorless	160	160	130	40	0.6
"	200	Schiller	1200	1200	1000	40	"
Itrongay Orthoclase		Yellow	200	310	80	40	1.0
Eifel Sanidine		Colorless	69	1160	50	40	1.0

*Sample was not magnetized before measurement

¶All μ values are in pico-Teslas

7.7 Visible Spectroscopy of Lake County Labradorite

7.7.a Characteristics of the colored zones

Absorption spectra of red zones show that the color results from a weakly anisotropic band at 560 nm with 1600 cm^{-1} full width at half height (Figure 7.2). Comparison of these spectra to those of common stones (Figures 3.3 and 3.12) or colorless zones of colored stones shows that a large tail from the ultraviolet (UV) is present. The green color is due to the superposition of a 2800 cm^{-1} wide band at 630 nm polarized (mostly in alpha) on a similar UV tail (Figure 7.3). The red color is present in this particular green zone as indicated by the weak band at 560 nm. The shiller bearing zones do not have definite absorption features, but instead exhibit a slight drop in absorptivity at 560 nm (Figure 7.4 and 7.5), which is probably due to reflections from the copper-red platelets. To preserve the color zonation in this particular sample, a perpendicular face was not polished.

Comparison of the spectra from the differently colored zones of one crystal (Figure 7.4 and 7.5) shows that the tail from the UV extends into the near-infrared wavelengths. The intensities of the Fe^{3+} absorptions at 380 nm are the same for all zones, if the effect of the UV tails are considered. This agrees with results of EPR spectroscopy (Section 7.5). From Figures 7.4 and 7.5 it also appears that the Fe^{2+} absorption intensities are also constant, which is expected because total iron is nearly constant for all phenocrysts measured (Section 7.3).

Spectroscopic measurements made of three green crystals and two red crystals in addition to those presented here show that the absorptivity of the two peaks was sample dependent. Intensity of the green peak varies from 1.2 to 2.5 cm^{-1} , and the red from 0.6 to 0.9 cm^{-1} . Green zones always

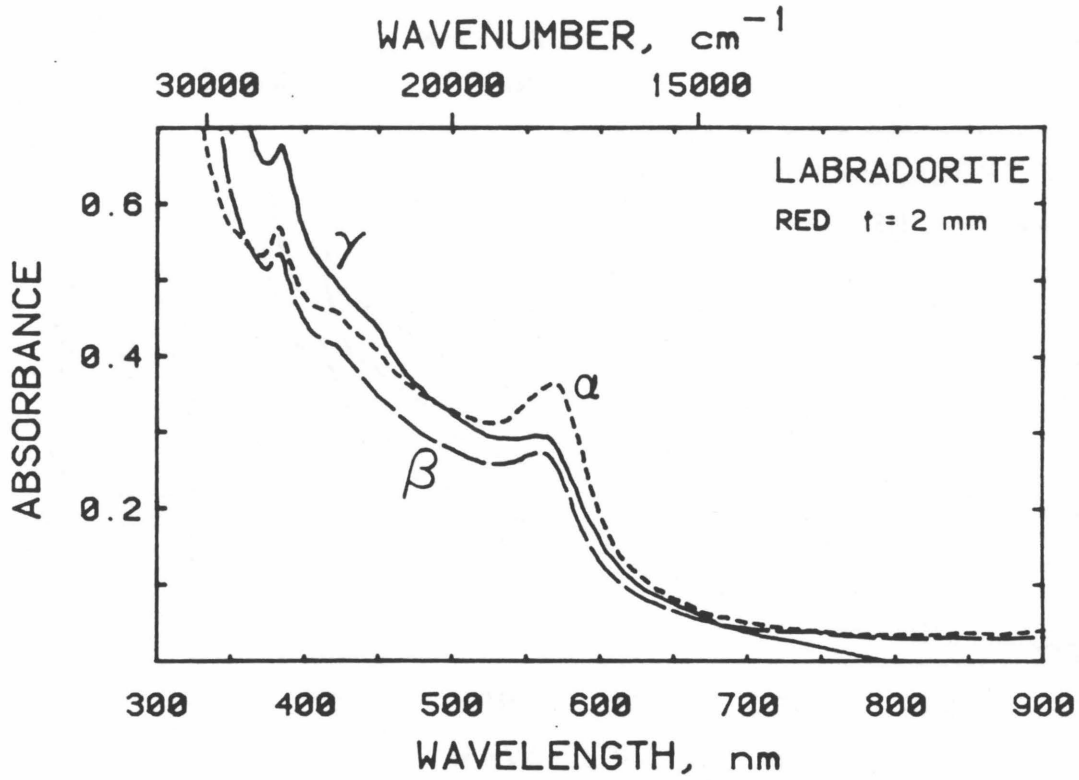


Figure 7.2 Polarized absorption spectra of the red area of Lake County labradorite #200. Scaled for 2 mm thickness. The weakly polarized peak at 560 nm produces the color. Fe^{3+} bands occur between 350 and 500 nm. The color is accompanied by an increase in the UV tail.

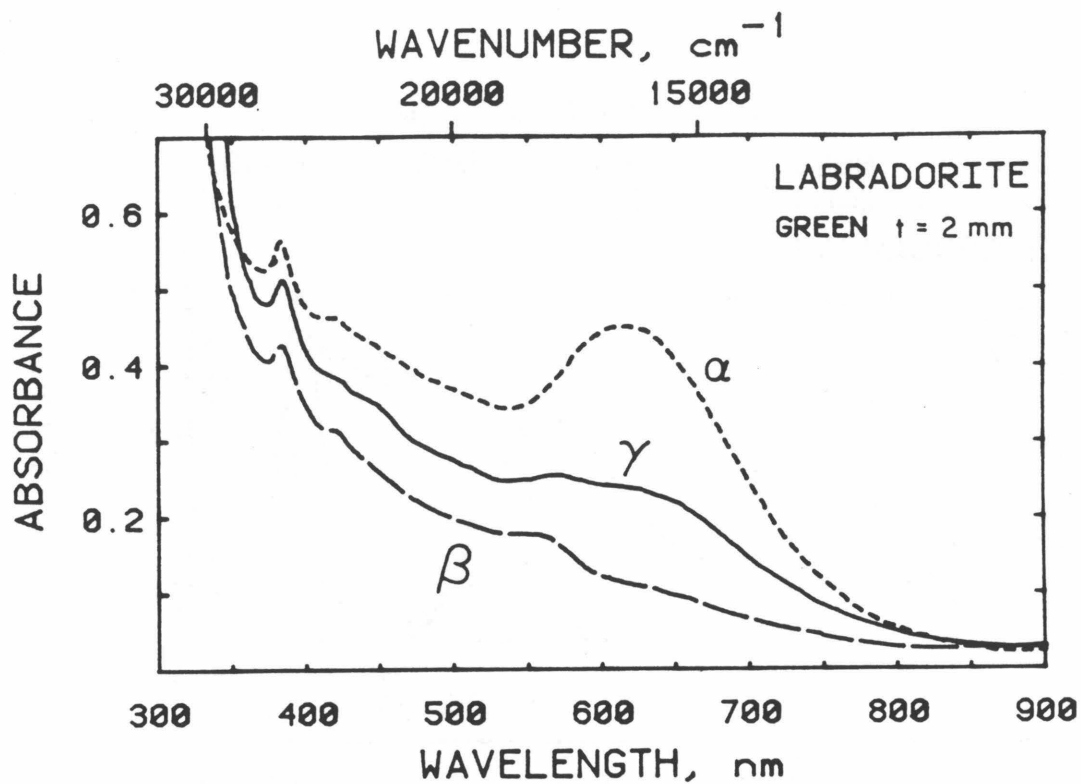


Figure 7.3 Polarized absorption spectra of the green area of Lake County labradorite #300. Scaled for 2 mm thickness. The green color results from a strongly anisotropic band at 630 nm. An increased UV tail is also present, as is the red color (weak band at 560 nm in α .) Fe^{3+} bands occur between 350 and 500 nm.

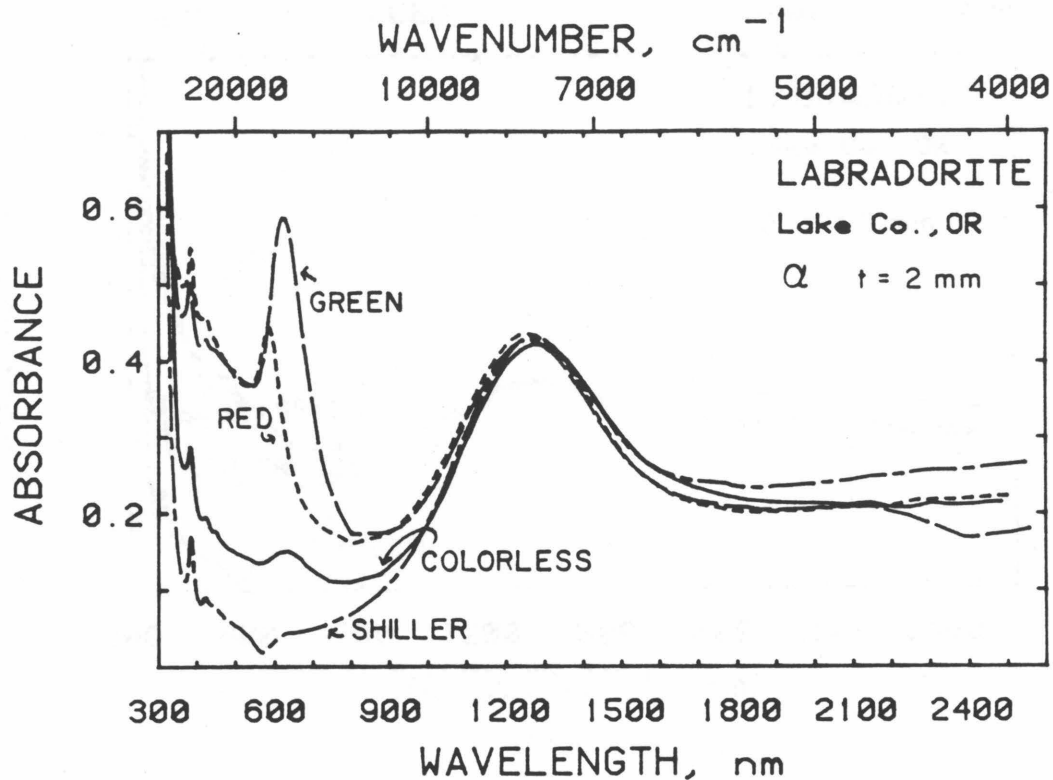
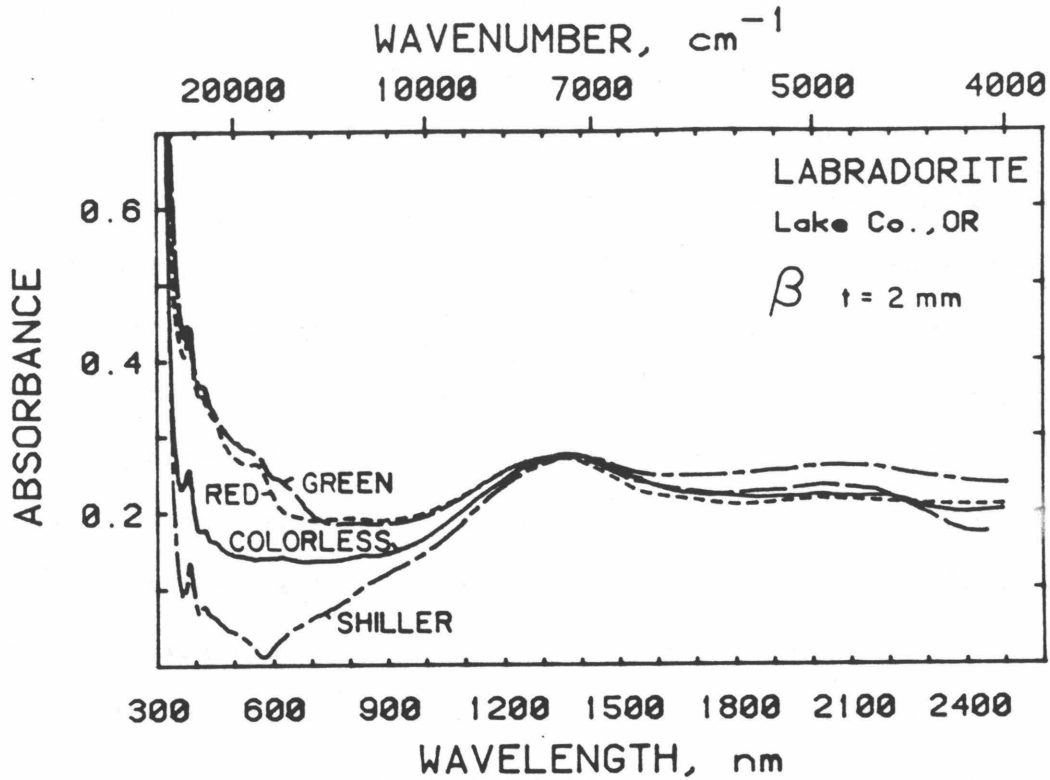


Figure 7.4 Alpha spectra from the four zones of Lake County labradorite #400. The colorless zone is actually slightly "green" from the weak band at 630 nm. The schiller zone has an absorbance minimum at 560 nm which is probably due to reflections from the Cu^0 flakes. Fe^{2+} absorptions at 1250 nm are nearly the same intensity. Fe^{3+} bands between 350 and 500 nm are also very close to the same intensity. The difference in UV tails between the colored and uncolored zones is large.



+

Figure 7.5 Beta spectra of the same four zones of labradorite #400 shown in Fig. 7.4. Fe^{3+} bands occur between 350 and 500 nm; Fe^{2+} bands are below 1100 nm. The zone with schiller exhibits a drop in intensity at 560 nm which is probably due to reflections from the Cu^0 platelets. The green zone has a slight amount of red color because it shows a weak band at 560 nm. The UV tail is polarized, being much weaker in the beta of the red and green zones than in the alpha polarization.

have a slight red component. The ratio of the two peaks' intensities varied among the different crystals from 0.02 to 0.13. (compare Figures 7.3, 7.4, and 7.5). For one sample, the red peak was near detection limits in a 1 mm thick sample. For the more deeply colored green samples, the tint appears blue to the eye because the minimum between the 630 nm peak and UV tail shifts as a result of higher absorptivity. The ratio of green to red peak intensity can also affect the position of the minimum.

Comparison of spectra taken at liquid nitrogen temperature to those taken at room temperature shows that the 630 nm peak is unaffected by cooling, while the 560 nm peak sharpens and increases in intensity such that the area is nearly constant for the two temperatures (Figure 7.6). For both zones and also for a colorless zone, the intensity of the Fe^{2+} band at 1200 nm in alpha increased by 27% upon cooling for the green and 24% for the red and colorless crystals. The difference in value is probably due to analytical uncertainty and baseline approximations.

7.7.b Comparison of red and green colors to transition metal colors

Several transition metals present in Lake County labradorite are capable of producing color through d-d transitions. These are Cu, Cr, Mn, Ti, and Fe. Because Fe^{2+} is the source of bands near 1200 and 2000 nm, and Fe^{3+} absorptions occur near 400 nm (Section 3.3), the red and green colors are not due to either of these elements by themselves. Ti^{3+} can be ruled out because it is unlikely to occur in a terrestrial silicate with Fe^{3+} . The distinctive Mn^{2+} spectra is unlike either the red or the green absorptions, so it need not be further investigated.

Cu^{2+} in an octahedral site is a likely source for the green color because it produces a broad polarized band between 630 and 820 nm (Section

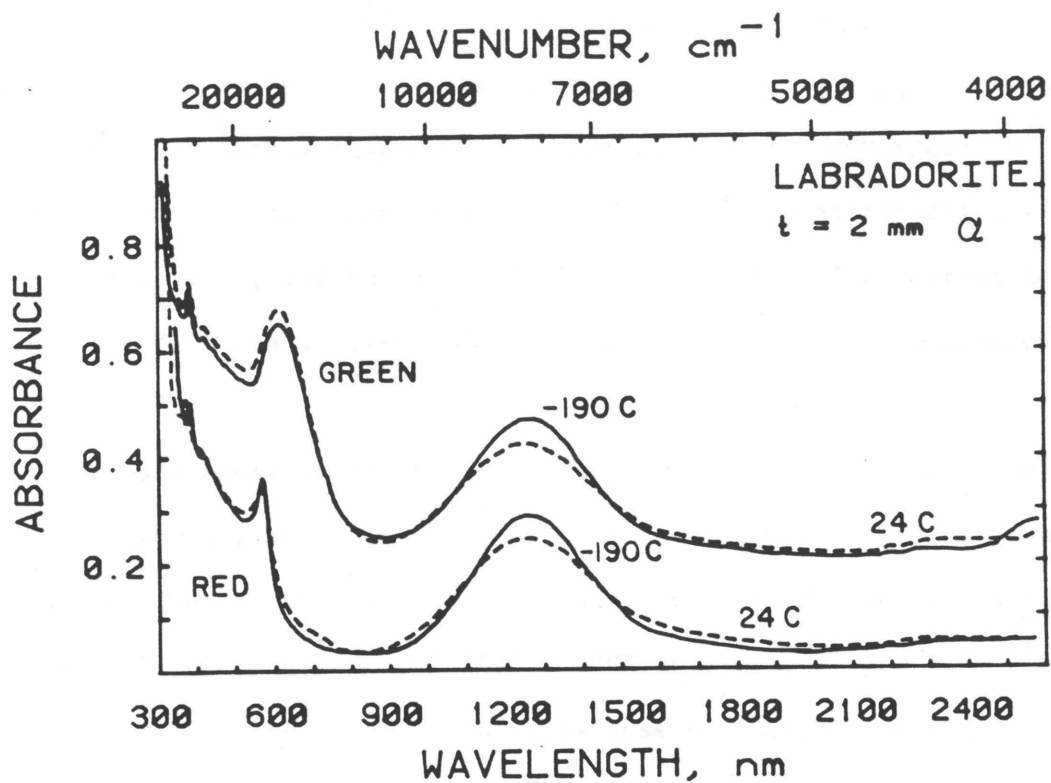


Figure 7.6 Comparison of alpha spectra at 24°C and -190°C for the red and green colors of Lake County labradorite. The red peak sharpens and increases in intensity, but maintains equal area. The UV tail of the green zone may have increased in intensity, but this might be due to a slight change in the baseline. The green peak's area remained constant upon cooling. The Fe^{2+} band sharpened slightly, increased strongly in intensity, so that its band area increased by about 15%.

1.2.b.i). Assuming Cu^{2+} is the chromophore for the green color, the molar absorptivity was calculated from the measured copper content and the range of intensities of the green color as 350-800 l/mole·cm. This is an order of magnitude larger than Cu^{2+} molar absorptivities in diopside [Rossman, 1980], and rules out Cu^{2+} as the source of the green color. Cr^{3+} and Mn^{3+} can similarly be ruled out due to their low concentration (Table 7.7).

A more probable coloration mechanism for transition metal elements in the labradorite is intervalence charge transfer (IVCT), because this produces deep colors for trace amounts. Likely reaction pairs are $\text{Fe}^{2+}/\text{Fe}^{3+}$, $\text{Fe}^{2+}/\text{Ti}^{4+}$, $\text{Cu}^{2+}/\text{Cu}^{1+}$ or $\text{Cu}^{1+}/\text{Cu}^{\circ}$. IVCT between Fe^{2+} and Fe^{3+} could produce either red or green bands because sufficient amounts of these charge states are present. However, the energy is usually lower than that of the red peak, and neither the red nor the green colors are seen in Crater Elegante labradorite which has a similar ferrous to ferric iron ratio. Iron-titanium charge transfer can similarly be discounted because uncolored Crater Elegante labradorite has at least as much titanium as the Lake County labradorite. Moreover, the band widths of the green and red (2800 and 1600 cm^{-1} , respectively) are much too small for charge transfer involving iron, which typically has 5000 cm^{-1} widths. In fact, these bands are no wider than Fe^{2+} d-d transitions (Sec. 3.3).

IVCT between different copper charge states could possibly cause either of the colors because copper content varies among the differently colored zones of the labradorite. Unfortunately, I am not aware of quantitative measurement of such processes in the literature.

Table 7.7 Comparison of Known Molar Absorptivities to Those Calculated for Labradorite

Coloring Mechanism	Reference Material				Labradorite	
	$\epsilon(\lambda)$ 1/mole·cm	λ nm	Substance	Reference	$\epsilon(\text{Green})$ 1/mole·cm	$\epsilon(\text{Red})$ 1/mole·cm
Cu ²⁺	18-39	819	MgSiO ₃ :Cu	Rossman [1980]	350-800	100-151
Cr ³⁺	15-45 29-59	646 442	MgSi ₃ O ₈ :Cr	Rossman [1980]	760-1700	380-570
Mn ³⁺	100 10	~580	Piedmontite Other silicaltes	Burns [1970]	470-1000	240-360
Fe ²⁺ /Fe ³⁺ IVCT	200	550-900	Silicates	Smith & Strens [1976]	18-40	10-14
Fe ²⁺ Ti ⁴⁺ IVCT	>800	480-780	Silicates	"	50-100	24-35
Pb ³⁺	4300 >100	630 614	KAlSi ₃ O ₈ :Pb Oligoclase:Pb	§ 6.8.c § 6.10	9000-19000* "	- -
Cu-ruby = Cu ⁰ colloids	900†	550	Glass	Weyl [1951]	-	180-260

*Pb concentration assumed to be 10 ppm

†Determined from Cu-ruby spectra (Figure 7.8) and Cu content (Table 7.2)

§Section

7.7.c Comparison of the green color to amazonite

The green color of the labradorite occurs at nearly the same position as the type B amazonite-potassium feldspars and the amazonite-sodic plagioclases (Figure 7.7). The colors are all polarized in similar crystallographic directions because beta in both amazonites and alpha in the labradorite are nearly perpendicular to the c axis. The width of the peak in the green labradorite (2800 cm^{-1}) is slightly less than those of the singlets in potassium feldspar (ranging from 3000 to 3700 cm^{-1}) and that of the blue sodic plagioclases (4000 cm^{-1} , Section 6.3 and 6.10). The occurrence of one peak in the 300-900 nm range in the labradorite mimics the behavior of the Na-amazonites and the type G color found in orthoclase-amazonite. Also, the green peak in the labradorite maintains equal area upon cooling as did the potassium amazonites (Section 6.3.c). Thus, spectral parameters of the green peak in labradorite are entirely consistent with an origin similar to amazonite color in potassium feldspar. The colors differ to the eye because of the various UV tails.

To directly test if the green labradorite has Pb^{3+} , comparisons were made between the EPR spectra of the different zones. The Pb^{3+} signal was not observed, even at the highest magnifications and power attainable. The high structural state of the labradorite probably precludes measurement of such a signal as was the case for the gemmy green orthoclases and gemmy blue sodic plagioclases (Sections 6.6 and 6.10).

Indirect tests for an amazonite mechanism in labradorite are (1) the presence of lead, (2) the presence of structural water, and (3) the removal of the color by heat and regeneration by irradiation. Lead could not be detected with XRF which shows that the lead concentration is definitely below 100 ppm and probably below 50 ppm. Because most

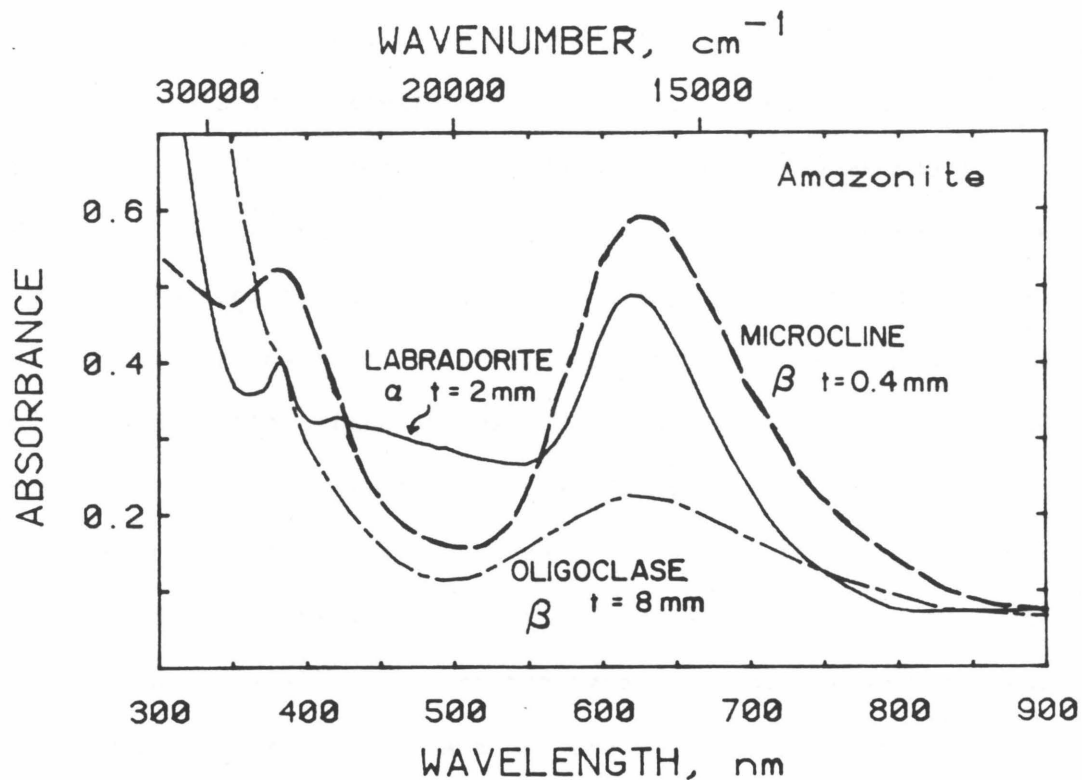


Figure 7.7 Comparison of green labradorite with amazonites. Labradorite is Lake County # 300. The oligoclase is from South Carolina. Microcline is type B, # 12 from Lake George, Colorado. The two plagioclases have sharp Fe^{3+} bands at 380, 421, and 450 nm, and steep UV tails partially due to O^{2-} to Fe^{3+} charge transfer. All have a broad intense band at 630 nm that is polarized close to the c axis. The type B microcline has an additional radiation band at 380 nm, but type G orthoclases do not.

plagioclases have about 10 ppm Pb, and because feldspars contain most of the lead present in igneous rocks [Wedepohl, 1956], and nearly all the lead of a volcanic rock without glass [L.T. Silver, pers. comm., 1983], lead is likely to be present in Lake Co. labradorite at the 10 ppm level. Assuming a Pb content of 10 ppm gives a molar absorptivity of 9000-19000 l/mole·cm for the green color, which is two to four times that of type B amazonites. If the labradorite's Pb content is nearly 50 ppm, which is below the detection limit of the XRF, then ϵ would be 1800 to 3800 l/mole·cm, which is reasonable for amazonite.

Structural water was not observed in any of the plagioclases examined, although OH^- was present in variable amounts (Section 4.3.c). It is possible that a small amount of hydrogen is present as H_2O because sufficiently thick (~10cm) samples were not available for quantitative measurement of near-infrared bands. The OH^- band at 2200 nm was detected in one of the thicker green labradorites, so that OH^- is likely to be present in all.

The green color can be removed by heating above 850°C for 1/2 hour. For this time scale noticeable dehydration did not take place in sanidine, suggesting that the similar OH^- species in the green labradorite was not removed.

Radiation did not return the green color once removed, nor did it generate the green color in any non-green samples. To the eye, the green color was not enhanced by gamma-radiation.

If the green color in the labradorite is due to Pb^{3+} , then it cannot be generated by the same mechanism as proposed for amazonite (Section 6.11). This discussion will be continued in Section 7.11.

7.7.d Comparison of the red color to copper-ruby color in glass

Copper bearing glasses come in a limited variety of colors, including a red, transparent type known as copper-ruby (Sections 1.2.b.i and 1.2.b.ii). The color results from intrinsic absorption at 560 nm of Cu^0 particles too small to scatter light (approximately a few to 70 nm). The similarity of a copper-ruby spectrum to that of red labradorite (Figure 7.8) strongly suggests that the red color of the feldspar results from the same mechanism. Not only are the band positions and half-widths nearly the same, but both colors involve a large UV tail extending into the near-infrared. The molar absorptivity measured for the glass is higher (900 l/mole·cm) than that computed for the feldspar (about 200 l/mole·cm). The difference is partially due to use of total copper to compute ϵ because not all Cu present would be exsolved and would contribute to the color. Also, ϵ for the glass has a high uncertainty because the thickness of the red coating on the glass was estimated.

The maxima of the red band for most of the labradorites observed was located at 560 nm, but one band (Figs. 7.4 and 7.5) was seen at 585 nm. This behavior is comparable to that observed in gold-ruby glasses by Williams et al [1981] wherein 4-5 nm sized particles produced a 530 nm (intrinsic) band and 22 nm particles involved a peak shifted to 570 nm. For the labradorite, the 560 nm intrinsic bands were observed for homogeneously red crystals, while the 585 nm band was from a red zone that graded into a copper-schiller, and thus is more likely to have larger sized copper colloids.

Because of the gradation of the red color into Cu^0 -schiller of the labradorite, the high Cu concentration in the red zones, and the remarkable similarity of the red color to copper-ruby of glasses, I conclude that the red color of the labradorite results from the intrinsic absorption of light by

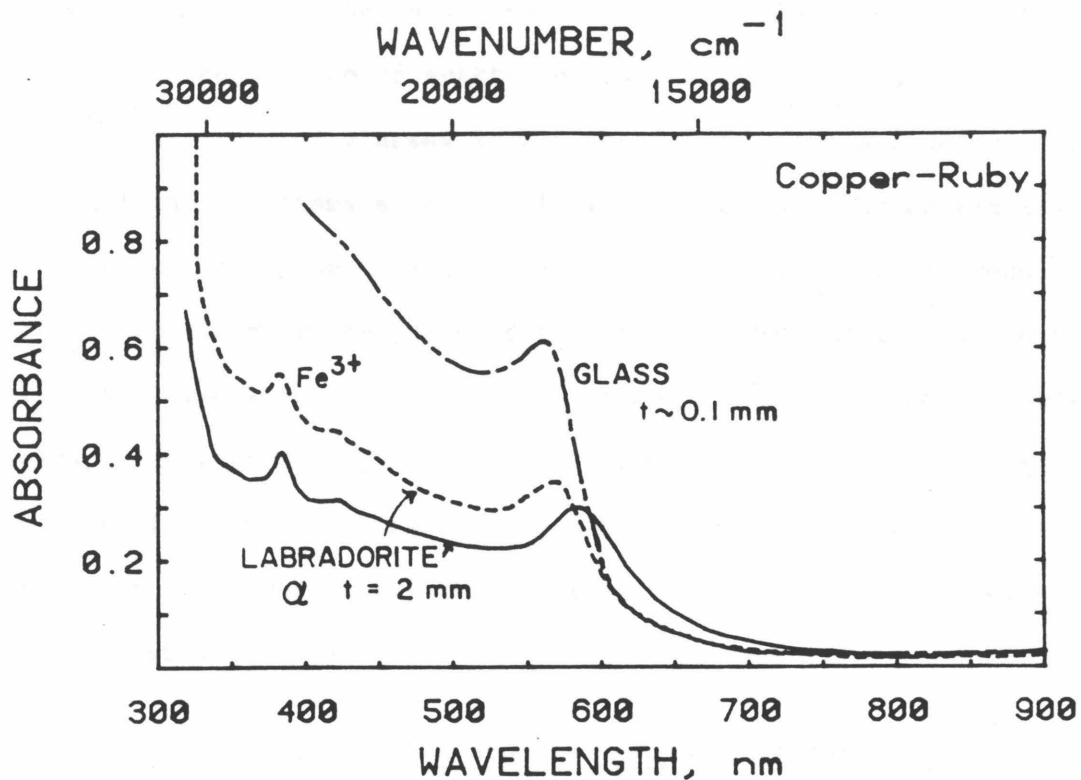


Figure 7.8 Copper ruby glass and red labradorite visible spectra. Glass is unpolarized. The α polarization is shown for the labradorite. Dots are sample #200, which had only the pure red color and no schiller visible to the microscope. Solid line is from sample #400's red zone which graded into the shiller. The shift and broadening of the peak from the uniformly colored to the zoned sample most likely reflects an increase in colloid size from about 4 nm to about 22 nm in the zoned sample.

Cu-metal colloids. The particles must be less than a few hundred nanometers because of the absence of scattering (which would be indicated by a brown or livery appearance of glasses in reflected light, but a blue color in transmitted light [Williams et al, 1981]). Colloids in unzoned samples are likely to be less than 20 nm in analogy with Williams et al [1981] results. The lower size limit of the colloids for color production is unknown and may be of atomic dimensions as proposed by Zsigmondy [1909]. The colloids in feldspar must be close to spherical because asymmetric shapes of colloids in glass lead to splitting of the isotropic band into two polarized bands of higher and lower energy than that of the metal's intrinsic absorption [Stookey et al, 1978].

7.8 TEM Observations of Red and Green Colored Labradorites

Crushed pieces of red labradorite #1100 and green #1700 were examined using a Phillips 400T TEM with a Tracor-Northern EDS system by Judy Konnert (USGS) under the guidance of Peter R. Buseck (Arizona State University) at the Tempe facility. Qualitative chemical results are that the red labradorite showed copper and iron in a variable ratio of 2 to 4 (Cu/Fe), while the green samples ratio ranged from 0.55 to 1 (Cu/Fe), confirming XRF results that the red sample's copper content is twice that of the green's. Cu/Si ratios varied greatly. Discrete inclusions were not seen. From the magnifications used, the upper limit for the size of the Cu^0 colloids is a few nanometers, in agreement with the upper limit inferred from the spectroscopy of the pure red color (Section 7.7d).

7.9 Heating Experiments

The red and green colors of the labradorite are relatively stable: the green can be removed by heating in air at 850°C for 24 hours; the red

at 900°C, and the schiller at temperatures between 1000 and 1100°C. The pink color also disappeared after heating at the magnetite-wustite fugacity buffer at 1000°C for 24 hours. The high temperatures, long times, and independence of fugacity conditions involved for the removal of the red color (Cu⁰ colloids) imply that diffusion controls the process rather than oxidation of the copper. This is reinforced by visual inspection of the schiller bearing phenocrysts: after 6 hours at 1000°C in air, the Cu⁰ flakes are about one half as large.

The temperatures of resorption are all less than the extrusion temperature of basalt (~1200°C) and the solidus temperature of labradorite (1400°C) which demands that the coloration occurred in the cooling flow and thus after the labradorite had crystallized and cooled.

From the heating experiments in air, copper solubility in labradorite depends linearly on temperature (Fig. 7.9) for homogenization experiments at constant time. It is likely that curves for different times would parallel these. This was not investigated due to sample availability. The oxygen fugacity did not prevent resorption of the Cu⁰ colloids at 1000°C, but whether the temperature of resorption changes with f_{O_2} was not tested.

Removal of the red color proceeds simply by reduction in the band's intensity (Fig. 7.10). Neither broadening or shifting in position was observed which proves that the colloidal color is intrinsic because an absorption band due to scattering would change in shape and position as the colloids shrank in size (Mie, 1908; Perenboom et al, 1981). Similar experiments were attempted on one green labradorite, but the color was totally removed by the time the sample was measured. Due to sample availability, the experiment was not repeated.

Heating also removed the UV tail. Fe²⁺ and Fe³⁺ bands were measured

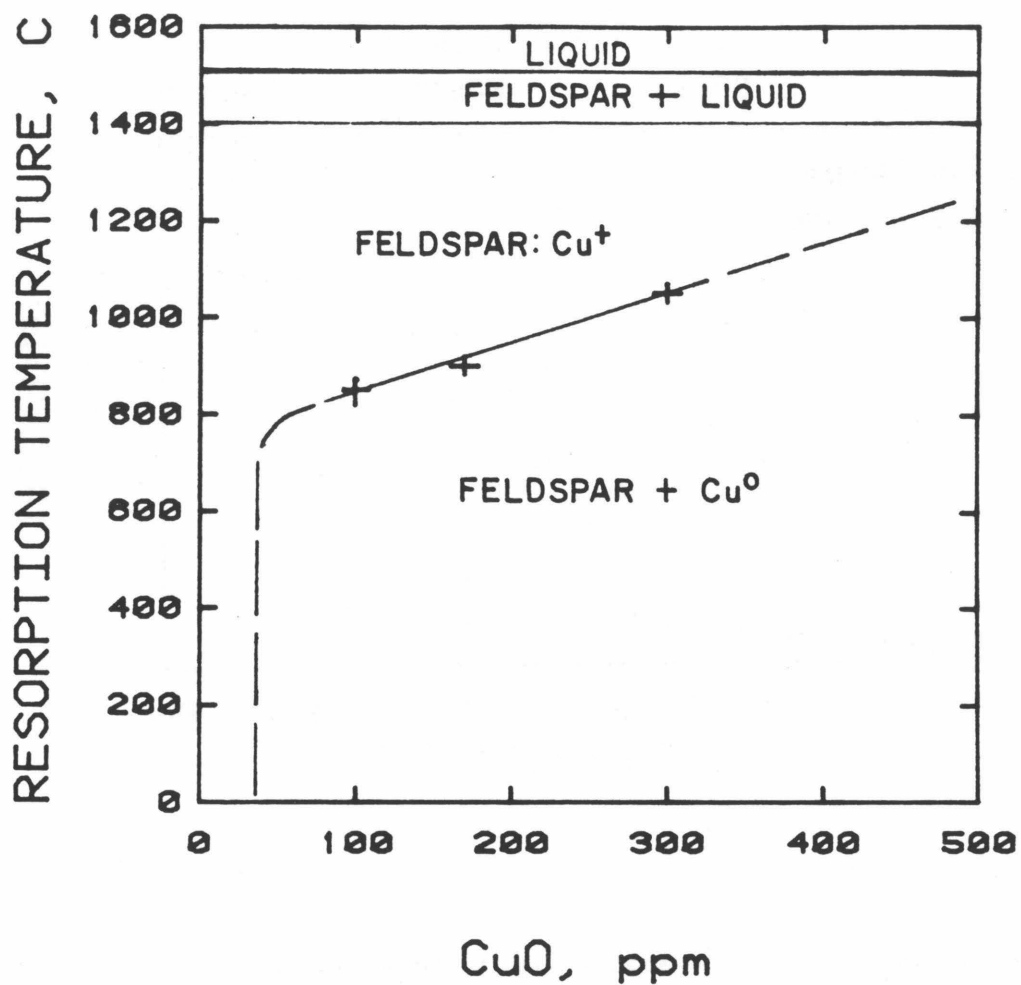


Figure 7.9 Partial phase diagram for Cu° and plagioclase, showing regions of solid solution and two phases. The boundary is for heating in air. At lower oxygen fugacities this may shift upward to favor Cu in the metallic state.

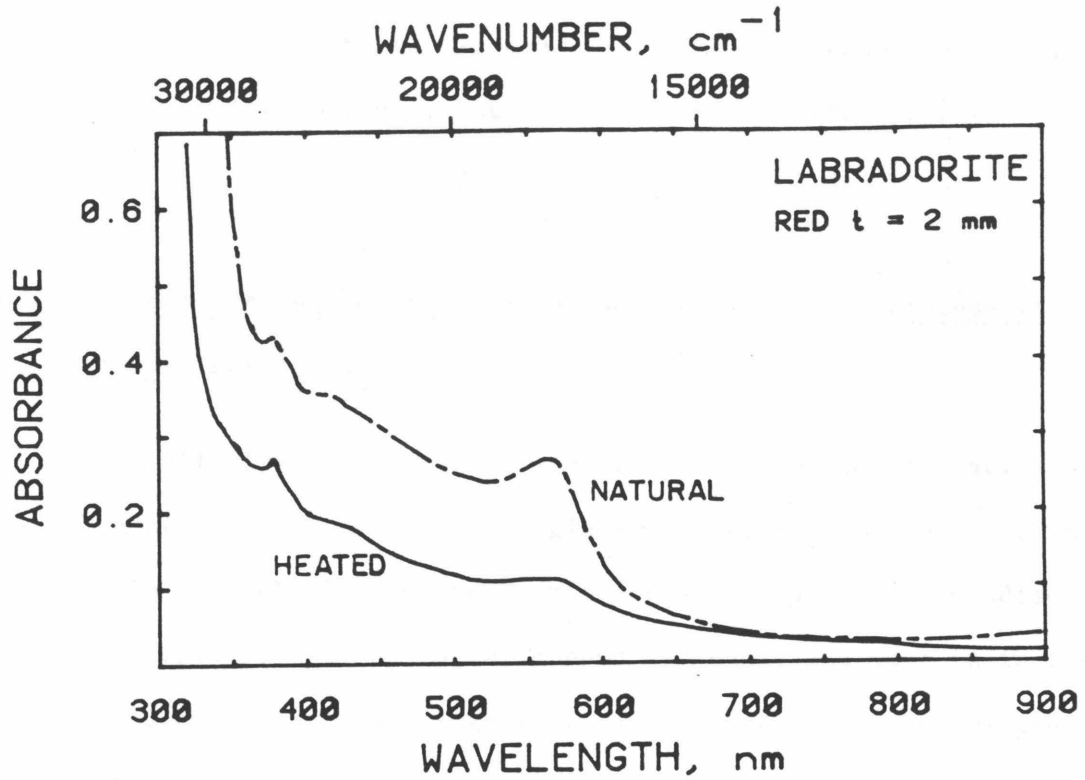


Figure 7.10 Unpolarized absorption spectra of red labradorite before and after heating. Scaled for 2 mm thickness. A decrease in both the 560 nm band and UV tail is apparant. No shifting of the 560 nm band was detected indicating that this color is intrinsic rather than due to scattering.

before and after heating in air and heating at the magnetite-wustite boundary at 1000°C for 24 hours, but no differences in the spectra were ascertained.

7.10 A Model for the Coloring Mechanism and Exsolution Process in Lake County Labradorite

The similarity of chemistry, spectra, and response to heating between the labradorite and copper-bearing glasses suggests that the process of exsolution in the labradorite should mimic the process in glass (discussed in Section 1.2.b.ii). In the magma, copper is ionic, and must be in the Cu^{1+} state because of low oxygen fugacity. It is certainly incorporated as Cu^{1+} in the growing labradorite phenocrysts, because the blue color and visible and EPR spectra of Cu^{2+} were not observed. For crystals with low concentrations of CuO (<40 ppm) Cu^{1+} remains in solid solution with the labradorite as it cools, so that the crystal is colored only by Fe^{3+} . For CuO concentrations higher than 40 ppm, the temperature resorption occurs at depends on the copper concentration (Fig. 7.9), so that exsolution temperature is also likely to depend on Cu content. The association of schiller with high copper content substantiates this conclusion because high temperatures during exsolution would aid diffusion and yield the largest clusters of Cu^0 . Exsolution of smaller amounts of copper at lower temperatures would tend to form smaller clusters because of slower diffusion rates: this is undoubtedly the case for the red color.

The fact that up to 40 ppm CuO can remain in solution coupled with the dependence of exsolution temperature on Cu content, means that the exsolution process operates continuously (over a temperature range) as the labradorite

cools. At one stage, schiller can be formed, and later the red of copper-ruby may develop to form the irregularly zoned crystals. Diffusion constants are not available for Cu^0 in feldspar, but within an order of magnitude, should be equal to those of the large ions Pb^{2+} or K^+ (which have $D =$ to 10^{-9} cm^2/sec and 10^{-10} cm^2/sec for anhydrous conditions, respectively [Smith, 1974, v.II, p. 169]). Using a cooling time of 1 year for the thin flow (which is probably an overestimate judging from measured cooling times for crust on a lava lake [Wright et al, 1976] and distance = $(D \cdot \text{time})^{1/2}$, gives maximum diffusion distances for Cu^0 in the labradorite of 0.06 to 0.17 cm. Thus, the copper metal could not create the centimeter scale zonation of red into schiller seen in some of the samples.

Reduction of Cu^{1+} is likely to occur while the copper is still in the labradorite structure because in the glass-copper system it is the reduction which precipitates the exsolution. One possible reaction would be:



This has been observed for glasses [Dietzel, 1945]. For the red and schiller zones this reaction would lead to a 7 to 13% decrease in the Fe^{2+} band's intensity. Because this small but detectable change was not observed, and because Fe^{2+} bands could not be oxidized under prolonged heating in air, I conclude that reaction (7-1) is unlikely.

For glass, schiller formation may occur through simple dissolution. The equivalent reaction in feldspar would be



At high temperature the "hole" would migrate among oxygen. Upon cooling, the $\text{Al}-\text{O}^-$ hole centers may result that were observed (Section 5.4).

For glass, formation of copper-ruby requires the presence of polyvalent ions to control the oxygen fugacity such that $\text{Cu}^0/\text{Cu}^{1+}$ increases

during cooling (Section 1.2.b.ii; Fig. 1.20). The presence of polyvalent ions (Pb, Sn, Se etc.) may not be necessary for the labradorite because fO_2 is not constant during cooling of the basalt; instead, the quartz-fayalite-magnetite (QFM) buffer is followed. Because most of the transition metal oxidation-reduction curves and the buffers are parallel, the reaction $Cu^0 \rightarrow Cu^{1+}$ is likely to be nearly parallel to the QFM buffer, so that the Cu^0/Cu^{1+} ratio is probably constant during cooling. The buffer would control the pO_2 or would free electrons which would then monitor the progress of reaction 7.2.

The resemblance of the green color in labradorite to Pb^{3+} absorptions in potassium feldspar and sodic plagioclase has been noted. In the labradorite, Pb is probably 1 to 10 ppm. In glass, the presence of lead aids in copper-ruby formation through



[Dietzel, 1945]. The analogous reaction in labradorite could be the two step process:



These reactions explain the properties of the green color. It forms at a lower temperature because otherwise the "hole" in eq. (7-4a) would migrate. Green can form after schiller or red in the same crystal during the final stage of exsolution. In an unzoned crystal green is accompanied by red because the reduced copper would diffuse somewhat to form small clusters. Green color would define the outer zone in crystals where the Cu content was lowest. The green would be the rarest color because its formation requires that the crystal have a moderate amount of Cu^{1+} (80 ppm) in solid solution when the proper temperature for eq. (7-4) is reached

Table 7.8 A Model For Coloration Of Lake County Labradorite

COLOR	Cu ppm	COLORING AGENT	STATE OF COPPER	REDUCTION TEMP.OF Cu	EXSOLUTION TEMP.OF Cu
PALE YELLOW	<16	Fe ⁺³	Cu ⁺¹	--	--
COLORLESS	35	--	Cu ⁺¹	--	--
GREEN	80	Pb ⁺³	(1) Cu ⁺¹ + O ²⁻ → Cu ⁰ + O ⁻ (2) Pb ²⁺ + O ⁻ → Pb ³⁺ + O ²⁻ (3) Cu ⁰ diffuses and collects to form small clusters (faint red color)	>850	--
RED	135	Cu ⁰	(1) Cu ⁺¹ + O ²⁻ → Cu ⁰ + O ⁻ (2) Hole diffuses; Cu ⁰ diffuses and aggregates into 40-220 Å clusters	>900	<900
SCHILLER	~240	Cu ⁰	(1) Cu ⁺¹ + O ²⁻ → Cu ⁰ + O ⁻ (2) Hole diffuses; Cu ⁰ diffuses and collects into 5-40 μm platelets	>1000	<1000

(approximately 850°C). It may also require incorporation of Pb in the neighborhood of Cu^{1+} .

This model for coloration of Lake County labradorite is summarized in Table 7.8.

7.11 Implications of Coloration on Geologic Conditions of Formation

The chemistry of the Steens basalts has been shown to result from fractionation of plagioclase, coupled with extrusion of fractionated liquid and labradorite cumulates [Gunn and Watkins, 1970; see Section 1.2.e]. Based on the usually low concentrations of ferromagnesian elements in plagioclase, Gunn and Watkins [1970] concluded that labradorite addition and subtraction produced the trends of Fig. 7.11 and 7.12. The chemistry determined for the labradorite in this thesis supports Gunn and Watkins [1970] conclusions. The labradorite is located on the trends for all the transition metals (Fe, Mg, Mn, Ti, and Cu) if the average composition is used. For Sr, the labradorite chemistry does not follow the trend, which may be related to a poor value for Sr. If the Crater Elegante standard had slightly more than the average value measured by Gutmann and Martin [1976], then my determination would be in error.

The major element trends of Gunn and Watkins [1970] also fit closely with the average chemistry for the Lake County labradorite. Use of the exact chemistry for labradorite would change the trends shown in Fig. 1.33 a very small amount.

For the trends of Fig. 1.33, 7.11 and 7.12 to hold, the labradorite chemistry must have been fairly constant. This is probably true of major elements, because the data for the samples in this study are consistent and nearly equal to prior measurements (Table 1.7). The phenocrysts mea-

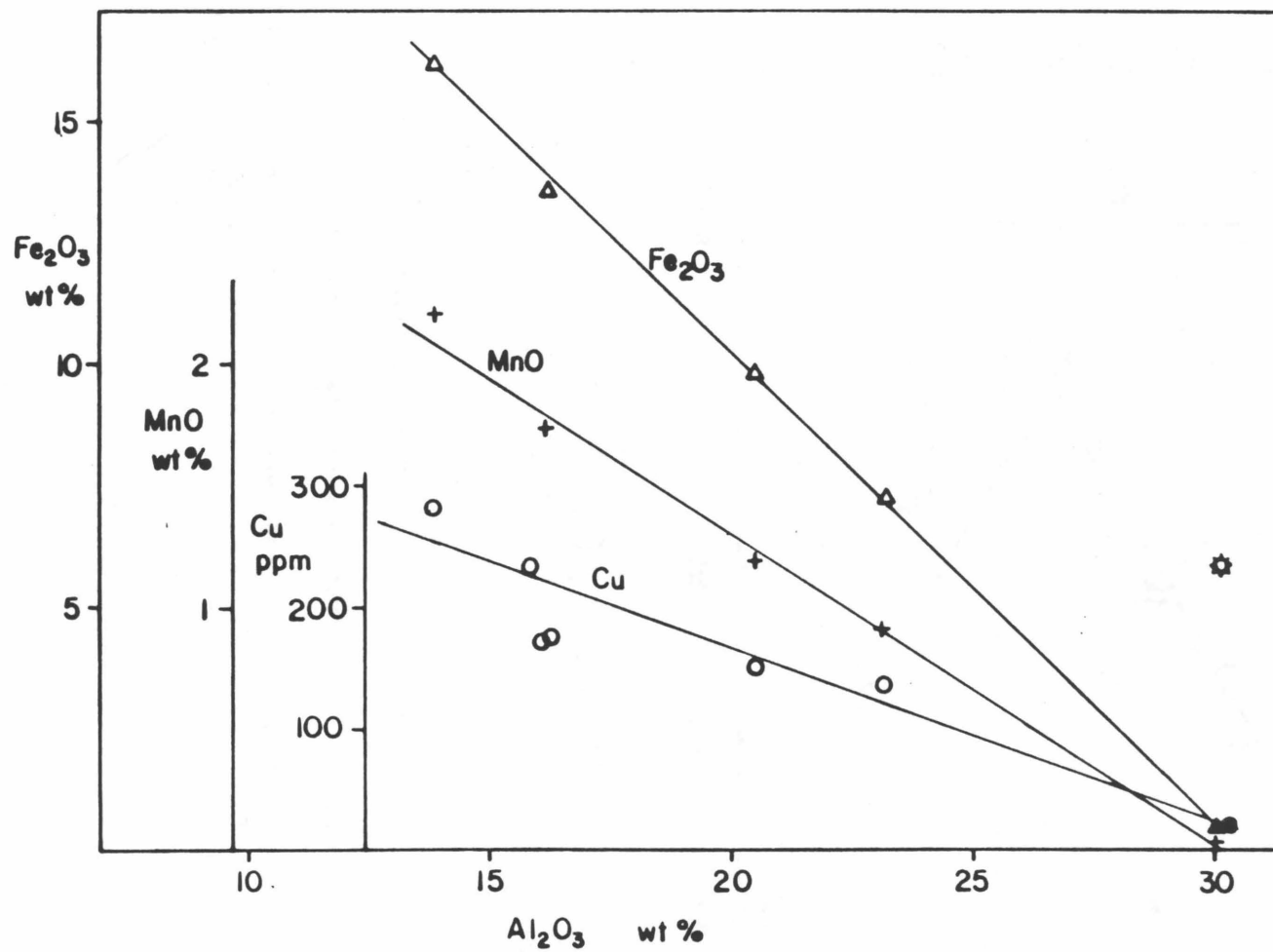


Figure 7.11 Relationship of Fe, Mn, and Cu trends in the Steens Mountain basalts to Lake Co. labradorite chemistry. Open symbols, basalt chemistry of Gunn and Watkins [1970]. Filled symbols, average values for labradorite. The star indicates the highest measured Cu content for labradorite.

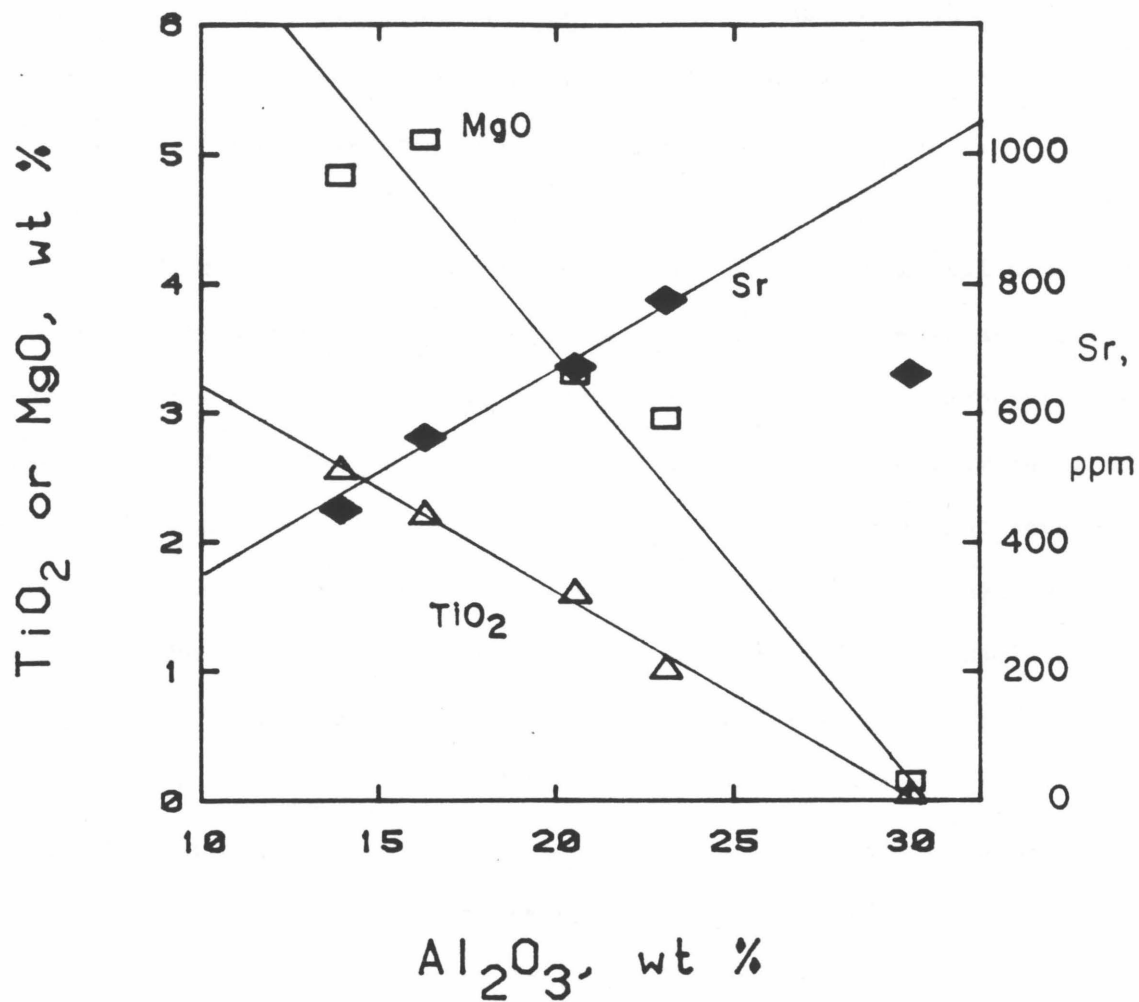


Figure 7.12 Relationship of MgO, TiO₂, and Sr trends in Steens Mountain basalts to Lake County labradorite chemistry. Symbols at 30 wt % are for the labradorite, others are averages for the groups of lavas from Gunn and Watkins [1970].

sured were probably all from the same flow (the Rabbit Hills locality), but because the major element chemistry of the phenocrysts is essentially the same as the groundmass labradorites [Stewart et al, 1967], this is probably not a problem.

The minor elements are consistent, given the experimental uncertainty, except that copper varies widely, and iron seems to decrease as copper increases (Table 7.3). The range of copper content in the phenocrysts nearly equals that of the basalt, the largest value for a single flow being 400 ppm Cu [Gunn and Watkins, 1970]. The Cu content of the phenocrysts varies not only between different crystals but also among color zones in a single crystal. The copper zonation may reflect diffusion during exsolution, but because it is doubtful that Cu^0 atoms migrated across 1 cm during the quick cooling of the basalts and because Cu content varies widely between crystals in a single flow, the present zonation is mostly original.

Almost all of the phenocrysts have about 16 ppm Cu (common stones). It is apparent that not all the labradorite took the same proportion of Cu from the melt, which suggests that the Cu content of the melt rose at one time, forcing more copper into the labradorite. This is compatible with Gunn and Watkins's [1970] conclusion that the magma chamber was successively recharged, in that before input of fresh melt, the fractionated older melt would be enriched in such elements as copper.

It is problematical that only copper would be enriched, and not all of the transition metal elements. Clinopyroxene and/or olivine crystallization may remove the ferromagnesian elements, but for this case, olivine should also remove Cu from the melt. The answer may be partially enhanced visibility of the copper variation in the form of the red and green colors and the schiller, yet for the samples enriched in Cu, no other enrichments were

observed. Perhaps the answer is a change in the chemistry of the melt-- possible enrichment of Cu itself, but more likely depletion of elements such as sulfur or chlorine which would usually complex with copper. Segregation of the labradorites is also related to Cu-enrichment because the colors and schiller have only been noticed for the large phenocrysts of the Rabbit Hills flow.

CHAPTER 8

SUMMARY AND CONCLUSIONS

This thesis concerns a variety of problems, including the use of spectral techniques to quantitatively determine speciation and concentration of iron and protons in feldspar, the production of radiation defects in feldspar and the effect of water on this process, and the mechanism of Cu^{1+} exsolution from feldspar to form Cu° schiller. The following discussion enumerates the principal observations and conclusions of this study, and provides a brief comparison of the findings on feldspar to previous work on other solids.

(1) Optical spectroscopy was used to determine Fe^{2+} and Fe^{3+} concentrations in feldspar to $\pm 15\%$ at levels as low as 0.02 wt% Fe, while EPR spectroscopy can measure Fe^{3+} concentrations of 0.003 wt% Fe within $\pm 10\%$. The methods were limited by the availability of suitable standards and the accuracy of their chemical data. The methods are complementary in that the optical spectroscopy works best at high concentrations, while EPR spectroscopy works best at low Fe^{3+} concentrations. The technique allows measurement of $\text{Fe}^{2+}/\text{Fe}^{3+}$ ratios in situ.

(2) Except for perthites, all Fe^{3+} in feldspar is tetrahedrally coordinated in sites with varying degrees of distortion, such that the number of sites depends on the structure and not on the chemistry of the feldspar. Perthites display an additional signal in the EPR attributable to axially coordinated Fe^{3+} , the intensity of which is proportional to the red color, and thus the hematite in the feldspar. The axial signal probably represents an intermediate stage of hematite deposition within the feldspar. Fe^{2+} replaces calcium in two distorted sites that do not experience major structural variations with changing plagioclase composition. For both Fe^{2+}

and Fe^{3+} absorption bands, molar absorptivities calculated using peak areas were independent of feldspar composition. The equivalent statement does not hold for EPR spectra because small differences in site geometries result in very different peak shapes and intensities.

(3) Protons occur as OH^- in sanidine, poorly ordered orthoclase and plagioclase; as structurally bound H_2O and fluid inclusions in microcline and ordered orthoclase; and as NH_3^+ in microcline from Amelia, Virginia. The speciation may be controlled by the temperature of the melt because plagioclase and the higher polymorphs of KAlSi_3O_8 have "disassociated" water. As suggested by Solomon and Rossman [1982], the speciation may also be related to H_2O content of the melt. These two factors are probably not separable because "cooler" melts are generally more hydrous. It is equally probable that the feldspar structure determines whether water speciation is OH^- or H_2O . Molar absorptivities derived from water contents measured by hydrogen manometry enabled determination of concentrations as low as a few parts per million H_2O for structurally bound H_2O through IR spectroscopy.

(4) Smoky radiation color in feldspar results from the combination of four polarized bands plus a UV tail, which were correlated with the sum of two centers seen in EPR spectra. Disorder in sanidine blends the two patterns into one asymmetric broad pattern, but in microcline the centers are well resolved. Comparison to EPR spectra of glass established that the two centers are: H_I , a hole trapped on one nonbonding oxygen (NBO) on silicon with a potassium near by and H_{II} , a hole shared between two NBO's on silicon. In analogy to smoky quartz and glasses the 16200 and 27200 cm^{-1} absorption bands are due to H_I , the 11600 cm^{-1} band is due to H_{II} , and the 19100 cm^{-1} band is due to an aluminum-oxygen hole center. This must be $\text{Al-O}^- -\text{Al}$,

rather than Al-O^- because the latter occurs unaccompanied by smoky color. The UV tail is possibly due to an electron trapped at an oxygen vacancy, although an EPR signal attributable to an electron trap was detected in only one smoky feldspar.

(5) Smoky color is inhibited in feldspars with high aluminum contents, but irradiation does produce Al-O^- and electron centers. The high aluminum content inhibits hole centers on oxygen near silicon simply because as the Al/Si ratio approaches unity, the odds of a bond breaking near aluminum (rather than an Si-O-Si bond) approach unity.

(6) Smoky color is inhibited by the presence of structurally bound H_2O in the lattice, but not by OH^- or fluid inclusion water. The process involves diffusion because irradiation of structurally hydrous samples at liquid nitrogen temperature produces a grey color. Radiation disassociates the H_2O molecule, whereupon the H and OH radicals mend broken bonds, attach to NBO's and combine with freed electrons and holes, thus preventing radiation centers from forming. Radiation may move the protons bound as OH^- , but this would have no discernible influence because OH^- concentrations are much lower than aluminum or silicon content and thus probably much lower than defect concentrations.

(7) Blue to green colors in KAlSi_3O_8 are due to electronic transitions of Pb^{3+} . This unusual charge state is relatively stable (once formed by radiation) because of its similarity to Au^0 , its electron delocalization (the hole is 31% on lead and 69% on oxygen), and possibly by the configuration of the irregular M-site.

(8) Formation of Pb^{3+} in KAlSi_3O_8 by radiation requires the presence of structurally bound H_2O , but the speciation was not observed to change upon irradiation. Water is partially incorporated through the coupled

substitution

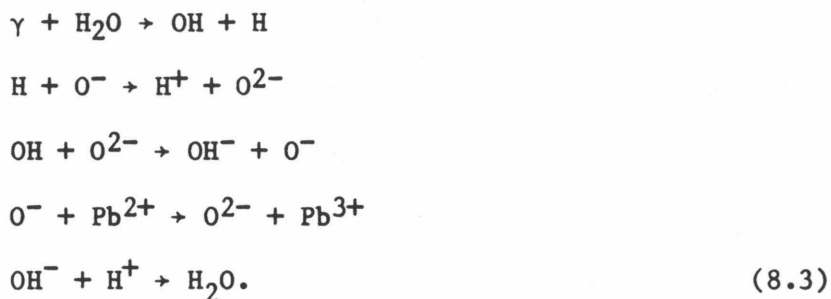


because M-site charge-compensation extends further than nearest neighbors. These sites can produce color upon irradiation. Lead is also incorporated as



but these sites will not produce color.

(9) The proposed mechanism for amazonite coloration by radiation is



After disassociation with the water molecule, the radical H should more readily diffuse than OH because of its size. The radical OH is likely to produce hole centers on oxygen, which if located near Pb^{2+} would react with it, forming the chromophore. Mending of hole centers not connected with lead by hydrogen is likely in view of the suppressive properties of structural H_2O discussed in (6). Recycling of water is required due to the fact that changes of the H_2O bands were not apparent even after the color doubled.

(10) Incorporation of H_2O and lead ions separately influence the Al/Si order of the feldspar, such that increasing either component decreases the maximum order attainable. For very high PbO contents (~ 2%) only disordered structure occurs. The range of amazonite colors depends on the order of the feldspar, such that microcline structure of the color site produces a blue color (630 nm band), while orthoclase structure gives a green color (720 nm band). Samples with intermediate lead contents thus

have a mixture of environments and both bands. A few samples with maximum order possible have M-sites intermediate between microcline and orthoclase, as indicated by multiple Pb^{3+} peaks in the EPR, and by a shift of the absorption band of up to + 20 nm.

(11) Both amazonite and smoky colors are produced through the internal decay of ^{40}K . The darker colors of the blue Colorado amazonites are produced in 300-400 myr.

(12) The color zonation in Lake County labradorite (colorless → green → red → schiller) corresponds to an increasing concentration of copper. The schiller consists of 5 to 40 μm diameter Cu^0 platelets which are at least 90% pure. The red color is a natural analog of copper-ruby color in glasses, and results from the intrinsic absorption of light by Cu^0 colloids of roughly 4 nm diameter. Larger colloids (~22 nm) are found in areas where the red color is transitional into the schiller. The spectral similarity of the green color to amazonite implies that Pb^{3+} is the source of this color.

(13) The formation of the schiller and colors is subsolidus and occurs in the cooling flow because resorption temperatures range from 850-1100°C. The copper must have exsolved from the feldspar (rather than being precipitated inside) because (a) unlike precipitated hematite flakes, the Cu^0 platelets are oriented with respect to the feldspar lattice, (b) oxygen isotopic studies indicated pristine $\delta^{18}O$ values and negligible differences among color zones, and (c) formation of similar color (copper-ruby and schiller) in glass occurs via reduction and then exsolution.

(14) The exsolution temperature depends on copper content. Because diffusion is strongly dependent on temperature, larger aggregates form in

crystals with higher copper content. The exsolution process is continuous during cooling so that in one crystal the schiller may form first, and then the red color. At crystallization, labradorite may incorporate up to 250 ppm Cu^{1+} , but by 800°C , only 35 ppm can remain in solid solution.

(15) Formation of amazonite color in Lake County labradorite implies that reduction at low temperature occurs via the reactions:



Thus reduction precedes exsolution. Equation (8.5) may occur at high temperatures, but in this case, the hole would readily diffuse. The reaction



was not observed within the labradorite. The reduction of copper is probably buffered by the basalt; i.e. $p\text{O}_2$ follows the QFM buffer and because this is parallel to transition metal oxidation/reduction curves, the ratio $\text{Cu}^{1+}/\text{Cu}^{\circ}$ decreases slowly during cooling. If $f\text{O}_2$ were constant, $\text{Cu}^{1+}/\text{Cu}^{\circ}$ would decrease rapidly and thus all Cu would exsolve at high temperatures.

(16) Not only are the chemical trends for the major elements controlled by crystallization and accumulation of plagioclase [Gunn and Watkins, 1970], but the minor elements (Fe, Mg, Mn, Cu, and Ti) are also controlled in the same manner. During the fractional crystallization, labradorite composition was not constant (especially with respect to copper which varies from 0 to 250 ppm Cu among different crystals), implying that the composition of the phenocrysts changed in response to fractionation of the melt.

The coloration process in feldspar is remarkably similar to that in quartz, glass, and other solids. Colloidal coloring of glass by noble metals

necessarily results in the same spectra as in feldspar because the color is due to the intrinsic absorption of the metal. The same statement holds for coloration by metallic schiller except that reflection of light and not absorption occurs. The process of Cu^0 exsolution in feldspar resembles that in glass: schiller develops for high copper content, whereas ruby develops for low. For the glass, ruby color requires slow cooling; in geological environments this occurs automatically. For glass, polyvalent ions are needed to attain small particle sizes and hence a good ruby color. But for feldspar, the buffering is achieved externally through other reactions in the basalt. Under special conditions in feldspar the reduction of Cu^{1+} is mediated by the polyvalent Pb^{2+} .

Besides amazonite, Pb^{3+} can be produced by irradiation of 14 different crystalline solids, including natural calcite (Section 1.2.b.v). In all cases, the hole is delocalized. Many of these centers are stable at room temperature, but other than feldspar, only Pb^{3+} in KCl has been definitely associated with color. For KCl:Pb^{3+} and KCl:Tl^{2+} , four transitions are observed, one of which is located in the visible region. In amazonite, at least three transitions were observed, and one is at the low energy end of the visible region. Like amazonite, the Tl^{2+} center is not produced directly by radiation, but requires a catalyst (Cl_2) [Delbecq et al, 1966]. Pb^{3+} centers do not develop upon irradiation of Pb-bearing glasses; instead ubiquitous O^- hole centers form.

Irradiation of feldspar, quartz, and alkali- and alumino-silicate glasses produces very similar EPR centers (H_I , H_{II} , and Al-O^-) and also absorption spectra (four strong UV and visible bands plus a UV tail which yield a smoky color). For both feldspar and glass, the most commonly observed EPR signals come from oxygen-associated hole traps. For glass

the unaccounted for electrons may be trapped on alkalis or shared among alkali clusters yielding broad band signals [Griscom, 1973], or trapped in pairs, in which case no EPR signal would be produced [Friebele and Griscom, 1979].

The similar response of feldspar, quartz, and glass to radiation is expected in view of their similar chemistry and the fact that their structures are all based on an interlocking framework of SiO_4 tetrahedra, which are modified to varying degrees by introduction of aluminum and alkalis into the network. Differences are reflected in the energies of the absorptions: for a given color center, the energy of the glass and quartz are roughly the same, but that of feldspar is much less.

Feldspar, quartz, and glass are also similar in that the presence of hydrogen species reduces production of smoky color by irradiation. These three examples indicate that irradiation of hydrogen bearing glasses and minerals creates atomic hydrogen which diffuses through the lattice and is trapped at existing defects. Very often the defect in which hydrogen is eventually trapped is related to the defect from which the hydrogen atom was removed. There is evidence that alkali atoms are also displaced by irradiation, and that the difference in behavior between alkali and hydrogen atoms is that hydrogen can diffuse at room temperature. Atomic hydrogen can eliminate both hole and electron centers by several processes: displacing electrons, mending broken bonds, and attaching itself to non-bonding oxygens.

The structural and chemical resemblances between feldspar, quartz, and glass probably aid in forming colors which have similar properties and develop through analogous mechanisms. But some of the similar colors occur in solids very unlike feldspar, which suggests that, for the most part, it is the behavior of the chemical substituent on an atomic level that controls these processes.

REFERENCES

- Abraham, A. and Bleaney B. [1970], Electron Paramagnetic Resonance of Transition Ions, Clarendon Press, Oxford, 911 pp.
- Acocella, J., Takata, M., Tomozawa, M., Watson, E. B. and Warden J. T. [1982], Effect of γ radiation on high-water-content glasses. J. Amer. Ceram. Soc. 65, p. 407-410.
- Aines, R. D., and Rossman, G. R. [1983, in press], Water in minerals? A peak in the infrared. J. Geophys. Res.
- Aitkens, I. [1931], Feldspar Gems. U.S. Bureau of Mines Infor. Circ. 6533, 10 pp.
- Andersen, O. [1915] On adventurine feldspar. Am. J. Sci. 40, p. 351-399.
- Andersen, O. [1917] Adventurine labradorite from California. Am. Min. 2, p. 91.
- Andlauer, B., Schneider, J. and Tolksdorf, W. [1973], ESR analysis of Pb^{+3} ions in $Y_3Ga_5O_{12}$. Phys. Rev. B. 8, p. 1-5.
- Appleman, D. E., Nissen, H.-U., Stewart, D. B., Clark, J. R., Dowty, E., and Huebner, J. S. [1971], Studies of lunar plagioclases, tridymite, and cristobalite. Proc. 2nd Lunar Sci. Conf., Geochim. Cosmochim. Acta Supplement 2, Vol. 1, p. 117-133.
- Arafa, S. and Bishay, A. [1969], A gamma induced centre in potassium borate glass. Phys. Chem. Glasses 10, p. 192-197.
- Arnold, G. W. and Compton, W. D. [1959], Radiation effects in silica at low temperatures. Phys. Rev. 116, p. 802-808.
- Auger, V. [1907], Theorie de la formation du verre d'aventurine an cuive. Comptes Rendus 144, p. 422-424.
- Bakhtin, A. I., Khasanov, R. A., and Vinokurov, V. M. [1973], Electron paramagnetic resonance and optical absorption spectra of some defect centers in barites and celestites. Sostav. Strukt. Svoista. Mineral., p. 84-90.
- Baksi, A. K., York, D., and Watkins, N. D. [1967], Age of the Steens Mountain geomagnetic polarity transition. J. Geophys. Res. 72, p. 6299-6308.
- Ballhausen, C. J. and Gray, H. B. [1964] Molecular Orbital Theory. Benjamin-Cummings Inc., Reading, Massachusetts, p. 127.
- Bambauer, H. U. [1961], Spurenelementgehalte und γ -Farbzentren in Quarzen aus Zerrklüften der Schweizer Alpen. Schweiz. Min. Petr. Mitt. 41, p. 335-369.

- Barasov, L. Sh., Kosals, Ya. A., and Senina, V. A. [1972], Temperature of formation of Zinwaldite-Amazonite-Albite Apogranite. *Doklady Earth Sci. Sec.* 203, p. 197-199.
- Barker, R. S., McConkey, E. A. G., and Richardson, D. A. [1965], Effect of gamma radiation on the optical absorption of lead silicate glass. *Phys. Chem. Glasses* 6, p. 24-29.
- Barkatt, A., Angell, C. A., and Miller, J. R. [1981], Visible spectroscopy of irradiated high-alkali borate and mixed-alkali phosphate glasses. *J. Amer. Ceram. Soc.* 64, p. 158-162.
- Bartholomew, R. F., Butler, R. L., Hoover, H. L., and Wu, C. K. [1980], Infrared spectra of a water-containing glass. *J. Amer. Ceram. Soc.* 63, p. 481-485.
- Basset, H. [1956], The colouring agent in amazonstone (amazonite). *Records Geol. Survey Tanganyika* 3, p. 97-99.
- Bell, P. M., and Mao, H. K. [1972], Measurements of the polarized crystal field spectra of ferrous and ferric iron in seven terrestrial plagioclases. *Carnegie Inst. Yrbk.* 72, p. 594-576.
- Bell, P. M., and Mao, H. K. [1973], Optical and chemical analysis of iron in Luna 20 plagioclase. *Geochim. Cosmochim. Acta* 37, p. 755-759.
- Bernstein, L. R. [1979], Coloring mechanisms in celestite. *Amer. Min.* 64, p. 160-168.
- Bethe, H. [1929], *Termaufspaltung in Kristallen.* *Annalen der Physik* 3, p. 133-208.
- Beyersdorfer, P., and Beyersdorfer, K. [1943], Studies of adventurine glasses. *Glastechn. Ber.* 21, p. 1-7.
- Bill, H. and Calas, G. [1978], Color centers, associated rare earth ions and origin of coloration in natural fluorites. *Phys. Chem. Min.* 3, p. 117-131.
- Binns, R. A. [1964], Zones of progressive regional metamorphism in the Willyama Complex, Broken Hill District, New South Wales. *J. Geol. Soc. Australia* 11, p. 283-330.
- Bishay, A. [1970], Radiation induced color centers in multicomponent glasses. *J. Non-Crystalline Solids* 3, p. 54-114.
- Bishay, A. and Maklad, M. [1966], Radiation induced optical absorption in lead borate glasses in relation to structural changes. *Phys. Chem. Glasses* 7, p. 149-156.
- Boone, G.M. [1969], Origin of clouded red feldspars: petrologic contrast in a granitic porphyry intrusion. *Am. J. Sci.* 267, p. 633-668.

- Born, G., Hofstaetter, A., and Scharman, A. [1970], EPR investigations on $\text{CaWO}_4:\text{Pb}$ single crystals. *Phys. Stat. Sol.* 37, p. 255-265.
- Born, G., Hofstaetter, A., and Scharmann, A. [1971a], Superhyperfine-interaction in the EPR-spectrum of Pb^{+3} -ions in $\text{CaWO}_4:\text{Pb}$ single crystals. *Zeit. Physik.* 245, p. 333-346.
- Born, G., Hofstaetter, A., and Scharmann, A. [1971b], $^2\text{S}_{1/2}$ -states of Pb^{+3} -ions: correlations between g-values and hyperfine splitting constants A in the EPR Spectra. *Zeit. Physik* 248, p. 7-12.
- Born, G., Hofstaetter, A., Scharmann, A., and Vitt, B. [1974], Anisotropic hyperfine interaction of Pb^{3+} ions in $^2\text{S}_{1/2}$ -state EPR. *Phys. Stat. Sol. B.* 66, p. 305-308.
- Born, G., Hofstaetter, A., Scharmann, A. and Vitt, B. [1976], Pb^{+3} -ions in CaWO_4 : temperature dependence of hyperfine interaction. *Zeit. Physik B.* 23, p. 307-309.
- Boyd, F. R., and England, J. L. [1960], Apparatus for phase-equilibrium measurements at pressures up to 50 kilobars and temperatures up to 1750°C . *J. Geophys. Res.* 65, p. 741-748.
- Brauns, R. [1909], Der Einfluss von Radiumstrahlen auf die Faerbung von Sanidin, Zircon, und Quarz. *Zbl. Mineral. Geol. Palaont.* p. 721.
- Breit, G., and Rabi, I.I. [1931], Measurement of nuclear spin. *Phys. Rev.* 38, p. 2082-2083.
- Breithaupt, A. [1847], Vollstandiges Buch der Mineralogie, III. Dresden und Leipzig.
- Brown, F. F., and Pritchard, A. M. [1969], The Mössbauer spectrum of iron orthoclase. *Earth Planet. Sci. Lett.* 5, p. 259-260.
- Bruno, E., and Facchinelli, A. [1972], Al,Si configurations in lead feldspar. *Zeit. Krist.* 136, p. 296-304.
- Bugaets, A. N. [1967], Characteristics of amazonite granites of Kazakhstan. *Zap. Vses. Mineral. Obshch.* 96, p. 641-651, (in Russian).
- Bukarnov, V. V., and Markova, G. A. [1969], The smoky and citrine color of natural quartz. *Dokl. Akad. Nauk. Translations, Earth Sci. Section* 187, p. 115-117.
- Burns, R. G. [1970], *Mineralogical Applications of Crystal Field Theory*, Cambridge University Press, Oxford, England, 224 pp.
- Cameron, E. N., Jahns, R. H., McNair, A. H., and Page, L. R. [1949], Internal structure of granitic pegmatites. *Econ. Geol. Mono. 2*, Economic Geology Publishing Co., Urbana, Illinois, 115 pp.
- Canina, V. G. and Priqueler, M. [1962], Diffusion of protons in $\text{SiO}_2+\text{Al}_2\text{O}_3$ glass in an electric field. *Phys. Chem. Glass.* 3, p. 43-45.

- Carlson, E. H., and Kircher, M. A. [1976], A pleochroic variety of gem labradorite from the Rabbit Hills area, Lake County, Oregon. *Gems and Gemology* 15, p. 162-167.
- Carmichael, I. S. E. [1967], The mineralogy and petrology of the volcanic rocks from the Leucite Hills, Wyoming. *Contrib. Mineral. Petrol.* 15, p. 24-66.
- Catanzaro, E. J., and Gast, P. W. [1960], Isotopic composition of lead in pegmatitic feldspars. *Geochim. Cosmochim. Acta* 19, p. 113-126.
- Cech, F., Misar Z., and Povondra, P. [1971], A green lead-containing orthoclase. *Tschermaks Mineral. Petrol. Mitt.* 15, p. 213-231.
- Chodos, A. A., Albee, A. A., Gancarz, A. J., and Laird, J. [1973], Optimization of computer-controlled quantitative analyses of minerals. *Proc. 8th Nat. Conf. on Electron Probe Analysis, New Orleans, LA*, p. 45a-45c.
- Clark, M. G., and Burns, R. G. [1967], Electronic spectra of Cu^{+2} and Fe^{+2} square planar coordinated by oxygen in $\text{BaXS}_{14}\text{O}_{10}$. *J. Chem. Soc. A* 1967, p. 1034-1038.
- Cohen, A. J., and Makar, L. N. [1982], Models for color centers in smoky quartz. *Phys. Status Solidi A*, 73, p. 593-596.
- Coombs D. S. [1954], Ferriferous orthoclase from Madagascar. *Mineral. Mag.* 30, p. 409-427.
- Copley, P. A., and Gay, P. [1978], A scanning electron microscope investigation of some Norwegian aventurine feldspars. *Norsk. Geol. Tidsskr* 58, p. 93-95.
- Copley, P. A., and Gay, P. [1979], Crystallographic studies of some Norwegian aventurized feldspars by optical, X-ray, and electron optical methods. *Norsk. Geol. Tidsskr* 59, p. 229-237.
- Davydov A. S. [1968], Theory of Urbach's rule. *Phys. Status Solidi*, 27, p. 51-56.
- Deer, W. A., Howie, R. A., and Zussman, J. [1966], *An Introduction to the Rock Forming Minerals*. Longman, London, England, 528 pp.
- Delbecq, C. J., Ghosh, A. K., and Yuster, P. K. [1966], Trapping and annihilation of electrons and positive holes in KCl-TlCl . *Phys. Rev.* 151, p. 599-609.
- Deuser, W. G., and Herzog, L. F. [1962], Rubidium-strontium age determinations of muscovites and biotites from pegmatites of the Blue Ridge and Piedmont. *J. Geophys. Res.* 67, p. 1997-2004.
- Dietzel, A. [1945], *Über das Anlaufen der durch Metallkolloide Gefärbten Glaser*. *Zeit. Elektrochem.* 51, p. 32-37.

- DiSalvo, R., Roy, D. M., and Mulay, L. N. [1972], EPR studies of radiation damage in hydrogen-impregnated glass. *J. Amer. Ceram. Soc.* 55, p. 536-537.
- Divljan, S. [1960], The results of field and laboratory studies of adventurine plagioclases from some Norwegian pegmatites. *Rept. 21st Intern. Geol. Congr. Norden* 17, p. 94-101.
- Donnay, G., Wyart, J. and Sabatier, G. [1959], Structural mechanism of thermal and compositional transformations in silicates. *Zeit. Kristallog.* 112, p. 161-168.
- Draganic, I. G., and Draganic, Z. D. [1971], *The Radiation Chemistry of Water.* Acad. Press, New York, 242 pp.
- Dreybrodt, W., and Silber, D. [1967], Electron spin resonance of Tl^{++} centers in KCl crystals. *Phys. Status Solidi* 20, p. 337-346.
- DuVarney, R. C., and Garrison, A. K. [1975], Electron paramagnetic resonance of divalent thallium in cadmium telluride. *Phys. Rev. B* 12, p. 10-14.
- Eaton S. S., and Eaton G. R. [1979] Signal area measurements in EPR. *Bull. Magnetic Resonance* 1, p. 130-138.
- Ebell, P. [1874], *Der Kupferrubin und die verwandten Gattungen von Glas.* *Dinglers Polyt. J.* 213, p. 53-59, 131-145, 212-220, 321-326, 401-410, and 497-506.
- Eliseev, E. N. [1949], *Okraska amazonita.* *Zap. Vses. Miner. Obshch.* 78, p. 26-39, (Abstracted in *Min. Abst.* 11 [1950], p. 285).
- Emmerling, L. A. [1773] *Lehrbuch der Mineralogie,* Griesen.
- Emmons R. C. (ed) [1953] *Selected petrogenetic relationships of plagioclase.* *Geol. Soc. Amer. Mem.* 52, p. 1-142.
- Ernst, W. G. [1960], Diabase-granophyre relations in the Endion Sill, Duluth, Minnesota. *J. Petrol.* 1, p. 286-303.
- Faile, S. P. [1969], *New Materials and Reactions in High Pressure Gas-Glass Systems.* PhD Thesis, Pennsylvania State Univ.
- Faile, S. P., and Roy, D. M. [1970], Mechanism of color center destruction in hydrogen impregnated radiation resistant glasses. *Materials Res. Bull.* 5, p. 385-390.
- Faraday, M. [1857], Experimental relations of gold (and other metals) to light. *Phil. Mag.* 14, p. 401-417, 512-539.
- Faust, G. T. [1936], The fusion relations of iron orthoclase. *Amer. Mineral.* 21, p. 735-763.
- Faye, G. H. [1969], The optical absorption spectrum of tetrahedrally bonded Fe^{3+} in orthoclase. *Canad. Mineral.* 10, p. 112-117.

- Folk, R. L. [1955], Note on the significance of "turbid" feldspars. *Amer. Mineral.* 40, p. 356-357.
- Foord, E. E. [1977], Famous mineral localities: the Himalaya dike system, Mesa Grande district, San Diego County, California. *Mineral. Record* 8, p. 461-474.
- Foord, E. E., and Martin, R. F. [1979], Amazonite from the Pikes Peak Batholith. *Mineral. Record* 10, p. 373-382.
- Forst, E., Jr., and Kreidl, N. J. [1942], Red Silver Glasses. *J. Amer. Ceram. Soc.* 25, p. 278-280.
- Fremy, E. and Clemandot, G. [1846], Note sur la production de l'Aventurine artificielle. *Comptes Rendus* 22, p. 339-342.
- Friebele, E. J., and Griscom, D. L. [1979], Radiation effects in glass. *Treatise on Material Science and Technology* 17, Glass II, Edited by M. Tomozawa and A.H. Doremus, Academic Press, New York, p. 257-351.
- Friebele, E. J., Jaeger, R. E., Siegel, G. H., Jr., and Gingerich, M. E. [1978], Effect of ionizing radiation on the optical attenuation in polymer-clad silica fiber-optic wave guides. *Appl. Phys. Lett.* 32, p. 95-97.
- Friedman, I. [1953], Deuterium content of natural waters and other substances. *Geochim. Cosmochim. Acta* 4, p. 89-103.
- Fron del, C., Ito, J. and Hendricks, J. G. [1966], Barium feldspars from Franklin, New Jersey. *Amer. Mineral.* 51, p. 1388-1393.
- Fuller, R. E. [1931], The Geomorphology and Volcanic Sequence of Steens Mountain in Southeastern Oregon. *Wash. Univ. Geol. Publ.* 3, p. 1-130.
- Gaite, J.-M., and Michoulier, J. [1970], Application de la resonance paramagnetique electronique de l'ion Fe^{3+} a l'etude de la structure des feldspaths. *Bull. Soc. Fr. Mineral. Cristallogr.* 93, p. 341-356.
- Gans, R. [1912], Uber die Form ultramikroskopischer Goldteilchen. *Ann. Physik* 37, p. 881-900.
- Gay P. [1955], The structures of the plagioclase feldspars: VI. Natural intermediate plagioclases. *Mineral. Mag.* 31, p. 21-40.
- Geake, J. E., Walker, G., Mills, A. A., and Garlick, G. F. J. [1971], Luminescence of Apollo lunar samples. *Proc. 2nd Lunar Sci. Conf.*, *Geochim. Cosmochim. Acta. Suppl.* 2, V. 3, p. 2265-2275.
- Godfrey, J. D. [1962], The deuterium content of hydrous minerals from the East-Central Sierra Nevada and Yosemite National Park. *Geochim. Cosmochim. Acta* 26, p. 1215-1245.

- Golding R. M., Kestigian M., and Tennant C. W. [1978] EPR of high-spin Fe^{3+} in calcium tungstate, CaWO_4 . *J. Phys. C.: Solid State Phys.* 11, p. 5041-5049.
- Golding R. M., Singhasuwich T., and Tennant W. C. [1977], An analysis of the conditions for an isotropic g-tensor in high-spin d^5 systems. *Molecular Physics* 34, p. 1343-1350.
- Goldman, D. A., and Rossman, G. R. [1977], The spectra of iron in orthopyroxene revisited: The splitting of the ground state. *Amer. Mineral.* 62, p. 151-152.
- Goldman, D. A., and Rossman, G. R. [1979], Determination of quantitative cation distribution in orthopyroxenes from electronic absorption spectra. *Phys. Chem. Minerals* 4, p. 43-53.
- Goldstein, E. [1902], Uber die durch Strahlungen erzeugten Nachfarben. *Physik. Zeit.* 3, p. 149-151.
- Goodman, B. A. and Raynor, J. B. [1970], Electron spin resonance of transition metal complex. *Advances in Inorganic Chemistry and Radiochemistry* 13, p. 135-363.
- Granger, A. [1923], Opaque and colored glasses and ceramic glazes of the same nature. *J. Soc. Glass Tech.* 7, p. 291-295.
- Griffith, J. S. [1961], *The Theory of Transition-Metal Ions*. University Press, Cambridge, England, 455 pp.
- Griffiths, J. H. E., Owen, J., and Ward, I. M. [1954], Paramagnetic resonance in neutron-irradiated diamond and smoky quartz. *Nature* 173, p. 439-440.
- Griscom, D. L. [1971], ESR and optical studies of alkali-associated trapped-electron centers in alkali borate glasses irradiated at 77°K. *J. Non-Crystalline Solids* 6, p. 275-282.
- Griscom, D. L. [1973], ESR studies of radiation damage and structure in oxide glasses not containing transition group ions: a contemporary overview with illustrations from the alkali-borate system. *J. Non-Crystalline Solids* 8, p. 251-285.
- Guermazi, M., Thevanard, P., Dupin, J. P., and Dupuy, C. H. S. [1980], Effects of implantation in rutile with metallic ions. *Radiation Effects* 49, p. 61-64.
- Gunn, B. M., and Watkins, N. D. [1970], Geochemistry of the Steens Mountain Basalts, Oregon. *Geol. Soc. Amer. Bull.* 81, p. 1497-1516.
- Gutlich, P. H., Odar, S., Fitzsimmons, B. W., and Erickson, N. E. [1968], Mössbauereffekt-Untersuchungen an γ -bestrahlten Eisenkomplexen. *Radiochimica Acta* 10, p. 147-153.
- Gutmann, J. T. [1974], Tubular voids within labradorite phenocrysts from Sonora, Mexico. *Amer. Mineral.* 59, p. 666-672.

- Gutmann, J. T. [1976], Geology of Crater Elegante, Sonora, Mexico. Geol. Soc. Amer. Bull. 87, p. 1718-1729.
- Gutmann, J. T. [1977], Textures and genesis of phenocrysts and megacrysts in basaltic flows from the Pinacate Volcanic field. Amer. J. Sci. 277, p. 833-861.
- Gutmann, J. T., and Martin, R. F. [1976], Crystal chemistry, unit cell dimensions and structural state of labradorite megacrysts from Sonora, Mexico. Schweiz. Mineral. Petrogr. Mitt. 56, p. 55-64.
- Hafele, H.-G. [1960], Über die Absorption des Quarzes in nahen Ultrarot. Zeit. Phys. 160, p. 420-430.
- Hafner, S. S. [1975], Mössbauer spectroscopy in Lunar geology and mineralogy. Topics in Applied Physics Vol. 5, Mössbauer Spectroscopy, Springer-Verlag, Heidelberg, Germany, p. 167-194.
- Hafner, St. and Laves, F. [1957], Ordnung/Unordnung und Ultrarotabsorption II. Variation der Lage und Intensität einiger Absorptionen von Feldspäten. Zur Struktur von Orthoklas und Andular, Zeitschrift Kristallog. 109, p. 204-225.
- Hafner, S. S., Virgo, D., and Warburton, D. [1971], Oxidation State of Iron in Plagioclase from Lunar Basalts. Earth Planet. Sci. Lett. 12, p. 159-166.
- Hartwig, C. M. [1977], The radiation-induced formation of hydrogen and deuterium compounds in silica as observed by Raman scattering. J. Chem. Phys. 66, p. 227-238.
- Hashimoto, S. and Ohiwa, Y. [1980], Absorption spectra of Pb^{++} centers in alkali iodides. J. Phys. Soc. Japan 48, p. 1655-1660.
- Haskell, B. S. [1959], The Geology of a Portion of the New York Mountains and Lanfair Valley. Masters thesis, Univ. of Southern California.
- Hautefeuille, P., and Perrey, A. [1888], Sur la preparation et les proprietes de l'orthose ferrique. Comptes Rendus 107, p. 1150-1152.
- Hawthorne, F. C. [1983], Quantitative characterization of site-occupancies in minerals. Am. Min. 68, p. 287-306.
- Helmke, P. A., and Haskin, L. A. [1973], Rare-earth elements, Co, Sc, and Hf in the Steens Mountain Basalts. Geochim. Cosmochim. Acta 37, p. 1513-1529.
- Hewett, D. F. [1956], Geology and mineral resources of the Ivanpah quadrangle, California and Nevada. U.S. Geol. Surv. Prof. Paper 275, 172 pp.
- Hill, F., and Lehmann, G. [1978], Atomic hydrogen in the mineral Brazilianite $NaAl_3(PO_4)_2(OH)_2$. Zeit. Naturforsch. 33a, p. 1484-1486.

- Hintze, C. [1897], Handbuch der Mineralogie II, p. 1354-1357. Verlag von Weit, Leipzig.
- Hobbs, L. W., Hughes, A. E., and Chassagne, G. [1974], Direct observation of alkali metal colloids in alkali halide crystals. *Nature* 252, p. 383-385.
- Hochli, U. [1964], Electron spin resonance of Fe^{+3} in feldspars. *Proc. Colloq. Ampere. (Electronic magnetic resonance and solid dielectrics)* 12th, p. 191-197.
- Holton, W. C., and Watts, R. K. [1969], $^2\text{S}_{1/2}$ -state centers in II-VI compounds. *J. Chem. Phys.* 51, p. 1615-1620.
- Hutchinson, R. M. [1976], Granitic-tectonics of the Pikes Peak Batholith. *Prof. Contrib. of the Colorado School of Mines, Vol. 8, Studies in Colorado Field Geology*, eds. R.C. Epis and R.J. Weimer, p. 32-43.
- Iida, T., and Watanabe, H. [1968], Ge- and Pb-Associated Hole-Traps in ZnTe Crystals. *Phys. Lett.* 26A, p. 541-542.
- Iiishi, K., Tomisaka, T., Kato, T., and Umegaki, Y. [1971], Isomorphous substitution, infrared, and far-infrared spectra of the feldspar group. *Neues Jahrbuch Miner. Abh.* 115, p. 98-119.
- Ioffe, V. A., and Yanchevskaya, I. S. [1968], Electron paramagnetic resonance and thermoluminescence of irradiated single crystals of the aluminosilicate $\text{NaAlSi}_3\text{O}_8$ and LiAlSiO_4 . *Soviet Phys. Solid State* 10, p. 370-374
- Isshiki, N. [1958], Red coloration of anorthite from Hachijo-Jima. *J. Geol. Soc. Japan* 64, p. 644-647.
- Jahns, R. H. [1955], The Study of Pegmatites. *Econ. Geol. 50th Anniv. Volume*, p. 1025-1130.
- Jahns, R. H., and Wright, L.A. [1951], Gem and lithium bearing pegmatites of the Pala district, San Diego County, California. *Calif. Div. Mines, Special Rept. 7-A*, 72pp.
- Jennings, C. W. [1958], Death Valley Sheet, *Geol. Map of California, Div. of Mines and Geology*.
- Johannes, W., Bell, P. M., Mao, H. K., Boettcher, A. L., Chipman, D. W., Hays, J. F., Newton, R. C., and Seifert, F. [1971], An interlaboratory comparison of piston-cylinder pressure calibration using the albite-breakdown reaction. *Contrib. Mineral. Petrol.* 32, p. 24-38.
- Karapetyan, G. O., Stepanov, S. A., and Yudin, D. M. [1964], Color centers in sodium aluminosilicate glasses. *Fizika Tverdogo Tela*, 6, p. 1531-1539, (English translation: *Soviet Physics-Solid State*, 6, p. 1197-1203).
- Kats, A. [1962], Hydrogen in alpha-quartz. *Phillips Res. Repts.* 17, p. 133-195, 201-279.

- Kevan, L. [1969], Radiation chemistry of frozen polar systems. *Actions Chim. Biol. Radiat.* 13, Ed. M Haissinsky, Masson Et Cie, Paris, p. 57-117.
- Kim, Y. M., and Bray, P. J. [1968], Electron spin resonance studies of gamma-irradiated glasses containing lead. *J. Chem. Phys.* 49, p. 1298-1301.
- Koenig, G. A. [1876], Microcline, Pikes Peak region, El Paso and Douglass counties, Colorado. *Philadelphia Acad. Nat. Sci. Proc.* 28, p. 155.
- Kordas, G., and Oel, H. J. [1982], Structure of radiation-induced hole centers in alkali silicate glasses. *Phys. Chem. Glasses* 23, p. 179-183.
- Kraeft, U. and Saalfeld, H. [1967], *Über die adventurin-oligioklase von Tvedestrand und Bjordan (Norwegen)*. *Schweiz. Mineral. Petrogr. Mitt.* 47, p. 247-256.
- Kreffft, G. B. [1975], Effects of high-temperature electrolysis on the coloration characteristics and OH-absorption bands in alpha-quartz. *Radiation Effects* 26, p. 249-259.
- Lee, S., and Bray, P. J. [1962], Electron-spin paramagnetic resonance studies of irradiated alumino-silicate glasses. *Phys. Chem. Glasses* 3, p. 37-42.
- Lell, E., Kreidl, N. J., and Hensler, J. R. [1966], Radiation effects in Quartz, Silica, and Glasses. *Progress in Ceramic Science* 4, Ed. J. E. Burke, Pergamon Press, Oxford, England, p. 1-94.
- Levy, P. W. [1960], The kinetics of gamma-ray induced coloring of glass. *J. Amer. Ceram. Soc.* 43, 389-395.
- Low, W. [1968], Electron spin resonance - a tool in mineralogy and geology. *Adv. in Electronics and Physics* 24, p. 51-108.
- Luettig, G. W. [1980], General geology of the Federal Republic of Germany. *Geology of the European Countries: Austria, Federal Republic of Germany, Ireland, The Netherlands, Switzerland, and The United Kingdom*. *Comite National Francais de Geologie, Paris, 26th Geological Congress*, p. 88-127.
- MacGregor, A. G. [1931], Clouded feldspars and thermal metamorphism. *Mineral. Mag.* 22, p. 524-538.
- Mackey, J. H., Jr. [1963], EPR study of impurity-related color centers in germanium-doped quartz. *J. Chem. Phys.* 39, p. 74-83.
- Mackey, J. H., Jr., Smith, H. L., and Nahum, J. [1966a], Competitive trapping in sodium disilicate glasses doped with Eu^{+3} . *J. Phys. Chem. Solids* 27, p. 1773-1782.
- Mackey, J. H., Jr., Smith, H. L., and Halperin, A. [1966b], Optical studies in X-irradiated high purity sodium silicate glasses, *J. Phys. Chem. Solids* 27, p. 1759-1772.

- Manning, P. G. [1970], Racah parameters and their relationship to lengths and covalences of Mn^{2+} and Fe^{+3} oxygen bonds in silicates. *Canadian Mineral.* 10, p. 677-688.
- Marfunin, A. S. [1979], Spectroscopy, Luminescence and Radiation Centers in Minerals. Springer-Verlag, Berlin, Germany, 352 pp.
- Marfunin A. S., Bershov L. V., Meilman M. L., and Michoulier, J. [1967], Paramagnetic resonance of Fe^{+3} in some feldspars. *Schweiz. Mineral. Petrogr. Mitt.* 47, p. 13-20.
- Marfunin, A. S. and Bershov, L. V. [1970], Paramagnetic centers in feldspar and their possible crystallochemical and petrological significance. *Dokl. Akad. Nauk. Trans.* 193, p. 129-130.
- Martin, R. F. [1968], Hydrothermal synthesis of low albite, orthoclase, and non-stoichiometric albite. PhD thesis, Stanford Univ., Stanford, CA.
- Maschmeyer, D., Niemann, K., Hake, H. Lehman, G. and Rauber, A. [1980], Two modified smoky quartz centers in natural citrine. *Phys. Chem. Minerals* 6, p. 145-156.
- Matyash I. V., Bagmut N. N., Litovchenko A. S., and Proshko, V. Ya. [1982], Electron paramagnetic resonance study of new paramagnetic centers in microcline perthites from pegmatites. *Phys. Chem. Minerals* 8, p. 149-152.
- Michoulier, J., and Gaite, J.-M. [1972], Site Assignment of Fe^{3+} in low symmetry crystals. Applications to $NaAlSi_3O_8$. *J. Chem. Phys.* 56, p. 5205-5213.
- Mie, G. [1908], Beitrage zur Optik truber Medien, speziell kolloidaler Metallosungen. *Ann. Physik* 25, p. 377-445.
- Mita, Y. [1965], Luminescent centers in lead- and tin-activated zinc sulfide, *J. Phys. Soc. Japan* 20, p. 1822-1826.
- Nakamoto, K. [1978], Infrared and Raman Spectra of Inorganic and Coordination Compounds, 3rd Edition. John Wiley and Sons, New York, 448 pp.
- Nassau, K., and Prescott, B. E. [1975], A reinterpretation of smoky quartz. *Phys. Status Solidi A* 29, p. 659-663.
- Nassau, K., and Prescott, B. E. [1977], Smoky, blue, greenish yellow, and other irradiation-related colors in quartz. *Mineral. Mag.* 41, p. 301-312.
- Nelson, C. M., and Weeks, R. A. [1960], Trapped electrons in irradiated quartz and silica: I, optical absorption. *J. Amer. Ceram. Soc.* 43, p. 396-399.
- Neumann, H., and Christie O. H. J. [1962], Observations on plagioclase adventurines from Southern Norway. *Norsk. Geol. Tidsskr.* 42, p. 389-393.
- Newnham, R. E., and Santoro, R. P. [1967], Magnetic and optical properties of diopside. *Phys. Status Solidi* 19, p. K87-K90.

- Niebuhr, H. H., Zeira, S., and Hafner, S. S. [1973], Ferric iron in plagioclase crystals from anorthosite 15415. Proc. Lunar Sci. Conf. 4th Supp., Geochim. Cosmochim. Acta 1, p. 971-982.
- Niggli, P. [1914], Einige vorlaufige hydrothermale Synthesen. Zeit. Anorg. Chem 84, p. 31-55.
- Nishi, M., Hara, H., Ueda, Y., and Kazumata, Y. [1977], ESR study of Pb^{3+} ions in cubic PbF_2 crystals irradiated with γ -rays and neutrons at low temperatures. J. Phys. Soc. Japan 42, p. 1900-1905.
- Nunes, J. L. [1979], Amazonites de Mocambique-Novos dados sobre a sua composicao. Comunic. Serv. Geol. Port. LXIV, p. 71-79.
- O'Brien, M. C. M. [1955], The structure of color centres in smoky quartz. Proc. Royal Soc. A 231, p. 404-414.
- Odiorne, H. H. [1978], Colorado Amazonstone. Forum Publishers, Denver, CO, 50 pp.
- Oftedal, I. [1957], Heating experiments on amazonite. Mineral. Mag. 31, p. 417-419.
- Onaka, R., Fukuda, A., and Mabuchi, T. [1965], A new type of absorption band in NaCl:Pb and KCl:Pb. J. Phys. Soc. Japan 20, p. 466.
- O'Neil, J. R., and Taylor, H. P., Jr. [1967], The oxygen isotope and cation exchange chemistry of feldspars. Amer. Mineral. 52, p. 1414-1437.
- Orville, P. M. [1960], Petrology of several pegmatites in the Keystone district, Black Hills, South Dakota. Geol. Soc. Amer. Bull. 71, p. 1467-1490.
- Orton, J. W., Auzins, P., Griffiths, J. H. E., and Wertz, J. E. [1961], Electron spin resonance studies of impurity ions in magnesium oxide. Proc. Phys. Soc. of London 78, p. 554-568.
- Parke, S., and Webb, R. S. [1973], The optical properties of thallium, lead and bismuth in oxide glasses. J. Phys. Chem. Solids 34, p. 85-95.
- Parsons, I. [1978], Feldspars and fluids in cooling plutons. Mineral. Mag. 42, p. 1-17.
- Perenboom, J. A. A. J., Wyder, P., and Meier, F. [1981], Electronic Properties of Small Metal Particles. Phys. Repts. 78, p. 175-292.
- Perlson, B. D., and Weil, J. A. [1974], Atomic hydrogen in α -Quartz. J. Magnetic Resonance 15, p. 594-595.
- Peterson, N. V. [1972], Oregon "sunstones". The Ore Bin (State of Oregon, Dept. Geol. and Min. Industr.) 34, p. 197-215.

- Pivec, E., Sevcik, J., and Ulrych, J. [1981], Amazonite from the alkali granite of the Avdar Massif, Mongolia. *Tschermaks Mineral. Petrogr. Mitt.* 28, p. 277-283.
- Plimer, I. R. [1976], A plumbian feldspar pegmatite associated with Broken Hill orebodies, Australia. *Neues Jahrbuch Mineral. Monat* 6, p. 272-288.
- Plyusnin, G. S. [1969], On the coloration of amazonite. *Zap. Vses. Mineral. Obshch.* 98, p. 3-17, (In Russian).
- Poldervaart, A., and Gilkey, A. K. [1954], On clouded plagioclase. *Amer. Mineral.* 39, p. 75-91.
- Popescu, F. F., and Grecu, V. V. [1975], Temperature dependence of Pb^{3+} EPR spectrum. *Phys. Status Solidi B* 68, p. 595-601.
- Przibram, K. [1956], *Irradiation Colors and Luminescence*, Pergamon Press, London, England, 332 pp.
- Ramsey, N. F. [1956], *Molecular Beams*. Clarendon Press, Oxford, 466 pp.
- Reed, J. S. [1973], Optical spectra of Cu^{+2} and Ni^{+2} in intermediate aluminate spinals. *J. Amer. Ceram. Soc.* 56, p. 525-527.
- Ribbe, P. H. [1975], Exsolution textures and interference colors. *Feldspar Mineralogy*, 1st Edition, *Reviews in Mineralogy*. Mineral Society of America, Washington, D.C., p. R73-R96.
- Riederer, J. [1965], Die Kalifeldspate der moldanubischen Granite. *Neues Jahrbuch Mineral. Abteilungen* 5, p. 291-339.
- Rinneberg, H., and Weil, J. A. [1972], EPR Studies of $Ti^{3+}-H^{+}$ centers in X-Irradiated -quartz. *J. Chem. Phys.* 56, p. 2019.
- Rohrig, R. and Schneider, J. [1969], ESR of Pb^{3+} in ThO_2 . *Phys. Letters* 30A, p. 371-372.
- Rontgen, W. C. (partially in collaboration with A. Joffe) [1921], Über die Elektrizitätsleitung in einigen Kristallen und über den Einfluss einer Bestrahlung darauf. *Annalen der Physik* 64, p. 1-195.
- Rose, H. [1848], Über das goldhaltige Glas. *Dinglers Polytech. Jour.* 107, p. 129.
- Rosenqvist, I. T. [1965], Electron-microscope investigations of Larvikite and Tonsbergite feldspars. *Norsk Geol. Tidsskr.* 45, p. 69-71.
- Rossmann, G. R. [1980], Pyroxene spectroscopy. *Pyroxenes, Reviews of Mineralogy*, Vol. 7. Mineralogical Society of America, Washington, D.C., p. 93-116.
- Rudenko, S. A. and Vokhmentsev A. Ya. [1969], Plagioclase-amazonite. *Dokl. Akad. Nauk. Trans.* 184, p. 113-115.

- Samoilovich, M. I. [1971], Study of sulfur-containing ion-radicals in minerals studied by the EPR method. *Geokhimiya* 4, p. 477-483.
- Scala, C. M., Hutton, D. R., and McLaren, A. C. [1976], NMR and EPR studies of some chemically intermediate plagioclase feldspars. *Phys. Chem. Minerals* 3, p. 33-44.
- Schawlow, A. L., Hume, J. N. P., and Crawford, M. W. [1949], Hyperfine structure and nuclear moment of Pb^{207} . *Phys. Rev.* 76, p. 1876.
- Scheel, H. J. [1971], Lead feldspar. *Zeit. Krist.* 133, p. 264-272.
- Scherrer, P., and Staub, H. [1931], Rontgenographische Untersuchung des Koagulationsvorganges bei kolloidem Gold, *Z. Phys. Chem.* 154 A, p. 309-321.
- Scheurs, J. W. H. [1967], Study of some trapped hole centers in X-irradiated alkali silicate glasses. *J. Chem. Phys.* 47, p. 818-830.
- Schirmer, O. F. [1976], Smoky coloration of quartz caused by bound small polaron optical absorption. *Solid State Commun.* 18, p. 1349-1351.
- Schnadt, R., and Schneider, J. [1970], The electronic structure of the trapped-hole center in smoky quartz. *Phys. Kondens. Materie* 11, p. 19-42.
- Schoemaker, D., and Kolopus, J. L. [1970], Pb^{++} as a hole trap in KCl: ESR and optical absorption of Pb^{+++} . *Solid State Commun.* 8, p. 435-439.
- Scholze, H. [1959], Der Einbau des Wassers in Glasern. *Glastech. Ber.* 32, p. 81-88, p. 142-145, 278-281.
- Scholze, H. [1966], Gases and water in glass. *Glass Ind.* 47, p. 546-551, 622-628.
- Schulman, J. H., and Compton, W. D. [1962], Color centers in solids. *International Series of Monographs on Solid State Physics* vol. 2. Pergamon Press, New York, 368 pp.
- Schulte-Frohlinde, D., and Eiben, K. [1962], Solvatisierte Elektronen in eingefrorenen Losungen. *Zeit. Naturforsch.* 17a, p. 445-446.
- Schurmann, K., and Hafner, S. S. [1972], On the amount of ferric iron in plagioclases and lunar rocks. *Proc. 3rd Lunar and Planet. Sci. Conf. I*, p. 615-621.
- Shelby, J. [1979], Radiation effects in hydrogen impregnated vitreous silica. *J. Appl. Phys.* 30, p. 3702-3706.
- Shmakin, B. M. [1968], Enigma of amazonstone. *Priroda* #8, p. 52-57, (in Russian).
- Sidorovskaya, T. I., Alekseeva, E. P., and Shmakin, B. M. [1982], New data on luminescent properties of amazonite. *Prikladnoe Spektroskopii* 35, p. 30-35 (in Russian).

- Siedentopf, H. [1905], Ultramikroskopische Untersuchungen uber Steinsalzfarbungen. *Physikalische Zeitschrift* 6, p. 855-866.
- Silverman, A. [1932], Colloids in glass. *Colloid Chemistry Vol. III*, Ed. J. Alexander. Chemical Catalog Co., Inc. New York, p. 855-866. (cited in *Ceramic Abstracts* 11, p.212.)
- Sinkankas, J. [1976] *Gemstones of North America II*. Van Nostrand and Reinhold, New York, 494 pp.
- Smekal, A. [1928], On the Structure of Real Crystals. *Atti. del Cong. Internatl. dei Fisici*, Como.
- Smith, G., and Strens, R. G. J. [1976], Intervalance transfer absorption in some silicate, oxide, and phosphate minerals. *The Physics and Chemistry of Minerals and Rocks*. Ed. R. G. J. Strens. John Wiley and Sons, New York, p. 583-612.
- Smith, H. L., and Cohen, A. J. [1964], Color centers in X-irradiated soda-silica glasses. *J. Am. Ceram. Soc.* 47, p. 564-570.
- Smith, J. V. [1974], *Feldspar Minerals: I. Crystal Structure and Physical Properties. II. Chemical and Textural Properties*. Springer-Verlag: Heidelberg, 627 and 690 pp.
- Solomon, G. C., and Rossman, G. R. [1979], The role of water in structural states of K-feldspar as studied by infrared spectroscopy. *Geol. Soc. Amer. Abst. with Prgms.* 11, p. 521.
- Solomon, G. C., and Rossman, G. R. [1982], Water in feldspars. *Geol. Soc. Amer. Abst. with Prgms.* 14, p. 622.
- Sorrel, C. [1962], Solid state formation of Ba, Sr, and Pb feldspars in clay-sulfate mixtures. *Amer. Mineral.* 47, p. 291-309.
- Speit, B., and Lehmann, G. [1976], Hole centers in the feldspar sanidine. *Phys. Status Solidi A* 36, p. 471-481.
- Speit, B., and Lehmann, G. [1982], Radiation defects in feldspars. *Phys. Chem. Minerals* 8, p. 77-82.
- Spencer E. [1937], The potash-soda feldspars. I. Thermal stability. *Mineral. Mag.* 24, p. 453-499.
- Stacey, J. S., and Kramers, J. D. [1975], Approximation of terrestrial lead isotope evolution by a two stage model. *Earth Planet. Sci. Lett.* 26, p. 207-221.
- Steubing, W. [1908], Uber die Optische Eigenschaften Kolloidaler Goldlosungen. *Ann. Physik* 26, p. 329-371.

- Stewart, B., Walker, G. W., Wright, T. L., and Fahey, J. J. [1966], Physical properties of calcic labradorite from Lake County, Oregon. *Amer. Mineral.* 51, p. 177-197.
- Stolper, E. [1982], Water in silicate glasses: an infrared spectroscopic study. *Contrib. Mineral. Petrol.* 81, p. 1-17.
- Stookey, S. D. [1949a], Coloration of glass by gold, silver, and copper. *J. Amer. Ceram. Soc.* 32, p. 246-249.
- Stookey, S. D. [1949b], Photosensitive glass. *Ind. Engr. Chem.* 41, p. 856-861.
- Stookey, S. D., and Araujo, R. J. [1968], Selective polarization of light due to absorption by small elongate silver particles in glass. *Applied Optics* 7, p. 777-779.
- Stookey, S. D., Beall, G. H., and Pierson, J. E. [1978], Full-color photosensitive glass. *J. Appl. Phys.* 40, p. 5114-5123.
- Stroud, J. S. [1962], Color centers in a cerium-containing silicate glass. *J. Chem. Phys.* 37, p. 836-841.
- Stroud, J. S., Scheurs, J. W. H., and Tucker, R. F. [1966], Color centers in alkali-silicate glass. *Proceedings VII Internatl. Cong. on Glass, Brussels, 1965, Gordon and Breach, New York.* p. 413-424.
- Suto, K., and Aoki, M. [1968], Impurity state of Pb in ZnTe. *J. Phys. Soc. Japan* 24, p. 955-956.
- Tagai, T., Joswig, W., and Korekawa, M. [1980], Die Bestimmung der Al/Si-Verteilung Mittels Neutronenbeugung in einem Plagioklas An₆₆. *Zeit. Krist.* 151, p. 77-89.
- Tarashchan, A. N., Serebrennikov, A. I., and Platonov, A. N. [1973], Peculiarities of the lead ion's luminescence in amazonite. *Konst. Svoist. Mineral.* 7, p. 106-111.
- Taylor, A. L., and Farnell, G. W. [1964], Spin-lattice interaction experimentation on color centers in quartz. *Canad. J. Phys.* 42, p. 595-607.
- Taylor, H. P., Jr. [1968], The oxygen isotope geochemistry of igneous rocks. *Contrib. Mineral. Petrol.* 19, p. 1-71.
- Taylor, S. R., Heier, K. S., and Sverdrup, T. L. [1960], Trace element variations in three generations of feldspar from the Landsverk I pegmatite, Evje, Southern Norway. *Norsk. Geol. Tidsskr.* 40, p. 133-156.
- Telfer, D. J., and Walker, G. [1975], Optical detection of Fe⁺³ in Lunar plagioclase. *Nature* 258, p. 694-695.

- Telfer, D. J., and Walker, G. [1978], Ligand field bands of Mn^{+2} and Fe^{+3} luminescence centers and their site occupancy in plagioclase feldspars. *Modern Geology* 6, p. 199-210.
- Tibballs, J. E., and Olsen, A. [1977], An electron microscope study of some twinning and exsolution textures in microcline amazonites. *Phys. Chem. Minerals* 1, p. 313-324.
- Treinin, A. [1968], Trapped radicals in inorganic glasses. *Radical Ions*, edited by E.T. Kaiser and L. Kevan, John Wiley and Sons, New York, p. 525-578.
- Tress, H. J. [1962a], Ruby and related glasses from the standpoint of chemical potential of oxygen in glass. Part I. Chemical potential of oxygen in glass. *Phys. Chem. Glasses* 3, p. 28-36.
- Tress, H. J. [1962b], Ruby and related glasses from the standpoint of the chemical potential of oxygen in glass. Part II. Gold and copper glasses. *Glass Technology* 3, p. 95-106.
- Tullis, J., and Yund, R. A. [1980], Hydrolytic weakening of experimentally deformed Westerly granite and Hale albite rock. *J. Struct. Geol.* 2, p. 439-451.
- Urbach F. [1953], The long-wavelength edge of photographic sensitivity and of the electronic absorption of solids. *Phys. Rev.* 92, p. 1324.
- Van Wieringen, J. S., and Kats, A. [1957], Paramagnetic resonance and optical investigation of silicate glasses and fused silica, coloured by X-rays. *Phillips Res. Repts.* 12, p. 432-454.
- Van Wieringen, J. S., and Kats, A. [1959], Paramagnetic resonance of hydrogen in fused silica. *Archives des Sci.* 12 (Maxwell-Ampere Conference), p. 203-204.
- Veremeichik, T.F., Grechusnikov, B.N., Varina, T.M., Sviridov, D.T., and Kalinkina, I.N. [1975], Absorption spectra and calculation of energy-level diagram of Fe^{3+} and Mn^{2+} ions in single crystals of yttrium aluminum garnet, orthoclase, and manganese silicate. *Kristallografiya* 19, p. 1194-1199. (*Trans. Sov. Phys. Crystallogr.* 19, p. 742-744).
- Watanabe, H. [1960], G-value of S-state ions with $(ns)^1$ configuration. *Phys. Rev.* 149, p. 402-405.
- Watkins, N. D. [1969], Non-dipole behavior during an upper Miocene geomagnetic polarity transition in Oregon. *Geophys J. (Royal Astron. Soc.)* 17, p. 121-149.
- Watts, R. K. [1977], *Point Defects in Crystals*. John Wiley and Sons, New York, 312pp.
- Weast, R. C.(ed.) [1973], *Handbook of Chemistry and Physics*. Chemical Rubber Co., Cleveland, Ohio.

- Wedepohl, K. H. [1956], Untersuchungen zur Geochimie des Bleis. *Geochim. Cosmochim. Acta* 10, p. 69-148.
- Weeks, R. A. [1956], Paramagnetic resonance of lattice defects in irradiated quartz. *J. Appl. Phys.* 27, p. 1376-1381.
- Weeks, R. A. [1963], Paramagnetic spectra of E_2' centers in crystalline quartz. *Phys. Rev.* 130, p. 570-576.
- Weeks, R. A. [1973], Paramagnetic spectrum of Ti^{+3} , Fe^{+3} , and Mn^{+2} in lunar plagioclases. *J. Geophys. Res.* 78, p. 2393-2401.
- Weeks, R. A., and Abraham M. [1964], Electron spin resonance of irradiated quartz: atomic hydrogen. *J. Chem. Phys.* 42, p. 68-72.
- Weeks, R. A., and Lell, E. [1964], Relation between E' centers and hydroxyl bonds in silica. *J. Appl. Phys.* 35, p. 1932-1938.
- Weeks, R. A., and Nelson, C.M. [1960], Trapped electron in irradiated quartz and silica: II, E.S.R. *J. Amer. Ceram. Soc.* 43, p. 399-404.
- Weil, J. A. [1975], The aluminum centers in α -quartz. *Radiation Effects* 26, p. 261-265.
- Wells, A. F. [1962], *Structural Inorganic Chemistry*, 3rd edition. Oxford, England, 1055pp.
- Wells, L. D., Jones, D. K., and Schaub, W. J. [1983], Celestite from Salem, Indiana. *Mineral. Record* 14, p. 7-12.
- Wenk, H. R., Joswig, W., Tagai, T., Korekawa, M., and Smith, B. K. [1980], The average structure of An 62-66 labradorite. *Amer. Mineral.* 65, p. 81-95.
- Weyl, W. A. [1951], *Coloured Glasses*. Dawsons, London, 541pp.
- Weyl, W. A. [1953], Metals in the atomic state in glasses. *J. Phys. Chem.* 57, p. 753-757.
- Wilkins, R. W. T., and Sabine, W. [1973], Water content of some nominally anhydrous silicates. *Amer. Mineral.* 58, p. 508-516.
- Williams, A. E. [1914], Notes on the development of the ruby color in glass. *Trans. Amer. Ceram. Soc.* 16, p. 284-306.
- Williams, J. A., Rindone, G. E., and McKinstry, H. A. [1981], Small-angle X-ray scattering analysis of nucleation in glass: III, gold ruby glasses. *J. Amer. Ceram. Soc.* 64, p. 709-713.
- Wohler, Fr. [1983], *Über die Zusammensetzung des Aventuringlasses*. *Ann. de Chimie et de Pharmacie* 45, p. 134-136.
- Wong, J. and Angell, C. A. [1976], *Glass: Structure by Spectroscopy*. Marcel Dekker, Inc., New York, 864 pp.

- Wright, T. L., Peck, D. L. and Shaw, H. R. [1976], Kilauea lava lakes: natural laboratories for study of cooling, crystallization and differentiation of basaltic magma. The Geophysics of the Pacific Ocean Basin and its Margin, Amer. Geophy. Union Mono. 19, American Geophysical Union, Washington, D.C., p. 375-390.
- Yamashita, N., and Asano, S. [1976], ESR of $^2S_{1/2}$ -state centres in CaS: Sn³⁺, CaSe:Sn³⁺ and CaSe:Pb³⁺. J. Phys. C: Solid State Phys. 9, p. L65-L67.
- Yokota, R. [1954], Color centers in alkali silicate and borate glasses. Phys. Rev. 95, p. 1145-1148.
- Yund, R. A., and Anderson, T. F. [1978], The effect of fluid pressure on oxygen isotope exchange between feldspar and water. Geochim. Cosmochim. Acta 42, p. 235-239.
- Yund, R. A., and Tullis, J. [1980], The effect of water, pressure, and strain on Al/Si order-disorder kinetics in feldspar. Contrib. Mineral. Petrol. 72, p. 297-302.
- Zhirov, K. K., and Stishov, S. M. [1965] Geochemistry of amazonitization. Geochem. Int. 2, p. 16-24.
- Zsigmondy, R. [1914], Colloids and the Ultramicroscope. John Wiley and Sons, New York, 245 pp. Translation by J. Alexander of Zur Erkenntnis der Kolloids [1905].

APPENDIX I. DERIVATION OF EPR PARAMETERS FOR Pb^{3+} IN AMAZONITE

Resonance occurs when the difference between the two energy levels is $h\nu$. From Section 6.6, the energy levels $W(F,m)$ are given as

$$W(1,0) = -ha/4 + (ha/2)(1 + z^2)^{1/2}$$

$$W(1,-1) = -ha/4 + g_n\mu_n B + (ha/2)(1 - 2z + z^2)^{1/2}$$

$$W(0,0) = -ha/4 - (ha/2)(1 + z^2)^{1/2}$$

where

$$z = (-g\mu_B + g_n\mu_n)B/ha = GB/ha. \quad (I-1)$$

From Figure 1.26, the higher energy transition occurs in the $F=1$ manifold, when $B = B_2$. Thus, the two resonances in amazonite occur at

$$\begin{aligned} h\nu &= W(1,0) - W(1,-1) \\ &= (ha/2)(1+(GB_2/ha)^2)^{1/2} - g_n\mu_n B_2 - (ha/2)(1-2GB_2/ha+(GB_2/ha)^2)^{1/2} \\ &= (ha/2)(1+(GB_2/ha)^2)^{1/2} - g_n\mu_n B_2 - (ha/2)(1-GB_2/ha), \end{aligned} \quad (I-2)$$

and

$$\begin{aligned} h\nu &= W(1,-1) - W(0,0) \\ &= g_n\mu_n B_1 + (ha/2)(1-2GB_1/ha+(GB_1/ha)^2)^{1/2} + (ha/2)(1+(GB_1/ha)^2)^{1/2} \\ &= (ha/2)(1+(GB_1/ha)^2) + g_n\mu_n B_1 + (ha/2)(1-GB_1/ha). \end{aligned} \quad (I-3)$$

Next, the square roots are eliminated. Equation (I-2) becomes

$$\begin{aligned} h^2 a^2 + G^2 B_2^2 &= (2h\nu + 2g_n\mu_n B_2 + ha - GB_2)^2 \\ &= (2h\nu+ha)^2 + 2(2h\nu+ha)(2g_n\mu_n B_2-GB_2) + (2g_n\mu_n B_2-GB_2)^2 \\ &= 4h^2\nu^2 + 4h\nu ha + h^2 a^2 + 8h\nu g_n\mu_n B_2 + 4ha g_n\mu_n B_2 \\ &\quad - 4h\nu GB_2 - 2ha GB_2 + (2g_n\mu_n B_2)^2 + G^2 B_2^2 - 4g_n\mu_n GB_2^2. \end{aligned} \quad (I-4)$$

Cancelling terms, multiplying both sides by $1/4h^2\nu^2$, and using

$$C = h\nu/2g_n\mu_n \quad (I-5)$$

gives

$$0 = 1+a/\nu + B_2/C + aB_2/2C\nu - GB_2/h\nu - aGB_2/2h\nu^2 + B_2^2/4C^2 - GB_2^2/2C h\nu. \quad (I-6)$$

Similarly, eq. (I-3) becomes

$$\begin{aligned}
 h^2 a^2 + g^2 B_1^2 &= (2h\nu - ha - 2g_n \mu_n B_1 + GB_1)^2 \\
 &= (2h\nu - ha)^2 + 2(2h\nu - ha)(GB_1 - 2g_n \mu_n B_1) + (GB_1 - 2g_n \mu_n B_1)^2 \\
 &= 4h^2 \nu^2 - 4h^2 a\nu + h^2 a^2 + 4h\nu GB_1 - 2haGB_1 + 4hag_n \mu_n GB_1 \\
 &\quad - 8h\nu g_n \mu_n B_1 + G^2 B_1^2 - 4g_n \mu_n GB_1 + 4(g_n \mu_n B_1)^2. \quad (I-7)
 \end{aligned}$$

Cancelling like terms, multiplying both sides by $1/4h^2\nu^2$, and using equation (I-5) gives

$$\begin{aligned}
 0 &= 1 - a/\nu + GB_1/h\nu - aGB_1/2h\nu^2 + aB_1/2C\nu - B_1/C \\
 &\quad - GB_1^2/2C h\nu + B_1^2/4C^2. \quad (I-8)
 \end{aligned}$$

Equation (I-6) is now solved for G:

$$\begin{aligned}
 G/h\nu &= [1 + a/\nu + B_2/C + B_2^2/4C^2 + aB_2/2C\nu] \\
 &\quad [B_2 + B_2^2/2C + aB_2/2\nu]. \quad (I-9)
 \end{aligned}$$

Once an expression for a is obtained, equation (I-9) can be used to compute G and hence g . Rearranging (I-8) and substituting (I-9) gives

$$\begin{aligned}
 0 &= [1 - a/\nu - B_1/C + B_1^2/4C^2 + aB_1/2C\nu] [B_2 + B_2^2/2C + aB_2/2\nu] \\
 &\quad + [B_1 - B_1^2/2C - aB_1/2\nu] [1 + a/\nu + B_2/C + B_2^2/4C^2 + aB_2/2C\nu]. \quad (I-10)
 \end{aligned}$$

This equation may be simplified by multiplying both sides by $1/c$ and defining $A = a/\nu$ and $D_1 = B_1/C$:

$$\begin{aligned}
 0 &= [1 - A - D_1 + D_1^2/4 + AD_1/2] [D_2 + D_2^2/2 + AD_2/2] \\
 &\quad + [D_1 - D_1^2/2 - AD_1/2] [1 + A + D_2 + D_2^2/4 + AD_2/2]. \quad (I-11).
 \end{aligned}$$

After multiplying, terms with the same powers of A are collected.

$$\begin{aligned}
 0 &= A^2 [D_1 D_2/4 - D_2/2] + A [D_2/2 - D_1 D_2/2 + D_1^2 D_2/8] + A [D_1 D_2/2 - D_2] \\
 &\quad + [D_2 - D_1 D_2 + D_1^2 D_2/4] + A [D_1 D_2^2/4 - D_2^2/2] \\
 &\quad + [D_2^2/2 - D_1 D_2^2/2 + D_1^2 D_2^2/8] - A^2 [D_1 D_2/4 + D_1/2] \\
 &\quad - A [D_1/2 + D_1 D_2/2 + D_1 D_2^2/8] + A [D_1 + D_1 D_2/2] + [D_1 + D_1 D_2 + D_1 D_2^2/4] \\
 &\quad - A [D_1^2/2 + D_1^2 D_2/4] - [D_1^2/2 + D_1^2 D_2/2 + D_1^2 D_2^2/8]. \quad (I-12)
 \end{aligned}$$

Equation (I-12) can be simplified to

$$0 = A^2[D_1 - D_2] + A[D_1/2 - D_2/2 D_1^2/2 - D_2^2/2 - D_1^2 D_2/8 + D_1 D_2^2/8] + [D_2 + D_1 + D_2^2/2 - D_1^2/2 - D_1^2 D_2/4 - D_1 D_2^2/4]. \quad (\text{I-13})$$

The solution for a is therefore

$$a/v = [-y \pm (y^2 - 4xz)^{1/2}]/2x$$

where $x = [D_1 - D_2]$,

$$y = [D_1 - D_2 - D_1^2 - D_2^2 - D_1^2 D_2/4 + D_1 D_2^2/4]$$

and

$$z = [2D_1 + 2D_2 - D_1^2 + D_2^2 - D_1^2 D_2/2 - D_1 D_2^2/2]. \quad (\text{I-14})$$

For Pb^{207} , μ_n is $0.5837\beta_n$, where $\beta_n = 0.50505 \times 10^{-23}$ erg/Gauss

[Goodman and Raynor, 1970, p. 141]. For amazonite #12, ν is 9.194 GHz,

B_2 is 4730 Gauss, and B_1 is 3590 Gauss. These quantities give $C =$

1.033×10^7 Gauss, $x = -1.1036 \times 10^{-4}$, $y = -1.1069 \times 10^{-4}$, and $z =$

1.6109×10^{-3} . Because the signal broadens as the temperature rises

towards room temperature, the sign of a is assumed to be positive [DuVarney

and Garrison, 1975]. Therefore equation (I-13) gives $a = 0.852 \text{ cm}^{-1}$ and

equation (I-9) gives $g = -2.189$.

APPENDIX II. BLUE AND RED-BROWN RADIATION COLORS IN BARITE AND CELESTITE

A model has been proposed for amazonite formation involving H₂O, lead and radiation. To test if this mechanism is valid for other minerals, I investigated the blue radiation color in sulfates. Spectra were taken on natural, heated, and irradiated fragments of two blue and one colorless barite (Table II.1), and on two blue celestites from Wayne Co., Utah, and Durango, Mexico (Caltech #3378), and on two colorless celestites from Boron, California, and Sicily, Italy (Caltech #8369). The chemistry of the barites (Table II.1) shows that iron is probably not involved in the coloration, and that lead is present in the blue samples. Lead was also found in a colorless section, but this piece turned blue upon irradiation.

Visible spectra of Sterling, Colorado, barite (Fig. II.1) show that the blue color results from a broad band ($W_{1/2} = 2800 \text{ cm}^{-1}$) at 622-625 nm in beta. A large band also occurs at 330 nm. After heating ($\sim 300^\circ$ for 1/2 hour) and irradiation, a red-brown color develops (Fig. II.2) having broad peaks at 559 nm in α , 560 nm in γ (red-violet pleochroism), and 600 nm in β (yellow-brown pleochroism). The red-brown color can be superimposed on the blue if the blue is only partially bleached. The blue and red-brown occurred naturally together in the Phrizington sample.

Blue celestite possesses essentially the same spectra as the blue barite, with a peak position of 622 nm. A red-brown color similar to that of the barite developed after irradiation of a colorless celestite from Boron, California. Both colors developed in celestite from Sicily. Zonations were seen from colorless to deep blue or to deep red-brown.

The blue color of barite can be enhanced through gamma-radiation. Saturation is reached at about 8 MRads (Figure II.3), which is much lower than the dose required for amazonite color saturation. Like amazonite,

Table II.1 Sample Description and Microprobe Analyses of Barite

Sample Number	Oke # 69	Oke # 86	Oke # 86
Location	Phrizington England	Sterling Colorado	Sterling Colorado
Color	Blue	Blue	White to colorless end of blue piece
Description	Gemmy	Gemmy	Gemmy to turbid
BaO	66.04	62.95	64.34
SO ₃	35.77	35.03	33.54
FeO	0.03	BLD	0.04
CaO	0.07	BLD	0.04
SrO	0.24	1.20	1.03
PbO	0.19	0.11	0.23
Total	100.34	99.29	99.21

Table II.3 Response of Blue Celestite to Heat and Irradiation

Dose* Mrads	Heat † time Minutes	I(622, β) cm ⁻¹	I(622, γ) cm ⁻¹	I(2680, β) cm ⁻¹
0	-	0.21	0.01	ND
2.47	-	1.73	0.15	0.19
2.47	15	1.25	0.12	0.08
2.47	25	0.87	0.05	0.03

*Cumulative
†200°C

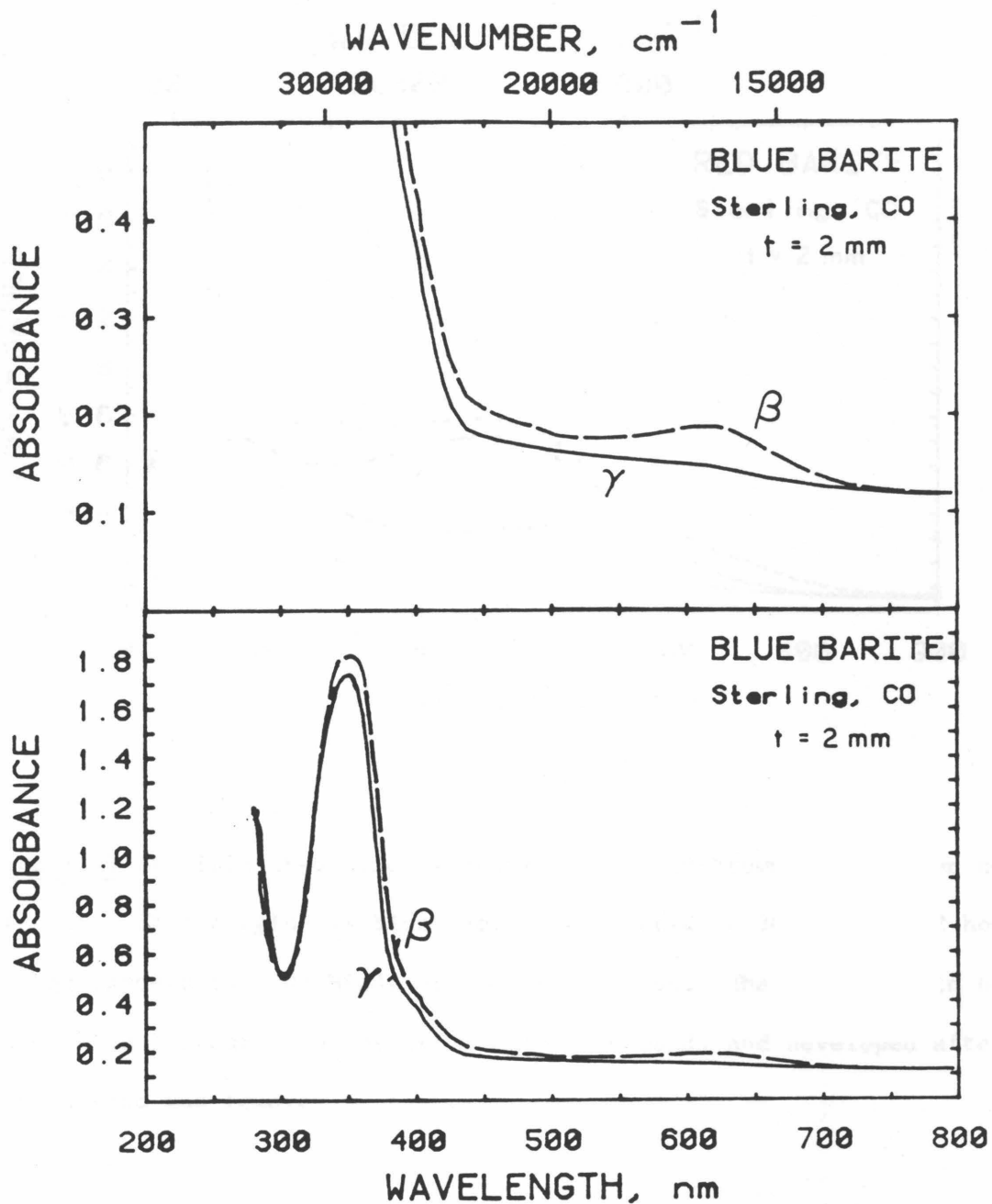


Figure II.1 Visible absorption spectra of naturally blue barite from Sterling, Colorado. The upper figure is an expanded version of the lower. The color is due to the absorption minima between the large band at 350 nm and the weak band at 624 nm in beta. The shoulder at 400 nm may be due to Fe^{3+} .

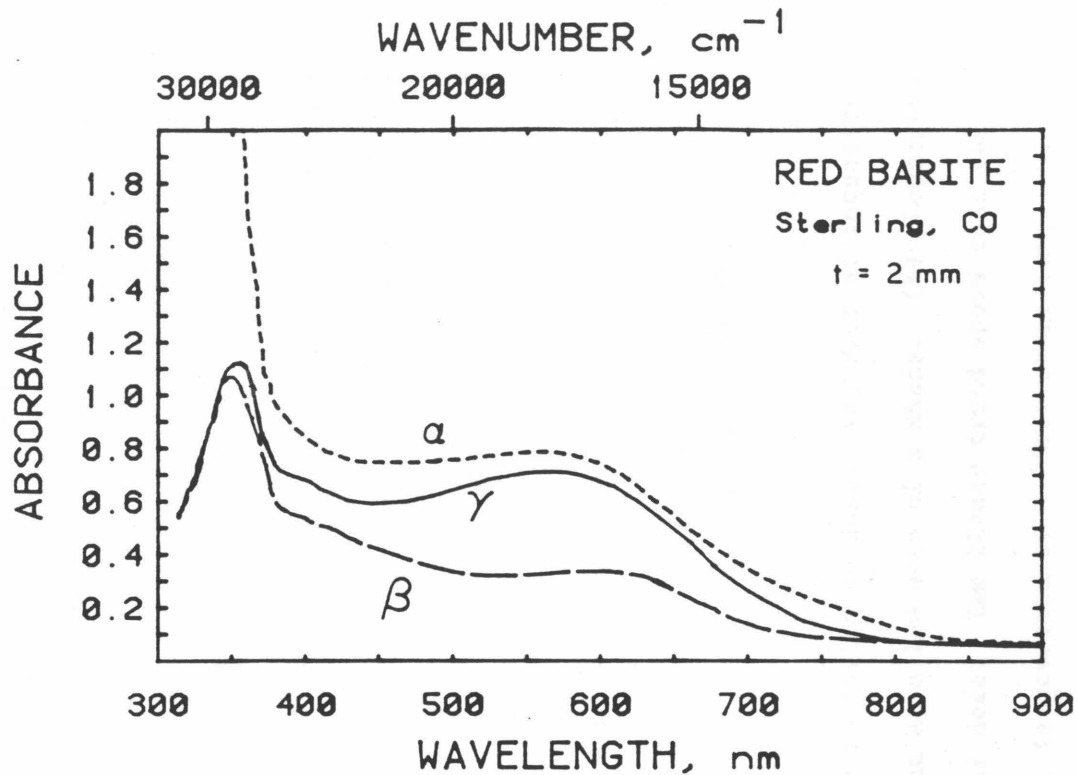


Figure II.2 Visible absorption spectra of the red-brown irradiation color of barite. This originally blue sample was heated at 300°C for 1/2 hour and then exposed to 7.02 MRads of gamma-radiation. The weak band in beta at 600 nm is broader than the originally blue band, and developed after the blue band was removed by heat.

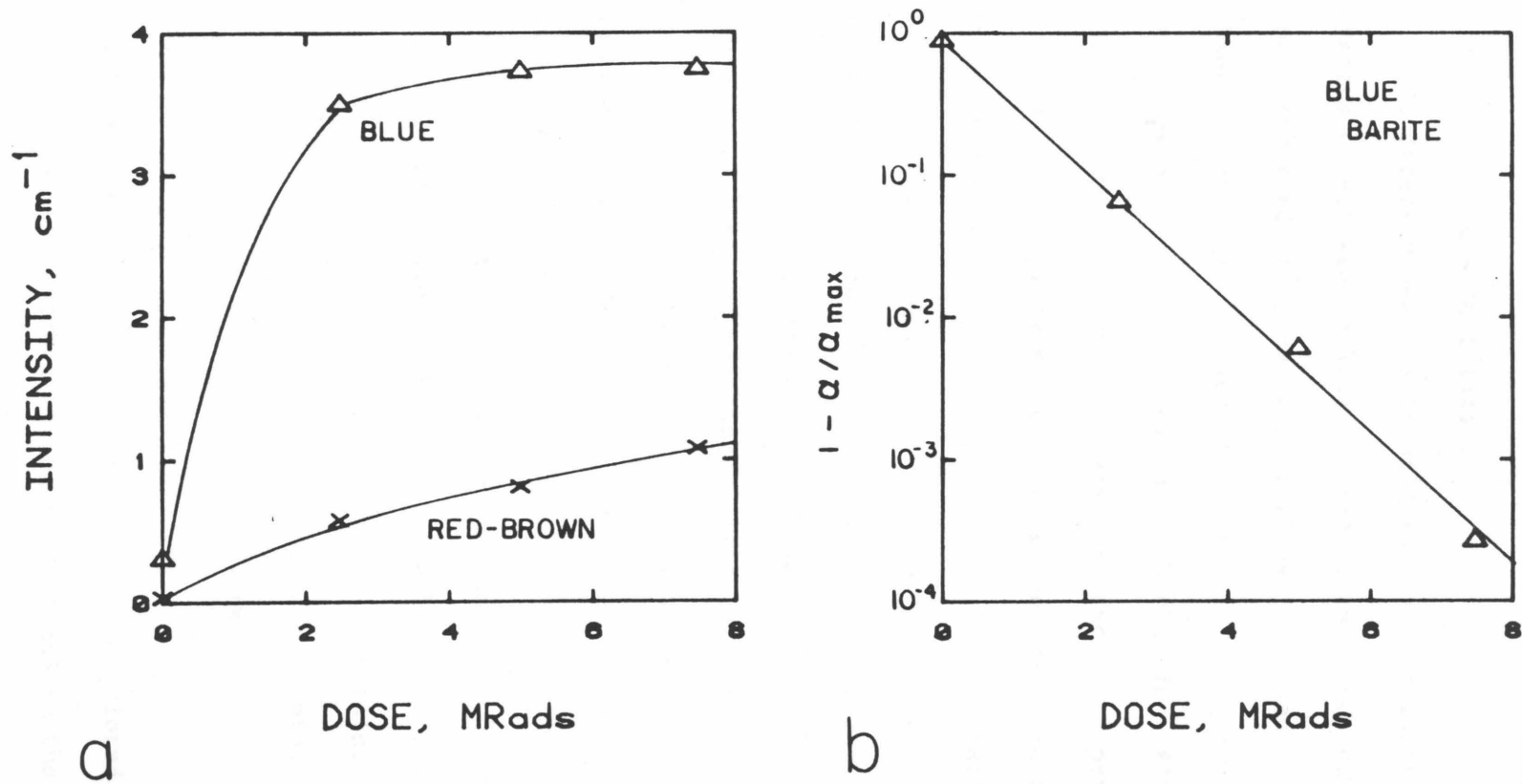


Figure II.3 Dependence of absorption band intensity in barite on dose. (a) Plot of intensity against dose. Only the blue color reached saturation at a low dose of 8 MRads. (b) Logarithmic plot of intensity of the 622 nm band as a function of dose. The linear trend shows that the development of blue color in barite, like amazonite, is governed by a first order rate law.

the kinetics follow a first order rate law (Fig. II.3; Section 6.3.b). Unlike amazonite, barite is not self-irradiating because no counts were detected by the scintillator.

To directly measure if Pb^{3+} is involved in the barite coloration, EPR spectra were taken on blue, heat-bleached, and red-brown (heat-bleached and irradiated) samples from Sterling, Colorado. No triplet of signals was observed near g_{eff} of 1.83, 1.56, and 1.39. Strong signals were observed near g_{eff} of 2.011 and 2.001 for both the blue (Fig. II.4) and red-brown samples. The structure suggests that two overlapping signals occur at 2.011. In this region, signals from barite and celestite have previously been attributed to O^- , SO_2^- , SO_3^- , and SO_4^- (see summary by Bernstein, 1979). An EPR signal also occurs for both colors at g_{eff} of 1.954, which probably is an electron trap as indicated by the negative g -shift. Because these signals were observed after the blue color was removed by heating and replaced by the red-brown, these centers cannot directly cause the blue color of sulfates. The EPR signals could be connected with the red-brown color. As cited by Bernstein [1979], Samoilovich [1971] calculated SO_2^- to absorb at 300-400 nm and SO_4^- to absorb at 200-250 nm, and Bakhtin et al [1973] calculated SO_3^- to absorb at 600 nm, and O^- to absorb at 620-650 nm, which suggest the following assignments for the red-brown color:

SO_4^- 210 nm [Bernstein, 1979],

SO_2^- 330 nm [Bernstein, 1979],

SO_3^- 559-564 nm,

and O^- 590 nm.

The first two peaks also occur in the blue colored samples.

Because the absence of the Pb^{3+} signal in the EPR could be due to structural disorder or to relaxation effects, an amazonite mechanism is

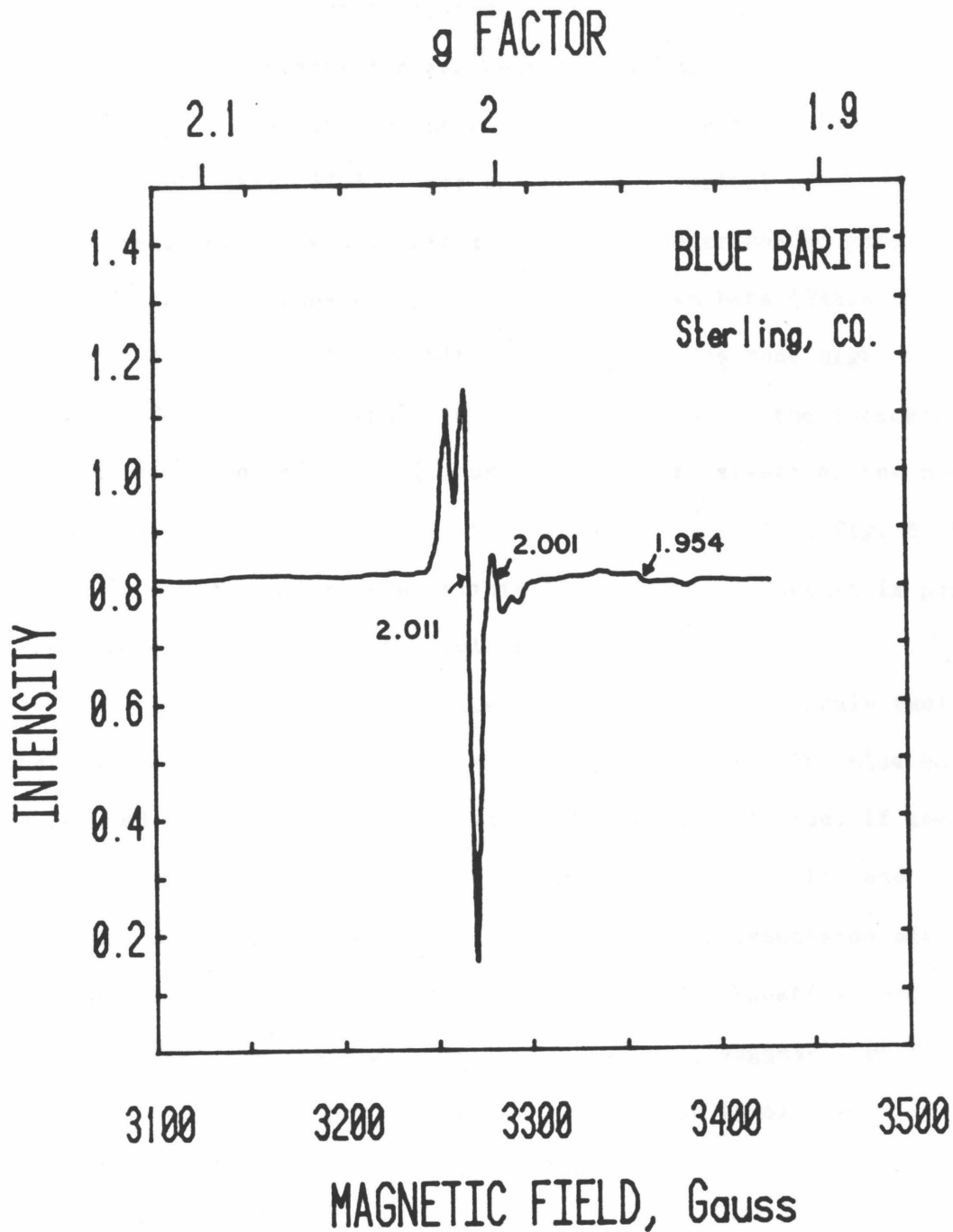
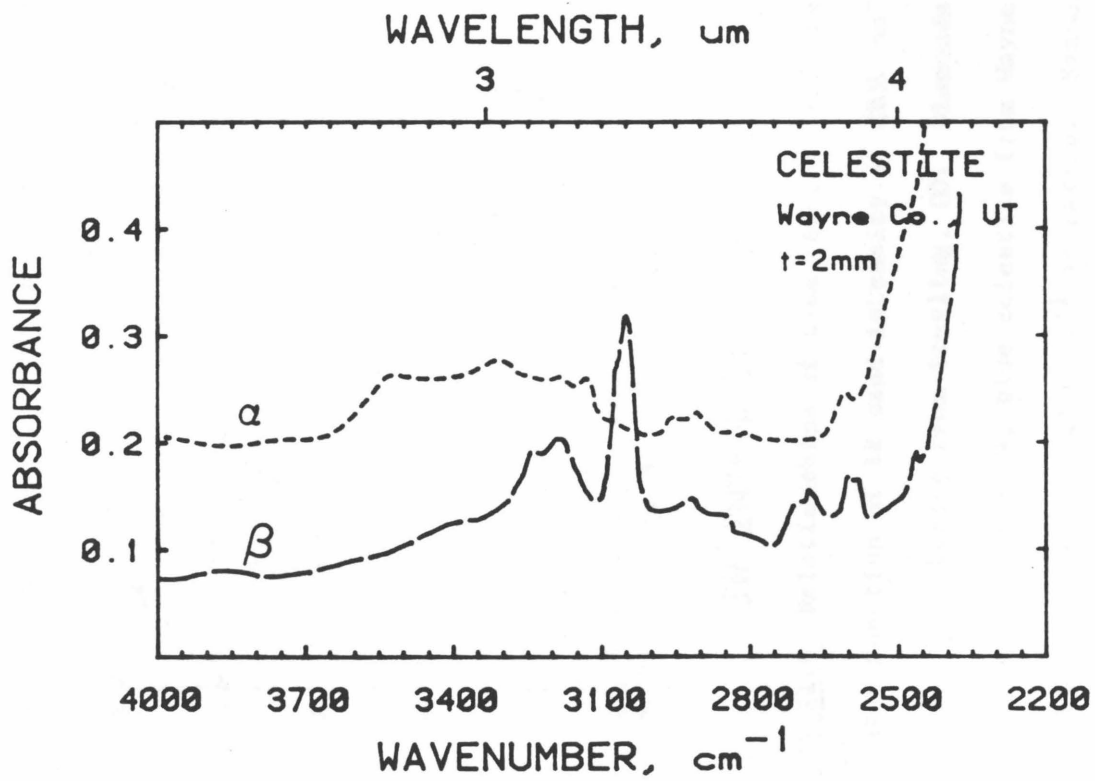
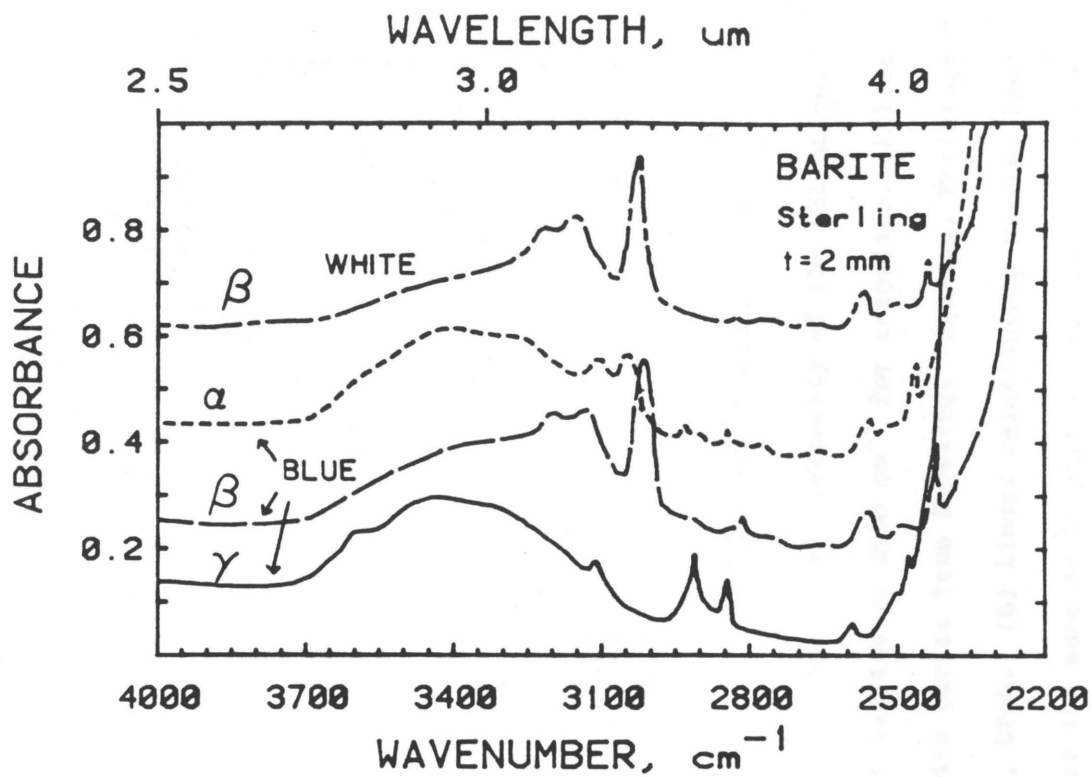


Figure II.4 EPR powder spectrum of blue barite from Sterling, CO, which was irradiated 2.47 MRads. The spectrum is scaled for 100 mg sample and run conditions of 1 Gauss modulation amplitude, 1 mWatt power, and x1 gain. Cross-over points for the first derivatives are labeled by g_{eff} . Several signals may be superimposed at $g = 2.011$ to 2.001 .

still possible. To indirectly test this hypothesis, changes in the volatiles during irradiation and heating were monitored through IR spectroscopy. Water is present as indicated by a broad band in the IR near 3500 cm^{-1} (Fig. II.5). For the Sterling barite, 0.010 ± 0.005 wt % H_2O was measured using hydrogen manometry. Comparison of peak intensities in the IR to the intensity of color at 624 nm in beta (Table II.2) shows that the color does not vary with any of the bands that might be attributable to OH^- or H_2O , but that the color is proportional to the intensities of bands at 2440 and 2830 cm^{-1} (Figure II.6). For celestite, the blue color is proportional to band intensity at 2680 cm^{-1} (Table II.3; Fig. II.6). None of the IR modes involved can definitely be assigned, but it is possible that these are overtones involving sulfur-oxygen bonds.

This incomplete study of blue color in sulfate minerals indicates that there are some similarities to amazonite properties. The blue color can be removed by heating and regenerated through irradiation, if the heating is mild; strong heating permanently removes the blue color and removes the IR bands, whereupon a new color develops that is associated with oxygen-related hole centers. This fact, the first order kinetics, and the possible involvement of lead (see also Section 1.2.b.vi), suggest that Pb^{3+} is likely to be the color, but that the mechanism does not involve water as in amazonite, but possibly some other volatile.

Figure II.5 Infrared absorption spectra of the water region of barite (upper) from Sterling, CO., and blue celestite (lower) from Wayne Co., Utah. The broad band near 3400 cm^{-1} is probably due to fluid inclusion water. Other sharper bands could not be assigned. The two barite spectra are from the same sample before (white) and after irradiation (blue).



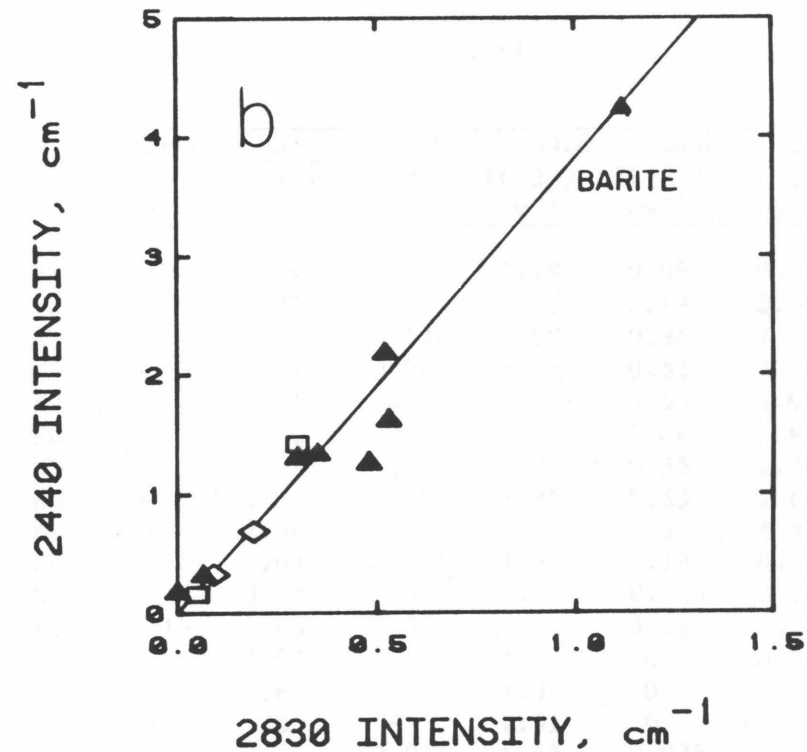
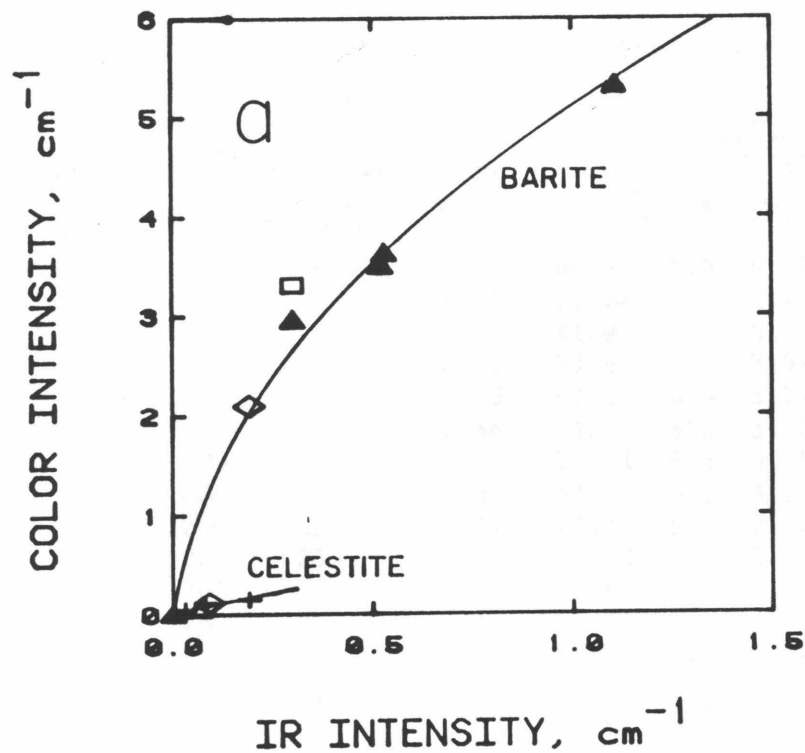


Figure II.6 Relationships of blue color in sulfates to IR bands. (a) Intensity of the 621 nm color band as a function of IR band intensity at 2830 cm^{-1} for barites or 2680 cm^{-1} for celestite. Filled triangles, blue barite from Sterling, CO. Diamonds, white barite from Sterling. Squares, Phrizington, England barite. Crosses, blue celestite from Wayne Co., Utah. (b) Linear relationship between band intensities at 2440 and 2830 cm^{-1} in barite. Symbols are the same as in part a. Because of this trend, the blue color also depends on 2440 cm^{-1} intensity.

Table II.2 Response of Blue Barite to Heating and Irradiation

Location	Temp. °C	Heat time Minutes	Dose Mrads	Color	λ nm	Blue band		Red-brown band		3500	3020	2830	2440
						$I(\beta)$ cm ⁻¹	$I(\alpha)$ cm ⁻¹	$I(\beta)$ cm ⁻¹	$I(\gamma)$ cm ⁻¹	$I(\gamma)$ cm ⁻¹	$I(\beta)$ cm ⁻¹	$I(\beta)$ cm ⁻¹	$I(\beta)$ cm
Sterling	-	-	-	None	625	0.119	ND	-	0.149	-	1.29	0.09	0.327
Colorado	-	-	2.47	Lt Bl	621	2.10	1.33	-	1.29	0.12	1.40	0.19	0.69
	-	-	-	Blue	622	0.32	ND	-	-	0.128	1.58	0.94	2
	-	-	2.47	Blue	622	3.51	ND	-	0.61	0.06	1.54	0.52	2.20
	-	-	4.99	Blue	623	3.74	ND	-	0.81	0	1.55	0.50	2.00
	-	-	7.46	Blue	623	3.76	ND	-	1.08	0	1.55	0.44	1.94
	200	15	-	Lt Bl	623	0.45	ND	-	0.09	0	1.33	0.35	1.36
	200	15	2.47	Blue	623	3.64	ND	-	0.79	0.09	1.35	0.53	1.64
	200	15	2.47	R/Bl	623	2.97	ND	-	2.09	0	1.25	0.30	1.33
	200	20	2.47	B/Red	621	5.28	ND	-	1.02	0.104	1.46	1.19	4.13
	200	30	-	None	625	0.069	ND	-	0.002	0.014	1.28	0.065	0.34
	200	30	2.47	Red	-	-	ND	1.15	2.63	0.03	1.3	0.065	0.23
	250	30	-	None	620	<0.02	ND	-	<0.02	<0.02	1.5	0	<0.2
	250	30	2.47	Red	-	-	ND	0.489	2.61	0.03	1.34	0	0.065
	300	30	-	None	ND	ND	ND	ND	ND	-	1.51	0	<0.1
	300	30	7.05	Red	-	-	1.24	1.24	3.70	<0.025	1.43	<0.025	0.075
Phrizington	-	-	-	Blue	624	3.31	ND	-	0.87	-	-	0.30	1.42
England	-	-	-	Red	-	-	ND	1.75	3.00	-	-	<0.05	0.16

APPENDIX III RECOMMENDATIONS FOR FUTURE STUDIES

A few loose ends remain for the amazonite study. The first would be to complete the work on blue sulfates by establishing lead as the chromophore through hydrothermal synthesis or by EPR at liquid helium temperature and to identify the volatiles involved in the radiative coloring. The second would be to establish the presence of Pb^{3+} in orthoclase, oligoclase, and Lake County labradorite through EPR at liquid helium temperature.

The study of smoky color could be expanded upon by investigating how the diffusion of protons works to inhibit color. One point left undone is whether OH^- suppresses color. This could be checked by measuring the OH content of a number of samples (plagioclase would be the choice due to availability of gemmy crystals) and comparing color against OH content for a constant dose.

Measurement of lead content would fill one hole in the labradorite study. More important (and interesting) would be to use a TEM to study the transition zone between the red and the shiller in sample #400, in order to determine the mechanics of exsolution and aggregation of Cu^0 in the feldspar. Also, a laboratory study of cooling conditions might be feasible if very high concentrations of copper were used.